

Analysis of Axial-Flow Ventilation Fans **by** **Vortex-Lattice Method**

by

Richard Anthony Hardin

B.S. Mechanical Engineering, University of Kansas, 1986

M.S. Mechanical Engineering, University of Kansas, 1988

Submitted to the Department of Mechanical Engineering
and the Faculty of the Graduate School of the University of Kansas
in partial fulfillment of the requirements for the degree of Doctor of Philosophy

Dissertation Committee:

Redacted Signature

Chairman

Redacted Signature

Redacted Signature

Redacted Signature

Redacted Signature

Committee Members

(4)

Dissertation defended:

April 1994

MAY 15 1994

Diss

1994

H372

C.2

Engineering

ABSTRACT

A steady vortex-lattice method was used to solve the lifting surface equation for an axial flow fan. The type of fan studied was designed for industrial and ventilation applications and in thermofluid systems such as cooling towers. The fan blades were thin cambered surfaces manufactured from metal sheets. The numerical approach was inviscid and results in a boundary value problem with viscous effects partially accounted for by application of drag coefficient data. A non-linear wake alignment procedure was used to account for the effects of vorticity shedding in the wake and variation in wake geometry with operating conditions. The wake alignment procedure was semi-free with wake input parameters required for accurate use of the technique. A study of the wake parameters gave trends in the variation of their values with flow rate. At "free-air" conditions, flow visualization estimates of these parameters were found to agree with those from the computations. Comparisons between the measured and predicted fan performance with and without a surrounding duct were especially good at the "free-air" condition for wake parameters determined from flow visualization and an inlet velocity profile measured using hot-wire anemometry.

To enable better understanding of basic flow phenomena and to provide data for verification of numerical analyses, a method for measuring unsteady surface pressure on a rotating axial-flow fan blade was devised. Unsteadiness of pressure on the blade surfaces was due to the effects of upstream fan motor supports and other installation features. A pressure transducer and signal amplification circuit were mounted on a circuit board at the rotating hub with signals taken off the rotating shaft through copper disk-mercury slip rings. Tubing was run from the transducer, along the trailing edge of the blade, to the radial location of the pressure taps and then at a constant radius to the taps. One blade was instrumented to measure suction-side surface pressures; another was instrumented to measure pressure-side surface pressures. The pressure difference across the blade was determined and the data were corrected for time lag and distortion caused by the tubing.

The pressure difference measurements were compared with aerodynamic loading computed using the vortex-lattice method. Both unsteady pressure measurements and their time-averaged values were utilized in the comparison. The best agreement between the predicted and unsteady loading measurements was found in the most uniform regions of the inlet flow.

ACKNOWLEDGEMENTS

I express my gratitude to Dr. Louis C. Burmeister for his initiative in setting up this project, his guidance and his patience in seeing the project through to its completion. Further gratitude is offered to Dr. Burmeister for the hands-on research experience I have gained working with him on projects unrelated to this thesis. I also acknowledge the members of my committee, Dr. Saeed Farokhi, Dr. Charles Reese, Dr. Peter Ten Pas and Dr. Bedru Yimer and thank them for participating in the examination and evaluation of this thesis. I also thank them for developing my knowledge of engineering through the coursework in which they instructed me.

I am grateful for the assistance given me by technicians during the course of this project, particularly: Mr. Ron Schorr who, with his breadth and depth of technical knowledge, was always ready to assist; Mr. Ed Achison who could always be counted on for good advice on instrumentation and Mr. Charles Gabel who was always ready to help me get the job done in the machine shop. The Department of Aerospace Engineering is acknowledged for the use of its helium bubble generator and lighting equipment.

The Mechanical Engineering Department is thanked for its generous support through a Robert M. Carey Scholarship which provided the resources to make the study more complete. In addition, the Department of Mechanical Engineering is thanked for acquiring the strobe light and digital oscilloscope without which the experimental parts of the project could not have been performed. Additional thanks go to Mr. Donald Smith and Mr. Samir Khouzam of Lenexa Products for their support of this project, the purchase of computer software, the use of the hot-wire anemometer and the fan testing facility. Also, this project could not have been performed without the computer facilities in the School of Engineering.

Finally, I thank my family for their support and encouragement during this effort. There is no way I could ever hope to repay my mother and father, who reared their children well and well-rounded, to be humanists and musicians; even so, their sons still became engineers. To my wife, Janis, I will forever be grateful for her patience, love and support through two graduate degrees. A last acknowledgement goes to my own family, Janis, Claire and Anna, who were always there during the most discouraging times to remind me of what is truly important in life.

TABLE OF CONTENTS

Nomenclature	vii	
List of Figures	x	
List of Tables	xxvi	
Chapter 1	Introduction	1
Chapter 2	Review of Flow Visualization Techniques	3
2.1	Overview	3
2.2	Smoke Flow Visualization	3
2.2.1	Smoke Illumination	5
2.3	Particle Tracing Techniques	5
2.3.1	Applying the Tracer Technique	6
2.3.2	Lighting and Photographing Particle Tracers	7
2.3.3	Examples and Applications	8
2.3.4	Helium Bubbles	9
2.3.5	Other Tracer Methods	11
2.4	Surface flow visualization techniques	13
2.4.1	Oil Film Technique	13
2.4.2	Tuft Methods	16
2.4.3	Tuft Grids	19
Chapter 3	Survey of Methods of Analysis	20
3.1	Introduction	20
3.2	Axial-flow Fan Studies and Analyses	21

3.2.1	Fan Design and Measurement Literature	24
3.3	Propeller Lifting-surface and Other Panel Method Analyses . .	28
3.3.1	Marine Propeller Studies	29
3.3.2	Airplane Propeller Studies	38
3.4	Helicopter Analysis	43
3.4.1	Helicopter Rotor Lifting-line and Lifting-Surface Analyses	45
3.4.2	Rotor Wake and Tip Vortex Visualization Applied to Analysis	49
Chapter 4	Review of Theory and Development of a Vortex-Lattice Method for the Analysis of Axial-Flow Fan	52
4.1	Introduction	52
4.2	Momentum Theory for Propellers, Rotors and Fans	52
4.3	Efficiency of Propellers, Rotors and Fans	59
4.3.1	Types of Fans and Their Efficiencies	65
4.4	Blade Element Theory	66
4.4.1	Isolated Airfoils	67
4.4.2	Cascade Approach	69
4.5	Development of Vortex-Element Methods	80
4.5.1	Introduction to Vortex Elements	80
4.5.2	Induced Velocity for a Vortex Filament Segment	84
4.5.3	The Lifting Surface	90
4.5.4	The Lifting Surface Equation and Its Solution	93
4.5.4.1	Discretization	95

4.5.4.2	Application of the Boundary Condition and Vorticity Conservation	101
4.5.4.3	Kutta Condition	112
4.5.4.4	Wake Alignment	113
4.5.5	Lifting-Line Theory	114
4.6	Outline of Calculation Procedures	115
4.7	Details of Running the PSF-2 Code	127
4.7.1	Data files	129
4.8	Description of the Modified Program	138
Chapter 5	Experimental Methods and Equipment	148
5.1	Introduction	148
5.1.1	Description of the Fans Studied	148
5.2	Flow Visualization Equipment	154
5.3	Hot-wire Anemometry Equipment	158
5.4	Pressure Measurements	165
5.4.1	Pressure Measurement Apparatus	167
5.4.2	Pressure Data Acquisition and Correction	174
Chapter 6	Results	184
6.1	Introduction	184
6.2	Unducted LP-36 Fan Results	185
6.3	Ducted LP-36 Fan Results	193
6.4	Comparison of Performance Measurements and Computations	214
6.4.1	PSF-2 Input Variable Trend Study	215

6.4.2	PSF-2 Input Variable "Fitting" for the LP-36 Fan . . .	224
6.4.3	Computed Performance Using FSF	229
6.4.3.1	Computed Performance Using FSF at 600 and 1100 rpm	238
6.5	Results of Unsteady Blade Aerodynamic Loading Measurements	241
6.5.1	Comparison of Measured and Computed Aerodynamic Loading	250
6.6	Conclusions and Recommendations	257
6.6.1	Recommendations for Future Work	258
Appendix A	Thin-Airfoil Theory	261
Appendix B	Pressure Data Acquisition Program	269
Appendix C	Pressure Measurement System Calculations and Data	273
C.1	Geometry Data for the Pressure Tubing and the Pressure Transducer	273
C.2	The Transducer-to-Tubing Volume Ratio Computation	273
C.3	The Effect of Tubing Elasticity on Speed of Sound	274
Appendix D	Fast Fourier Transform and Pressure Data Correction Program	275
Appendix E	Integration of Measured Inlet Axial Velocities	282
Appendix F	Surface Flow Visualization of the LP-36 Fan at Rotational Speeds of 600, 850 and 1100 RPM	283
Appendix G	Unsteady Blade Surface Pressure Difference Measurements	294
References	301

NOMENCLATURE

a	acceleration, ft/sec ²
A	area, ft ²
BHP	brake horsepower, hp
c	chord length, ft
C_D	drag coefficient
C_L	lift coefficient
C_P	power coefficient
C_{PI}	induced power coefficient
C_{P, lost}	lost power coefficient
C_Q	torque coefficient
C_T	thrust coefficient
D	diameter, ft; and drag force, lbf
D_s	specific diameter
F	force, lbf
g	gravitational acceleration, ft/sec ²
g_c	gravitational constant, 32.174 lbm ft/lbf s ²
H	total pressure, lbf/in. ² , in. H ₂ O
i	cascade incidence angle
J	advance coefficient
L	lift force, lbf
m	mass, lbm
\dot{m}	mass flow rate, lbm/sec
M	helicopter rotor figure of merit
N_{blades}	number of blades
P	static pressure, lbf/in. ² , in. H ₂ O
Q	torque, ft lbf
r	radial distance from center of rotor, ft
r_{tip}	tip radius of rotor, ft
R	distance from vortex singularity
s	angular spacing between cascade rotor blades
t	time, sec
T	thrust, lbf
v	velocity, ft/sec, ft/min
u, v, w	velocity components in the x, y, and z directions, ft/sec, ft/min
\dot{V}	volumetric flow rate, ft ³ /min
w	specific work
\dot{W}	rate of work, power, hp
x, y, z	rectangular coordinates
Z	pressure head elevation, ft

Greek Letters

α	angle of attack
β_1	cascade flow inlet angle
β_2	cascade flow outlet angle
$\beta_1\text{-}\beta_2$	cascade flow turning angle
β_m	cascade mean flow angle
γ	vorticity density, ft/sec
Γ	circulation, concentrated strength of a vortex segment
δ	cascade deviation angle
ΔD	net drag force, lbf
ΔH	net total pressure rise, lbf
ΔL	net lift force, lbf
ΔP	net static pressure rise, pressure impulse across actuator disk, lbf/in. ² , in. H ₂ O
ΔQ	net torque, ft lbf
ϵ	swirl coefficient
η	efficiency
θ	blade pitch
θ_c	cascade camber angle
λ	cascade local flow coefficient
ν	specific volume, ft ³ /lbm
ρ	density, lbm/ft ³
σ	blade solidity
ϕ	perturbation velocity potential, flow coefficient
Φ	velocity potential
Ψ	total pressure coefficient, stream function
ω	rotational speed, rpm, rad/sec
ω	vorticity, ft/sec
ω_r	specific rotor speed

Subscripts

atm	atmospheric
a	axial
c	camber
d	difference
disk	actuator disk
D	drag
e	exit
fan	fan
i	induced, inlet
l	lower surface
L	lift

m	mean
p	preswirl
Q	torque
R	relative to rotor blade, in blade frame of reference
s	specific, afterswirl
shaft	variable required to operate device
static	static pressure
t	thickness
tip	rotor tip
total	total pressure
T	thrust
u	upper surface
useful	component of variable put to desired use
w	wake excursion variable far downstream
θ	rotational
1	upstream of rotor
2	downstream of rotor
∞	free stream, i.e. craft velocity for advancing propeller

Overstrike

\cdot	rate
-	average

LIST OF FIGURES

Chapter 2

- Figure 2.1** Generally accepted appearance of flow separation and reattachment lines as they appear in experiments and, in this case, from the PLOT3D program 14

Chapter 3

- Figure 3.1** An example of an axial fan designed by EXFAN (Tong, 1985) 27
- Figure 3.2** An example of a propeller, DTNSRDC propeller 4384, designed with large amounts of rake and skew and modelled by author with data from Kerwin and Lee (1978) 27
- Figure 3.3** Comparison of predicted and experimental performance data, K_T and K_Q (thrust and torque coefficients, respectively), modified from Greeley (1982) with Kerwin et al. (1978) data added 32
- Figure 3.4** Model of leading-edge vortex sheet from Greeley (1982) 32
- Figure 3.5** Comparison of vortex-lattice calculations for radial circulation distribution with and without hub effects and experimental measurements (Wang, 1985) 34
- Figure 3.6** At left, a conventional panelling scheme as tested by Kerwin et al. (1987) and at right an improved panel arrangement with a helical pitch (usually set to match the propeller tip pitch) 37
- Figure 3.7** Panel scheme used by Kerwin et al. (1987). A cosine spacing was used on the duct in keeping with the blade panelling scheme 37
- Figure 3.8** Panel discretization for a four-rotor counter-rotating propeller model (Valarezo, 1991) 41

Figure 3.9	Detail of counter-rotating prop/airframe interference model (Valarezo, 1991)	41
Figure 3.10	Inner and outer computational domains from Egolf and Sparks (1987)	51
Figure 3.11	Vortex box model as used by Kocurek and Tangler (1977)	51
Chapter 4		
Figure 4.1	Momentum theory for flow through an axial flow device	53
Figure 4.2	One-dimensional actuator disk momentum theory for a fan operating in an enclosed system	58
Figure 4.3	Ideal performance curve from Chueng (1987)	58
Figure 4.4	Normal view of fan rotational plane for blade element theory derivation	68
Figure 4.5	Two-dimensional blade section in blade element theory	68
Figure 4.6	A cascade of two-dimensional airfoils	71
Figure 4.7	A single blade in the two-dimensional cascade flow	73
Figure 4.8	Blade angles	74
Figure 4.9	Velocity induced at P due to volume V_r of vorticity	83
Figure 4.10	Construction of a vortex filament from a volume of vorticity	83
Figure 4.11	Geometry of a straight line vortex filament (from P_1 to P_2) and the point P of induced velocity	86
Figure 4.12	Special case for evaluating the induced velocity at P due to a line vortex	89
Figure 4.13	A lifting surface with velocity vectors shown at point P in the plane of the lifting surface	91

Figure 4.14	The vortex sheet strength γ as derived from calculating the circulation about a small contour (Kerwin, 1986)	91
Figure 4.15	Three primary methods of VLM discretization	97
Figure 4.16	A vortex lattice of four panels in the chordwise direction with vortex element and control point locations indicated	98
Figure 4.17	A vortex-lattice representation of the Lenexa Products 36 in. fan blade with important lattice features and variables indicated	100
Figure 4.18	An arbitrary section of the vortex-lattice showing vorticity conservation at the m,n-th lattice intersection node	104
Figure 4.19	Detail of separation of chordwise tip vortex elements as used in PSF-2 on the Lenexa Products 36 in. fan blade (the blade tip is at the abrupt change in vortex line slope)	110
Figure 4.20	Graphical demonstration of an explicit Kutta condition for an unsteady VLM application (Kerwin and Lee, 1978)	110
Figure 4.21	Outline of a design computation procedure using a VLM technique (Greeley and Kerwin, 1982)	116
Figure 4.22	Blade geometry notation (Greeley and Kerwin, 1982)	119
Figure 4.23	Cylindrical blade section showing pitch angle ϕ , the thickness function $t(s)$ and the camber function $f(s)$ (Greeley, 1982)	120
Figure 4.24	PSF-2 wake variables	120
Figure 4.25	Transition and ultimate wakes of a computation for the Lenexa Products 36 in. fan	124
Figure 4.26	Outline of the PSF-2 analysis code	128
Figure 4.27	Fan coordinate axis	128

Figure 4.28	Schematic drawing of the PSF2BVP program; the eight source code files are given in the boxes shown, all subroutines are given and the routing of calls from the main program is shown	136
Figure 4.29	Schematic drawing of the PSF2FOR program; the four source code files are given in the boxes drawn in dotted lines, all subroutines are given and the routing of calls from the main program is shown	137
Figure 4.30	Typical PSF-2 panelling scheme for Lenexa Products fan using 144 panels on the key blade (viewed from downstream)	140
Figure 4.31	Detail of separated tip vortex showing only the chordwise tip vortex elements	140
Figure 4.32	A vortex-lattice model for the author's modified PSF-2 program with like discretization and tip vortex on all blades (only part of trailing wake is shown as viewed from the front or upstream side)	142
Figure 4.33	Side view of a vortex-lattice model from the author's modified PSF-2 code	143
Figure 4.34	View of a duct or venturi panel lattice added to the original PSF-2 panelling scheme (as seen from the upstream/side)	144
Figure 4.35	View of a duct or venturi panel lattice using the author's panelling scheme (as seen from the downstream/side)	145
Chapter 5		
Figure 5.1	Test tunnel arrangement used by Lenexa Products; known as the multiple nozzle in chamber setup (AMCA, 1985)	149
Figure 5.2	The ACME Engineering 36 in. diameter fan blade geometry as represented by a vortex lattice	149

Figure 5.3	The Lenexa Products 36 in. diameter (LP) fan and venturi panel as viewed from the front and side with and without shipping crate (proceeding from left to right)	151
Figure 5.4	The LP fan and venturi panel viewed from the upstream side with dimensions of motor supports and reference points for pressure measurements and flow visualization indicated (all dimensions in in.)	151
Figure 5.5	Light chopper for use with a light sheet produced from a projector light source (all dimensions in in.)	152
Figure 5.6	Blade position encoder and variable position strobe light trigger with an electro-magnetic sensor and variable time delay circuit	157
Figure 5.7	Trace of signal output from strobe light triggering circuit	157
Figure 5.8	Fan laboratory for conducting flow visualization, hot-wire measurements and unsteady pressure measurements on the LP at free air conditions	159
Figure 5.9	Fan laboratory with more of the backdrop shown	159
Figure 5.10	Welding system used to reattach tungsten hot-wire to probe prongs (after Sandborn, 1972)	161
Figure 5.11	Typical calibration curve for a reattached hot-wire probe	161
Figure 5.12	Test of velocity angle sensitivity of a reattached hot-wire probe	163
Figure 5.13	Velocity components and angles of incidence at a hot-wire sensor (Fingerson and Freymuth, 1983)	164
Figure 5.14	(a) A hot-wire sensor aligned in the direction of one of the components to be measured in a two-dimensional flow field, (b) rotated by a known angle Δ in the plane of the velocity	164

Figure 5.15	Pressure tap tubing running along the blade trailing edge to the tap on the opposite side of the blade surface to be measured	169
Figure 5.16	Detail of pressure tap tube for measuring suction side blade surface pressures	169
Figure 5.17	Detail of pressure taps on pressure side of the blade	170
Figure 5.18	Slip-ring "box" mounted on the motor with cover plate to the mercury reservoir (empty) removed showing a shaft-mounted copper disk	170
Figure 5.19	Pressure sensor and amplifier circuit located at the center of rotation to measure pressures on the LP fan blade surface	171
Figure 5.20	SenSym SX01DN pressure transducer calibration curve	172
Figure 5.21	Battery pack mounted to the fan hub between the four posts used to secure the transducer/circuit board	172
Figure 5.22	Example of oscilloscope voltage data input for the pressure difference post-processing program	175
Figure 5.23	Example of measured pressure data ($P_{ref} - P_{measured}$) as determined from "raw" voltage, and pressure difference data ($P_{pressure-side} - P_{suction-side}$) from the post-processing program	176
Figure 5.24	Measurement of pressure signal response time showing data with and without air injected, and the difference between them (data for pressure difference up to the response time is also shown)	178
Figure 5.25	Pressure difference data and its FFT representation, and corrected pressure difference data for δ_o computed using Equations (5.14) and (5.15)	183

Chapter 6

Figure 6.1	Surface-oil flow pattern developed on the suction side of the unducted LP-36 fan operating as a free-air circulating fan at 850 rpm	186
Figure 6.2	Flow visualization of the unducted LP-36 fan using fluorescent minitufts on the suction side of the blade surface	187
Figure 6.3	Flow visualization of the unducted LP-36 fan using marabou tufts on the suction side of the blade surface	187
Figure 6.4	Surface tufts at the trailing edge of the unducted LP-36	189
Figure 6.5	Photographs of tufts placed at the edge of the blade tip used to experimentally determine the value of DISP _N : a) edge view of tip, b) four scanned images of the blade tip and c) photograph from which one scanned image was taken	189
Figure 6.6	Photograph of helium bubbles entrained into the fan inlet from well upstream	190
Figure 6.7	A longer exposure of helium bubble streaklines showing more of the wake flow, particularly the recirculation through the tip at top of picture	191
Figure 6.8	Detail of rotor tip flow with helium bubble injected into the rotor tip region from the inlet side showing the recirculation region	191
Figure 6.9	Detail of rotor tip flow with helium bubble injected into the rotor tip region from downstream showing the flow around the tip from the downstream side to the inlet side	194
Figure 6.10	Hot-wire measurements of the inlet velocity profile for a number of traverses with wire aligned in the vertical direction	194

Figure 6.11	Comparison of inlet velocity profiles measured by the vertical traverses and the horizontal traverse using the hot-wire and that taken from Wallis (1983)	195
Figure 6.12	Orientation of vertical light sheets for visualizing the fan inlet flow	197
Figure 6.13	Photograph of helium bubble streaklines at the wall in the fan inlet	197
Figure 6.14	Photograph of helium bubble streaklines in the fan inlet 2 in. from wall	198
Figure 6.15	Photograph of helium bubble streaklines at 2-3/4 in. from wall in the fan inlet	198
Figure 6.16	Photograph of helium bubble streaklines at 6 in. from wall in the fan inlet	199
Figure 6.17	Photograph of helium bubble streaklines at 8 in. from wall in the fan inlet	199
Figure 6.18	Photograph of helium bubble streaklines at 10 in. from wall in the fan inlet	200
Figure 6.19	Photographs of helium bubble streaklines at 17-3/4 in. from wall in the fan inlet	200
Figure 6.20	Photographs of helium bubble streaklines at 20 in. from wall in the fan inlet	201
Figure 6.21	Photograph of fluorescent minitufts at the mid-region on the side wall of the inlet	201
Figure 6.22	Photographs of marabou tufts on the suction side of the blade at positions in Figure 5.4: a) A, b) B, c) C, d) D, e) E, f) F, and g) tufts on trailing edge and aft portion of suction side	203
Figure 6.23	Photographs of marabou tufts on the suction side of the blade at positions G-H in Figure 5.4 at the window in the side of the duct	204

Figure 6.24	Photographs of marabou tufts on the suction side of the blade at positions H-I in Figure 5.4 at the window in the side of the duct	205
Figure 6.25	Blade surface flow pattern on suction side at position K	207
Figure 6.26	Comparison of marabou tufts (upper) and mini-tufts (lower) on the pressure side of the blade at position A	207
Figure 6.27	Blade surface flow patterns for marabou tufts (upper) and mini-tufts (lower) on pressure side at position F	208
Figure 6.28	Marabou tufts on the pressure side of the blade at position E	208
Figure 6.29	Marabou tufts on the pressure side of the blade at position H	209
Figure 6.30	Marabou tufts at the fan blade tip viewed from the pressure side of the blade	209
Figure 6.31	Photograph of helium bubble streaklines demonstrating the general wake flow pattern	210
Figure 6.32	Photographic data for wake contraction angle (DCD) versus radius	212
Figure 6.33	Side view (left) and view from downstream (right) of trailing edge streamer at $R = 6$ in. and streamer on duct (blade in horizontal position)	212
Figure 6.34	Side view (left) and view from downstream (right) of trailing edge streamer at $R = 11$ in. and streamer on duct (blade in horizontal position)	213
Figure 6.35	Side view (left) and view from downstream (right) of trailing edge streamer at $R = 13$ in. and streamer on duct (blade in horizontal position)	213
Figure 6.36	Axial and radial inlet velocities measured with the hot-wire anemometry	213

Figure 6.37	Performance tests of the LP-36 fan at 600 and 1100 rpm	216
Figure 6.38	Performance tests of the LP-36 fan rotors at their 850 rpm design rotational speed	217
Figure 6.39	Plots of efficiency, power and P_{total} versus PSF-2 input variable DCD, wake contraction angle at blade tip	219
Figure 6.40	Plots of efficiency, power and P_{total} versus PSF-2 input variable RULT, radius of the ultimate wake	219
Figure 6.41	Plots of efficiency, power and P_{total} versus PSF-2 input variable RHULT, radius of the hub vortex line in the ultimate wake	220
Figure 6.42	Plots of efficiency, power and P_{total} versus PSF-2 input variable SFC, leading edge suction efficiency factor	220
Figure 6.43	Plots of efficiency, power and P_{total} versus PSF-2 input variable XTW, axial extent of transition wake	221
Figure 6.44	Plots of efficiency, power and P_{total} versus PSF-2 input variable XULT, distance downstream where wake pitch ceases to change	221
Figure 6.45	Plots of efficiency, power and P_{total} versus PSF-2 input variable DISPN, normal displacement of tip vortex collection point from trailing edge	222
Figure 6.46	Plots of efficiency, power and P_{total} versus PSF-2 input variable CDRA, section drag coefficient	222
Figure 6.47	Measured and computed performance for the LP-36 fan at 850 rpm (computations before and after input variable "fitting" process)	223
Figure 6.48	Input variable values which best match measured performance for the LP-36 fan at 850 rpm	225
Figure 6.49	Measurements and PSF-2 computations of performance using "fitted" input variables at 600 and 1100 rpm	227

Figure 6.50	Measurements and PSF-2 computations of performance for the ACME fan using "fitted" input variables and the modified PSF-2 program	228
Figure 6.51	Drag data as a function of lift coefficients for thin plate blades of various amounts of camber (data from Wallis, 1983 and Milgram, 1971)	230
Figure 6.52	Computational lattice for LP-36 fan at 850 rpm and 10800 cfm (free-air) as modelled with FSF with a 12 x 12 blade grid	230
Figure 6.53	Computed and measured performance for the LP-36 at 850 rpm fan using FSF without the venturi duct capability	232
Figure 6.54	Duct panelling scheme used in FSF for all "duct" results presented in this section with 15 x 20 blade panels (computation at 850 rpm and "free-air")	233
Figure 6.55	Side view of 15 x 20 panel blade lattice and trailing wake for the ducted LP-36 fan at 850 rpm and 10960 cfm (duct, used in calculation, not shown)	233
Figure 6.56	Computed and measured performance for the LP-36 at 850 rpm fan using FSF with the venturi duct capability (duct discretization shown in Figure 6.54)	234
Figure 6.57	Side view of the blade lattice and wake elements for the 12 x 12 blade panels case at 850 rpm, 5730 cfm and with the venturi duct (duct, used in calculation, not shown)	235
Figure 6.58	Side view of a 20 x 20 panel blade lattice and trailing wake for the ducted LP-36 fan at 850 rpm, 6760 cfm (duct, used in calculation, not shown)	235
Figure 6.59	Computed and measured performance for the LP-36 at 1100 rpm fan using FSF without and with the venturi duct capability (duct discretization shown in Figure 6.54)	237

Figure 6.60	Computed and measured efficiency for the LP-36 at 1100 rpm fan using FSF without and with the venturi duct capability for cases shown in Figure 6.59	239
Figure 6.61	Computed and measured performance for the LP-36 at 600 rpm fan using FSF for a coarse lattice without and with a fine lattice with the venturi duct capability	240
Figure 6.62	Uncorrected, "raw", unsteady pressure difference measurements at position A ($R = 15.68$ in.)	244
Figure 6.63	Uncorrected, "raw", unsteady pressure difference measurements at position B ($R = 10.87$ in.)	245
Figure 6.64	Uncorrected, "raw", unsteady pressure difference measurements at position C ($R = 7.67$ in.)	246
Figure 6.65	Unsteady pressure difference measurements at position A ($R = 15.68$ in.) corrected for tubing dynamic response	247
Figure 6.66	Unsteady pressure difference measurements at position B ($R = 10.87$ in.) corrected for tubing dynamic response	248
Figure 6.67	Unsteady pressure difference measurements at position C ($R = 7.67$ in.) corrected for tubing dynamic response	249
Figure 6.68	Circumferentially averaged blade pressure differences at the radial sections A, B and C at pressure tap chordwise locations	251
Figure 6.69	Comparison of measured computed pressure differences for the LP-36 fan at 850 rpm and "free-air" conditions at radial position A ($R = 15.68$ in.)	253
Figure 6.70	Comparison of measured computed pressure differences for the LP-36 fan at 850 rpm and "free-air" conditions at radial position B ($R = 10.87$ in.)	254
Figure 6.71	Comparison of measured computed pressure differences for the LP-36 fan at 850 rpm and "free-air" conditions at radial position C ($R = 7.67$ in.)	255

Figure 6.72	Measured pressure difference at azimuthal position (7-12 msec) compared with pressure predictions from FSF with a 400 panel (20 x 20) grid without duct at radial positions A, B and C	256
--------------------	--	-----

Appendix A

Figure A.1	Concept of decomposition of the potential flow problem into camber and thickness problems (Lan, 1988, p. 65)	264
Figure A.2	The cambered surface with elemental vorticity γds (Anderson, 1984, p.196)	264
Figure A.3	Locations of vortex and control points in the VLM (Lan, 1988, p.73)	264

Appendix F

Figure F.1	Efficiency versus volumetric flow data for LP-36 fan at 600 rpm (S and P signify data for suction and pressure side photographs, respectively)	284
Figure F.2	Surface flow at 8141 cfm on suction side (left) and 7976 cfm on pressure side (right) for 600 rpm test data	284
Figure F.3	Surface flow at 7516 cfm on suction side (left) and 7356 cfm on pressure side (right) for 600 rpm test data	284
Figure F.4	Surface flow at 6432 cfm on suction side (left) and 6346 cfm on pressure side (right) for 600 rpm test data	285
Figure F.5	Surface flow at 5442 cfm on suction side (left) and 5390 cfm on pressure side (right) for 600 rpm test data	285
Figure F.6	Surface flow at 4456 cfm on suction side (left) and 3442 cfm on pressure side (right) for 600 rpm test data	285

Figure F.7	Surface flow at 2537 cfm on suction side (left) and 2492 cfm on pressure side (right) for 600 rpm test data	286
Figure F.8	Surface flow at 1554 cfm on suction side (left) and 1537 cfm on pressure side (right) for 600 rpm test data	286
Figure F.9	Surface flow at 1247 cfm on suction side (left) and 1249 cfm on pressure side (right) for 600 rpm test data	286
Figure F.10	Efficiency versus volumetric flow data for LP-36 fan at 1100 rpm (S and P signify data for suction and pressure side photographs, respectively)	287
Figure F.11	Surface flow at 14096 cfm on suction side (left) and 13962 cfm on pressure side (right) for 1100 rpm test data	287
Figure F.12	Surface flow at 13578 cfm on suction side (left) and 13036 cfm on pressure side (right) for 1100 rpm test data	287
Figure F.13	Surface flow at 12208 cfm on suction side (left) and 12379 cfm on pressure side (right) for 1100 rpm test data	288
Figure F.14	Surface flow at 11578 cfm on suction side (left) and 11692 cfm on pressure side (right) for 1100 rpm test data	288
Figure F.15	Surface flow at 11002 cfm on suction side (left) and 11072 cfm on pressure side (right) for 1100 rpm test data	288
Figure F.16	Surface flow at 8729 cfm on suction side (left) and 8865 cfm on pressure side (right) for 1100 rpm test data	289
Figure F.17	Surface flow at 4200 cfm on suction side (left) and 4252 cfm on pressure side (right) for 1100 rpm test data	289

Figure F.18	Surface flow at 3002 cfm on suction side (left) and 3434 cfm on pressure side (right) for 1100 rpm test data	289
Figure F.19	Surface flow at 0 cfm on suction side (left) and 0 cfm on pressure side (right) for 1100 rpm test data	290
Figure F.20	Efficiency versus volumetric flow data for LP-36 fan at design speed of 850 rpm (S and P signify data for suction and pressure side photographs, respectively)	290
Figure F.21	Surface flow at 10947 cfm on suction side (left) and 11339 cfm on pressure side (right) for 850 rpm test data	290
Figure F.22	Surface flow at 10327 cfm on suction side (left) and 10609 cfm on pressure side (right) for 850 rpm test data	291
Figure F.23	Surface flow at 9903 cfm on suction side (left) and 10101 cfm on pressure side (right) for 850 rpm test data	291
Figure F.24	Surface flow at 9270 cfm on suction side (left) and 9474 cfm on pressure side (right) for 850 rpm test data	291
Figure F.25	Surface flow at 8497 cfm on suction side (left) and 8883 cfm on pressure side (right) for 850 rpm test data	292
Figure F.26	Surface flow at 7548 cfm on suction side (left) and 7711 cfm on pressure side (right) for 850 rpm test data	292
Figure F.27	Surface flow at 3640 cfm on suction side (left) and 3712 cfm on pressure side (right) for 850 rpm test data	292
Figure F.28	Surface flow at 2972 cfm on suction side (left) and 2940 cfm on pressure side (right) for 850 rpm test data	293

Figure F.29	Surface flow at 0 cfm on suction side (left) and 0 cfm on pressure side (right) for 850 rpm test data	293
Appendix G		
Figure G.1	Uncorrected, "raw", unsteady pressure difference measurements at position A ($R = 15.68$ in.)	295
Figure G.2	Uncorrected, "raw", unsteady pressure difference measurements at position B ($R = 10.87$ in.)	296
Figure G.3	Uncorrected, "raw", unsteady pressure difference measurements at position C ($R = 7.67$ in.)	297
Figure G.4	Unsteady pressure difference measurements at position A ($R = 15.68$ in.) corrected for tubing dynamic response	298
Figure G.5	Unsteady pressure difference measurements at position B ($R = 10.87$ in.) corrected for tubing dynamic response	299
Figure G.6	Unsteady pressure difference measurements at position C ($R = 7.67$ in.) corrected for tubing dynamic response	300

LIST OF TABLES

Chapter 5

Table 5.1	Azimuthal positions in degrees and temporal location during pressure measurement cycle for positions of interest	153
------------------	--	-----

Chapter 6

Table 6.1	Percent change in PSF-2 output caused by changes of input variables shown in Figures 6.39-6.46	223
Table 6.2	Pressure tap locations as a fraction of chord from blade leading edge on the LP-36 fan; position A at R = 15.68 in., position B at R = 10.87 in. and position C at R = 7.67 in.	243

CHAPTER 1

INTRODUCTION

Axial-flow fans have been built since even before the Industrial Revolution. These machines are a subset of axial-flow turbomachines which can range in application from machines designed to move large amounts of fluid against low pressures to multi-stage axial-flow compressors. This study is concerned with the former, a device commonly used in ventilation applications. While the rotor blades of some of these machines have airfoil cross-sections, the fans explored in this study do not; their blades are thin-plate blades. Usually, the methods of analysis or design are determined on the basis of blading solidity and assumptions about the inlet and outlet flow. Generally, the designer will select the blading solidity best suited to the flow requirements by making use of either design or analysis methods such as those presented by Wallis (1983) or their own experience and methods. One complaint voiced about these techniques is the large amount of information that must be known from experience or assumed in order to approach the problem.

However, with the age of the digital computer has come the possibility of taking an arbitrary three-dimensional blade geometry, a given rotational speed and a given flow rate and computing the flow field using computational fluid dynamics (CFD). From the flow field solution, pressures and forces on the blade can be determined; from these results the fan efficiency can be determined. Three-dimensional full field solvers can be used to solve such problems but the computational costs are still too high for routine analysis and optimal design. The purpose of this study was to see whether or not a CFD technique which has been used in helicopter rotor and marine and ship propeller applications is also applicable to axial-flow fans. This method, the vortex-lattice method (VLM), is a singularity-based panel method which gives the aerodynamic loading of a lifting surface assuming potential flow outside of the discretized vortex sheets. The VLM is a full three-dimensional potential flow field solver with the added advantages that aerodynamic forces on the lifting surface are directly computed and velocities are only computed on the blade surface, where they are of immediate interest. The VLM is recognized in the aerospace industry as a robust routine design and analysis tool; its many applications will be discussed in Chapter 3.

The ultimate objective of this work is to develop such a robust design and analysis tool for axial-flow fans, a tool which could be used as the "engine" in an optimal design program or "expert" system. The VLM meets important requirements, being fast and capable of handling complex geometries, for the computational method in such an optimization procedure. Highly sculptured marine and ship propellers and helicopter rotor tips have been shown to have improved low noise characteristics and it appears that experimental results for fans

show similar acoustic improvements (Brown, 1977 and Wei and Zhong, 1988). In order to take advantages of the benefits of three-dimensional flow effects, an efficient three-dimensional flow solver such as the VLM is needed.

The immediate objectives of the current study represent the first step toward the ultimate objectives. An examination of the literature of flow visualization techniques was undertaken to identify techniques which would provide insight into the flow field. The results of this review are presented in Chapter 2. Flow visualization techniques were used with the goals of providing a fundamental understanding of the flow through the fan, assisting in the interpretation of hot-wire anemometry measurements and determining wake parameters required for input to the VLM. An important immediate objective was to see whether or not providing the velocity profile and wake input parameters from observations and measurements at "free-air" (zero static pressure rise) conditions enables the VLM to accurately predict the measured performance.

Another, important objective of the study was to measure the blade surface pressures and determine the pressure difference, or aerodynamic loading, across the blade. The measurement of blade surface pressures also gives insight into the flow over the fan blade and provides a basis other than total fan performance for comparison with computations. The measured unsteady pressure on the blade provides details as to the degree of unsteadiness of the aerodynamic loading which the blade experiences due to upstream motor supports and other inlet flow phenomena. A comparison between the VLM results and the pressure measurements establishes the degree to which the VLM-predicted aerodynamic loading matches the unsteady measurements. The blade surface flow visualization performed in this study gives supporting physical evidence to the unsteady pressure measurements.

CHAPTER 2

REVIEW OF FLOW VISUALIZATION TECHNIQUES

2.1 Overview

As stressed by Wallis in his comprehensive work on axial-flow fans (Wallis, 1983, p. 361) flow visualization should be an integral part of axial-flow fan research and development. The major qualitative goals of visual study are to establish flow directions, and determine regions of separated, recirculating and disturbed flow in order to understand and improve fan design. In general, instrumental measurements without some physical picture of the flow field can lead to improper conclusions. Furthermore, following the evaluation of the flow field by visual means (especially a complex erratic flow field such as the present in situ fan flowfield), the type of instrumentation required and the extent of study to be applied to the problem can be decided upon in a more informed manner. An overview of recent developments and future expectations and trends in flow visualization is given by Settles (1986). In this work, the use of flow visualization techniques is farther reaching.

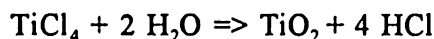
In the present work flow visualization techniques were used to analyze and evaluate the fan inlet conditions and the wake geometry qualitatively and quantitatively in order to estimate some parameters used in the numerical study. In addition, the existence of non-ideal flow phenomena such as flow separations and regions of unsteady flow was investigated and documented. As good inlet flow velocity data are required to effectively use the PSF-2 steady lifting surface computer model, the hot-wire anemometry measurements of the inlet were assisted by flow visualization techniques in both the orientation of the probe and prevention of misinterpretation of measurements. Also, the identification of flow separation regions aided interpretations of the blade pressure measurements conducted in the current study, and a correlation between blade surface flow visualization and pressure measurements lent credibility to the latter.

2.2 Smoke Flow Visualization

Often classified as a particle tracer flow visualization technique, smoke has been used in many applications to visualize flow, and these applications are generally non-turbulent and low speed flows. Smoke is a difficult technique to use for a swirling flow. However, the smoke tube method is similar to the use of colored dye injection in water. It is the use of the dye technique (and a hope to adapt the technique using the smoke tube for air flows) as in the study of large area flows in plexiglass model chambers by Sucker and Boenecke (1982) which is of interest here in the study of wake and inlet flow properties. Wallis (1983)

stated that smoke is useful in visually testing fans, but gives no examples of its use. The personal experience of this author shows it to be tough to use.

Essentially the smoke provides for visualization of a flow structure or a flow field by scattering incident light. A smoke of adequate light scattering quality for flow visualization must be employed; TiCl_4 was one possibility (i.e. Freymuth, Bank and Palmer, 1985) and was the only type of smoke used in the present study. TiCl_4 produces smoke by the reaction



There is enough moisture in the air of even the most arid climates for production of the desired titanium dioxide smoke. Also, the hydrochloric acid released in TiCl_4 smoke can be greatly diminished by bubbling through a water bath before releasing it. TiCl_4 smoke also has the tendency to form additional precipitates which can clog filament tubes. These problems can be overcome by adding CCl_4 to the TiCl_4 in the mixing chamber. TiCl_4 smoke is generally only suitable for flows up to 5 fps.

For higher speed applications one could use a mist of α -bromonaphthalene ($\text{C}_{10} \text{H}_7 \text{Br}$), which has been applied to the study of flows in axial compressors at speeds up to 500 fps, Maltby and Keating (1962). The high luminosity of these organic mists does have a price in that they are extremely toxic, and should never be inhaled.

A tracer gas can be used to visualize flows. Such techniques are desirable because a tracer can more exactly follow the motion of the main flow. The ozone (O_3) flow visualization technique of Stedman and Carignan (1985) appears to be an excellent method for this reason, and it has the same properties of air in turbulent flow conditions. The developers of this method were studying rates of photolysis of ozone in the atmosphere when a release of dilute ozone between a mercury lamp and a "black light" poster made them think there was smoke in the room. They thought this would be of interest not only because they could see the shadow of an invisible object, but also they thought it might be of benefit to those studying turbulence for the reasons previously mentioned. Ozone cannot be stored in any way; it must be produced at the time of use. They produced a stream of about 1% ozone by passing air through a strong electric corona. Ozone is toxic, but does not have to be produced in high enough quantities with this technique for toxicity to be of concern. The components of an ozone flow visualization technique required are an ozonizer, ultraviolet light source and fluorescent backdrop. Ozone appears as a dark cloud on the fluorescent backdrop when it passes between the backdrop and an ultraviolet light source. This is due to ozone's absorption of ultraviolet light, and the luminescence of the fluorescent backdrop. This potentially useful technique has yet to be used (to the writer's knowledge).

This also serves as an example of the serendipity sometimes involved in the development of flow visualization techniques.

2.2.1 Smoke Illumination

Illumination is of the utmost importance to the visualization of smoke lines or smoke flow. When illuminating smoke lines or filaments from smoke tubes, the illumination is generally from the front with conventional light sources (spot lights, halogen lights, etc.). In this type of illumination the photographs are made from the same direction as the illumination. Larger volumes or sheets of smoke which reveal boundary layers, flow separations, and wakes are best illuminated using sheets of light which are recorded by photographing normal to this plane.

Light sheets can be produced from conventional light sources, and one of the best conventional light sources can be made from a slide projector, using a slide with a small slit in it to produce a light plane of several millimeters width which can be focused and manipulated. Lasers provide the best sources of light planes, and this technique has made a dramatic impact on the visualization of smoke seeded flows; see Philbert, Beaupoil, and Faléni (1979), Mueller (1985) and Stanislas (1985). One of the earliest implementations of this technique was at the ONERA (Office National d'Etudes et de Recherches Aérospatiales) wind tunnel as presented by Philbert et al. (1979). Lasers can produce very narrow sheets of intense light, about 0.3 mm in width, and also provide a variety of power levels which make a dramatic improvement in the visualization of these structures. Such laser light sheets are produced by first passing the laser beam (He-Ne, Ar, and pulsed ruby have been used) through a cylindrical lens or a glass rod to get a plane of light. This plane is then narrowed and focused by passing the beam through a converging lens. Laser light sheets have the added advantage of producing fluorescence in molecular seeding particles such as iodine and sodium (Settles, 1986). Lasers used in laser induced fluorescence techniques must be tunable and quite powerful; the smoke-like seeding materials are corrosive.

2.3 Particle Tracing Techniques

Although smoke consists of foreign particles which are often classified as tracer particles, the term particle tracing technique generally refers to techniques where the flow is seeded with a concentration of particles low enough that their individual motion can be discerned (Emrich, 1983). The movement of a single particle can be observed and recorded. But, does the motion of such a particle in the flow truly reproduce the motion of the fluid? There is general agreement that it does not on a microscopic level; however, in some cases the differences between particle and fluid motions are so small that the technique provides useful qualitative and quantitative information. Foreign particle-flow interaction has been the subject of numerous theoretical and experimental works due to its importance

in such applications as laser-doppler anemometry, optical probe velocimetry, and multi-phase flows. For deeper discussion of the theories of particle-free flow in non-turbulent flows, the interested reader is directed to Merzkirch (1987, p. 39) and Somerscales (1981). In turbulent applications there are important considerations about the limiting turbulent frequencies a particle is capable of following. This is investigated in detail by Somerscales (1981) and Hinze (1975).

Tracer particles must meet a number of criteria. Other than those already discussed concerning smokes, the two remaining criteria are a minimum of slip (difficult to measure) between the particle and the fluid in which it is borne and high visibility. These two criteria are not easily met together. If the particle density approaches that of the fluid, then it is almost neutrally buoyant, and the first criterion (negligible slip) is met. Generally, this criterion is met if the particle is small enough. However, a small particle is difficult to detect with the naked eye, let alone record photographically. A description of particles used in some of the most difficult flow visualization applications, thermally driven flows, is given by Matisse and Gorman (1984). Of great concern in applications of particle tracing (Matisse et al., 1984), is that the sedimentation time of a seeded particle be much less than the characteristic time over which the experiment is performed. The sedimentation time t_s is determined by the characteristic length of the flow being investigated divided by the sedimentation velocity v_s . The sedimentation velocity can be approximated by the terminal velocity of a sphere falling through a fluid of differing density; this terminal velocity is given by the Stokes formula (Matisse and Gorman, 1984)

$$v_s \approx v_{\text{terminal}} = \frac{2}{9} \frac{r^2 g}{\nu} \left(\frac{\rho'}{\rho} - 1 \right) \quad (2.1)$$

for a particle of radius r and density ρ and a fluid of density ρ' and kinematic viscosity ν .

2.3.1 Applying the Tracer Technique

Generally, the particle traces are photographed normal to the light plane in which they are illuminated and, whether or not the flow field is three dimensional, a two dimensional image is usually recorded. There are examples of efforts to record the three-dimensional motion. The particle trace has a length that is actually proportional to the average local fluid velocity at that point. The most serious source of error in this technique is the accuracy of the shutter speed. Also, care must be taken in flows with great differences in velocities. The faster the flow, the shorter the exposure needed to capture good flow streaks. This trade off (between faster and slower velocities) can be hard to achieve in fields with wide ranges of velocities. Also there is a question of contrast; a fast moving particle

exposes itself at given points on the film for a shorter length of time than does a slow particle. This variety of contrast can lead to problems in developing and printing the film.

This technique can be misleading or ambiguous in flows which have regions of reversed flow. Providing a burst of light at the start of a photographic exposure to mark the particle starting point assists in the determination of flow direction in these difficult instances. Measurements of the particle streaks when mapping out the velocity field are generally performed using negatives, and the accuracy of these measurements introduces a possible source of error.

2.3.2 Lighting and Photographing Particle Tracers

In order to capture the entire flow field (or at least a large portion), its qualitative characteristics as well as the velocity field at the given instant, suitable lighting and recording (photographic equipment) are needed. The flow must be seeded with particles, and this is done with equipment not unlike the smoke generators which have been previously described. Except for the case of particle deposition, the characteristics of the equipment are less critical. However, a critical parameter in these experiments is the camera shutter speed or exposure time. The distance a particle travels in the photograph is assumed to have been traversed during the length of exposure, and it is from these two sources of information that the particle velocity is calculated.

Illumination for particle tracing is usually some variation of two methods; light sheets and stroboscopic lighting. Light sheets are the most common, and have been described earlier as produced by a conventional projector or by expanding a laser beam through a cylindrical lens. The laser systems used range from 5 mW Helium-Neon lasers up to 5 W Argon lasers. The light sheets used are no thicker than about 1 mm, and the plane is generally no higher than 10 cm. Such a plane reveals a two-dimensional velocity field only, and only so long as the particle remains illuminated in the plane. This major drawback can not only be misleading, but also can render the technique useless in determining velocity components normal to the plane. This is, however, not a difficulty for flows which lack a complex three-dimensional structure. There are limited solutions to the problem: Van Meel and Vermij (1961) used several parallel light sheets of different colors to discern motion normal to the planes by particle color changes. Illumination by the use of stroboscopic light planes can be used to give information on the residence time of the particle in the light plane. With a steady light plane one has no idea whether or not the particle streak began in the plane, let alone whether it stayed in the plane during the entire exposure; but with longer exposure times and a flashing light plane, particle motion entering and leaving the plane is readily observed. Still, interpretation and skill is required in making decisions about such observations.

2.3.3 Examples and Applications

Sparks and Ezekiel (1977) developed LSV (Laser Streak Velocimetry) from a desire for full field velocity mapping, and additionally to develop a non-obtrusive velocity measuring method. A criticism of LDV (Laser doppler velocimetry) techniques is that they are limited to point by point measurements and it is desirable to develop a "full-field" non-obtrusive technique. Very small particles were introduced into the flow, and illuminated by a 3.5 W argon laser formed into a 0.3 mm sheet by passing it first through a cylindrical lens and then through a spherical lens. The cylindrical lens (that forms the plane) is mounted on a rotor so the plane can be easily and precisely oriented to any given angle. The flow they examined was that of air around a 1.6 cm cylinder placed in a wind tunnel. The experiments were viewed and recorded in the test section of the wind tunnel, a 10 cm x 10 cm section. The speed of the flow was limited to velocities under 10 m/s due to the shutter speed limitation of 1 ms. These exposure constraints (lengths of particle streaks and lighting) restricted them to using high speed film (ASA 3000). The best results were achieved using 10 μm diameter talc particles dispersed at an appropriate distance upstream of the test section by manually squeezing a plastic bottle. No effort was made to sort or sieve the particles other than to allow larger particles to naturally settle out in the wind tunnel during the course of the experiment. Water particles (aerosols) were also attempted (diameter 5 μm), but were found to be weak light scatterers. Streak particle photographs were taken in increments of 0.2 mm above the surface of the test section, and extended to 5 mm above the section. Sparks et al. compared the results of their technique to the well-known theoretical solution of boundary layer flow and found their results to be within 4% provided they used only the longest streaks. At that time they said there was no way to measure instantaneous velocities in such an unsteady flow, and also no theory for such an unsteady vortex flow. LSV provided the only means of measuring the velocities.

Chen and Emrich (1963) used lycopodium powder, oil droplets, and cigarette smoke in their investigations of shock-tube boundary layer flow. They say (but provide no data) that they investigated the tracing characteristics of aluminum flakes, silica, and zinc oxide. The strength of the shock used in their investigation (P_{12} , the ratio of pressures across the shock) ranged from 1.2 to 2. For this thesis, the pertinent information is their study of the various particles used as tracers, the response of the tracer particle to the flow, and the influence of particle size on the technique's use and validity. In order to predict the response time of their technique, the time it would take a particle entrained in the flow to acquire the mean flow velocity, Chen et al. derived an expression for the relationship between particle and gas velocity as a function of time. This derivation began with the assumption of a particle size of about 20 μm .

2.3.4 Helium Bubbles

One way of producing neutrally buoyant particles is to use the helium bubble method. In this method soap bubbles down to about 1 mm in diameter can be produced using a bubble generator. The neutral buoyancy of the bubbles emitted into the flow can be further improved on by passing the generated bubbles through a settling chamber before emitting them to the flow. This eliminates bubbles which are either too heavy and too light. This technique produces bubbles which are capable of faithfully following torturous paths with minimal bursting. One must tolerate some mess when using the technique, and the models used must also withstand moisture. This technique provides information about the nature of streaklines in the flow, but is difficult to use in giving whole-field information as do some of the tracer techniques. The use of helium bubbles for axial-flow fan application is unreported in the literature, but would be similar to the air bubble injection technique which has been used with success on marine propellers (Yausa and Ishii, 1982) and helium bubble injection in helicopter rotor work (Gray, 1992).

Helium bubble generators are used a great deal in wind tunnel testing in the study of aerodynamics. It can, however, be used in more ways than it has been, and it is with this in mind that this sort of literature has been reviewed. Santanam and Tietbohl (1985) working at the boiler manufacturer, Riley Stoker Corporation, investigated complex three-dimensional flows of which there are many in the field of power generation (burners, furnaces, piping networks, heat exchangers, deaerators, condensers etc.). Needless to say, such three-dimensional flows are difficult to analyze mathematically. With these difficulties in mind, Riley Stoker implemented a program of flow visualization using helium bubble techniques. Scale models of the equipment are made of clear plastic so the flow might be seen and recorded, and through these models was blown air seeded with helium bubbles which traced out the streaklines of the flow. Their generator produced neutrally buoyant bubbles of about 1/8 in. diameter. Generally, they used video tape to record their experiment for closer analysis. The importance of lighting was stressed. Helium bubbles require very bright directional lighting with dark backdrops to achieve good contrast. Lights with too wide a diffusion angle may illuminate stray objects and cause blotches on the film. At Riley Stoker several different lighting techniques were used. For very large exterior flows, they used a six-foot long light box in which were seated five, 150 W spot lights, and the sides of this box were high in order to reduce the beam expansion for the reasons given above. Conventional slide projectors were used in some cases for illumination, but they lacked control of the diffusion of light. Adjustable beam angle lamps of 150 W and 300 W were also employed in small area illumination. These adjustable beam lamps were capable of narrowing the beam to the size of a quarter when the source is ten feet away. Generally Riley Stoker employed light sources with the beam direction opposite to that of the flow. Flows were then observed and recorded normal to the streaklines.

If still photographs were taken, the camera was usually placed about 5 feet from the model, and the f-stop set between 1.4 and 2.8. Exposure times depended on the flow and the desired streak length, but for applications at Riley Stoker this meant between 1/8 to 1/2 of a second. These exposure constraints generally meant using films (black and white) of relatively high speeds, an ASA of 1000 or 1250. When films of this high speed cannot be found, they suggested using ASA 400 film (easily obtainable) shot with the camera exposure of 800 ASA. This makes the resulting exposure times lower than applicable for the ASA 400 film. To offset this, the film development is lengthened, and this process is called push-processing. Santanam et al. suggested doubling the development time for this reason and to improve the contrast of the bubble streaks. In making prints of streak photographs Santanam et al. recommended using Kodak Polycontrast RC2 Grade F paper. This is a high contrast paper which allows the preparer to vary the contrast through the use of filters. Magenta filters provide the highest contrast in printing. The ultimate goal in this technique is the production of clear flow patterns, bubble streak lines with good contrast to the dark background. Although the technique provided for excellent flow visualization, Santanam et al. said it is a time consuming affair in which there are many variables that effect the quality of the photographic record. They pointed out that subject contrast, film exposure, film development times, negative contrast and lighting are all interrelated, making the technique as much an art as it is a science.

Kent and Eaton (1982) described He-filled bubbles as a new technique in their work on three-dimensional fluid motion studies in engine cylinders. That is not to say that it was a new technique, because as pointed out earlier it has been used to study steady external flows in studies of aerodynamics, but it was the first application (to their knowledge) of the technique to transient three-dimensional internal flow fields.

Kent et al. (1982) and Colladay and Russell (1976, in turbine blade boundary layer visualization) both used a Sage Action Incorporated (SAI) helium bubble generator in their work. The generator consists of a bubble-blowing head and a console which controls the flow of bubble soap solution, helium, and air to the head through the use of micrometering valves. Carefully controlled bubble solution flow through the annulus is formed into a bubble filled with helium (flowing through the concentric tube of the annulus). Bubbles formed at the tip of these concentric tubes are then blown off and carried from the generator head by the compressed air flowing around the tube. Neutral buoyancy is achieved through careful ratios of bubble soap solution to helium flow. These flow rates also determine the rate of helium bubbles generated. Sage Action Inc. claims the device can form up to 200 bubbles per second; however, some researchers using this device say it is capable of 300 bubbles per second.

2.3.5 Other Tracer Methods

It has been mentioned that there are no truly neutrally buoyant particle tracers for the visualization of air and gas flows, other than of the helium bubble technique. Zinc stearate dust, though not as neutrally buoyant as the previously mentioned bubbles, has been used in the study of low velocity flows induced by natural convection (i.e. Hsieh, 1977 and Eichorn, 1959). Just as in the case with talc and lycopodium particles, microphotography techniques must be employed to visualize the flow of the zinc stearate dust particles (6 μm in diameter). The physical model that Hsieh (1977) studied using this technique was a heated plate of constant temperature which induces through natural convection a vertical boundary layer in which there is the obstacle of a forward facing step. This particular problem has become important in the area of heat transfer due to the increased interest in the cooling of printed circuit boards. The limitations of this technique were due to the fact that the field observed is relatively small.

Eichorn (1959), for instance, used a camera lens with a magnification of 18, and was limited to a field of vision $2.04 \times 1.36 \text{ mm}$ in his early work with the technique. Since then most of the researchers using the technique have attempted to visualize larger areas, but this increases the depth of the field on which the lens focuses. The depth of field increase means that the photographs are more difficult to survey. Hsieh was able to evaluate a velocity field in a $6 \times 8 \text{ cm}$ area. The zinc stearate dust was introduced to the convection chamber by first using a blower to carry the dust from the fluidized bed, a fine mesh screen on which the dust was sprinkled, to a mixing chamber. The mixing chamber served to mix the air and dust, settle out larger dust particles, and minimize the forced draft caused by room air disturbances. Then the air was forced into the convection chamber through an opening at the bottom of the chamber. Hsieh, apparently, did a good bit of trial and error work to control and achieve just the right amount of dust concentration in the air which was accomplished by blocking off the blower intake. The general operating procedure consisted of first sealing the convection chamber and turning on the plate heaters and allowing the temperature to reach steady-state (this would take about 12 hours, the plate was usually 71°C , the air 27°C). Next the blower was turned on (for about 15 minutes) to slowly force air with a good quantity of dust into the convection chamber. The blower was turned off after about 15 minutes for a period of about 30 minutes to allow the larger particles of dust to settle out and for the chamber to again reach steady-state. After this wait, the illumination equipment was turned on and a series of photographs of flow over the plate and step were taken.

Hsieh used a 1000 W calibration lamp with focusing lenses and a chopper mounted on an optical bench for illumination. The optical equipment thus arranged creates an intense flashing light source. The area of illumination used was a $1.27 \times 12.7 \text{ cm}$ strip, and could be varied through the use of the focusing

lenses. A single lens reflex camera was used with the best results using an aperture setting of f2 and 1/8 second exposure time. Kodak Tri-X film was used, but it was not sensitive enough at the rated speed of ASA 400. However, with special (increased) processing times it was possible to push it to ASA 4000 speed rating using Kodak HC-110 developer (no specific development times are provided by Hsieh). A 7.62 μm diameter thermocouple wire was placed in all photographs to provide a reference for the magnification of the velocity field which was needed when evaluating the average velocities. All photographs were evaluated by using images from the film negatives projected onto a large screen using a slide projector.

Akiyama, Suzuki and Nishiwaki (1979) showed that it is possible to visualize flow fields of a much larger area than these previous methods which employ microphotography. Akiyama et al. visualized a ventilating flow through a chamber (18 cm x 18 cm) using zinc stearate particles which have been seeded into the flow. Their illumination source was a 16mm projector focused on the test chamber after passing in through a 4mm slit. Tri-X film was used in all photographs with shutter speeds ranging from 1 to 1/8 second. Further examples of this technique by Akiyama et al. showed the periodic growth and decay of a recirculating region in the chamber in a series of pictures. It was reported that this technique could be used to accurately determine (barring motions in the third dimension and other uncertainties (see Akiyama et al., 1979) velocities ranging from 5 mm/s to 1 m/s.

The flow visualization technique used by Howarth, Morton and Sherratt (1972), and was first used by Daws (1967), consisted of injecting small visible white particles into the room. Particles of up to 6 mm in diameter which had the appearance of snow flakes were produced by the heating of metaldehyde tablets. These particles are crystalline in appearance and lightweight. Vertical planes of light projected through the ceiling were used to illuminate the particles in mutually perpendicular planes of interest. These planes could be observed and recorded through either of the transparent walls with the dark walls providing the needed contrast. The two-dimensional flow fields were then photographed at shutter speeds of 1/4, 1/2, and 1 second. From photos taken during testing, quantitative measurements of the velocity field were made.

Magness, Utsch and Rockwell (1990) described a flow visualization rig for a water tunnel which generated grids of hydrogen bubbles. The hydrogen bubble technique allowed for continuous or intermittent particle generation and their bubble sheets were generated for arbitrary duration and separation. Laser sheet illumination which used a 2 W argon-ion laser swept with a 500 cycle per second frequency were positioned normal to the free stream in order to visualize arbitrary cross sections of the flow over an oscillating delta wing.

The extension of particle flow visualization to the quantitative study of flow fields takes a number of forms and is currently a field of great interest. There are a variety of techniques in use, most notably particle imaging velocimetry (PIV) and particle tracking velocimetry (PTV). Adrian (1989) and Khalighi (1989) provide examples of the applications of PIV and PTV, respectively. The lighting sources used with the PIV technique are pulsed lasers, while the PTV technique can be used with light choppers and conventional lamps as lighting sources. For instance, a 500 W quartz-halogen lamp was used by Kumar, Conover and Pan (1993) in an application of the PTV technique to a swirling turbulent flow. A collection of PIV and PTV papers is contained in Khalighi, Braun and Freitas (1991).

2.4 Surface flow visualization techniques

A group of techniques which may yield results without the technical difficulties of some of the previously mentioned procedures are the methods of surface flow visualization. Such techniques show interactions of fluid flow with the surface of a body in the form of pressure, heat transfer, mass transfer or shear forces. Of particular interest to this project are the advances being made in quantitative surface pressure mapping using pressure sensitive paints or PSP (Morris, Dnonvan, Kegelmann, Schwab, Levy and Crites, 1993 and Bell and McLachlan, 1993). However, PSP formulations currently in use are for higher pressures than those experienced by the axial-flow fans used in this study.

Surface flow visualization techniques generally provide qualitative information about the surface flow field. The visualization methods surveyed here exploit the mechanical interaction between the flow and the surface to visualize flow at the surface. The techniques examined are oil films, surface tufts and tuft screen methods. Questions about the reliability of these techniques will be discussed as will be their limitations because of their interference with the boundary conditions of the flow studied, and because they only provide information about the boundary layer of the flow. Also, when being using on rotating surfaces, as in the present project, stroboscopic lighting is required.

2.4.1 Oil Film Technique

Perhaps the most commonly used technique to acquire qualitative surface flow information is the oil film technique (i.e. Sallam, Kaji, Nakanishi and Ishigai, 1982). This technique reveals patterns of air flow over a surface that can be interpreted to discern the characteristics of flow close to the body surface. Many aerodynamicists in the wind tunnels of the future, their computers, use a computational form of the oil film technique to interpret fluid flow behavior or to compare numerical experiments with flow visualization (Walatka and Buning, 1989) as shown in Figure 2.1.

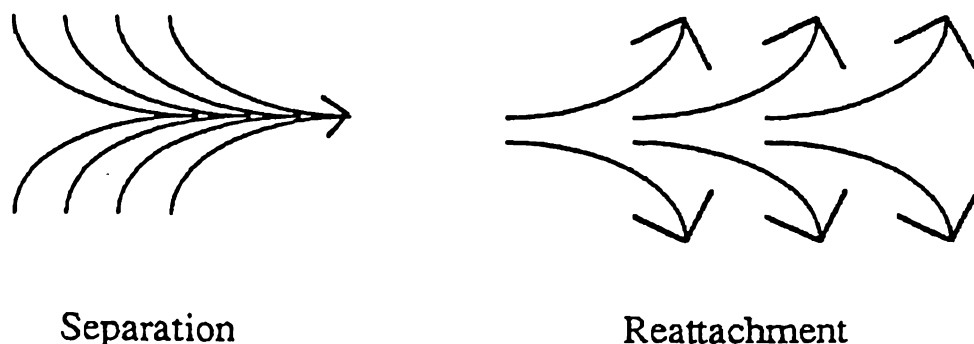


Figure 2.1 Generally accepted appearance of flow separation and reattachment lines as they appear in experiments and, in this case from the PLOT3D program

In its general form, this technique involves applying a paint, a mixture of a light oil and a portion of powdered pigment (usually mixed in ratios of 4:1 or 5:1 oil to pigment, by weight) to the surface of interest. Kerosene appears to give the best general purpose results as an oil (oil of wintergreen has also been employed among others), and the pigments used are generally lampblack, titanium dioxide, or tempera paint as in the case of Portiero, Norton and Pollock (1985). Many mixtures are possible and some of these involve additives such as oleic acid. Casale, Onorato, Quagliotti and Savorelli (1985) used a mixture of 70% kerosene, 6% oleic acid, and 24% Dayglo Saturn Yellow Pigment on their models and illuminated them with ultra-violet light to observe detailed surface flows. This improved the contrast in the photographs recording the results of the experiments. Generally, the pigment-oil mixtures cited are useful only as a starting point in using the technique. The correct mixture for a given application is found only through trial and error.

After the surface is coated with the paint, and the flow is initiated over the surface, the shear forces at the oil-fluid interface move the oil over the surface in the mean flow direction. The flow of oil carries with it the pigment that leaves streaks deposited along the mean flow direction. There is general agreement that the oil streaks can, when examined by an experienced eye, reveal qualitative information about the nature of the boundary layer (whether the flow is laminar or turbulent, points of transition from laminar to turbulence, points of flow separation and reattachment etc.).

Squire, Maltby, Keating and Stanbrook (1962) gave a thorough discussion and analysis of the motion of a thin oil sheet under the boundary layer on a body. The solutions to various flow conditions for an oil film on the surface of a body with a moving boundary layer led Squire to three conclusions.

1. The oil flow will follow the boundary layer streamlines except where there is a separation. The oil flow will form an envelope (or ridge) upstream of the actual separation envelope.
2. The disturbance to the boundary layer motion is very small for most of the applications of this technique. Disturbing influences become a concern, however, as the oil viscosity decreases.
3. Interpretation of the oil flow pattern at low Reynolds numbers must be done cautiously. It is sometimes difficult to pick out the difference in the flow streaks between laminar-turbulence transition and flow separation.

Squire et al.'s resulting equations for oil film streamlines showed that the direction of the oil flow streamlines depends upon the wall shear stress of the air flow and on the pressure gradient. For most flows the wall shear term is much larger than the pressure term and the oil film streamlines formed are a good representation of the true wall streamlines. However in regions where the pressure term becomes large, such as near a separation point or reattachment, the oil flow decelerates and the oil film thickness increases, oil piles up, and the oil streamlines do not provide a representation of what is happening at the body surface. Squire et al. showed that it is possible for the oil buildup to affect the point of separation or reattachment.

More recent investigations into the physical processes responsible for the formation of oil-flow patterns have used interferometric (Tanner, 1982) and shadowgraph methods (Murai, Ihara and Narasaka, 1982). However, there seems to be no complete agreement on all of the physical processes responsible for the formation of oil flow patterns.

Maltby and Keating (1962) discussed and compared various oil film testing strategies involving changing the oil medium used, the use of additives (commonly oleic acid) to improve flow patterns, the effects of different types of pigments, methods of application, recipes for mixing the oil film paint, and the interpretation of the oil-flow pattern. The ratio suggested by Maltby et al. for a oil-pigment mixture is a 3:1 oil-to-pigment by weight. Applications of the suggestions presented by Maltby et al. are primarily for low speed flows. A similar overview of the oil-flow technique for use in high speed flows was given by Stanbrook (1962).

Settles and Teng (1962) suggested using a kerosene-pigment ratio of 4:1, but go on to say that ratios of 2:1 might be required for especially high speed, high shear flows. Settles et al. also used large sheets of Scotch tape (20 cm x 66 cm) carefully placed over the dried flow pattern and rubbed vigorously to remove and

preserve the flow pattern. The tape was then be placed on a sheet of paper as a record of the experiment. They claimed that with practice even patterns of complex geometries can be preserved in this manner. This technique also recorded the experiment in a way not possible from photographing the model since the camera cannot focus on the depth of view needed to capture three-dimensional patterns.

Additional applications (left to the interested reader) of the oil streak technique are many and include; the effect of various wind/nozzle conditions on a space shuttle's surface heat transfer to prevent damage to the ceramic tiled surface of the ship during the loading of cryogenic propellants (Portiero et al., 1985), the study of water surface flows over rotating disks and axial-flow pump blades (Arakawa and Tagori, 1982), flow around propeller blades (Yuasa et al., 1982), flows over impulse turbine cascades (Stastny, 1982) and use of the "oil-dot" technique (Atraghji, 1982). Also, an aluminum oxide and kerosene coating was employed by Ahmed (1983) to study the influence of base slant (angle of the rear window with the horizontal of the top of the car) on drag and wake structure of automobiles.

Examples of the oil flow technique on rotating blades are of particular interest. The technique has been applied by Vaczy and McCormick (1987) to counter-rotating prop-fans in order to substantiate the existence of leading edge vortex flow. Vaczy et al. used a fluorescent paint pigment (manufactured by Day-Glo) as a tracer mixed with 90 or 120 weight oil (the higher the rpm the more viscous the oil) in a 1:1 ratio by volume. The props were run up to the desired speed, which took approximately 1 minute, and then allowed to remain at the desired operating point for 5 to 15 minutes, once again depending on the rpm. They gave no actual rpm values for the tests in their paper, but indicated changes in rpm by showing results at various advance coefficients. The existence of the leading edge vortex as the flow separates along the leading edge of the upper or suction surface on swept blades or, more commonly, delta wings is known to provide extra lift, and this lift can be predicted rather well (Polhamus, 1966 and 1968). The blades of an axial-flow fan were removed and placed in a wind tunnel to confirm the boundary layer control achieved by the use of leading edge slats (Javur, Murthy and Kar, 1982) by the use of oil flow patterns. Another example of the use of the technique on rotating propellers was given by Stefko, Paulovich, Greissing and Walker (1982).

2.4.2 Tuft Methods

Because tufts enable visualization of the direction of streamlines in a flow, a tuft's length is customarily chosen to be smaller than the expected radius of curvature of the streamline at the given tuft point in the flow. In this way, unsteady motion of the tuft due to the crossing of several streamlines is minimized.

In unsteady flows, tufts will exhibit unsteady motion, which cannot be helped. This whipping motion of tufts is a shortcoming with the technique; if it is due to the self-excitation of the tuft and not a feature of the flow, errors can result while interpreting test results. Tuft whip depends upon tuft length and material. Reducing tuft whip can also lead to longer tuft life, and improved photographic recording of test results. The effects of corrugation of flow surfaces by the tape or glue affixing the tufts can be reduced by reducing tuft whip and the resulting loads at the point of attachment.

Tufts can be glued to the surfaces of models to discern qualitative information about the direction and steadiness (or lack of it) of flow in the boundary layer of a surface. It is true that the rough surface created by gluing and applying tufts to the surface can alter the true nature of a flow. The tufts can produce a transition in a laminar boundary layer, for instance, and can also thicken the boundary layer, leading to such things as premature separation in aerodynamic testing. Bradshaw (1970) suggests applying tufts progressively to detect and prevent such problems. Crowder (1982, 1982a and 1985) has overcome these difficulties among others associated with using tufts by developing fluorescent minitufts. When appropriately illustrating flow phenomena, tufts can show transition to turbulence through their unsteady motion, and separation by their lifting motion.

The fluorescent minituft technique is a revolutionary weapon in the arsenal of flow visualization techniques. Developed at Boeing by J.P. Crowder for wind tunnel testing in 1980, they became a routine method of testing in both low speed and transonic testing. As briefly mentioned above, they are less obtrusive to flows than traditional yarn or string tuft techniques, and also improve performance and durability. Minitufts are also more sensitive than any other tuft technique, and because they are much less sensitive to centrifugal forces (caused by the tuft material) they can be used on rotating surfaces (Crowder, 1985), in this case an automobile wheel. An example of a minituft test photograph given the work cited above shows an automobile moving past a stationary camera at a speed of 160 kilometers per hour. It is reported that more than 90% of the tufts remain fixed to the models after many hours of testing, and speeds up to Mach 2.7. Force and moment coefficient tests with and without tufts show a negligible difference. Also negligible were the tufts' effect on the integrated wake profile drag (as calculated by traversing the wake); $C_D = 0.00945$ on a clean model and $C_D = 0.00949$ for a tuft-covered model with slightly more data scatter for the tuft-covered model.

Minitufts are made from thin monofilament line about 20 to 30 μm in diameter, and are invisible in ordinary light even if inspected closely. They can, however, be treated with fluorescent dye, causing them to be luminescent under ultraviolet light and making them visible and recordable. The range of ultraviolet illumination techniques that have been used for the technique range from black

lights (long-wave ultraviolet, not a hazard to the human eye) to high intensity (or short-wave ultraviolet lighting) ultraviolet lighting which provides better results, provided that the researcher takes care with these dangerous light sources. One also has to use a barrier filter on the camera recording these experiments. This filter will pass the visible fluorescence of the minitufts while preventing reflected ultraviolet light from damaging the photograph.

Crowder provides little details to the novice as to what sort of dye, method of attachment, type of nylon line, and method of dyeing the line to use. Crowder also gives the interested reader few clues as to how best to photograph the experiments. Stinebring and Treaster (1985) can help such an interested reader. Stinebring et al.¹ adapted the use of the minituft technique for use in high speed water tunnels, and they give a detailed description of how to dye the nylon fiber. They started with commercial nylon rope which they unravelled down to the individual fibers; approximately 30 μm in diameter. The fibers were treated using a fluorescent dye (Leucophor) manufactured by the Sandoz Corporation as a commercial fabric brightener. A dyeing solution of 1% dye, 2% acetic acid, and 97% water was mixed and heated to 180 F. The fibers were then soaked in the solution for 15 minutes, and allowed to dry. This drying set the dye into the fibers, making them waterproof. For high speed applications, Stinebring et al. were careful to clean the model surface with acetone or methyl-ethyl ketone to provide a firm hold for the tuft adhesive. The fibers were fixed to the model surface using small drops of cyanoacrylate adhesive applied by either the point of a straight pin or the edge of a dull razor blade. Stinebring et al. used a Kodak Wratten 2A barrier filter over the lens of their 35 mm camera. Kodak Plus-X film was used at shutter speeds of 1 second and f/5.6. They mentioned difficulties with some of the plastics used in their water tunnel which absorbed some of the energy of the ultraviolet light source. It was a bad enough problem that they replaced the troublesome sections with ultraviolet transmitting materials. Crowder's minitufts solved another problem with the tuft technique, that conventional tufts do not show true flow direction at low speeds and do not follow rapid changes in the flow direction.

Applications of flow visualization in diffusers of pumps or fans are of particular interest to the search for techniques applicable to the problem at hand. One such application is to the study flows in vaned diffusers was given by Brownell, Flack, Davis and Rice (1987). Diffusers in turbomachines turn a portion of the kinetic energy which the impeller put into the fluid into static pressure. Vaned diffusers offer performance improvements over vaneless diffusers provided that separation in the diffuser vanes can be avoided. Brownell et al. combined

¹ Also mentioned in this article are their research activities with fluorescent helium bubbles. Mixing a 10% solution of Leucophor dye (used to dye the tuft fibers) with a standard bubble mixture produces brightly fluorescent bubbles if illuminated by UV light. They had not, at the time of this article perfected the technique, and no results were shared.

both tuft and dye injection in their plexiglass flow visualization tank and swirl generator to visualize flow through four- and six-vaned diffusers. Tufts and dye were used to indicate flow directions and points of separation. This was important information when examining the influence of diffuser angle on performance of the turbomachine. The tufts used in these tests were apparently unique. The tufts were 1.3 cm long and made from the tip of a black marabou plume. The tufts were placed along anticipated streamlines of the flow, and were also applied with more density in areas where separation was suspected.

2.4.3 Tuft Grids

In addition to surface flows, tufts can be used to explore external flows, or flows in planes. By this is meant the use of tuft grids, tufts supported on wires or entire grids of wires with the tufts affixed at the nodes of the wire mesh which are placed perpendicular to a flow. Such tuft grids are commonly used in wind tunnel testing and are observed and photographed from the downstream side of the flow. Tuft grids can also be made of taut strands of wires run in one direction with tufts attached at intervals along these wires.

Grids of tufts can be used in conjunction with measurements made by hot-wire anemometry made at the tuft points to provide both velocity direction and magnitude. Such an experimental method was employed by Akiyama et al. discussed earlier in the survey of particle tracing techniques. The flow inspected was a ventilating flow through a rectangular room, a chamber 18 cm x 18 cm. The grid wires used were 0.29 mm in diameter. The tuft material used is described as being shiny silk threads of 25 mm in length, and they have been secured at the nodal points of the grid. These tufts showed a velocity direction at a minimum velocity of 10 centimeters per second. The nodal points of the grid are 20 mm apart. Tuft grids have been made from a variety of materials and for many applications. Aluminum-tuft grids have been employed in studies of helicopter lifting rotors, rotor down wash, and rotor ground vortices (Wada and Hayafuji, 1985). Also in conjunction with anemometer studies (as they are used quite frequently), tuft grids (made of silk fibers on a steel wire, 0.8 mm in diameter with 30 mm separation) have been employed in studying gas flow fields in coal-fired natural circulation boilers (Obata, Miyao, Kurata and Kusakari, 1979).

CHAPTER 3

SURVEY OF METHODS OF ANALYSIS

3.1 Introduction

Panel methods (sometimes referred to as boundary element methods) and lifting-surface (or vortex-lattice) methods have long been important design and analysis tools in the aerospace industry. These methods model the equations of ideal, or potential flows, but can, when coupled with other methods (finite difference for example, using a hybrid computation scheme as described by Egolf and Sparks, 1987), model viscous and compressible effects. Viscous effects can also be accounted for through the use of drag coefficients and nonlinear free vortex sheet calculations. Panel and vortex-lattice methods (VLM) of computational fluid dynamics are typically introduced to students of aerodynamics in textbooks (Anderson, 1984) for fundamental aerodynamics courses. Finite difference and finite element techniques are certainly important and useful, but the statement given above is meant to express the tradition and acceptance of panel methods for giving estimates of aerodynamic loading in many applications. Generally speaking, those with a mechanical engineering background seldom become familiar with panel methods and the VLM. There is certainly a wealth of literature and accepted panel codes for aerodynamic applications, from isolated wings through entire aircraft bodies. In the rotating-frame-of-reference category, the available panel and lifting-surface literature shows uses for helicopter rotor (in hover and forward flight), airplane and ship propeller, and wind turbine analyses. There appears to have been little or no published work involving the use of the VLM in axial-flow fan studies, although a proprietary report (Van Houten, 1986) which is said to consider the application of a ducted propeller lifting-surface code to the ducted fan problem is mentioned in the literature. In the United Kingdom there has apparently been more effort to use vortex element techniques in axial and mixed-flow fan studies, judging from the literature cited by Lewis (1991), but this literature is difficult to acquire.

There may be several reasons for the paucity of literature in the public domain that demonstrates the effectiveness of panel methods in the modelling of axial-flow fans. The effectiveness of blade element theory, which must be applied judiciously and with experience due to its empirical aspects, is mixed. Such general factors of axial-flow fan design (for use in HVAC, warehouses, and poultry industry applications) as cost of design and manufacture, strength and safe performance generally do not warrant expensive computation. The profile of companies producing this type of fan is that they are small to medium sized and regional. The products are produced close to market in order to decrease shipping costs, and, therefore, a number of these companies have emerged whose market

geographic areas overlap relatively little. For these reasons, the need for expensive research and development, including computational analysis, is not pressing. However, as computer costs have decreased and capabilities have increased, and markets have expanded and become more competitive, there has come to exist a need for analysis and design tools which are trusted, worth the effort of using, robust, and not too computationally expensive. While there may be a need for a tool which could be used for optimization computations, there is an initial need for tools which provide engineers with analysis; torque and horsepower requirements to meet certain flow rate, pressure loading and rotational speed conditions for various design geometries.

A goal of the present work is to demonstrate the efficacy of a lifting-surface technique, the vortex-lattice method, in analyzing axial-flow fans. It is expected that this work will lead to analysis of axial-flow fans with more three-dimensional flow characteristics than can be attempted by blade element theory. Such machines, incorporating greater skew and rake variation than current designs, might exhibit improved performance characteristics. Lifting-surface (or vortex-lattice) methods are well suited to the flow around thin airfoils such as fan blades fabricated from stamped sheet metal, and they are similar to propellers for which the method had earlier success. Such blades are commonly employed because they are cheaper than airfoil shaped blades and have but little less performance. Based upon these factors and upon consultations with persons in the field of computational fluid dynamics in turbomachinery, it appeared that the most promising method of predicting performance characteristics of complex three-dimensional axial-flow fan blading would be a lifting-surface method (Burmeister and Amadian, 1988). Before looking at panel method applications which are similar to axial-flow fans, a review is first presented of the body of axial-flow fans analysis that has been reported in the open literature.

3.2 Axial-flow fan studies and analyses

In general, three-dimensional, viscous, and compressible analysis of axial-flow fans is not warranted. The majority of designers use an analysis that is based on two-dimensional potential flow with the more complicated flow behavior accounted for by empirical adjustments (Wallis, 1983 and Bass, 1987). These two-dimensional analyses of axial-flow fans are used in two ways; either as an isolated airfoil or as a rotating cascade. The method used depends upon the solidity ratio of the blade. The blade solidity is defined as the chord length to circumferential spacing length at a given rotor radius; another way of defining it is as the ratio of blade surface area (projected in the direction of the flow) to annulus flow area. Either method can be used for the analysis of a given machine, depending on the solidity at that radius, with the cascade method used for solidities greater than about 0.7, and an airfoil approach used for solidities less than 0.7. The fans of interest in the present study will produce small pressure rises and have a low

blading solidity. These blades previously have been designed based on the two-dimensional approach without cascade correction. Interference factors are often used in designing the blading near the root to take into account blade-to-blade interference. Since these interference problems are also viscous in nature, designs primarily have been based on testing and operating experience.

A recent example of this design/analysis approach is given by Wright and Ralston (1987) using computer codes developed by the Carrier Corporation. The breakdown in the analysis was believed to be caused by flow reversal and recirculation in the hub/spider region of the fan. Flow conditions for through flow in axial-flow fans can be considered as those of a two-dimensional cascade of blading. The deflection of flow along the blade will vary, but the flow conditions at various radial sections of blading are considered as "two-dimensional" flow. This concept, which has been used for a number of years in axial-flow turbomachinery design (NASA SP-36, 1965), holds for the case of radial equilibrium and stems from the early work of Glauert (1926). Essentially, it appears Wright and Ralston are using blade element theory with NACA two-dimensional cascade corrections from NASA SP-36 with additional corrections for deviation from the mean flow turning angle due to viscous effects, viscous losses, mild three-dimensionality, flow leakage, flow blockage, blade solidity and flow separation. While these techniques work to produce a rough fan design, they do not appear to bear up to scrutiny for plate blading fans as found by Wright and Ralston (1987);

"A fan that is considerably more difficult to analyze is ... characterized by having four stamped sheet metal blades mounted on a steel "spider" without having a true aerodynamic hub installed. Although such a fan may be typical of HVAC practice the absence of the hub leads to predictions of reversed flow in the hub region of the fan, causing a breakdown in the analysis because of flow reversal and recirculation through the open region. The performance estimates ... were achieved by artificially including a hub for the fan and systematically reducing hub diameter to a minimum "acceptable" size. While the results are similar to the test data, they must be viewed with a little caution. In a more general sense, the limitations and approximations of the computer codes must be kept in mind..."

Wright and Ralston's efforts are admirable, considering the complexity of the problem, and their results for fans with aerodynamic hubs and shrouds show good agreement with measured performance curves at design conditions. Their programs are useful in that they appear to predict the trends and trade-offs in fan design and the interaction of many fan variables including noise prediction.

Dhaubhadel, Akay, and Charles (1988) gave results of a three-dimensional potential and compressible flow finite element analysis applied to flow through a rotating fan. Their computations were performed using a mesh specialized for the complicated geometry of forward- and back-swept, twisted blades and applied to a rotating coordinate system. The grid generation used was automated (basically by using polynomials) in such a way that the complicated geometry of the fan (in this case an automotive cooling fan) can be efficiently and conveniently varied, resulting in a design and experimentation tool. The authors have surveyed the literature, finding no previous finite element analysis publications for such fans. The utility of the finite element method for the computation of complex potential flows was said to be demonstrated by the agreement between measured and predicted efficiencies at design conditions. Verification by direct comparison between velocities and pressures predicted by the computations and measurements at design conditions was not provided. Comparison between measured and predicted efficiencies at off-design conditions was not nearly so good, as one would expect, due to stall and other non-ideal flow phenomena. An improved design based on pressure rise, lift, and fan efficiency was computed (though not experimentally verified). This was accomplished through trial and error computations to increase the blade loading where possible, while also preventing blade unloading over the blade surface. The particular geometry of the fan, motor size, and motor rpm were not given. Flow rates in the range of 125 to 1600 cfm were computed.

The effect of blade skew on noise production and aerodynamic performance was investigated by Brown (1977) and Wei and Zhong (1988). Wei and Zhong performed a comparative experiment in aerodynamic performance and noise emitting characteristics between a straight radial rotor and a skewed bladed rotor. As was found earlier by Brown (1977), the overall efficiency was better than for radial blades, especially at low volumetric flow rates. However, a low total pressure rise was associated with forward skewed rotors at the same volumetric flow coefficient. The rotors tested were followed by a stator and were in a tube with a hub/annulus wall diameter ratio of 0.39. The skewed blade showed a greatly reduced noise level from rotor stator interaction. The improvements in efficiency were believed to occur due to less aerodynamic loss, and to better secondary and blade flow characteristics. It was shown that axial velocity and stagnation pressure rise decrease from root to tip for a forward swept (skewed) blade, while the opposite is true for a straight radial-bladed fan. Lower wake and tip losses were said to occur when using a forward swept blade. Another example of investigation into blade sweep as a means of reducing noise while not adversely affecting performance was given Wright and Simmons (1990).

Measurements of axial-flow fan entry flow were made with both static and rotating hot wire anemometers by Scoles et al. (1981). The paper described measurements which were made to study the effects of inflow conditions on the

noise generated by a 40 kW, 0.56 m diameter, seven-blade ducted fan at speeds up to 5000 rpm. The focus of the study was a 1.25 m diameter, hemispherical honeycomb flow conditioner which could also be fitted with an internal gauze liner.

A singularity technique, similar in approach to the vortex element method, was used by Yadav and Singh (1987) to analyze vaned centrifugal pump flow fields. The theoretical model used was two-dimensional and used a source and displacement (rotational component of velocity) singularity to represent the impeller. The vanes on which vorticity and pressure distribution were computed were modelled using vortex elements.

3.2.1 Fan Design and Measurement Literature

Eventually, a fan analysis program should be turned into a design tool. Considering this fact, a brief review of design oriented literature is presented. A simple method for the prediction of the performance of cooling tower axial-flow fans using blade element theory was given by Forman and Kelly (1961). The method assumes that the performance of the entire fan can be represented by blade element analysis at the 3/4 radius (from center). The calculation neglects tip losses and non-uniform inlet velocity distributions and numerous other non-ideal effects. The intent of the technique is not design, or analysis, but rather, a method by which a prospective buyer of a fan might verify performance data given by the fan's manufacturer.

Pierzga (1980) verified the results of a streamline curvature numerical analysis method. He conducted an investigation in which comparisons were made between analytical and experimental data of an axial-flow fan. Using loss model calculations to determine the proper outlet flow deviation angles, the flow field in the hub-to-tip plane of the turbomachine was calculated. To obtain the necessary data to verify the blade-to-blade solution, internal blade row data were also collected. The internal blade row measurements were obtained by using a rotating circumferential traversing mechanism which was designed and implemented during that investigation. Along with this set of survey data, the static pressure distributions on the pressure and suction surfaces of the test rotor were also obtained.

Homicz, Lordi and Ludwig (1979) reported the results of a program designed to study the influence of three-dimensional effects on the aerodynamics and acoustics of axial-flow fans and compressors. To avoid numerical solutions of the full nonlinear three-dimensional equations, a linearized analysis was employed. The blades were represented by pressure dipole singularities in a lifting-surface formulation. Comparisons are presented between the present results and those of two-dimensional strip theory.

Franke (1978) undertook a project to investigate the distribution of unsteady pressure on the blades of a stator blade row in an axial-flow turbomachine which operated in the wakes of an upstream rotor. These unsteady pressure distributions were measured using a blade instrumented with a series of miniature pressure transducers which were developed in that project. Several geometrical and flow parameters (rotor/stator spacing, stator solidity and stator incidence angle) were varied to determine the influence of these parameters on the unsteady response of the stator.

A scheme to accelerate the design of axial-flow fans was presented by Caglar (1988). He described a method founded on blade element theory with aerodynamic effects of a variety of geometrical parameters taken into account. In order to minimize the outlet losses in axial-flow fans and to boost the static efficiency, Blaho (1975) found from measurements on cascades made up of cambered blades that cascades "steeper" than usual seem to offer the most favorable design. The "steepness" of cascades are defined relative to the approach angle to the cascade (the angle between the approach velocity and the normal to the cascade plane of rotation). A steep cascade is one where the approach angle is small.

A design method based on the use of carpet plots for optimum operating conditions for a variety of airfoil sections was presented by Hay and Metcalf (1978). These plots are taken from data and replotted optimum values of angle of incidence versus camber angle. Airfoils considered applicable for the axial-flows fans studied were: NACA 65, Göttingen, C4, and cambered flat plates. Although many airfoil sections (F-series, NACA 65-series, Clark Y, Göttingen, and RAF 6E to name a few) have been used for axial-flow fan blading, this study (Hay and Metcalf, 1978) was limited to improving the utility of plate blading. This topic was of special interest to fan manufacturers because of the possibility of fabricating sheets of steel into exotic geometries. It may also be possible to produce flat underside blades similar to the Göttingen airfoil from sheet or plate metal by adding a manufacturing stage where the flat undersurface is created by bending under the flat surface. According to Wallis (1983), a flat underside blade is most suitable for high performance low pressure fans.

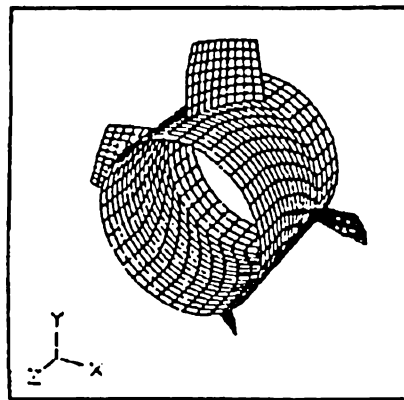
Recently, a meeting in the United Kingdom held by the Institution of Mechanical Engineers offered insight into current design and analysis techniques for industrial fans. A sample design calculation based on using plots with a two-dimensional cascade analysis employing interference coefficients, and empirical data was demonstrated by McKenzie (1987) and Hay, Mather and Metcalfe (1987). McEwen, Wilson and Neal (1987), working on a prototype mixed-flow cooling fan for a quiet heavy vehicle (QHV), presented an interesting design example. They formed prototype fan blades by hot pressing sheet steel on dies produced on a numerically controlled milling machine. The results they presented for a flat-

bladed fan (thus eliminating the need for the dies and pressing operation) were comparable to the results of the pressed blades. Smith (1987) described the implementation of the design methodology for axial-flow fans (with or without guide vanes), using radial equilibrium with a series of concentric blade sections. Calculations were performed on the six boundaries of these sections were performed either as a cascade of airfoils or as an isolated airfoil, depending on blade solidity. Essentially the goal of the work was to predict the pressure rise achieved as calculated from the average change of momentum, using radial equilibrium, actuator disc theory, and various empirical data (cascade data, lift and drag coefficients, diffusion factor, etc.).

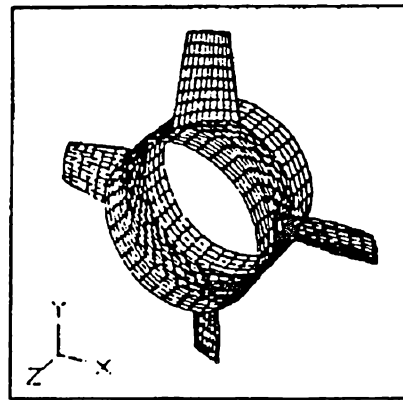
Wallis has made numerous contributions to the study of axial-flow machines. In addition to his comprehensive text on the subject (Wallis, 1983), he has written numerous articles. In Wallis (1968a), he applied theoretical analyses along with experimental data and experience to guide blade element theory in design and he extended this to optimization studies in Wallis (1968b). Wallis (1972) makes a study of published airfoil data and identifies an optimum aerodynamic fan blade airfoil section.

The ultimate stage of evolution of the design method is the expert design system. Andrew (1988) presented the concept, and made reference to its use in a fan design expert system as given by Tong (1985). Little information about the axial-flow fan code used by Tong (1985) was given in his paper. The design code is described as a "fast quasi-3D indirect axial fan design code used to obtain the relationship between flow conditions and blade geometry parameters." Judging from the inputs to the program (the tip and hub diameters, chord lengths, rotational speed, number of blades, mass flow rate, static pressure rise distribution and other control parameters) and the program output (various flow conditions, chamber angle, stagger angle and power consumption), it was probably a blade element model. The goals of that design study were to minimize noise produced and power required, while meeting pressure and flow requirements and other constraints. When the design code was coupled with Tong's expert design system and appropriate rules were provided to the system, the "artificially intelligent" system produced an improved design, as illustrated in Figure 3.1.

It is interesting to restate Tong's observations in comparing the design program operation by the human expert versus the computer expert. The computer was able to examine an estimated ten times more numerous trial geometries than the human could and could do so with smaller trial increments. The subsequent increase in computation time was offset by the computer's ability to setup and analyze the design program's input and output at a much faster pace than the human designer. The result was that the design time required by the computer was somewhat less than for the human, and the computer designed fan performed as well (if not better than) the human designed fan.



Initial Fan



New Fan Design Using AI Technique

	Initial Fan	New Fan	Difference
Tip Diameter	16.5 cm	18.5 cm	+ 12%
Chord Length	10.2 cm	7.6 cm	- 25%
Energy Consumption	2.19 Watts	1.44 Watts	- 34%
Noise Level	48.3 db	46.8 db	- 1.5 db

Initial and Final Designs Using EXFAN

Figure 3.1 An example of an axial fan designed by EXFAN (Tong, 1985)

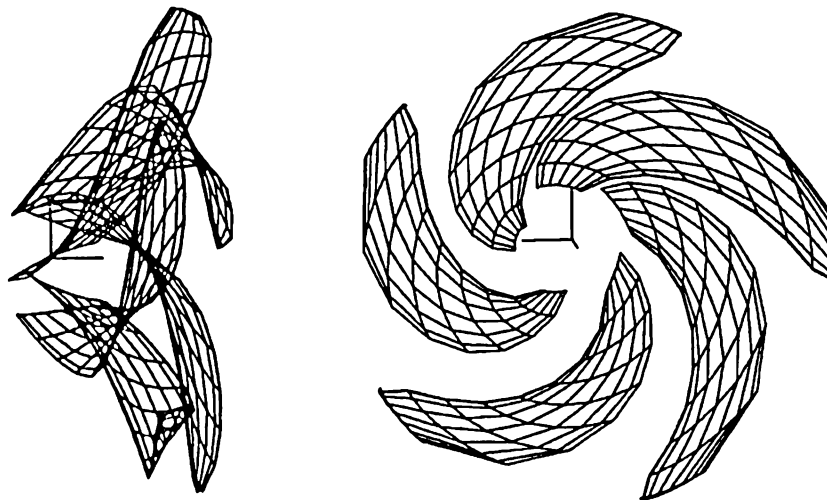


Figure 3.2 An example of a propeller, DTNSRDC propeller 4384, designed with large amounts of rake and skew and modelled by author with data from Kerwin and Lee (1978)

With this last study from the literature in mind, why don't we turn the problem over to such an expert system? First, it was not known how well the machines in Tong's study actually performed as no testing was done. Second, it has previously been found that the analysis/design tool that Tong presumably used (blade element theory) does not provide adequate results for all machines (Wright and Ralston, 1987). Third, unconventional blade geometries incorporating large amounts of skew and rake and, therefore, highly three-dimensional flow phenomena violate some of the assumptions of blade element theory. Some axial-flow fan studies (Brown, 1977; Wei and Zhong, 1988 and Wright and Simmons, 1990) have shown that these more "exotic" geometries can have performance benefits and produce less noise.

An example of an exotic marine propeller is given in Figure 3.2. Interest in marine propeller designs such as this are fueled by their improved vibration, noise and cavitation characteristics. In a similar design application, advanced turboprop propulsion for aircraft provides greater efficiency than existing turbofan powerplants at similar performance according to Maser, Fertis, Aiello and Chamis (1990) in their study of the SR5 blade. In addition to the possibility of fuel saving, such designs are said to have significantly less noise and be capable of operating well in the transonic flow regime. However, the complexity of the blade's geometry must be balanced with practical structural and fabricating constraints. Lifting-surface and boundary element methods have provided a good way to analyze these "highly sculptured" rotors.

3.3 Propeller Lifting-surface and Other Panel Method Analyses

The use of lifting-surface methods employing the vortex-lattice method applied to the investigation of axial-flow fans is not reported, but its use in the analysis of marine and airplane propellers can be found. While the surface panel and vortex-lattice method techniques have been used for years with great utility in aerodynamic analyses, their application to marine and airplane propeller work as demonstrated by Kerwin and Lee (1978), Greeley and Kerwin (1982), Hess and Valarezo (1985), and Kerwin, Kinnas, Lee and Shih (1987) is more recent and continues to be a topic of ongoing research.

The lifting-surface theory is based on the assumption of small disturbances and is, therefore, best suited to thin blades as the singularities are placed on the mean camber surface. In the case of the vortex-lattice method, the lattice end points can be placed on the blade mean camber surface without considering thickness, and with thickness taken into account by using source singularities also placed on the camber line. In order to more accurately account for thickness (either "thicker" blades or the ducts surrounding a ducted propeller) a panel (or boundary element) method with singularities covering the object's actual surface is used. This technique was demonstrated by Hess et al. (1985), Kerwin et al.

(1987), Morino and Kuo (1974) and Kinnas and Coney (1988). A direct formulation of the boundary element method for thin airfoils was given by Dragos and Dinu (1990).

A detailed discussion of the vortex-lattice technique is left until Chapter 4 when the basic concepts of lifting-surface (or vortex-lattice) methods will be outlined. Because the lifting-surface techniques might be new to mechanical engineers (they are normally of concern to aero- and hydrodynamicists), only descriptive review is presented, leaving theoretical and formulation issues to later discussions. References will be made to works in which more rigorous derivations are presented. Works of particular assistance in understanding the fundamentals of the technique include Kerwin (1989), Anderson (1984) and Lan (1988).

3.3.1 Marine Propeller Studies

Kerwin (1986) provided an excellent review of the topics related to, and techniques applied to, solution of the analysis and design problems of marine propellers. This discussion as well as much of Kerwin's work addressed single propulsors operating under the assumption of no cavitation. Since the present work of this study uses the results of Kerwin and various colleagues and students, this article is an excellent starting place to review past work. For the interested reader, reviews of techniques and literature for marine propeller design and analysis in unsteady flow were given in Kerwin (1986), and this discussion will not detail these topics.

Kerwin and Lee (1978) presented a lifting-surface technique to analyze propeller performance in both steady and unsteady flow which is named **Propeller Unsteady Flow-2 (PUF-2)**. Much of their work remains in the **Propeller Steady Flow-2 (PSF-2)** code, as will be seen in Chapter 4. Their approach used a vortex-lattice and line source representation of blades where highly complex blade geometries could be described and discretized. Trailing wake elements were prescribed to contract and roll up, and a mechanism (used also in **PSF-2**) for tip vortex separation was included. An ultimate wake consisting of a single hub and concentrated tip vortices were used in the same manner as in the **PSF-2** code. A highly discretized "key" blade with coarse singularity spacings on subsequent blades was used. Non-ideal flow phenomena were accounted for in a number of ways, all of which are also employed in the **PSF-2** code. A viscous drag force was calculated by making use of experimental values for viscous drag coefficient; in this case a constant drag coefficient was used over the entire blade span. A constant suction efficiency factor (which is actually a decreasing function of radius) of $1/3$ was used at all radial locations on the leading-edge suction force. The effect of boundary-layer thickness and separation on lift was approximately taken into account by reducing the pitch angle at a given radius according to an empirical correction. The inlet velocities were arbitrarily allowed to vary with

radius. In the unsteady case, the boundary value problem with unsteady vortex shedding was solved at angular intervals through several revolutions of the blade until the oscillating pattern of the blade loading develops and converges, usually this required two revolutions. It was shown, as with non-rotating wing lifting-surface analyses, that increasing the number of panels in the spanwise direction does not affect solution convergence as much as increasing the panel number in the chordwise direction. This technique was later extended to include predictions of cavitation inception in a code called **PUF-3** (Lee, 1979).

The **PSF-2** code used and modified in this study was the work of Greeley (1982). However, from the statement in the preceding paragraph it is noted that much was built-up from earlier work. Not only did Greeley address the problem of propeller steady flow, but also he developed (along the lines of **PSF-2**) a computer code, **Propeller Blade Design-10**, which solved the inverse, or design, problem for a propeller in steady flow (Greeley and Kerwin, 1982).

Greeley (1982) constructed a "semi-free" wake model for **PSF-2** so that the users need not necessarily know experimentally observed features of the propeller wake as with the earlier work of Kerwin et al. (1978). Kerwin et al. (1978) required the user to set the radius of the trailing wake roll up points, the angle between the trailing edge and the roll-up point, the pitch angle of the outer extremity of the transition wake, and the pitch angle of the ultimate tip vortex helix. A parameter study undertaken by Kerwin et al. (1978), showed that the wake pitch was a critical parameter in performance prediction. It appeared that it would be better if this value (transition wake pitch) were computed as part of the problem solution rather than providing it in the beginning. Greeley (1982) devised a wake alignment scheme which provided for a radial and axial distribution of pitch through the transition wake that more accurately predicted the wake behavior. Through a set of interpolation functions, the wake geometry in Greeley (1982) is calculated from estimating the radius of the ultimate wake (both the hub and tip vortices), the axial extent of the transition wake, and the contraction angle of the tip vortex. Greeley (1982) also used the laser doppler anemometry measurements of Min (1978) to arrive at an ideal vortex core size to account for the viscous effects on the self induced velocities of the trailing tip vortices in the transition wake. More details of the iterative wake alignment scheme will be given in Chapter 4.

Results from Greeley (1982) and Greeley et al. (1982) demonstrated improved agreement between the numerical predictions and experimental performance data over Kerwin et al. (1978). Comparisons were made in both Greeley (1982) and Kerwin et al. (1978) with a variety of propeller geometries. An idea of the uncertainty in the performance predictions is given by Greeley as he provides experimental data from two water tunnels for the same type of blade. The results of both Kerwin et al. (1978) and Greeley (1982) appeared to predict

thrust and torque coefficients within this uncertainty provided the blade geometry incorporates little rake and skew. When blades having more rake and skew were studied, Greeley showed some improvement in agreement over Kerwin et al., but Greeley's results still lacked good agreement at off-design conditions for the most highly skewed and raked propellers. However, it must be pointed out that even the two experimental studies cited by Greeley disagree more noticeably at off-design (low) advance coefficients as shown in Figure 3.3.

Greeley (1982) also added a "local" tip-flow vortex-lattice model which was computed following a calculation that used PSF-2 for the global boundary value problem. The tip flow model allowed for flow separation along the leading-edge, and a very fine discretization of the blade in the "local" tip-flow domain which provided a more accurate blade loading estimate in the tip region where cavitation is of particular concern. An example of the "local" flow domain problem is given in Figure 3.4. Calculations were performed in the "local" flow domain for the singularities, now the only unknowns, in the tip flow region. Since the induced velocities due to singularities on all other blades, wakes, and the rest of the key blade are part of the global problem which has already been solved, these effects are included as part of the inflow velocity. The local flow analysis also includes a technique which predicts the point of separation, after which flow over the entire outboard section of the blade is assumed to be separated. An analysis of data for leading-edge vortex breakdown led Greeley (1982) to include the effect of vortex breakdown in his analysis of the leading edge separated flow.

Results from numerical studies using the leading-edge vortex sheet model led to the following conclusions (Greeley and Kerwin, 1982). The blade loading in the extreme tip region of the blade was low as evidenced by a drop in bound circulation. Inboard, from about the 0.95 full span to the point of local re-discretization (R_{cut} in Figure 3.4), blade loading is seen to be higher by about 5%. Plots of bound vorticity showed that, as expected, separated flow decreased the loading near the leading-edge; the flow converged to the non-separated solution from the latter half of the chord to the trailing edge. The computed thrust coefficient for the separated flow model was about 2% below the global solution, and the torque coefficient was about 6% below that from the global solution. Difficulties in computing induced drag on a swept vortex-lattice were said to be the cause for a larger increase than expected in computed torque. A final recommendation was that more work needed to be done with the leading-edge vortex-sheet modeling. Good sources for vortex-sheet modeling can be found in studies of high angle of attack aerodynamics (Rom, Almosnino and Gordon, 1987), the study of free vortex sheets using a time-dependent procedure as given by Behr and Wagner (1988), and a variety of discussions on these topics given in workshop proceedings (NASA SP-405).

The PSF-2 computer code was extended by Kim and Kobayashi (1984) to

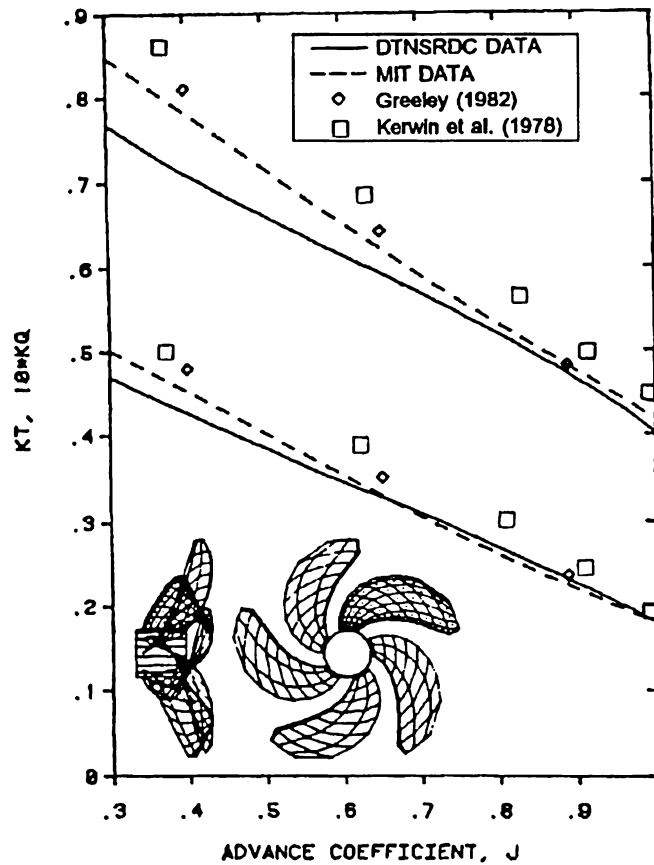


Figure 3.3 Comparison of predicted and experimental performance data, K_T and K_Q (thrust and torque coefficients, respectively), modified from Greeley (1982) with Kerwin et al. (1978) data added

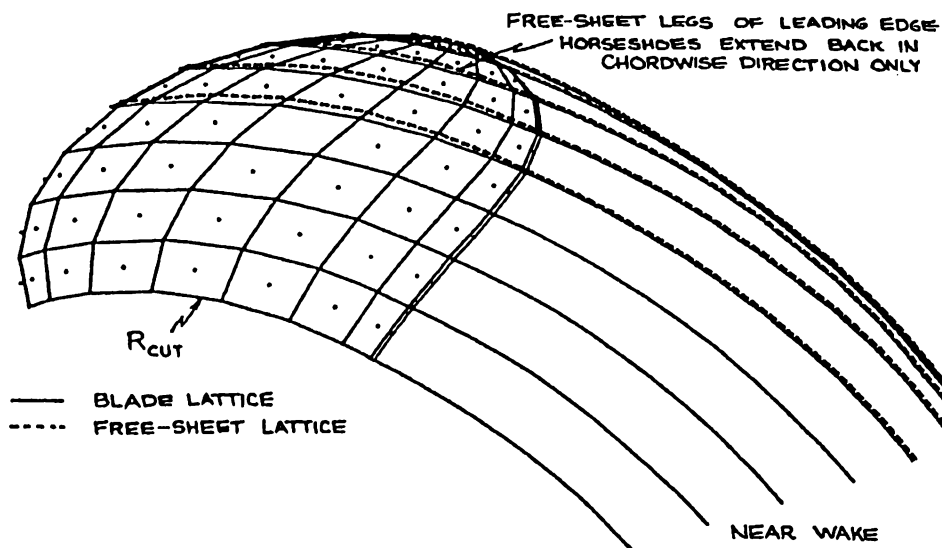


Figure 3.4 Model of leading-edge vortex sheet from Greeley (1982)

the computation of blade surface pressures. Hess and Valarezo (1985) compared results from their panel method with those of Kim and Kobayashi, and found that away from the leading-edge (an approximate chord fraction of 0.2) the results agreed both with each other and with measurements. Nearer the leading-edge, where no measurements were taken, the computations diverge, and the panel method is able to capture a pressure minimum at the leading-edge that is known to exist from two-dimensional conformal mapping solutions. This behavior of the solutions of panel methods near the leading-edge is a strength of panel methods over vortex-lattice methods for thick blades. However, this deficiency of vortex-lattice methods could be rectified by the use of a Lighthill correction as discussed by Greeley and Kerwin (1982), and is only important for the case of finite leading-edge radii. The application at hand seems better suited to the vortex-lattice method in that the fan blades under consideration are thin, cambered plates.

Another modification to the **PSF-2** program was undertaken by Wang (1985), who included hub effects through a surface panel representation of the hub. The hub was modelled using surface panel elements of concentrated vorticity, and the solution to the hub problem was solved in an iterative manner. First, the **PSF-2** program was run and the singularity strengths without the hub were then found. Then the induced flow due to the hubless blades was used as the boundary condition for the hub singularity problem, and the hub singularity strengths were found. For the second and succeeding iterations, the induced velocities of the hub singularities were included in the fan program, and a new set of blade singularities were then computed, this time the hub effect was included. This procedure was said to converge to a solution after three or four iterations. From laser-Doppler anemometry measurements of the circumferentially averaged tangential velocity just downstream of the blades, Wang found the distribution of circulation given in Figure 3.5. Except for the spike near the hub which was due to viscous effects not modelled by the calculations, the vortex-lattice calculations which include the hub showed a definite improvement over the calculations which did not include the hub.

More recently, ducted propeller studies can be found in the literature. A low order velocity potential-based panel method was used to model ducts (with a vortex-lattice blade model) and unducted blades by Kerwin, Kinnas, Lee, and Shih (1987). The potential-based method offered the following advantages over velocity-based panel methods: more accurate results for thin bodies, influence coefficients one order of magnitude less singular with subsequent less sensitivity to panelling errors, the data storage requirement is less since the potential is a scalar value, and greater accuracy of potential for internal flows. Potential-based panel methods do, of course, require post processing to determine pressures, velocities, and forces. The code developed for this application is called **Ducted Propeller Steady Flow, DPSF-2**.

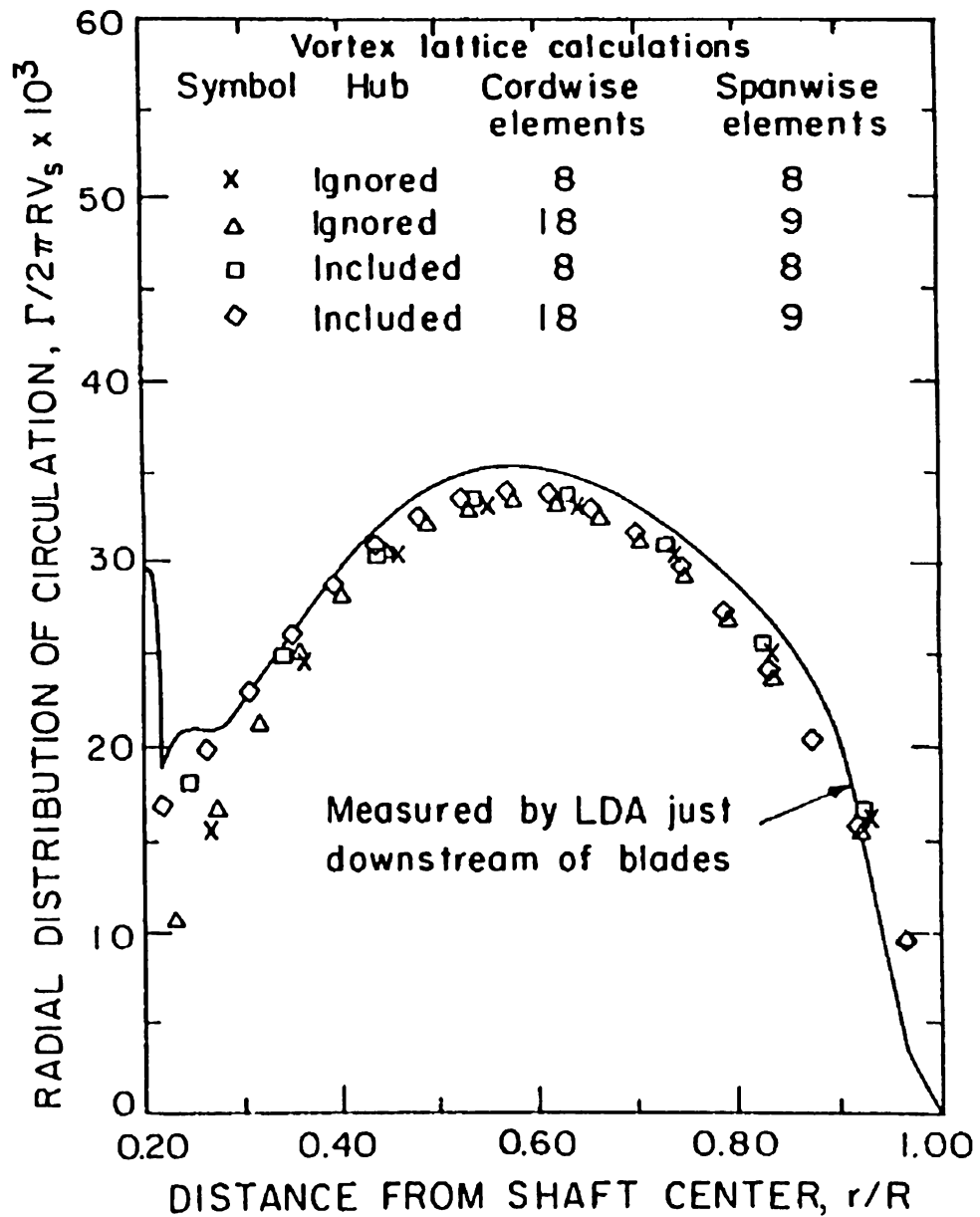


Figure 3.5 Comparison of vortex-lattice calculations for radial circulation distribution with and without hub effects and experimental measurements (Wang, 1985)

The wake model used by Kerwin et al. (1987) was essentially that used **PSF-2** by Greeley (1982). But, instead of using vortex elements, dipole panels of strength determined by a trailing edge Kutta condition were used in the wake. The Kutta condition used by Kerwin et al. (1987) to determine the wake dipole strengths was iterative, and used the difference between the potentials on the upper and lower panels at the trailing edge as an initial guess.

When Kerwin et al. (1987) turned to the problem of a ducted propeller they chose to use the vortex-lattice model of the blade in **PSF-2** and modeled the duct using the panel method. The problem was solved in an iterative manner similar to Wang (1985) in his solution of the hub effects. The main difference (besides the added complexity of the duct panel method) was that now the duct/hub problem involves solving for the velocity potential, and the blade solution used the vortex-lattice method where velocity enters into the boundary conditions. Initially, the potential flow problem around the hub and duct were solved. Using the potential field from the duct/hub problem, velocities were computed at the control point locations on the vortex-lattice model of a blade. The vortex-lattice singularities were then computed using the velocities due to the duct/hub model as part of the spatially varying inlet flow applied at each control point. The velocities induced by the vortex-lattice model of a blade were calculated and converted to a perturbation velocity potential which was added to the boundary condition applied at each collocation point when the duct/hub problem was solved during the next iteration. The calculation was said to converge within seven iterations.

In order to reduce numerical errors for the zero-tip gap assumed in the ducted propeller they studied, Kerwin et al. (1987) found it necessary to modify the more conventional panelling procedure, shown on the left in Figure 3.6. It was found that a better solution was given with a panelling arrangement such as that shown at the right in Figure 3.6, where the panels are arranged in a helical manner with a pitch matching that of the propeller blade tip. This arrangement resulted in very elongated panels if the pitch of the tip was quite low. For such cases, it might be better to compromise and use the best available pitch angle on the duct (Hughes, Kinnas, and Kerwin, 1992). An example of the duct, hub and blade panelling arrangement used by Kerwin et al. (1987) is given in Figure 3.7. An analysis was provided by Kerwin et al. (1987) where they argued that the potential flow model was valid for tip gaps of zero (ideal) and tip gaps of greater than 1% of the blade radius. For tip gaps between these values, they pointed out that viscous effects on the crossflow in the tip gap were of concern.

A further innovation used by Kerwin et al. in **DPSF-2** was their choice of matrix solver. The simultaneous equations solved in panel methods result in fully populated matrices, and this is the case with the VLM also. Typically, as is the case with **PSF-2**, these matrices are then solved using Gaussian elimination which is a tried and true method, but becomes computationally more expensive as the

size of the matrix increases. An iterative matrix solver then becomes an attractive tool. Kerwin et al. (1987) employed an "accelerated" iterative matrix solver originally developed for use with velocity formulation panel method (Clark, 1985). Kerwin et al. (1987) gave the following example: if a system of 2000 unknowns was solved on a DEC Microvax II, the iterative matrix solver took about fifteen minutes; for the Gaussian elimination case, they estimated that it would require an hour provided that it could be performed in memory. However, the memory limitations for this case were such that external storage was required, and the resulting time for the operation took more than an hour. Results for duct discretizations of 80x80 (or 6,400 unknowns) were given by Kerwin et al. (1987) with good convergence for 60x60 panels. The need for an iterative solver in these cases was, therefore, apparent.

Kinnas and Coney (1988) employed a lifting-line representation of propeller blades, combined with panel method models of the airfoil ducts in which they operated, in their study of optimal radial distribution of circulation for ducted propellers. An iterative wake alignment procedure was not used due to the necessity of repanelling required on the duct. The requirement of having matching grids on the duct and blade tip is discussed by Kerwin et al. (1987). The technique of representing the duct by using an image vortex system is also discussed, but is left to future, more detailed, study. Using this technique would save a great deal in panelling calculations, and would be capable of representing cylindrical ducts. Kinnas and Hsin (1992) have extended the boundary element analysis to the unsteady regime, using a time marching procedure.

Another boundary element analysis of the propeller flow problem was given by Yon, Katz and Ashby (1991) who (like Kerwin et al., 1987) used a velocity potential formulation. Yon et al. presented results and comparisons with surface pressure from other sources for marine propellers. However, their stated goal was to produce a technique that could be used for other applications; aircraft propellers or any other unsteady problem where aerodynamic bodies are moving relative to each other. This unsteady class of problems of aerodynamic bodies changing with time includes a propeller rotating relative to a solid body moving with a constant velocity, and an aircraft wing with flaps moving relative to the wing. They added their modified formulation incorporating the rotational and unsteady effects into the latest version of the panel method code PMARC. An unsteady free-wake shedding procedure where the wake develops as the unsteady problem was solved by shedding dipole panels downstream whose orientation was such that they remain aligned with the flow. No viscous effects were considered; that was an area of future work. Approximately 3000 (about 2400 on the propeller, and the rest on the solid body) panels were run to steady state (when thrust and torque computations stabilize) after 20 time steps, or less than one revolution, and this took 10 minutes on a CRAY-YMP computer. Some difficulty in convergence was noted at low advance ratios, and higher advance ratios were found to converge quickly and

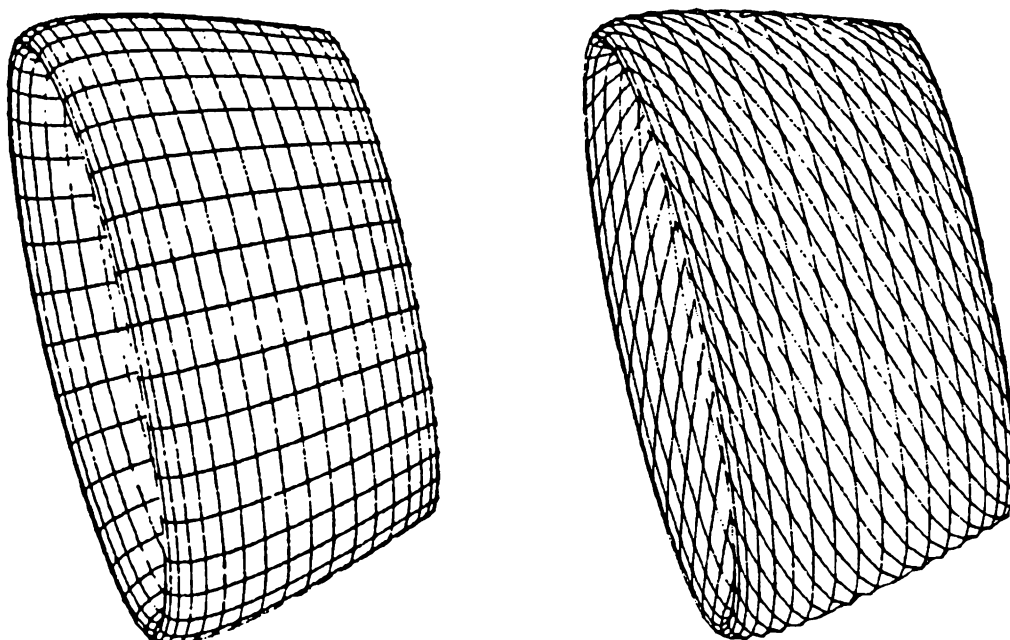


Figure 3.6 At left, a conventional panelling scheme as tested by Kerwin et al. (1987) and at right an improved panel arrangement with a helical pitch (usually set to match the propeller tip pitch)

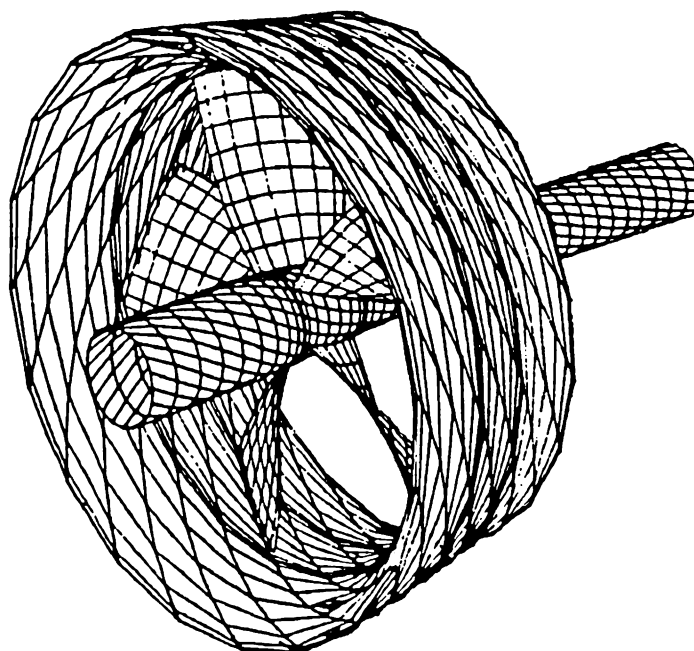


Figure 3.7 Panel scheme used by Kerwin et al. (1987). A cosine spacing was used on the duct in keeping with the blade panelling scheme.

easily.

3.3.2 Airplane Propeller Studies

Masquelier (1982) gave a basic application of the vortex-lattice method to airplane propeller analysis. The propeller in this case was assumed to be a twisted, rotating, planar wing. The following details were not considered in Masquelier's model; spanwise variation in axial inlet velocity and camber, thickness and hub effects. His study lacked any discussion or calculation of leading-edge suction forces or induced drag forces. There was no inclusion of viscous effects using drag coefficients. Masquelier assumed the wake to be made up of short, straight, vortex line segments whose length was set to 1/100th of a revolution following a convergence study. The wake was also assumed to be fixed with a constant helix angle and its effect was truncated after five diameters downstream. This was determined after a parameter study that showed the blade lift coefficient was unchanged after the five diameter length. This model is arguably only acceptable for blades at small angles of attack. Results from his code were compared with those from a blade element theory analysis, and basic agreement in trend was noted. No comparison was made with experimental propeller performance data. Masquelier realized the elementary nature of his analysis, and many of his recommendations for further work can be found (for example) in the codes created by Kerwin et al.

Rather than using a traditional panel method or source singularities to include thickness effects, Cheung (1987) chose to use a vortex-lattice system covering the upper and lower surfaces of thick propeller blades. Along with his lifting-surface model, Cheung presented a comprehensive review of propeller theory. Cheung constructed a computer model of the blades using a single vortex-lattice discretized on the mean camber line of thin blades, or the two layers of elements for thick blades mentioned above. Quadrilateral vortex rings were chosen by Cheung as the lattice elements instead of the more usually used horseshoe arrangement, and Cheung (1987) provided a thorough derivation of their formulation. The problem of using two layers of vortex elements when analyzing a thin blade was noted, and for thin blades a single layer gave the best results when compared with performance data. Data from the analysis of four blades was presented in Cheung (1987) along with experimental measurements from the literature. When the problem was not ill-conditioned as in the case of thin blades, the two-layer lattice performed better than the single mean-camber layer. The addition of viscous drag data as a function of two-dimensional lift coefficient provided only a slight improvement in agreement with the measurements. A lifting-line analysis of the propeller is also given in Cheung (1987), and this was found to be adequate for thin blades with no camber. A constant diameter and pitch helical wake model was used and no hub effects were considered. The trailing wake assumptions, i.e. neglecting wake contraction, probably limits the

analysis to lightly loaded propellers. The blade forces contributed by the chordwise vortex elements were neglected which assumes that spanwise flow effects were neglected there. Spanwise flow components were, of course, considered when computing the forces on the spanwise running vortex elements.

The performance of advanced turboprop rotors (SR-1 and SR-3) has been calculated by Kobayakawa and Onuma (1985) by the use of a vortex-lattice method. The effects of compressibility are approximated using the Prandtl-Glauert similarity rule, which is said to be useful below Mach 0.6 in providing a better estimate for compressibility than not using any correction at all. The trailing wake vortices were considered to be constant helices, and the induced velocity due to the wake was calculated for two revolutions of the wake. The effect of velocity increase through the propeller on the shed wake in its axial position downstream was approximated by making use of the "displacement velocity" concept from classical propeller theory. In applying the Biot-Savart law to compute the velocities induced by the vortex singularities, Kobayakawa et al. used the method given by Sullivan (1977). A source distribution was placed along the axis of the rotor with a strength distribution that satisfies tangential flow over the spinner and nacelle. Inclusion of the nacelle offered improvement in performance prediction. Performance predictions for the SR-1 propeller were closer to measured values than those for the SR-3 rotor, a blade with more sweep than the SR-1. Distortion of the SR-3 blade near the tip due to centrifugal forces was thought to be a contributing factor.

In the study of computational fluid dynamics by panel methods few researchers have as long and distinguished a track record as John L. Hess of the Douglas Aircraft Company. Recently, he has written a survey article on panel methods (Hess, 1990). His earlier work included the calculation of potential flows about lifting aerodynamic bodies (Hess, 1974) and the extension of this technique to higher-order panel methods (Hess, 1975) where the singularity strength is prescribed to vary within a panel. A more notable innovation (considering the work at hand) was his work in the computation of propeller flow and performance by panel method (Hess and Valarezo, 1985). Prior to Hess and Valarezo a number of lifting surface propeller studies had been published, but Hess and Valarezo appear to have presented the first panel method investigation of propellers. Hess and Valarezo used source and dipole singularities on the blades (lifting/thick bodies) and concentrated vortex singularities (straight-line) were used to model the trailing wake. A fixed helical wake model was used in Hess and Valarezo (1985), but the wake allowed for a fixed helix angle to be provided at a given radius. The distance downstream at which this helical wake was computed was determined by the number of segments (22 segments seen to be mostly used), the advance ratio, the helix angle and, of course, blade geometry. Typically, extending the calculation of the helical wake downstream a distance of 1.5 blade radii was adequate, and results using more wake segments changed the loading on the

elements only in the fourth significant figure. A "far-wake" approximation was used in which, after the helical wake, the wake lines were replaced by semi-infinite cylindrical wake elements, the influence coefficients for which may be derived in closed form. This resulted in an economical far-wake approximation. Predictions of pressure distributions using the Hess and Valarezo technique compared favorably with experiments and the computations of Kim and Kobayashi (1984). However, overall estimates of thrust and torque were typically over predicted. This was said to be due to viscous losses, which were not modeled or taken into account using viscous drag coefficients, and due to the fixed helical wake model which differs from the real flow substantially at low advance coefficients. Valarezo (1991) extended the implementation of the Hess panel code to multiple and counter-rotating propellers (see Figure 3.8) and extended the analysis to propeller/airframe interference models as shown in Figure 3.9. Valarezo has also used the technique to analyze proplet and windmill flows (Valarezo and Liebeck, 1988 and Valarezo, 1989).

An extension to the VSAERO panel method (Maskew, 1982) investigating the unsteady flow problem of propeller-wing interaction was undertaken by Rangwalla and Wilson (1987). The unsteady potential flow problem was attacked by solving the Laplace equation in each time step as the propeller was allowed to rotate relative to the wing. After the flow over the wing and propeller were started impulsively, the wake of the propeller was allowed to convect downstream and where a vortex core-size model was used to keep velocities bounded in the vicinity of a vortex singularity. A "vortex snipping" approach was also used in the interaction of the shed vortex ring panels with the wing (or any other surface). This was based on the physical phenomena of vorticity diffusion at or near solid bodies, and was taken into account by eliminating from the model any vortex panel which intersects a solid boundary. Propeller and wing interaction was also considered by Fratello, Favier and Maresca (1991) using a panel method code (COHV) to model the wing coupled with a free-wake lifting-line code (SMEHEL) to model the propeller. Primarily of interest to Fratello et al. was the interaction of the propeller slip-stream on the wing and, therefore, the influence of the wing on propeller performance was left to future work.

Examples of compressible lifting-surface theory applied to advanced turboprops were given by Hanson (1983), and Williams and Hwang (1986). In both of these applications the helicoidal lifting-surface theory employed was the equivalent of a planar wing in lifting-surface theory. The blades were assumed to be adequately represented by a helical surface and the wake was composed of rigid helical lines. The Hanson paper unified the aerodynamics and acoustic theoretical calculations using an unsteady potential formulation involving monopole, dipole and quadrupole sources. While Hanson presented the derivations of his approach, results and comparisons with measurements were lacking in this work. This technique while not an accurate three-dimensional model of the rotor blade (in that

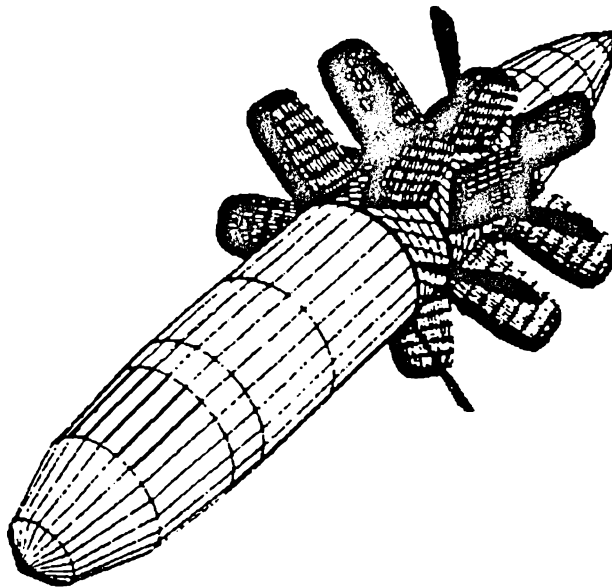


Figure 3.8 Panel discretization for a four-rotor counter-rotating propeller model (Valarezo, 1991)

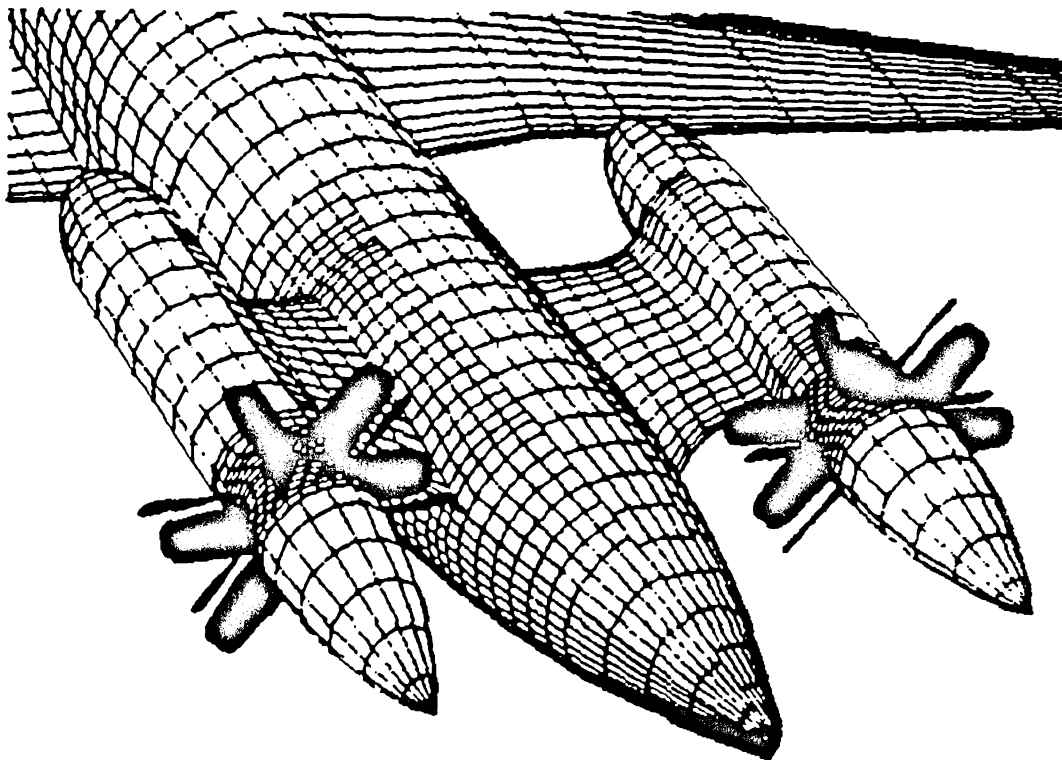


Figure 3.9 Detail of counter-rotating prop/airframe interference model (Valarezo, 1991)

camber and thickness were ignored) could be used to investigate the effects of different planforms.

The method of analysis mentioned above, linear compressible flow, was also chosen by Williams and Hwang (1986) in their turboprop study. Their approach was said to be adequate provided that the blades are thin, at low angle of attack, and free of embedded shocks and transonic flow. Blades were approximated using discretized doublet sheets on a helical surface rather than the actual blade surface. The blades were assumed to be equally spaced and the hub is ignored. The wake is considered to be a rigid helix of vortex lines. Doublet singularities of the type used in this analysis predict a pressure difference across each panel, and was considered to be constant over a given panel. It was found that an 85% panel chord length location for control points gave the best convergence with increasing number of panels; this value is in contrast with the 75% chord length normally used. An aeroelastic structural analysis was performed on the blades loaded with forces resulting from the program; however, the need for more steady and unsteady pressure data for code validation is mentioned.

There are, of course, techniques other than panel and lifting-surface methods to analyze the propeller problem. A method for solving a small disturbance form of the three-dimensional potential equation in helical coordinates for a rotating frame of reference was presented by Snyder (1987). A detailed discussion of the formulation, boundary conditions, and problem solution with the alternating-direction implicit (ADI) Douglas-Gunn algorithm (Douglas and Gunn, 1964) was presented. Snyder's results, using the above mentioned formulation, were compared with an Euler code; enough differences existed between the two numerical solutions to cause concern and led them to concede that further investigation was needed. Possibly the discrepancies were due to differences in the computational meshes used in the two models. Turboprop rotors have been analyzed using Euler solutions by Yamamoto, Barton and Bober (1986), and unsteady counter-rotating turboprops were studied by Whitfield, Swafford, Janus, Mulac and Belk (1987) who also used an Euler analysis. Euler methods are usually described as being between the full potential flow and Navier-Stokes equations in terms of computational intensity. When the flow is influenced by significant vorticity effects such as leading edge separation and curved shocks, Euler equation solvers should be employed.

A primitive variable Navier-Stokes analysis, using the finite-element method, of flow fields near propellers was given by Pelletier and Schetz (1985). The main focus of this study was the improved prediction of swirl velocities in the flow-field, and the blade was treated as an actuator disk. Therefore thrust and torque were considered known and were provided as inputs to generate the rotor flow field. No performance predictions were made or discussed, and little was known about the distribution of loading on the actuator disk. A trapezoidal

distribution was assumed, and the actuator disk was given a thickness and radius equal to that of the rotor. Results from the computer model for axial velocity predictions (upstream and downstream of the rotor) and swirl velocities (only downstream) compared favorably with wind tunnel test measurements for a rotor acting as a propeller and a windmill.

3.4 Helicopter analysis

Although quite different in application and, to some degree blade solidity and flow physics, there are similarities between an axial-flow fan and a helicopter rotor in hover. There is much the axial-flow fan researcher can learn from the use of analytical and experimental work that has been done on helicopter rotors. A good deal of what Wilson (1987) wrote about ongoing work on helicopter rotors is equally true for how axial-flow fan problems should be attacked. Wilson stressed the need for coordinated experimental and analytical work so that analysis is used to guide experimental work in setting test objectives, and experimental work verifies and evaluates the analysis. Codes used at NASA Langley are; **UTRC Free-wake, CAMRAD, VSAERO, HESS, AMI HOVER, C-81, Langley momentum hover, and Langley DO 865**. Of the most important areas of investigation (airfoil, rotor performance, blade loading, and interaction of rotor and air-frame being the others), rotor inflow and ability to understand the many variables that affect it is most germane to axial-flow fans. Furthermore, he raised the point that, definition of rotor inflow and wake studies are key elements in predicting loading, performance and acoustic characteristics. Unfortunately there exist few data to evaluate the current methods used to define inflow and wake effects. Wilson (1987) stated there was an effort to develop a knowledge base for the many parameters (advance ratio, thrust coefficient, number of blades, blade planform and proximity to the rotor) influencing the inflow and wake.

In the area of helicopter research, lifting-line and surface techniques have long been important techniques. The problem of the helicopter rotor in forward flight is indeed challenging, involving unsteady rotor wake fuselage, transonic and viscous phenomena. Fortunately the research most appropriate to the study of axial-flow fans is the problem of the helicopter rotor in hover. Not too long ago, according to Johnson (1986), "Navier-Stokes calculations of the entire rotor flow are well beyond present capabilities, so a hybrid method is likely to be used." To some extent, this statement has been taken out of context, as it was known that such Navier-Stokes calculations were possible, but at what cost was (and still is) the primary concern. In 1986 potential flow analyses were the most popular approach for advanced rotor analyses. Unsteady and compressible effects could be conveniently handled by such inviscid models. Current research in the area, as outlined by Singleton (1992), include three-dimensional, compressible, unsteady Navier-Stokes solvers focusing on areas such as new blade tip geometries to inhibit blade stall.

Recent reviews of research efforts by Singleton (1992), Cardonna (1990) and Johnson (1986) reveal trends, names and types of programs currently in use. Representing perhaps the most computationally intensive, the transonic unsteady rotor Navier-Stokes (**TURN**S) program solves the thin-layer Navier-Stokes (TNS) equation, and it has been used to compute aerodynamic loading in hover and forward flight, study rotor wake systems in hover and predict impulsive noise and rotor acoustics. Studies using TNS solvers typically reported in the literature required such supercomputers as the CRAY2. Given the computer power, TNS solvers have been used by Srinivasan and McCroskey (1988) to study rotor tip vortex formation and roll-up processes in the wake. If one is to model the complex viscous flow-field in the tip region, this is the present state of the art. The tip vortex formation and blade-vortex-interactions (BVIs) with following rotor blades are important aspects of rotor noise prediction and tip drag. Srinivasan, Baeder, Obayashi and McCroskey (1992) gave results of the state-of-the-art **TURN**S numerical code for a lifting rotor in hover which required no wake specifications (such as were used in the earlier versions of **TURN**S by Srinivasan and McCroskey, 1988). The results of Srinivasan et al. showed a noticeable improvement of agreement with experimental measurements over their earlier prescribed wake model (Srinivasan and McCroskey, 1988). A criticism of their approach that may be of concern to some was the computer time required; Srinivasan et al. reported 1 hour for coarse grids (109 x 36 x 31) and 15 hours for the fine grid of "nearly a million points" on a CRAY2 supercomputer.

Potential-flow CFD codes provide today's helicopter designers with fast and robust design tools. The **ROT22** three-dimensional full-potential code for rotary wings developed from a fixed wing code **FLO22** developed by Jameson and Caughey (1977). Arieli, Tauber, Saunders and Caughey (1986) developed **ROT22** to compute quasi-steady flow about lifting rotors throughout the subsonic and transonic regimes. Egolf and Sparks (1987) coupled a lifting-line/vortex-lattice wake method with a full potential finite difference method. Their method, **ROT22/WAKE**, allows for the influence of the wake on the finite difference solution of the full potential equation by treating the wake vortex elements in the finite difference mesh with a vortex embedding technique. There are, thus, two domains of computation, the wake (outer domain) and the inner, finite difference domain, as shown in Figure 3.10. The merits of their efficient solution process were demonstrated through showing agreement with their results and subsonic and transonic hover pressure coefficient data. According to Cardonna (1990) **ROT22** was one of the most used codes in industry; its simplicity and robustness made it user friendly. It was useful in initial designs of rotor planform and profile. Unfortunately **ROT22** used the non-conservative form of the full potential equations, known for its "shock errors". A full-potential code which did not have this drawback was **FPR**, developed by Strawn and Caradonna (1986). **ROT22/WAKE** and **FPR** use the so-called hybrid method of analysis in which various blade element and wake domains are assembled to produce a total

aerodynamic analysis. Steinhoff and Ramachandran (1989,1990) have developed a "unified" code, **HELIX I**, treating blade and wake as a single domain. This approach allows the wake surface to move through the flow field without concern as to its location in the flow domain and imposing boundary conditions between more than one domain. **HELIX I** is applicable currently only to axisymmetric blades in hover mode and has produced good results with a variety of planforms. There are several improvements and modifications to the code which are said to be ongoing, extending application to forward flight and incorporation of a "circulation coupled" wake geometry model to accelerate wake formation computations being among them.

3.4.1 Helicopter Rotor Lifting-line and Lifting-surface Analyses

Because of the lifting-surface nature of this study, two areas of the literature, the lifting-line studies and the lifting-surface studies, will be explored. Lifting-surface studies began appearing feasible in the late 1970's as computational power increased. A literature review of lifting-surface techniques used during this period is given by Stepniewski (1979). It was debated at first whether going from a line singularity of distributed circulation to either a zero thickness vortex-lattice representation, or a "thick" upper-lower surface distribution of the singularities was warranted. With increasing computational ability, the lifting-surface technique became more attractive and, more importantly, (unlike lifting-line analyses) it was able to predict the aerodynamic effects of rotor tip shapes.

In addition, there appears to have been (perhaps still is) a debate in the literature of the free-wake versus prescribed-wake approaches to vortex-wake modeling. Classical non-contracting wake models (Glauert, and Goldstein-Lock) proved inadequate when it was realized the improvement in prediction that could be obtained by considering the actual contracting wake in the hover mode. The free-wake approach requires an iterative procedure, and takes a variety of forms, but basically aligns vortex elements with the local velocity in the wake so that they remain force-free. The prescribed-wake model relies on flow visualization or other measurement techniques to provide parameter values to the model in order to arrive at reproduction of the actual rotor wake at the operating condition to be modeled. This has the drawback of requiring knowledge of the wake flowfield or some empirical model of the wake for the performance at a given flow condition to be accurately predicted. Indeed some (Shenoy and Gray, 1981) had success with using a prescribed tip vortex wake while using a free-wake procedure for determining the inner sheet geometry.

The North Atlantic Treaty Organization's Advisory Group for Aerospace Research and Development (**AGARD**) has held a number of meetings during the last twenty years to survey the status of the aerodynamics of rotor aircraft and the technology. From these, if one looks at the list of papers of the older meetings

(AGARD-CP-111) and the most recent (AGARD-R-781), a picture of the evolution of the field is painted. Landgrebe and Cheney (1972) provide a survey of rotor aerodynamics from the Rankine-Froude momentum theory (developed in 1865), to blade element theory, to lifting line theory as it stood in 1972. They stress the importance of wake (free, prescribed, empirical, in hover and in forward flight) modeling. Gray and Brown (1972) present a free-wake lifting line analysis of a single blade rotor. Zimmer (1972) looked at lifting-line and blade element calculations for rotors in a wide range of axial-flow conditions: hover, fast descent, autorotation (windmilling) and vortex-ring state. The importance of flow visualization data to early rotor analysis is seen in Gilmore and Gartshore (1972) as they experimented with various vortex filament wake models in an attempt to reduce the size of the wake modeled and include effects of tip vortex core size in a lifting-line analysis.

Landgrebe's (1969) use of a lifting-line and free-wake approach to predicting rotor wake geometry was one the early studies which showed that a computer coded free-wake analysis was able to indicate real rotor wake behavior as observed in flow visualization tests. Later (Landgrebe, 1972) extensive flow visualization studies of the rotor wake using smoke rakes led Landgrebe to develop a prescribed-wake performance model. These findings led Landgrebe to develop this wake model for a variety of operating conditions, and his qualitative observations of increasing rotor wake instability with increasing distance from the rotor. It was shown (Landgrebe, 1972) that a more realistic wake geometry could lead to improved prediction of rotor wake performance characteristics.

Another important early work in the development of computational methods for the prediction of hovering rotor performance was by Clark and Leiper (1970). Clark and Leiper (1970) used a lifting line representation and a free-wake model. Sadler (1971) used a procedure similar to the start-up of a rotor in a free stream with a lifting line representation of the rotor blade to predict steady rotor induced aerodynamic loads and rotor wake flow for advancing helicopter rotors through a transient startup process. He allowed for the possibility of nonuniform inflow due to a free-wake and the behavior of flexible blades in response to the applied loads (flapping). The Sadler method for computing the velocity induced by a vortex element on itself is used in the **PSF-2** code.

A translation of a Russian text on helicopter rotor theory by Baskin, Vil'dgrube, Vozhdayev and Maykapar (1976), in which lifting-line and lifting-surface were discussed in detail, represented typical methods of analysis of rotors during the mid-70's. Also, Baskin et al. discussed many other aspects of helicopter rotor technology including flow visualization of rotor wakes. An analytical solution for semi-infinite cylindrical wake elements was also given by Baskin et al. which is of interest in far wake approximation. Another example of the methods of rotor analysis during this period was given in Kocurek and Tangler (1977).

Kocurek and Tangler (1977) presented an improved prescribed-wake model using a lifting surface analysis. The improved wake model was the result of Schlieren flow visualization studies of the wake and tip vortex. A vortex-box representation of the lifting surface was used as shown in Figure 3.11 rather than a vortex-lattice. The collocation points were located at the panel chordwise position; the results at these points were made to match two-dimensional thin airfoil theory.

Shenoy and Gray (1981) had success predicting pressures except for the final 1% span (i.e. the tip) of a single rotor in hover, using a hybrid method using both lifting-line/blade element and lifting-surface techniques. Using a lifting-line/blade element method as an initial estimate of strengths of the upper and lower surface vortex sheets, they performed iterations on the inner vortex filaments while fixing the tip vortex to a prescribed wake geometry. Following convergence of the trailing sheet geometry using a lifting line procedure, they used a lifting-surface technique incorporating panels on the rotor surface and the rounded rotor tip with the converged wake for the final calculation. This article is interesting from the standpoint of comments as to the effectiveness and proper use of such methods. In these authors' experience, free-wake modeling is computationally expensive and does not appear to produce correct tip vortex geometries. Lifting-line/blade element methods which use prescribed wakes had two major draw backs. First, they could not predict tip vortex geometries, thus requiring observations of an operating condition before simulation. Second, the lifting-line could not determine the effect of tip shape on rotor performance. They stress that accurate modeling of the tip-vortex geometry in the near flow field wake is important to predicting performance. It is further remarked that different wake geometries can give the same integrated thrust. Also, the wake geometry generated is sensitive to the induced angle of attack along the blade span. This sensitivity might show itself adversely in poor prediction of torque.

Miller (1982) and Flax (1983) examined the benefits of classical vortex lifting-line theories for hovering rotors which include wake contraction. Miller's technique was used to compute wake geometry and bound circulation, using both a simplified two-dimensional vortex lifting-line and a three-dimensional model using vortex rings and cylinders with 10% accuracy (compared with experimentally determined circulation values). The comparison of integrated thrust coefficient is considerably better, especially for the two-dimensional model (versus the three dimensional model). It was hoped that this technique could be used as a guide to optimum circulation distributions for rotors in hover mode in that the computational requirements are considerably less than a free-wake analysis.

The analysis of straight or curved helicopter rotors in hover was performed by Rosen and Graber (1988) using the vortex-lattice method and a free-wake analysis. The free-wake was analyzed in a two part scheme with a near wake composed of straight-line segments and a far wake consisting of semi-infinite

helical curve. The positions of the near wake elements were computed in an iterative manner where the elements were "force-free". Actually, Rosen and Graber's far wake was not actually "free"; it remain fixed in radius but had a helix angle which was allowed to vary in a prescribed manner with reference to the near wake end elements. The velocities induced by the semi-infinite helical vortex lines was computed in the manner given by Graber and Rosen (1987). The free-wake calculations were shown to have converged after 26 iterations which is somewhat larger than the number of iterations to convergence of other free-wake analyses on propellers.

A novel method of analytically predicting helicopter rotor characteristics in vertical descent was given by Shi-cun (1990). In considering the vortex-ring and the windmill modes of operation, he used an argument that circulation in the trailing vortices of the wake are dissipated by viscous phenomena. Therefore, rather than assuming conservation of vorticity as in the ideal wake, "a decay or dissipation of circulation in the real wake is assumed." As a simple physical argument, he considered the fact that far enough down stream from a fan an observer will feel no effect. Shi-cun showed that with the assumption of linear decay of circulation for trailing vortices and the assumption of the distance to zero circulation being proportional to transport velocity of the trailing vortices, an analytical/empirical model can be constructed which predicts induced velocity, torque and thrust with an accuracy adequate for engineering calculations and preliminary design. This approach with a lifting-line or lifting-surface simulation might be of use in analyzing fan performance.

As modern helicopter designs have incorporated larger stabilizers (or lifting-surfaces) there has come about the need for tools able to explore the dynamic (vibration) and aerodynamic interactions of rotating and non-rotating surfaces. In response to this need, Mello and Rand (1991) developed a vortex-element lifting-surface model to predict unsteady loading on non-rotating lifting surfaces. Rather than considering the problem in the time domain using a time marching procedure, Mello and Rand used a frequency domain analysis via Fourier series for solving the periodic loading of a stabilizer operating in the rotor downwash. The model considered the lifting surface without camber or thickness, and no wake deformation was allowed in the model. A double-cosine was used in the chordwise direction to resolve the steep loading gradients at the leading edge and to accurately calculated the loading on the trailing edge as this effects the periodic wake calculations. General trend and magnitude of the periodic loading was a good match to experimental data. This technique has the distinct advantage over time domain procedures as it can be carried out in a single numerical step.

Gray (1992) provided a retrospective examination of lifting-surface analysis in helicopter rotor research. In his early studies, the flow field of a single rotor blade was investigated using smoke flow visualization with the goal being to

determine the boundary for the rotor wake in hover. This was accomplished by tracking the tip vortex and then defining the surface along which it moved by curve fitting the flow visualization data. In comparing this prescribed wake model with the 1955 "state-of-the-art" Goldstein-Lock method, which did not include wake contraction; the measured thrust was 7.8 pounds, Gray's method gave 7.73 pounds, and the Goldstein-Lock method (with extrapolation to a single blade) gave 7.00 pounds. This led Gray to the conclusion (well acknowledged today) that "relatively small errors in wake geometry can lead to significant errors in blade loadings." In addition, Gray demonstrated the importance of tip vortex core modeling on calculation of free-wake geometries for a hovering rotor using a lifting-line analysis. Gray discussed some more recent efforts. The current importance of classical lifting-surface techniques in their "close correspondence of the modeling with flow visualization studies" was stressed and a need to now how well these classical techniques answered questions about rotor phenomena was also addressed. Then after knowing the limits of the lifting-surface method, researchers can more effectively apply "Euler and Navier-Stokes formulations for those regions where classical modeling was shown to be inappropriate." Hybrid techniques are the way of the future, according to Gray.

3.4.2 Rotor Wake and Tip Vortex Visualization Applied to Analysis

The importance of tip vortex geometry studies is exemplified by Norman and Light (1987). They remarked that the ability to measure rotor tip vortex geometry has and will continue to be useful to our understanding of rotor wake distortion, their use in empirical prescribed wake models and in the verification of computer codes for wake modeling (free-wakes etc.). They employed the shadow-graph technique to quantify tip vortex geometry and trajectory by measure its axial and radial coordinates in a large outdoors testing environment. The strobe light used was approximately 15 meters from the 2.14 meter rotor used in this study. Also, a technique was developed to predict the ability of the shadowgraph technique to visualize tip vortices.

Evidence of a mid-span vortex was published by Müller (1990) who explored them via a non-rotating water tunnel study using air bubble flow visualization and laser anemometry measurements. The mid-span vortex was believed to be created by the interaction of the tip vortex with following blades. Müller had generated a finely discretized free-wake analysis which yield this mid-vortex roll-up. Other vortex structures were discussed by Müller (1990) and examples of these structures were visualized using vapor or smoke visualization techniques. The flow visualization techniques were not discussed in any detail which is unfortunate.

A variation on this theme of quantifying flow visualization data of rotor wakes is given by Brand, Komerath and McMahon (1989). Seeding the wind

tunnel with droplets of atomized mineral oil, and illuminating the desired plane of visualization with a 5 W argon ion laser they were able to visualize (quantitatively) the interaction of the tip vortex interaction with the airframe. Strobing the laser is necessary when visualizing the unsteady flow field. Airframe pressure data correlated well with observed flow visualization of the vortex regarding its interaction with the airframe; this allows for improved physical interpretation of the periodic airframe surface pressure measurements. The tip vortex was made visible owing to the relative scarcity of droplets in the vortex core; the core appeared as a dark spot against the bright background of light scattering oil droplets.

From these last studies, we have come back around to discussing the joint importance of flow visualization studies (as discussed in Chapter 2) and numerical analysis (as discussed here in Chapter 3). This is appropriate given the goals of this thesis. Through this in-depth discussion, a background of literature to this study has been drawn and now this thesis can be put in proper perspective with regard to the past literature. It is now time to present the physical, mathematical and numerical approximation theories that are behind the lifting-surface approach to fluid dynamic analysis as used in this thesis.

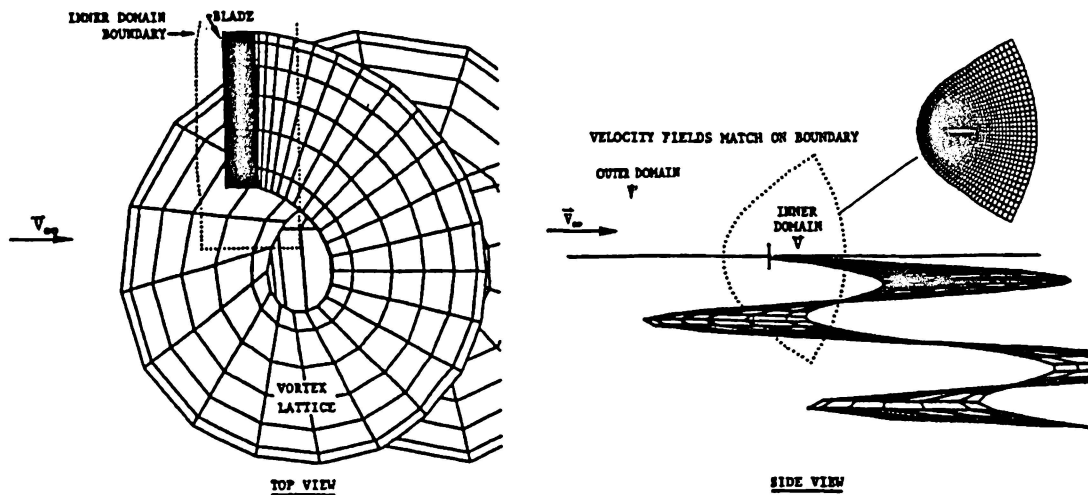


Figure 3.10 Inner and outer computational domains from Egolf and Sparks (1987)

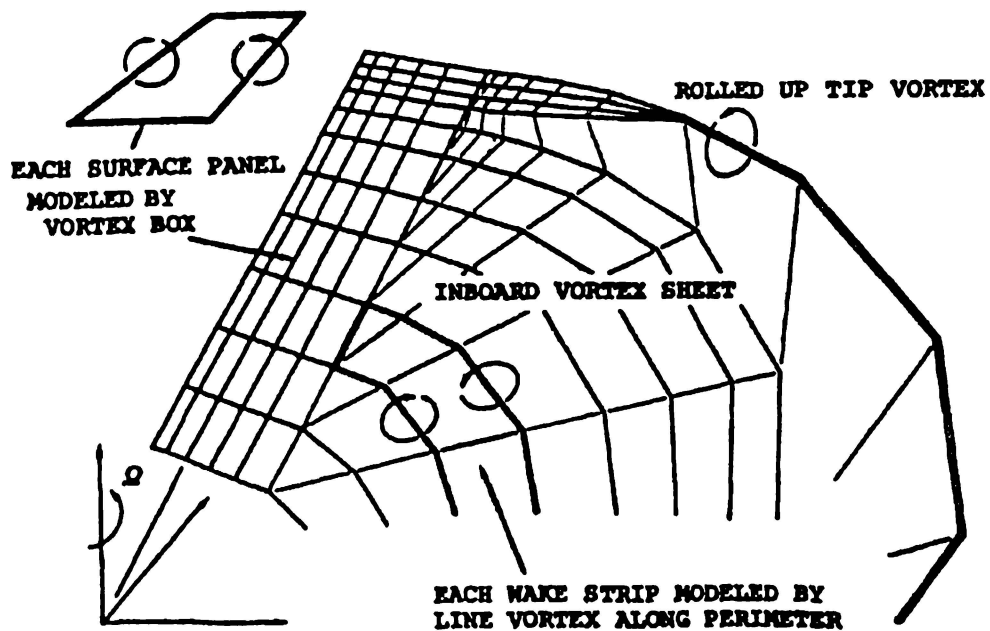


Figure 3.11 Vortex box model as used by Kocurek and Tangler (1977)

CHAPTER 4

REVIEW OF THEORY AND DEVELOPMENT OF A VORTEX-LATTICE METHOD FOR THE ANALYSIS OF AXIAL-FLOW FANS

4.1 Introduction

In this chapter is presented an overview of topics in axial-flow device theory, and many aspects of this discussion can be applied with minimal changes to axial-flow fans, propellers, helicopter rotors and windmills. It begins with a presentation of momentum theory and efficiency. Later, basic blade element theory is presented along with a brief exposition on the fundamental of cascade momentum theory. This is followed by background of lifting-surface theory, the vortex-lattice method, thin-airfoil theory and related topics. Finally a discussion of the implementation of the vortex-lattice method used in this study is given, including discussions of geometry and discretization techniques, input file formats and input variables.

4.2 Momentum Theory for Propellers, Rotors and Fans

The application of Newtonian mechanics to the problem of one-dimensional flow through an axial-flow device is commonly called **momentum theory**, as derived by Rankine and Froude in the 19th century. By using the conservation laws of mass, and momentum, theoretical relationships for the performance variables for the device can be derived. These relationships give insight into such variables as induced velocity, pressure rise (or thrust), and first-law efficiency. The development and use of a first-law efficiency is common in analyzing both axial flow propulsion, and such turbomachinery as axial-flow fans. Because this figure of merit will be used, and because the method of analysis to be used is from the concept of a propeller system, the fundamentals of this efficiency are examined along with their application to axial-flow fans.

The flow is assumed to be incompressible and inviscid. Therefore, no energy is lost by dissipation. This means that the flow on either side of the disk, shown in Figure 4.1, is of constant energy. Furthermore it is assumed the fluid flowing through the actuator disk forms a "column-like" stream-tube at distances far upstream and downstream from the disk. Downstream of the device this stream-tube (also called the wake, slipstream, or propeller race) is, in reality, a turbulent three-dimensional flow. In this application of momentum theory, the flow is considered to be only in the axial direction. The axial-flow device, be it a propeller or fan, is assumed to impart an instantaneous, uniform increase in momentum to the fluid. This "ideal" device is called an actuator disk. Looking at the conservation of momentum as expressed in the Bernoulli equation, this

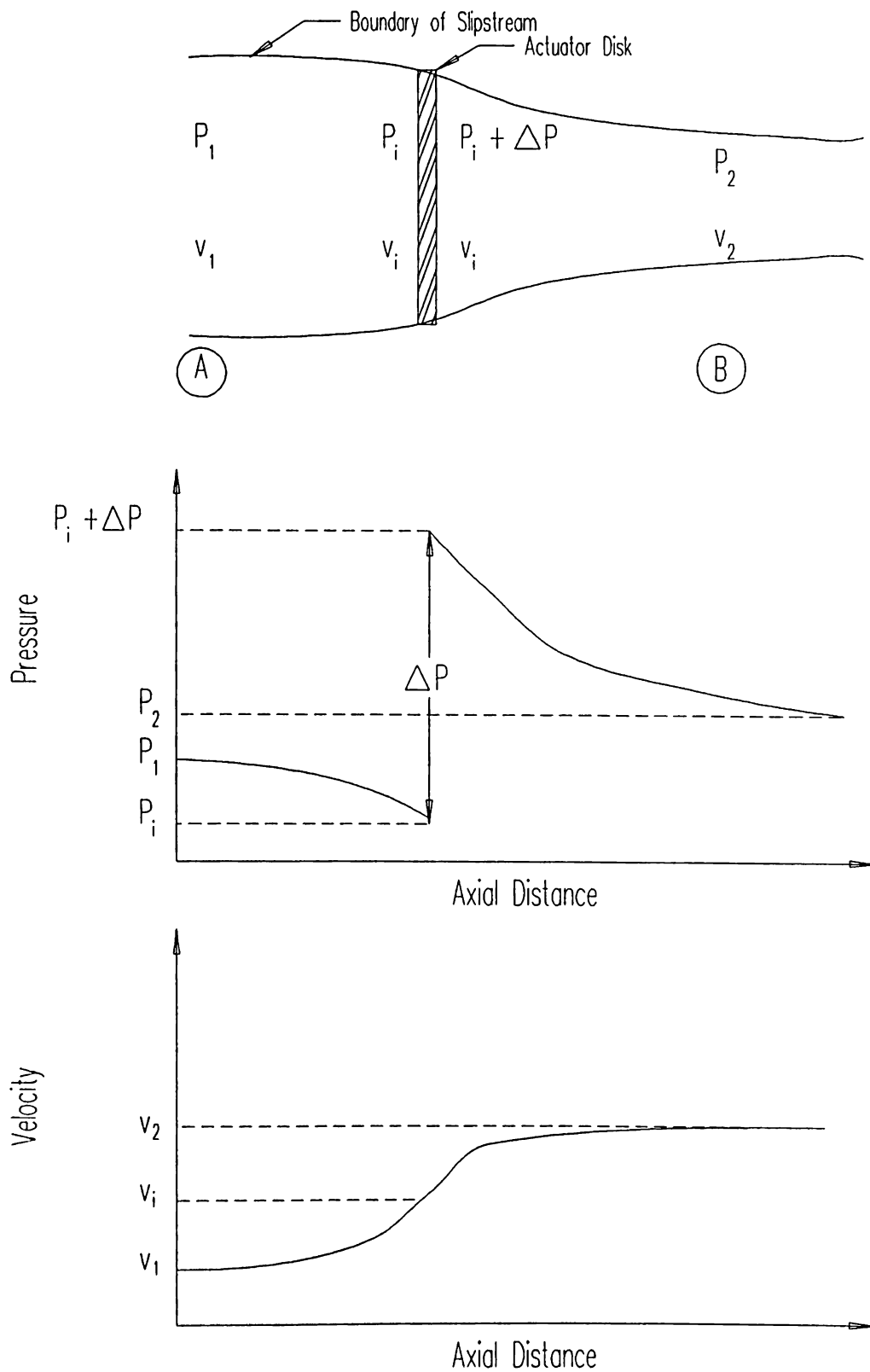


Figure 4.1 Momentum theory for flow through an axial flow device

momentum (or energy, since the two are redundant for such a flow) could be added either as static or dynamic pressure. The Rankine-Froude momentum theory maintains that energy added to the flow at such a disk must be in the form of increased static pressure. To conclude otherwise is to admit the existence of an instantaneous acceleration at the disk, and admission of velocity discontinuity in a constant area streamtube for an incompressible flow. Once again all velocity is in the axial direction and rotation of the slipstream is neglected for this analysis.

The momentum theory will first be presented in a form where few stipulations on the flow will be made. Then stipulations on the flow for a propeller, helicopter rotor, and fan will be made. As can be seen from Figure 4.1 and discussed above, the velocity is considered continuous at the disk. On the upstream side, far ahead of the disk at point A, the flow upstream of the disk is of constant energy. The velocity and static pressure at this point are denoted by the subscript 1. Because flow will be drawn through the disk, the static pressure at the disk on the upstream side of the disk must be less than that at A, and an induced velocity v_i develops. By the Bernoulli equation for the flow upstream of the disk

$$P_1 + \frac{\rho v_1^2}{2} = P_1 + \frac{\rho (v_1 + v_i)^2}{2} \quad (4.1)$$

the total velocity just upstream of the disk must be higher than at points further upstream from the disk, and continuity tells us that the slipstream must be contracting since the velocity increases nearing the disk. This is reflected in Figure 4.1.

At the actuator disk, the uniform increase in pressure ΔP is produced in the fluid as work is applied to the device ($P < 0$ in the analysis of a windmill). From the assumed flow behavior, the energy and the pressure on the downstream side of the actuator disk are also constant. The velocity, however, is unchanged. The energy equation for the downstream side is

$$(P_1 + \Delta P) + \frac{\rho (v_1 + v_i)^2}{2} = P_2 + \frac{\rho v_2^2}{2} \quad (4.2)$$

where the static pressure at a distance far downstream has reached P_2 . The pressure P_2 at point B is determined by the boundary conditions of the device, and is the point of maximum slipstream contraction and maximum speed v_2 of the fluid on which the disk acted. In a propeller or helicopter rotor device P_2 would be equal to the atmospheric pressure, and for a fan system it is determined by the pressure/flow rate characteristics of the duct system downstream.

The point where the static pressure becomes equal to the atmospheric

pressure is sometimes called the starting point of the ultimate wake. Subtracting Equation (4.1) from (4.2), an expression for the pressure impulse transferred to the fluid is obtained as

$$\Delta P = P_2 - P_1 + \frac{\rho}{2} (v_2^2 - v_1^2) \quad (4.3)$$

Assuming a uniform disk loading, the pressure jump across the actuator disk is equal to the thrust per unit area on the disk. Thus

$$\Delta P = \frac{T}{A_{\text{disk}}} \quad (4.4)$$

Considering that the thrust produced by the disk is equal to the change of momentum of the fluid upon which it acts, the thrust (without any momentum loss or rotation in the wake) can be expressed as

$$T = m a = m \frac{\Delta v}{\Delta t} = \rho A_{\text{disk}} (v_1 + v_i) (v_2 - v_1) \quad (4.5)$$

At the disk the pressure impulse ΔP can also be expressed as

$$\Delta P = \rho (v_1 + v_i) (v_2 - v_1) \quad (4.6)$$

With Equations (4.3) and (4.6) one can derive fundamental relationships for the cases of a propeller advancing through a fluid, a helicopter rotor in hover, and a fan. An expression for the induced velocity can be found by equating Equations (4.3) and (4.6) and solving for v_i

$$v_i = \frac{P_2 - P_1 + \frac{\rho}{2} (v_2^2 - v_1^2)}{\rho (v_2 - v_1)} - v_1 \quad (4.7)$$

Just as insight into the problem can be gained by expressing the inlet velocity as an induced velocity added to the far upstream value, for similar reasons we can express the far-downstream value in the wake as an excursion above the far-upstream value. Or, as shown in Figure 4.1,

$$v_2 = v_1 + v_w \quad (4.8)$$

where v_w is the excursion velocity in the ultimate wake.

If the actuator disk is considered for the problem of a propeller in a propulsion system (Harvald, 1983), the flow is considered with reference to the advancing propeller. In this case the analysis is of a propeller moving with speed

v_∞ , and the static pressure far upstream and downstream must be equal to the atmospheric pressure. For this case

$$\begin{aligned} v_1 &= v_\infty \\ P_1 &= P_2 = P_{\text{atm}} \end{aligned} \quad (4.9)$$

From Equation (4.7) the induced velocity for the propeller becomes

$$v_i = \frac{0 + \frac{\rho}{2} ((v_\infty + v_w)^2 - v_\infty^2)}{\rho ((v_\infty + v_w) - v_\infty)} - v_\infty \quad (4.10)$$

which gives the result that the induced velocity at the actuator disk is one half the induced velocity in the ultimate wake

$$v_i = \frac{1}{2} v_w \quad (4.11)$$

Or, for a propeller according to these assumptions, one half the total velocity increase occurs before the fluid enters the propeller. From Equation (4.5) the relationship between thrust and induced velocity is

$$T = \rho A_{\text{disk}} (v_\infty + v_i) v_w = 2 \rho A_{\text{disk}} (v_\infty + v_i) v_i \quad (4.12)$$

For a propeller then, the induced velocity in the ultimate wake is shown to be larger than that at the disk, and the total velocity in the wake is larger than that, v_∞ , of the free stream. The more heavily loaded the propeller is, or the lower the advance coefficient is, the more the slipstream will contract and the greater v_w becomes. Similarly, a propeller operating at ideal cruise conditions has smaller induced velocities and less wake contraction and, as we shall soon see, operates at a higher ideal efficiency.

The momentum theory analysis of a helicopter rotor operating in hover mode is equivalent to a stationary fan drawing air through it with a velocity $v_1=0$ far upstream and at free air conditions (or no static pressure difference). The static pressure far upstream and downstream from the rotor must be equal, and the total velocity in the ultimate wake will be the induced ultimate wake velocity v_w . Thus

$$\begin{aligned} v_1 &= 0 \\ v_2 &= v_w \\ P_1 &= P_2 = P_{\text{atm}} \end{aligned} \quad (4.13)$$

From Equations (4.7) and (4.12) the induced velocity for the ideal helicopter rotor in hover is

$$v_i = \frac{1}{2} v_w \quad (4.14)$$

which was the same result obtained for the propeller. The torque for the helicopter rotor can be expressed in terms of induced velocity at the disk using Equation (4.5) with values from Equations (4.12) and (4.13)

$$T = 2 \rho A_{\text{disk}} v_i^2 \quad (4.15)$$

An estimate of the induced velocity can be made (if the thrust is known) as

$$v_i = \sqrt{\frac{T}{2 \rho A_{\text{disk}}}} = \sqrt{\frac{\Delta P}{2 \rho}} \quad (4.16)$$

where the pressure impulse ΔP is sometimes termed the disk loading and the induced velocity v_i is sometimes called the rotor downwash.

It has been shown for the case of a still or advancing axial-flow device in an infinite fluid reservoir that the momentum theory leads to ideal relationships between the induced velocity and actuator disk loading. The case of a fan in a duct system is similar to a propeller (in that the fan puts energy into the fluid), but they differ in that the entire fluid is enclosed by the duct system. Therefore, far upstream and downstream of the actuator disk the velocities must be equal for an incompressible fluid. This situation is shown in Figure 4.2. However, the static pressures will now not be equal. In Figure 4.2, a boundary for the slipstream is shown, and it is known that it will contract as the fluid velocity increases after passing through the disk. This kinetic energy added to the stream will be converted to a specific energy change (in the thermodynamic sense) as the increased dynamic pressure is converted to static pressure. Since

$$v_2 = v_1 \quad (4.17)$$

from Equation (4.3) the pressure rise across the actuator disk becomes

$$\Delta P = P_2 - P_1 \quad (4.18)$$

This simple approach of the actuator disk should not be confused with actuator disk models used by Hawthorne and Horlock (1962) (and others cited therein) which were of utility in describing the flow fields upstream and downstream of

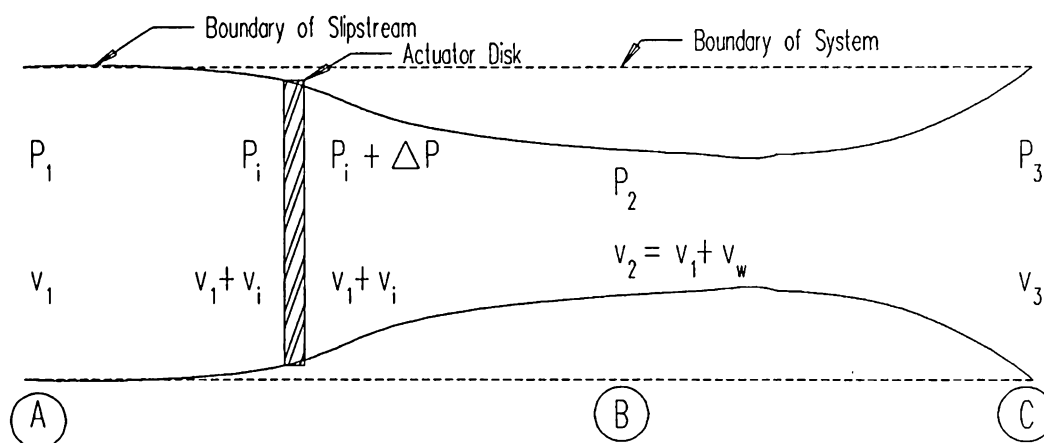


Figure 4.2 One-dimensional actuator disk momentum theory for a fan operating in an enclosed system

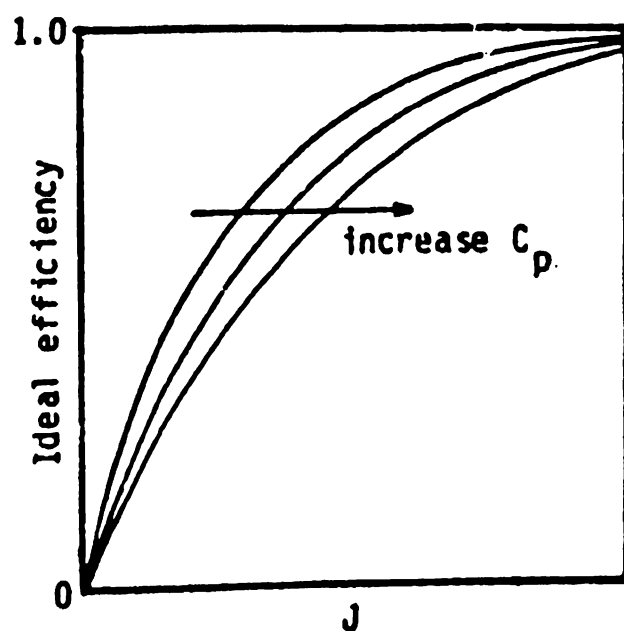


Figure 4.3 Ideal performance curve from Chueng (1987)

axial-flow rotors. From these more detailed actuator disk studies, contracting streamlines downstream of the rotor are apparent (though somewhat exaggerated) in Figure 4.2.

4.3 Efficiency of Propellers, Rotors and Fans

The thrust T produced by the actuator disk from Equation (4.4) is

$$T = \Delta P A_{\text{disk}} \quad (4.19)$$

The useful power delivered to a ship or aircraft results in the craft moving at a velocity v_{∞} through the fluid medium. This power is obtained by multiplying the speed v_{∞} of the craft by the thrust causing its motion, or

$$\dot{W}_{\text{useful}} = T v_{\infty} \quad (4.20)$$

The power supplied to the propulsor is total change in energy of the air flowing through the disk, or the thrust developed by the disk times the velocity of the flow through the disk

$$\dot{W}_{\text{shaft}} = T (v_{\infty} + v_i) \quad (4.21)$$

This leads to an efficiency η defined as the useful power divided by the power put into the propulsion device. Here the efficiency is the effective power delivered by the propeller divided by the power supplied to the propeller as

$$\eta = \frac{\dot{W}_{\text{useful}}}{\dot{W}_{\text{shaft}}} = \frac{v_{\infty}}{v_{\infty} + v_i} \quad (4.22)$$

If the torque of the propeller is known at the operating rotational speed ω , the shaft power can also be expressed as

$$\dot{W}_{\text{shaft}} = Q \omega \quad (4.23)$$

Therefore the efficiency can also be expressed as

$$\eta = \frac{\dot{W}_{\text{useful}}}{\dot{W}_{\text{shaft}}} = \frac{T v_{\infty}}{Q \omega} \quad (4.24)$$

While the preceding discussion is not directly applicable to axial flow fans, the efficiency given above is that predicted by the PSF-2 program. The computer program PSF-2 computes $\dot{W}_{\text{shaft}} = \omega Q$, where the torque Q is part of the program computations and ω , the rotational speed, is provided as input. Similarly in the numerator, the thrust for the propeller is also computed by the lifting surface

solutions and the craft velocity is provided as input. From the one-dimensional momentum theory as given in Equation (4.22), note that efficiency approached unity for ever smaller values of v_i . Equation (4.22) gives the ideal efficiency for a given operating condition, but does not tell us how to predict the performance of the device. Thrust and torque, for instance, cannot be determined by simple momentum theory for a given operating condition.

Applying the Buckingham pi theorem (White, 1974, p. 86), the number of dimensionless groups equals the number of the variables (v_∞ , ω , D , T , \dot{W}_{shaft} and ρ) minus the number of dimensions (three; one of space, one of mass and one of time). From this, three dimensionless variables can be formed which describe the problem, and give relationships for efficiency, thrust and torque (power). The dimensionless variables representing thrust and power (or torque) are the thrust coefficient

$$C_T = \frac{T}{\rho \omega^2 D^4} \quad (4.25)$$

the power coefficient

$$C_P = \frac{\dot{W}_{\text{shaft}}}{\rho \omega^3 D^5} \quad (4.26)$$

and the advance coefficient

$$J = \frac{v_\infty}{\omega D} \quad (4.27)$$

which are convenient and formed from independent variables. The efficiency of a propeller can then be described by

$$\eta = \frac{T v_\infty}{\dot{W}_{\text{shaft}}} = \frac{v_\infty}{\omega D} \frac{C_T}{C_P} = J \frac{C_T}{C_P} \quad (4.28)$$

Cheung (1987) gives the relationships for η , C_P , and C_T as

$$1 - \eta - \eta^3 \frac{2 C_P}{\pi J^3} = 0 \quad (4.29)$$

and

$$1 - \eta - \eta^2 \frac{2 C_T}{\pi J^2} = 0 \quad (4.30)$$

where an example of the ideal performance curve, Equation (4.29), is given in Figure 4.3.

An ideal efficiency, also known as the *figure of merit* (Seddon, 1990), can also be developed from momentum theory for the case of a helicopter rotor in hover. The rate of work done on the air passing through the actuator disk for this case is equal to the change in kinetic energy of the air per unit time, which is called the induced rotor power \dot{W}_i is

$$\dot{W}_i = \frac{\rho A_{\text{disk}} v_i}{2} v_w^2 \quad (4.31)$$

from Equations (4.14) and (4.15) and the induced power is

$$\dot{W}_i = 2 \rho A_{\text{disk}} v_i^3 = T v_i \quad (4.32)$$

or from Equation (4.16)

$$\dot{W}_i = \sqrt{\frac{T^3}{2 \rho A_{\text{disk}}}} \quad (4.33)$$

The dimensionless coefficients describing thrust and power for the hovering helicopter rotor are similar to those used in the advancing propeller case. The rotor tip speed ωr_{tip} is used as a reference velocity, and the induced velocity coefficient C_i replaced the advance coefficient in the hovering rotor application, where

$$C_i = \frac{v_i}{\omega r_{\text{tip}}} \quad (4.34)$$

The thrust coefficient is

$$C_T = \frac{T}{\rho A_{\text{disk}} (\omega r_{\text{tip}})^2} \quad (4.35)$$

From Equations (4.15) and (4.32) the thrust coefficient can also be written

$$C_T = 2 C_i^2 \quad (4.36)$$

The power coefficient as used in hover helicopter rotor performance is given by

$$C_P = \frac{\dot{W}_{\text{shaft}}}{\rho A_{\text{disk}} (\omega r_{\text{tip}})^3} \quad (4.37)$$

The induced power coefficient C_{Pi} is given by

$$C_{Pi} = \frac{\dot{W}_i}{\rho A_{\text{disk}} (\omega r_{\text{tip}})^3} = \frac{T v_i}{\rho A_{\text{disk}} (\omega r_{\text{tip}})^3} = C_i C_T = \sqrt{\frac{C_T^3}{2}} \quad (4.38)$$

where Equations (4.32), (4.34), (4.35), and (4.36) have been used to simplify the expression written above. Extensions of the momentum theory which included the effects of swirl energy in the wake, radially varying induced velocity, and operating conditions other than hover may also be explored in a similar way.

The figure of merit M , which is taken to be the idealized efficiency of a helicopter rotor, is the ratio of power desired from the rotor (the rate of work done on the air) to the total power supplied to the rotor. The total power \dot{W}_{shaft} supplied to the rotor is the sum of the induced (useful) power \dot{W}_i and lost power \dot{W}_{lost} applied to overcome viscous drag, tip losses, wave drag and other effects so that

$$\dot{W}_{\text{shaft}} = \dot{W}_i + \dot{W}_{\text{lost}} \quad (4.39)$$

The lost power coefficient $C_{P, \text{lost}}$ is given by

$$C_{P, \text{lost}} = \frac{\dot{W}_{\text{lost}}}{\rho A_{\text{disk}} (\omega r_{\text{tip}})^3} \quad (4.40)$$

So, the figure of merit M is

$$M = \frac{\dot{W}_i}{\dot{W}_i + \dot{W}_{\text{lost}}} = \left(1 + \frac{\dot{W}_{\text{lost}}}{\dot{W}_i} \right)^{-1} = \left(1 + \frac{C_{P, \text{lost}}}{C_{Pi}} \right)^{-1} \quad (4.41)$$

or, from Equation (4.38),

$$M = \left(1 + C_{P, \text{lost}} \sqrt{\frac{2}{C_T^3}} \right)^{-1} \quad (4.42)$$

Typically, a value of $M = 0.6$ is achieved, and Equation (4.42) shows that M increases as C_T does. However, with increasing thrust (or lift for the blade) comes the eventual stall. As with the advancing propeller case (analogous to a rotor in vertical climb), the momentum theory for a rotor in hover mode does not predict performance; instead, it provides insight into ideal efficiency and the overall effects of such variables as rotational speed, rotor size, thrust and induced velocity.

Just as the pi theorem may be applied to rotors and propellers, its application to the fan yields dimensionless variables for the dependent variables (pressure rise and power, essentially resulting from the aerodynamic forces in the axial and tangential directions, respectively) and these determine the fan efficiency. These variables are dependent on the flow rate, size and speed of rotation, and the density which is taken as a constant for an incompressible flow. The non-dimensional output of a fan test or calculation is typically given in terms of a head (total pressure rise) coefficient ψ

$$\psi = \frac{\Delta P_{\text{total}}}{\rho \omega^2 D^2} \quad (4.43)$$

and power coefficient C_p

$$C_p = \frac{\dot{W}_{\text{shaft}}}{\rho \omega^3 D^5} \quad (4.44)$$

The values of ψ and C_p are usually plotted in terms of the dimensionless flow coefficient ϕ given by

$$\phi = \frac{\dot{V}}{\omega D^3} \quad (4.45)$$

The use of ϕ is analogous to the advance coefficient J used in propeller work to present performance data. Plotting fan performance with respect to dimensionless rotational speed and size (diameter) for a variety of different blade parameters leads to a better understanding of the trends in performance affected by a design parameter. The dimensionless variables used for rotational speed and diameter are the specific speed ω_s ,

$$\omega_s = \omega \dot{V}^{\frac{1}{2}} \left(\frac{\rho}{\Delta P} \right)^{\frac{3}{4}} \quad (4.46)$$

and the specific diameter D_s ,

$$D_s = \frac{D \left(\frac{\Delta P}{\rho} \right)^{\frac{1}{4}}}{\dot{V}^{\frac{1}{2}}} \quad (4.47)$$

The efficiency η_{fan} of a fan can be taken from the analysis of a propeller (given above in Equation 4.24) by considering the useful work as the work done at the impeller on the fluid rather than the work done to move a craft a given velocity. In this definition the efficiency of an ideal fan is given by

$$\eta_{\text{fan}} = \frac{(A_{\text{disk}} \Delta P v_1)}{\dot{W}_{\text{shaft}}} \quad (4.48)$$

This same result can be obtained by looking at the first and second laws of thermodynamics, and considering the cases of two processes; either a reversible adiabatic process or a reversible isothermal process occurring at the actuator disk. In Sonntag and Van Wylen (1985) it is shown that the reversible work output per unit mass is given by

$$w = -\int_1^e v \, dP + \frac{(v_1^2 - v_e^2)}{2} + g (Z_1 - Z_e) \quad (4.49)$$

If, in the process at the fan, we assume there is negligible change in kinetic and potential energy and that the flow is incompressible (constant density), the useful work produced by the fan would be

$$-w = \int_1^e v \, dP = v(P_e - P_1) = v \Delta P \quad (4.50)$$

The rate of useful work done by the fan is the work per unit mass given above times the mass flow rate through the fan as

$$-\int \dot{m} \, dw = \dot{W}_{\text{useful}} = \dot{m} v \Delta P = \dot{V} \Delta P \quad (4.51)$$

Efficiency of a fan is then the useful power divided by the shaft power supplied to the motor, and this brings us to the commonly used definition of fan efficiency

$$\eta_{\text{fan}} = \frac{\dot{V} \Delta P}{\dot{W}_{\text{motor}}} = \frac{\dot{V} \Delta P}{Q \omega} \quad (4.52)$$

In terms of the dimensionless variables ψ , C_p and ϕ , the efficiency can be expressed as

$$\eta_{\text{fan}} = \frac{\phi \psi}{C_p} \quad (4.53)$$

From the energy equation (the Bernoulli equation) it can be shown that changes in kinetic and potential energy can be included if additional information about the

device or system in which it operates is known. However, the definition of efficiency normally used by fan manufacturers in their catalogs does not normally include them (static pressure efficiency is used).

The use of the dimensionless variables has important implications. By plotting the ψ versus ϕ curve for a given device, the operating performance for new conditions in the dimensional variables can be estimated with reasonable accuracy. The rules used to estimate the new performance variables are known as the **fan (or pump) laws**. For instance, if the device is to operate at a different rotational speed, equality of flow coefficient means that

$$\frac{\dot{V}_{\text{old}}}{\omega_{\text{old}}} = \frac{\dot{V}_{\text{new}}}{\omega_{\text{new}}} \quad \text{and} \quad \frac{\Delta P_{\text{old}}}{\omega_{\text{old}}^2} = \frac{\Delta P_{\text{new}}}{\omega_{\text{new}}^2} \quad (4.54)$$

If the C_p versus ϕ relationship for a given device is known, the torque Q required at a different speed can be estimated by

$$\frac{Q_{\text{old}}}{\omega_{\text{old}}^2} = \frac{Q_{\text{new}}}{\omega_{\text{new}}^2} \quad (4.55)$$

if the size is unchanged. Other relationships can also be derived for the case of similar (in the dimensionless sense), but different sized machines running at the same speed.

4.3.1 Types of Fans and Their Efficiencies

Free-air, or circulating, fans have no orifice or surrounding duct. These fans circulate air within the space in which they are located. These are regularly in a large space, operate against minimal pressure drop and produce maximum velocity pressure. All but the simplest and lightest duty fans operate without a surrounding duct or venturi panel. The types of fans operating within an orifice are the so-called propeller fans, and ducted fans. Propeller fans consist of an impeller within an orifice mounted to a supporting structure and motor. Propeller fans are usually mounted in a wall and move air from one large space to another. The design and type of orifice and placement of the fan blade in the orifice are known to affect the overall performance of the propeller fan.

The term "ducted fan" refers to an axial fan mounted in a duct which encases the impeller, the intake, and the discharge areas of the fan. These fans are generally referred to as either tube-axial fans or vane-axial fans depending on whether or not stationary (normally) flow-conditioning vanes are employed. Tube-axial fans do not use the aforementioned vanes, and have static efficiencies in the range of 40 to 45 percent. The static efficiency cited by manufacturers is

$$\eta_{\text{static}} = \frac{\dot{V} \Delta P_{\text{static}}}{6356 \cdot \text{BHP}} \quad (4.56)$$

where \dot{V} is the volumetric flow of air(cfm), P_{static} is the static pressure overcome in producing this flow (in. H₂O), and BHP is brake horse power applied to the motor. Though tube-axial fans offer improvements in an integral design of mounting structure, motor, duct and impeller, the efficiency range quoted above is about the same as achieved by propeller fans enclosed in a sharp-edged orifice.

The rotational motion imparted to the air by the impeller dissipates energy that might be useful. This energy can be recovered to some degree by adding vanes to the discharge opening of the fan, making it the already-mentioned vane-axial fan. These vanes straighten out the air flow and, in doing so, convert rotational air velocity to static pressure. This additional conversion can give a vane-axial fan total efficiencies of up to 90%. Total efficiency is defined as

$$\eta_{\text{total}} = \frac{\dot{V} \cdot \Delta P_{\text{total}}}{6356 \cdot \text{BHP}} \quad (4.57)$$

where now the total pressure $\Delta P_{\text{total}} = \Delta P_{\text{static}} + \Delta P_{\text{dynamic}}$ difference is used instead of static pressure.

Guide vanes are also used at the intake to impart a compensating swirl to the inflow. Beyond the issue of guide vanes, a variety of other geometric design concerns are of importance. Blade geometry, airfoil design (or camber shape in the case of cambered plates), tip-to-duct clearance, and hub(if used)-to-diameter ratio are some of the factors affecting the overall design. In ducted fan design the orifice shape, tip clearance, duct depth and position of the plane of rotation in the duct are also factors of interest.

4.4 Blade Element Theory

Low solidity rotor blades, whether they be propeller, helicopter or axial-flow fan blades, can be analyzed by making use of two-dimensional airfoil theory. This method of predicting performance is known as blade element theory. As demonstrated in Figure 4.4, the rotor blade is considered to be a wing of span $r_{\text{tip}} - r_{\text{hub}}$ rotating about a center. At a given radius r of the blade, a section of the blade of elemental width Δr can be treated as a two-dimensional airfoil independent of the rest of the blade. This assumes insignificant spanwise or radial velocities. The forces over a section of the blade can be computed and summed over the entire span to arrive at a loading for a single blade. In the case of low blade solidity (0.5 or less), an isolated blade element approach has provided a rough estimate of performance. For larger blade solidities, the isolated airfoil with interference

effects accounted for by the use of interference factors can be used. However, for blade solidities much larger than 0.5 the blade cascade approach must be used. A brief description of each approach will be given below, but for details see Wallis (1983) for a fan and Seddon (1990) for helicopter rotors.

4.4.1 Isolated Airfoils

At a radius r the two-dimensional blade element shown in Figures 4.4 and 4.5 will experience a relative velocity v_R which is dependent on the axial inflow and the net rotational velocity in the rotational plane. The relative velocity shown in Figure 4.5 equals

$$v_R = \sqrt{(\omega r)^2 + v_a^2} \quad (4.58)$$

The rotational component could include pre-swirl which is not considered here. Also, the axial component of velocity v_a could include induced components (especially important for propellers and helicopter rotors) which are not discussed here. The axial inlet velocities for a fan analysis are known if one assumes an inlet profile, knows the fan annulus area and the flow rate for which performance is wished. Most often used is a constant velocity profile. Such a profile is the result of radial equilibrium of pressure and centrifugal forces, and results in an assumed flow condition called free vortex flow.

The angle between the plane of rotation and the total velocity relative to the blade is known as the inflow velocity angle, ϕ in Figure 4.5, and is given by

$$\phi = \arctan \left(\frac{v_a}{\omega r} \right) \quad (4.59)$$

The blade pitch θ at the radial element under consideration is given in Figure 4.5. If the blade geometry is known, then the angle of attack of the relative velocity to the blade is given by

$$\alpha = \theta - \phi \quad (4.60)$$

The elemental lift ΔL on the radial section of area $c \Delta r$ is defined perpendicular to the relative velocity (as shown in Figure 4.5) as

$$\Delta L = \frac{1}{2} \rho v_R^2 C_L c \Delta r \quad (4.61)$$

Similarly, the elemental drag ΔD on the airfoil element is given by

$$\Delta D = \frac{1}{2} \rho v_R^2 C_D c \Delta r \quad (4.62)$$

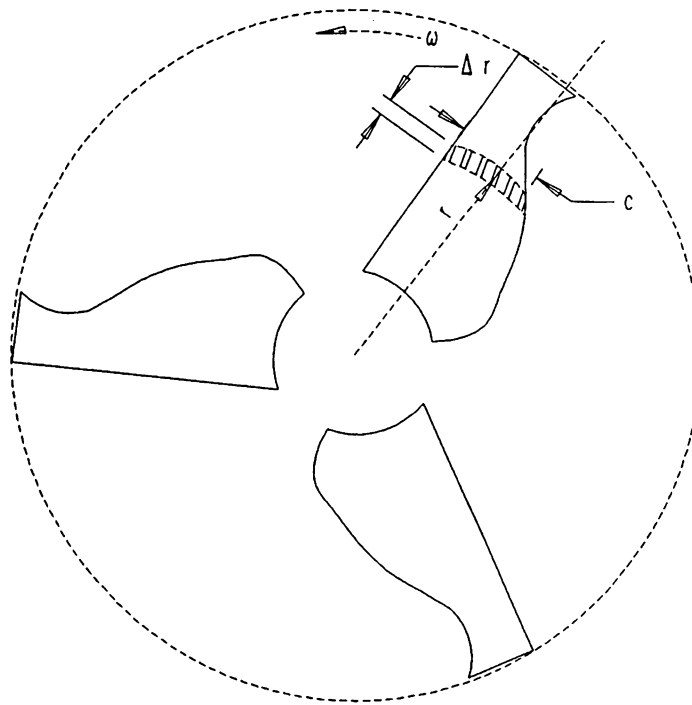


Figure 4.4 Normal view of fan rotational plane for blade element theory derivation

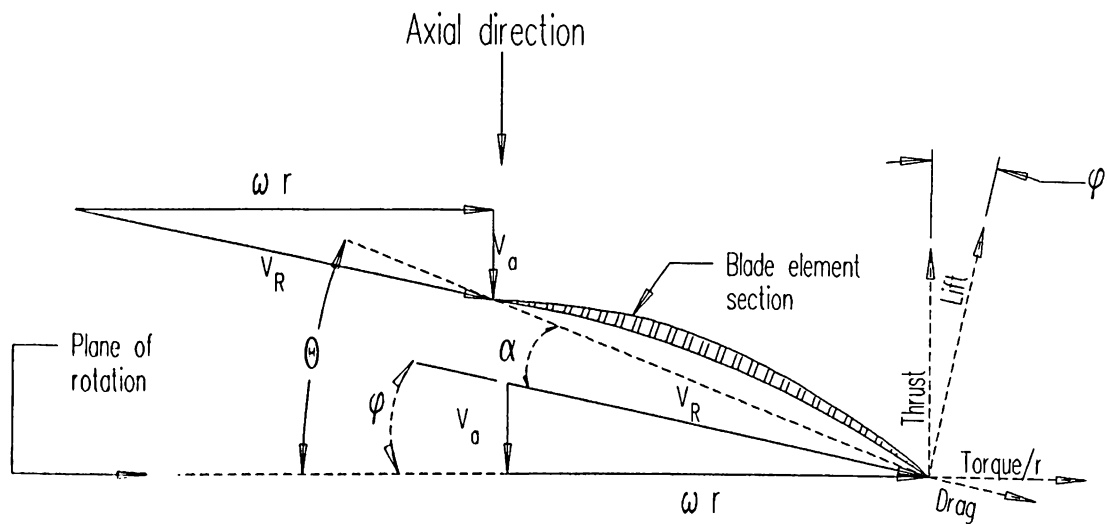


Figure 4.5 Two-dimensional blade section in blade element theory

and must be parallel to the direction of v_r . Using the known inflow angle ϕ these forces can be resolved into the axial and rotational directions of the rotor so that they may be related to the performance variables of thrust and torque respectively. The elemental thrust ΔT is given by

$$\Delta T = \Delta L \cos \phi - \Delta D \sin \phi \quad (4.63)$$

or, from Equations (4.61) and (4.62),

$$\Delta T = \frac{1}{2} \rho v_R^2 c \Delta r (C_L \cos \phi - C_D \sin \phi) \quad (4.64)$$

The elemental torque ΔQ on the section of blade at radius r is given by

$$\Delta Q = (\Delta L \sin \phi + \Delta D \cos \phi) r \quad (4.65)$$

or

$$\Delta Q = \frac{1}{2} \rho v_R^2 c \Delta r r (C_L \sin \phi + C_D \cos \phi) \quad (4.66)$$

After summing the elemental torque and thrust components over a blade span, the total value of thrust and torque for a blade can be estimated. The values of C_L and C_D can be taken or calculated from airfoil characteristic curves as functions of α and section Reynolds number for a given inlet condition. Total pressure rise and power can be calculated once torque and thrust are known. While performance can be estimated using this blade element theory, no prediction of the flow field about the rotor is made, and interactions of the wake with the rotor are also not predicted. Alternative forms of these equations can be derived by substituting dimensionless variables, and can be found in Seddon (1990) for example.

4.4.2 Cascade Approach

The cascade approach to rotor analysis is applied to high solidity blading as stated above. In the cascade approach a radial section of the rotor (see Figure 4.4) would reveal not an isolated airfoil but, rather, an infinite cascade of two-dimensional airfoils a section of which is shown in Figure 4.6. In this way, a radial section, or annulus of width (depth into the paper) Δr , of flow through the rotor can be represented as a cascade of airfoils. As with blade element theory, spanwise flow is not addressed directly by the technique, and corrections for mildly three-dimensional flows can be added. In the cascade momentum theory that follows, a discussion of the forces which produce pressure rise and torque on a rotor will be presented. A brief discussion of blade section geometry and

associated variables is also given. Pressure rise and torque developed on the rotor are then related to lift and drag on a single section of the cascade, and a brief outline of a rotor analysis procedure is given as presented by Wallis (1983). For more details on these techniques the reader should consult either the book by Wallis (1983) (after whose work this discussion is patterned), or another turbomachinery reference such as the excellent one by Vavra (1974).

As seen in Figure 4.6, the entire cascade experiences a uniform velocity v_1 which can be decomposed into axial v_a and tangential $v_{\theta 1}$ components. It is assumed the flow is incompressible, lacking radial components, so that there is no flow of momentum across the sides of the control volume. The axial component upstream equals that component downstream as shown in Figure 4.6. However, the flow is deflected by the cascade and, as a result, the tangential (or rotational) component is changed. The angles which the inflow velocity vector v_1 and inflow velocity vector v_2 make with the axial direction are known as the inlet angle β_1 and outlet angle β_2 , respectively. The rotational components of velocity upstream and downstream of the rotor are given in Figure 4.6 as $v_{\theta 1}$ and $v_{\theta 2}$, respectively, and can have preswirl or rotational components other than ωr as will be discussed. Also in Figure 4.6, the chord length of an airfoil in the cascade is shown as c , and the blade spacing is s . The solidity σ of a rotor is then

$$\sigma = \frac{c N_{\text{blades}}}{2 \pi r} = c \frac{N_{\text{blades}}}{2 \pi r} = \frac{c}{s} \quad (4.67)$$

As discussed by Wallis (1983), a control volume shown in Figure 4.6 is constructed on symmetric streamlines a width s apart about the blade with the control volume inlet experiencing the uniform velocity v_1 and the outlet velocity v_2 . The axial force on the control volume is given by summing the axial components of rate of momentum and pressure forces

$$F_T = \left(\rho s \Delta r v_a^2 \right)_{\text{downstream}} + p_2 s \Delta r - \left(\rho s \Delta r v_a^2 \right)_{\text{upstream}} - p_1 s \Delta r$$

Or,

$$F_T = (p_2 - p_1) \Delta r s \quad (4.69)$$

and the force in the plane of rotation (contributing to torque) is

$$F_Q = s \rho v_a \Delta r (v_{\theta 2} - v_{\theta 1}) \quad (4.70)$$

In the development of this cascade theory, constant pressure is assumed in the planes upstream and downstream of the rotor.

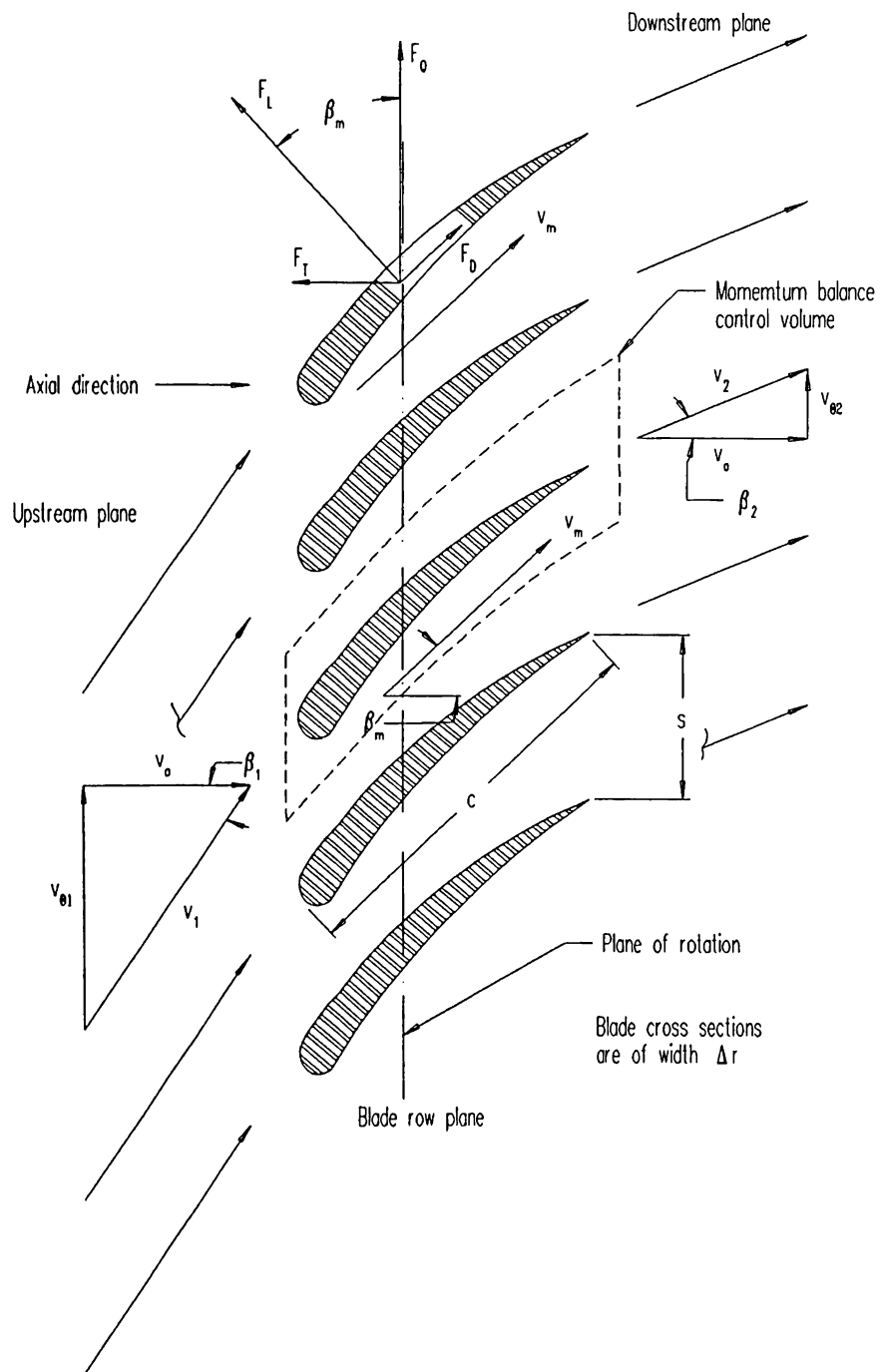


Figure 4.6 A cascade of two-dimensional airfoils

As discussed by Wallis (1983), a control volume shown in Figure 4.6 is constructed on symmetric streamlines a width s apart about the blade with the control volume inlet experiencing the uniform velocity v_1 and the outlet velocity v_2 . The axial force on the control volume is given by summing the axial components of rate of momentum and pressure forces

$$F_T = \left(\rho s \Delta r v_a^2 \right)_{\text{downstream}} + p_2 s \Delta r - \left(\rho s \Delta r v_a^2 \right)_{\text{upstream}} - p_1 s \Delta r$$

Or,

$$F_T = (p_2 - p_1) \Delta r s \quad (4.69)$$

and the force in the plane of rotation (contributing to torque) is

$$F_Q = s \rho v_a \Delta r (v_{\theta 2} - v_{\theta 1}) \quad (4.70)$$

In the development of this cascade theory, constant pressure is assumed in the planes upstream and downstream of the rotor.

Turning our attention to a single representative blade of the cascade as shown in Figure 4.7, first recall that this momentum theory is derived in a blade-fixed reference system. It is assumed, in keeping with Wallis's (1983) derivation, that there is a preswirl velocity $v_{\theta p}$ which is opposite the direction of rotation. The effect of this preswirl in the blade reference system is an increase in the tangential velocity seen by the blade. It is also assumed that there is an afterswirl velocity $v_{\theta s}$ in the outlet flow, and that this swirl velocity component is in the same rotational direction as the blade rotation. In the downstream plane the flow exiting the blade is, therefore, the difference between this swirl velocity and the rotational component ωr of the blade element. Also, in keeping with the convention of Wallis (1983), the preswirl $v_{\theta p}$ and afterswirl $v_{\theta s}$ will both be considered as positive in terms of the convention mentioned above even though they are in opposite directions in a blade-fixed coordinate system. The total pressure rise across the rotor disk can be expressed

$$\Delta H = H_2 - H_1 = \left[p_2 + \frac{1}{2} \rho (v_a^2 + v_{\theta s}^2) \right] - \left[p_1 + \frac{1}{2} \rho (v_a^2 + v_{\theta p}^2) \right] \quad (4.71)$$

Or, the static pressure difference is given by

$$p_2 - p_1 = \Delta H - \frac{1}{2} \rho (v_{\theta s}^2 - v_{\theta p}^2) \quad (4.72)$$

Wallis (1983) then uses a total pressure loss term ΔH_{loss} to account for the

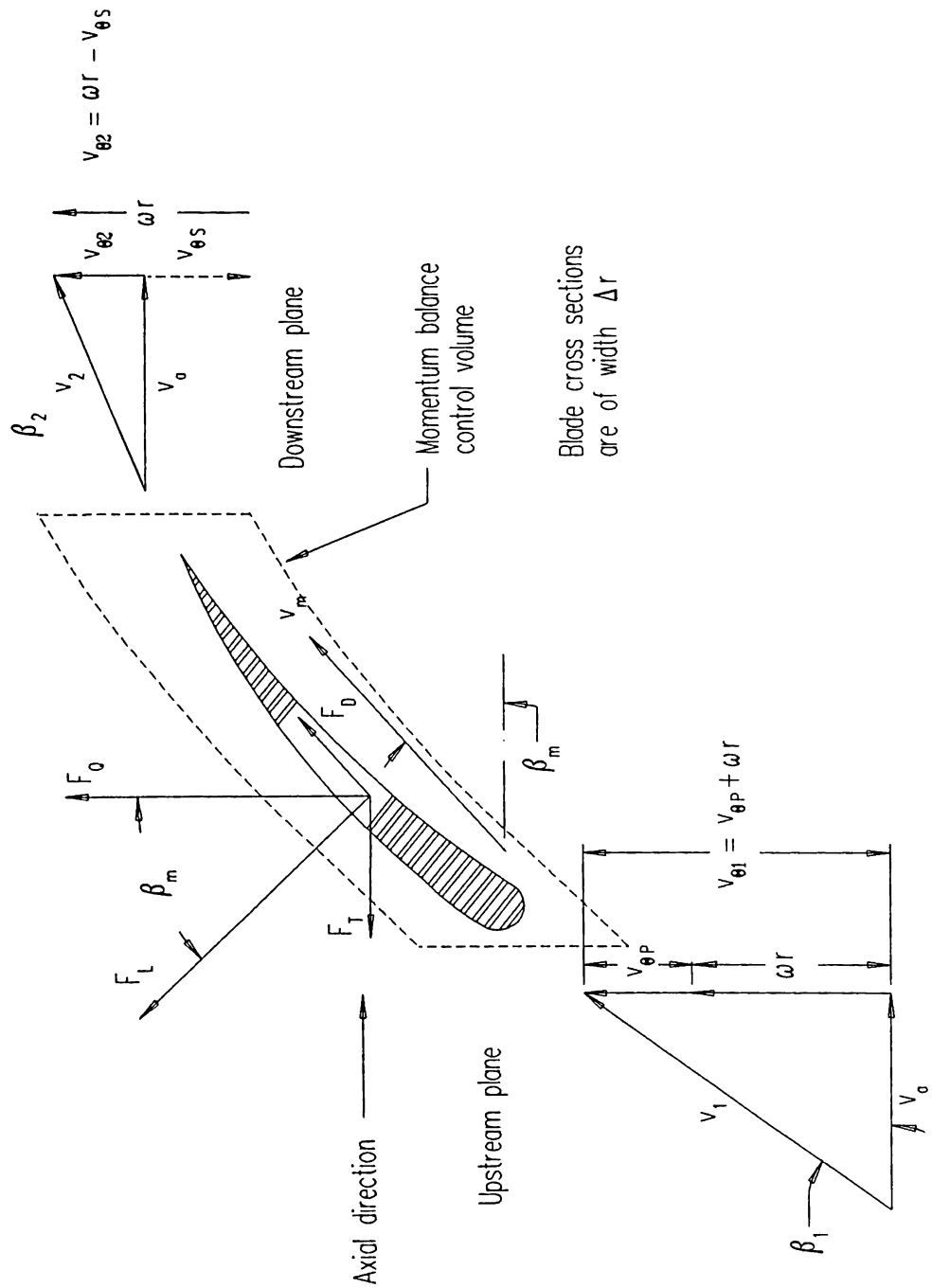


Figure 4.7 A single blade in the two-dimensional cascade flow

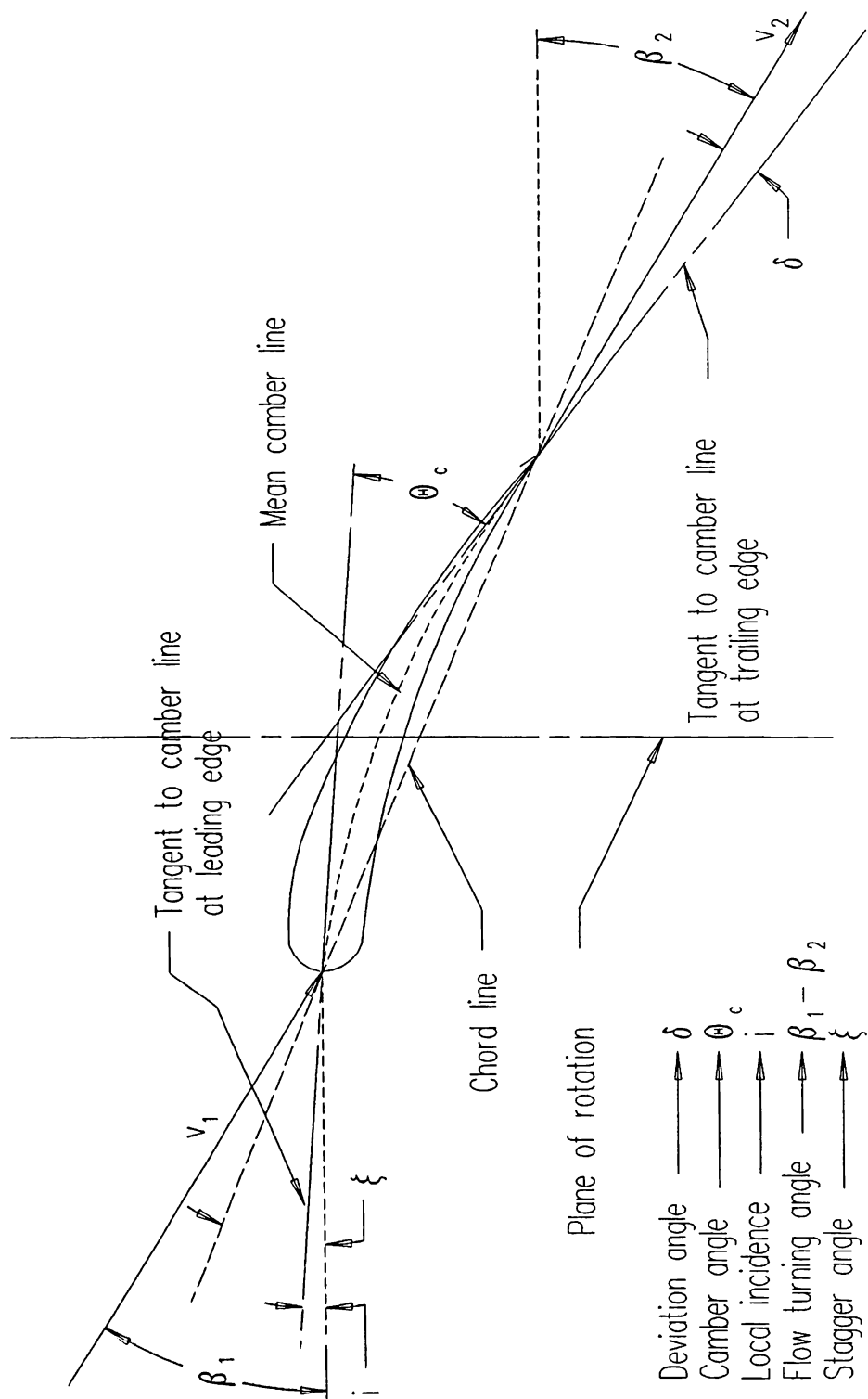


Figure 4.8 Blade angles

departure from the theoretical ideal total pressure rise ΔH_{th} so that

$$p_2 - p_1 = \Delta H_{th} - \Delta H_{loss} - \frac{1}{2} \rho (v_{\theta s}^2 - v_{\theta p}^2) \quad (4.73)$$

Non-dimensionalizing Equation (4.72) using the axial velocity as reference velocity, it is found that

$$p_2 - p_1 = \frac{1}{2} \rho v_a^2 \left[\psi_{th} - \psi_{loss} + \epsilon_p^2 - \epsilon_s^2 \right] \quad (4.74)$$

where the theoretical total pressure coefficient ψ_{th} is given by

$$\psi_{th} = \frac{\Delta H_{th}}{\frac{1}{2} \rho v_a^2} \quad (4.75)$$

the lost total pressure coefficient ψ_{loss} is

$$\psi_{loss} = \frac{\Delta H_{loss}}{\frac{1}{2} \rho v_a^2} \quad (4.76)$$

and the swirl coefficients ϵ are

$$\epsilon = \frac{v_{\theta}}{v_a} \quad (4.77)$$

As discussed earlier, the rate of useful work done on the fluid in the cascade annulus is given by the total pressure rise across the rotor cascade times the volumetric flow rate

$$\dot{W}_{useful} = \Delta H \dot{V} = \Delta H (2 \pi r \Delta r v_a) \quad (4.78)$$

The rate of work put into the motor shaft is ωQ . If all torque is ideally transferred to the fluid as evidenced by its rate of change of angular momentum, the shaft work can be expressed as

$$\dot{W}_{shaft} = \omega (2 \pi r \Delta r v_a \rho) (v_{\theta s} + v_{\theta p}) r \quad (4.79)$$

where the change in rotational velocity across the rotor disk is given by

$$v_{\theta 1} - v_{\theta 2} = (\omega r + v_{\theta p}) - (\omega r - v_{\theta s}) = v_{\theta s} + v_{\theta p} \quad (4.80)$$

as demonstrated in Figure 4.7. If there are no rotor losses and the total pressure rise is equal to the ideal total pressure rise ΔH_{th} then the useful work would be

equal to the actual shaft work so that Equations (4.77) and (4.78) are equated to give

$$\Delta H_{th} (2 \pi r \Delta r v_a) = \omega (2 \pi r \Delta r v_a \rho) (v_{\theta s} + v_{\theta p}) r \quad (4.81)$$

or

$$\Delta H_{th} = \omega \rho (v_{\theta s} + v_{\theta p}) r \quad (4.82)$$

If radial equilibrium holds, the total pressure rise must be constant over the span of the rotor, and therefore should not depend upon r as it appears in Equation (4.81). The total pressure rise will be constant if $v_{\theta s} + v_{\theta p}$ is inversely proportional to r . In the case of a fan with zero preswirl, of particular interest in this study, it is observed that the outlet swirl velocity must be inversely proportional to r , or $v_{\theta s} \propto r^{-1}$, if the condition of radial equilibrium or free-vortex flow is to be satisfied. Equation (4.81) can be non-dimensionalized based on $\frac{1}{2}\rho v_a^2$ to give

$$\psi_{th} = \frac{2}{\lambda} (\epsilon_p + \epsilon_s) \quad (4.83)$$

where λ is termed the local flow coefficient and is given by

$$\lambda = \frac{v_a}{\omega r} \quad (4.84)$$

If an estimate of performance is to be made based on a single representative blade element calculation, the mean axial velocity \bar{v}_a is used to make the expressions written above dimensionless. However, for the commonly used free-vortex assumption in fan design and analysis $v_a = \bar{v}_a$. Bars are similarly placed over the swirl, flow and pressure coefficients to denote that they are a mean approximation.

The lift and drag on a given blade element in a cascade are determined based on the mean velocity in the rotor plane \bar{v}_m as shown in Figure 4.7. In the rotor plane the tangential velocity component is given by

$$\bar{v}_{\theta m} = \omega r - \frac{1}{2} (v_{\theta s} - v_{\theta p}) \quad (4.85)$$

The angle β_m between the mean velocity in the rotor plane and the axial direction is

$$\tan \beta_m = \frac{\omega r - \frac{1}{2} (v_{\theta s} - v_{\theta p})}{\bar{v}_a} \quad (4.86)$$

as shown in Figure 4.7. In terms of the dimensionless coefficients this becomes

$$\tan \beta_m = \frac{1}{\lambda} - \frac{1}{2}(\epsilon_s - \epsilon_p) \quad (4.87)$$

In Figure 4.7 the forces in the axial and tangential (rotational) directions are denoted F_T and F_Q , respectively. Considering Equations (4.68) and (4.69) from a force or rate of momentum balance on a control volume as shown in Figure 4.7, the axial force relative to the blade is given by

$$F_T = (p_2 - p_1) \Delta r s \quad (4.88)$$

and the tangential force is given by

$$F_Q = s \rho v_a \Delta r (v_{\theta s} + v_{\theta p}) \quad (4.89)$$

which, in terms of swirl coefficients, is

$$F_Q = s \rho v_a^2 \Delta r (\epsilon_s + \epsilon_p) \quad (4.90)$$

Considering the force diagram in Figure 4.7, the lift and drag are defined for a given blade cross section as perpendicular and parallel to the mean velocity in the blade plane. The lift and drag can be expressed as

$$F_L = F_Q \cos \beta_m + F_T \sin \beta_m \quad (4.91)$$

and

$$F_D = F_Q \sin \beta_m - F_T \cos \beta_m \quad (4.92)$$

Taking the drag force first, it will be shown that the drag coefficient can be expressed in terms of the solidity ratio, the total pressure loss coefficient and the mean velocity vector direction. This has advantages in making experimental measurements which can both guide the design of the machine and assist in verification of analyses. Taking Equation (4.91) and substituting in Equations (4.87) and (4.89) for F_T and F_Q results in

$$F_D = s \rho v_a^2 \Delta r (\epsilon_s + \epsilon_p) \sin \beta_m - (p_2 - p_1) \Delta r s \cos \beta_m \quad (4.93)$$

Expressing the drag force in terms of the drag coefficient requires dividing both sides by $\frac{1}{2}\rho v_m^2 c \Delta r$. Also, the static pressure difference can be expressed using Equation (4.73), and $\cos \beta_m$ can be substituted for v_a/v_m to give

$$C_D = \frac{s}{c} \cos^3 \beta_m \left[2 (\epsilon_s + \epsilon_p) \frac{\sin \beta_m}{\cos \beta_m} - (\psi_{th} - \epsilon_s^2 + \epsilon_p^2) \right] + \frac{s}{c} \psi_{loss} \cos^3 \beta_m \quad (4.94)$$

The bracketed term in Equation (4.93) is equal to zero by use of Equations (4.82) and (4.86) which gives the result that

$$C_D = \frac{s}{c} \psi_{loss} \cos^3 \beta_m \quad (4.95)$$

The expression is not just of practical use, but is also an expression of the fact that without losses included in the derivation the drag must be zero as one would expect for an ideal flow.

Returning to the expression for lift in Equation (4.90), and substituting in Equations (4.87) and (4.89) for F_T and F_Q , the lift force is

$$F_L = s \rho v_a^2 \Delta r (\epsilon_s + \epsilon_p) \cos \beta_m + (p_2 - p_1) \Delta r s \sin \beta_m \quad (4.96)$$

Determining the lift coefficient requires dividing both sides by $\frac{1}{2} \rho v_m^2 c \Delta r$. Also, as before, the static pressure difference can be expressed using Equation (4.73), $\cos \beta_m$ can be substituted for v_a/v_m , and with additional manipulations one obtains

$$C_L = \frac{s}{c} \cos^3 \beta_m \left[2 (\epsilon_s + \epsilon_p) + (\psi_{th} - \epsilon_s^2 + \epsilon_p^2) \frac{\sin \beta_m}{\cos \beta_m} \right] - \frac{s}{c} \psi_{loss} \cos^3 \beta_m \frac{\sin \beta_m}{\cos \beta_m} \quad (4.97)$$

After manipulation using Equations (4.82), (4.86), and (4.94) the bracketed term becomes

$$\left[2 (\epsilon_s + \epsilon_p) + (\psi_{th} - \epsilon_s^2 + \epsilon_p^2) \frac{\sin \beta_m}{\cos \beta_m} \right] = \frac{2 (\epsilon_s + \epsilon_p)}{\cos^2 \beta_m} \quad (4.98)$$

and the lift coefficient is found to depend on the solidity ratio, the mean velocity vector direction, the swirl coefficients and the total pressure loss coefficient as

$$C_L = 2 \frac{s}{c} (\epsilon_s + \epsilon_p) \cos \beta_m - C_D \tan \beta_m \quad (4.99)$$

A blade loading factor $C_L \sigma$ is often used in fan rotor work, and typically is used in families of curves of $C_L \sigma = f(\epsilon, \lambda)$. In terms of Equation (4.98), the blade loading factor is

$$C_L \sigma = 2 (\epsilon_s + \epsilon_p) \cos \beta_m - C_D \sigma \tan \beta_m \quad (4.100)$$

The relationship between the mean flow direction, and the swirl and flow coefficients was established in Equation (4.86). Also, through manipulation of Equation (4.86) and geometry as shown in Figure 4.7, the mean flow angle is related to the inlet and outlet flow angles via

$$\tan \beta_m = \frac{1}{2} (\tan \beta_1 + \tan \beta_2) \quad (4.101)$$

There also exists a relationship between the blade camber and the degree of flow turning (or deflection) which is commonly termed the flow turning angle, $\beta_1 - \beta_2$. This relationship is given by

$$\beta_1 - \beta_2 = \theta_c + i - \delta \quad (4.102)$$

where the blade angles are defined in Figure 4.8. This relationship is valuable in correlating and presenting experimental measurements of two-dimensional cascades which can be used in the design or design evaluation process.

Wallis (1983) and Johnsen and Bullock (1965) provide valuable compilations of data and charts relating to the behavior of deviation and incidence angles as functions of the cascade geometry, and much more. The incidence angle i has an optimum value according to Wallis (1983) which is a function of solidity and blade camber. Also, for example, there exist experimental cascade data for the estimation of deviation angle δ as a function of solidity, camber and stagger angle. However, the deviation angle is difficult to estimate as it is dependent on boundary layer phenomena. Other examples of design guidelines in Wallis (1983) include recommendations (via charts) of camber for a given amount of flow turning, recommended stagger angle for given camber and inlet conditions, and optimum solidity as a function of flow and swirl coefficients.

It has been shown that, ideally, $\beta_m = f(\lambda, \epsilon_p, \epsilon_s)$ in Equation (4.86). From this and the force relationships, it is note worthy that the performance of a blade element cascade rotor can be estimated primarily based on given flow and swirl coefficients $(\lambda, \epsilon_p, \epsilon_s)$. Actual methods of performance estimation or design are given by Wallis (1983) and Johnsen and Bullock (1965), and require more detail than can be given here. This purpose of this presentation has been to provide a background to a cascade blade element theory which can be used to design or perform evaluations of designs for axial-flow fans (for another example of the technique see Wright and Ralston, 1987).

4.5 Development of Vortex-Element Methods

In the vortex-element (or vortex-lattice) method and other potential flow panel methods it is assumed that the fluid behaves in an ideal manner. In this case it is also assumed that the flow is steady with reference to the rotating blade. This ideal flow field is said to be an incompressible, irrotational, inviscid and homogeneous continuum. In such flow fields the Mach number is zero and the Reynolds number is infinity. It will be shown that a surface in this flow can be represented using a surface singularity distribution of vortex elements. The ideal fluid field is therefore theoretically considered to be unbounded so that the perturbations in the flow field caused by the singularities vanish at infinity. The body in an external flow or the boundaries of an internal flow field will also be streamlines of the unbounded flow field, and can have no normal velocity component at their surfaces.

The vortex singularity and its associated (or induced) flow field (which cause the perturbations in the flow field mentioned above) is a mathematical model which represents the physical response of the ideal fluid to the pressure distribution on the body or boundaries. Thus, even though the velocity field is often said to be induced by vortex elements, it is convenient to think of the irrotational flow field and the rotational vortex elements as a single model of a flow field which is responding to pressure disturbances (Gray, 1992). In this case the flow field is ideal and there is no mechanism for diffusion of vorticity, and pressure disturbances are propagated instantaneously throughout the flow field. There are several important rules and mathematical relationships that are observed when using vortex systems to describe ideal flow fields. However, the essential point of the technique is to use the concept of vortex elements and their associated circulation to predict flow related forces on a surface via the Kutta-Joukowski law. With this in mind, this section presents various aspects of the vortex element technique covering some of the basic concepts of vorticity, induced flow, lifting surfaces and the presentation of a computational lifting surface technique.

4.5.1 Introduction to Vortex Elements

The vortex-lattice method is based on relationships derived from the description of fluid motion using vortex dynamics. The topic of vortex dynamics is discussed in many texts such as those by Panton (1984), Kerwin (1986) and Lan (1988). The discipline of vortex dynamics predates the contributions of Helmholtz and Stokes in the mid-nineteenth century upon whose works much of this section is based. Helmholtz and Stokes were the primary contributors to a mathematical technique, sometimes called the Helmholtz decomposition, by which the velocity field can be divided into irrotational and rotational fields. It was shown by Stokes that a continuous vector field could be split into an irrotational vector field and a rotational (or solenoidal) vector field provided that this vector field and its first

derivatives approach zero at infinity. Consider a velocity vector field \vec{v} which is split as described above

$$\vec{v} = \vec{v}_i + \vec{v}_r \quad (4.103)$$

where the rotational field \vec{v}_r is defined as one with zero divergence ($\nabla \cdot \vec{v}_r = 0$) and the irrotational field \vec{v}_i has zero curl ($\nabla \times \vec{v}_i = 0$).

In an irrotational flow field, the rotational field component is zero which means that

$$\nabla \times \vec{v} = \nabla \times \vec{v}_i = 0 \quad (4.104)$$

This is true for the particular case that the velocity field is equal to the gradient of a scalar function called the velocity potential ϕ

$$\vec{v}_i = \nabla \phi \quad (4.105)$$

For an ideal incompressible fluid, the continuity equation then gives the Laplace equation in velocity potential as

$$\nabla \cdot \vec{v} = \nabla^2 \phi = 0 \quad (4.106)$$

A fundamental solution to Equation (4.105) is a surface distribution of sources (Panton, 1984, p. 351). The general solution to the Laplace equation is given by Lan (1988, p.49) as

$$\phi(x,y,z) = \frac{1}{4\pi} \int_S \left[\frac{\partial \phi}{\partial n} \frac{1}{r} - \phi \frac{\partial}{\partial n} \left(\frac{1}{r} \right) \right] dS \quad (4.107)$$

where r is the distance from the point of surface singularity to the point where the potential is to be computed, n is the surface normal direction of the surface on which the singularities are distributed, and S and dS are the surface area and differential area respectively. Equation (4.106) describes in a mathematical sense that the velocity potential anywhere in the flow field can be calculated from a surface source distribution (the first term of the integral) and a surface doublet distribution (the second term).

Of greater importance to this discussion is the rotational velocity field of Equation (4.102). Consider an amorphous volume V_r of vorticity $\vec{\omega}$ in a three-dimensional flow as shown in Figure 4.9 using a Cartesian coordinate system. A single point of vorticity P_r is defined via the subscript r , and is separated from a point P in the flow by the vector \vec{r} . As discussed above, in the region of vorticity the divergence of \vec{v}_r is zero and the curl of \vec{v}_r is $\vec{\omega}$ in the region of vorticity. From vector analysis, it can be shown that any vector field whose divergence is zero and whose curl is non-zero in any portion of the field can be expressed as the curl of a vector field \vec{A} which has a zero divergence. In the present context this is

expressed as

$$\vec{v}_r = \nabla \times \vec{A} \quad \text{and} \quad \nabla \cdot \vec{A} = 0 \quad (4.108)$$

The vorticity is now expressed as

$$\vec{\omega} = \nabla \times \vec{v}_r = \nabla \times (\nabla \times \vec{A}) = \nabla (\nabla \cdot \vec{A}) - \nabla^2 \vec{A} \quad (4.109)$$

or, by Equation (4.107),

$$\vec{\omega} = - \nabla^2 \vec{A} \quad (4.110)$$

This is the Poisson equation in vector form which has a solution at point P in Figure 4.9 that is

$$\vec{A} = \frac{1}{4\pi} \int_{V_r} \frac{\vec{\omega} \, dV_r}{r} \quad (4.111)$$

The resultant velocity induced by this region of vorticity from Equations (4.107) and (4.110) is

$$\vec{v}_r = \nabla \times \vec{A} = \frac{1}{4\pi} \int_{V_r} \frac{(\vec{\omega} \times \vec{r}) \, dV_r}{r^3} \quad (4.112)$$

a result commonly called the Biot-Savart law (although it is sometimes called Ampere's law when applied to electricity and magnetism). If the region of vorticity is an infinitesimally thin sheet of vorticity, such as a lifting surface, the Biot-Savart law takes the form

$$\vec{v}_r = \frac{1}{4\pi} \int_S \frac{(\vec{\gamma} \times \vec{r}) \, dS}{r^3} \quad (4.113)$$

where $\vec{\gamma}$ is the surface vorticity per unit length on the vortex sheet, and $\vec{\gamma}$ is capable of varying in direction on the surface. The surface vorticity can be described in terms of bound and free vorticity, but for the time being this possibility is not pursued. After boundary conditions are applied to Equation (4.112), an expression for the integral equation to be solved via the vortex-lattice method results. The boundary conditions imposed are that the total velocity at the body surface is tangent to it, that vorticity is conserved over the surface S, and that the flow leaves the surface tangentially. Without applying boundary conditions it is difficult to see how Equation (4.112) can be solved since both \vec{K} and \vec{v}_r are unknown.

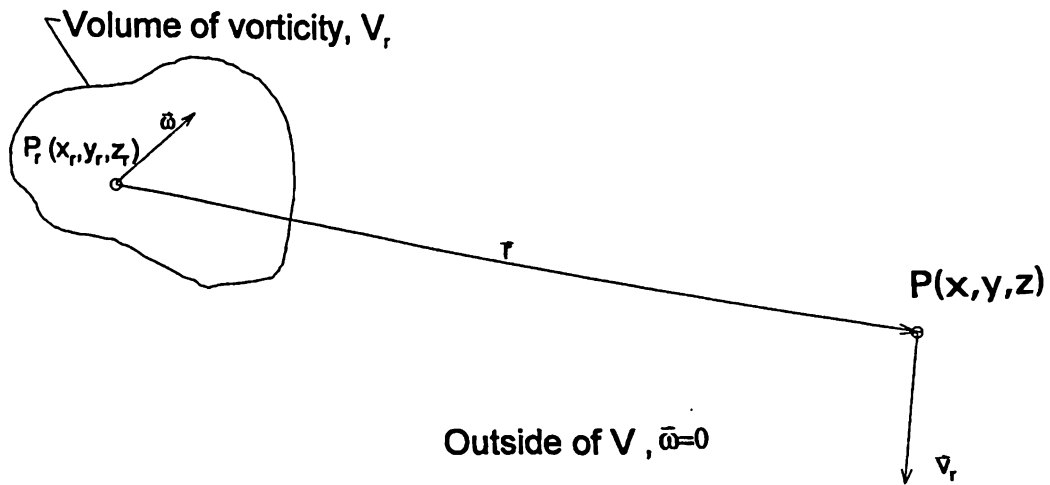


Figure 4.9 Velocity induced at P due to volume V_r of vorticity (after Kerwin, 1986)

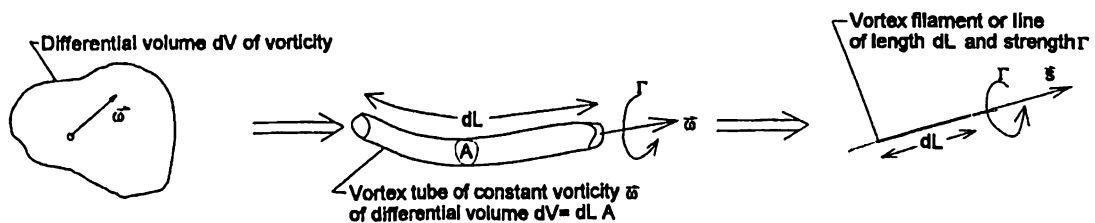


Figure 4.10 Construction of a vortex filament from a volume of vorticity (after Kerwin, 1986)

In order to describe sheets of vorticity, which will come to represent the lifting surface, a lattice of vortex filaments will be used to discretize the vortex sheets. The process of constructing a vortex filament from a volume of vorticity is shown in Figure 4.10. In order, to develop what follows, several definitions and relations of vortex dynamics developed by Thompson (1869), also known by the title Lord Kelvin, will be employed. Kelvin defined the circulation Γ as the line integral of the tangent velocity around a closed contour which is expressed mathematically as

$$\Gamma = \int_C \vec{v} \cdot d\vec{C} \quad (4.114)$$

The relationship between the circulation and the vorticity is given by Kelvin's relation as

$$\Gamma = \int_S \omega_n dS \quad (4.115)$$

where the vorticity $\vec{\omega}$ is defined in Equation (4.108) and ω_n is the component of vorticity normal to the surface S which is bounded by the contour C in Equation (4.113) and over which the integral is computed. For a more complete discussion, see Panton (1984, p. 476).

Now consider the vortex tube shown in Figure (4.10); the vorticity flux for a vortex tube is not dependent on the tube cross-sectional area A . Therefore the vortex tube is defined so that it is a conduit of vorticity of constant strength, and the vorticity is normal to the cross sectional area of the tube and constant. The circulation about the vortex tube as given by Equation (4.114) is $\Gamma = \omega A$. For a segment of tube length dL , the induced velocity as described by the Biot-Savart law is

$$\vec{v} = \frac{1}{4\pi} \int_V \frac{\left(\frac{\Gamma}{A} \vec{s} \right) \times \vec{r} (A dL)}{r^3} = \frac{\Gamma}{4\pi} \int_L \frac{\vec{s} \times \vec{r} dL}{r^3} \quad (4.116)$$

where \vec{s} is the unit tangent vector of the vorticity. The Biot-Savart law as given in Equation (4.115) for a segment of a vortex filament is commonly the starting point of many VLM papers.

4.5.2 Induced Velocity for a Vortex Filament Segment

The velocity due to a vortex filament will now be derived in the manner given by Kerwin and Lee (1978) and others cited therein since this is used in the PSF-2 program. There are other variations on the application of the Biot-Savart

law such as those given by Lan (1988).

Consider the three-dimensional line vortex segment shown in Figure 4.11, which lies between P_1 and P_2 . The velocity induced by the line vortex at a point P is to be calculated by the Biot-Savart law, Equation (4.115). The vortex has a strength Γ and the distance between a small segment of the vortex $d\xi$ and the point P is given by the vector \vec{r} in keeping with the previous notation. Even though \vec{r} varies along the integration path, the line vortex and point of induced velocity calculation lie in a plane. Then for this case application of the Biot-Savart law leads to a scalar calculation. Then the direction of the velocity determined separately from the cross product of \vec{s} and \vec{r} will always be normal to plane of Figure 4.11. For a given field point P and line vortex, a two-dimensional "local" coordinate system can be used in the plane of P , P_1 and P_2 . These are the ξ and η axes shown in Figure 4.11 with η chosen so that P lies upon it. Therefore the distance d in Figure 4.11 is the shortest distance between P and the line vortex. The coordinates of P , P_1 and P_2 are given in both the global cartesian coordinate system and the local coordinate system in Figure 4.11 for the sake of clarity. The vortex element direction vector is $\vec{s} = \langle 1, 0 \rangle$ and field point vector is $\vec{r} = \langle \xi, \eta \rangle$ as defined in the local coordinate system. Putting these vectors into the Biot-Savart law, Equation (4.11), and leaving out the direction of the induced velocity, the induced velocity at P is given by

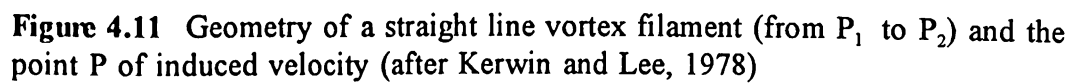
$$\begin{aligned} v(\eta) &= \frac{\Gamma}{4\pi} \int_{\xi_1}^{\xi_2} \frac{\vec{s} \times \vec{r} d\xi}{r^3} \\ &= \frac{\Gamma}{4\pi} \int_{\xi_1}^{\xi_2} \frac{\eta d\xi}{(\xi^2 + \eta^2)^{3/2}} = \frac{\Gamma}{4\pi\eta} \left[\frac{\xi}{\sqrt{\xi^2 + \eta^2}} \right]_{\xi_1}^{\xi_2} \end{aligned} \quad (4.117)$$

The result of Equation (4.116) can be manipulated further, using geometry and the angles θ_1 and θ_2 (see Figure 4.11), to give

$$v(\eta) = \frac{\Gamma}{4\pi\eta} \left[\frac{\xi_2}{\sqrt{\xi_2^2 + \eta^2}} - \frac{\xi_1}{\sqrt{\xi_1^2 + \eta^2}} \right] = \frac{\Gamma}{4\pi\eta} [\cos\theta_2 + \cos\theta_1] \quad (4.118)$$

where the sign of ξ_1 is taken into account when using the trigonometric functions. It is interesting that an infinite line vortex, where θ_1 and θ_2 are zero, gives the result $v(\eta) = \Gamma/2\pi\eta$ for a two-dimensional point vortex.

Equation (4.117) needs to be converted to a general three-dimensional result which can be used to compute induced velocities in the global coordinate



system. For the cartesian coordinates given in Figure (4.11), the result is

$$\mathbf{v} = \frac{\Gamma}{4\pi d} \left[\frac{\mathbf{e}}{c} - \frac{\mathbf{a} - \mathbf{e}}{b} \right] \quad (4.119)$$

where the lengths of a, b, c, d, and e shown in Figure 4.11 can be determined from geometry as

$$\begin{aligned} a &= \sqrt{(x_2 - x_1)^2 + (y_2 - y_1)^2 + (z_2 - z_1)^2} \\ b &= \sqrt{(x_2 - x)^2 + (y_2 - y)^2 + (z_2 - z)^2} \\ c &= \sqrt{(x_1 - x)^2 + (y_1 - y)^2 + (z_1 - z)^2} \\ d &= \sqrt{c^2 - e^2} \\ e &= \frac{a^2 + c^2 - b^2}{2a} \end{aligned} \quad (4.120)$$

The expression for d in Equation (4.119) can be expressed entirely in terms of variables a, b and c by substituting for e into the expression for d in Equation (4.119) which leads to

$$d = \frac{1}{2a} \sqrt{2(c^2a^2 + b^2a^2 + c^2b^2) - (a^4 + b^4 + c^4)} \quad (4.121)$$

or, after factoring, as

$$d = \frac{1}{2a} \sqrt{-(c + a - b) \cdot (c + a + b) \cdot (c - a - b) \cdot (c - a + b)} \quad (4.122)$$

However, the expressions given in Equations (4.118) and (4.119) are used in the computational work owing to the complexity of Equations (4.120) and (4.121). The point of representing the induced velocity at a point in terms of only the lengths a, b and c explicitly, emphasizes that only the end point coordinates of a line vortex segment, its strength and the coordinates of the field point are required to calculate the induced velocity.

There are special cases to be considered since Equation (4.118) becomes poorly behaved should the distance d become very small. Kerwin and Lee (1978) included two special cases taken from the work of Tsao (1975) for evaluating Equation (4.118) should d approach zero (less than 1×10^{-8} in the PSF-2 computer program). These cases are demonstrated in Figure 4.12. In both cases shown in

Figure 4.12, the distance between the vortex line and the field point may be quite large even if d is small.

For Case A in Figure 4.12, the condition that $b > c$ and $d \rightarrow 0$ can be used to perform the special calculation for Case A. For Case A the approximation to Equation (4.118) used is

$$v = \frac{\Gamma d}{8\pi} \left[\frac{1}{e^2} - \frac{1}{(a - e)^2} \right] \quad (4.123)$$

since $\cos \theta_1$ and $\cos \theta_2$ are approximated by

$$\cos \theta_1 \approx -1 + \frac{d^2}{2(a - e)^2} \quad \text{and} \quad \cos \theta_2 \approx 1 - \frac{d^2}{2e^2} \quad (4.124)$$

For Case B in Figure 4.12, the condition that $e > a$ and $d \rightarrow 0$ can be used to test for Case B. For Case B the approximation to Equation (4.118) used is

$$v = -\frac{\Gamma d}{8\pi} \left[\frac{1}{e^2} - \frac{1}{(a - e)^2} \right] \quad (4.125)$$

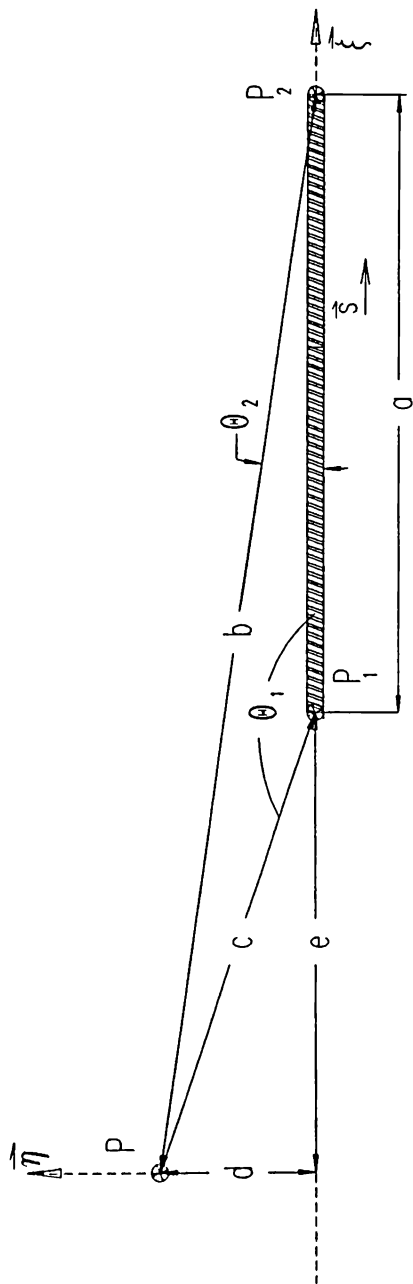
since $\cos \theta_1$ and $\cos \theta_2$ are now approximately given by

$$\cos \theta_1 \approx 1 - \frac{d^2}{2e^2} \quad \text{and} \quad \cos \theta_2 \approx -1 + \frac{d^2}{2(a - e)^2} \quad (4.126)$$

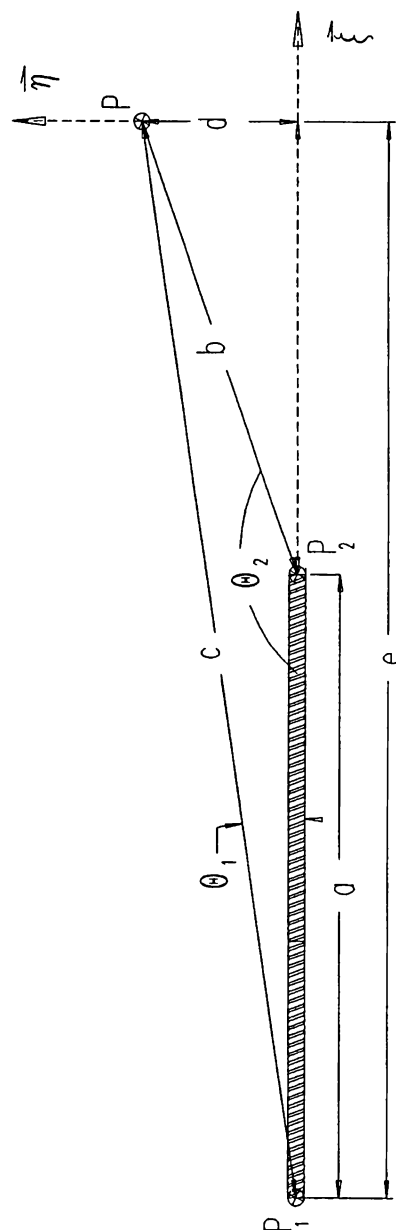
All that remains is to determine the velocity direction, the unit direction of the induced velocity vector. As discussed previously, it can be determined from the cross product of the vector \vec{a} (defined by the line vortex as $\vec{a} = \langle (x_2 - x_1), (y_2 - y_1), (z_2 - z_1) \rangle$) and any other vector (shown as \vec{r} in Figure 4.11) from the line vortex to the field point normalized by the magnitude of the cross product. The vector \vec{r} could be taken from the mid-point of the line vortex to the field point as $\vec{r} = \langle (x - x_m), (y - y_m), (z - z_m) \rangle$ where, for example, $x_m = 0.5 \times (x_2 + x_1)$. The direction $\hat{\phi}$ of the induced velocity is, therefore, given by

$$\hat{\phi} = \frac{\vec{a} \times \vec{r}}{|\vec{a} \times \vec{r}|} \quad (4.127)$$

which means the induced velocity is given by $\vec{v} = v \hat{\phi}$.



Case A



Case B

Figure 4.12 Special case for evaluating the induced velocity at P due to a line vortex (after Kerwin and Lee, 1978)

4.5.3 The Lifting Surface

Issues involved with both a surface of vorticity and a vortex element will now be discussed in order to complete the development of the VLM as used in the PSF-2 program. Consider a surface (see wire frame surface in Figure 4.13) of negligible thickness and arbitrary shape. About this surface there is an incompressible and inviscid flow. In assuming inviscid flow, only the flow problem outside the boundary layers on the surface and outside the viscous wake that leaves the trailing edge of this surface is considered. It is, therefore, assumed that the thicknesses of the viscous flows are negligible in comparison with the dimensions of the lifting surface. Classic derivations of the lifting surface equation, an integral equation which relates the normal component of induced velocity (the downwash) to the pressure difference on a wing, are given by Küssner (1940), Lan (1988) and Anderson (1984).

The surface (known as a lifting surface due to a finite pressure difference across it) does not have sources or sinks and, therefore, the flow velocities on the surface should be everywhere tangent to it. This means that at a given point P on the surface there exist velocities on the upper and lower side of the surface that are coplanar, but not necessarily of either equal magnitude or direction. These vectors on the surface under consideration are shown in detail in Figure 4.13. The vector subscripts denote the upper surface by u , lower surface by l , the mean velocity by m and the difference velocity by d. The vectors are related by

$$\begin{aligned}\vec{v}_u &= \vec{v}_m + \vec{v}_d \\ \vec{v}_l &= \vec{v}_m - \vec{v}_d\end{aligned}\tag{4.128}$$

where

$$\begin{aligned}\vec{v}_m &= \frac{1}{2} (\vec{v}_u + \vec{v}_l) \\ \vec{v}_d &= \frac{1}{2} (\vec{v}_u - \vec{v}_l)\end{aligned}\tag{4.129}$$

In the study of a two-dimensional vortex sheet, or curve, (see Anderson, 1984, p.197) a non-zero difference velocity implies the existence of a local vortex sheet of strength γ (where the notation is switched from ω for the strength of a three-dimensional vortex sheet to γ for the two-dimensional strength) as

$$\gamma = v_u - v_l\tag{4.130}$$

where the absence of vector notation denotes magnitudes. In Equation (4.129) is expressed the fact that A non-zero velocity difference for a surface in three dimensions similarly indicates a vortex sheet with a strength at the point of consideration (P) of

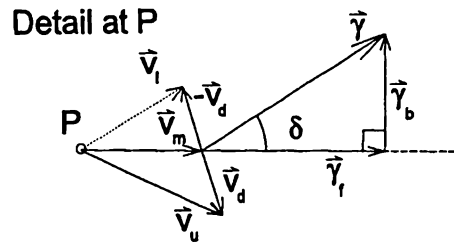
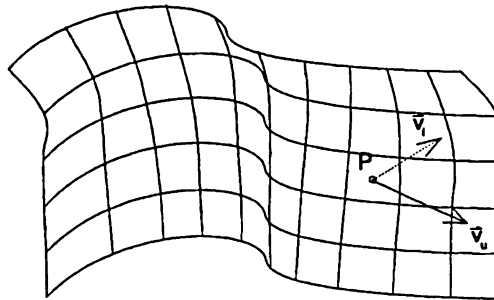


Figure 4.13 A lifting surface with velocity vectors shown at point P in the plane of the lifting surface (after Kerwin, 1986)

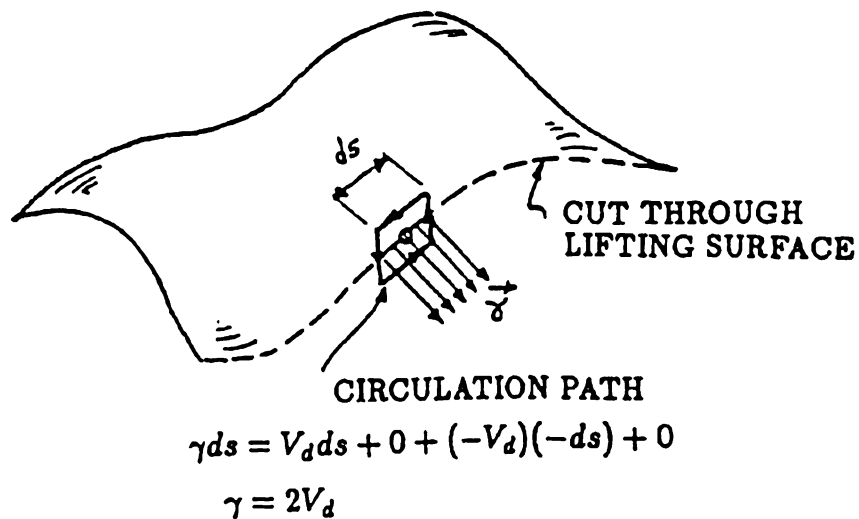


Figure 4.14 The vortex sheet strength γ as derived from calculating the circulation about a small contour (Kerwin, 1986).

$$\gamma = 2 \mathbf{v}_d \quad (4.131)$$

which will have a direction normal to the plane formed by the normal vector to the surface and the difference velocity vector \vec{v}_d . The derivation of Equations (4.129) and (4.130) comes from the calculation of circulation about the surface due to the velocity difference as shown in Figure 4.14. The contour of integration selected to compute γ in Equation (4.130) is taken in a plane normal to the lifting surface at point P. Therefore the vorticity is, as expected, a vector quantity in the lifting surface. Vortex elements will be used to discretize this surface vorticity.

An angle δ is defined between the mean velocity vector \vec{v}_m and the vorticity vector $\vec{\gamma}$ as; this is shown in Figure 4.13. Since Bernoulli's equation holds for the flow, the pressure jump ΔP across the lifting surface can be calculated as

$$\Delta P = P_l - P_u = \frac{1}{2} \rho (v_u^2 - v_l^2) \quad (4.132)$$

The pressure difference can be shown (Kerwin, 1986) to be dependent on the mean velocity magnitude, the vorticity strength γ and the angle δ in the manner

$$\Delta P = \rho v_m \gamma \sin \delta \quad (4.133)$$

It is interesting to note two orientations of the vorticity vector. When the vorticity is aligned with the mean velocity vector \vec{v}_m so that $\delta = 0$, there is no pressure difference between the upper and lower surfaces. In the case of the vorticity vector aligned orthogonally to the mean velocity at an angle $\delta = \pi/2$, the pressure difference is equal to

$$\Delta P = \frac{dL}{dA} = \rho V_m \gamma \quad (4.134)$$

which is the same as that found from the Kutta-Joukowski theorem (soon to be discussed in more detail) for the lift force per unit area on a vortex density γ in two-dimensional flow.

As shown in Figure 4.13 and from the considerations given above, it is desirable to resolve the vorticity vector $\vec{\gamma}$ into a component $\vec{\gamma}_t$ tangent to the mean flow \vec{v}_m and one $\vec{\gamma}_n$ normal to it. The component tangent to or aligned with the mean flow is called the free vorticity, of magnitude

$$\gamma_f = \gamma \cos \delta \quad (4.135)$$

The free vorticity is seen to not contribute to the lift, and is perhaps called free

vorticity as it can be thought of as being transported force free from the surface into the wake. Bound vorticity is the name given to the component normal to the mean velocity vector. This component is

$$\gamma_b = \gamma \sin\delta \quad (4.136)$$

and is the vorticity component contributing to any pressure difference or lift across the surface.

The discussion of this section led to the relationship between the strength of a vortex sheet and the pressure difference across it. This relationship is expressed through the Kutta-Joukowski law (see discussion and derivation by Panton, 1984, p. 476) which for a two-dimensional arbitrary (Joukowski) airfoil is given by

$$\bar{L}' = \rho \bar{v} \times \bar{\Gamma} \quad (4.137)$$

where \bar{L}' is the lifting force per unit span of the airfoil. For a point on a lifting surface where the vorticity strength is $\bar{\gamma}$ and velocity \bar{v} , the force at this point would be

$$\delta\bar{F} = \rho \bar{v} \times \bar{\gamma} \delta A \quad (4.138)$$

where the elemental force is given by $\delta\bar{F}$ and the elemental area about the point on the lifting surface is δA . For a vortex element the Kutta-Joukowski law is

$$\bar{F}_e = \rho l_e (\bar{v}_e \times \bar{\Gamma}_e) \quad (4.139)$$

where the subscript e denotes a variable at a vortex element, l is the length of the element, and the velocity and vortex strength (circulation) are evaluated at the element. The velocity and circulation strength are evaluated using the lifting surface equation by the vortex lattice method which will now be discussed.

4.5.4 The Lifting Surface Equation and Its Solution

The distribution of vorticity on a surface can be found by applying four conditions (to be outlined in this section) to the vorticity distribution and its induced velocity:

1. the flow must be tangent to the surface;
2. Kelvin's circulation, or vortex, conservation theorem must be employed;
3. the Kutta condition that the velocity at the trailing edge must be finite,

the velocity vectors on the upper and lower surfaces must leave the trailing edge smoothly, and these velocity vectors must be collinear though not necessarily of the same magnitude and

4. the trailing vorticity cannot support forces and must, therefore, be aligned with the local flow.

After applying the first condition, the basic lifting surface equation is produced. The other conditions must be considered owing to issues of fundamentals of vorticity dynamics, uniqueness of solutions and numerical discretization.

The lifting surface equation results from applying the condition that the lifting surface (fan blade in this case) becomes a streamline in the potential flow. By assuming a potential flow, the problem can be solved by assembling the solutions of elementary flows (vortex elements, which are themselves solutions) in a linear manner. The vortex elements, sometimes referred to as singularities, are fundamental solutions to the Laplace equation which describes potential flow. However, only when the boundary condition that the surface be a streamline of the flow and the effect of a given singularity must vanish far away from that singularity are applied can a given flow problem be solved. The latter boundary condition, the "infinity condition", is satisfied for a vortex element. The former boundary condition, that the surface be a streamline of the flow, is satisfied by imposing flow tangency at the surface. Specifically, the normal component of the velocity (due to the onset flow and all surface vorticity) must vanish at the surface. Application of the Biot-Savart law (Equation (4.112)) to account for the velocity \vec{v}_r due to all surface vorticity, adding this to a total onset velocity \vec{v}_{total} (composed of the freestream component and a rotational component, since the problem is to be solved in a blade-fixed coordinate system), and imposing the flow tangency condition leads to the lifting surface equation, given here as

$$\left[\vec{v}_r + \vec{v}_{total} \right] \cdot \hat{n} = \left[\frac{1}{4\pi} \int_s \frac{(\vec{\gamma} \times \vec{r}) dS}{r^3} + \vec{v}_{total} \right] \cdot \hat{n} = 0 \quad (4.140)$$

where the equation is satisfied over the lifting surface itself, \hat{n} being the unit vector normal to the lifting surface. The problem to be solved is entirely determined by variables on the boundary of the problem, hence it is called a boundary value problem. The lifting surface equation can be presented in a variety of forms, and in some references (i.e. Lan, 1988 and Anderson, 1984) assumptions as to surface geometry are made in its presentation. Equation (4.139) is a generic form of the lifting surface equation without any stipulations as to surface geometry.

There are a number of important issues left to be resolved before solving the integral equation given by Equation (4.139). The distribution of vorticity over

the surface (on the body and the wake) needs to be discretized in some way. Another issue, related to the manner of discretization, is the method of satisfying the boundary conditions. The points where the boundary conditions are satisfied are called the control points in the VLM. In many numerical integral equation solutions used in panel methods and boundary element methods, the boundary conditions are satisfied by making use of a kernel function or a weighted residual method such as a collocation or Galerkin method. Essentially, the VLM uses a point collocation method to satisfy the boundary conditions. The VLM is simple to apply to problems in steady and unsteady flow even where free wake or nonlinear calculations are done; it, however, lacks the strong mathematical basis which the kernel function methods possess. Whether or not the issue of "mathematical correctness" amounts to anything is moot, since many successful past and recent applications of the VLM to rotating lifting surfaces are discussed in the literature review conducted during this work. The important applications of the VLM to non-rotating lifting surfaces are even more numerous. A mathematically rigorous, and quite novel, approach to the integration of the lifting surface equation is presented by van Niekirk (1986).

4.5.4.1 Discretization

The discretization of the lifting surface (fan blade) and subsequent computations in the VLM are performed using vortex line elements having an induced velocity which was discussed earlier (see Equations (4.118) to (4.126)). In Figure 4.15 are shown three popular techniques of discretizing the surface vorticity (Lewis, 1991) by dividing the surface into quadrilateral panels. A panel of the lifting surface (shown cross-hatched in Figure (4.16)) is defined by a quadrilateral whose vertices lie on the body surface, and the vortex elements must be discretized in some way within this panel. The methods of discretization differ on the basic singularity element is used, and how the Kelvin vortex conservation theorem is applied to the lifting surface.

The classical application of the VLM uses vortex elements arranged in a lattice of "horseshoe vortices" on the quadrilateral panels which define the lifting surface. The wake of the lifting surface is represented by vortex line elements which, by Kelvin's conservation of vorticity theorem, extend an infinite distance downstream into the wake. In many applications of the VLM (i.e. Lan, 1988), a horseshoe singularity (consisting of a spanwise vortex element and two vortex elements trailing from the end points of the spanwise element in a semi-infinite manner) is the basic building block of the model as shown in Figure 4.15, drawing (a). In other words, the induced velocity due to the surface vorticity is computed based on these horseshoe vortex elements rather than single line vortex elements. The horseshoe vortex application of the VLM given by Lan (1988) is really only suitable for flat lifting surfaces. An application using the horseshoe vortex singularity which treats camber effects and free wake effects using vortex line

segments is possible, and Lan has included this in his VORSTAB code.

Another method of vorticity discretization is the "ring" vortex singularity technique shown in Figure 4.15 (b). Chueng (1987) used this technique in his propeller VLM work and provides an excellent discussion of its application. The singularity is actually represented by a square "ring" created by terminating a horseshoe vortex at the next element downstream. While this method leads to relatively straightforward influence coefficients (the normal velocity induced by a vortex "ring" at a control point), the final vorticity distribution must be calculated by subtracting the strengths of adjacent vortex "rings". There appear to be problems associated with this technique since vorticity conservation is not built into the solution process; instead, it is applied when computing the forces. As mentioned by Lewis (1991), the effect of this appears to be cumulative, resulting in poor accuracy (in some cases) when the number of "ring" elements is increased.

The method used in this work is based on individual vortex line segments (Kerwin and Lee, 1978), one of which is shown in Figure 4.15 (c). By this technique each element in the lattice is a singularity of unknown strength. On the face of it, this means a blade lattice of $M \times N$ panels would have $2 \times M \times N$ vortex elements of unknown vortex strengths where the boundary conditions are applied at only $M \times N$ locations. This problem, if solved directly, requires solving a matrix twice as large as in the methods previously mentioned. Alternatively, the unknowns can be represented by two sets of $M \times N$ equations to be solved iteratively which overcomes memory usage problems of the increased matrix size, but requires longer run times. Vorticity conservation could be applied to the solution afterwards as a check on the solution. Or, vorticity conservation could be applied to the vortex lattice in assembling the set of simultaneous equations which means the set of equations can be reduced to solving for either only the chordwise vortex elements or the spanwise elements. While this results in complex recurrence relationships as discussed, though not derived, by Lewis (1991, p. 239) and it reduces the system of equations to be solved, it requires an additional calculation of the vortex element strengths not determined in the solution of the boundary value problem. This method of vortex-lattice discretization has proved accurate and robust (Kerwin and Lee, 1978 and Greeley, 1982), and is used in PSF-2.

As displayed in Figures 4.16 where four vortex-lattice panels are shown (distributed over a lifting surface only one element wide in the spanwise direction), each panel consists of a spanwise vortex line element and two trailing chordwise vortex line element segments. The spanwise vortex (sometimes called the bounder or bound vortex since it will be mostly responsible for lift) is located at the $1/4$ panel chord length in the VLM, and the boundary condition (flow tangency) is applied at the mid-span of the panel at the $3/4$ panel chord length. This method of satisfying the boundary condition is essentially a point collocation method. It is

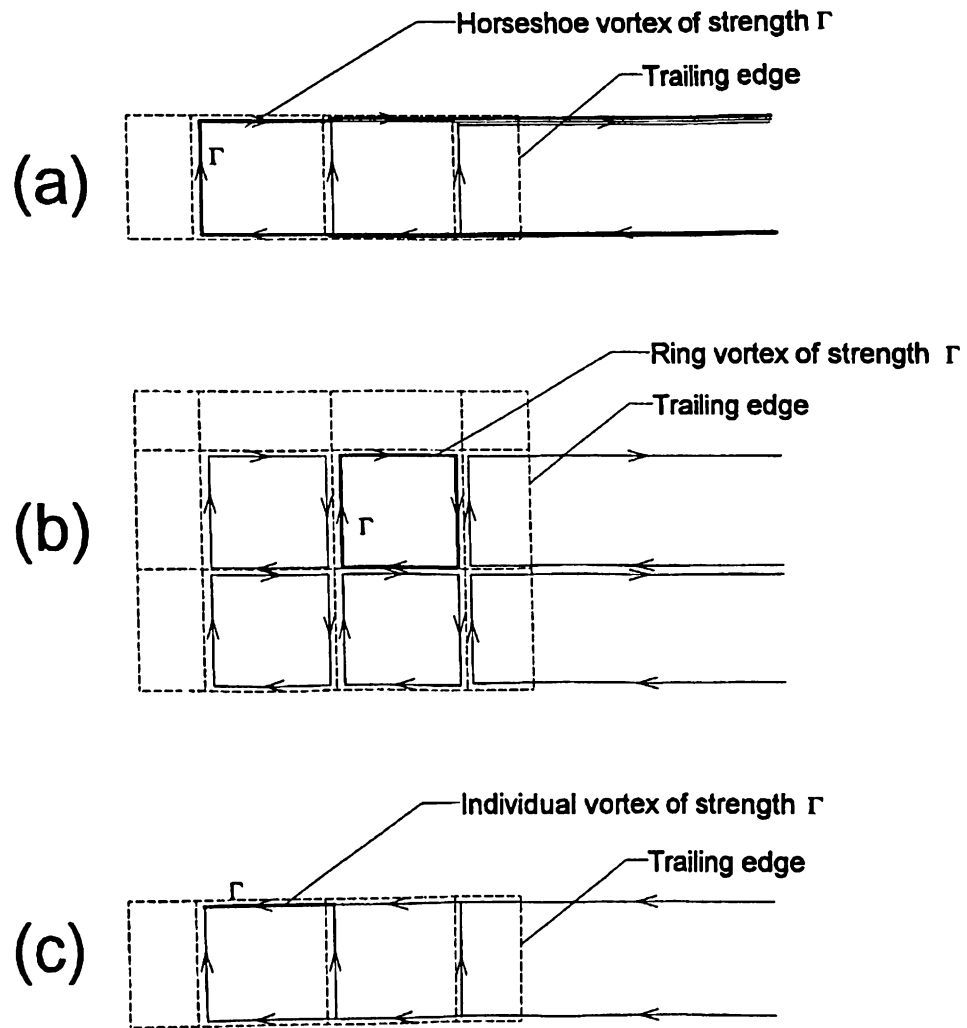


Figure 4.15 Three primary methods of VLM discretization

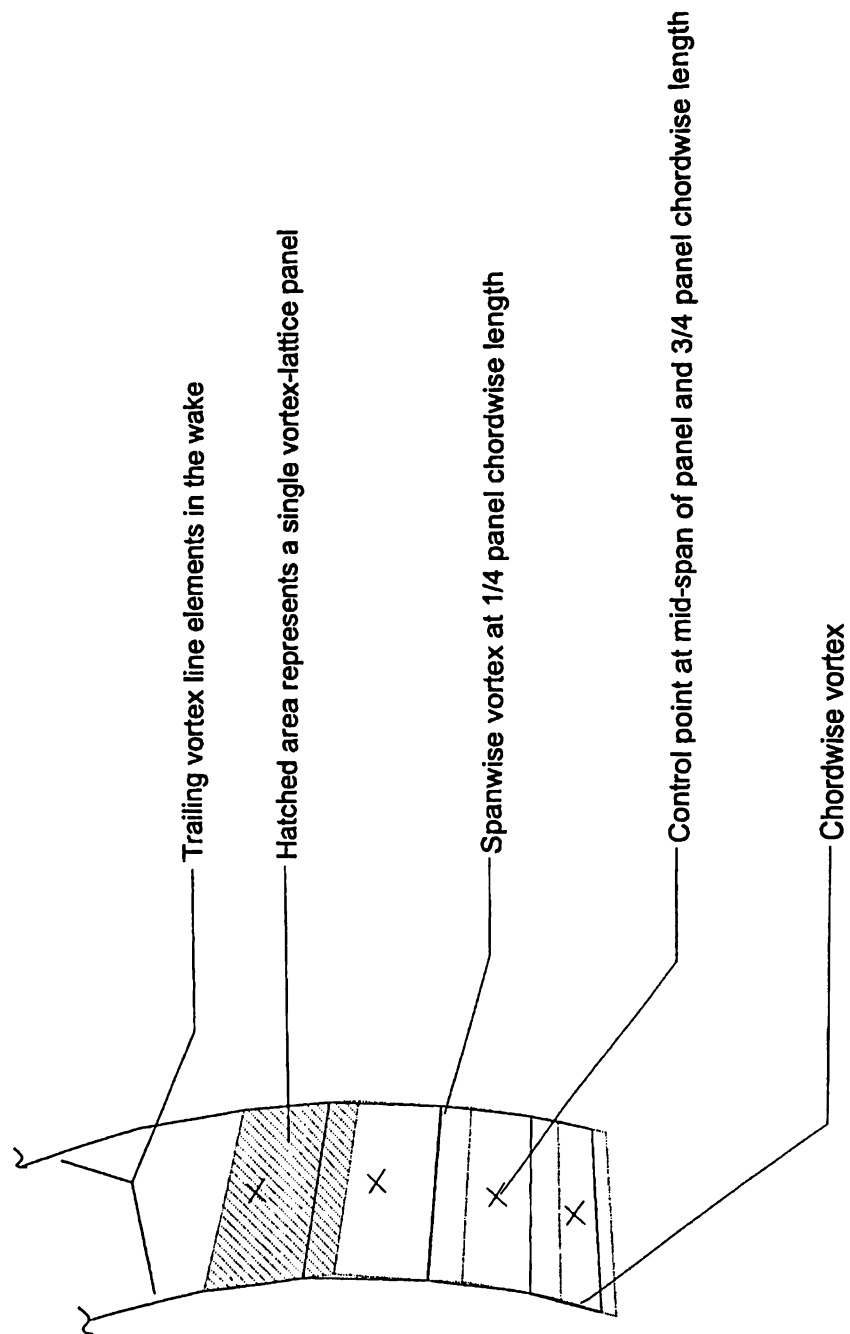


Figure 4.16 A vortex lattice of four panels in the chordwise direction with vortex element and control point locations indicated

based on the "three-quarter-chord theorem" originally derived by Pistoiesi in 1933 (Lan, 1988, p.72). As discussed by Lan (1988), it can be shown that if a discrete vortex is placed at the 1/4 chord point and the boundary condition (flow tangency) is applied at the 3/4 chord point of any number of panels over a two-dimensional flat plate, the resulting circulation (or lift coefficient) is the same as that given by thin-airfoil theory (see Appendix A). The VLM, therefore, applies the boundary condition based on a method verified by thin-airfoil theory as was discussed in detail by James (1969). Also, as discussed by James (1972), the Kutta condition at the trailing edge is implicitly satisfied by this application of the VLM. A further improvement on the VLM was made by Hough (1973), who demonstrated that vortex-lattice panels uniformly spaced in the spanwise direction yield improved accuracy and convergence if the tip lattice elements (at the surface span-extremities) are inset by one-quarter panel. This feature, the one quarter extremity inset, has been included in PSF-2 (Greeley, 1982) at both the blade root and tip.

The blade discretization used in this work is shown in Figure 4.17. Also given in Figure 4.17 are important features in describing the lattice to be used in the detailed development of this application of the VLM. Figure 4.17 is a view of the vortex-lattice from above the suction surface (the upwind side) of a blade. The surface normal vector is defined as positive in the lift force direction. By this definition the surface normal is directed out of the paper toward the reader. The directions of positive vorticity are indicated by arrows on some of the outer-most lattice elements, and are defined on the spanwise direction in such a way that a positive vortex strength produces a force in the positive surface normal direction. The convention of choosing the direction of the chordwise vortex elements is arbitrary, but must be consistently followed when the conservation of vorticity principle is applied at each lattice node point as will soon be discussed. The indices used to identify a number of lattice features; panels, vortex elements, control points, and lattice coordinates, are m in the spanwise direction, and n in the chordwise direction. The enumeration of indices begins at the leading edge for the chordwise direction and at the root for the spanwise direction. The number of panels in the spanwise direction is M and in the chordwise direction N . This means that the total number of panels is $M \times N$, and the number of vortex elements on the blade surface is $(M+1) \times (N+1)$. The convention used for representing a vortex element is to use superscripts c , s , and w to represent whether a given element is a chordwise, spanwise or wake element respectively. Subscripts are then used to represent an element's spanwise and chordwise position with the spanwise index m given first. Several vortex elements are indicated using this notation in Figure 4.17, for example (as represented by $\Gamma_{7,5}^s$ and $\Gamma_{7,3}^c$ where Γ is the element's strength). For the wake elements (essentially consisting only of chordwise elements), the chordwise (really streamwise since they are located in the wake) vortex elements' indices start re-numbering from one with the first element in the wake. A wake element $\Gamma_{6,3}^w$ is pointed out in Figure 4.17 where the 3 subscript denotes it is the third element in the wake from the last trailing element on the blade lattice.

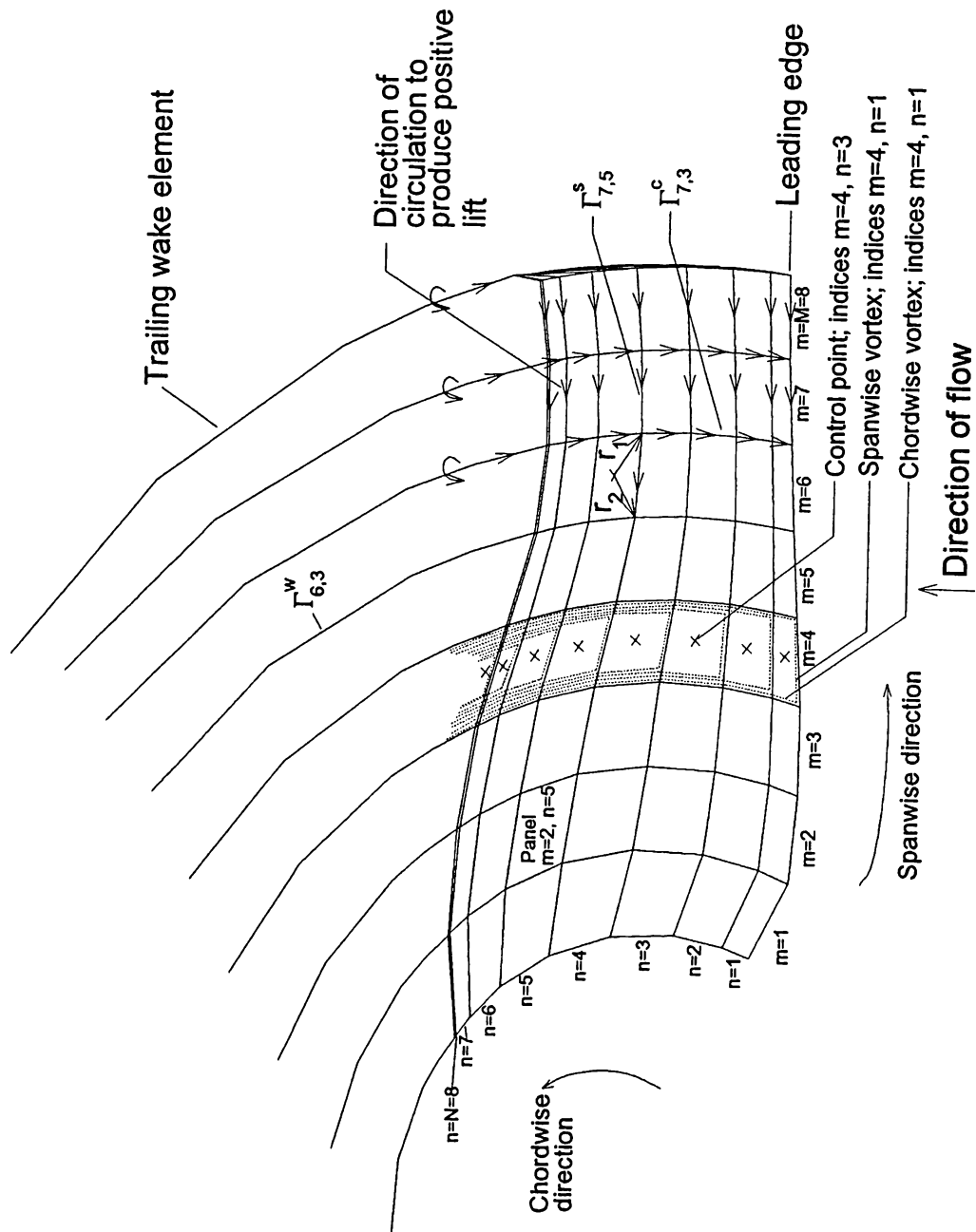


Figure 4.17 A vortex-lattice representation of the Lenexa Products 36 in. fan blade with important lattice features and variables indicated

It should be noted that the direction of the trailing circulation vectors shown in Figures 4.15 and 4.17 differ for the horseshoe, ring and individual vortex element discretizations. The direction convention is model dependent (for instance the ring model forms a closed loop) and arbitrary. However, the convention, once decided upon, must be steadfastly observed when developing the discretized lifting surface equation. This will be done in detail for the individual element discretization shown in Figure 4.15 (c).

4.5.4.2 Application of the Boundary Condition and Vorticity Conservation

Returning to the lifting surface equation (Equation (4.139)), its discretized form will be solved at the control point locations on the lifting surface. In doing so, the total normal velocity at the surface at the i -th (i is the control point index) control point will be set to zero. Since this will be performed at each panel control point (one in each panel), a system of $M \times N$ equations will be solved after Kelvin's vorticity conservation theorem is applied.

The influence coefficient $(A_{m,n})_i$ is defined as the normal velocity at the i -th control point due to the m,n -th vortex line segment of unit strength. From Equations (4.118) and (4.126) the influence coefficient is given by

$$(A_{m,n})_i = \frac{1}{4\pi d} \left[\frac{e}{c} - \frac{a - e}{b} \right] \left(\frac{\vec{a} \times \vec{r}}{|\vec{a} \times \vec{r}|} \cdot \hat{n}_i \right) \quad (4.141)$$

where it is recalled that the vector describing the line vortex segment \vec{a} is $\langle (x_2 - x_1), (y_2 - y_1), (z_2 - z_1) \rangle$, and the vector \vec{r} is from the mid-point of the line vortex to the control point so that $\vec{r} = \langle (x_p - x_m), (y_p - y_m), (z_p - z_m) \rangle$. The surface normal at the i -th control point is given by that panel's spanwise vortex and control point coordinates as

$$\hat{n}_i = \frac{\vec{r}_2 \times \vec{r}_1}{|\vec{r}_2 \times \vec{r}_1|} \quad (4.142)$$

where $\vec{r}_1 = \langle (x_p - x_1), (y_p - y_1), (z_p - z_1) \rangle$, $\vec{r}_2 = \langle (x_p - x_2), (y_p - y_2), (z_p - z_2) \rangle$, and the subscript i indicates these coordinates are the geometry value evaluated for the panel associated with the i -th control point. For example, the vector positions \vec{r}_1 and \vec{r}_2 for the panel at the 6,5 index (panel or control point index) are indicated in Figure 4.17. The influence coefficient for the m,n -th vortex element can then be multiplied by that vortex strength to give the normal velocity at a given control point. Now, the "influence" of all the vortex elements at a given control point can be added to the onset flow to arrive at the discretized form of Equation (4.139).

The discretized form of Equation (4.139) for a given blade lattice, the summed effect of the total induced velocity due to all vortex elements and the

onset velocity (relative to the rotating blade) normal to the surface at the i-th control point be zero, is given by

$$\begin{aligned} & \sum_{m=1}^M \sum_{n=1}^N \Gamma_{m,n}^s (A_{m,n}^s)_i + \sum_{m=1}^{M+1} \sum_{n=1}^N \Gamma_{m,n}^c (A_{m,n}^c)_i \\ & + \sum_{m=1}^{M+1} \sum_{n=1}^{NWAKE} \Gamma_{m,n}^w (A_{m,n}^w)_i + \vec{v}_{total,i} \cdot \hat{n}_i = 0 \end{aligned} \quad (4.143)$$

where the superscripts s,c and w denote spanwise, chordwise and wake elements, NWAKE is the number of wake elements at spanwise index m, and the subscript i indicates that this "single" equation is evaluated at the i-th control point.

In Equation (4.142) the influence of the vortex elements on only one of the rotor blades are considered, and this blade is taken to be the one on which the control points are located. This blade was termed the "key" blade by developers of the PSF-2 program. If the blades of the rotor are equally spaced, one may assume symmetry and equal blade loading. The vortex strength at a given location on each blade would, therefore, be equal. The PSF-2 developers use this feature of the problem to save computation time (actually this concept is disputed by Hess and Valarezo, 1985). The other blades on the rotor are discretized in a coarser mesh than on the key blade, and then influence of the other blades at the control points on the key blade were included by using interpolated estimates of other blade vortex strengths from those of the key blade. The interpolation is solely dependent on blade geometry, the coarse discretization on the non-key blades and the fine "key" blade discretization. Essentially, these interpolations lead to influence coefficients of more complexity, which involve performing this interpolation on the other blades. This author has taken this feature out of his modified version of the PSF-2 program for reasons to be discussed. For the sake of the current discussion, assume that the influence coefficients due the other blades can be formulated in such a way that it is as if each blade on the rotor is equally discretized (as is the case in the author's modified PSF-2 code), and in the case of PSF-2 these influence coefficients actually involve calls to interpolation subroutines. For such a case the discretized lifting surface equation becomes

$$\begin{aligned} & \sum_{m=1}^M \sum_{n=1}^N \Gamma_{m,n}^s \left(\sum_{k=1}^{KBLADE} (A_{k,m,n}^s)_i \right) \\ & + \sum_{m=1}^{M+1} \sum_{n=1}^N \Gamma_{m,n}^c \left(\sum_{k=1}^{KBLADE} (A_{k,m,n}^c)_i \right) \\ & + \sum_{m=1}^{M+1} \sum_{n=1}^{NWAKE} \Gamma_{m,n}^w \left(\sum_{k=1}^{KBLADE} (A_{k,m,n}^w)_i \right) + \vec{v}_{total,i} \cdot \hat{n}_i = 0 \end{aligned} \quad (4.144)$$

where k is the blade index with $k = 1$ signifying the "key" blade and $k = \text{KBLADE}$ denoting the final blade (or the total number of blades). Given inlet velocity conditions (provided in terms of cylindrical coordinate components; axial v_a , radial v_r and rotational v_θ) and a given rotor speed of revolution ω , the onset flow term is known and becomes

$$\vec{v}_{\text{total},i} \cdot \hat{n}_i = \left\{ v_a \hat{x} + v_r \hat{r} + (v_\theta + \omega r) \hat{\theta} \right\}_i \cdot \hat{n}_i \quad (4.145)$$

where r is the radius at the i -th control point and all velocities are given at the i -th control point. The inlet velocity conditions may vary with radius, and are circumferentially averaged for this steady flow problem. The onset term, Equation (4.144), can be moved to the right-hand side of the equal sign in Equation (4.143), and will become the right-hand side array in the $M \times N$ (the number of control points) system of simultaneous equations to be solved to determine the vortex element strengths. If thickness effects are to be included using a source distribution which yields the desired surface thickness, it would be included in the right-hand side.

However, when revisiting Equation (4.143), it is noted that more than $M \times N$ unknown vortex element strengths appear. The wake vortex element strengths $\Gamma_{m,n}^w$ are determined from the final chordwise vortex element in the blade lattice by Kelvin's theorem; or at a given spanwise position m , $\Gamma_{m,n}^w$ is

$$\Gamma_{m,n}^w = \Gamma_{m,N}^c \quad (4.146)$$

After substituting Equation (4.145) into Equation (4.143), the unknown spanwise $\Gamma_{m,n}^s$ and chordwise $\Gamma_{m,n}^c$ vortex strengths are still too numerous. By repeated application of conservation of vorticity the chordwise vortex strengths can be expressed in terms of the spanwise vortex strengths (Kerwin and Lee, 1978). Then the number of unknowns will be reduced to $M \times N$, the number of spanwise vortex elements. Applying the previously discussed sign convention and Kelvin's conservation of vorticity theorem at an arbitrary lattice node, as shown in Figure 4.18, the flux of vorticity into and out of the m,n -th node (shown as a small circle in Figure 4.18) must be equal, or

$$\Gamma_{m,n}^c + \Gamma_{m,n}^s = \Gamma_{m-1,n}^s + \Gamma_{m,n-1}^c \quad (4.147)$$

The m,n -th chordwise vortex element is

$$\Gamma_{m,n}^c = \Gamma_{m,n-1}^c + \Gamma_{m-1,n}^s - \Gamma_{m,n}^s \quad (4.148)$$

Applying this procedure in a recursive manner gives

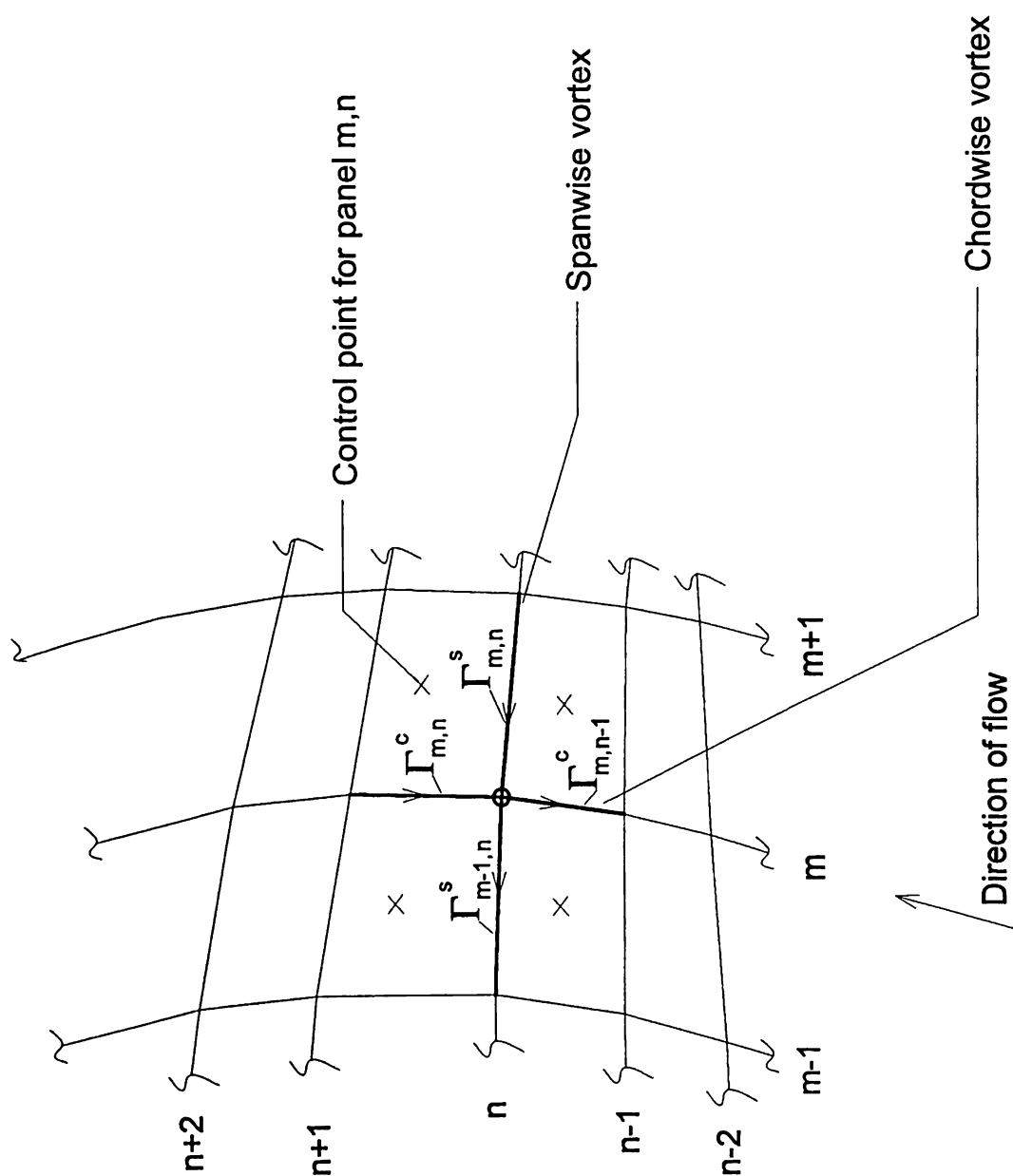


Figure 4.18 An arbitrary section of the vortex-lattice showing vorticity conservation at the m,n -th lattice intersection node

$$\Gamma_{m,n}^c = \Gamma_{m,n-2}^c + (\Gamma_{m-1,n-1}^s - \Gamma_{m,n-1}^s) + (\Gamma_{m-1,n}^s - \Gamma_{m,n}^s) \quad (4.149)$$

Or,

$$\Gamma_{m,n}^c = \sum_{v=1}^n (\Gamma_{m-1,v}^s - \Gamma_{m,v}^s) \quad (4.150)$$

Rewriting the influence coefficients for economy, the spanwise term is

$$\sum_{k=1}^{KBLADE} (A_{k,m,n}^s)_i = S_{m,n} \quad (4.151)$$

the chordwise term becomes

$$\sum_{k=1}^{KBLADE} (A_{k,m,n}^c)_i = c_{m,n} \quad (4.152)$$

and the wake term is

$$\sum_{k=1}^{KBLADE} (A_{k,m,n}^w)_i = W_{m,n} \quad (4.153)$$

Substituting Equations (4.145), (4.149), (4.150), (4.151), and (4.152) into Equation (4.143) makes the discretized lifting surface equation appear as

$$\begin{aligned} \sum_{m=1}^M \sum_{n=1}^N \Gamma_{m,n}^s S_{m,n} + \sum_{m=1}^{M+1} \sum_{n=1}^N \left(\sum_{v=1}^n (\Gamma_{m-1,v}^s - \Gamma_{m,v}^s) \right) c_{m,n} \\ + \sum_{m=1}^{M+1} \sum_{n=1}^{NWAKE} \left(\sum_{v=1}^N (\Gamma_{m-1,v}^s - \Gamma_{m,v}^s) \right) W_{m,n} = - \vec{v}_{total,i} \cdot \hat{n}_i \end{aligned} \quad (4.154)$$

where now the equation is written in terms of only spanwise vortex elements. However, Equation (4.153) cannot easily be put into the form of an influence coefficient matrix, unknown array of spanwise vortex strengths, and right-hand side since it involves complicated terms of both the $m-1$ and m spanwise indices. It would be desirable to cast Equation (4.153) into a form more suited for solution as a system of simultaneous linear equations. The $m-1$ spanwise vortex terms will be

eliminated from Equation (4.153) to facilitate this.

First, working only on the chordwise vortex term, the second term, of Equation (4.153), and expand the summations of n and v (only four terms shown) to obtain

$$\begin{aligned}
& \sum_{m=1}^{M+1} \sum_{n=1}^N \left(\sum_{v=1}^n (\Gamma_{m-1,v}^s - \Gamma_{m,v}^s) \right) c_{m,n} = \sum_{m=1}^{M+1} c_{m,1} (\Gamma_{m-1,1}^s - \Gamma_{m,1}^s) \\
& + c_{m,2} (\Gamma_{m-1,1}^s - \Gamma_{m,1}^s + \Gamma_{m-1,2}^s - \Gamma_{m,2}^s) \\
& + c_{m,3} (\Gamma_{m-1,1}^s - \Gamma_{m,1}^s + \Gamma_{m-1,2}^s - \Gamma_{m,2}^s + \Gamma_{m-1,3}^s - \Gamma_{m,3}^s) \\
& + c_{m,4} (\Gamma_{m-1,1}^s - \Gamma_{m,1}^s + \Gamma_{m-1,2}^s - \Gamma_{m,2}^s + \Gamma_{m-1,3}^s - \Gamma_{m,3}^s + \Gamma_{m-1,4}^s - \Gamma_{m,4}^s) \\
& + \dots =
\end{aligned} \tag{4.155}$$

After collecting like terms of Γ the right-hand side, Equation (4.154) becomes

$$\begin{aligned}
& \sum_{m=1}^{M+1} [\Gamma_{m-1,1}^s (c_{m,1} + c_{m,2} + c_{m,3} + c_{m,4} + \dots) \\
& + \Gamma_{m-1,2}^s (c_{m,2} + c_{m,3} + c_{m,4} + \dots) \\
& + \Gamma_{m-1,3}^s (c_{m,3} + c_{m,4} + \dots) + \Gamma_{m-1,4}^s (c_{m,4} + \dots) + \dots \\
& - \Gamma_{m,1}^s (c_{m,1} + c_{m,2} + c_{m,3} + c_{m,4} + \dots) - \Gamma_{m,2}^s (c_{m,2} + c_{m,3} + c_{m,4} + \dots) \\
& - \Gamma_{m,3}^s (c_{m,3} + c_{m,4} + \dots) - \Gamma_{m,4}^s (c_{m,4} + \dots) - \dots] =
\end{aligned} \tag{4.156}$$

The index on the Γ_{m-1}^s is now shifted from $m-1$ to m , which alters the summation indices as well, so that Equation (4.155) becomes

$$\begin{aligned}
& \sum_{m=0}^M [\Gamma_{m,1}^s (c_{m+1,1} + c_{m+1,2} + c_{m+1,3} + c_{m+1,4} + \dots) \\
& + \Gamma_{m+1,2}^s (c_{m+1,2} + c_{m+1,3} + \dots) \\
& + \Gamma_{m,3}^s (c_{m+1,3} + c_{m+1,4} + \dots) + \Gamma_{m,4}^s (c_{m+1,4} + \dots) + \dots] \\
& - \sum_{m=1}^{M+1} [\Gamma_{m,1}^s (c_{m,1} + c_{m,2} + c_{m,3} + \dots) + \Gamma_{m,2}^s (c_{m,2} + c_{m,3} + \dots) \\
& + \Gamma_{m,3}^s (c_{m,3} + \dots) + \Gamma_{m,4}^s (c_{m,4} + \dots) + \dots] =
\end{aligned} \tag{4.157}$$

Now, keeping in mind that an arbitrary vortex-lattice is considered, assumptions can be made about the blade lattice used. Specifically, in our notation for the blade lattice shown in Figure 4.17 there can exist no spanwise vortex element with indices of $m = 0$ and $m = M+1$. Applying this condition and using a summation notation for the summed influence coefficients shown in brackets in Equation (4.156), Equation (4.156) becomes

$$\begin{aligned} & \sum_{m=1}^M \left[\Gamma_{m,1}^s \left(\sum_{v=1}^N c_{m+1,v} \right) + \Gamma_{m,2}^s \left(\sum_{v=2}^N c_{m+1,v} \right) \right. \\ & + \Gamma_{m,3}^s \left(\sum_{v=3}^N c_{m+1,v} \right) + \dots - \Gamma_{m,1}^s \left(\sum_{v=1}^N c_{m,v} \right) \\ & \left. - \Gamma_{m,2}^s \left(\sum_{v=2}^N c_{m,v} \right) - \Gamma_{m,3}^s \left(\sum_{v=3}^N c_{m,v} \right) - \dots \right] = \end{aligned} \quad (4.158)$$

Equation (4.157) then simplifies to

$$\begin{aligned} & \sum_{m=1}^M \left\{ \sum_{n=1}^N \left[\Gamma_{m,n}^s \left(\sum_{v=n}^N c_{m+1,v} - c_{m,v} \right) \right] \right\} = \\ & \sum_{m=1}^{M+1} \sum_{n=1}^N \left(\sum_{v=1}^n (\Gamma_{m-1,v}^s - \Gamma_{m,v}^s) \right) c_{m,n} \end{aligned} \quad (4.159)$$

where the result is equated to the original expression from the left-hand side of Equation (4.154) involving the influence of the chordwise vortex elements.

Through a similar exercise the wake vortex element term in Equation (4.153) can be rewritten as

$$\begin{aligned} & \sum_{m=1}^{M+1} \sum_{n=1}^{NWAKE} w_{m,n} \left(\sum_{v=1}^N \Gamma_{m-1,v}^s - \Gamma_{m,v}^s \right) \\ & = \sum_{m=1}^M \sum_{n=1}^N \Gamma_{m,n}^s \left(\sum_{v=1}^{NWAKE} w_{m+1,v} - w_{m,v} \right) \end{aligned} \quad (4.160)$$

The discretized lifting equation (sometimes called a boundary value problem), Equation (4.153), can now be entirely written in terms of the m,n -th unknown spanwise vortex strength $\Gamma_{m,n}^s$, the influence coefficients and onset flow term, all which are known from geometry and given inlet conditions. Equation (4.153) for the i -th control point then can be written as

$$\begin{aligned}
& \sum_{m=1}^M \sum_{n=1}^N \Gamma_{m,n}^s S_{m,n} + \sum_{m=1}^M \sum_{n=1}^N \Gamma_{m,n}^s \left(\sum_{v=n}^N c_{m+1,v} - c_{m,v} \right) \\
& + \sum_{m=1}^M \sum_{n=1}^N \Gamma_{m,n}^s \left(\sum_{v=1}^{NWAKE} w_{m+1,v} - w_{m,v} \right) \\
& = - \left\{ v_a \hat{x} + v_r \hat{r} + (v_\theta + \omega r) \hat{\theta} \right\}_i \cdot \hat{n}_i
\end{aligned} \tag{4.161}$$

which can be expressed more concisely as

$$\begin{aligned}
& \sum_{m=1}^M \sum_{n=1}^N \Gamma_{m,n}^s \\
& \left(S_{m,n} + \left(\sum_{v=n}^N c_{m+1,v} - c_{m,v} \right) + \left(\sum_{v=1}^{NWAKE} w_{m+1,v} - w_{m,v} \right) \right)_i \\
& = - \left\{ v_a \hat{x} + v_r \hat{r} + (v_\theta + \omega r) \hat{\theta} \right\}_i \cdot \hat{n}_i
\end{aligned} \tag{4.162}$$

Equation (4.161) represents one equation in a system of equations to be solved, where the right-hand side is a vector of $M \times N$ (the number of control points) components in length (the array representing the vector is taken to be 1, $M \times N$), as also is the length of the vector of unknown spanwise vortex strengths. Then, each row in the system of equations represents the problem defined at a corresponding i -th control point. The influence coefficient matrix is made up of elements given in the brackets above as

$$\left\{ S_{m,n} + \left(\sum_{v=n}^N c_{m+1,v} - c_{m,v} \right) + \left(\sum_{v=1}^{NWAKE} w_{m+1,v} - w_{m,v} \right) \right\}_i \tag{4.163}$$

and is entirely dependent on geometry. In PSF-2 the wake influence coefficients (w in Equation (4.162)) are solved in each iteration of the free-wake analysis since the wake geometry is variable (as will be discussed later). The first two terms of Equation (4.162), however, are entirely determined by blade geometry. This means for a given blade many operating points, or cases, can be executed without having to recalculate this part of each term in the coefficient matrix. Also, note that the influence coefficient matrix elements, one of which is Equation (4.162), can be viewed as a "horseshoe-like" vortex structure composed of a spanwise vortex element (on which the force will be computed by the Kutta-Joukowski law) and the difference between the chordwise vortex elements extending from each end of $\Gamma_{m,n}$ to the end of the wake (at NWAKE). It is with this point in mind that the

reader will note the horseshoe-like structures indicated by dotted lines in Figure 4.17. Ideally, each vortex structure is closed, meaning that the wake extends to infinity where a "start-up" vortex must exist (connecting the ends of the trailing vortex elements in the wake). Such a horseshoe vortex structure satisfies vorticity conservation. Therefore, after using the individual vortex element technique and applying the conservation of vorticity to the lattice, an influence coefficient matrix results whose individual elements are "horseshoe-like" vortices.

The resulting systems of equations to be solved for the vortex element strengths, Equation (4.161), is similar in some respects to that given by Kerwin and Lee (1978). However, their formulation was derived for an unsteady flow, and indeed there also appears to be a typographical error in their published result. However, the result given here is the procedure of assembling the coefficient matrix performed in PSF-2. That is, the derivation given here confirms the procedure used by Greeley in the PSF-2 code, as determined by examining the code (in subroutine HSKEY). It should be noted that Greeley (1982) gives no discussion of the development of the boundary value problem beyond the presentation of the basics. In particular, according to Greeley (1982), the system of equations to be solved for the vortex strengths Γ_j is given by

$$\sum_{j=1}^{M \times N} A_{ij} \Gamma_j = - \hat{n}_i \cdot \vec{v}_{total_i} \quad (4.164)$$

where A_{ij} are the elements of the influence coefficient matrix (no more information about them is given by Greeley), i is the control point index, j is the spanwise vortex index and the right-hand side is the onset flow term (which actually includes source terms which have their origin in the non-zero blade thickness). Though the results of the present derivation appear similar to the results of Kerwin and Lee (1978), they are different. And, the complete discussion of these basic details of the method (such as that given here) is absent from the literature this author has seen on PSF-2. It is likely that the PSF-2 developers recorded it at some point, though.

In order to represent the tip vortex separation which occurs at increasing angles of attack (particularly on swept wings of low aspect ratio), the developers of the PSF-2 code included the ability for the outermost chordwise vortex elements to separate from the blade (as shown in Figure 4.19) in a prescribed or semi-free manner (as will be discussed shortly). As a consequence of this modelling feature, some improvement in the prediction of the increased lift resulting from this tip-vortex is obtained. Germane to the present discussion is the fact that this feature alters the discretized lifting surface equation on the outermost panels (at $m = M$). These $(M+1)$ -th chordwise vortex elements separate from the blade and collect at the same point (shown near the trailing edge in Figure 4.19), altering the influence coefficient matrix at elements where $m = M$. For this case, after applying vorticity

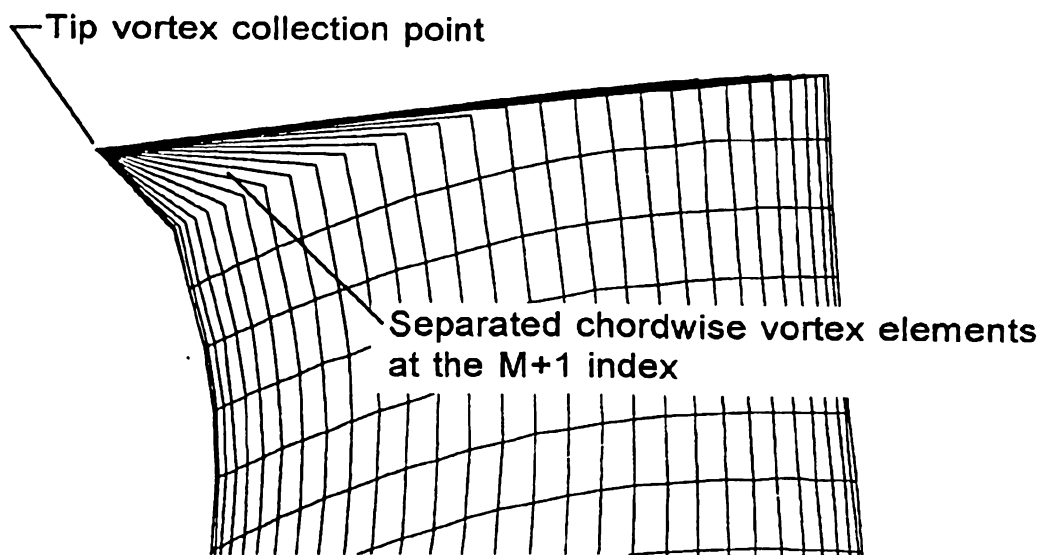


Figure 4.19 Detail of separation of chordwise tip vortex elements as used in PSF-2 on the Lenexa Products 36 in. fan blade (the blade tip is at the abrupt change in vortex line slope)

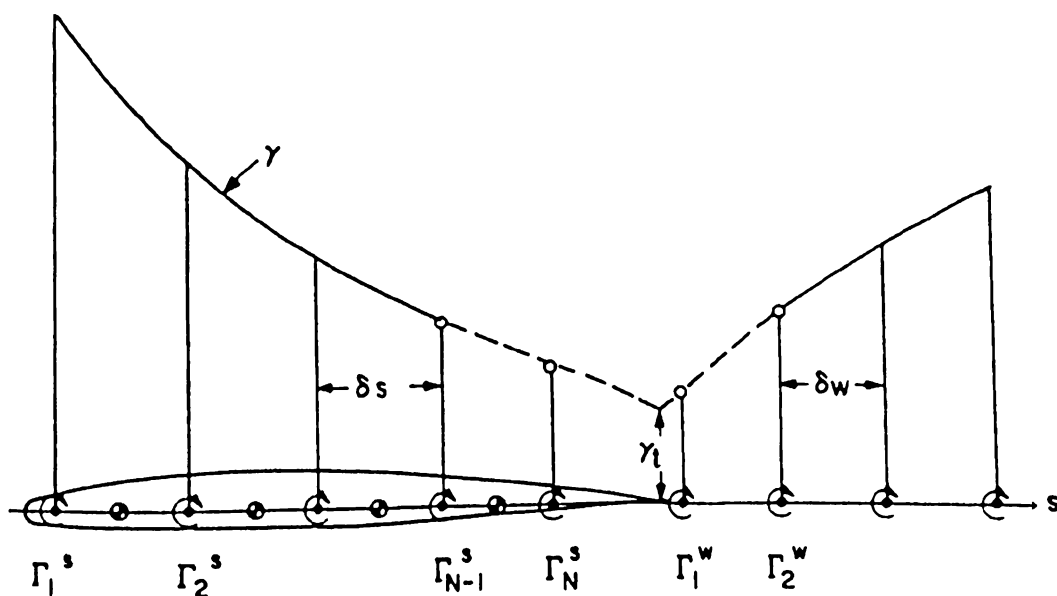


Figure 4.20 Graphical demonstration of an explicit Kutta condition for an unsteady VLM application (Kerwin and Lee, 1978)

coefficient matrix at elements where $m=M$. For this case, after applying vorticity conservation and using the same vorticity direction convention as previously used, the outermost chordwise vortex element strengths become

$$\Gamma_{M+1,n}^c = -\Gamma_{M,n}^s \quad (4.165)$$

and the strength of the tip-vortex (after the collection point) is given by

$$\Gamma_{M+1,n}^w = \sum_{n=1}^N \Gamma_{M+1,n}^c = -\sum_{n=1}^N \Gamma_{M,n}^s \quad (4.166)$$

The discretized lifting surface equation for the outermost panels where the tip chordwise vortex elements are allowed to separate and collect in the manner shown in Figure 4.19 can be found after removing the $M+1$ term from the sum in Equation (4.153), reworking all chordwise and wake element terms and applying the conservation of vorticity for the separated tip vortex model as given by Equations (4.165) and (4.166) in the derivation. At an intermediate stage in the derivation, where essentially four new terms appear, the discretized boundary value problem appears as

$$\begin{aligned} & \sum_{m=1}^{M-1} \sum_{n=1}^N \Gamma_{m,n}^s \left\{ S_{m,n} + \left(\sum_{v=n}^N c_{m+1,v} - c_{m,v} \right) + \left(\sum_{v=1}^{NWAKE} w_{m+1,v} - w_{m,v} \right) \right\}_i \\ & + \sum_{n=1}^N \left(\Gamma_{M,n}^s S_{M,n} \right)_i - \sum_{n=1}^N \Gamma_{M,n}^s \left(\sum_{v=n}^N c_{M,v} + c_{M+1,n} \right)_i \\ & - \sum_{n=1}^N \Gamma_{M,n}^s \left(\sum_{v=1}^{NWAKE} w_{M,v} \right)_i - \sum_{n=1}^{NWAKE} w_{M+1,n} \left(\sum_{ns=1}^N \Gamma_{M,ns}^s \right)_i \\ & = - \left\{ \mathbf{v}_a \hat{\mathbf{x}} + \mathbf{v}_r \hat{\mathbf{r}} + (\mathbf{v}_\theta + \omega \mathbf{r}) \hat{\boldsymbol{\theta}} \right\}_i \cdot \hat{\mathbf{n}}_i \end{aligned} \quad (4.167)$$

Or, when reduced to its final form, it can be written as

$$\begin{aligned} & \sum_{m=1}^{M-1} \sum_{n=1}^N \Gamma_{m,n}^s \left\{ S_{m,n} + \left(\sum_{v=n}^N c_{m+1,v} - c_{m,v} \right) + \left(\sum_{v=1}^{NWAKE} w_{m+1,v} - w_{m,v} \right) \right\}_i \\ & + \sum_{n=1}^N \Gamma_{M,n}^s \left\{ S_{M,n} - c_{M+1,n} - \sum_{v=n}^N c_{M,v} - \sum_{v=1}^{NWAKE} (w_{M,v} + w_{M+1,v}) \right\}_i \\ & = - \left\{ \mathbf{v}_a \hat{\mathbf{x}} + \mathbf{v}_r \hat{\mathbf{r}} + (\mathbf{v}_\theta + \omega \mathbf{r}) \hat{\boldsymbol{\theta}} \right\}_i \cdot \hat{\mathbf{n}}_i \end{aligned} \quad (4.168)$$

where the equation for all but the outermost (where $m = M$) is the same as before,

and a new form of the influence coefficients appears for the M-th panel as would be expected. Once again vorticity conservation has been used and is, therefore, satisfied. Also, the sign convention of the vortex elements previously used has been observed, and must be carefully observed later when the chordwise vortex strengths are calculated for purposes of aerodynamic force computations via the Kutta-Joukowski law.

The vortex elements' strengths can now be calculated for the lifting surface either without tip vortex separation (Equation 4.161) or with separation (Equation 4.167), using a solver appropriate to the problem. PSF-2 uses Gaussian elimination; however, as mentioned previously, there is at least one iterative solver which offers an improvement in execution time for these fully populated matrices (Clark, 1985).

4.5.4.3 Kutta Condition

The discretization of the lifting surface and the formulation of the system of equations resulting from applying the boundary conditions and vorticity conservation have been presented. This means the first two conditions set forth (on p. 38) to solve the problem have been addressed. The third condition to be addressed is the application of a Kutta condition at the trailing edge of the lifting surface.

The Kutta condition is applied to the solution of both two- and three-dimensional ideal flows in order to uniquely solve for the circulation. As lucidly discussed by Anderson (1984, p.198), if there was flow around the trailing edge (not permitted by the Kutta condition), flow separation would result. This can be observed during startup flow until a stagnation point is established at the trailing edge (assuming the trailing edge has some definite angle, i.e. for a blunt trailing edge the stagnation point fluctuates unsteadily). Flow around the leading edge and large velocity gradients if the leading edge is sharp are not ruled out for two reasons. One reason is that if the actual surface has a rounded leading edge, a sharp edge will not adequately model it; when the actual rounded leading edge is accurately modelled, large velocities at the leading edge are not predicted. The second reason, of more importance to the plate fan blade case, is that separation will occur at the leading edge if the leading edge is sharp; but for moderate angles of attack, the flow will re-attach to the blade a short distance downstream. Because of this re-attachment, the circulation is about the same as that given by inviscid potential flow theory (Kerwin and Lee, 1978). For a steady flow, the Kutta condition is achieved if there is no lift produced at the trailing edge. In other words, there can be no "bound" vorticity at the trailing edge. If the flow is unsteady, the Kutta condition is achieved by allowing no accumulation of bound vorticity at the trailing edge, and the bound vorticity which flows into the trailing

edge must also be shed into the trailing wake during a given time interval.

Generally the Kutta condition is satisfied by what are termed implicit or explicit techniques. When the Kutta condition is satisfied by placing the control points and vortex elements at the appropriate locations on the discretized surface, it is known as an implicit Kutta condition technique. As mentioned earlier, James (1972) showed that the VLM (using the three-quarter chord rule as discussed earlier) implicitly achieves the Kutta condition at the trailing edge for a flat plate and a flat airfoil of parabolic camber. Explicit methods of satisfying the Kutta condition at the trailing edge require that the vortex elements near the trailing edge have some prescribed strength behavior to meet the Kutta condition. For example, Kerwin and Lee (1978) discuss an explicit technique where the last two element have strengths directly proportional to their distances from the trailing edge. Also, Kerwin and Lee use an explicit technique for satisfying the Kutta condition in their unsteady VLM flow model which prescribes a continuous functional behavior (the dashed lines on either side of the trailing edge) for γ as shown in Figure 4.20. In this figure, note that the strength γ_t of the vortex element at the trailing edge is non-zero. Note too that, by the prescribed behavior of the element strengths, the strengths given by the function (dashed line in Figure 4.20) just upstream and downstream of the trailing edge are approximately equal. In both the PSF-2 program, and the author's modified version of PSF-2 the Kutta condition is satisfied by an implicit technique.

4.5.4.4 Wake Alignment

Wake alignment, the fourth condition addressed on p. 94 to solve for the blade singularity strengths, is an improved representation of the lifting surface wake over "classical" wake models. The "classical" wake model for a non-rotating lifting surface is for the trailing vortex lines to proceed as straight semi-infinite lines from the last panel. The classical rotating lifting surface wake is a helix of constant pitch. The helix pitch is dependent on the speed of the onset flow and the rate of revolution or, in the case of a propeller, it is dependent on the advance ratio. A prescribed fixed wake model is a slight improvement over the classical wake in that the wake contracts and has variable pitch, but these variations are predetermined by detailed physical knowledge of the rotor wake gleaned from past experience. Ideally, wake alignment and rotor free-wake analysis can predict the wake geometry as part of the solution procedure, thus eliminating both guess work and wake geometry observations.

A solution of the strengths of the singularities on the blades and in the wake can proceed by solving a system of equations determined by the boundary conditions as previously discussed. Using the constraints of conservation of vorticity, as previously shown, the trailing wake strengths are dependent on the spanwise vortex element strengths on the blade surface (Equations (4.145) and

(4.149)). However, in order to calculate the vortex strengths the positions of the trailing wake elements must be known in order to compute their induced velocities normal to the blade surface at the control point locations. Therefore, wake geometry must be iteratively determined in the problem's solution. An assumed wake geometry is used on the first calculation; then the computed vortex strengths are used to calculate the velocity vector at trailing wake elements which must be aligned with their local velocity directions so that they remain force free. The position of the free vortex elements in the wake are then determined and their new positions (or in its entirety, the new wake geometry) can be used on the next iteration to calculate the vortex strengths. However, care must be taken in calculating the self-induced velocities of a given line vortex, and PSF-2 uses the method developed by Sadler (1971) (Sadler's work is readily available, but his method was derived from that of Crimi (1965), a harder to find reference) for free-wake helicopter rotor analysis where a finite vortex core size must be assumed.

The fourth and final condition for calculating the vortex strengths is not rigorously treated for the case of fixed wake or prescribed wake models. When this fourth condition (given on p. 38) is applied, it adds particular difficulties in the case of the lifting surface methods applied to rotating lifting surfaces (propellers, fan blades and helicopter rotors) since the wake structure is more complex than for, say, a lifting wing. Therefore, the inclusion of the fourth condition leads to a non-linear numerical lifting surface approach. The details used in PSF-2 are given by Greeley (1982), and will be discussed in more detail when discussing the PSF-2 program execution.

4.5.5 Lifting line theory

In extending the lifting surface theory to finite wings, it is customary to begin with lifting line theory before discussing the VLM. So the present discussion, traditionally speaking, is in the wrong order. However, a brief discussion of lifting line theory is included at this point with the realization that if the VLM method is already set forth. A discretized lifting line approach will subsequently be recognized as a VLM approach in which only one panel is used in the chordwise direction of the lifting surface. In the classical lifting line theory set forth for propellers by Betz (1919) and Goldstein (1929), the bound vorticity is given by a function over the blade span rather than being discretized. Betz and Goldstein developed the fundamentals of propeller theory by extending the lifting line theory to finite wing aerodynamics as developed by Prandtl in the 1911-1918 period and presented by Anderson (1984). This theory describes the interaction between the flow at the lifting line that represents the propeller blade and the wake flow downstream of the lifting line. The departure from wing lifting line theory in the propeller version is that the flows behind the rotating blade are considered to be rigid helical trailing vortex sheets. The trailing sheets which make up the wake

of the propeller develop into a helical sheet of constant pitch as the axial velocity of the wake in these analyses is considered constant. Goldstein examined the difference in circulation distribution between a perfect propeller (an infinite number of blades) and a real one with a finite number. However, the methods of Betz and Goldstein give only characteristic information about blade performance and distribution of bound circulation, and do not address the blade shape.

The lifting line theory as developed by Prandtl and presented by Anderson provide information about the spanwise distribution of circulation and the lift and drag on a planar surface such as a wing of arbitrary aspect ratio. This development assumes that the lifting surface and its free trailing wake lie in the same plane and that the steady problem is considered. Lifting line analysis mostly serves today as a learning tool and to provide a check on more sophisticated formulations.

Propeller lifting line developments are based on circulation theory. Circulation theory postulates that the lift developed by a propeller blade is due to a circulatory flow around the blade surface. When a body develops lift, the circulation about the body is defined as the line integral in Equation (4.113). Because of the combination of circulation with the freestream flow, there will be an increased local velocity and decreased pressure on the back (suction) side of the blade and the reverse on the blade face (pressure) side. From this, one can see the utility of circulation in the study of lifting surfaces, since the aerodynamic force on the blade can be readily computed using the Kutta-Joukowski law of Equation (4.138). PSF-2 uses a discretized lifting line method to estimate propeller forces for comparison with the VLM forces.

4.6 Outline of Calculation Procedures

The lifting surface method used, modified and reformulated during this project is an analysis method (as opposed to a design method). One project goal is to find the loading distribution on an axial-flow fan blade when operating with specified flow rate, rotational speed, blade geometry and so forth. The analysis problem stated here is in contrast to the design problem of determining a blade geometry that will give a specified blade loading. Essentially, this is equivalent to specifying a distribution of circulation on the blade surface and finding the geometry that results. A program has been developed by Greeley et al. (1982) which solves the design problem for marine propellers. The solution of the design problem is important, but would probably be the final stage of a program in which the current work would be the first stage. The outline of the design program of Greeley et al. (1982) is similar to that of PSF-2 and is given in Figure 4.21.

An accurate and flexible description of the blade geometry which is capable

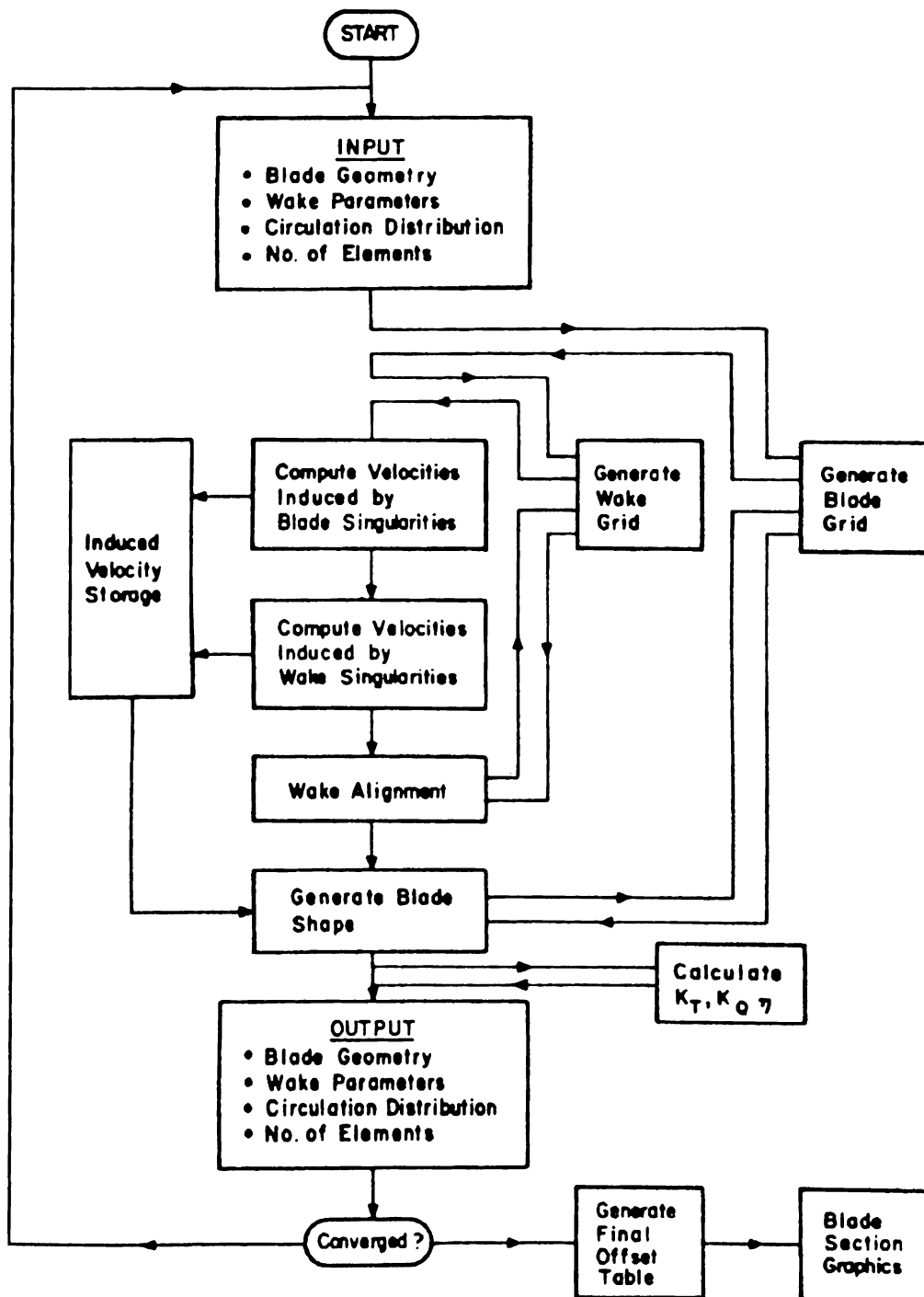


Figure 4.21 Outline of a design computation procedure using a VLM technique (Greeley and Kerwin, 1982)

of modelling complex blade shapes is needed to ease the computations. If the computational method is to be used in an optimization study, or as the workhorse in an artificially intelligent CFD system such as those discussed by Andrews (1988), thought needs to be given to a parametric description of blade shapes. In this sense, polynomials or cubic spline functions involving constants that are design variables to be optimized should be used in describing the blade geometry. More generally, the method used should be able to accurately compute the coordinates of an arbitrary point on the blade surface given the overall geometry of the blades. The method used by Kerwin and Lee (1978) to describe complex three-dimensional blades appears to fit these criteria.

The blade geometric notation is presented in Figure 4.22. The x-coordinate axis is positive in the downstream direction, the y axis is defined by the blade geometry relative to the "key" blade, and the z axis then fills out the orthogonal coordinate system. Cylindrical coordinates are used in the y-z plane to describe parametric curves, but all computations are performed based on the Cartesian coordinates. In the y-z plane, clockwise rotation of θ is positive when viewed in the positive x direction. The radial coordinate r is given by

$$r = \sqrt{y^2 + z^2} \quad (4.169)$$

The angle measured from the y axis to the midchord curve at a given radius when viewed in the y-z plane is defined as the angle of skew $\theta_m(r)$. This defines the midchord curve in the y-z plane parametrically as a radial skew distribution. The rake distribution is similarly defined as a radial distribution of distance $x_m(r)$ (from the y-axis to the midchord curve) as viewed in the projected x-y plane. Having provided the radial distributions of skew and rake, a midchord curve in space will be constructed about which the remainder of the blade geometry is to be described and discretized into a vortex lattice.

The leading and trailing edges of the blade are constructed by advancing a length $+c(r)/2$ (to leading edge), or retreating (to trailing edge) a distance $-c(r)/2$ from the midchord line along a helix making a pitch angle $\phi(r)$ (also varying with r) with the y-z plane. At a given radius the chord length $c(r)$ (nose to tail length in the cylinder of radius r), helix angle $\phi(r)$, rake $x_m(r)$ and skew $\theta_m(r)$ can be used to determine the cartesian coordinates of points on the leading and trailing edges as

$$\begin{aligned} x_{l,t} &= x_m \mp \frac{c}{2} \sin \phi \\ \theta_{l,t} &= \theta_m \mp \frac{c}{2r} \cos \phi \\ y_{l,t} &= r \cos \theta_{l,t} \\ z_{l,t} &= r \sin \theta_{l,t} \end{aligned} \quad (4.170)$$

The radial blade section camber and thickness (if it were to be used) are then defined in a the manner similar to that for two-dimensional airfoils. The functions that describe the thickness $t(s)$ and camber $f(s)$ distributions are shown in Figure 4.22. For convenience and utility the chordwise coordinate is non-dimensionalized into a coordinate s , varying from 0 at the leading edge to 1 at the trailing edge. The distribution of camber is then measured in the cylindrical surface normal to the nose-tail helix as shown in Figure 4.23. Any point on the camber surface at a radius r , as s varies from 0 to 1, can now be expressed in either cylindrical or cartesian coordinates in terms of the parametric functions of r , rake x_m , skew θ_m , pitch ϕ , camber $f(s,r)$ and chord length $c(r)$. The camber point coordinates can then be computed from an extension of Equation (4.169)

$$\begin{aligned}
 x_c &= x_m + c \left(s - \frac{1}{2} \right) \sin \phi - f(s) \cos \phi \\
 \theta_c &= \theta_m + c \left(s - \frac{1}{2} \right) \frac{\cos \phi}{r} + f(s) \frac{\sin \phi}{r} + \delta_k \\
 y_c &= r \cos \theta_c \\
 z_c &= r \sin \theta_c \\
 \delta_k &= \frac{2\pi(k-1)}{K} \quad \text{with} \quad k=1,2,\dots,K
 \end{aligned} \tag{4.171}$$

where the expressions given above are for the k -th blade, where K is the number of blades and $k = 1$ corresponds to the key blade.

In PSF-2 this geometric development is represented by cubic spline functions based on data either provided as input or computed from input at a set of radial or chordwise locations. Although the number and radial spacing of data are arbitrary, the program was intended to have data every tenth of the outer (tip) radius. The chordwise section data is fixed at 17 values, in keeping with NACA section data. Use of cubic spline functions readily enables integration, differentiation and interpolation of geometric data.

Using the discretization shown in Figure 4.18, vortex elements of constant strength with endpoints on the camber surface are used to compute loading as described earlier; to represent thickness, line source elements are used in PSF-2 (not discussed because not used in this thin sheet metal blade study). The camber surface is known from its cubic spline representation. In the radial direction, the panel spacing is given by dividing the span into M radial intervals from hub radius r_H to the tip radius R with extremities of the lattice inset $\approx 1/4$ of the panel width from the tip and root of the blade. This has been found to improve the

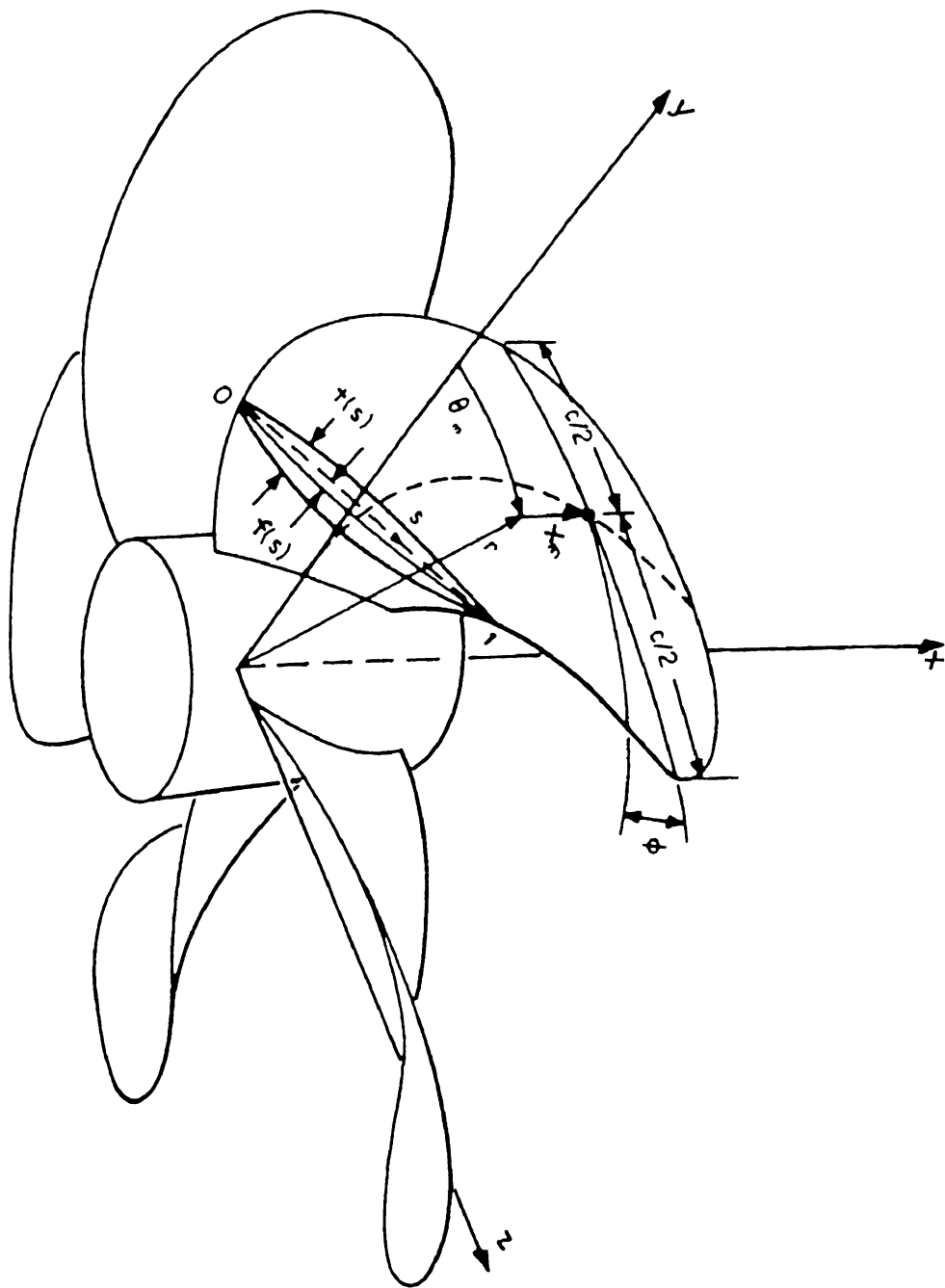


Figure 4.22 Blade geometry notation (Greeley and Kerwin, 1982)

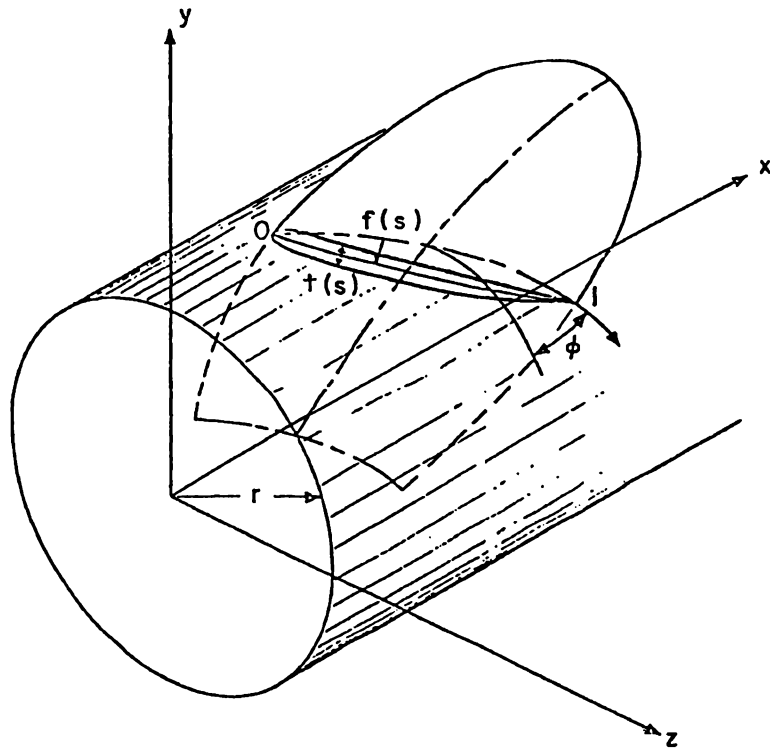


Figure 4.23 Cylindrical blade section showing pitch angle ϕ , the thickness function $t(s)$ and the camber function $f(s)$ (Greeley, 1982)

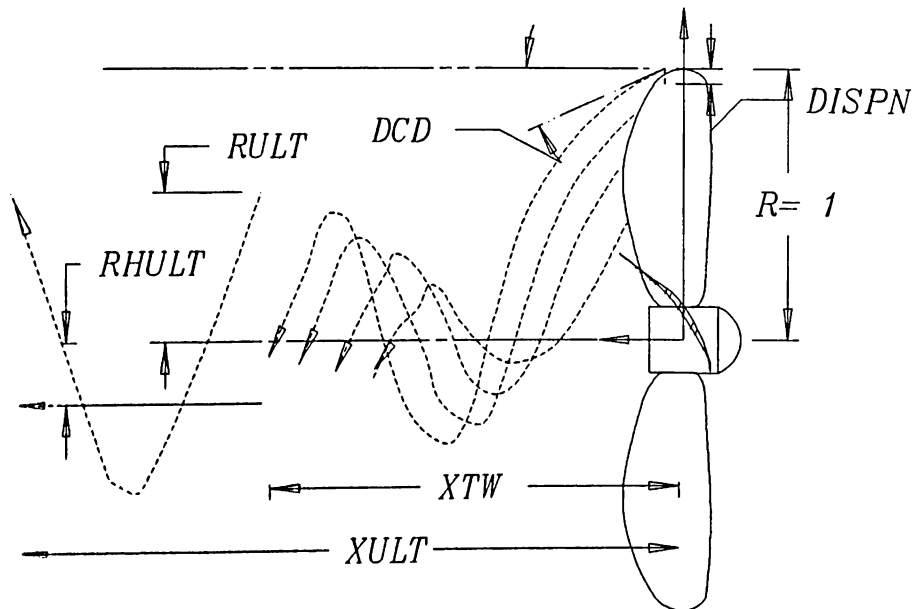


Figure 4.24 PSF-2 wake variables

convergence, as mentioned earlier. The best lattice-inset factor has been demonstrated to vary with the loading distribution (i.e. for elliptical loading this has been found to be 16% instead of 25%). End points of discrete vortices will be located at radial locations given by

$$\rho_m = \frac{(R - r_H)(4m - 3)}{4m + 2} \quad \text{where } m = 1, 2, 3, \dots, M+1 \quad (4.172)$$

The PSF-2 user has the choice of either uniform or cosine chordwise spacing. Cosine spacing is known to have distinct advantages over uniform spacing, and was primarily used in this study. It was the preferred method used by Greeley (1982), the developer of PSF-2. A chordwise spacing (the quasi-vortex lattice method or QVLM) has three advantages:

- according to Lan (1988), this technique takes into account leading edge singularities which were completely ignored in vortex lattice development previously
- it enables the leading edge suction to be readily calculated
- two-dimensional calculations show that it forces the distribution of vorticity to have the correct behavior near the trailing edge, satisfying the Kutta condition implicitly, and the last control point can be placed at the trailing edge.

In PSF-2, the blades are discretized using a coarse spacing on the non-key (force not computed for) blades. Also, the numbers of panels on the key blade in a given direction (M in the spanwise, and N in the chordwise) must be an integer multiple of the number of panels on a given coarser blade.

It is important to collect the assumptions, some previously mentioned, employed by the PSF-2 program which relate to modelling the Lenexa Product fan. It is assumed there are K identically spaced blades arranged about a common axis. The blades rotate about a common axis in an unbounded and incompressible fluid. The presence of a hub or "spider" is ignored. Blades are assumed to be thin and operate at a small angle of attack α , and are modeled by source singularities (in the case of thick airfoil shapes) and vortex sheets which are discretized on the mean camber surface. The perturbation velocity due to the presence of the blades is considered irrotational outside the boundary layers and the trailing vortex wake. The boundary layer is not explicitly taken into account. However, slight empirical corrections account for the loss of lift caused by the boundary layers by altering the effective shape of the blade (by changing the blade pitch).

The above-described method leads to a surface integral equation which is

approximated numerically and solved by a system of linear algebraic equations as outlined in Section 4.6. Additionally, in PSF-2, a source strength distribution is used to represent the jump in normal velocity at the blade camber surface due to thickness. The source singularity strengths are computed by a strip-wise application of thin-wing theory at each radius. Once again no thickness representation of the blade was used in this study because of simplicity. Although, the author is aware that the apparent "potential flow" shape of the blade (as altered by separation etc.) may be taken into account by the using of the source singularities. As discussed earlier, the vortex element distribution is employed to represent the jump in tangential velocity across the camber surface and across the trailing vortex sheets where the vortex elements are conveniently resolved into spanwise and chordwise components.

Therefore, following the discretization of the blade singularities on the blade surface (see Figure 4.17), the resulting boundary value problem is solved as described earlier in Section 4.6. The system of equations to be solved for the strength of the j th discrete "horseshoe-like" vortex where the boundary condition is

$$\sum_{j=1}^{M \times N} A_{ij} \Gamma_j = -\vec{n}_i \cdot \vec{v}_i \quad \text{and} \quad i=1,2,\dots,M \times N \quad (4.173)$$

satisfied at the i th control point is

where Γ_j is the spanwise vortex strength, A_{ij} is an influence coefficient matrix determining the induced velocity at the i -th control point by the j th horseshoe vortex of unit strength (this is a complex expression resulting from the application of the law of Biot-Savart and vorticity conservation, Equation (4.163)), \vec{n}_i is the unit normal vector at i (computed by constructing a normal vector from the cross-product of the diagonal vectors of the panel) and \vec{v}_i is the velocity vector at i from inflow and rotation.

A recurring idea in the literature review is that the geometry of the trailing vortex wake greatly influences the calculation of the induced velocities on the blade and the blade loading. Out of this need, the PSF-2 developers have included a wake model which includes some aspects of both free- and prescribed-wake analysis. The wake alignment method used in PSF-2 (and all true free-wake rotor models) depends on the Γ distribution over the blade, which in turn depends on the geometry of the wake (trailing vortices). An iterative method is, therefore, used to solve for the correct wake and blade geometry. In the PSF-2 program the geometry of the trailing wake is really not entirely free, as will be discussed. At least not as "free" as in methods where every single vortex element in the wake is aligned with the local velocity vector, as in a "vortex chasing" free-wake analysis. The variables which help determine the wake geometry, and rotor performance and

which must be provided as input to the PSF-2 program are shown in Figure 4.24.

The wake of trailing vortex elements is divided into two parts; a transition wake region where contraction and deformation of the slipstream occurs, and an ultimate wake region, which is composed of K (number of blades) helical tip vortices and a single rolled up hub vortex. These regions are shown in Figure 4.25 for the Lenexa Products three-blade fan rotor and wake. The radii of the discrete vortices of the trailing wake are determined by a set of parameters (variable names refer to those used in PSF-2 and shown in Figure 4.24); the radius $RULT$ of the rolled up tip vortices, the radius $RHULT$ of the hub vortex at the end of transition wake region, the length XTW of the transition wake region and the contraction angle DCD of the tip vortex as it leaves the blade tip. The trailing vortices comprising the transition wake region are extensions of the chordwise vortices. In the transition wake, the radii of innermost and outermost trailers are set by smooth curves and the intermediate end points are obtained by interpolation at any downstream location. Since the trailing wake, like the blade lattice, is modeled by a series of short straight segments it is necessary to specify the angular extent subtended by each vortex segment in order to specify their length. In the transition wake this is set by the $\delta\theta_{tw}$ parameter, the angular extent of each element. However for the ultimate wake each tip vortex is formed by at most three complete turns of its helix, and the angular extent of each straight vortex element is determined by specifying the number of points in the ultimate tip vortex and $XULT$.

A critical parameter in determining the wake geometry is the wake pitch because it sets the distance between the key blade and the wake of the blade immediately ahead of it. The transition wake pitch is allowed to vary in both the radial and downstream directions, and the correct pitch results in the wake being force-free (i.e. no pressure jump across the trailing vortex wake). This is met if the total velocity vector is parallel to the vorticity vector on the trailing vortex sheet. In the present code the correct pitch is calculated at a series of points just downstream of the blade trailing edge and at another series of points at $0.70 XTW$. The pitch everywhere else in the transition wake is obtained by interpolation. The ultimate wake pitch is calculated in PSF-2 using the Loukakis (1971) wake model. This involves making an estimate of the strength of the ultimate tip vortex (obtained by solving the global boundary value problem with an approximate wake geometry) and an estimate of the tip vortex core radius size (an assumed, constant parameter within the source code). From these estimates the axial and tangential self-induced velocities at the ultimate tip vortex and the ultimate wake pitch are calculated from a table of data within the source code. The PSF-2 model assumes a (tip vortex core radius)/(tip helix radius) of 0.02. The iterative wake alignment used in PSF-2 is discussed in detail by Greeley (1982).

Since the wake geometry affects the calculation of the correct pitch, this

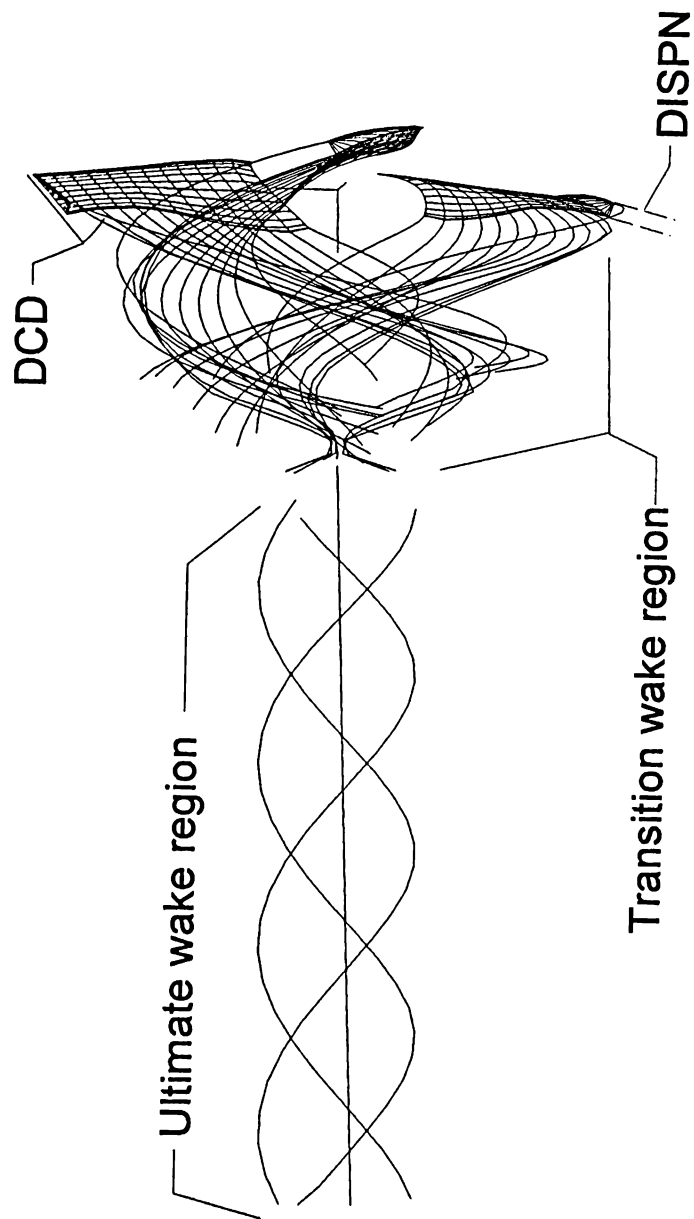


Figure 4.25 Transition and ultimate wakes of a computation for the Lenexa Products 36 in. fan

wake alignment procedure requires an iterative solution: for a given wake geometry the correct pitch is calculated at several points in the wake, the wake geometry is updated to reflect the newly calculated pitch distribution and the process is repeated until the wake geometry stops changing. All of the wake calculations discussed above require knowing the vorticity distribution on the blade and in the wake, which are unknowns to be determined. It is then necessary to iterate not only on the wake geometry but also on the blade vorticity distribution used to calculate the final wake geometry. The iteration procedure can be summarized into three steps:

1. The global boundary value problem is solved for a blade vorticity distribution using an assumed wake geometry. The assumed wake geometry can be a helix, the wake resulting from an earlier calculation, or a shape specified by the user input.
2. Using the vorticity distribution from step 1. calculate the correct (force-free) wake geometry.
3. Solve again the boundary value problem using the updated (aligned) wake geometry and determine a new vorticity distribution. Continue to iterate through steps 1 and 2 until the vorticity distribution stops changing.

The procedure has been shown to converge rapidly for well-behaved propeller-like flows. In the current program, the user must initiate and run each iteration. So far this aspect of running the program has been found to be tedious, and it would be desirable for users to set their own convergence criteria.

Several corrections for non-ideal flow behavior are included in the PSF-2 calculations. In PSF-2, vortex sheet separation is included by allowing the vortices at the blade tip (only) to separate from the blade and coalesce at a point above the trailing edge of the blade at the tip. This concept previously has been addressed in this work from the standpoint of conservation of vorticity. The distance of this separation Δ (or DISPN, the PSF-2 program variable, see Figure 4.25) can either be stipulated or calculated, as outlined below, from the flow conditions at the tip. In order to determine the tip vortex collection points, assumptions about the geometry of the tip vortex are made. The pitch angle of the vortex leaving the trailing edge is assumed to be

$$\bar{\beta} = \frac{1}{2} (\beta + \beta_T) \quad (4.174)$$

where β is the undisturbed inflow angle at the tip and β_T is the pitch of the transition wake tip vortex as it leaves the blade. The displacement Δ of the trailers

above the trailing edge of the blade tip is then given by

$$\Delta = c \tan(\phi - \bar{\beta}) \quad (4.175)$$

where c is the chord length of the tip panel, and ϕ is the pitch angle at the blade tip. In closing it should be pointed out that if accurate information about the wake geometry is known, the solution to the problem could be accelerated through the use of a prescribed wake model. However, it is impossible to have detailed information about rotor wake behavior under all operating circumstances beforehand.

The forces acting on a vortex sheet can then be calculated by the Kutta-Joukowski theorem. Also, assuming that the average velocity over the length of a singularity can be represented by the velocity at its midpoint, then the force on the j -th key blade singularity can be expressed as

$$\vec{F}_j = \rho \Delta l_j (\vec{v}_j \times \vec{\Gamma}_j) \quad (4.176)$$

where

Δl_j is the length of the line singularity

\vec{v}_j is the total velocity at the line singularity midpoint

$\vec{\Gamma}_j$ is the line singularity strength

In PSF-2 forces are computed on spanwise and chordwise elements. This is in contrast to many other methods which assume that the chordwise vortex elements produce no loading effect which assumes the flow lacks spanwise velocity components. The PSF-2 program also estimates the force due to the line source effect of the elements when thickness effects are included. Since they were not used during this work this aspect will not be discussed further. However, the interested reader is directed to Greeley and Kerwin (1982). The computation of Equation (4.175) is made over the entire blade except for the tip chordwise vortex elements which are assumed to be separated from the blade.

Viscous drag forces are included in PSF-2 through user-supplied estimates of viscous drag coefficients in the program input data. These estimates of drag are modeled as additional forces on the spanwise vortex elements. The computed leading edge suction force (estimated using the Lan (1974) QVLM model) is multiplied by a recommended 1/3 suction efficiency factor to simulate the (experimentally observed) loss of leading edge suction at conditions other than the ideal angle of attack. Greeley, in his development of the PSF-2 code, uses an additional correction for the effective change in blade shape caused by the inequality in boundary layer thickness on the pressure and suction sides of the

blade. The method chosen was that used by Kerwin and Lee (1978) where the right-hand side of Equation (4.172) is modified to account for the loss of lift caused by boundary layer effects. This method uses a blade pitch correction by reducing the blade pitch by an amount $\Delta\alpha$ at each radial section given by

$$\Delta\alpha = 1.9454 \left(\frac{t_o}{c} \right) \left(\frac{f_o}{c} \right) \quad (4.176)$$

where $\Delta\alpha$ is in radians and t_o and f_o are the maximum blade thickness and camber at a given radial section, respectively.

4.7 Details of Running the PSF-2 Code

After a survey of the available computational codes, the PSF-2 computer program was chosen for use. Though it is designed for use in the analysis of steady, non-cavitating ship propeller flows, discussions with some of the program's developers Kerwin (1988) and Kinnas (1991) and others in the field (Burmeister and Amadian, 1988) it was found to be the most used and applicable program available. It is reported that this code was used to analyze plastic radiator cooling fans for Ford and Crysler. The version of PSF-2 to be used in the study dates from 5/27/85, and is written in FORTRAN. PSF-2 is based on the vortex-lattice method, the basic theory of which was previously discussed. The original PSF-2 program and the author's modified version was installed currently on the University of Kansas VAX computer, and has (in modified form) been installed on Apollo and Sun Workstations and on the author's 486 PC (not using a DOS compiler, however).

Figure 4.21, given earlier to outline the Greeley propeller design code, should be contrasted with the outline in Figure 4.26 for the analysis program, PSF-2, as presented by the author. The version of PSF-2 used consists of two main programs. Two input files, INPGEO and ADMIN, are needed to run the first stage of the program. INPGEO contains the description of the blade geometry in dimensionless form expressed through standard marine propeller dimensions and nomenclature. Arbitrary blade camber and thickness (not needed for plate blading analysis) can be given in this input data file. Within the ADMIN input file are placed the paneling arrangement and overall operating conditions of the fan. The first PSF2BVP of the two main programs then uses the information in the input files in solving the boundary value problem of potential, attached flow, generating an output file GBVPOUT. This process covers everything up to the converged wake in the calculation scheme shown in Figure 4.26. GBVPOUT contains the locations of the vortex-lattice grid points, the geometry of the transition and ultimate wakes (see Figure 4.25), and the singularity strengths obtained from solution of the boundary value problem. In the existing version of the program this file is unformatted, and cannot be examined as an ASCII text file. A

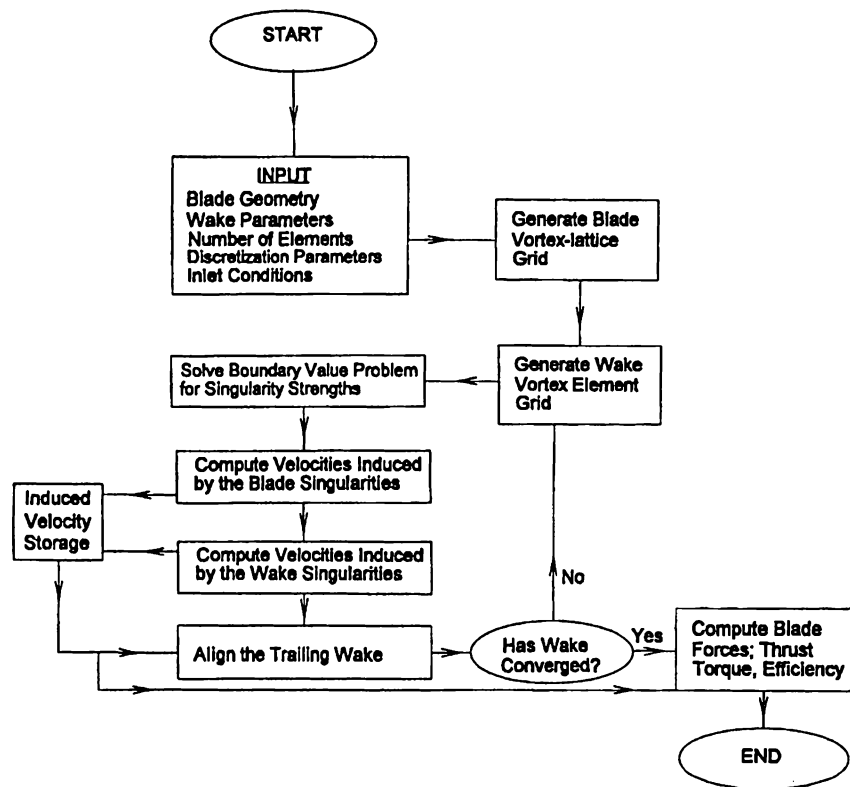


Figure 4.26 Outline of the PSF-2 analysis code

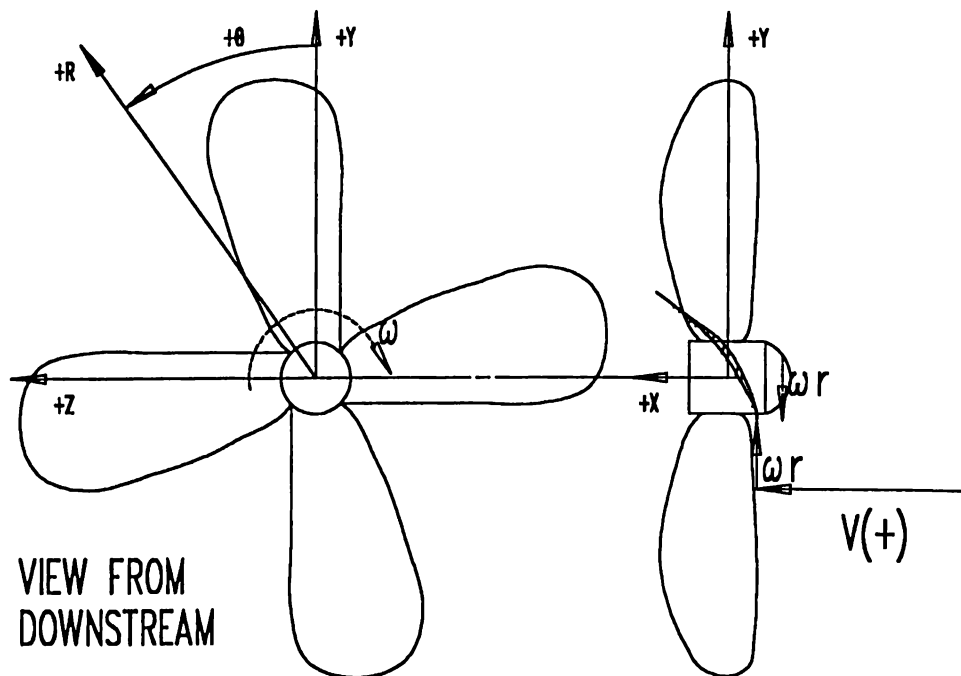


Figure 4.27 Fan coordinate axis

formatted version of the output file containing geometric information was added in the modified version of the code in order to extract grid information. The second stage of calculations takes place in the program PSF2FOR in which the forces and moments on the blade are computed based on the singularity strengths. The computations performed in this program are the final stage in the schematic diagram shown in Figure 4.26. Figure 4.27 is provided to clarify the coordinate directions and their sign conventions used in the PSF-2 data input. Note that the sign convention for positive rate of rotation is opposite the right-hand convention.

4.7.1 Data files

While a manual is provided with the PSF-2 program in which some of the information about to be presented appears, it was thought best to include the information in this section and expand on the information given in the manual. As previously mentioned there are two input data files. The first to be looked at in detail is INPGEO. A line-by-line description of the information in this file is given below with the line number in the file indicated at the far left of each list of input data for a given line, and the bold characters represent the input variables. A description of the variables for a given line then follows that line.

- 1 **IDGEOM**
 where
 IDGEOM= a descriptive header of up 72 characters

- 2 **NX NBLADE MLTYPE MTHICK KPCORR**
 where
 NX= number of radii at which geometric data is to be put in (15 is the maximum)
 NBLADE= number of fan blades (maximum of 12)
 MLTYPE= type of chordwise camber used for this blade
 1, designates mean line camber for NACA a=0.8 load distribution
 2, designates mean line camber for Brockett's approximation of 0.8 chord loading
 3, designates a parabolic arc camber
 4, read in manual camber offsets through XCS(N,J)
 MTHICK= type of chordwise thickness used for this blade
 1, designates modified NACA66 thickness form
 2, designates NACA16 thickness form
 3, designates elliptical section thickness form
 4, read manually set thickness form using array XTS(N,J)
 KPCORR= switch for setting an approximate viscous correction, reduces blade pitch to simulate the viscous effect on lift
 0, do not include viscous pitch correction
 1, include viscous pitch correction.

note: The camber geometry is set in the program at the following percent chord length locations; 1, 2.5, 5, 10, 20, 30, 40, 50, 60, 70, 80, 90, 95, 97.5, and 99. This is important to know when the user wishes to manually set camber and thickness.

- 3 **XR(1) XR(2) XR(3) ... XR(NX)**
 where
 XR(N)= non-dimensional radii at which blade geometry is specified from
 origin of the coordinate system; $XR(N) = R(N)/R_{tip}$; XR(1) must be
 for the hub radius, similarly XR(NX) is the tip radius (=1.0 always)
- 4 **XPI(1) XPI(2) XPI(3) ... XPI(NX)**
 where
 XPI(N)= pitch/diameter ratio of blade section; note that the pitch is that of
 the nose-tail line; $P(N)/D = \pi \times XR(N) \times \tan \phi$, where ϕ is the blade
 geometric pitch angle given in Figure 4.23
- 5 **XRAKE(1) XRAKE(2) XRAKE(3) ... XRAKE(NX)**
 where
 XRAKE(N)= rake/diameter ratio of the blade section; propeller rake is defined as
 the axial coordinate of the mid-chord line at each radius and is
 considered positive in the +X, downstream direction
- 6 **XSKEW(1) XSKEW(2) XSKEW(3) ... XSKEW(NX)**
 where
 XSKEW(N)= skew angle in degrees; the skew angle is the angular coordinate of
 the mid-chord line viewed in the plane of rotation; positive skew is
 clockwise rotation when viewed in the downstream
 direction
- 7 **XCHD(1) XCHD(2) XCHD(3) ... XCHD(NX)**
 where
 XCHD(N)= the (expanded chord)/diameter ratio of the blade section; the
 expanded chord length of a blade section is the length of the
 leading to trailing edge helix at that radius
- 8 **XCAM(1) XCAM(2) XCAM(3) ... XCAM(NX)**
 where
 XCAM(N)= the (maximum camber)/chord ratio of the blade section at a given
 radius
- 9 **XTHICK(1) XTHICK(2) XTHICK(3) ... XTHICK(NX)**
 where
 XTHICK(N)= the (maximum thickness)/diameter ratio of a given blade section
- 10 **XCS(1,1) XCS(2,1) XCS(3,1) ... XCS(NX,1)**
 XCS(1,2) XCS(2,2) XCS(3,2) ... XCS(NX,2)

 XCS(1,15) XCS(2,15) XCS(3,15) ... XCS(NX,15)
 where
 XCS(N,J)= these are the manual camber offsets in units of local chord length;
 the J index tracks the values at a given percent chord; values are
 given at 1, 2.5, 5, 10, 20, 30, 40, 50, 60, 70, 80, 90, 95, 97.5, and
 99 percent chord; so that 15 lines are required here
- 11 **XTS(1,1) XTS(2,1) XTS(3,1) ... XTS(NX,1)**

XTS(1,2) XTS(2,2) XTS(3,2) ... XTS(NX,2)

.....

XTS(1,15) XTS(2,15) XTS(3,15) ... XTS(NX,15)

where

XTS(N,J)= thickness offsets in units of local chord; once again, the J index tracks the values at a given percent chord; values are given at 1, 2.5, 5, 10, 20, 30, 40, 50, 60, 70, 80, 90, 95, 97.5, and 99 percent chord; so that 15 lines are required here

An example INPGEO file is given below:

```
ACME: SIX BLADE FAN
10 6 3 1 1
0.237 0.322 0.406 0.491 0.576 0.661 0.746 0.830 0.915 1.000
0.677 0.884 1.037 1.162 1.212 1.229 1.293 1.357 1.439 1.539
0.000 0.006 0.003 -0.004 -0.015 -0.027 -0.034 -0.042 -0.054 -0.067
0.00 -4.16 -7.24 -9.36 -11.46 -13.28 -13.96 -13.61 -12.52 -11.00
0.138 0.193 0.209 0.214 0.201 0.177 0.164 0.164 0.172 0.190
0.114 0.153 0.136 0.128 0.106 0.089 0.089 0.099 0.115 0.092
0.000 0.000 0.000 0.000 0.000 0.000 0.000 0.000 0.000 0.000
```

Actually, for all cases run during this project no thickness effects were used, and the MTHICK variable was not used in the geometry data file since it was never read.

The second input data file is the ADMIN data file. This file contains information to set up the lattice grid on the blades, put in the required operating conditions, stipulate such parameters as the inflow velocities seen at each radial blade section, fluid and wake properties, and more. The convention in describing this file line-by-line follows the format for the previous INPGEO file.

- 1 **NCASE**
 where
 NCASE= number of cases contained in this ADMIN file; a number of different cases (different rotational speeds and flow rates for instance) can be set up in one ADMIN file

- 2 **MPAN(1) MPAN(2) MPAN(3) ... MPAN(NBLADE)**
 where
 MPAN(N)= number of spanwise panels used on the Nth blade; the maximum number of such panels is 20; also, the ratio MPAN(1)/MPAN(N) must be an integer for all N, where MPAN(1) is the number of spanwise panels on the key blade

- 3 **NPAN(1) NPAN(2) NPAN(3) ... NPAN(NBLADE)**
 where
 NPAN(N)= number of chordwise panels used on the Nth blade; the maximum number of such panels is 20; the ratio NPAN(1)/NPAN(N) must be an integer for all N, where NPAN(1) is the number of chordwise panels on the key blade; on the key blade, the product MPAN(1)*NPAN(1) equals the number of control points for the key blade; the maximum number of control points is 144

- 4 **KSPACE**
 where
 KSPACE= a switch for controlling the method of chordwise spacing of singularities on the blade
 = 1, use cosine spacing
 = 2, use uniform spacing
- 5 **IDADMN**
 where
 IDADMN= a descriptive character string, up to 72 characters
- 6 **DIAM VSKTS RPM**
 where
 DIAM= the diameter of the blades in feet
 VSKTS= the speed of the free stream flow in knots, 1 knot= 1.6889 ft/sec
 RPM= the rotational speed of the blades, in revolutions per minute
- 7 **RULT RHULT DCD DTPROP XTW XULT NPUW**
 where
 RULT= a dimensionless value of the ultimate wake tip radius, (radius of the ultimate tip vortices)/propeller radius (if not known use 0.83 as this depends upon flow rate, rpm, geometry, skew, etc.)
 RHULT= a dimensionless value of the ultimate wake hub radius; (radius of the ultimate hub vortex)/propeller radius (if not known, 0.15 is recommended)
 DCD= contraction (in degrees) of wake at the blade tip (if not sure, use 30°)
 DTPROP= angular spacing (in degrees) between grid points in the transition wake (15° recommended).
 XTW= dimensionless axial extent of transition wake/blade radius, normally 1.0
 XULT= dimensionless downstream distance at which wake pitch ceases to change, there the ultimate wake begins (normally 1.5 is recommended)
 NPUW= number of points to be used in each ultimate tip vortex (36 is recommended, but maximum possible is 61)
- 8 **KSEPTV DISPN DISPR KTHICK**
 where
 KSEPTV= switch for controlling the calculation of DISPN, the displacement of the separated tip vortex normal to the blade.
 = 0, recompute DISPN from the transition wake geometry
 = 1, use DISPN as read from this ADMIN input data file without changing it
 DISPN= displacement of separated tip vortex normal to the blade, considered positive toward the suction side.
 DISPR= this features not used yet, set to 0 in this work; it is a displacement of separated tip in the radial direction, considered positive outward
 KTHICK= switch for ignoring the blade thickness
 = 0, ignore thickness
 = 1, include blade thickness

- 9 **RHO CDRAG SFCIWTEST ICDRAG ISFC**
 where
 RHO= fluid density (slug/ft³)
 CDRAG= blade section viscous drag coefficient (constant over radius); if
 radially variable, then this value is not used; the radial varying
 values will follow later, ICDRAG
 SFC= leading edge suction recovery factor (here put value if constant over
 the radius); if SFC=1.0 complete the suction recovery is assumed; a
 value of 1/3 is recommended; if radially varying values are to be
 used then this value is discarded; see radially variable values later,
 ISFC
 = 0.0, no suction recovery is to be used
 IWTEST= switch for controlling reading of the wake convection velocities
 = -1, use the previous convection velocities
 = 0, set the wake convection velocities to zero
 = 1, read induced velocities in the wake from lines 13, 14, 15, 16
 ICDRAG= switch for controlling the reading of radially variable drag
 coefficients
 = 0, use the value of CDRAG entered previously
 = 1, use the value of CDRAG from line 17 as indicated
 ISFC= switch for controlling the reading of radially variable suction
 recovery factors
 = 0, use the value of SFC entered previously
 = 1, use the value of SFC from line 18
 note: CDRAG and SFC can be changed during the interactive running of PSF-2.
- 10 **XVA(1) XVA(2) XVA(3) ... XVA(NX)**
 where
 XVA(N)= (axial inflow velocity)/VSKTS at input radii used to define the blade
 geometry; positive velocity is in the downstream, +X, direction; it is
 dimensionless; in the fan work it is the volumetric average velocity
 of the free stream flow at the inlet, as determined by the volumetric
 flow rate divided by the fan blade annulus area
- 11 **XVT(1) XVT(2) XVT(3) ... XVT(NX)**
 where
 XVT(N)= (tangential inflow velocity)/(average velocity of the free stream flow)
 at input radii used to define the blade geometry; positive velocity is
 in the rotational, + θ , direction, clockwise rotation in the plane of
 rotation when observer is facing downstream
- 12 **XVR(1) XVR(2) XVR(3) ... XVR(NX)**
 where
 XVR(N)= (radial inflow velocity)/(average velocity of the free stream flow) at
 input radii used to define the blade geometry; positive velocity is in
 the outward, +r, direction
- 13 **XUAN(1) XUAN(2) XUAN(3) ... XUAN(NX)**
 where
 XUAN(N)= (axial induced velocity)/(average velocity of the free stream flow)
 just behind blade trailing edge (at the input radii)

- 14 **XUAU(1) XUAU(2) XUAU(3) ... XUAU(NX)**
 where
 XUAU(N)= (axial induced velocity)/(average velocity of the free stream flow) at
 XULT behind blade (at the input radii)
- 15 **XUTN(1) XUTN(2) XUTN(3) ... XUTN(NX)**
 where
 XUTN(N)= (tangential induced velocity)/(average velocity of the free stream
 flow) just behind blade trailing edge (at the input radii)
- 16 **XUTU(1) XUTU(2) XUTU(3) ... XUTU(NX)**
 where
 XUTU(N)= (tangential induced velocity)/(average velocity of the free stream
 flow) at XULT behind blade (at the input radii)
- 17 **XCDRAG(1) XCDRAG(2) XCDRAG(3) ... XCDRAG(NX)**
 where
 XCDRAG(N)= blade section viscous drag coefficients at the input radii
- 18 **XSFC(1) XSFC(2) XSFC(3) ... XSFC(NX)**
 where
 XSFC(N)= leading edge suction force recovery factors at the input radii

An example ADMIN file is:

```

1
8 8 8
8 4 4
1
LENEXA PRODUCTS FAN TEST CASE
3.0 14.85 850 DIAM (FT), VFLOW(KNOTS;1 KNOT=1.6889 FT/SEC), RPI
0.853 0.150 15.00 15.0 1.00 1.50 36
0 0.0 0.0 0
0.00228 0.0070 0.333 0 0 0 3 3
0.958 0.997 0.999 0.997 1.000 1.012 1.034 1.079 1.027 0.640
0 0 0 0 0 0 0 0 0 0
0 0 0 0 0 0 0 0 0 0

```

Note that the input files are read by the program in free format.

The program PSF2BVP can be run in either a batch mode or an interactive mode. The steps required to run PSF2BVP interactively are:

1. The program prompts the user for the INPGEO file, appropriately named and correctly assembled (see above).
2. The user is prompted for the ADMIN data file to be used which may include several cases. Each time the PSF2BVP program command **ADINPT** is given another case is read from the ADMIN file.
3. Following the **ADINPT** command, the input data is assembled by the

program, and the boundary value problem can be solved by entering the **BVP** command if the correct wake convection velocities are presumed read in at the start of the computations (IWTEST=1) or, if wake alignment is not desired, the solution is completed after solution of the boundary value problem (BVP).

4. If wake alignment is used, the **ALIGN** command is entered and an iterative process of aligning the computed wake with the Loukakis wake model (1971) is undertaken. The parameters requested after the **ALIGN** command is entered are:

NWIMAX = maximum number of iterations during alignment process

ITUNNEL = switch for controlling the tunnel correction
 = 0, do not use tunnel correction
 = 1, use tunnel correction of APROP/ATUNNEL (blading disk area/cross sectional area)

IPRINT = flag for printing out details
 = 0, do not print out details
 = 1, print details

DAMPING = damping factor, which is advance coefficient dependent
 = 0.25, for moderate advance coefficient
 > 0.25, for a lower advance coefficient
 < 0.25, for a high advance coefficient

5. Following the wake alignment, the boundary value problem must be solved again with the converged wake geometry by using the **BVP** command, the **ALIGN** program is run again with the new circulation distribution, and this iterative process continues until stopped by the user when the circulation distribution is converged.

A detailed drawing of the files received with the PSF-2 code, and in particular the "flow" of the commands issued in the main program is given in Figure 4.28. Included in Figure 4.28 is such valuable information for modifying the original source code as the FORTRAN routines contained in each file and the functions they perform. This ends the discussion of the boundary value problem solution process performed in PSF-2, but the blade forces have still to be computed.

The second part of the PSF-2 programs is the PSF2FOR program which is laid out graphically in Figure 4.29. Once again, in Figure 4.29 the first level of subroutines called from the main program is shown by lines, an understanding that was of great help in rewriting the computer code. This program uses the unformatted GBVPOUT file as input, and computes the forces and moments on the blade in the previously solved boundary value problem. The GBVPOUT file output from PSF2BVP gives the entire blade and wake geometry, the key blade spanwise vortex element strengths and more. From the key blade spanwise vortex

Figure 4.28 Schematic drawing of the PSF2BVP program; the eight source code files are given in the boxes shown, all subroutines are given and the routing of calls from the main program is shown

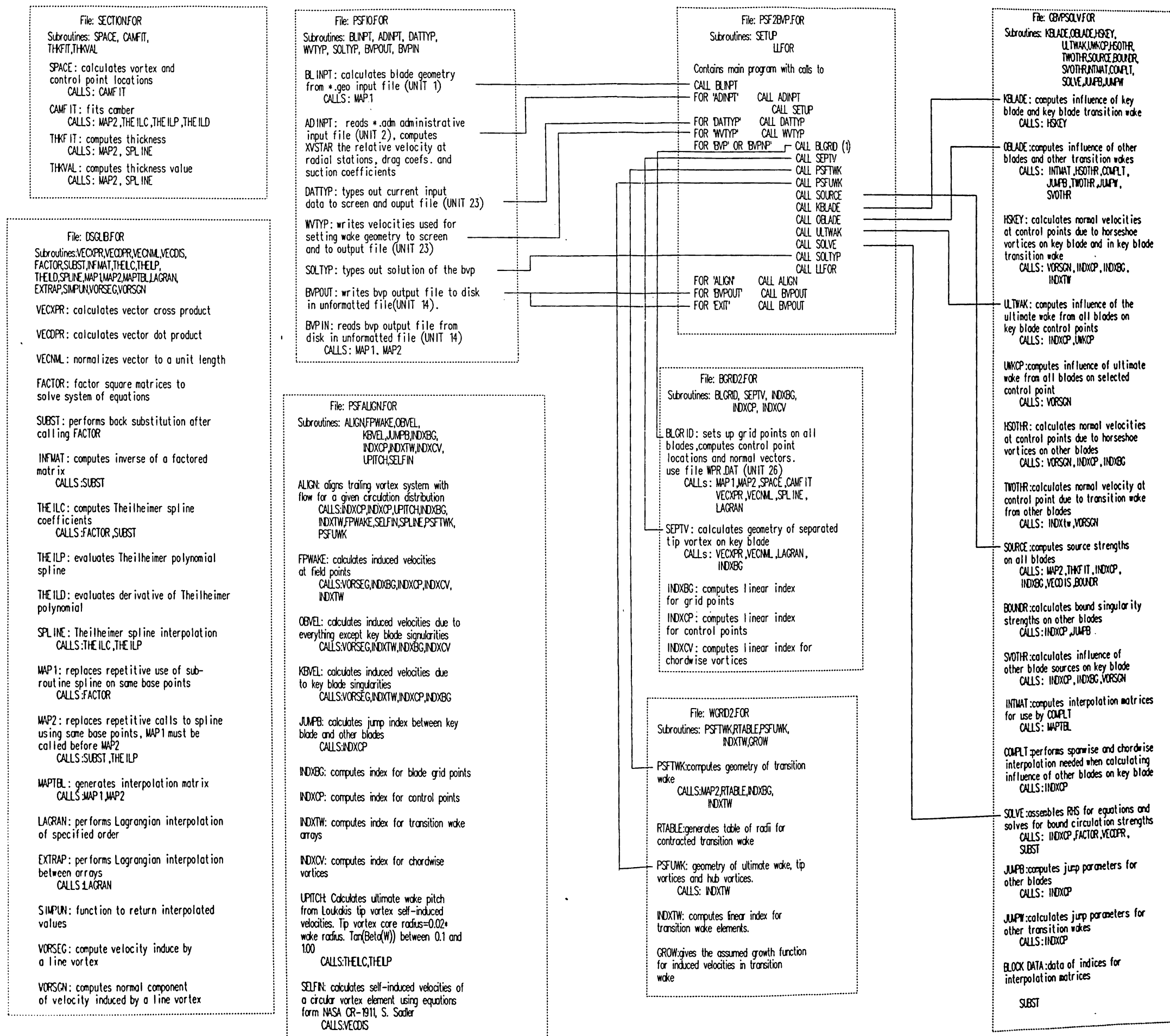
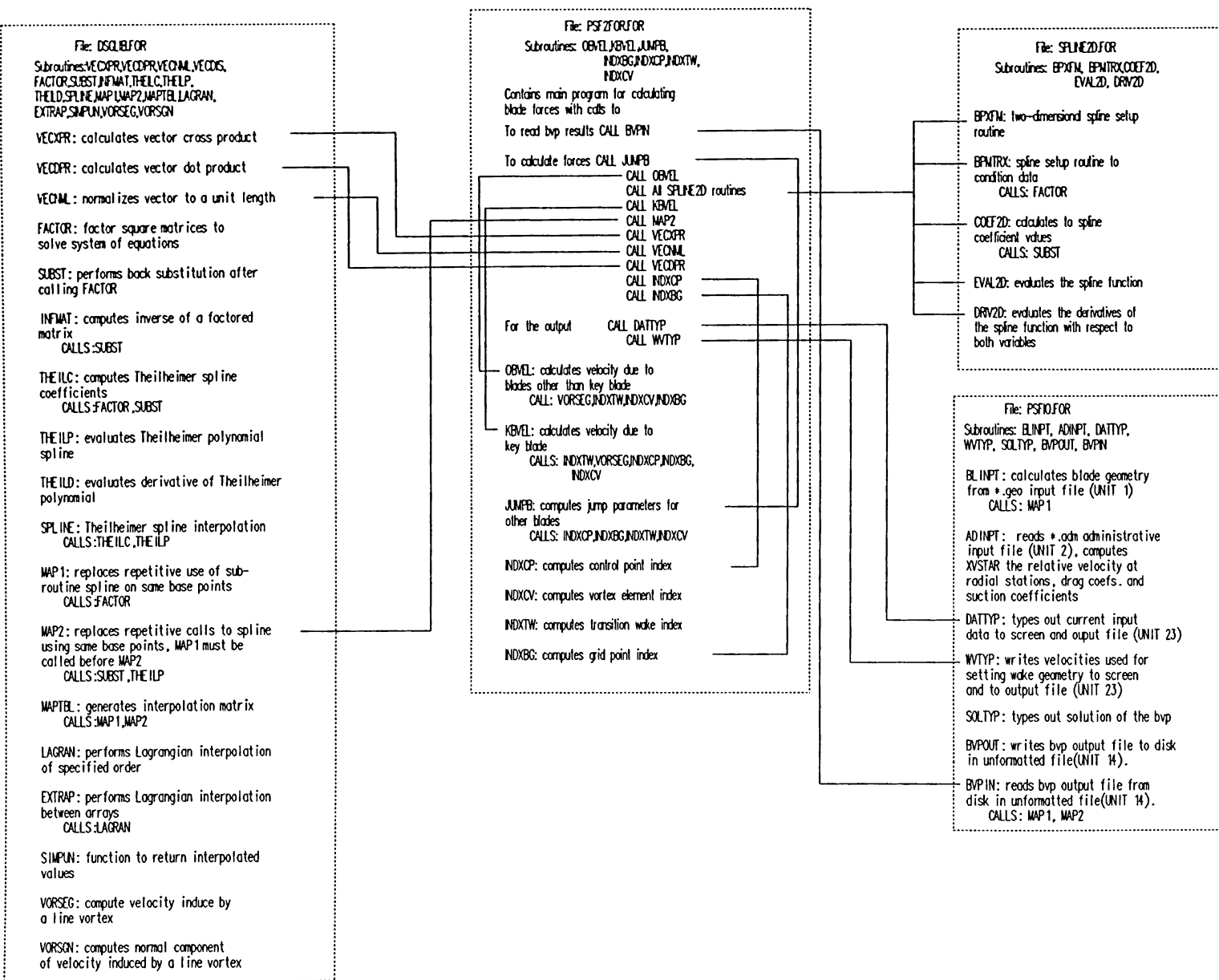


Figure 4.28 Schematic drawing of the PSF2BVP program; the eight source code files are given in the boxes shown, all subroutines are given and the routing of calls from the main program is shown

Figure 4.29 Schematic drawing of the PSF2FOR program; the four source code files are given in the boxes drawn in dotted lines, all subroutines are given and the routing of calls from the main program is shown



element strengths the strengths of the spanwise vortex elements on the other non-key blades are found by interpolation. Then the chordwise and trailing wake vortex element strengths are determined by applying the Kelvin vorticity theorem for the entire rotor. The PSF2FOR program then computes the velocity at the midpoint of each spanwise and chordwise vortex element; the spanwise and chordwise vortex elements are termed bounders and trailers, respectively, in the program. Greeley (1982) interpolates these velocities from those calculated at the control points in his design program. Then the elemental forces at the mid-point of each spanwise and chordwise vortex element segment on the blade are computed. The corrections are made for leading edge suction and drag. The components of the elemental forces are then summed into the total axial component which is the thrust and the tangential elemental force component is multiplied by its radial distance from the center of rotation before being summed into the total torque. The results of the force and torque calculations are generally presented in terms of the thrust and power coefficients as a function of advance coefficient. The dimensionless variables were discussed previously and presented in Equations (4.25), (4.26) and (4.27).

4.8 Description of the Modified Program

The PSF-2 program was modified in various stages, and as a result it is difficult to discuss all the different versions of the modified program developed along the way to the programs now in use and used in the results which will be presented in Chapter 5. The modifications and the reasons for undertaking them will be discussed.

The first work undertaken on the PSF-2 program dealt with performing some additional calculations on the program output so that the results might be compared with the Lenexa Products wind tunnel test results. The wind tunnel test results are given terms of the static and total pressure rise, the horsepower, and the volumetric flow rate. It was decided to present the results in these forms rather than use their dimensionless counterparts, and so volumetric flow rate and total pressure rise calculations were added to the PSF-2 program. The volumetric flow rate was determined by two methods which are performed as a check on each other. Both methods, involve integrating the inlet velocity profile (given as input, assumed to be the circumferential average and possibly varying over the radius) over the blade annulus. In the first method, simple trapezoidal integration is used. In the second method, the inlet velocity profile is represented by a curve fitted polynomial using least squares and then integrated using Gaussian quadrature. The inlet profiles are generally smooth functions except near the root and tip where the velocities tend to drop off dramatically. This technique has been validated for this idealized inlet flow by comparing the two methods above with results from Mathcad and routines from the IMSL libraries for realistic inlet profiles. The real inlet flow is more complicated than this particularly at radii less than the blade

root radius. The lack of a hub (a spider is used) and the motor complicate matters for the real flow at the rotor center.

The thrust, or total force on the rotor in the axial direction, is assumed (by force balance) to be the total force applied to the air at the rotor disk. Ideally, therefore, the total pressure rise of the air at the rotor disk is equal to the thrust force divided by the rotor disk area (Equation 4.4). This calculation is performed in PSF-2 and its modified form, along with calculation of the volumetric flow rate, so that fan performance test results and the vortex-lattice computations can be compared.

In order to begin modifications on PSF-2, the COMMON block statements were removed from the source code files given in Figures 4.28 and 4.29, and were replaced by INCLUDE file statements. This enables more straightforward changes to the code's arrays which were some of the earliest alterations made to the program. The limitation of 144 control points needed to be removed and, by changing the array sizes and appropriate traps in the code to check for discretization input errors, the PSF-2 code was capable of using up to about 200 control points. However, difficulties with the interpolation and discretization routines on the "other" blades appeared to be the reason for not being able to use more control points than this with the PSF-2 code.

An example of a 12 spanwise by 12 chordwise vortex-lattice panel model with the other blade modelled using a 6 by 6 panelling scheme is shown in Figure 4.30. Graphical output such as Figure 4.30 is important to have in computational fluid dynamics, and the PSF-2 program lacks this. A number of "post-processing" routines written during the course of this study served this purpose. The PSF-2 source code lacks almost any commented explanation of variable nomenclature, and has only sparse general comments as to what purpose a section of code serves. Therefore, the graphical output allowed for testing and confirming what various geometric variables were and their locations. The control points, lattice-element end points, transition and ultimate wake element end points and the geometric variable of the tip vortex (see detail in Figure 4.31) can all be determined and explored via graphical means. Without interpretation and understanding of the variables, the code modifications could not have proceeded.

The graphical output of the computational mesh also serves several other purposes. The shape of the computed wake can be examined and qualitatively compared with flow visualization pictures. This is also true of the separated tip vortex geometry, the outermost chordwise lattice elements, no matter whether it is prescribed or calculated. The wake visualization graphics routines have been written so that the shape of the tip vortex and wake can be examined visually at any point during the wake alignment process, and these results have assisted in identifying cases where, how, and why the wake alignment procedure breaks down.

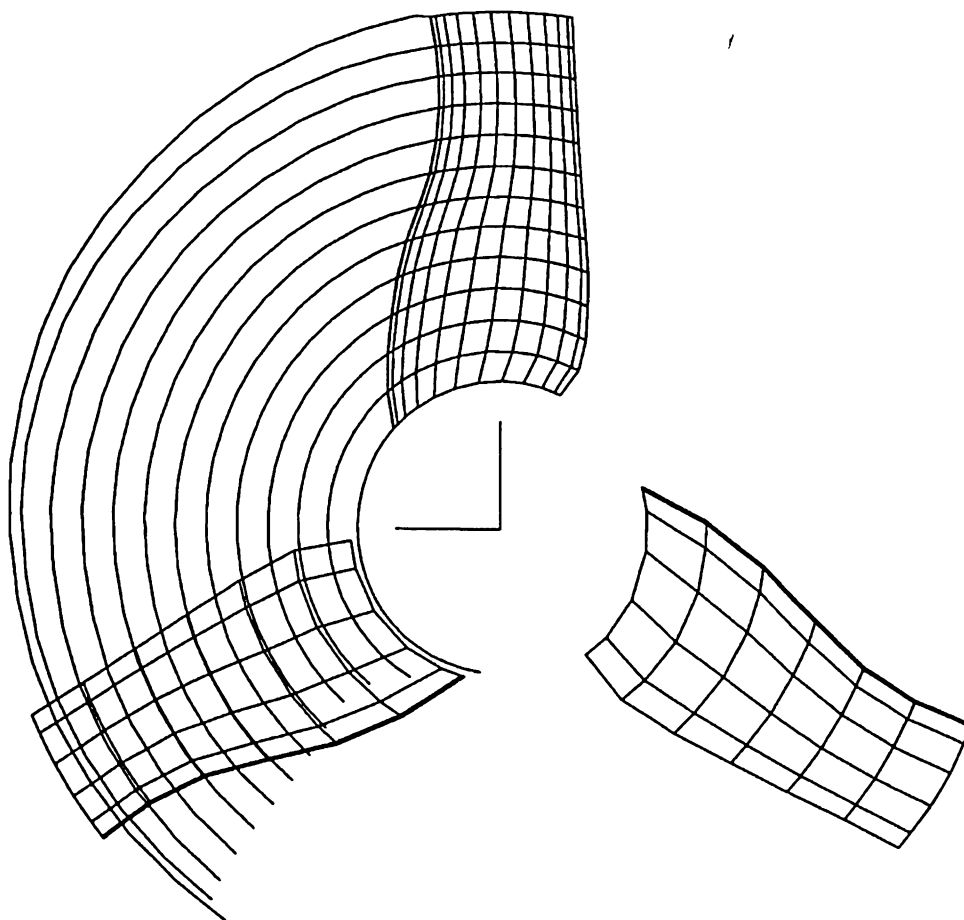


Figure 4.30 Typical PSF-2 panelling scheme for Lenexa Products fan using 144 panels on the key blade (viewed from downstream)



Figure 4.31 Detail of separated tip vortex showing only the chordwise tip vortex elements

Some of these cases show that the predicted flow directs the streamlines back upstream through the fan hub region. The graphical output routine also provided visual verification of the computational mesh and its accurate representation of the fan blades.

At the start of the project, the lattice graphical output was provided through writing the geometry to be read by the PLOT3D program, using only its mesh drawing function. The routines and additional programs were written using the PICASSO (Leinbach and Schmid, 1988) library of graphical subroutines for the IBM compatible PC. The graphical output given here and most used during this study to develop the code were performed using programs written using PICASSO. These programs allow the user to examine the vortex-lattice of the fan and (later) duct model using a PC with a graphics card; or, for hard copy, the output can be written to a file in Hewlett-Packard Graphics Language (HPGL).

In the modified version of PSF-2, it was decided to remove the coarse discretization that is performed on the non-key blades (also called the non-uniform blade lattice feature) for a number of reasons. The first reason being that difficulties were encountered with the interpolation routines involved in this function when attempting the increase the number of the lattice-elements on the key blade. This feature appeared to hamper progress in that direction. Also, more recent panel method codes do not create this type of lattice due increase in computer power, the complications involved, the belief that this type of lattice does not represent the problem adequately and the argument that this feature really doesn't save much computer time (Hess and Valarezo, 1985). Indeed, the additional calculations performed because of the increased number of panels on the other blades need only be done once for a given lattice geometry. Then for all additional performance cases, or alignment iterations in the case of a free wake model, these influence coefficients are the same and need not be re-computed. Therefore, for any multiple operating point computations, the non-uniform blade lattice feature doesn't save any time. The separated tip vortex feature was only used on the key blade in PSF-2, whereas in the author's modified version of the program this feature is included on all blades as shown in Figure 4.32. A side view of a vortex-lattice fan model created using the author's modified code is shown in Figure 4.33. The author's modified code can employ as many as 600 control point and panels on each blade from personal experience using the VLM to represent flat rectangular wings 400 panels is certainly enough to match the finite wing theoretical solutions, and really beyond about 300 there is no appreciable improvement. It is difficult, however, to make generalizations since a fan rotor geometry is more complex and issues of refinement must also play a role. This range of discretization (400 to 600 panels on a rotor surface) appears to be in the range used by many in the field.

The author also provided an additional feature to the force computation

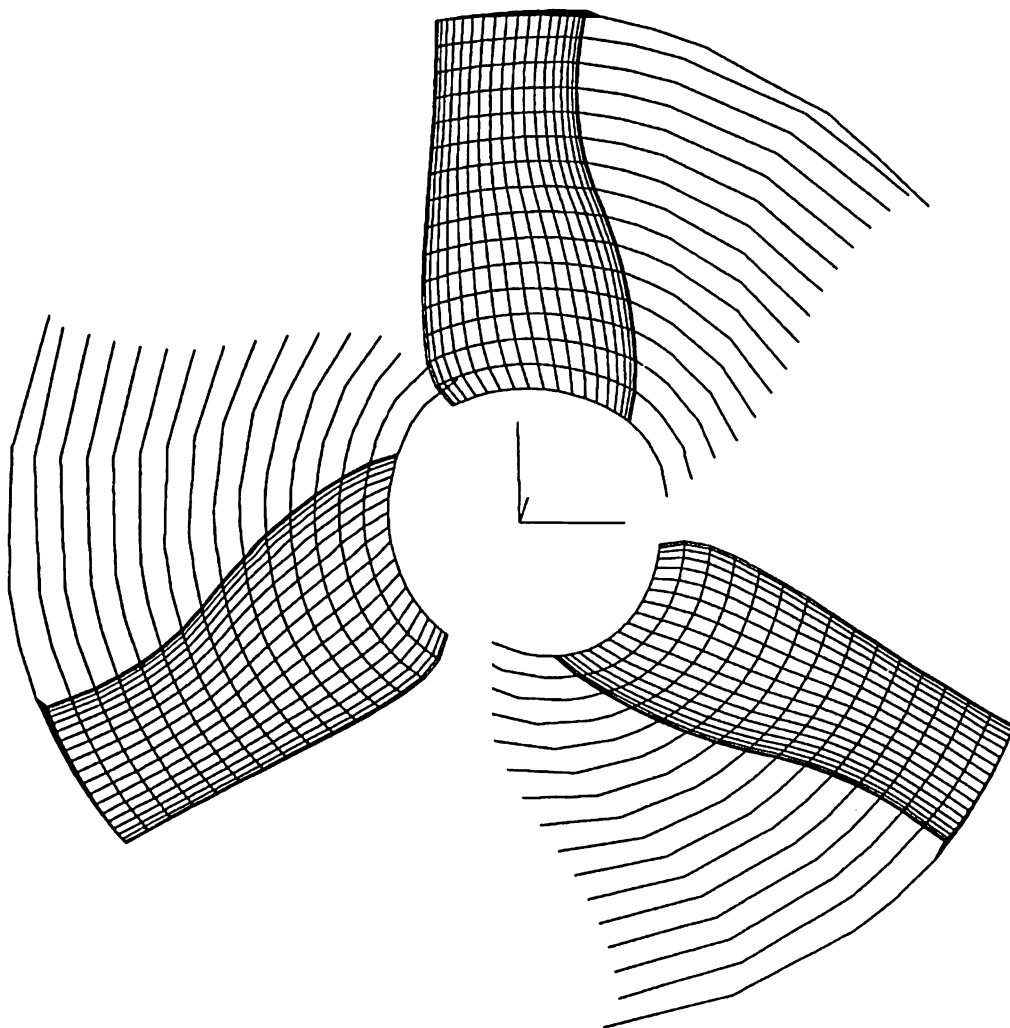


Figure 4.32 A vortex-lattice model for the author's modified PSF-2 program with like discretization and tip vortex on all blades (only part of trailing wake is shown as viewed from the front or upstream side)

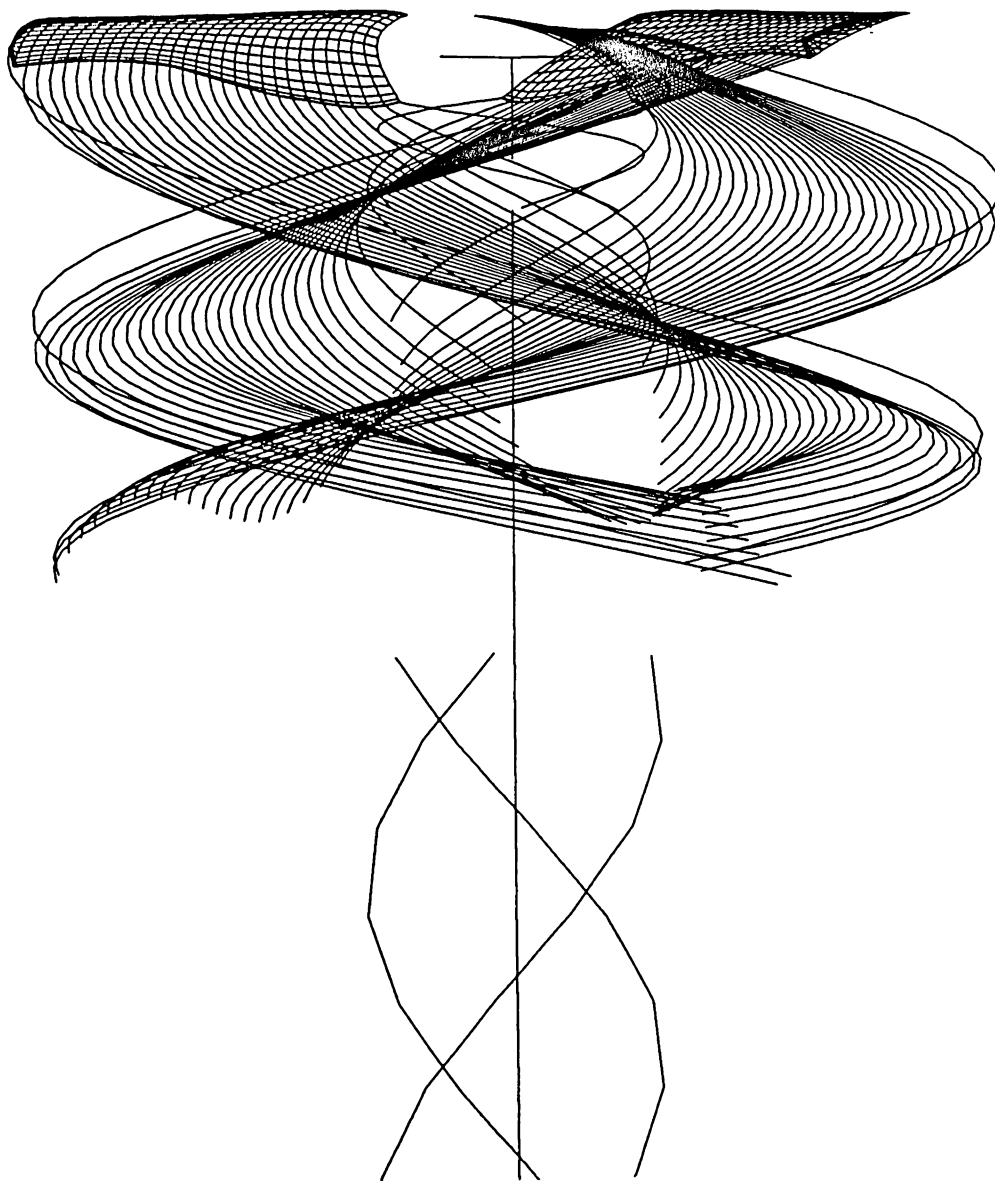


Figure 4.33 Side view of a vortex-lattice model from the author's modified PSF-2 code

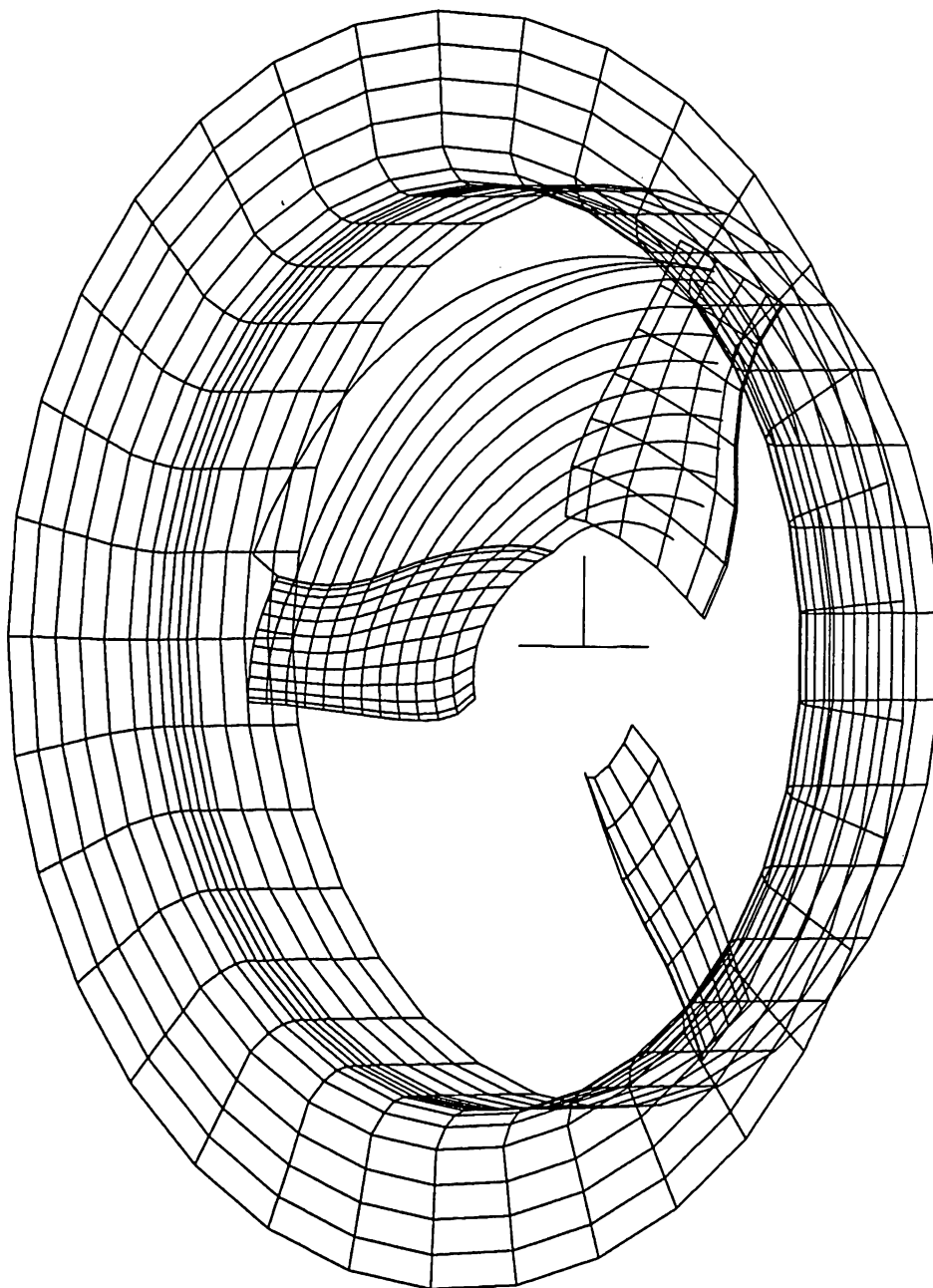


Figure 4.34 View of a duct or venturi panel lattice added to the original PSF-2 panelling scheme (as seen from the upstream/side)

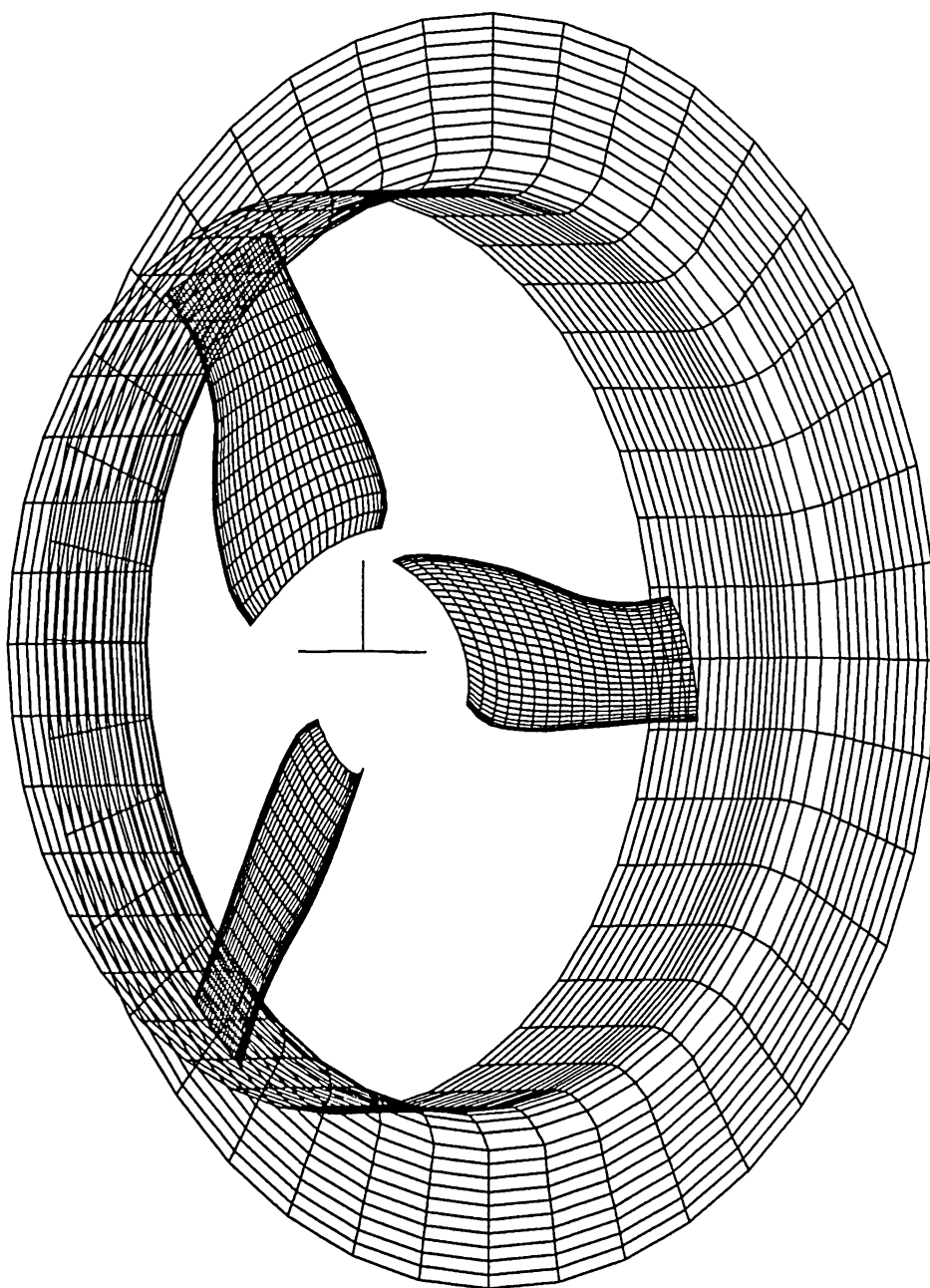


Figure 4.35 View of a duct or venturi panel lattice using the author's panelling scheme (as seen from the downstream/side)

program which accounts for the variation of the viscous drag coefficient with lift. Rather than estimating the viscous drag coefficient for a given radial blade section, the author has provided viscous drag coefficient versus lift coefficient from which the drag coefficient at a radial section can be interpolated after estimating the lift coefficient from the sum of the bound circulations for that radial blade section. The lift versus drag data for a number of flat cambered plate blades (Wallis, 1983 and Milgram, 1971) sections has been used. Prior to this, the viscous drag appeared to be used in an arbitrary manner as a "correction" parameter within the program. A drag coefficient value of 0.007 appears to have been used in many of the program developer's calculations.

A venturi panel or duct option has been added to the modified program, representing a major addition to the program. It has also been implemented on the non-uniform discretization (original) model as shown in Figure 4.34 which was later scrapped due to other difficulties in modifying that blade discretization. In its current form, the duct model is an option in the author's modified PSF-2 program, and its effect is computed in an iterative manner like the wake alignment procedure. The trailing wake elements on the duct extend from the trailing edge of the duct downstream to the end of the rotor's ultimate wake. The computation proceeds as normal for the rotor and wake until the user wishes to include the duct. Then the BVP is solved on the duct surface using the influences of the known blade and blade-wake vortex strengths and the unknown duct vortex element strengths and their trailing wake vortex strengths which are determined from solving that BVP. Then on the next iteration for the blade BVP, the effect of the duct lattice and its wake vortex elements on the blade is included in solving the blade BVP for the blade singularity strengths. The method currently used does not include the effect of the duct-related elements on the trailing blade wake during the wake alignment procedure. Instead, the effect of the duct is taken into account by the change in blade element strengths due to the duct. Usually, the method converges after about six iterations.

A final addition to the computer programs used with PSF-2 and its modified versions is a field point velocity program which post-processes the vortex lattice computations. Due to its utility, the developers of PSF-2 have produced a version of the field point velocity prediction code. However, the author's field point velocity (FPV) program was especially designed for the purposes of putting velocities in a format that can be read by the PLOT3D numerical flow visualization program and to calculate the blade surface pressure difference by computing the static pressure difference across the blade at the control points. The field point velocity program calculates the velocity at a given point by computing the velocities induced by all the singularities in the problem and adding the induced velocity to the onset flow. The problem is computed in the rotational reference frame and the velocities requested from the field point code can have the rotational effect either included or ignored, the latter to explore the appearance of

the velocities in the non-rotating (laboratory) reference frame for comparison with flow visualization photographs. The field point velocity program computes the velocities for three cases; an arbitrary (single) point in space, a plane of velocities at a constant axial coordinate value where the velocities are arranged on circles or circular sections and a given normal offset from the blade surface at the control point locations where the positive offset is taken in the direction of positive lift (from pressure, or downstream, to suction, or upstream, side). For the blade surface velocity case (a small offset, equal to the estimated boundary layer thickness, in the third case), the surface pressure difference is calculated following the velocity computations at the same offset from each side of the blade and application of the Bernoulli equation.

CHAPTER 5

EXPERIMENTAL METHODS AND EQUIPMENT

5.1 Introduction

The goals of this study are to document the flow phenomena associated with the axial-flow fan investigated, measure pressure measurements on a rotating blade surface and examine the ability of a VLM to predict fan performance. The methods and equipment used to accomplish these goals will be described in this chapter.

5.1.1 Description of the Fans Studied

In all the experimental work and most of the VLM computations, a fan manufactured by Lenexa Products (36 in. diameter, galvanized steel, vertical, direct-drive, poultry fan, model 3C675) was used. The fan is sold by the Dayton Electric Mfg. Co., and its performance is certified by the Air Movement and Control Association Inc. (AMCA) following the AMCA Standard 210 in the manufacturer's fan testing facility. Performance testing of the fans used in this work was conducted in the Lenexa Products fan testing facility. The testing facility is certified by the AMCA for conducting performance rating tests of axial-flow fans to ANSI/AMCA 210-85 and ANSI/ASHRAE 51-1985 standards. The method for testing follows that in AMCA (1985). There are over 15 different fan testing facility arrangements that could be used in the ANSI/AMCA/ASHRAE standard. The arrangement used by Lenexa Products is given in Figure 5.1. Lenexa Products manufactures and tests the following sizes of axial flow fans:

Fan Diameter (in.)	Rotational Speed (rpm)	Shaft Power (bhp)
24	650 to 945	0.25 to 0.75
30	470 to 720	0.25 to 1.0
36	415 to 660	0.33 to 1.5
42	382 to 520	0.50 to 1.5

The present range of peak total efficiencies achieved by the fans produced by Lenexa Products is from 57% for the 24 in. diameter model to 66% for the 48 in. diameter model.

The blade geometries used in the VLM computations were determined from measurements made by Lenexa Products with their three-dimensional coordinate measuring machine. These measurements were converted to the appropriate PSF-2 values and then stored in a PSF-2 geometry file for later specification of the

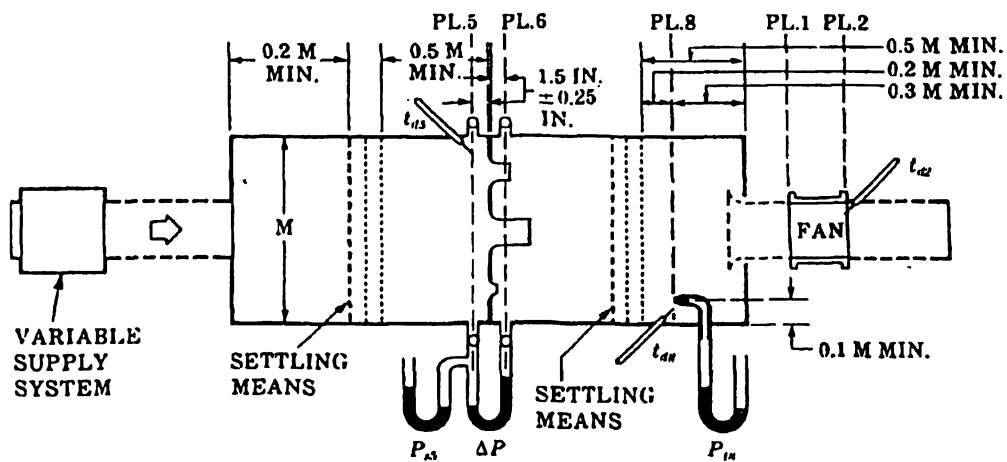


Figure 5.1 Test tunnel arrangement used by Lenexa Products; known as the multiple nozzle in chamber setup (AMCA, 1985)

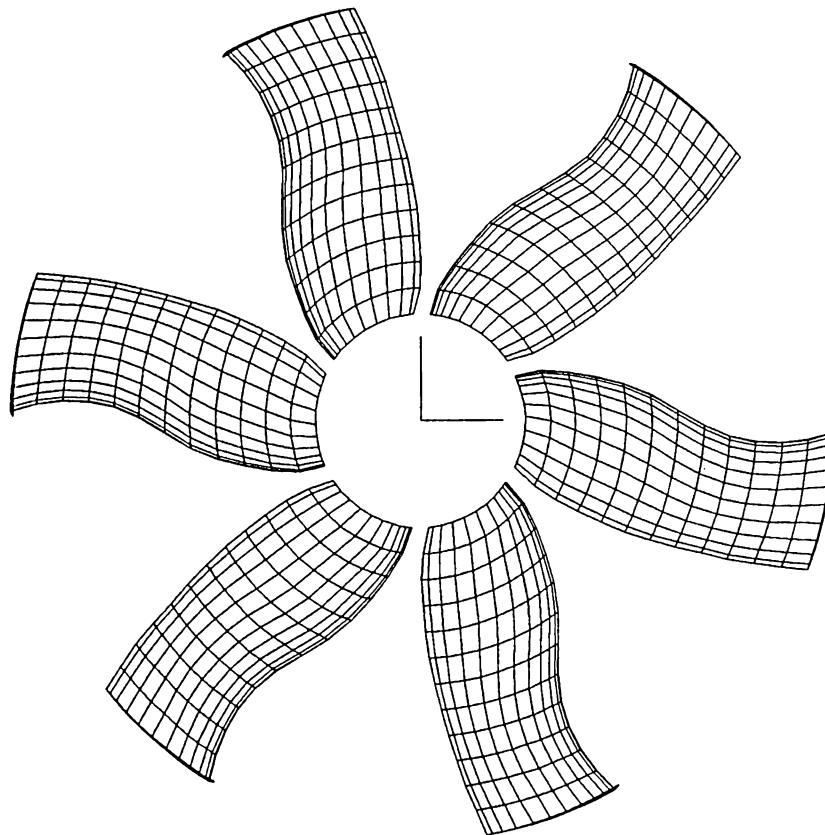


Figure 5.2 The ACME Engineering 36 in. diameter fan blade geometry as represented by a vortex lattice

computational grid as discussed previously. The results of this procedure have been verified by remeasuring by Lenexa Products and by the author's comparison of the actual blade with that from the author's graphical computational mesh visualization program that used their coordinate measurements. A computational mesh for the Lenexa Product 36 in. diameter fan was shown in Figure 4.32. Another fan blade used for VLM program verification of predicted performance was the ACME Engineering 36 in. diameter fan blade which is shown in Figure 5.2 as produced using the author's program. The thickness of the flat-plate fan blades is approximately 0.06 in.

The Lenexa Products 36 in. diameter fan was chosen for this study primarily because of the good performance data available for comparison with VLM. This performance data was taken with the motor support struts in place, the struts introducing a noticeable effect on the blade surface flow and pressure as measurements show. The Lenexa Products 36 in. diameter fan is mounted on the motor shaft downstream of the two motor support struts as shown in Figure 5.3. The motor supports are welded to the inlet side of the venturi panel, a 40 in. square piece of deep-drawn steel with an orifice of 36½ in. diameter (see the side views of Figure 5.3). The dimensions and locations of the motor supports are given in Figure 5.4. The fan-panel assembly is normally shipped to and often used by the customer in a 41 in. square outer dimension crate which is 16 in. deep. The fan-crate assembly was used in the pressure measurement and flow visualization work given here. Not only is this the manner of use, but the difficulty and expense of building a test rig which does not employ the motor supports, or which has the blades upwind of the motor supports and motor, is substantial. Even the manufacturer has no convenient way of running performance tests without the motor supports in place.

The VLM used is a steady-flow solver and cannot model the unsteady effects that exist in the "in situ" fan. The best that can be expected of the PSF-2 based VLM is that it can model the time-averaged rotor problem. The unsteadiness of the flow on the Lenexa Products 36 in. diameter fan will be demonstrated by unsteady surface pressure measurements and blade surface flow visualization. In order to identify the rotor position in presenting these unsteady results, points of reference were marked at azimuthal locations on the venturi panel as indicated by the positions marked A through P in Figure 5.4. The leading edge at the tip of the rotor blade was taken as the point of reference of the blade when determining its azimuthal position. For instance, the blade is taken to be at point A when the leading edge at the tip of the rotor blade is at the azimuthal position A. The pressure measurements were made with position F as the start of the data which will be given for an entire revolution. This will be discussed in more detail in the pressure measurement section. In Table 5.1 are presented the geometric data for these azimuthal positions from their measured point of reference, point D, at bottom center of the panel as viewed from the intake (upstream) side. Also in

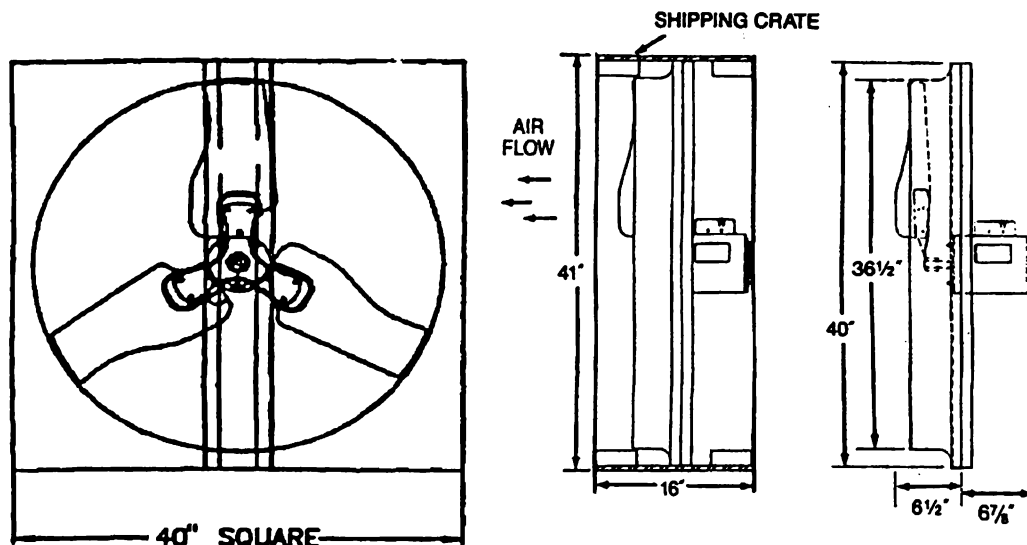


Figure 5.3 The Lenexa Products 36 in. diameter (LP) fan and venturi panel as viewed from the front and side with and without shipping crate (proceeding from left to right)

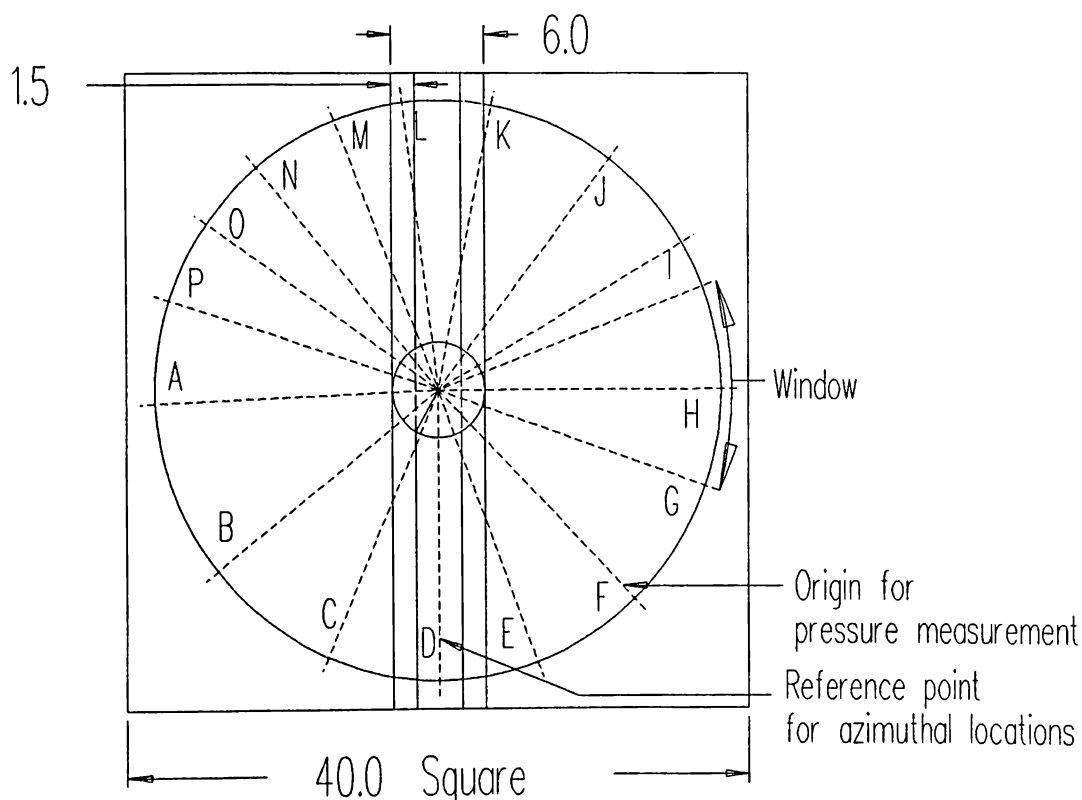


Figure 5.4 The LP fan and venturi panel viewed from the upstream side with dimensions of motor supports and reference points for pressure measurements and flow visualization indicated (all dimensions in in.)

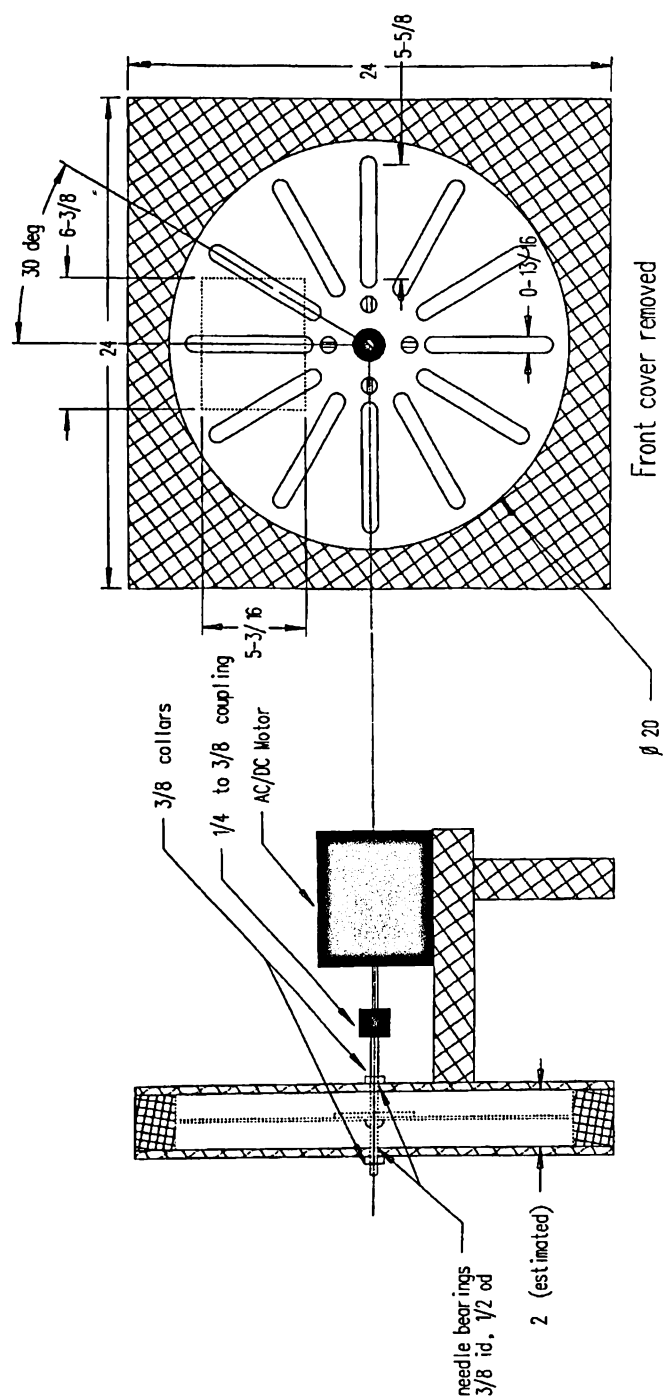


Figure 5.5 Light chopper for use with a light sheet produced from a projector light source (all dimensions in in.)

Table 5.1 Azimuthal positions in degrees and temporal location during pressure measurement cycle for positions of interest

Point Description	Position from D (deg.)	Time from Origin During Pressure Measurement Cycle (msec)
D, origin	0.0	62.0
E	19.1	65.7
F, pressure trace origin	43.8	0.0
G, start of window	70.6	5.3
H, blade horizontal in window	80.0	7.1
end of window	110.9	13.2
I	120.6	15.1
J	142.8	19.4
K	169.1	24.6
L	187.2	28.1
M	201.6	30.9
N	220.0	34.6
O	235.0	37.5
P	251.9	40.8
A	272.5	44.9
B	308.4	51.9
C	336.6	57.4
END, 360deg.	360.0	62.0

Table 5.1 are presented the time a given position is reached during a pressure measurement cycle with point F as the origin and an 850 rpm speed of rotation. Therefore, a complete cycle has a 70.6 ms period. For brevity, from now on in this work the Lenexa Products 36 in. diameter fan and the ACME Engineering 36 in. diameter fan will be referred to as the LP and ACME fans respectively.

5.2 Flow Visualization Equipment

A variety of flow visualization results will be discussed and presented in this chapter. These results represent the outcome of much experimentation in the fan laboratory and the darkroom. The flow visualization techniques were first tested in the lab where lighting, photography setup and flow conditions are among the primary variables in visually inspecting some qualitative aspect of the flow. Once the flow feature was seen in the lab, then the problem of photographing and recording the flow feature was tackled. Usually the record of the flow visualization revealed more information than simple visual inspection. However, no matter what flow visualization technique is used, photographically recording the flow visualization involves experimentation with conditions of both film exposure (aperture, shutter speed and film speed) and film processing. In short, it is a trial and error process where experience is invaluable.

All photographs were made with the Kodak T-MAX line of black and white films. The best and, unfortunately, most costly is Kodak T-MAX 3200 (TMZ) film which can be used at speeds of up to 25,000 ASA with special processing. The T-MAX 400 ASA film (TMY) worked well for the surface tuft techniques, but was more difficult to use for the streakline photography. Kodak (1989) provides guidelines and information when using and processing these films. Some experimentation was still required as many rolls of film processed resulted in poor-quality negatives. Flow visualization photographs were taken with the author's 35mm Minolta X-700 SLR camera, tripod, remote control and auto-winder. No matter what the flow visualization technique used, photographic experimentation involving taking photos at a number of shutter speeds and aperture settings (ranging from seconds to 1/60th of a second and 1.8 to 4 f-stop respectively) was first done before processing the film. After noting which method worked best, that method was then implemented for that technique. As a starting point, SAI (1991) recommended an f-stop of 2.8 and shutter speeds of 1/4th to 1/15th of a second when using Kodacolor 400 or 1000 ASA film to photograph helium bubble streaklines.

Particle streakline, surface tuft, tuft grid and TiCl_4 smoke techniques were attempted in identifying qualitative characteristics of the LP fan flow. The ACME fan was not studied in this way and only its performance measurements will be given here. These techniques were used to study inlet flow field qualities, blade

surface flow conditions, blade leading and trailing edge flow conditions, flow at the blade tip, conditions of the wake flow field and effects caused by the shipping crate and motor mounts for qualitatively checking the unsteady pressure measurements. The results given here are primarily particle tracing and surface tuft techniques.

The results for the particle tracing techniques were obtained by use of helium bubbles and small styrofoam bead particles. The helium bubble generator used was the Sage Action Inc. (SAI) Multi-Head Bubble Generator Model 33 using SAI 1035 Bubble Film Solution and the Vortex Filter chamber to remove bubbles which are either too light or too heavy¹. Use of the Vortex Filter produces helium bubbles which are neutrally buoyant particles. The styrofoam particles used were made by the author by heating polystyrene beads (the type commonly available in hobby store for making molds). The particles were then sized using particle-sizing sieves and introduced into the flow at a desired location through a 1 in. id. tube. The vacuum pressure in the fan inlet is adequate to draw the polystyrene particles into the flow from a holding container. Polystyrene particles are not buoyant and this must be considered when interpreting visualization photos in which they were used. Since they are considerably easier to photograph than helium bubbles, the author experimented with them for comparison with the helium bubbles and as a method of particle velocimetry.

The lighting equipment used for the particle flow visualization techniques included a slide projector, a SAI X6207 Xenon Illuminator (manufactured by the Eimac Division of Varian) with optical shroud, a Model 121 100 W mercury-vapor (Hg-vapor) UV arc-lamp from Shannon Luminous Materials Inc. and a Unilux 885 Xenon strobe light. The slide projector was used without and with slides made by the author to produce light sheets of various thicknesses. The author also made a light chopper (shown in Figure 5.5) which can be used to chop light sheets from the slide projector or from a laser. Most of the wake flow pictures were taken using the SAI X6207 Xenon Illuminator and optical shroud, but the Hg-vapor lamp without its UV filter (a glass that filters out the visible and allows the UV to pass through) gave similar results.

The Hg-vapor arc lamp is a much stronger source of UV light for the mini-tuft technique than the Unilux strobe, but since it lacked the strobing capability it could not be used to investigate the rotating fan blade. Efforts to use the light chopper (shown in Figure 5.5) with the Hg-vapor lamp proved futile due to the inability to match the speeds on the fan and chopper motor with the precision necessary to photograph the blade without blurring. With the UV filter the Hg-

¹ Provided by the Department of Aerospace Engineering at the University of Kansas

vapor lamp provided an excellent source of UV light in the range necessary for implementation of the fluorescent mini-tuft technique (Hardin, 1988) provided the tufts are on a stationary surface. Thus the Hg-vapor lamp was used to visualize mini-tufts on the motor, venturi panel, shipping crate and on grids placed in the inlet or wake flow field. Also, in the surface oil-pigment technique the Hg-vapor lamp provided excellent illumination when using a fluorescent pigment as the oil-flow tracer. Finally, without the UV filter, the Hg-vapor lamp provided a powerful source of light for particle tracer flow visualization.

Certainly, the Unilux 885 strobe was a valuable piece of equipment to have during this study. The equipment used with the Unilux 885 was the model H-95 spot light and the RSC-2 remote digital strobe control device. The Unilux 885 strobe unit has a flash rate range of 1 to 250 flashes per second with a 10 microsecond flash duration. This strobe unit is powerful and has sufficient power in the UV range to use the minituft technique on rotating surfaces. The energy per flash is 4 J for 125 flashes per second and 2 J at 250 flashes per second. Flash power in this range was reported by Stinebring and Treaster (1985) as necessary when using the minituft technique on rotating surfaces. The UV filter from the Hg-vapor lamp was used as the filter for the mini-tuft technique; the manufacturer could provided no data on the optical properties of this glass. More impressive results using the mini-tuft technique might be obtained if an optical band-pass filter were to be used. The Unilux strobe was also used without the UV filter in a blade surface flow visualization technique using individual tufts of marabou feathers (a common type of feather sold in hobby stores). The use of marabou tufts on non-rotating surfaces had been previously reported by Brownell et al. (1987), but their use on rotating surfaces appears to be new in this work. Marabou tufts were photographed without the special lighting conditions of the minituft technique and appear to be unaffected by the centrifugal forces in the rotor speed and size range considered here. Marabou tufts could be used in the manufacturer's fan testing facility where lighting conditions are difficult. While visual inspection at the fan testing facility using a strobe of lesser power might be possible using the marabou tufts, photography of the patterns was impossible without the powerful Unilux strobe light. The Unilux strobe light was also applied to investigate the use of helium bubble and styrofoam particle velocimetry in the wake flow.

The author built the apparatus that was both a blade position encoder and variable time delay strobe light trigger shown in Figure 5.6. When the signal output is used as the strobe light trigger, it allows the user to smoothly and accurately position the fan rotor at any azimuthal location. The signal output from the triggering circuit is stable and allowed shutter speeds as slow as several seconds without blur when photographing the rotating blade with the mini-tuft technique. The signal output from the circuit in Figure 5.6 is compatible with the Unilux strobe; the strobe is triggered by a negative-going pulse in the range of 3 to 10 V with a pulse width of longer than 100×10^{-6} s and a repetition rate between 1

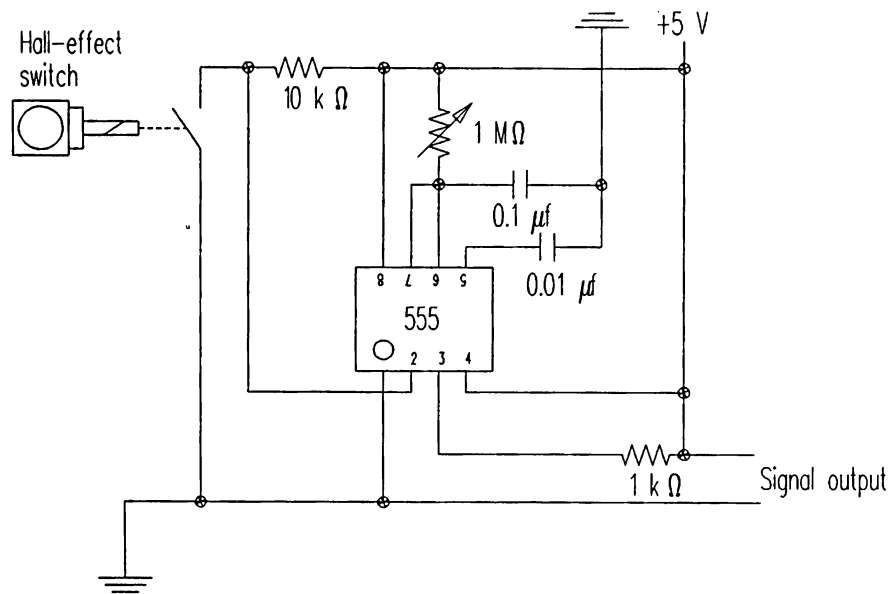


Figure 5.6 Blade position encoder and variable position strobe light trigger with an electro-magnetic sensor and variable time delay circuit

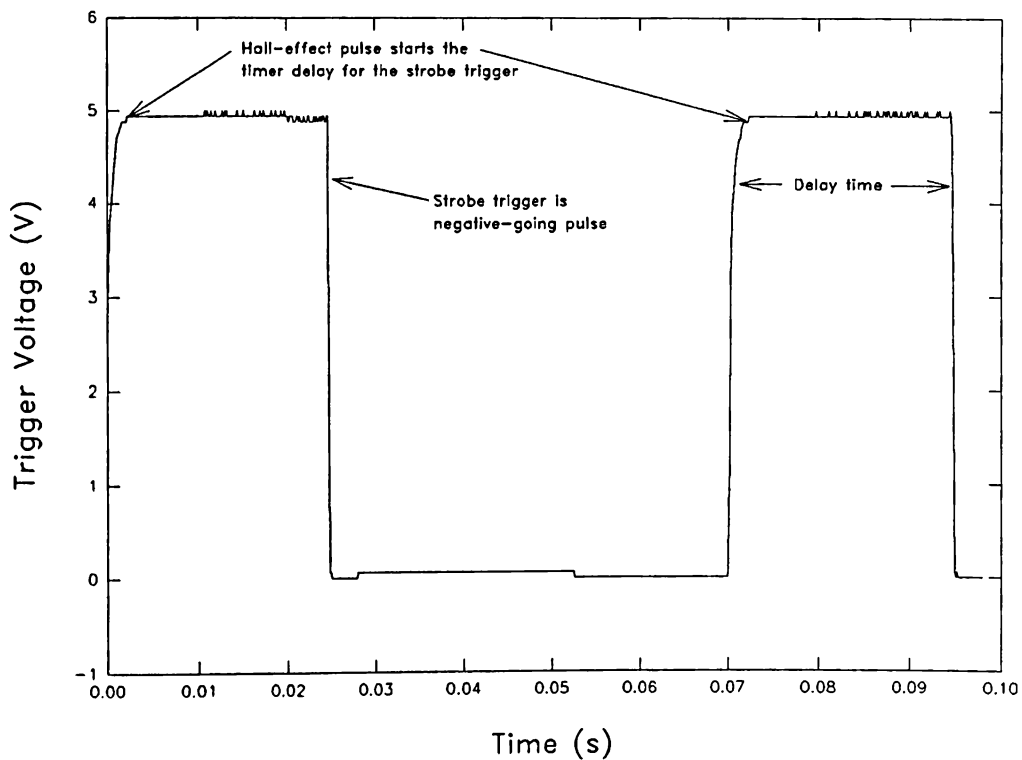


Figure 5.7 Trace of signal output from strobe light triggering circuit

and 125 pulses per second. The encoder/strobe trigger was useful in the unsteady pressure measurements as well as flow visualization as will be discussed shortly.

The Hall-effect sensor is fixed to a motor support in an adjustable manner so that the sensor can be precisely positioned for good trigger stability and response. A magnet is affixed to the "spider" of one of the blades to close the electromagnetic switch in the sensor on each pass of the rotor blade. If no time-delay circuit were used, the sensor switch could be used to flash the strobe in synchronization with the fan rotation, and in doing so the fan blade appears under strobe illumination to stand perfectly still with the magnet directly positioned by the Hall-effect sensor. The sensor signal in this case appears as a sharp spike from a base of 0 V to a sharp peak of 5 V. When using the time-delay circuit, the Hall-effect pulse begins the time-delay circuit where the delay time is dependent on adjusting the 1 M Ω potentiometer. After the set delay time, the signal voltage (which first went "high" to 5 V when the Hall-effect sensor was triggered) falls sharply back to 0 V, triggering the strobe light. This process is demonstrated in Figure 5.7 for the case of advancing the rotor 120 degrees past the Hall-effect pulse. Note that the position F marked in Figure 5.4 (the origin of reference for the pressure measurements) was chosen because this is the location where the rotor is positioned when no time delay is used and the blade on which the suction side is measured is located at F.

All testing and experimentation was performed in Room 2032 Learned Hall. The setup and the equipment used during the study are shown in Figures 5.8 and 5.9. In Figure 5.8, the LP fan with shipping crate sets on a table with one side of the crate replaced by a plexiglass sheet to ease flow visualization. Also, a section of the venturi panel (as indicated in Figure 5.4) has been replaced by a matching piece of plexiglass to enable flow visualization at the rotor tip. It was necessary for the particle and mini-tuft flow visualization work to be performed at night with black plastic sheeting covering the closed window shades in order to get good, consistent results. The black plastic sheets and a large wallboard backdrop painted flat black to provide needed contrast in the particle visualization techniques is visible in both Figures 5.8 and 5.9. Generally speaking, the larger the flow field to be visualized the more difficult it is to visualize the flow due the lighting restrictions. For example, the flow visualized here would be more straightforward to visualize if it were enclosed in a test tunnel instead of a large laboratory space.

5.3 Hot-wire Anemometry Equipment

The following hot-wire anemometry equipment was loaned by Lenexa Products for use over the course of this study:

- Dantec two-channel constant temperature hot-wire anemometer
- Two straight-pronged single quartz-fiber probes

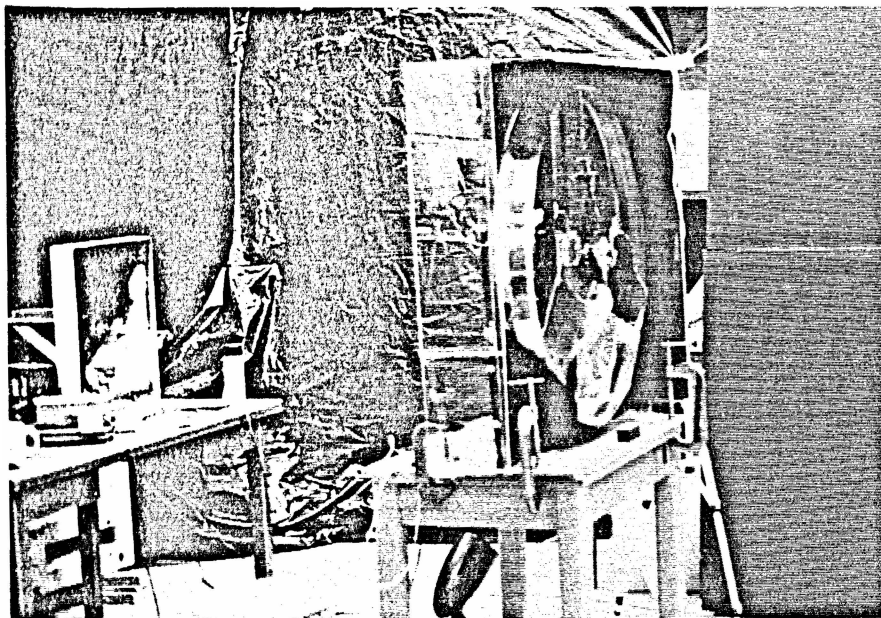


Figure 5.8 Fan laboratory for conducting flow visualization, hot-wire measurements and unsteady pressure measurements on the LP at free air conditions

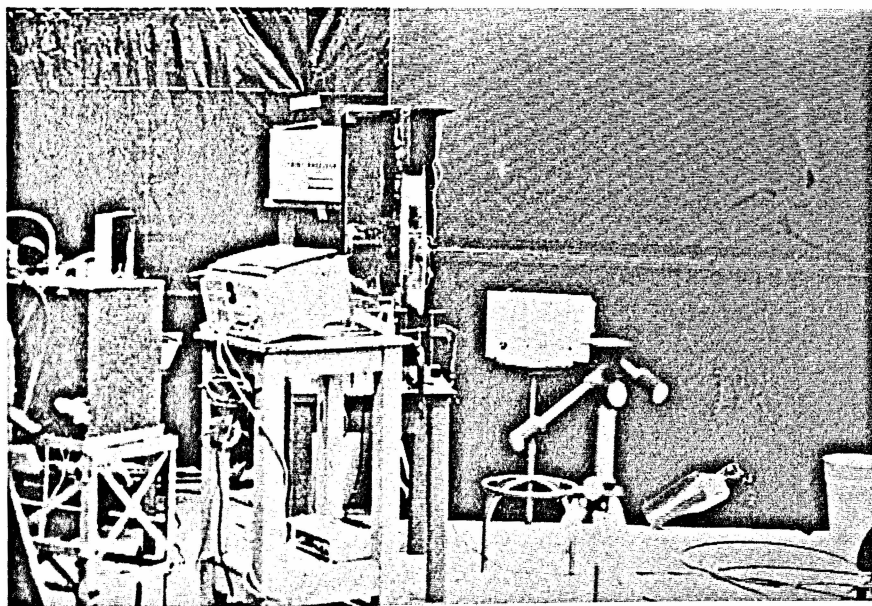


Figure 5.9 Fan laboratory with more of the backdrop shown

- One quartz-fiber x-probe for simultaneous measurement of flow velocity and direction in primarily two-dimensional flows
- 56C01 Constant Temperature Anemometer (CTA) and 56B10 Main Frame
- 56N20 Signal Conditioner
- 56N21 Linearizer
- 56N22 Mean Value Unit
- A manual traversing system and fixture

After it was realized how rough this application was on the probes, it was decided to replace the quartz fiber probes with a tungsten wire probe (a single straight wire). This type of probe can be repaired by the user reducing expense and turn around time on repairs. After experimentation, practice and (sometimes) luck the author had success in re-attaching replacement wire to the probe prongs. A welding circuit based on instructions given by Sandborn (1972) was constructed and used to spot-weld the fine tungsten hot-wire to the probe prongs. The welding circuit used is shown in Figure 5.10 and differs from Sandborn's by using a variable voltage supply to fine tune the welding power. Sandborn recommended an 18V supply which the author found to be too powerful, typically vaporizing the tungsten wire; the better success was had using 14 to 15 V. A fixture and micro-manipulator would simplify the task, but the author found that with the welding device, a dissecting microscope with makeshift means of positioning the wire, time and patience the wire could be reattached. A small drop of lacquer applied with a single bristle from a fine paint brush was applied to the weld for added strength before calibrating the reattached probe.

All probes were calibrated after first setting up the Dantec 56C01 CTA and 56B10 Main Frame for the appropriate overheat ratio and transient response. The Dantec probes were calibrated in a Thermo-Systems Inc. (TSI) Calibrator Model 1125 after new probe holders for the internal chambers on the TSI Calibrator. This equipment is capable of calibrating hot-wire or hot-film anemometers over the velocity range of 0.5 to 1000 ft/sec, following the manufacturer's instructions. A typical calibration curve is shown in Figure 5.11.

The response of the probe to direction was also tested and quantified as shown in Figure 5.12 where the angle on the ordinate axis is taken as that between the velocity vector at the probe wire and the normal vector to the probe wire at that point. A simple form of the describing equation for the effective velocity measurement at the sensor and the actual velocity and its direction is given by Hinze (1975), and Fingerson and Freymuth (1983) as

$$V_{\text{eff}} = V \sqrt{\cos^2 (\alpha - \delta) + k_t \sin^2 (\alpha - \delta)} \quad (5.1)$$

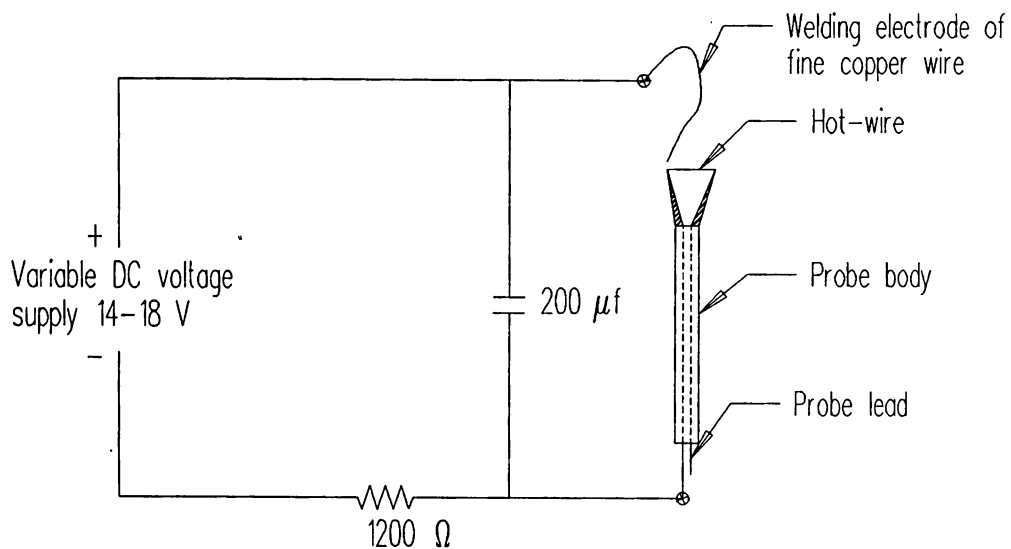


Figure 5.10 Welding system used to reattach tungsten hot-wire to probe prongs (after Sandborn, 1972)

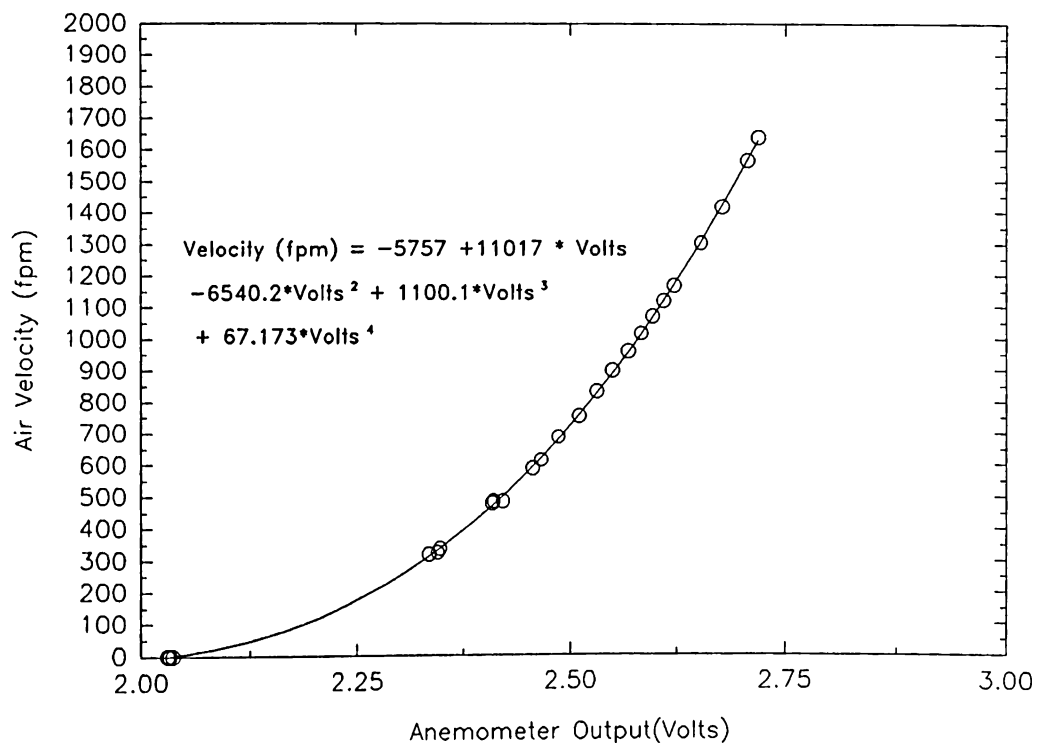


Figure 5.11 Typical calibration curve for a reattached hot-wire probe

where V_{eff} is the effective cooling velocity measured by the hot-wire, V is the total velocity incident to the hot-wire, α is the angle between the velocity vector and the normal vector to the sensor wire, and k_t is an empirically determined factor which is dependent on the length-to-diameter ratio of the sensor wire. The variable δ has been added to discern uncertainty in the positioning of the sensor element, which was done manually, and to determine the angle offset to the actual point of maximum velocity as determined by the data.

Directional sensitivity data were taken by positioning the hot-wire perpendicular to a flow of known velocity produced by the TSI Calibrator. The velocity versus incidence angle data was taken using the Dantec CTA. Directional sensitivity data for the hot-wire probe is plotted for $V = 2988$ ft/min is given by the circle symbols in Figure 5.12. A non-linear least square curve fitting of Equation (5.1) with the probe data indicates that $k_t = 1.45 \times 10^{-4}$ and $V = 2983$ ft/min for $\delta = 0$ deg. The curve derived from this non-linear least-squares procedure is the $\delta = 0$ curve in Figure 5.12. Next, the value of δ was determined by nonlinear least-squares using the maximum velocity determined from the curve for $\delta = 0$. The resulting curve is identified in Figure 5.12 as $\delta \neq 0$ where $k_t = 3.59 \times 10^{-5}$ and $\delta = 2.01$ deg for $V = 2983$ ft/min. The result, that $\delta = 2.01$ deg, is believable since the difference between where the sensor was thought to be and where it actually was perpendicular to the flow because it was positioned by hand. Since $k_t \approx 0$ for the data, the velocity along the sensor wire basically has no cooling effect, $k_t^{1/2} V \sin(\alpha) \approx 0$. This is typical (Fingerson and Freymuth, 1983) for a hot-wire probe with a large wire length-to-diameter ratio (greater than 800). The data is skewed at angles less than 0 as shown in Figure 5.12, believed to be caused by a slight bend in the probe wand. Even so, these measurements and the assumption of negligible effect of k_t are adequate for the task of measuring the fan inlet velocity profile using the probe in question.

The use of the hot-wire anemometer's directional sensitivity to measure a velocity's magnitude and direction is well known (Fingerson and Freymuth, 1983). In this project the hot-wire was used to measure the inlet-flow velocity profile of the LP fan at free-air conditions for the purpose of providing it as input to the PSF-2 and derivative programs. Flow visualization and examination of the hot-wire signal using the Hewlett-Packard HP 54601A digital oscilloscope have shown the flow often to be poorly behaved for accurate measurements (as will be shown later). Essentially, though, the inlet flow has only axial and radial components with radial components occurring near the tip and motor. Also, the inlet flow field is certainly affected by the motor supports, but also it is altered by the shipping crate. This means the fan rotor should see a periodic inlet-flow field of period $\pi/2$ with the effects of the motor supports seen on alternate periods. This will be borne out by the pressure measurements. Flow visualization showed that the inlet flow field is basically two-dimensional and that a velocity traverse made with the hot-wire aligned in the radial direction can determine these axial and radial

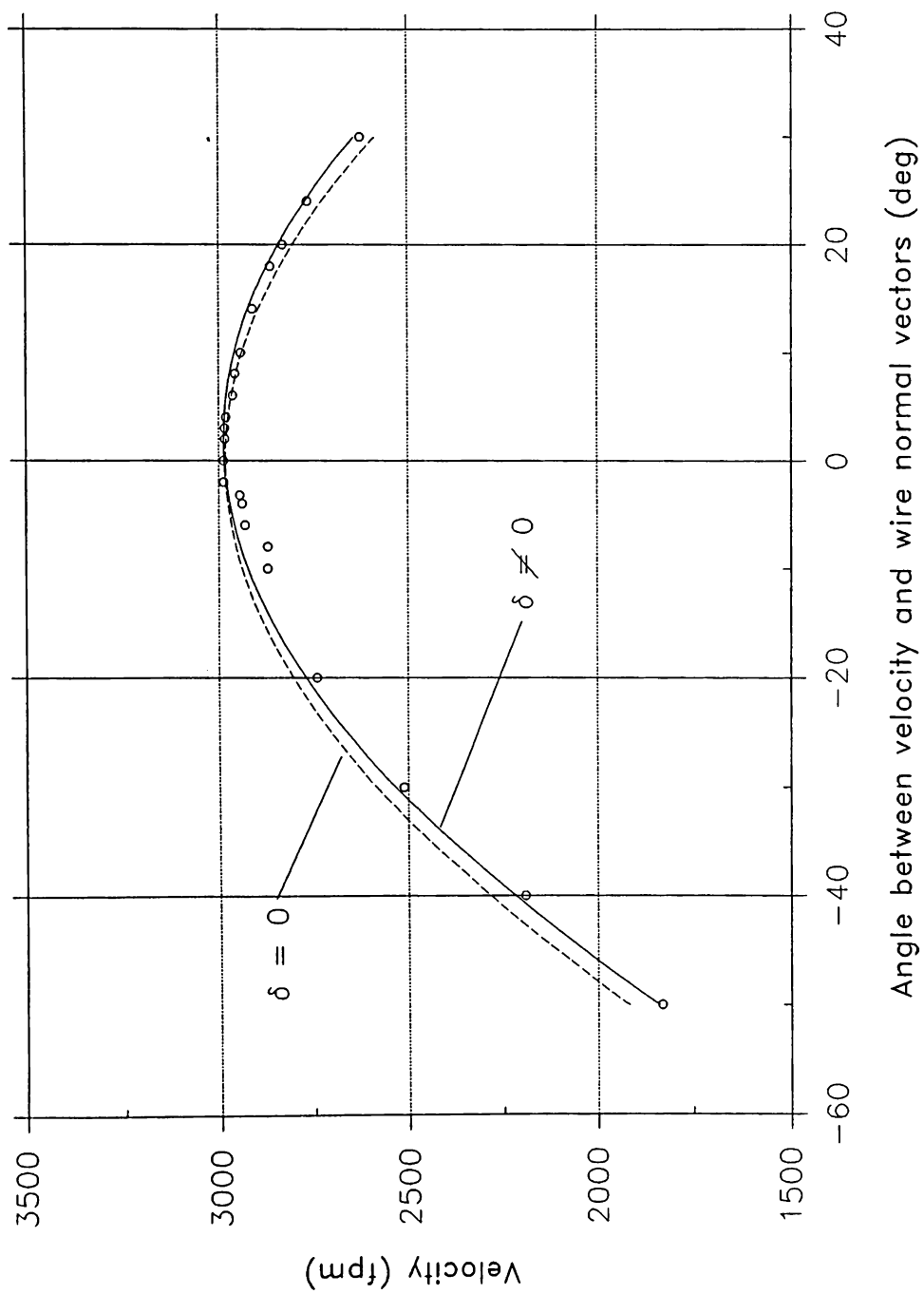


Figure 5.12 Test of velocity angle sensitivity of a reattached hot-wire probe

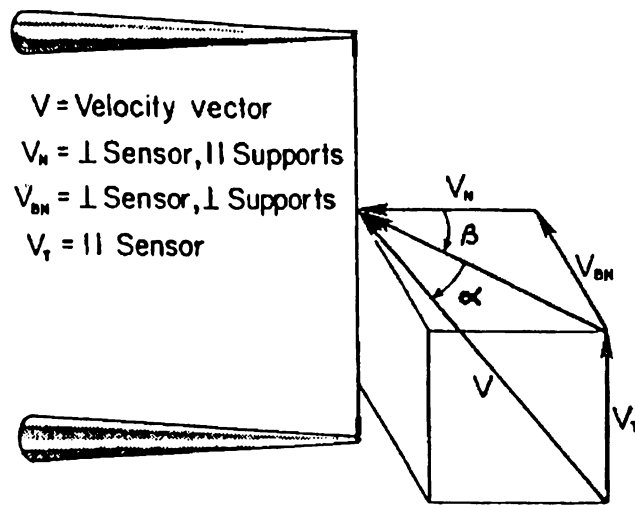


Figure 5.13 Velocity components and angles of incidence at a hot-wire sensor (Fingerson and Freymuth, 1983)

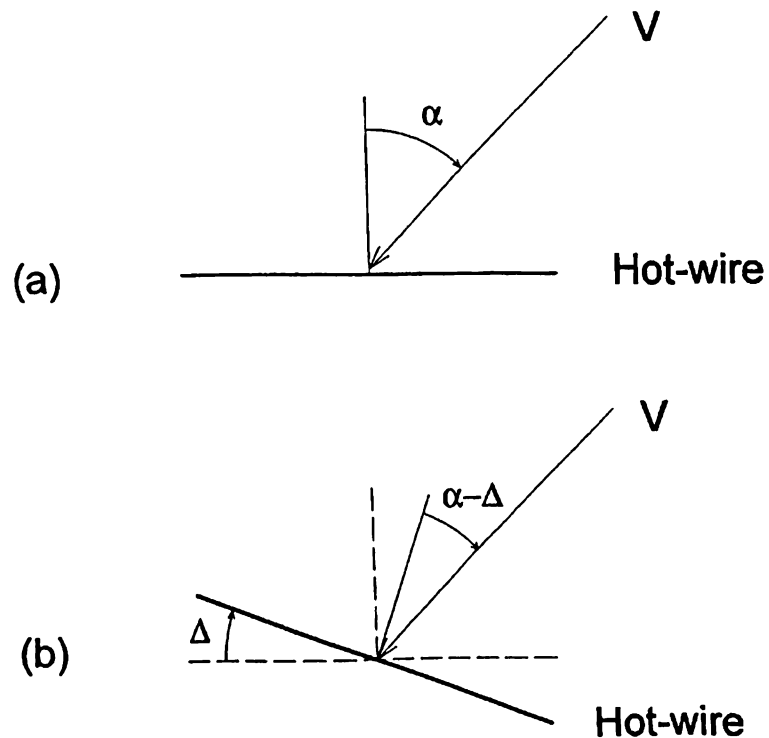


Figure 5.14 (a) A hot-wire sensor aligned in the direction of one of the components to be measured in a two-dimensional flow field, (b) rotated by a known angle Δ in the plane of the velocity

velocity components.

At the minimum, two measurements at a given traversing point are required to determine the components. When the hot-wire is aligned along the radial direction, it would appear in the two-dimensional flow field shown in Figure 5-14(a). The effective cooling velocity $V_{\text{eff}, a}$ sensed by the wire in this position as measured by the Dantec CTA is given by Equation (5.1) with $k_t = 0$ as

$$V_{\text{eff}, a} = V \cos \alpha \quad (5.2)$$

where the velocity V is angled to the wire normal vector by α . Measurement at a second point is made with the sensor wire turned by an angle Δ into the direction of the velocity V , which is presumed to be unchanged. Admittedly, the technique is valid for steady velocities and a poorly behaved flow requires measurements at multiple values of Δ to confirm the measurement. However, the velocity $V_{\text{eff}, b}$ sensed by the hot-wire in position (b) is given by

$$V_{\text{eff}, b} = V \cos (\alpha - \Delta) \quad (5.3)$$

Since Δ , $V_{\text{eff}, b}$ and $V_{\text{eff}, a}$ are known by measurement, Equations (5.2) and (5.3) can be solved to the velocity V and its direction α defined with respect to the hot-wire. Measurements at multiple Δ values enables V and α to be determined by minimization of the sum of the squares of the errors between the data (values of V_{eff} and Δ) and the predictions of the assumed function

$$V_{\text{eff}} = V \cos (\alpha - \Delta) \quad (5.4)$$

which was the method used in this work. Average velocities of V_{eff} over a period of 100 seconds were taken in the measurements given later in this work. The technique of using the directional sensitivity of the hot-wire to determine velocity components in a two-dimensional flow can be extended to three dimensions as discussed by Jackson and Lilley (1986) and others they cite. Multi-wired probes can also be used for this purpose.

5.4 Pressure Measurements

Vortex element methods, such as the vortex lattice method used to compute aerodynamic loading in this study, calculate the net force on the i -th vortex element using the Kutta-Joukowski law

$$\vec{F}_i = \rho \vec{V} \times \vec{\gamma}_i s_i \quad (5.5)$$

where \mathbf{V} is the velocity relative to the vortex element at its midpoint, γ_i is the vortex strength per unit length of vortex element, and s_i is the length of the given (i-th) vortex element. This force is perpendicular to the vortex element and, therefore, normal to the blade mean camber line that the sheet of vortex elements models. For the current method of analysis, this force is the resultant lifting force, and is considered constant over the area of the vortex lattice panel under consideration. A pressure difference on the i-th panel, constant over the area of the panel, can be calculated by dividing this force by that panel area as

$$P_i = \frac{|\vec{F}_i|}{A_i} \quad (5.6)$$

Perhaps the most direct way of verifying a vortex element code is to compare the "lifting" forces produced by the computation with the actual forces on the blade, and these forces, which can be directly measured as pressure, are the result of the aerodynamic flow characteristics over the blade surface.

It is of interest to look at other validation methods for comparison, some of which were discussed in Chapter 3. The ducted version of the PSF-2 code, **DPSF-2**, was the subject of validation work by Hughes et al. (1992). Dynamometer measurements of thrust forces on both the propeller and the duct along with dynamometer torque measurements were made at various advance coefficients and compared with DPSF-2 computations as thrust coefficient, torque coefficient, and efficiency. The results show good agreement, but the agreement appears much better for the propeller alone than for the propeller and duct results. Also the results are very good at the design advance coefficient and depart (particularly for the results with duct) at off-design coefficients. Velocities were measured upstream and downstream from the duct using a Laser Doppler Velocimetry system. Using the tangential velocities in the wake of the duct, it was possible to calculate a span-wise distribution of circulation on the propeller blades. This calculation was made using the method given by Wang (1985). These values were then compared with computed circulation distributions for several operating conditions. Also, the measured axial and tangential velocities 1 cm behind the duct edge were circumferentially averaged and compared with averaged calculation field point velocities. In the calculations the duct and hub were treated as a single unit; however, the duct/hub and propeller were treated as separate domains with their effect on each other being taken into account in an iterative manner. The propeller was modelled using a lifting surface technique (like the PSF-2 code) and the duct and hub were analyzed using a boundary element, or panel, method (using dipole/source panels on the duct and dipoles for its wake). Also, in an effort similar to the present pressure measurement study, Kim and Kobayashi (1984) extended the PSF-2 program code to compare computed blade surface pressures with their measurements as discussed in Chapter 3.

The results of the pressure measurements in this study, though at first sought for the purposes of code verification, are of interest in themselves. The measurement apparatus constructed and the technique used to extract the pressure difference across the blade is novel as are resulting unsteady measurements that capture the effects of the motor support struts and other in situ phenomena. There was no idea of the magnitude of the fluctuating aerodynamic loading on the blade at the project outset.

5.4.1 Pressure Measurement Apparatus

Measured of blade surface pressures gave insight into the actual flow over the blade and provided a basis other than total fan performance for comparison with the VLM predictions. The actual pressure loading on the blade provides insight into the degree of unsteadiness of the aerodynamic loading which the blade experiences due to motor supports, shipping crate and other "in situ" phenomena. These features could not be taken into account by the PSF-2 code or its derivatives. The comparison between the VLM and the measurements was made to investigate the degree to which the VLM-predicted aerodynamic loading matches the unsteady measurements and their time-averaged values.

The method finally used to measure the blade surface pressures evolved from experimentation. The measurement system met six major criteria:

- The method needed to be as unobtrusive as possible, which is difficult considering the "thinness" of the LP fan blade.
- The measurement system should not be influenced by centrifugal forces and rotational effects.
- A method to take the pressure signal off of the rotating blade needed to be developed.
- The response of the pressure measurement system must be fast enough to capture the unsteady effects.
- The unsteady data needed to be acquired and stored.
- The measurement system should be robust and inexpensive.

There are currently methods of surface measurement which are amazingly unobtrusive. Pressure sensitive paints are currently being researched and used for full-surface pressure data both in wind-tunnel testing and in in-flight testing (Morris et al., 1993, Bell et al., 1993 and works cited therein). The range of pressure studied here is believed to be too low to use this technique and

experimentation with this technique should be approached as a separate endeavor. Another technique, which would use 1 mm thick transducers, is described by Kimura and Nishio (1989) and uses strips of magnetic tape which deflect due to the surface pressure and become magnetized by a current-carrying wire running approximately 0.2 mm beneath it by an amount dependent on its deflection. Kimura and Nishio envision using the technique with many "transducers" contained in a single sheet and bonded to a surface. Thin pressure transducers are manufactured by Kulite (0.0013 in. thick and 1/16 in. diameter, approximately \$300 per transducer) and Endevco, which are cheaper than Kulite's but larger. Heidelberg (1992) at NASA-Lewis (from whom this information was learned) used the Kulite transducers to measure dynamic pressures on propellers and fans. However, pressure sensing devices located on a rotor surface must be corrected for centrifugal forces.

Given the cost constraints for this project, the pressure sensing device chosen, the SenSym SX01DN, was an economical pressure transducer which has an acceptably fast response time. Some of the characteristics of the SX01DN are a response time of 0.1 ms for 10% to 90% of full scale, a measurement range from 0 to 1 psi, a repeatability of 0.5% of full scale, and a full scale output of 20 mV unamplified. Since the fan blades are approximately 0.06-in. thick it is not possible to machine out pressure tap channels in the blade surface without compromising the blade strength. For this reason, and the difficulties associated accounting for the effects of rotational forces on the sensing element, it was decided to locate the pressure transducer at the center of rotation with the sensing element located in the plane of rotation to limit rotational forces on the sensor. Pressure tap lines were then run from the low pressure sensor side to the pressure tap location on the blade surface. The high pressure port (P1) was open to the ambient pressure at the fan rotor hub for all measurements.

Pressure tap tubing ran from the center of rotation, along the trailing edge of the blade, to the radial location and then along the constant radial distance to the point of pressure measurement. The Tygon tubing used has is of 0.092 in. (2.33 mm) o.d. and 0.027 in. (0.686 mm) i.d.. Because the tubing outer diameter is only 0.03 in. greater than the plate blade thickness, it does not visibly alter the flow at the trailing edge. The tubing was seated in place (the tap hole in the blade were drilled to provide a press fit to the tube) and a drop of Loctite industrial adhesive was used to secure the tubing in place. Thin metal tape and the adhesive were used to secure the tubing at the trailing edge and along the constant radial distance from the trailing edge. The situation just described is shown in Figure 5.15, where the tubing is on the blade pressure side and the measurement, therefore, is made on the suction side. In Figure 5.16 is given a detailed photograph of the tube running along the trailing edge to the pressure tap. The blade surface measured and the pressure taps were conditioned for testing as described by Pope (1984). However, the pressure tap hole were somewhat larger

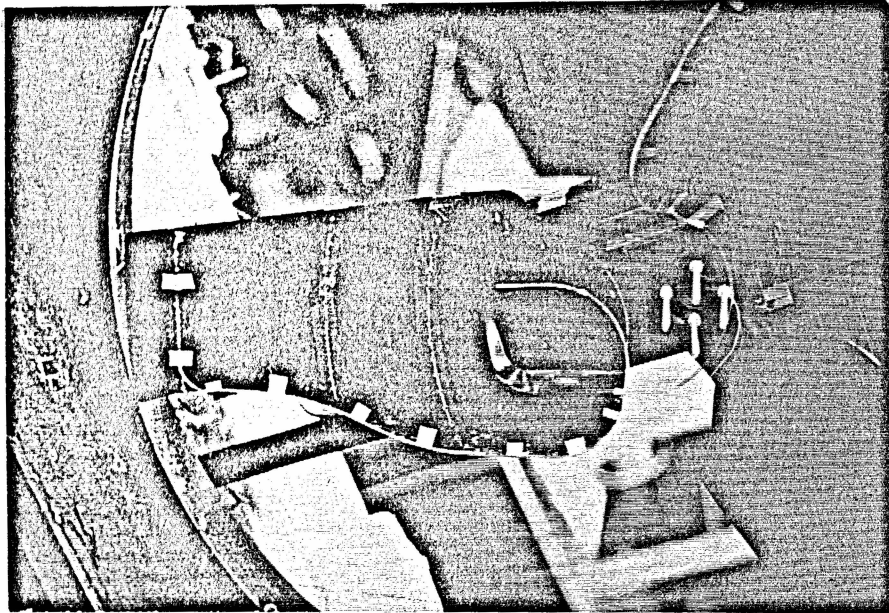


Figure 5.15 Pressure tap tubing running along the blade trailing edge to the tap on the opposite side of the blade surface to be measured

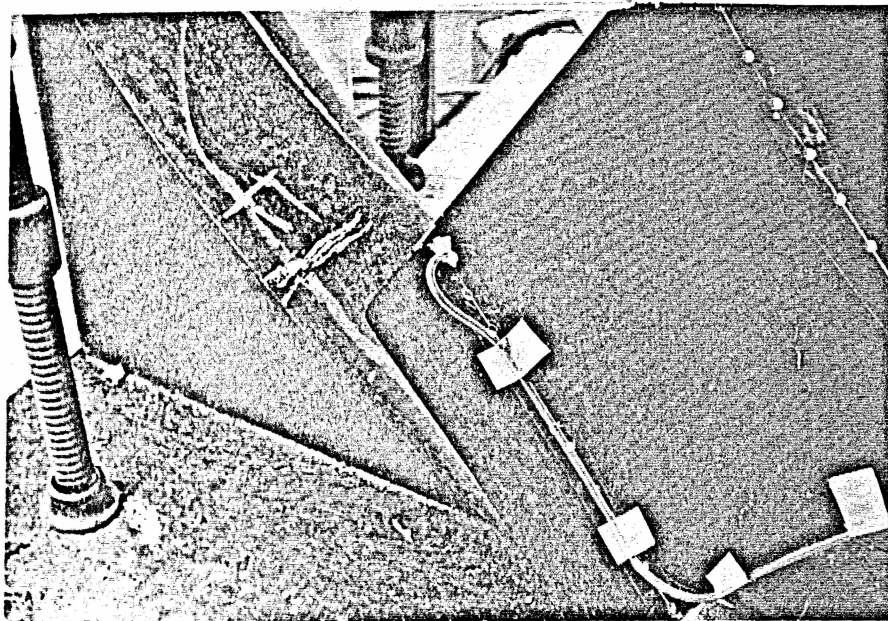


Figure 5.16 Detail of pressure tap tube for measuring suction side blade surface pressures

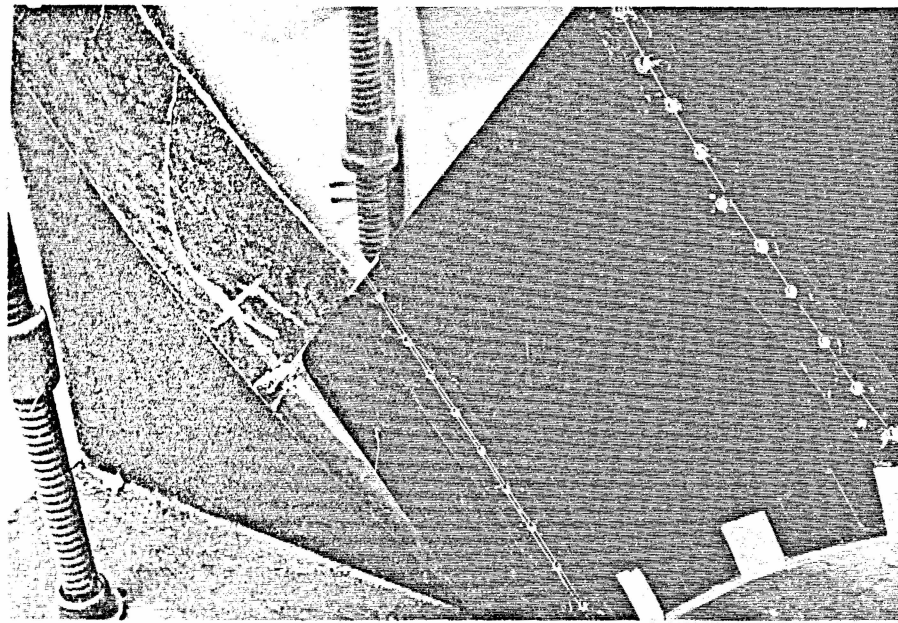


Figure 5.17 Detail of pressure taps on pressure side of the blade

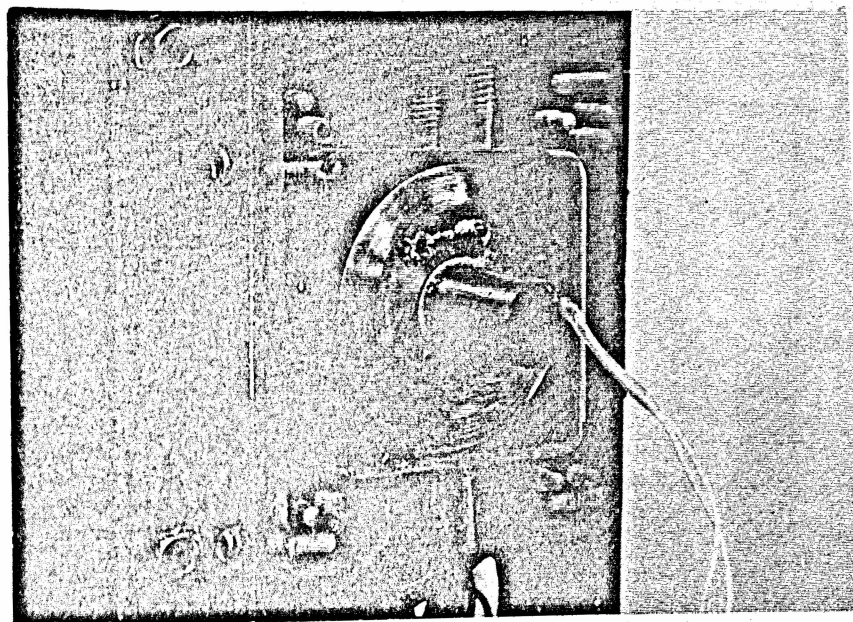


Figure 5.18 Slip-ring "box" mounted on the motor with cover plate to the mercury reservoir (empty) removed showing a shaft-mounted copper disk

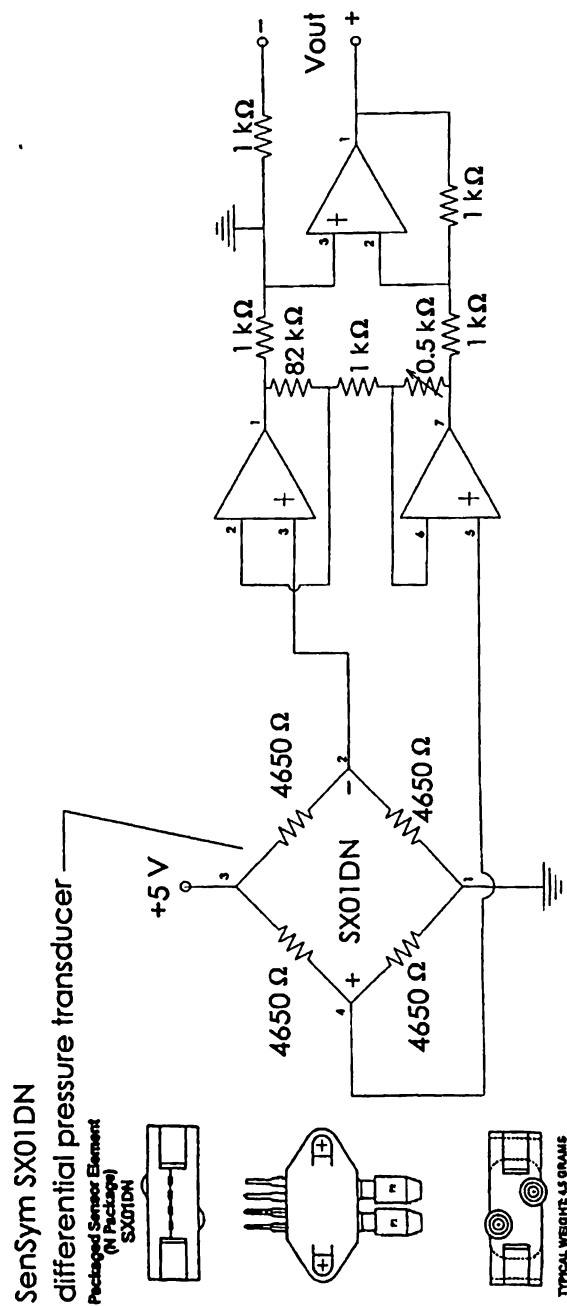


Figure 5.19 Pressure sensor and amplifier circuit located at the center of rotation to measure pressures on the LP fan blade surface

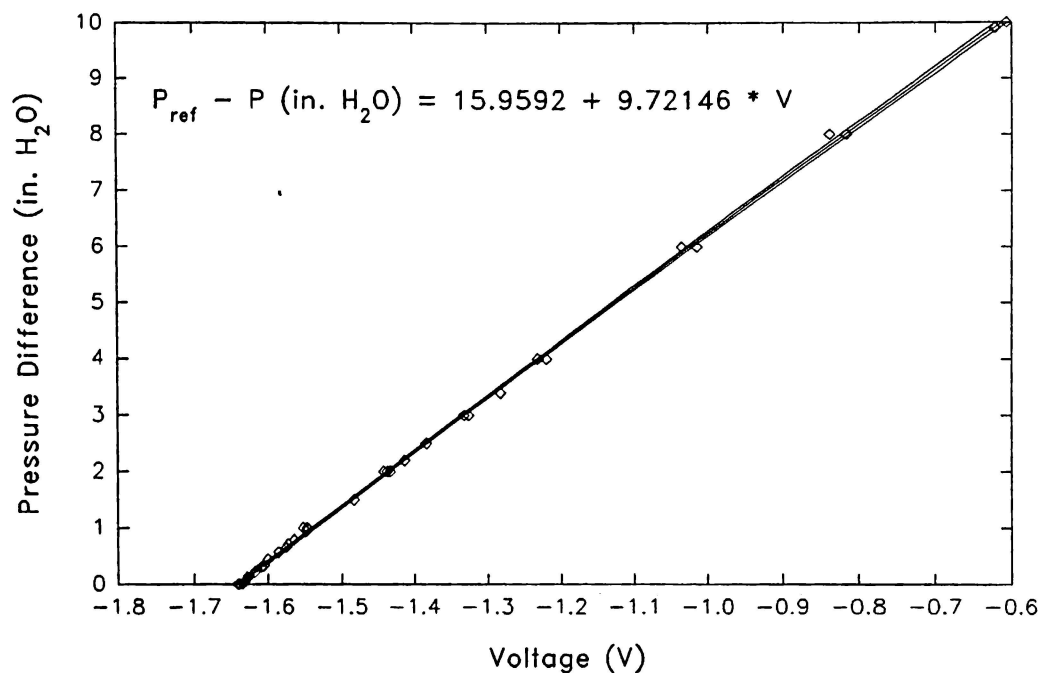


Figure 5.20 SenSym SX01DN pressure transducer calibration curve

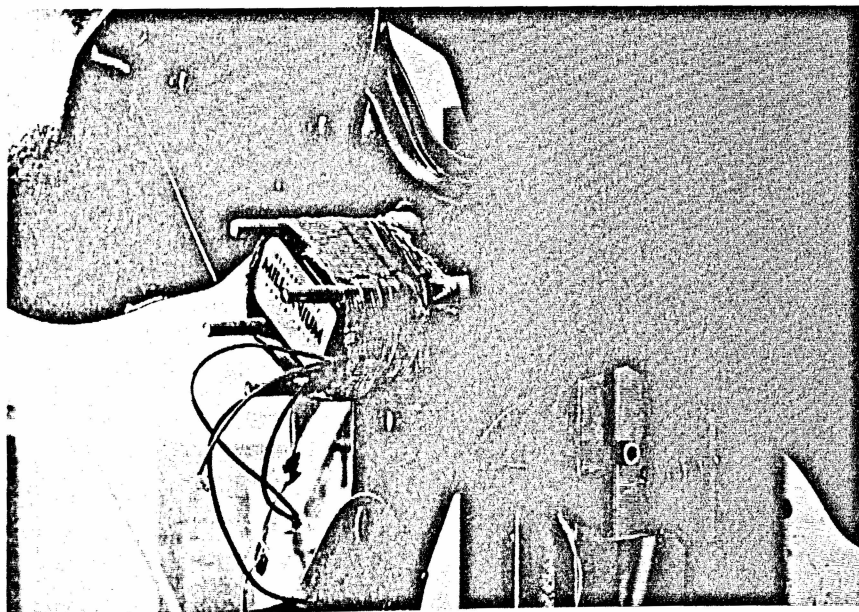


Figure 5.21 Battery pack mounted to the fan hub between the four posts used to secure the transducer/circuit board

than recommended by Pope (1984) and are shown for the pressure side of the blade in Figure 5.17. As will be shown in the presentation of the performance results, tubing on the blades showed no noticeable effect on fan performance. Also, blade surface flow visualization using mini-tufts showed no discernible changes in the overall blade surface flow caused by the tubing.

Several means of extracting the pressure data from a rotating shaft were investigated; telemetry devices tried were too slow, lacked temporal resolution and were not robust enough, and Scanivalve devices were too costly (however, if price is no object, they are the way to go). It was decided, finally, to construct a set of slip-rings to take the pressure measurement signal off the fan. A two-chambered box was machined out of plexiglass with cover plates attached by screws to seal the chambers. The chambers were filled to a level high enough to make contact with the copper disks rotating on the shaft. The slip ring "box" was custom made to fit on the fan motor and was mounted to the motor as shown in Figure 5.18. Shown in Figure 5.18, with the cover plate removed, is the shaft-mounted copper disk which rotates in the mercury as the shaft spins and the two white signal wires which were attached to the pressure measurement circuit. The two signal wires led from the pressure transducer and amplifier circuit to the copper disks, which were mounted to the shaft using teflon sleeves. The sleeves insulate the signals from the motor shaft and each other, and also served as a bearing and seal between the box and the shaft-mounted disks. The signal leads in the laboratory (non-rotating) reference frame ran from thin conducting strips at the bottom of the mercury chambers out of the bottom of the slip-ring box. The slip rings produced no detectable noise when comparisons were made without and with the fan on; a steady voltage signal from a battery was identical on the digital oscilloscope for both fan on and fan off cases with no noise introduced by the disk rotation.

The pressure transducer signal amplification was done on the rotating fan by a circuit mounted on the fan hub. The pressure transducer was also fixed to this circuit board. A simple means of amplifying the transducer output was used; the circuit performing this is given in Figure 5.19. Also in Figure 5.19 the SenSym pressure transducer is drawn nearly to full scale. Resistances indicated in the transducer bridge are the input impedance resistances as taken from the manufacturer's literature. The small numbers in Figure 5.19 indicate the pin-out locations on the integrated circuits used. Operational amplifiers were used rather than precision instrument amplifiers. The manufacturer says op-amps provide an accuracy of $\pm 2\%$ for temperatures limited to $25\text{ }^{\circ}\text{C} \pm 15\text{ }^{\circ}\text{C}$. While this was deemed acceptable for the present work, both the circuit used to condition the signal and its components could be improved. Nonetheless, as shown by the curve in Figure 5.20 along with 99% confidence interval lines, calibration data taken several months apart is good. One drawback of the circuit is that since it and the transducer are powered by two 9V batteries, the signal drifts as the batteries lose charge. This slight drift was compensated for by adjusting the $0.5\text{ k}\Omega$

potentiometer shown in Figure 5.19. This may also be the cause of any data scatter in Figure 5.20. The 9V batteries are shown in Figure 5.21 mounted to the fan hub (with slip-ring box also visible) between the four posts used to secure the pressure transducer and circuit board.

5.4.2 Pressure Data Acquisition and Correction

Pressure data was acquired using an HP 54601A digital storage oscilloscope with the Unilux strobe light and associated circuit (see Figure 5.7) as a trigger. The fan blade upon which the pressure was measured could be positioned in a pre-determined position for flow visualization purposes using the strobe light/triggering equipment. The output from the strobe light trigger circuit and the pressure sensing circuit was then sent to the oscilloscope where the strobe light trigger was used as the data sampling trigger. A complete revolution of data was acquired and averaged over 8, 64, or 256 revolutions using the oscilloscope's internal functions. All measurement results presented here were averaged over 256 revolutions. However, the author's experience shows that there is little difference between data averaged over 64 and 256 revolutions. The data averaged over 8 revolutions exhibit the same form as data incorporating more samples, but the slight fluctuations (though interesting) were less desirable than the extremely stable measurements made with 64 or 256 samples. The oscilloscope was controlled during data acquisition using the HP 54601A oscilloscope's programmable capabilities over an RS-232 port by using a personal computer. This technique is discussed in Hewlett-Packard (1991) and the program used to acquire the data in this project is given in Appendix B.

The data acquisition program allows the user to take the data, graphically inspect it, and store it on the PC hard disk for later use. Essentially, the information acquired in this process are the oscilloscope settings, voltage and time values for the trigger and the pressure measurement circuit output from which (following post-processing) the pressure difference across the blade at a given pressure tap will be found. Graphical inspection of the data gives confidence that the data stored was good and that the system worked properly. Also, in the initial stages of the pressure measurements the graphical display of the data allowed the author to experiment by placing jets of air and other disturbances at various azimuthal positions to test the measurement system's response, and to confirm the location of disturbances caused by the motor supports and other inlet flow disturbances.

As mentioned above, for a given pressure difference measurement the strobe light was used to position the blade to be measured at the azimuthal position taken as the beginning of a pressure data trace (position F in Figure 5.4). On one fan blade the pressure taps and tubing are instrumented for a suction-side

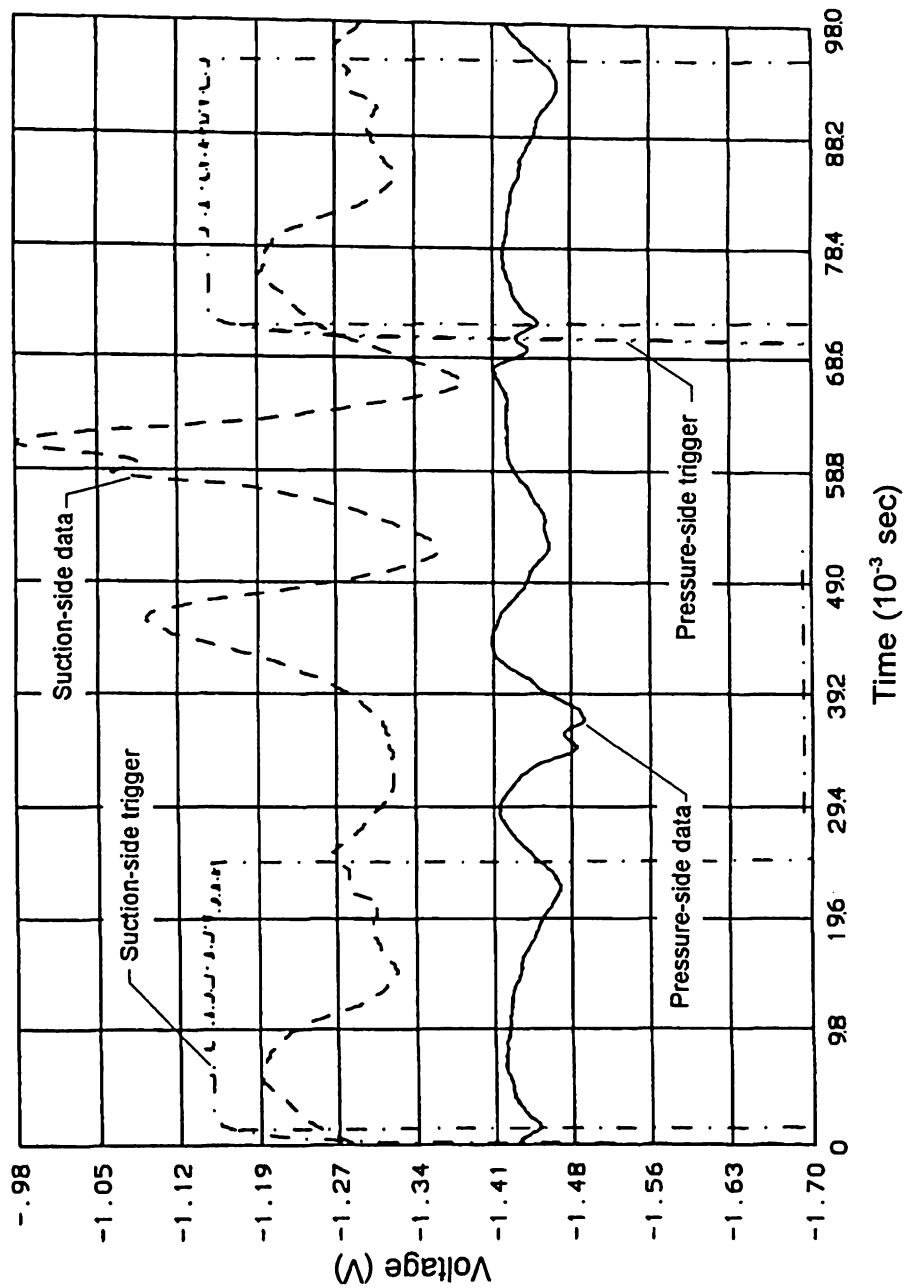


Figure 5.22 Example of oscilloscope voltage data input for the pressure difference post-processing program

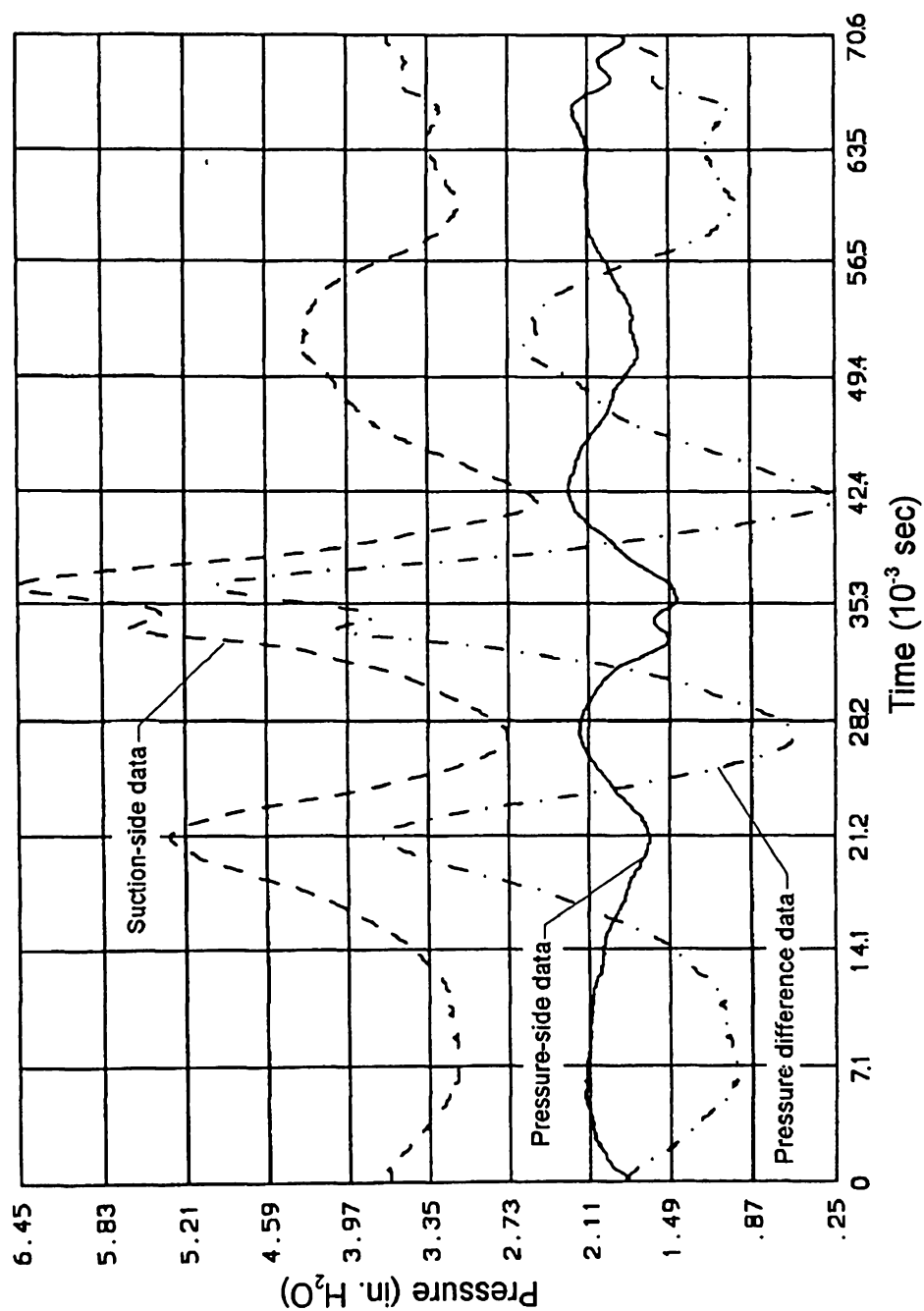


Figure 5.23 Example of measured pressure data ($P_{ref} - P_{measured}$) as determined from "raw" voltage, and pressure difference data ($P_{pressure-side} - P_{suction-side}$) from the post-processing program

measurement, and on another blade for the pressure-side. Using the negative going trigger pulse (shown in Figure 5.7) as the data marker for this reference position, the data for matching azimuthal positions was then determined from the suction and pressure-side data files when the data was processed to determine the pressure difference at a given blade position. Therefore, for a given pressure measurement, the rotor was first positioned at the reference point so that the leading edge of the suction-side blade was at position F in Figure 5.4 and the measurement was made. Next, the pressure-side blade was positioned at the reference position F using the time delay circuit along with the strobe light, and data for that side was taken. The data was then stored for processing on the author's 486 personal computer. The machine used to acquire the data, an XT-type personal computer, was not adequate for processing the data.

The pressure-side and suction-side data stored in files once stored were ready for processing. The treatment of the "raw" oscilloscope data was broken into five steps:

1. Pressure-side and suction-side oscilloscope data from a given location were retrieved and converted to the appropriate time and voltage scale as shown in Figure 5.22. The oscilloscope is triggered by the positive going pulse.
2. Using the negative going pulse as a data marker and initial reference point, data for one revolution were taken from that previously stored.
3. The voltage data values were converted to the pressure difference ($P_{ref} - P_{measured}$) sensed by the transducer as determined from the Sensym transducer calibration curve. See the pressure and suction-side data shown in Figure 5.23 taken directly from the program output.
4. The pressure data ($P_{ref} - P_{pressure-side}$) for the pressure-side was then subtracted from the suction-side data ($P_{ref} - P_{suction-side}$) to arrive at the pressure difference ($P_{pressure-side} - P_{suction-side}$) which determines the loading on the blade at that point. An example of this data (taken directly from the author's program) is shown in Figure 5.23.
5. Finally, the pressure-difference data was "corrected" for the time delay and attenuation of the pressure signal caused by the length of pressure tap tubing. The technique used will be discussed later in detail. However, it was assumed that correcting the difference is equivalent to correcting the two data sets prior to taking their difference with the advantage that only half as many computations

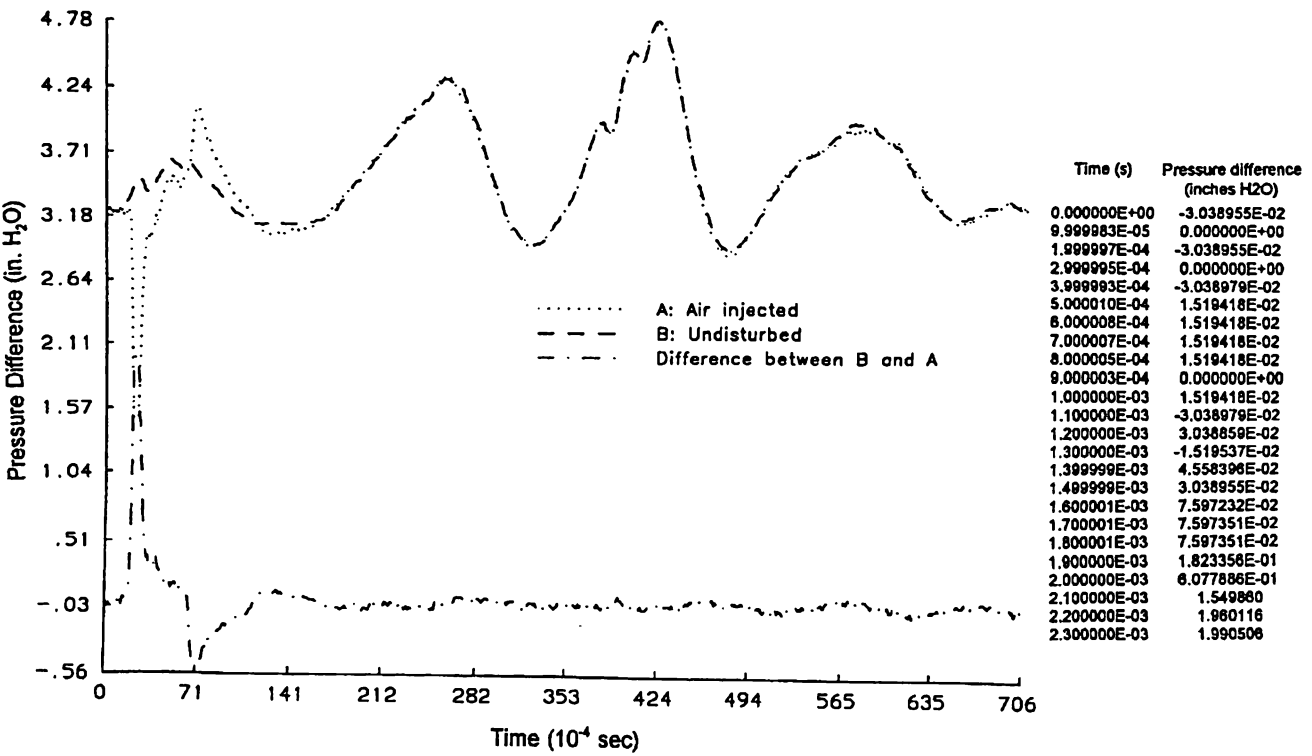


Figure 5.24 Measurement of pressure signal response time showing data with and without air injected, and the difference between them (data for pressure difference up to the response time is also shown)

need to be made, and test calculations to be presented will bear this out.

The "raw" data collected using the digital oscilloscope needs to be corrected for time lag and signal attenuation caused by the pressure tap tubing. Two classical cases of the influence of time lag and attenuation of a pressure signal in a tube are the pressure step input case (Schuder and Binder, 1959) and the oscillatory (sinusoidally varying pressure) pressure case (Iberall, 1950). For the measurement system used in this study, experimentation by injecting air at a given azimuthal location synchronized with the strobe light system revealed a time delay almost precisely equal to the time required for the pressure disturbance caused by the air jet to propagate down the tube at the speed of sound. In this case, the speed of sound was taken as that (1130 ft/s) at the room temperature of 70° F and the length of the pressure tap tubing was 28 in. The theoretical time for the pressure disturbance to traverse to tube (from tap to pressure transducer) was 0.00206 s. The actual measurement for this experiment is shown in Figure 5.24 for data with and without the air injection, and also the difference between them. The time versus pressure measurement data are also provided so that the extraordinary agreement between the measurement and the time response can be demonstrated. The measurements (taken on 0.1 millisecond intervals) indicate a delay time of 0.0021 s where the sharp pulse is evident. Another interesting phenomena is the reflection of the pressure pulse which occurs in all such air-injection tests. This reflection of the pressure wave from the tap back to the transducer occurs at about three times the initial time delay, and was not investigated in detail. There is also a time response for the pressure transducer which, according to the manufacturer's literature, would be much less than 0.0001 s for the test described here. In Figure 5.24, therefore, not only is the excellent agreement in the time response of the tubing demonstrated to be quite close to the theoretical value, but the good reproducibility between measurements is also demonstrated.

Before implementing the technique of data correction, two features of the measurement system were studied; the relative volumes of the pressure tap tube and the transducer, and the effect of the tubing elasticity on the velocity of the pressure wave. The first feature is addressed by Iberall (1950) by a ratio of the instrument (transducer) volume to the tubing volume. The attenuation of the pressure wave caused by a finite volume at the pressure sensing end of the tube is greater than if the volume is negligible. Fortunately, the pressure sensing port on the transducer used in this study was quite small, 0.001 cm³, compared to the volume of the pressure tubing, 0.262 cm³. The ratio of the instrument volume to tubing volume was 0.004 and so the effect of the sensing element volume was neglected, in keeping with Iberall (1950). The second feature studied was the possibility that the velocity of the pressure propagation (speed of sound) through the air in the tube may have been altered by elastic effects of the tubing. For a pressurized tube, for instance, the fluid might be effectively more elastic due to the

tension in the elasticity of the tubing wall (Binder, 1958). From Binder (1958) a correction for this effect may be calculated so that

$$c_{\text{corrected}} = c \sqrt{\frac{1}{1 + \frac{2 R_{\text{tube}} E_{\text{air}}}{t_{\text{tube}} E_{\text{tube}}}}} = c F \quad (5.7)$$

where $c_{\text{corrected}}$ is the speed of sound corrected for the tubing elasticity, c is the uncorrected speed of sound, R_{tube} is the tube internal radius, t_{tube} is the tubing wall thickness, and E_{tube} and E_{air} are the tube and air modulus of elasticity, respectively. Using the tubing dimensions provided by the manufacturer, and a tubing modulus of elasticity measured by the author, the value of F was found to be 0.9986. This correction (although small) was built into the data correction program. The information and calculations performed to reach the conclusions discussed for the two cases given above are provided in Appendix C.

It was decided to correct the "raw" data using the method of Iberall (1950) to compute attenuation and phase lag (time response) of sinusoidally oscillating pressures by applying the correction to the terms of a Fourier series for the uncorrected data. According to Iberall (1950), if sinusoidal pressure variations are experienced at the beginning of a tube as given by

$$P_o = P_m + \Delta P \cos \omega t \quad (5.8)$$

where ΔP is the amplitude of the oscillations about the pressure mean P_m , P_o is the pressure at the beginning of the tube, ω is the frequency of the oscillations, and t is time. The trigonometric function in Equation (5.8) may be either cosine (as shown) or sine. Based on a parameter z which determines the degree of damping of the pressure signal in the tube, a given correction regime is chosen. For values of z approximately six or greater (such as is the case with this regime) the equations used by Iberall (1950) are for the undamped case. The z parameter is defined as

$$z = \frac{D^2 \omega}{4 \nu_o} \quad (5.9)$$

where D is the internal tube diameter, ω is the frequency, and ν_o is the kinematic viscosity of the fluid in the tube. Iberall gives the undamped attenuation of the pressure signal as

$$\left[\frac{P_o}{P_L} \right]^2 = \frac{1}{2} + \frac{1}{2} \cos \frac{2\omega L}{c} - R \frac{\omega L}{c} \sin \frac{2\omega L}{c} + \frac{R^2}{2} \left(\frac{\omega L}{c} \right)^2 \left(1 - \cos \frac{2\omega L}{c} \right) \quad (5.10)$$

where P_L is the amplitude of the pressure at the sensing element end ($x = L$) of the tube, P_o is the amplitude of the pressure at the beginning of the tube, L is the tube length, c is the speed of pressure propagation, ω is the frequency, and R is a sensing element volume to tubing volume ratio. The value of R is approximately zero for this case as previously discussed. For the case of $R \approx 0$, Equation (5.10) becomes

$$\left| \frac{P_L}{P_o} \right| = \frac{1}{\cos \frac{\omega L}{c}} \quad (5.11)$$

If the pressure amplitude at the sensing element P_L is known, but the amplitude at the beginning of the tube is not, then the pressure amplitude at the beginning of the tube can be calculated from

$$P_o = \sqrt{P_L^2 \cos^2 \frac{\omega L}{c}} \quad (5.12)$$

The lagging phase angle δ_o for the undamped case is given by Iberall (1950) to be

$$\tan \delta_o = \gamma \frac{\omega L}{c} \sqrt{\frac{1}{2z}} \frac{\left(1 + R \frac{2 - \gamma}{\gamma} \right) \tan \frac{\omega L}{c} + R \frac{\omega L}{c}}{1 - R \frac{\omega L}{c} \tan \frac{\omega L}{c}} \quad (5.13)$$

which for the case of $R \approx 0$ becomes

$$\tan \delta_o = \gamma \frac{\omega L}{c} \sqrt{\frac{1}{2z}} \tan \frac{\omega L}{c} \quad (5.14)$$

However, the delay time of the measurement system was previously found to be L/c , which means that the lagging phase angle has been found to be

$$\delta_o = \frac{\omega L}{c} \quad (5.15)$$

A comparison between the values of δ_o computed from Equations (5.14) and (5.15)

will be made shortly. In this study, the pressure signal corrected will actually be the pressure difference, aerodynamic loading, as discussed with regard to Figure 5.23.

Before computing the data correction, the data was first treated with a discrete Fourier transform algorithm. The fast Fourier transform (FFT) routine used was developed by Swarztrauber (1975) and is available with the text by Kahaner, Moler and Nash (1989). Subroutines EZFFTF, EXFFTB and EZFFTI were used, and a detailed description of their use is given in Kahaner et al. (1989). However, an idea of their application is provided in the author's data correction program given in Appendix D which includes the calls to these subroutines. The "raw" data from the data acquisition program was provided as input to the program given in Appendix D which was then transformed into a Fourier series of the form

$$P(t) = A_0 + \sum_{n=1}^N \{ A_n \cos \omega_n t + B_n \sin \omega_n t \} \quad (5.16)$$

After establishing the values of A_n , B_n and ω_n in the individual terms of the series, each term was corrected for attenuation using Equation (5.12) and lagging phase angle from Equation (5.14). Essentially, then, for a given term the pressure signal at $x = 0$ is determined from that measured at $x = L$ by

$$P_n|_{x=0} = \{ A_n|_{x=L} \cos (\omega_n t + \delta_o) + B_n|_{x=L} \sin (\omega_n t + \delta_o) \} \left| \cos \frac{\omega L}{c} \right| \quad (5.17)$$

The resulting correction changes a small amount depending on whether δ_o is computed using Equation (5.14) or (5.15). The corrected and uncorrected Fourier transform representations of the data, as well as the "raw" data used, are shown in Figure 5.25. The main difference between the results from the Equation (5.14) and (5.15) corrections are shown in Figure 5.25, and are that the Equation (5.15) results appear to capture the delay time (demonstrated in Figure 5.24) slightly better than the (5.14) results. However, the results computed using Iberall (1950) and Equation (5.14) are comparable. It was decided to use Equation (5.14) to compute the phase lag term for the results presented in this project in Chapter 6. Also to be noted in Figure 5.25, there is no perceptible difference between the pressure difference data and its FFT representation. The maximum number of terms possible with the data and subroutines were used in the FFT representation of the data ($N=353$) as computed in all results that follow.

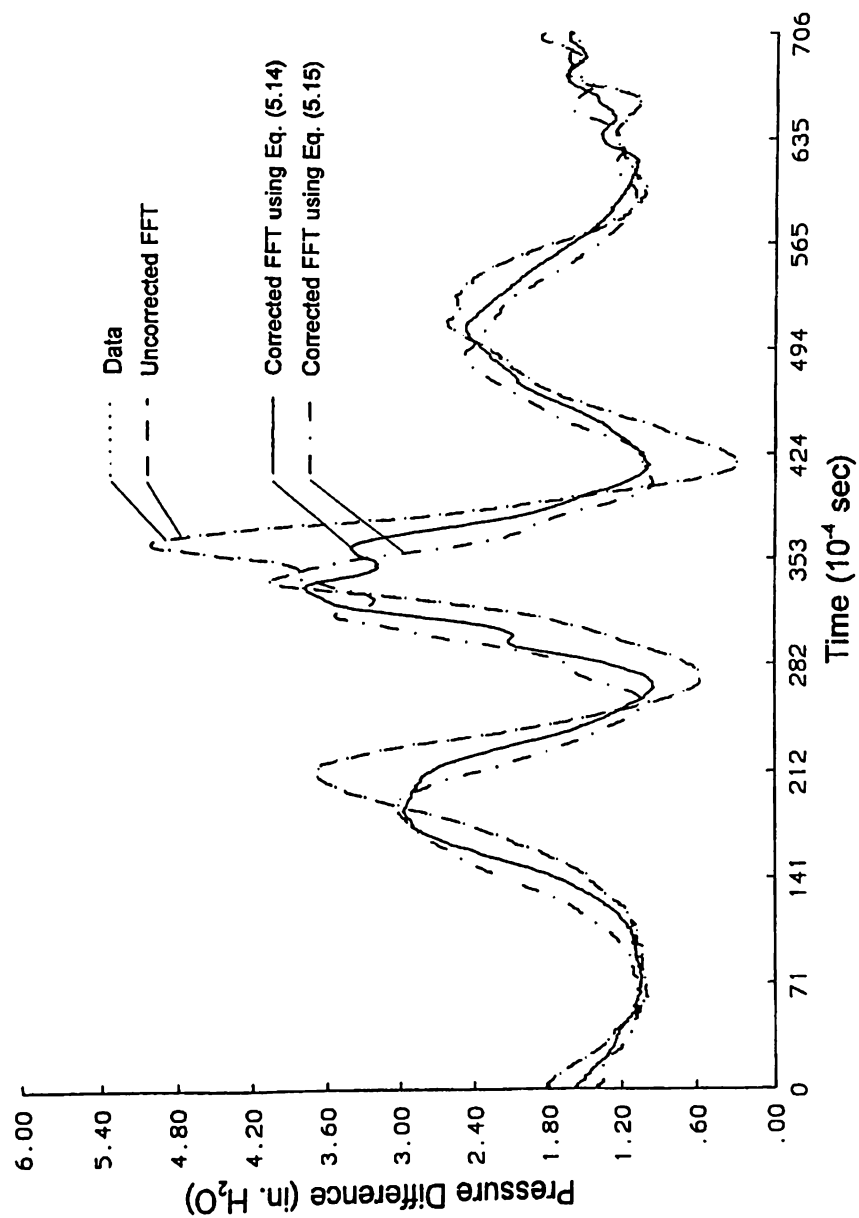


Figure 5.25 Pressure difference data and its FFT representation, and corrected pressure difference data for δ_0 computed using Equations (5.14) and (5.15)

CHAPTER 6

RESULTS

6.1 Introduction

Included in the results of this study the reader will find experimental results for the Lenexa Products 36 in. diameter (LP-36) fan with (also referred to as ducted) and without (also referred to as unducted) a surrounding venturi panel. The experiments performed without the venturi panel were done to determine the fundamental flow field involved for that case. Also, since the PSF-2 computer code includes no duct, it was thought that this unducted state would be the appropriate situation to compare with the PSF-2 program. However, as supported by the measurement results, the flow field is fundamentally different from that assumed in the PSF-2 model. Hot-wire measurements and a variety of flow visualization techniques were used to study the unducted fan. Only by the addition of a venturi panel to the computational model used can a computational comparison of unducted and duct fan results be made, and this was done. While these comparisons will be made, no performance testing of an unducted fan was made for comparison, owing in part to the testing difficulties involved.

Testing facilities were available to test the ducted fan as discussed in the previous chapter and these tests will be compared with the modified and unmodified versions of the PSF-2 computer program. A number of features of the ducted LP-36 fan were investigated experimentally. Flow visualization and hot-wire measurements of the LP-36 fan in the form in which it is normally received from the manufacturer were made. In this situation the fan operated at the so-called free-air state where it is assumed that no static pressure is developed. These investigations (which are given here) include a description of the inlet flow field by hot-wire measurement and streakline photography. A detailed recording of surface flow characteristics of the fan at various azimuthal positions by surface flow visualization (for reference see Figure 5.4) at free air is given. Surface flow visualization results for the fan at various operating points during testing in the manufacturer's fan testing facility are also presented. These surface flow patterns will be compared with others derived from postprocessing results obtained with the VLM. Additional flow visualization results for the fan wake at the free-air state are also given, and comparisons between these results and the computer model will be made. Performance test results of the LP-36 and the Acme (shown in Figure 5.2) fans as performed in the manufacturer's testing facility are given with comparison with results obtained with the VLM. The performance test results are used as a guide in exploring the effect of various input parameters in the PSF-2 program, and a trend study of the effects of the input parameters on performance output for the VLM is given.

Surface pressure measurements have been converted to pressure differences across the blade and will be presented for three spanwise (constant radius) locations. The unsteady (though cyclic) corrected and uncorrected (as discussed in Chapter 5) measurements will be presented, and are then averaged to produce a mean cyclic loading. Comparisons of the pressure difference measurements will be made with the resulting pressure difference produced by the VLM. The VLM pressure differences presented are the results of post-processing the results of the VLM computations by two techniques; first, use of the field point velocities and the Bernoulli equation and, second, vortex lattice force per panel divided by a given panel area. Finally, results of the field point velocity program using the PLOT3D program will be given.

6.2 Unducted LP-36 Fan Results

At the outset of this project it was thought that a study of the LP-36 fan in an unducted form would more closely match the capabilities of the PSF-2 program. However it was discovered that the flow regime of the unducted LP-36 fan was different from the propeller flows modelled by the PSF-2 code. As a result, the planned performance and surface pressure measurement study of the unducted LP-36 fan was not undertaken as it was doubtful that the VLM computations would be accurate. The results of the unducted fan study provide a general description of the flow field in that regime. The results mentioned here include hot-wire measurement and flow visualization of the inlet flow, and flow visualization of the wake and blade surface flow.

Surface flow visualization techniques revealed interesting flow features on the blade suction side. A mixture of 80-weight oil and a combination of fluorescent pigment (Flame Orange pigment #53 from Shannon Luminous Materials Inc.) and tempera paint was used in a surface-oil flow indicator technique. A thick mixture having an approximate 1:1 ratio by volume of dry to wet ingredients was used. The mixture used was arrived at by trial and error, guided by Vaczy et al. (1987). The fan blade was completely painted with this mixture, and the fan was run between 5 and 10 minutes to achieve the flow pattern. The resulting flow pattern was then recorded with a 35 mm camera equipped with a UV filter and using the Hg-vapor arc-lamp for illumination. The unducted fan results given here are with the fan motor operating at 850 rpm on a stand as a free-air circulating fan. The oil-flow test showed a region of separated flow at the leading edge of the blade on the suction (upstream) side from about a 5 in. radius to the tip radius as shown in Figure 6.1. The inset in Figure 6.1 is a negative of the photograph but with the region of separated flow a positive of the photograph to provide emphasis. The oil-flow is primarily in the radial direction under the centrifugal force. However, near the leading edge, in the region shown in Figure 6.1, the flow departs from its purely radial path and bends toward the leading edge. The flow at the blade surface which is altering the oil-flow in this

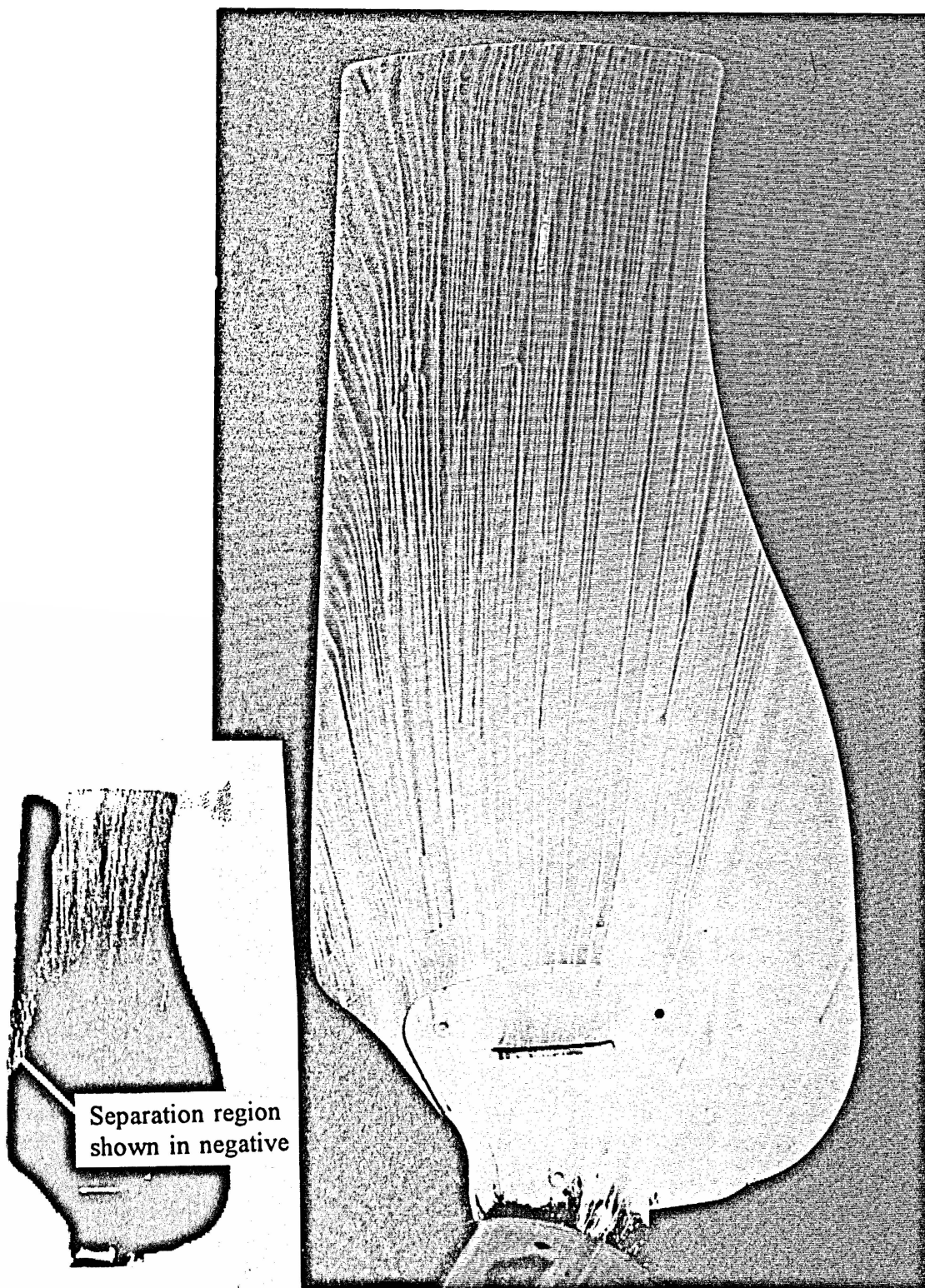


Figure 6.1 Surface-oil flow pattern developed on the suction side of the unducted LP-36 fan operating as a free-air circulating fan at 850 rpm

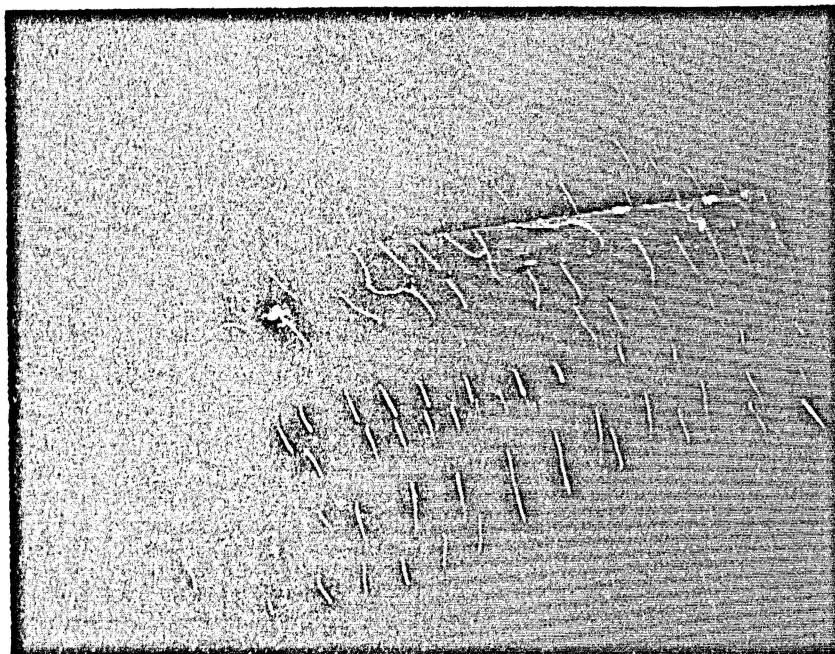


Figure 6.2 Flow visualization of the unducted LP-36 fan using marabou tufts on the suction side of the blade surface

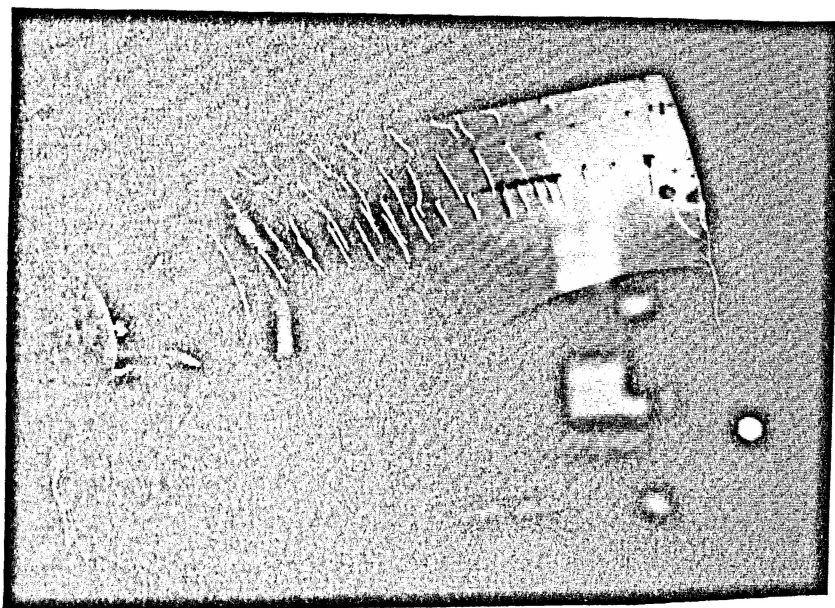


Figure 6.3 Flow visualization of the unducted LP-36 fan using fluorescent minitufts on the suction side of the blade surface

region toward the leading edge is due to the extreme low pressure near the leading edge. Owing to the thin cambered blade used on the LP-36 fan, the flow separates near the leading edge because of the abrupt change in flow direction there. The point of change in the oil-flow direction is also similar to the reattachment line flow structures reported in the literature (see oil-film references in Chapter 2). Elsewhere on the suction side of the blade, no departure from the radial oil-flow occurred. Photos were taken of the pressure side of the blade from similar testing, but are not included here since there was no departure from the radial flow pattern. This is the only application of the oil-flow technique on a rotating fan blade this author has seen. Its success in identifying the flow feature discussed above in spite of the centrifugal forces was confirmed by fluorescent mini-tufts.

The fluorescent minituft and marabou techniques applied to the unducted LP-36 (shown in Figures 6.2 and 6.3, respectively) show that over most of the aft portion of the blade the tufts are aligned along the blade chord constant radial line. Near the tip, however, (on the aft portion of the blade) the tufts are slightly aligned outward in the radial direction. The tufts at the leading edge have an unsteady behavior and have a pronounced radial direction for $R_{\text{blade}} > 8$ in. This indicates (again) the flow separation and possibly a leading edge vortex on the blade with a core of high velocity directing the flow outward in the direction indicated by the tufts.

Surface tufts were placed at the edges of the blade which, when photographed edgewise, provided information on the flow angles at the tip and the trailing edge. At the trailing edge, as shown in Figure 6.4, the outer third of the blade is experiencing a noticeably positive angle of attack. At the blade tip, the flow directions were investigated to provide guidance in selecting an appropriate value for the PSF-2 input variable DISPN, the separation of the tip vortex normal to the blade. The photographs were made before the strobe triggering device described in Chapter 5 was made, and therefore the camera shutter speed and exposure had to be carefully synchronized to catch a single flash of the strobe. The pictures given in this section are taken using a single flash and do not capture the unsteadiness that was observed. Using multiple images, such as those shown in 6.5 (in particular 6.5 b), the value of DISPN for this case (unducted and free-air) is estimated to be 0.21.

Helium bubbles were used to develop a qualitative understanding of the inlet and wake flows for the unducted LP-36 fan. This technique revealed a fundamental feature of the inlet flow into the unducted fan shown in Figure 6.6. When bubbles are introduced in a variety of positions upstream of the fan, well upstream of the motor, no flow was entrained through the rotor for $R_{\text{blade}} > 13$ in. This feature of the inlet flow and features of the wake flow are shown again in Figure 6.7 which also is provided to show features of the wake. The qualitative picture of the wake that developed from these flow visualization studies showed a

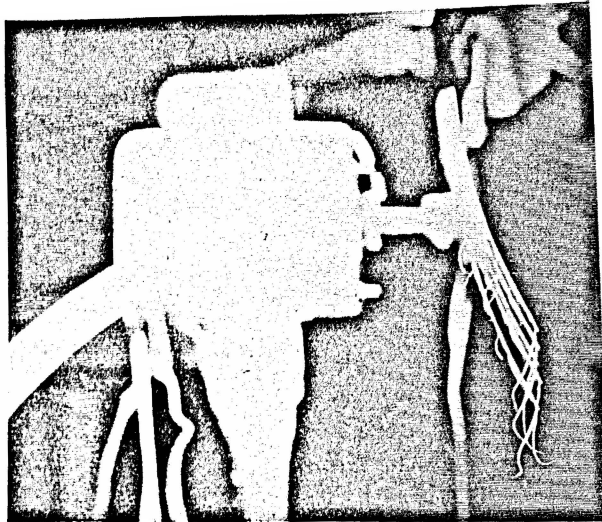


Figure 6.4 Surface tufts at the trailing edge of the unducted LP-36

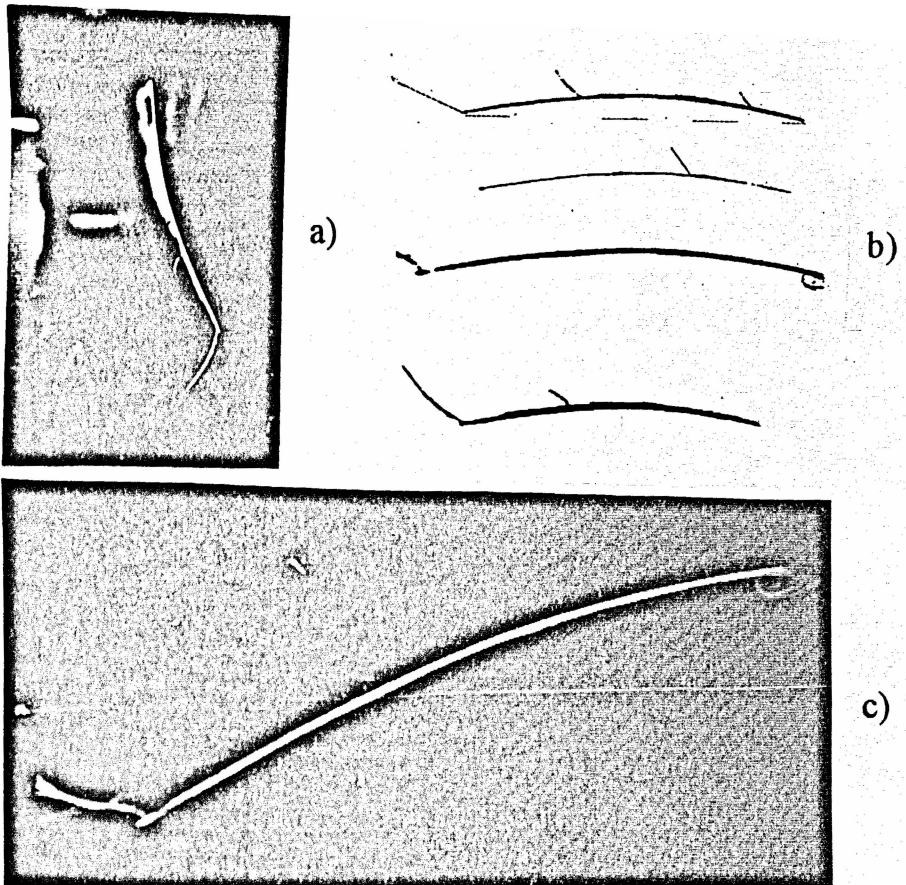


Figure 6.5 Photographs of tufts placed at the edge of the blade tip used to experimentally determine the value of DISPN: a) edge view of tip, b) four scanned images of the blade tip and c) photograph from which one scanned image was taken

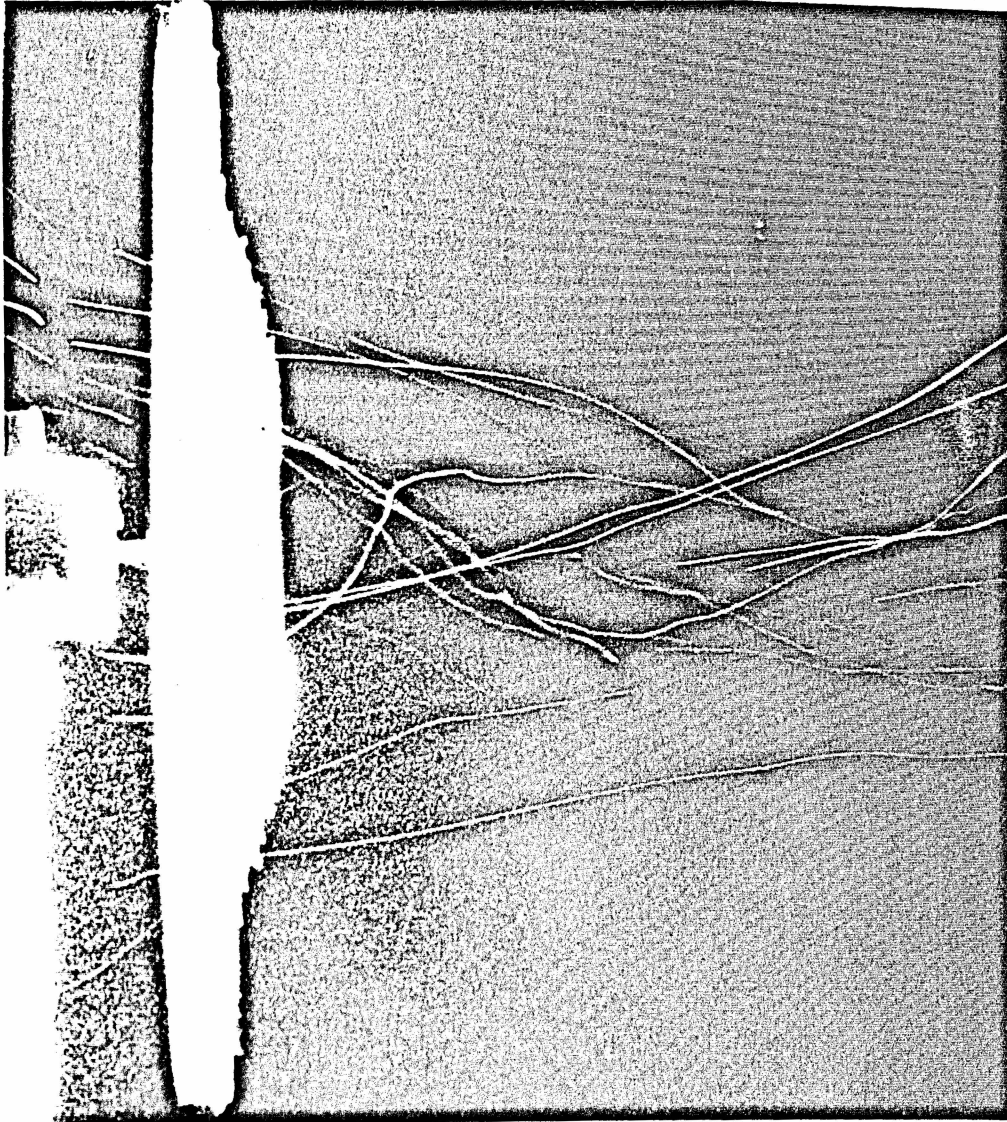


Figure 6.6 Photograph of helium bubbles entrained into the fan inlet from well upstream

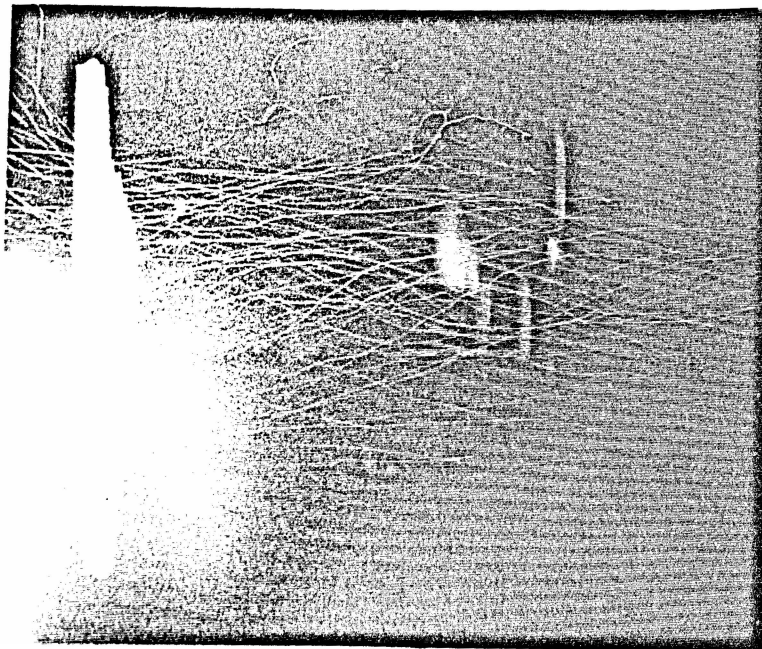


Figure 6.7 A longer exposure of helium bubble streaklines showing more of the wake flow, particularly the recirculation through the tip at top of picture

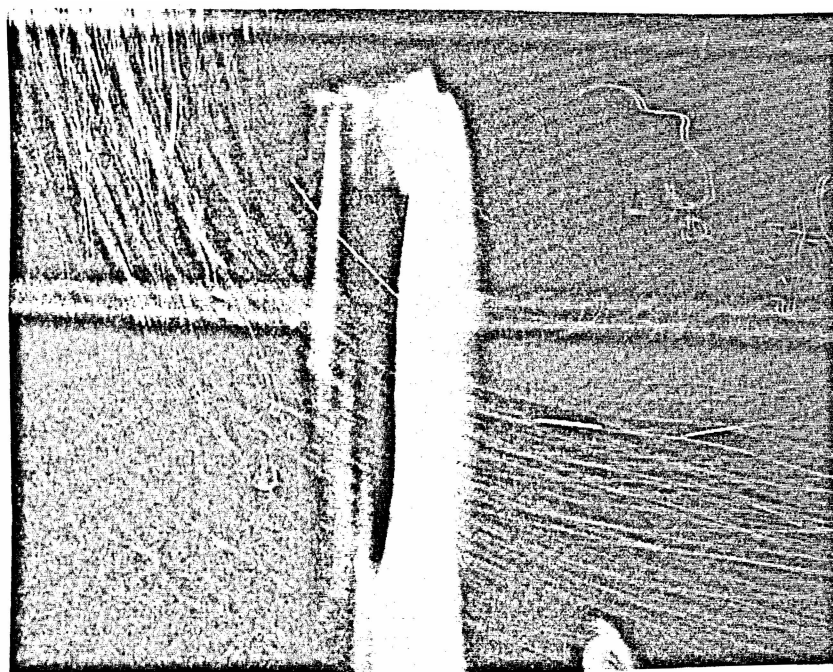


Figure 6.8 Detail of rotor tip flow with helium bubble injected into the rotor tip region from the inlet side showing the recirculation region

tight helical structure in the core and progressively less swirling at larger radii. At the outside of the wake there was entrainment of room air as shown in Figure 6.7. The structure is similar to that sketched by Wallis (1983, p. 412) taken from an unavailable report. The wake appears in Figures 6.6 and 6.7 to contract slightly and then expand as it mixes with the room air at a distance of greater than one diameter downstream. From photographs of the wake flow the initial contraction angle of the wake was found to range between about 7 deg. at the outside boundaries to about 20 deg. for the streaklines inside the wake.

Another important feature of the flow is seen at the tip of the fan in Figure 6.7 where a bubble from downstream is drawn back around to the inlet side. This basic phenomenon is quite different from the wake model used by the PSF-2 program, which was demonstrated for a typical case in Figure 4.33. The wake modeled in PSF-2 is appropriate for the inner wakes as shown in Figure 6.6. For the outer third of the rotor span, however, the flow is quite different as detailed with the close up picture of the rotor tip flow in Figure 6.8 where the flow is (as before) from left to right. The bubbles have been injected directly into the upstream tip region where the recirculation region is made evident. Another photograph is presented in Figure 6.9 with bubble injection downstream in the tip region to show the extent of the entrainment of the flow downstream of the rotor back to the inlet side. This flow state is quite similar to the vortex-ring state which occurs in propellers and helicopter rotors. The fundamental difference between the flow state of the unducted fan and the PSF-2 computer model is over the outer third of the blade.

Hot-wire anemometry measurements were made of the inlet flow velocity profile with the hot-wire placed in a vertical orientation and perpendicular to the axial flow direction. In this way a number of traverses were made, none of which were corrected for direction. Inlet profile data are given in Figure 6.10 for four vertical traverses and a single horizontal traverse taken in this manner. Beyond the scatter in the measurements, which were time averaged over several minutes, there is a marked difference between the velocities measured for the horizontal and vertical traverses. The horizontal traverse measurements showed a higher velocity than the vertical traverse measurements. Because there is a radial velocity component to the inlet flow (see Figures 6.8 and 6.9), the horizontal traverse experiences this additional velocity component while the vertical traverse does not. Hence, the vertical traverse velocity measurement should be a more accurate measurement of the axial velocity. Nonetheless, the horizontal traverse agrees more with the typical inlet velocity profile for unducted free-air circulating fans given in Wallis (1983). The comparison with the typical inlet profile from Wallis (1983) is given in Figures 6.11 and 6.12 for the vertical and horizontal traverses, respectively. These plots provide guidance for the general shapes of inlet profiles that should be used for input to the PSF-2 program.

6.3 Ducted LP-36 Fan Results

Several changes were made to the venturi panel housing of the ducted fan, shown in Figure 5.3, to remove obstacles to flow visualization. On one side, a side of the box around the duct was replaced by a sheet of plexiglass in order to enable visualization of the flow through the fan. Next, a portion of the circular venturi orifice was removed (on the side where the plexiglass wall was placed) and replaced with plexiglass. This section of the duct is shown as the "Window" in Figure 5.4. After these modifications, the inlet flow and blade surface flow could be visualized. As before, the flow in the ducted fan was visualized to provide the PSF-2 input parameters; inlet flow profile information, tip flow directions, and wake parameters. Additional information regarding the unsteady blade surface flow conditions is helpful in interpreting the unsteady pressure measurements. Visualization of the inlet flow is not only of interest in describing the inlet flow for purposes of running the PSF-2 program. It also could provide designers with a fundamental understanding of the inlet flow quality in their machine.

A slide projector was used as a light source in studying the inlet flow. By fashioning a slide with a vertical slot, a 3/8 in. wide vertical sheet of light was produced. The light sheet and flow planes observed are shown in Figure 6.12. The streaklines produced by particles scattering light in the sheet were recorded using a 35 mm camera. In the results given here the SAI helium bubble generator with settling chamber was used to produce the particles. The fan was placed on a laboratory table, and special lighting conditions were found to be necessary for all of the particle streakline pictures given in this study. The windows in the lab were covered with black plastic sheeting and a 8 ft square flat black wall was constructed as a background for the streakline photographs.

The results of the inlet flow visualization by streakline photography are given in Figures 6.13 to 6.20. The photographs are of one upper quadrant of the inlet side of the fan and show at their right edge (viewed after rotating the page so that the direction arrow is at the bottom) the inlet face of the venturi panel (see Figure 6.12). Overall flow direction is from left to right with approximately 10 in. of the flow field in the upstream direction shown in each photograph. Photographs of ten vertical planes of flow were taken, and from those results photographs which show details of interest are given here. These vertically oriented planes were positioned parallel to the plexiglass side wall as shown in Figure 6.12; the positions of the light sheets were at 0 in. (at the wall), 2 in. from the wall (toward the fan center), 2-3/4 in., 6 in., 8 in., 10 in., 12 in., 14-3/4 in., 17-3/4 in. and 20 in. from the side wall (center).

The first plane of streaklines is given in Figure 6.13 at the side wall. It shows a flow with two features. The first is that the flow on the mid-portion of the wall is up the wall (later confirmed by mini-tufts, see Figure 6.21)

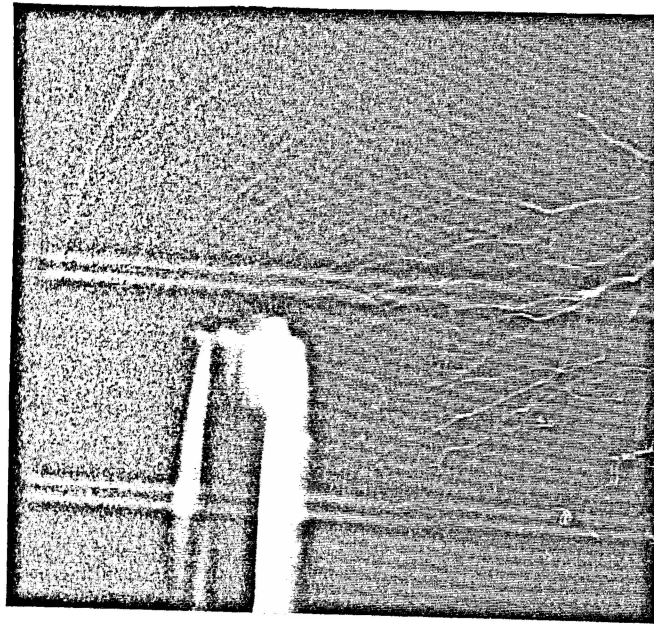


Figure 6.9 Detail of rotor tip flow with helium bubble injected into the rotor tip region from downstream showing the flow around the tip from the downstream side to the inlet side

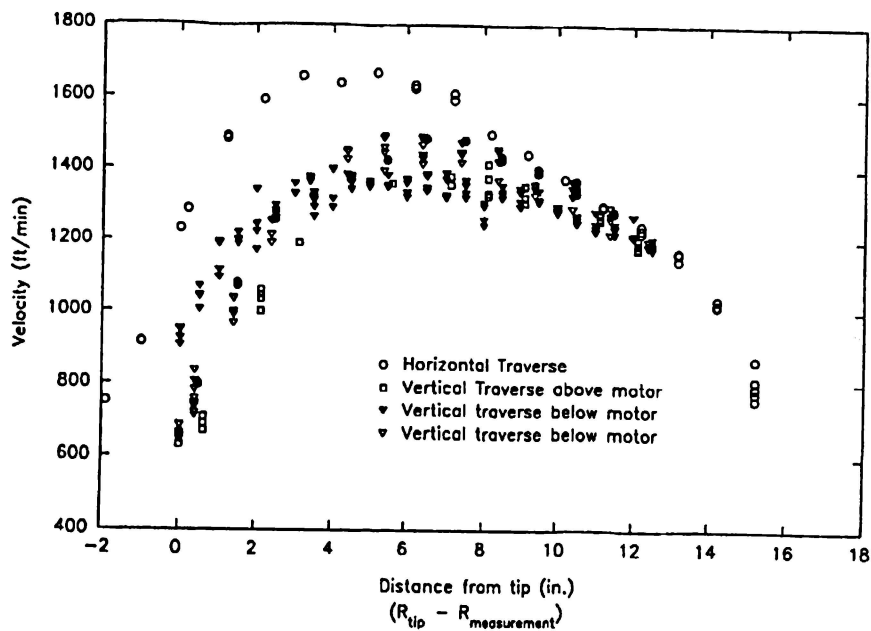


Figure 6.10 Hot-wire measurements of the inlet velocity profile for a number of traverses with wire aligned in the vertical direction

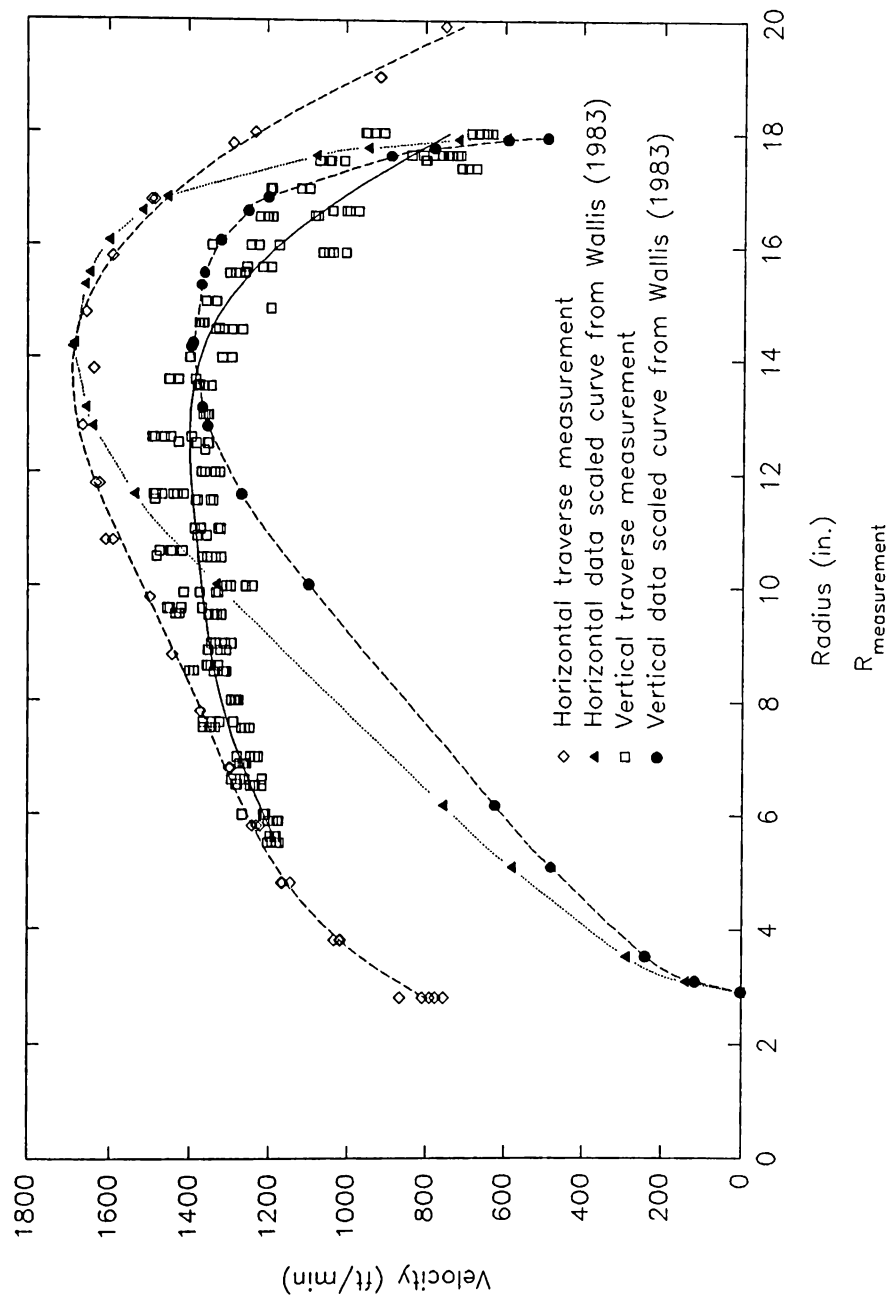


Figure 6.11 Comparison of inlet velocity profiles measured by the vertical traverses and the horizontal traverse using the hot-wire and that taken from Wallis (1983)

perpendicular to the overall flow direction through the fan. The second is that in the top and right corner of Figure 6.13 there is an eddy flow structure. At 2 in. offset from the side wall, shown in Figure 6.14, the flow is remarkable only in that it appears more unstructured. However, a light plane just $3/4$ in. closer to the fan center, shown in Figure 6.15, shows a more structured appearance with a strong eddy shown at the right (as viewed with the direction arrow at the bottom) photograph and streaklines in the left photo showing an upward trajectory entering the photo and bending in the axial direction as the particles are drawn into the fan. In Figure 6.16, at 6 in. from the wall, the particles are seen to be drawn into the fan and take on a mostly axial trajectory with more radial components farther from the center. Also, note (compared to later streakline pictures closer to the center) the particles do not remain in the light plane as long as particles closer to the fan center. The flow eddy still appears to exist at the top wall of the inlet, as shown in Figure 6.17, but is smaller with greater activity. At 10 in. offset from the wall the flow behavior is similar to that at 6 in. but with the particles remaining in the light plane longer than at 6 in. offset. From 10 to $17\text{-}3/4$ in. offset the flows are well behaved and approximately the same as seen by comparing Figure 6.18 and 6.19. Flow enters in the inlet at the top wall, as shown in the left photo of Figure 6.19, has a region into which no particles are drawn. This is typical of a recirculation flow structure visualized using particle streaklines. In the right-most streakline photograph in Figure 6.20 at the center of the fan inlet at 20 in. offset from the wall this recirculation region is clearly seen. Also, in the recirculation photo, close to the blade the streaklines appears to bend outward. The left-most photo in Figure 6.20 shows the flow over the motor to be good, mostly in the axial direction. When the light sheets were placed perpendicular to the axial flow direction, the streakline photographs reveal a qualitative feature of the flow which has already been alluded to in the previous discussion. The particles did not travel very long in the light sheet, mostly appearing as specks of light. However, near the outside of the fan there were noticeable streaks. This indicated radial components of velocity at $R > 15$ in. and no swirling in the light planes oriented in this way were noticed. No photographs of these streakline tests are presented here.

Visualization of the ducted fan blade surface offered insight into the unsteady (though cyclic) nature of the flow experienced by the blade through its revolution. Fluorescent mini-tufts and marabou tufts were used with the strobe light and time delay circuit for this portion of the study. Photographs were taken using both tuft techniques on the suction and pressure sides of the blade at azimuthal positions identified by the capital letters A-P in Figure 5.4. These results identify of the unsteady behavior of the flow on the blade experienced at various azimuthal positions and enable comparison of the unsteady pressure measurements. Tufts were placed on the blade in rows at constant radial positions. There was a small difference between the surface flow patterns visualized between marabou and mini-tuft techniques which is not believed to be caused by differing centrifugal and flow forces on the two types of tufts; rather the difference in tuft

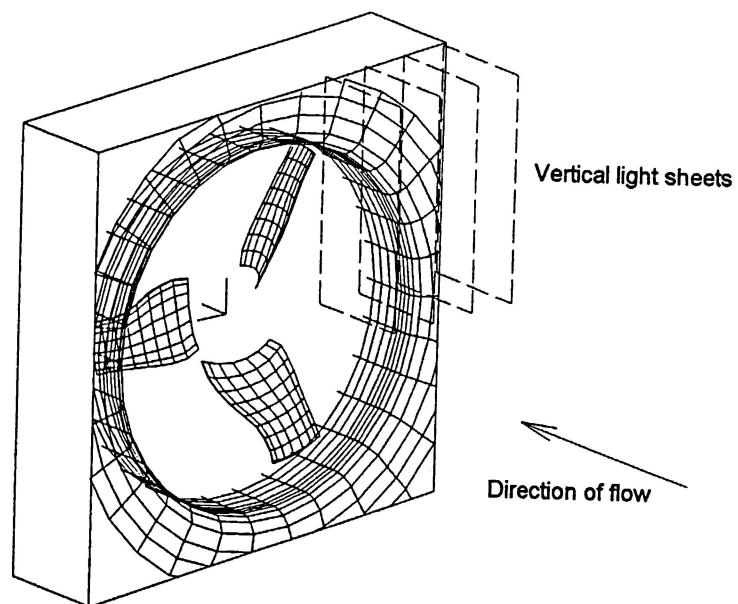


Figure 6.12 Orientation of vertical light sheets for visualizing the fan inlet flow

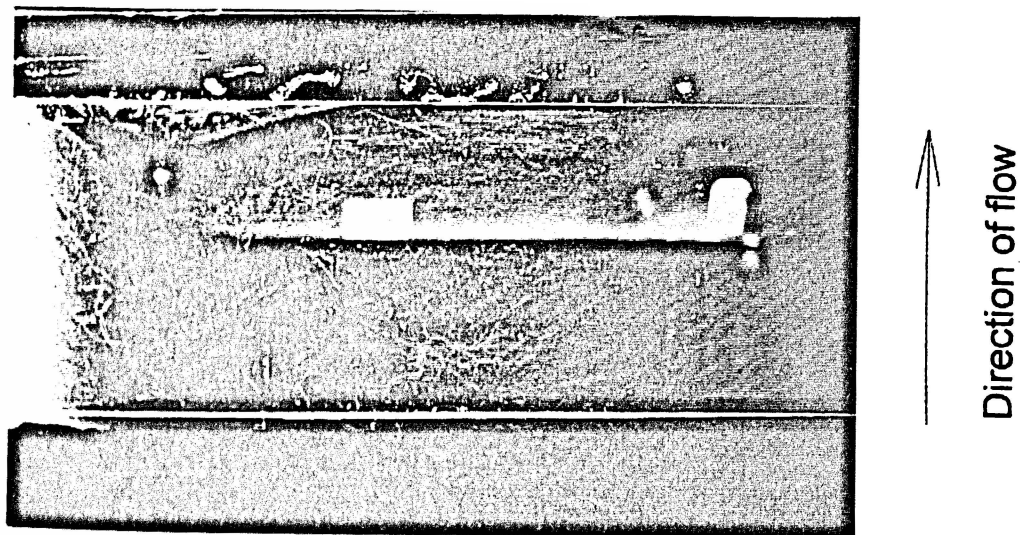


Figure 6.13 Photograph of helium bubble streaklines at the wall in the fan inlet

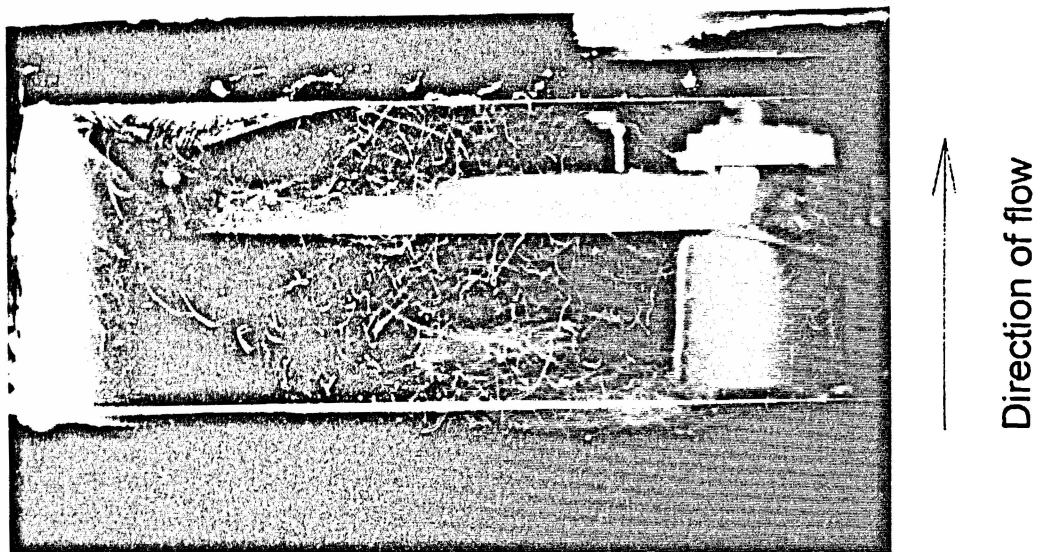


Figure 6.14 Photograph of helium bubble streaklines in the fan inlet 2 in. from wall

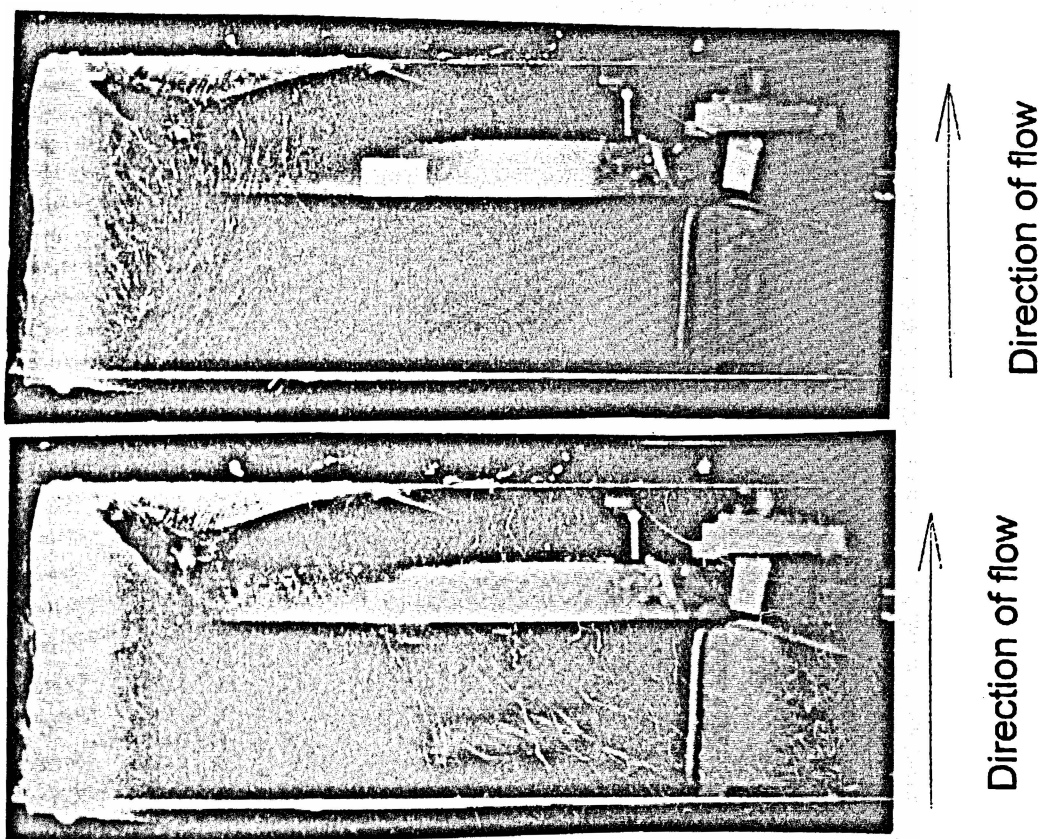


Figure 6.15 Photograph of helium bubble streaklines at 2-3/4 in. from wall in the fan inlet

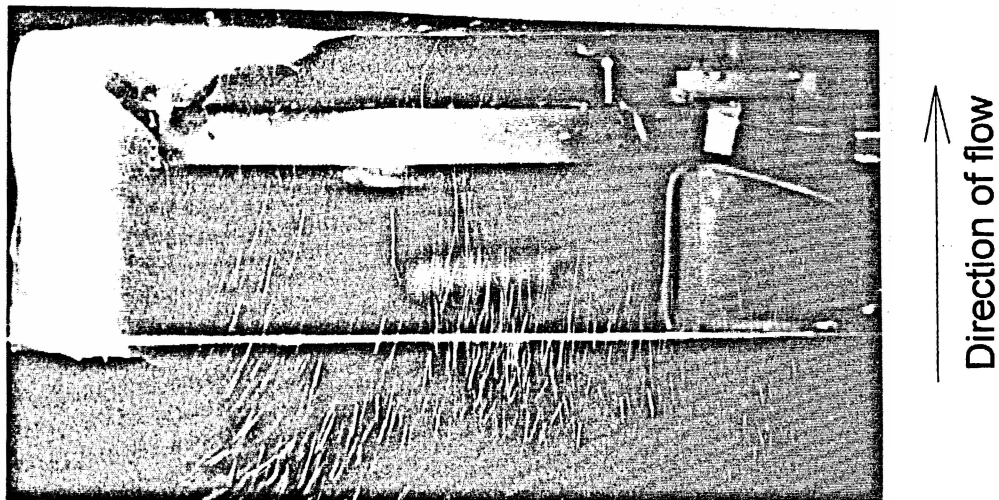
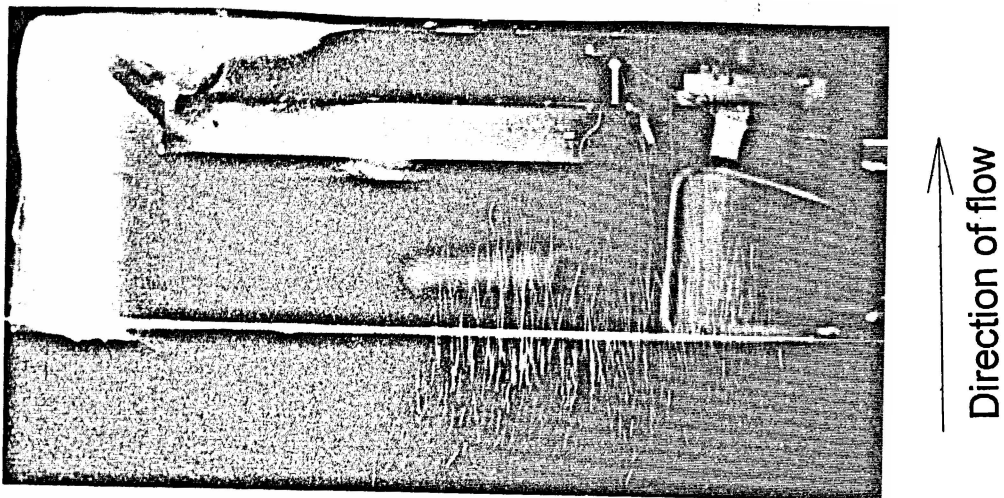


Figure 6.16 Photograph of helium bubble streaklines at 6 in. from wall in the fan inlet

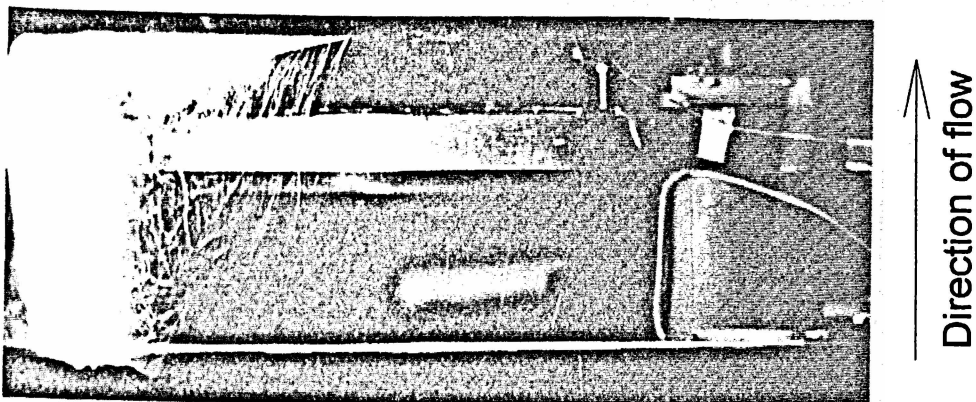


Figure 6.17 Photograph of helium bubble streaklines at 8 in. from wall in the fan inlet

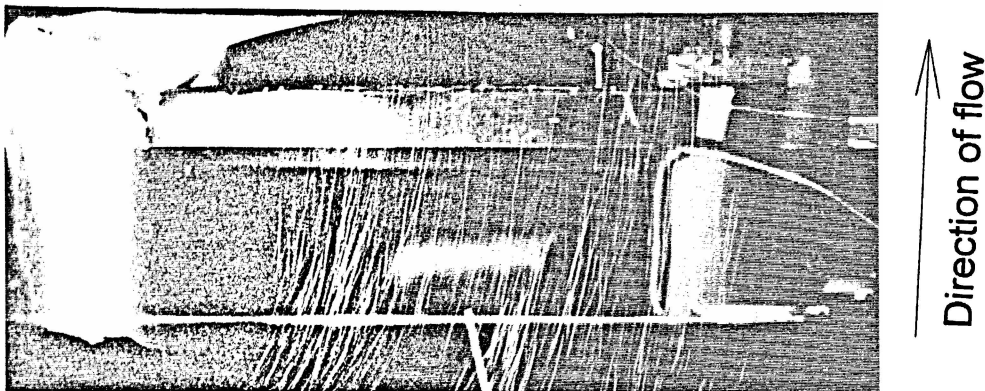


Figure 6.18 Photograph of helium bubble streaklines at 10 in. from wall in the fan inlet

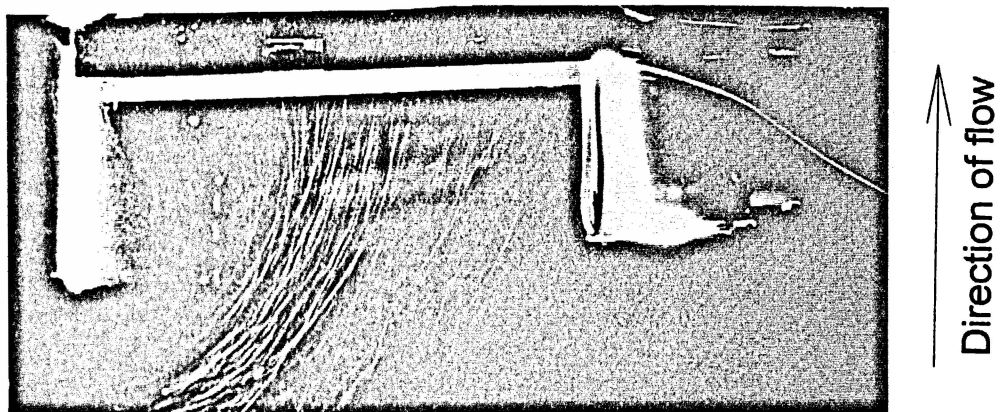
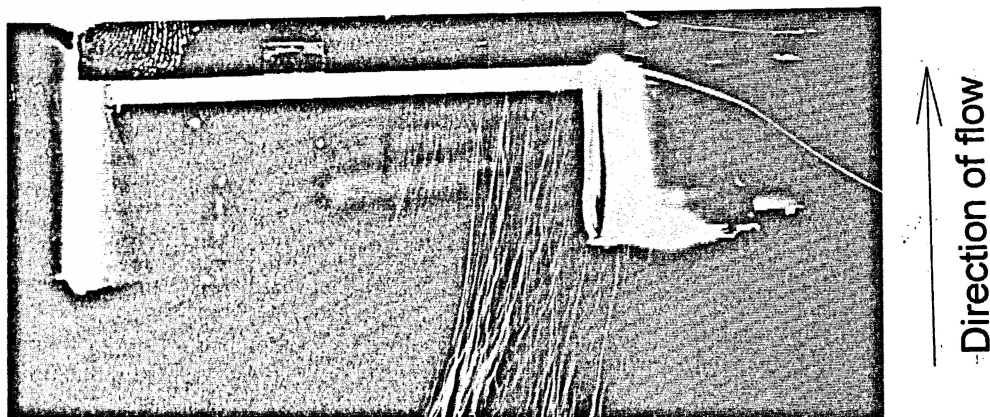


Figure 6.19 Photographs of helium bubble streaklines at 17-3/4 in. from wall in the fan inlet

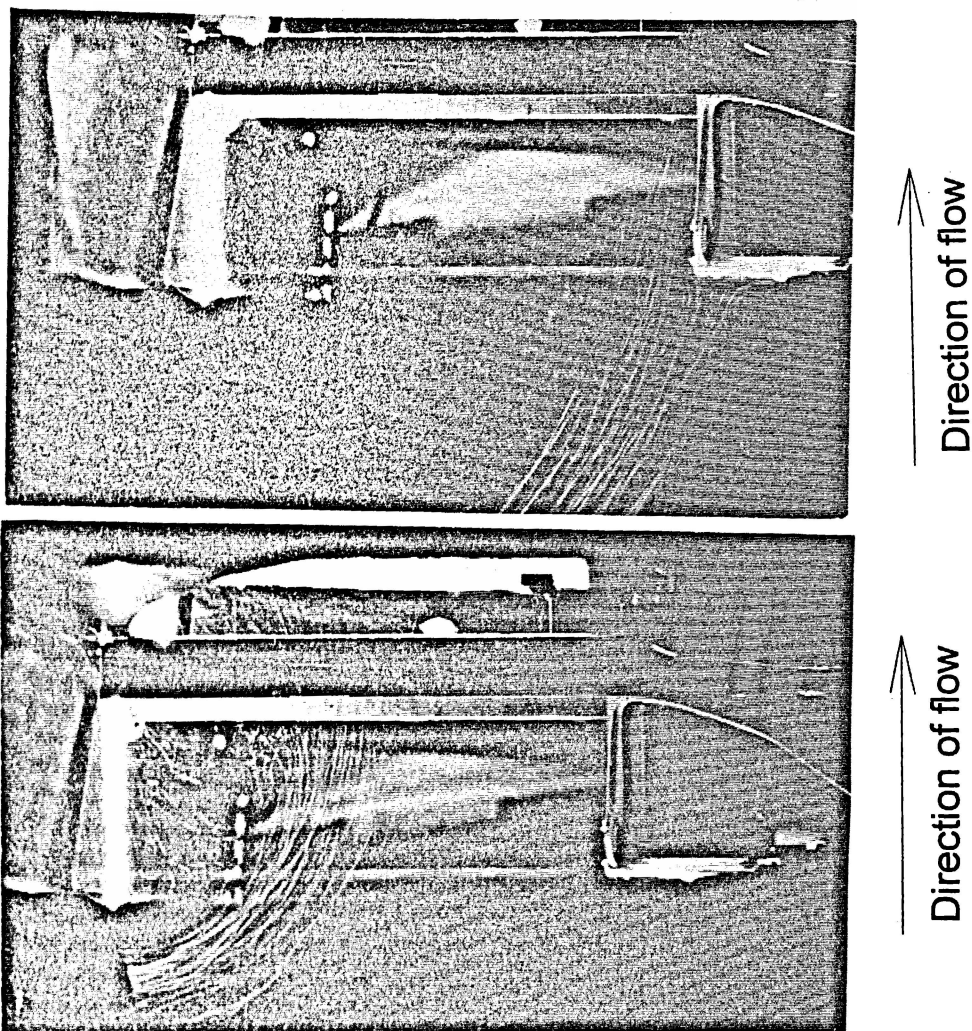


Figure 6.20 Photographs of helium bubble streaklines at 20 in. from wall in the fan inlet

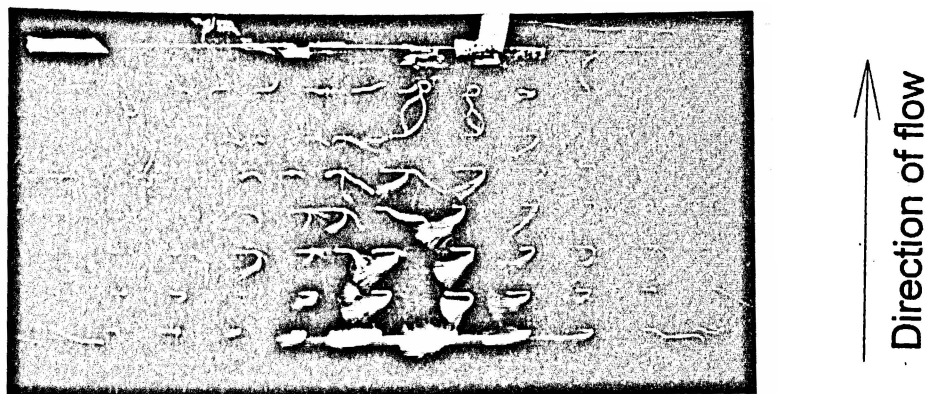


Figure 6.21 Photograph of fluorescent minitufts at the mid-region on the side wall of the inlet

sizes show flows at different displacements from the blade surface. Only, the marabou tuft photographic results are presented here because they photo-copy better than the minituft photographs. A comparison between the two tuft techniques will be presented for the pressure side of the blade. The surface tufts at the tip also provide a means of estimating the PSF-2 program variable DISPN as was done with the unducted fan.

Beginning with Figure 6.22, it is noted that position A, shown in Figure 6.22 a), shows tuft unsteadiness at the leading edge over the outer 3 in. of the blade. Also, the tufts show a slight outward direction to flow over much of the suction (upstream) side. In Figure 6.22 b), the leading-edge tufts in the tip region appear still and well behaved, as do the tufts at position C except those already in the motor support wake. A marked effect of the motor support and side wall inlet flow is seen at position D. The flow pattern at D is similar to that at A; tufts at the leading edge and their immediate downstream neighbors are seen to move violently, some pointing along the leading edge toward the tip. One possibility is that there is no flow force on the tuft at those points and centrifugal force alone causes them to point outward. The other possibility is that there is a flow structure at these points flowing outward to the tip aligning the leading edge, perhaps a weak leading edge vortex. The leading edge flow is seen to be better behaved though there are still oscillating tufts along the leading edge at position E (Figure 6.22 e), and by position F the leading edge flow appears stable and attached once again (just as observed at position B). Figure 6.22 g) is given to demonstrate the flow at the trailing edge, which for this "free-air" case appeared well behaved with no separation or lifting of tufts off the surface near the aft portion of the blade on the suction side.

Figures 6.23 and 6.24 are given to provide greater insight into the flow behavior as the blade passes through region G-I, where the side wall meets the circular duct. Beginning with Figure 6.23 a) the onset of the unsteady leading edge flow behavior was observed; this is slightly past point G, the start of the window. In Figure 6.23 b), it is noted that the disturbance at the leading edge appears to have developed over the outermost 2-3 in., and by Figure 6.23 d) the leading edge flow disturbance is noted over the outermost 5 in. along the leading edge. Shown in Figure 6.24 are a number of photographs of the marabou tufts on the blade surface at the end of the blade's path across the window. These show that the transition between the leading edge flow disturbance and the well behaved (tufts aligned with chord) leading edge flow occurs at the end of the window as shown in Figure 6.24 d). By position I, the flow at the leading edge appears well behaved again such as shown in Figure 6.22 b) and c). This surface flow visualization study assists interpretation of unsteady pressure measurements. For instance, the strongest leading edge flow disturbance was observed at the upper motor supports at positions K and L. In Figure 6.25 this disturbance is seen, all along the leading edge. The flow appears to be better behaved over the aft portion

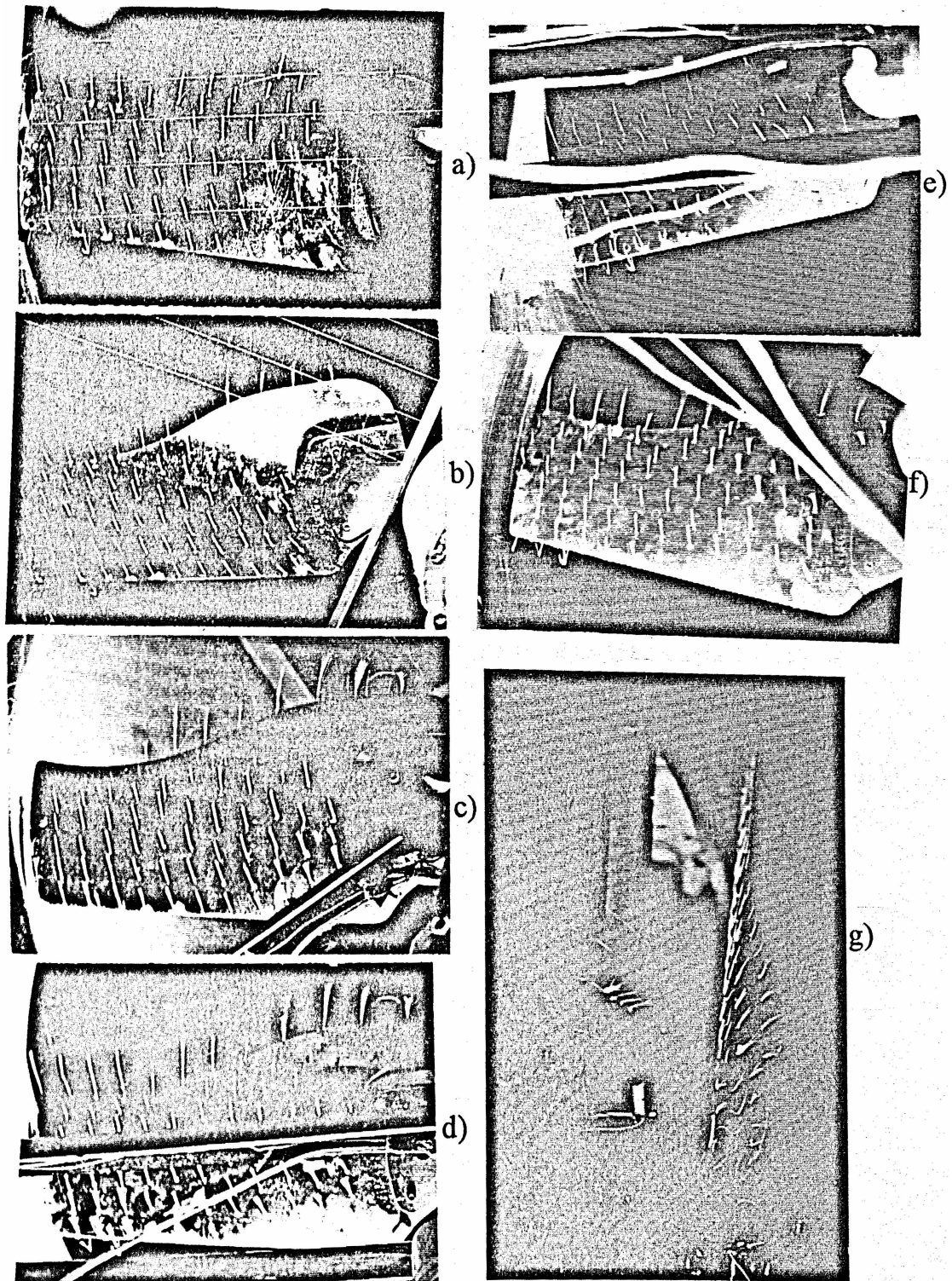


Figure 6.22 Photographs of marabou tufts on the suction side of the blade at positions in Figure 5.4: a) A, b) B, c) C, d) D, e) E, f) F and g) tufts on trailing edge and aft portion of suction side

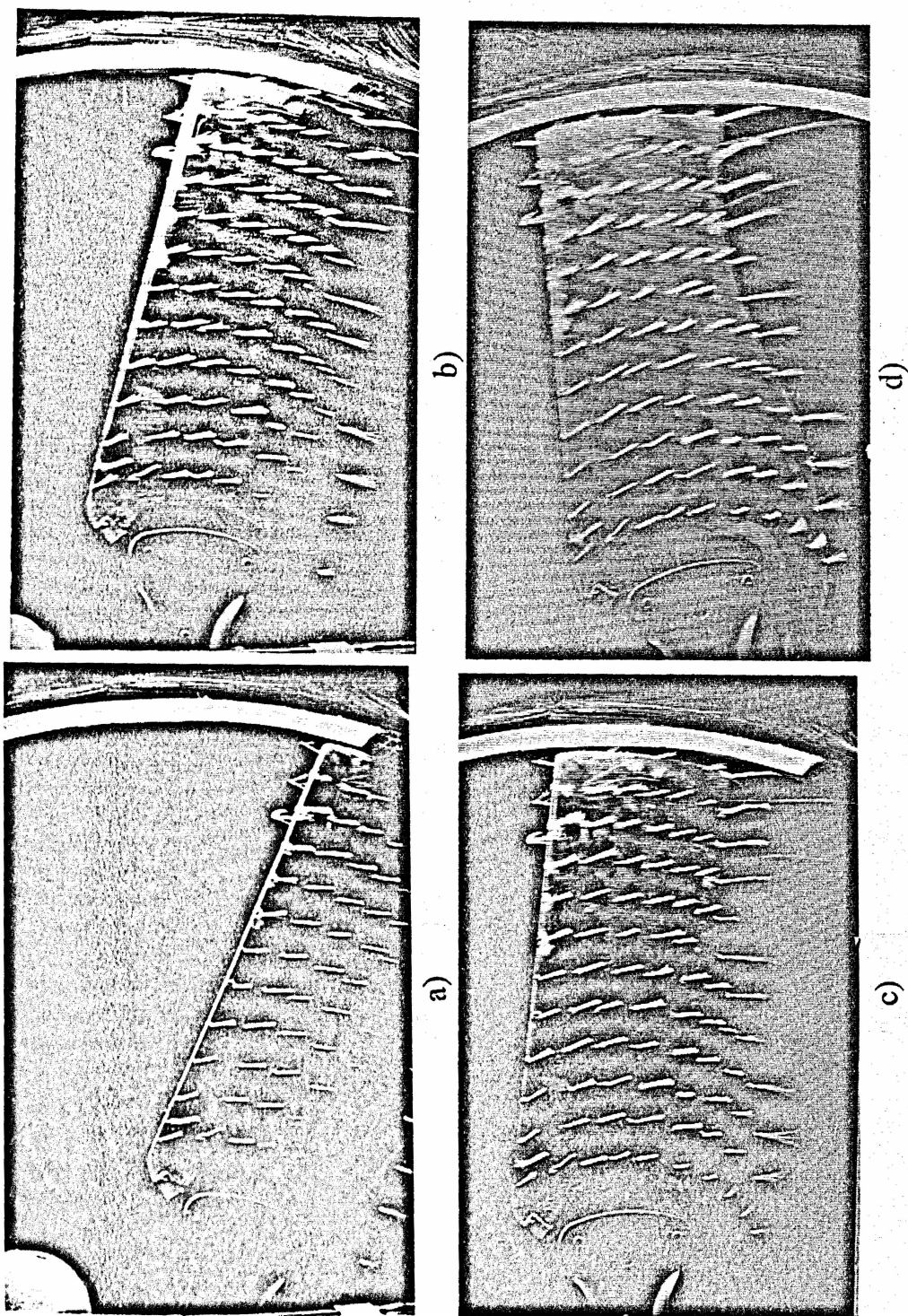


Figure 6.23 Photographs of marabou tufts on the suction side of the blade at positions G-H in Figure 5.4 at the window in the side of the duct

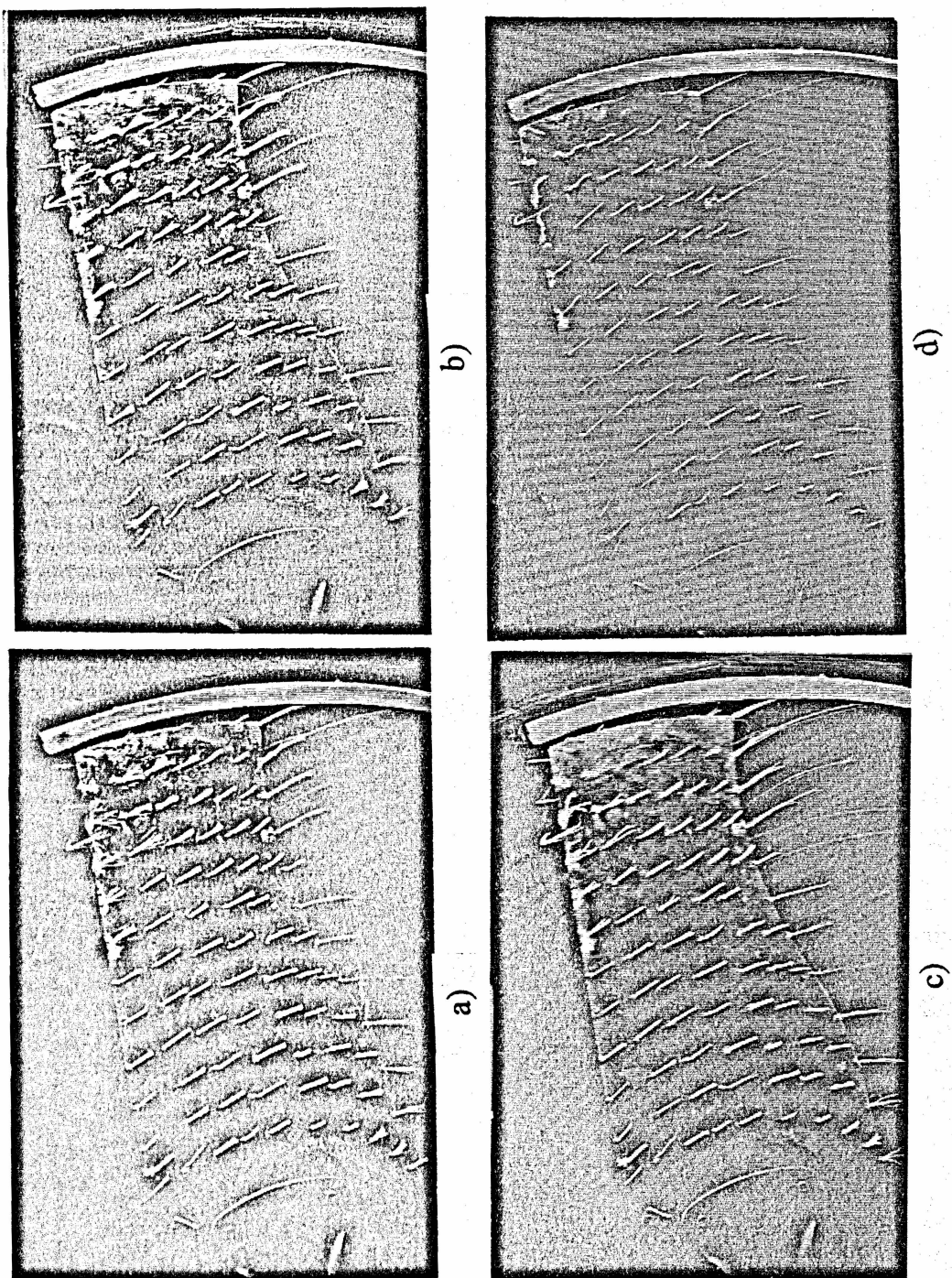


Figure 6.24 Photographs of marabou tufts on the suction side of the blade at positions H-I in Figure 5.4 at the window in the side of the duct

of the blade, but still showing some vortical effects as evidenced by the fuzziness of the tuft image.

Comparison of the fluorescent mini-tufts and the marabou tufts is made in Figure 6.26 on the pressure side of the blade at position A. The marabou tufts (the upper photo in Figure 6.26) lie farther off the surface than the mini-tufts and are heavier. Therefore, it was surprising to see the more outward direction favored by the mini-tufts compared to the marabou tufts (shown in the upper photo in Figure 6.26) for much of the blade. Since the effects of centrifugal forces can be excluded as the cause of this difference, a remaining possibility is that close to the surface there are layers of flow mixing at the thickness of the marabou tufts thickness that cause them to oscillate slightly. A comparison of the two tuft techniques is also presented in Figure 6.27 where the mini-tufts again show an outward direction. Also, note the features that are shown in all the pressure side photos given in this section; the wrapping of the tip chord line tuft to the suction side indicating the tip gap flow (not surprising) and the separated flow at the leading edge at $R_{\text{blade}} < 9$ in. This separation indicates that the blade there experiences a negative angle of attack capable of separating the flow at the leading edge at this free-air condition. A frequently seen feature of the surface flow on the pressure (downstream) side the rotor is an outward flow seen by the mini-tufts and leading edge flow separation seen by both mara- and mini-tufts over $R_{\text{blade}} < 9$ in. Effects of flow conditions at different azimuthal positions are not as pronounced on the pressure side as they are on the suction side. This is also indicated by the unsteady pressure measurements (see Figure 5.22). However, as is also indicated by the pressure measurements, there is a slight difference between the leading edge flow conditions when the blade passes behind the motor supports and when it is 90° from them (positions E and H, respectively). Comparison of the flow patterns are in Figure 6.28 at position E and Figure 6.29 at position H; reveals that the patterns do not vary greatly except at the leading edge just outside of the innermost chordwise row of pressure taps, by the ☺ symbol. This effect was also picked up by the pressure measurements on the blade surface.

As discussed earlier regarding Figure 6.5, the tufts placed at the blade tip in the ducted fan application were visualized through the window and photograph in order to estimate the value of DISPN, the PSF-2 input variable setting the tip vortex separation normal to the blade trailing edge. The value of DISPN estimated in this way for the ducted fan at free-air was found to be 0.08. The tufts at the tip are seen to angle outward in all of the surface flow visualization photos shown here, and in Figure 6.30 the upward angle of the outermost tuft can be seen along with the trailing edge tufts. The trailing edge tufts at free-air showed the flow leaving the trailing edge smoothly with the tufts remaining quite still under the strobe light.

The qualitative characteristics of the ducted fan wake were visualized to

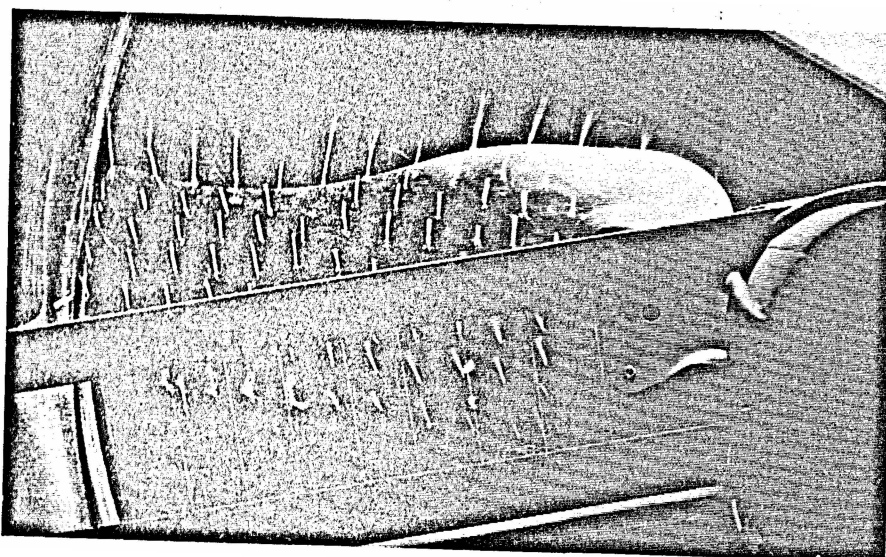


Figure 6.25 Blade surface flow pattern on suction side at position K

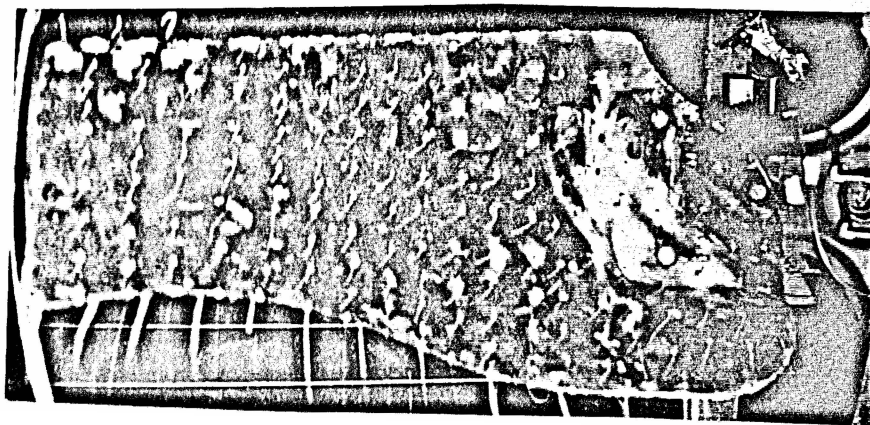
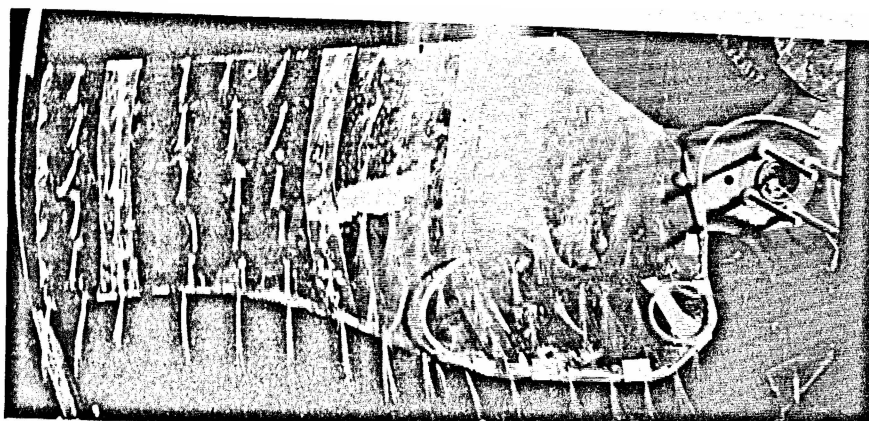


Figure 6.26 Comparison of marabou tufts (upper) and mini-tufts (lower) on the pressure side of the blade at position A

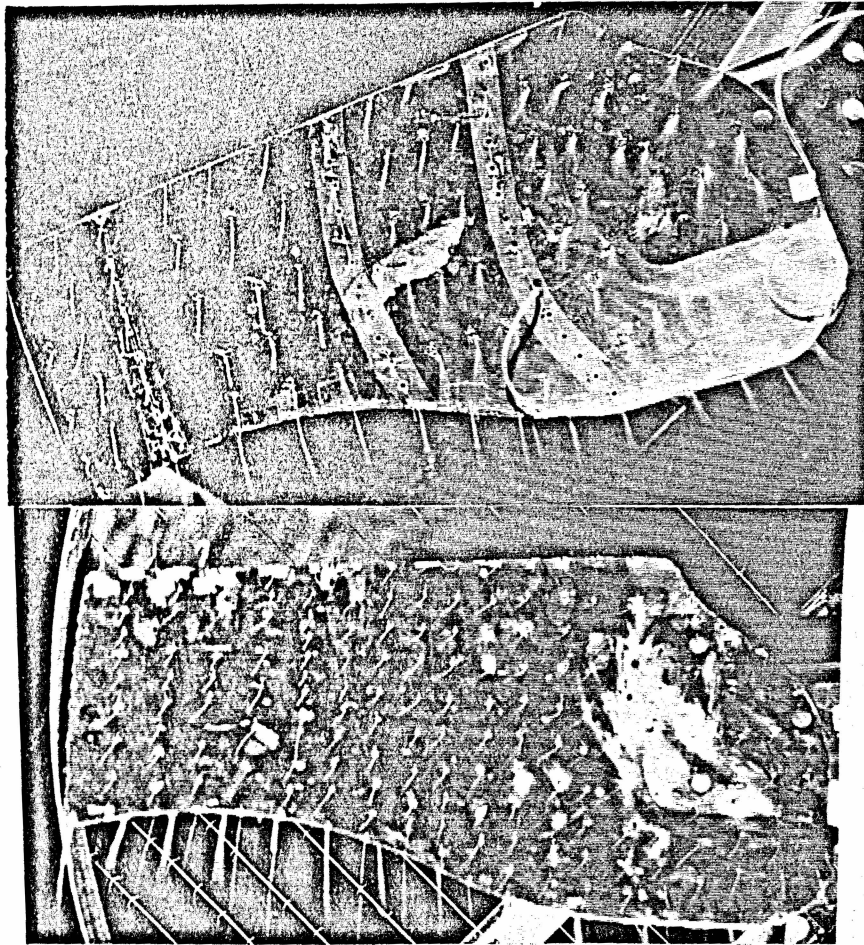


Figure 6.27 Blade surface flow patterns for marabou tufts (upper) and mini-tufts (lower) on pressure side at position F

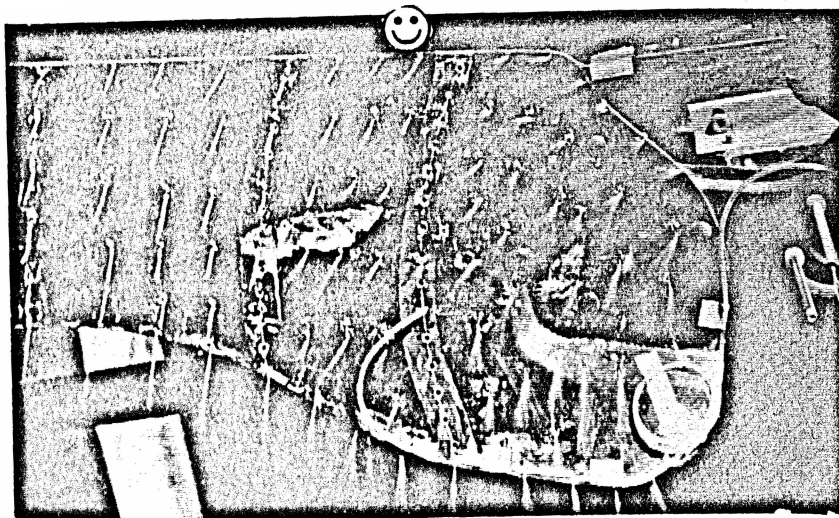


Figure 6.28 Marabou tufts on the pressure side of the blade at position E

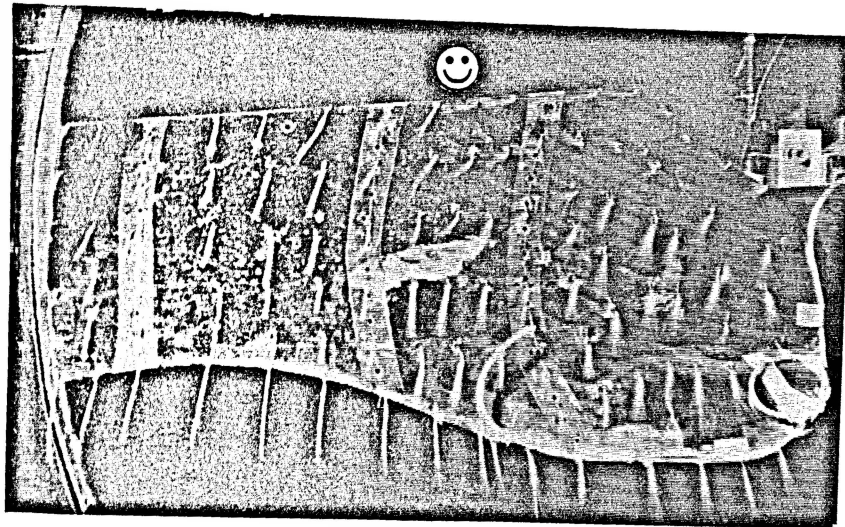


Figure 6.29 Marabou tufts on the pressure side of the blade at position H

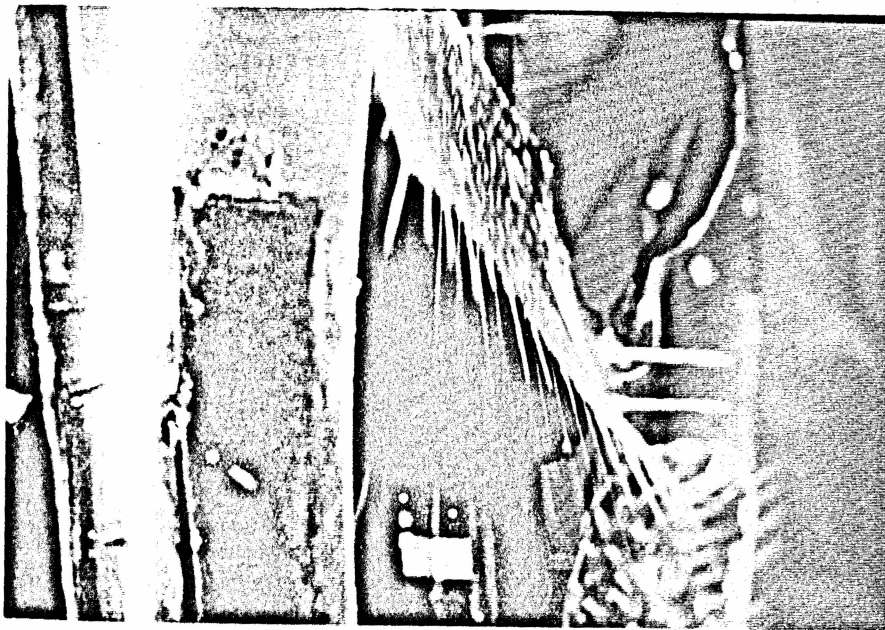


Figure 6.30 Marabou tufts at the fan blade tip viewed from the pressure side of the blade

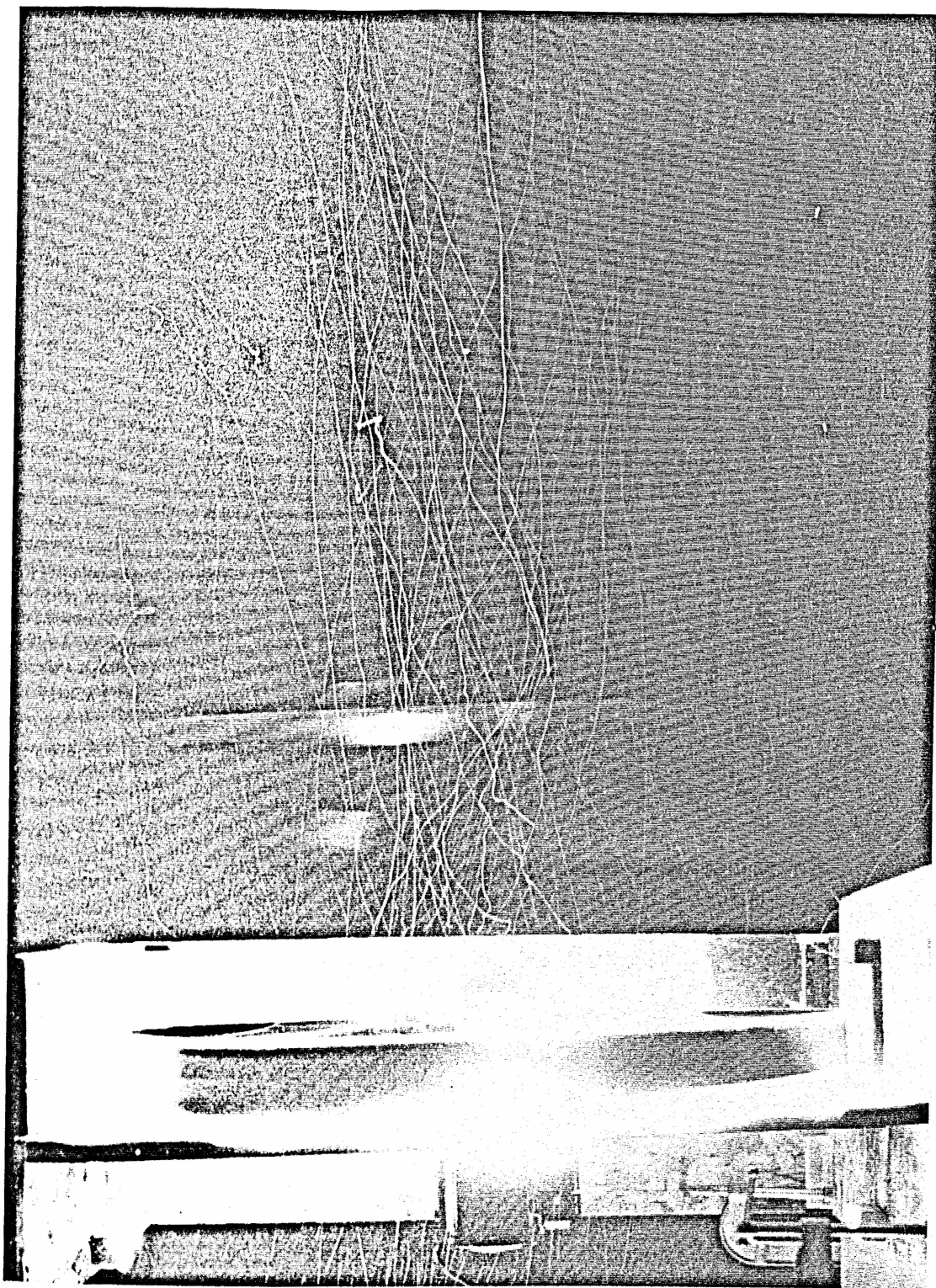


Figure 6.31 Photograph of helium bubble streaklines demonstrating the general wake flow pattern (flow is from left to right)

check that the physical wake matches that modeled by PSF-2, identify input parameters for the PSF-2 program and increase understanding of flow phenomena pertinent to this flow situation. Helium-bubble streaklines were used to learn more about the wake flow and identify DCD, the PSF-2 input parameter for the tip contraction angle of the wake. A general picture of the wake of the type used to identify the wake contraction angle immediately downstream of the rotor is in Figure 6.31. However, for the purposes of estimating the wake contraction angle, particles were injected at a given radial location immediately up stream of the rotor. Then the wake contraction angle was estimated from the resulting photograph at the radii where the bubbles appeared immediately downstream of the rotor. While this procedure is not illustrated in Figure 6.31, it is verbally provided here to give the reader an idea of the technique. Another reason for including the photo given in Figure 6.31 was to demonstrate how particles were drawn into the flow in a natural way from well upstream, illustrating the manner in which air enters and leaves the ducted fan. The Sage Action arc lamp illuminated the flow from well downstream, and the "chopped" streaklines on the inlet side of the fan are caused by the rotor blades. The results of the wake contraction angle study are given in Figure 6.32 where a general trend of increasing contraction angle with decrease radius in the wake is shown. The results of the wake contraction angle, while not nailing down a precise value, do give this parameter to be in the 0° to 15° range; values of $DCD = 7^\circ$ at $R = 18$ in. are believed to be the best estimation.

The trailing vortex elements in the wake are aligned with the local velocity vectors in a blade fixed frame of reference. They are, therefore, visually different from the wake streaklines visualized from a laboratory frame of reference in this section. In the author's field point velocity post-processing program, the rotation reference frame velocity is subtracted from the velocity at a given point. In this way, the velocity field is that seen by an observer in the laboratory reference frame. Also, streamlines as seen in the rotating frame of reference were visualized by placing streamers on the trailing edge and allowing them to flow behind the rotor, approximating the force-free path followed by the trailing vortex elements in PSF-2. Drag on the streamer causes its path not to be entirely force-free except for the last 10% or so of the streamer length. The streamer photographs presented here were made with the streamers at $R_{blade} = 6, 11$ and 13 in. as shown in Figures 6.33-6.35, respectively. A side and downstream view of each tuft is given in these figures. Notice the distinction between the flow lines produced in the rotating frame of reference (on the fan blade) and the behavior of the streamers in the laboratory reference frame. The pitches of the helices of the trailing edge streamers (as seen from the side) shows a definite trend in its variation with radius of attachment point.

Hot-wire anemometer measurements in the ducted fan inlet were corrected for direction in the manner described in Chapter 5 by changing the orientation of a single-wire probe. The author took measurements by taking radial traverses which

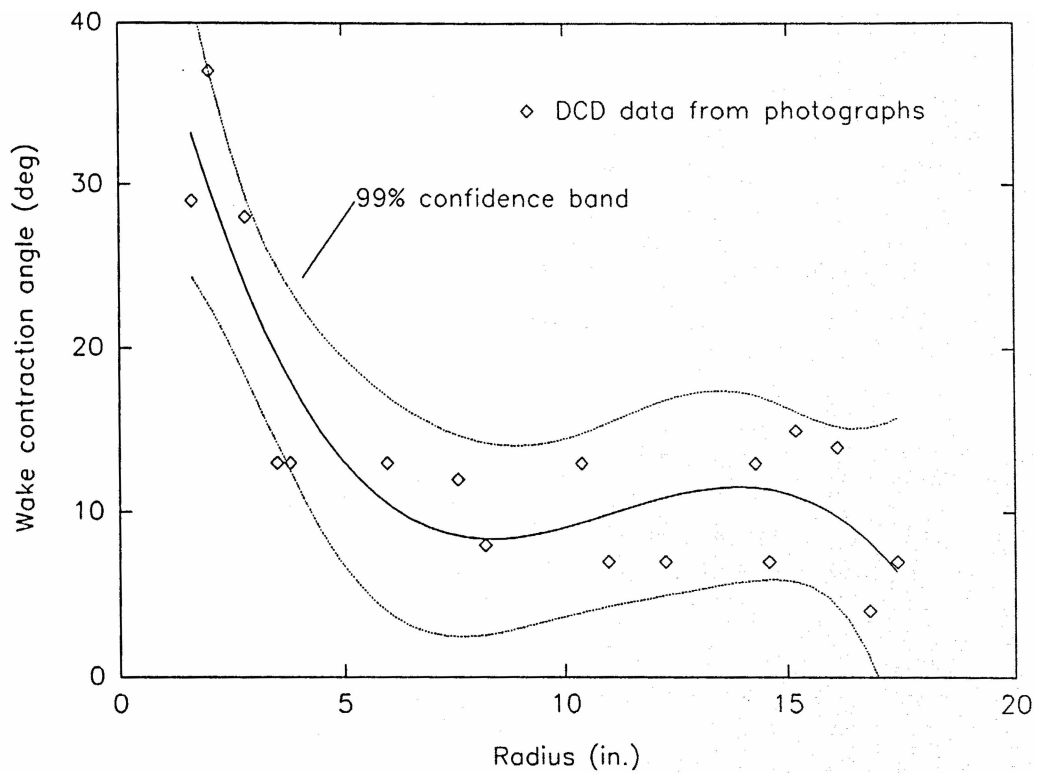


Figure 6.32 Photographic data for wake contraction angle (DCD) versus radius

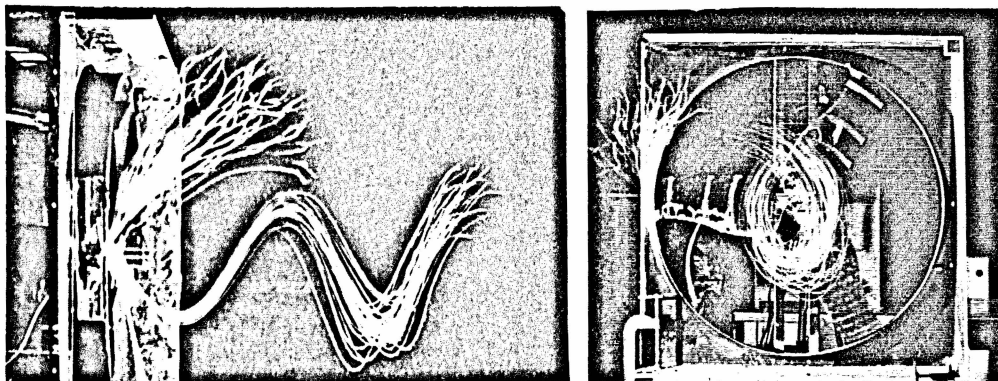


Figure 6.33 Side view (left) and view from downstream (right) of trailing edge streamer at $R = 6$ in. and streamer on duct (blade in horizontal position)

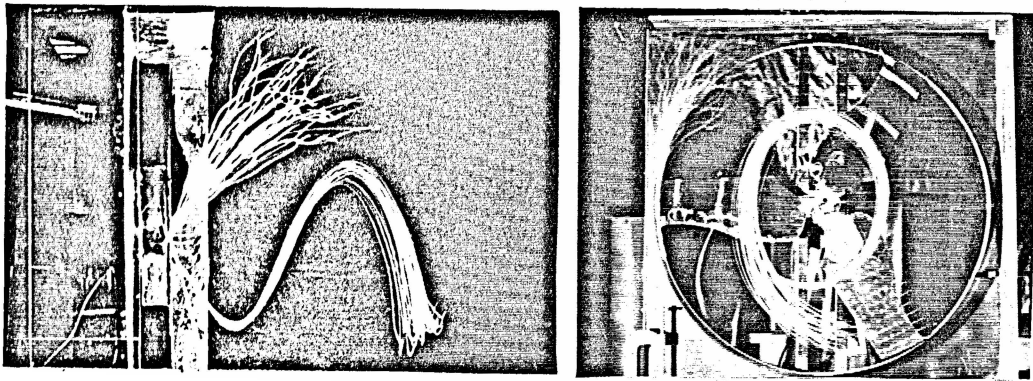


Figure 6.34 Side view (left) and view from downstream (right) of trailing edge streamer at $R = 11$ in. and streamer on duct (blade in horizontal position)

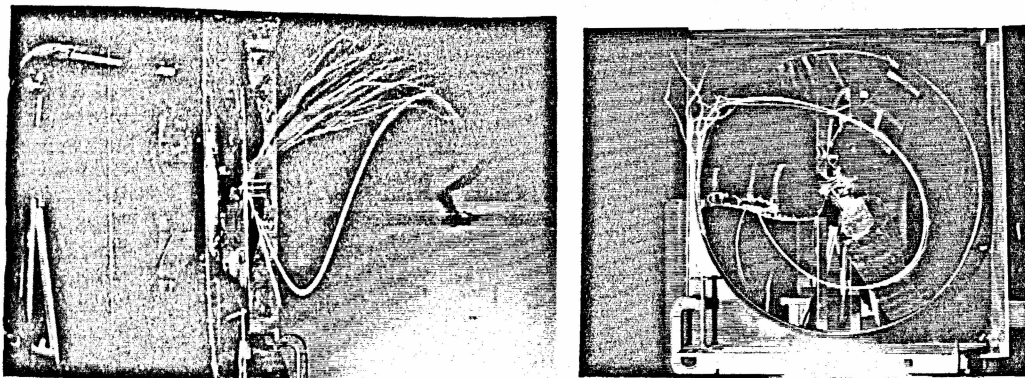


Figure 6.35 Side view (left) and view from downstream (right) of trailing edge streamer at $R = 13$ in. and streamer on duct (blade in horizontal position)

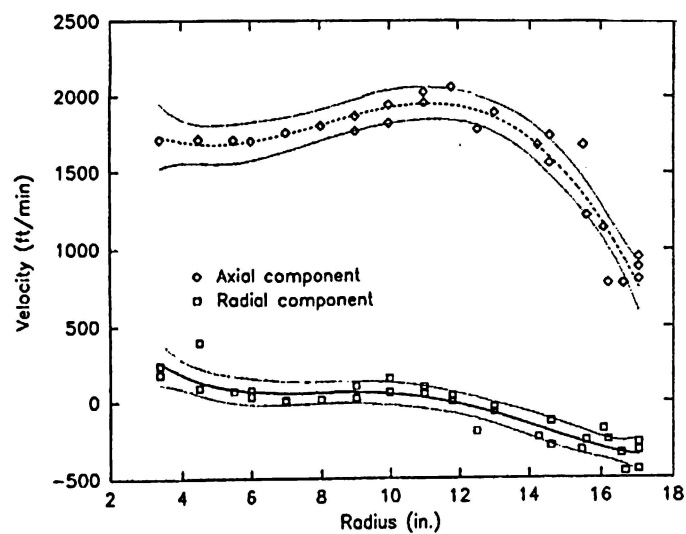


Figure 6.36 Axial and radial inlet velocities measured with the hot-wire anemometry

were limited to azimuthal position A in Figure 5.4. This limitation was due to the traversing equipment available. Measurements could be taken at other positions but, since the equipment was positioned by hand, the scatter and uncertainty in this data was quite considerable. The author's experience with the repeated measurements shows the uncertainty of measurements near the tip to be about 15% with the actual flow fluctuations between 25 and 30% about an average reading. From the flow visualization in the inlet, there are regions of ill-behaved flow (particularly at $R_{\text{blade}} > 15$ in.) which contribute to the data scatter. However, since the inlet flow profile is input for the steady PSF-2 program, the best data for this purpose is the data presented in Figure 6.36. This inlet velocity profile was also present at other azimuthal positions but with more scatter. The data for the axial components was integrated as described in Appendix E, and found to be within 7% of the volumetric flow rate at free-air conditions as tested by the manufacturer. Also, the general appearance of the radial velocity components match the qualitative flow visualization study results in the inlet.

6.4 Comparison of Performance Measurements and Computations

Performance measurements were made using the test cell described in Chapter 5 and the accuracy of these measurements is (according to the ASHRAE/AMCA standard) such that a least squares fit to the data does not depart by more than 0.5% from any data point. The test cell has also been certified to agree with the standard AMCA test cell within 2%. Also, a technician running tests at the manufacturer's test cell has said the measurements for a given rotor are reproducible within 3%. Greater reproducibility is observed for closely spaced tests, demonstrating that drift occurs and recalibration is required. In Figure 6.37 are presented results of performance tests for an LP-36 rotor at 600 and 1100 rpm taken approximately two hours apart so that no blade damage occurred in the intervening time, demonstrating that the performance tests for a given rotor are reproducible. Another issue is the variation in performance from one rotor to the next. On this point the test cell operator said that the performance of rotors coming off the assembly line can vary by about 5%. While this is to some extent a quality control issue, it is important to know these variations when comparing the VLM computations with measurements of the fan performance. Surface flow field direction was visualized (see Appendix F) using marabou tufts for the performance tests given in Figures 6.37 and 6.38.

Performance test results are given in Figure 6.38 for the LP-36 fan at 850 rpm. The manufacturer provided two LP-36 fan rotors and both were tested. These rotors (fan blades) will be referred to as Rotor A and Rotor B. Rotor A was instrumented with the pressure tap tubing and unsteady pressures were measured on its surface. As a result, Rotor A was subjected to more wear and tear than Rotor B. However, Rotor B was also used for some tests involving fitting it with leading edge flaps to control flow separation and improve performance. While

these tests are not discussed here, performance results using Rotor B without the flaps (in its unaltered form) are presented here for comparisons between rotors.

Comparisons between Rotor A, Rotor B and the benchmark LP-36 rotor (as certified by AMCA) at their design rotational speed of 850 rpm are given in Figure 6.38. The data presented in Figure 6.38 were chosen to illustrate: the effect of the shipping crate on performance, test reproducibility, the effect of pressure tap tubing on the performance testing and the variability of tests performed on different rotor blades of the same design. In this figure the data legends are in three columns with each column of data from a different test. Results referred to as "with panel" in Figure 6.38 mean they were made without the box or crate surrounding the venturi panel, i.e. panel only, and results identified as "with crate" were tested with the box and venturi panel together. Also, if "tubing" is used in the Rotor A data legend, it means that the test was performed with the pressure tap tubing in place. Overall in Figure 6.38, there is not a great variation in total pressure developed in the six tests. The most noticeable differences between the tests are seen in the power plot, the results of which are then reflected in the efficiency plot. The AMCA fan and Rotor B data agree well because both tests were made without the crate installed; the shipping crate affects test results. This comparison also shows that a given rotor performance can agree with the certified performance.

All of the Rotor A measurements depart from the AMCA curve. Since Rotor A was used for pressure measurements, it was used more than Rotor B. It is believed that numerous installations and removals of Rotor A during performance, pressure and flow visualization testing caused small changes in the rotor. The changes affected the performance in a gradual way over time. Two sets of data for Rotor A with crate and tubing taken in the same testing session are given in Figure 6.38 and demonstrate good reproducibility. Sets of data (∇ and \diamond) for Rotor A with and without pressure tap tubing (made without the crate and six months apart) show an increase in power; however data sets obtained during the same testing session (∇ and \square) agree, showing that the tubing effect on blade performance is negligible. The AMCA certified data will be used for comparison with the PSF-2 code for the LP-36 fan operating at 850 rpm.

6.4.1 PSF-2 Input Variable Trend Study

Of course, the input parameters (rotational speed, velocity profile and magnitude and blade geometry) of a VLM analysis using PSF-2 have a direct bearing on the output. Also, there are eight input variables, most of which contribute to wake modelling, which affect the output of the VLM analysis. Of these, the six variables (DISPN, DCD, RULT, RHULT, XTW and XULT) which deal with wake calculation were shown in Figure 4.24. The other two input variables are a leading edge suction recovery factor SFC and a blade section drag coefficient CD_{RAG}. There is provision in PSF-2 for these two to vary over the

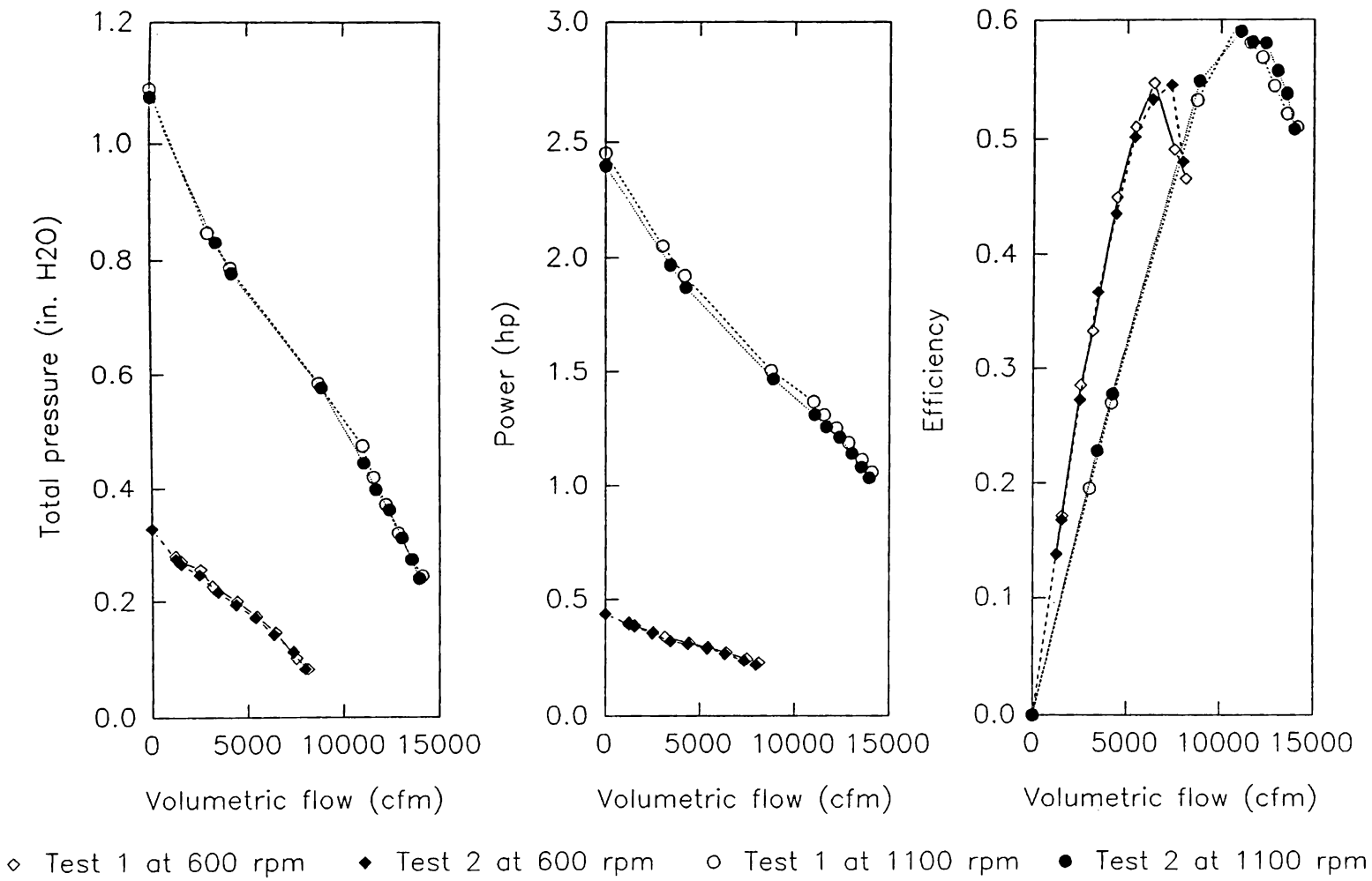
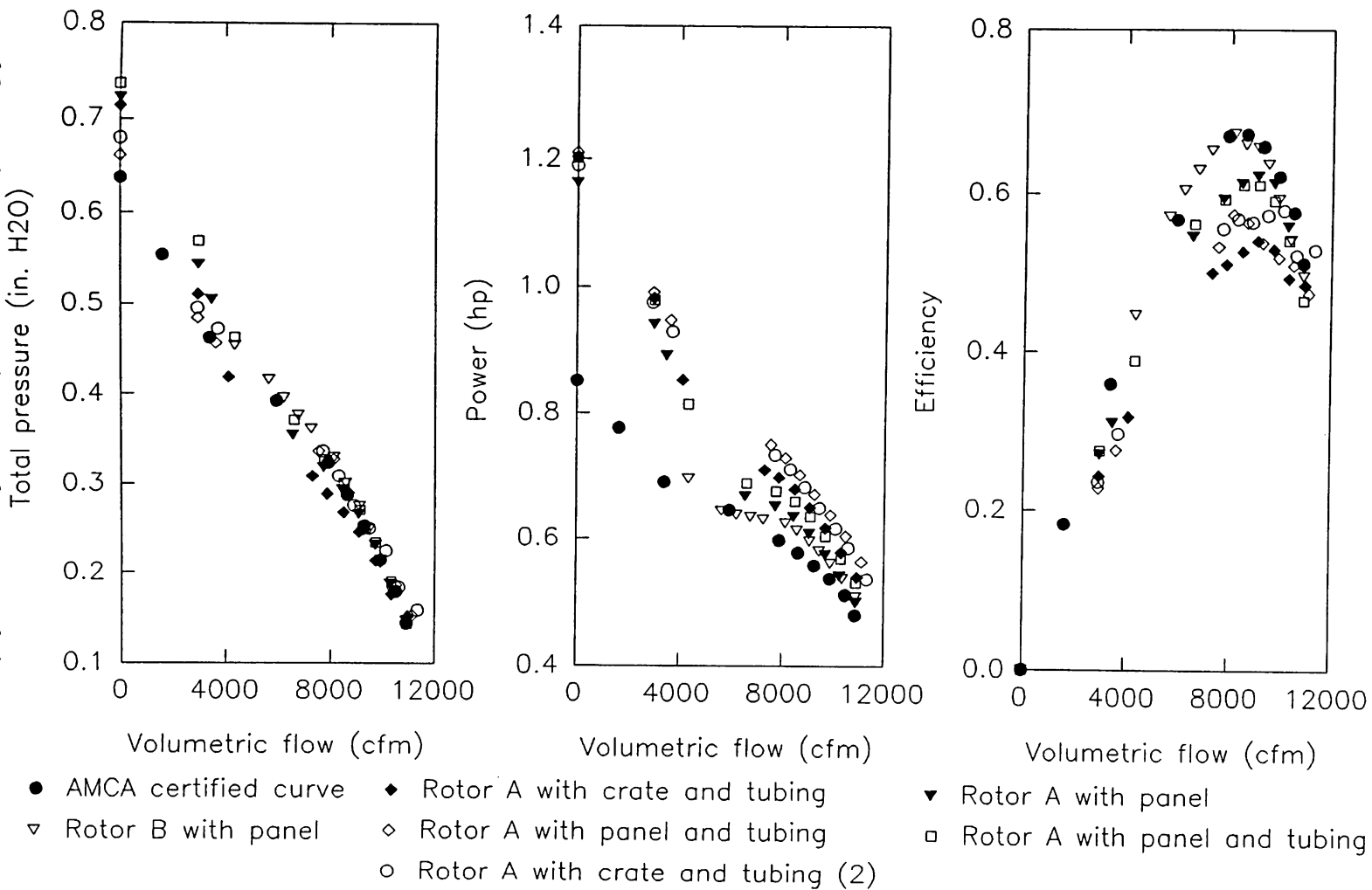


Figure 6.37 Performance tests of the LP-36 fan at 600 and 1100 rpm

Figure 6.38 Performance tests of the LP-36 fan rotors at their 850 rpm design rotational speed



blade span, although that provision was not used in this study.

A trend study of the effect of the input variables on the VLM analysis was conducted to determine how much and in what way they alter the program output (total pressure, power and the efficiency). By knowing the way a variable affects output, it is possible to select the variable value to give better agreement with measurement. In this way, the flow phenomena can be approximated in an empirical way. An operating point for the LP-36 fan was selected where the eight variables could be modified through a range of values that is large enough to show each variable's effects. At some operating points, for instance, the free-wake analysis will only converge for a range of some variables that is too small for their effects to be made apparent. A good point for modification of the variables is in the region of peak efficiency.

The operating point chosen for the trend study was at 7978 cfm using an inlet velocity profile that approximated the measured axial velocity. The values at which all other variables are held constant while the variable being studied is changed were: DISPN = 0.4, DCD = 20, RULT = 0.853, RHULT = 0.15, XTW = 1, XULT = 1.5, SFC = 0.333 and CDRAG = 0.007. The computed results are given in Figures 6.39-6.46 for the efficiency, power and total pressure as a function of the variable under consideration. The plots' scales were chosen to emphasize changes and are, therefore, different. Comparisons of the percentage change in output caused by a variable are given in Table 6.1 by taking the difference between the maximum and minimum values of an output variable and dividing by the minimum value. Numerical experimentation done at other operating points did not reveal substantially different effects, although exhaustive investigation was not undertaken. The important variables are seen in Table 6.1 to be RULT, DISPN and CDRAG. Other variables, which do not appear to be of much importance in Table 6.1 but which strongly affect the wake alignment convergence (and, therefore, RULT), are DCD and XTW. To achieve convergence over the full range of RULT, for example, it is necessary to vary DCD and XTW a bit. This interdependence can be more pronounced at operating points different from that of peak efficiency. Also, complicating matters further, there is a similar relationship between DISPN and the other five wake variables. For this reason, DISPN was computed (PSF-2 has provision for either stipulating a DISPN value as input or computing a DISPN value for output as discussed in Chapter 4) by the program during the seven trend studies when it was not studied. Then DISPN did not vary much from the 0.04 baseline value. This guidance in selecting input variables and understanding their effects, not provided with the PSF-2 code and related materials, assisted all the computations to be presented. Computations shown in Figure 6.39-6.49 were made using the maximum number of panels allowed in the PSF-2 program, 144 panels on the key blade.

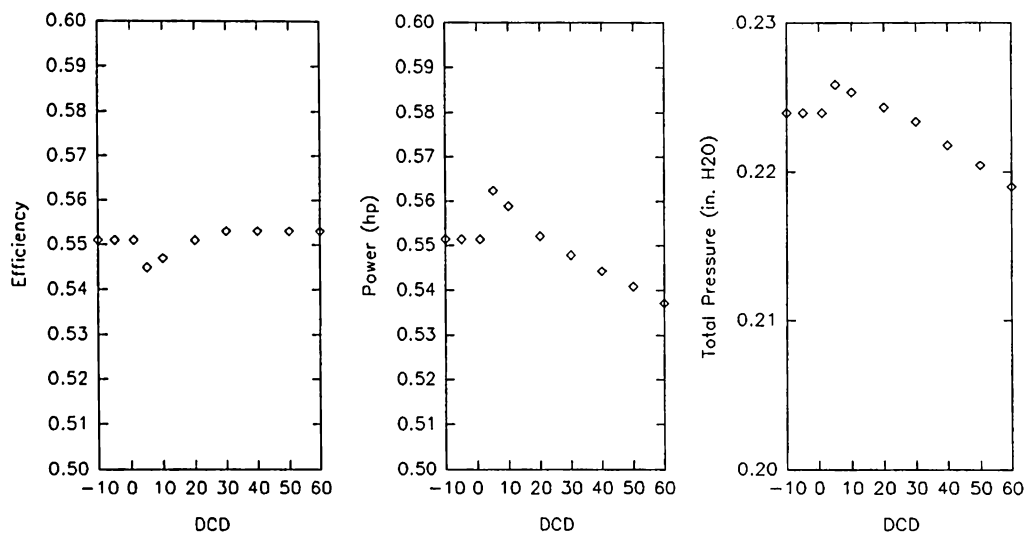


Figure 6.39 Plots of efficiency, power and P_{total} versus PSF-2 input variable DCD, wake contraction angle at blade tip

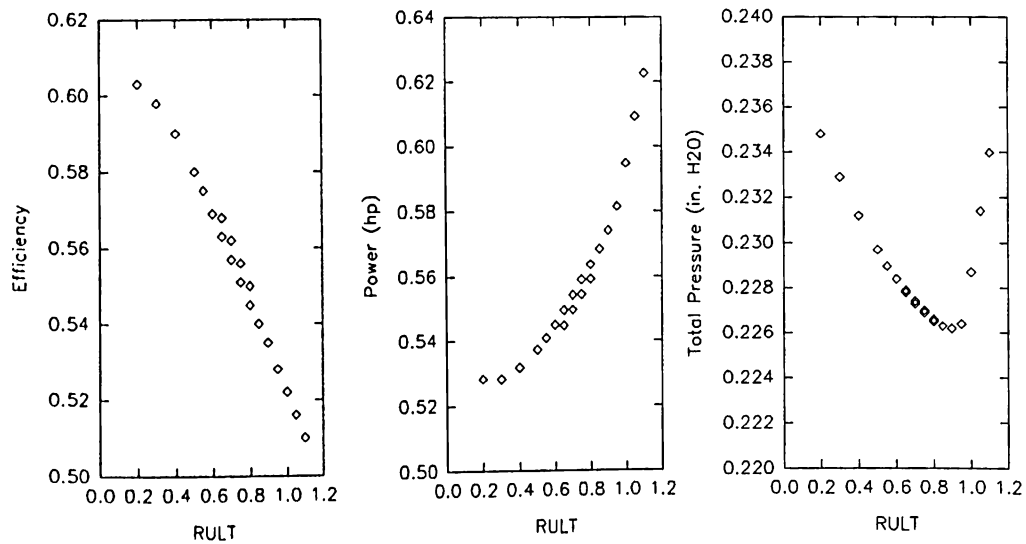


Figure 6.40 Plots of efficiency, power and P_{total} versus PSF-2 input variable RULT, radius of the ultimate wake

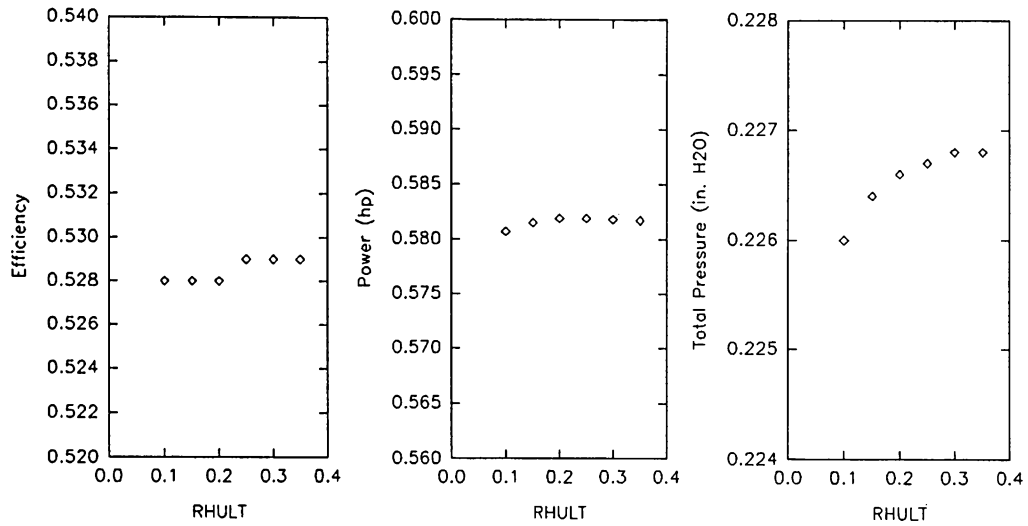


Figure 6.41 Plots of efficiency, power and P_{total} versus PSF-2 input variable RHULT, radius of the hub vortex line in the ultimate wake

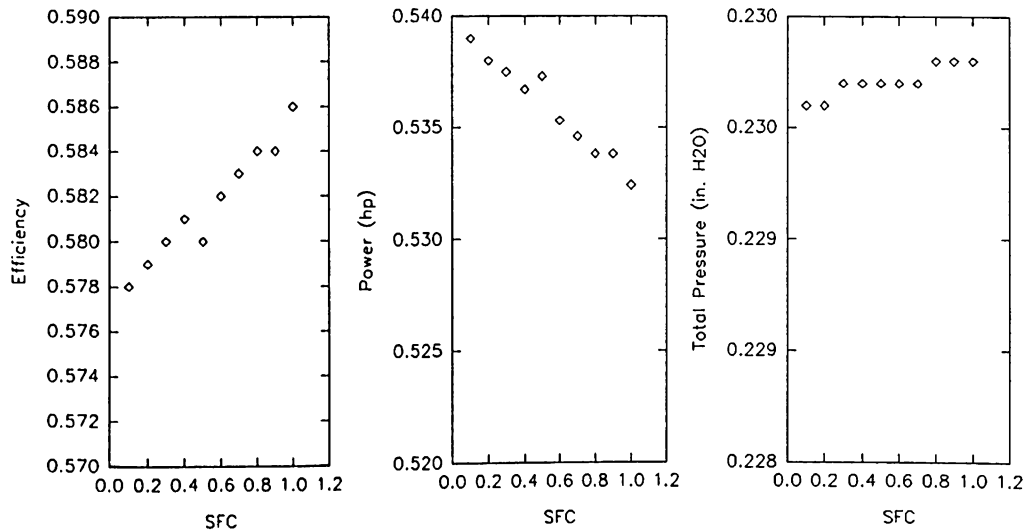


Figure 6.42 Plots of efficiency, power and P_{total} versus PSF-2 input variable SFC, leading edge suction efficiency factor

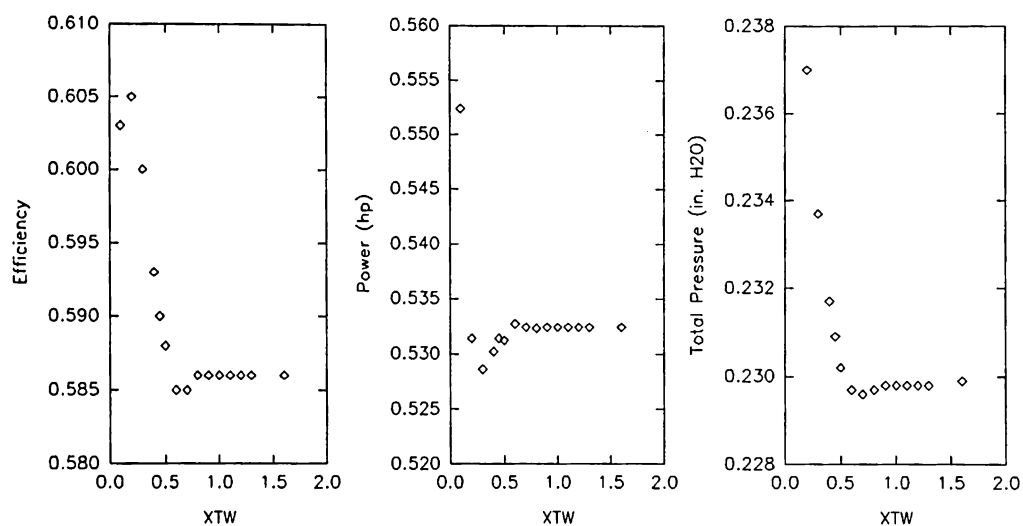


Figure 6.43 Plots of efficiency, power and P_{total} versus PSF-2 input variable XTW, axial extent of transition wake

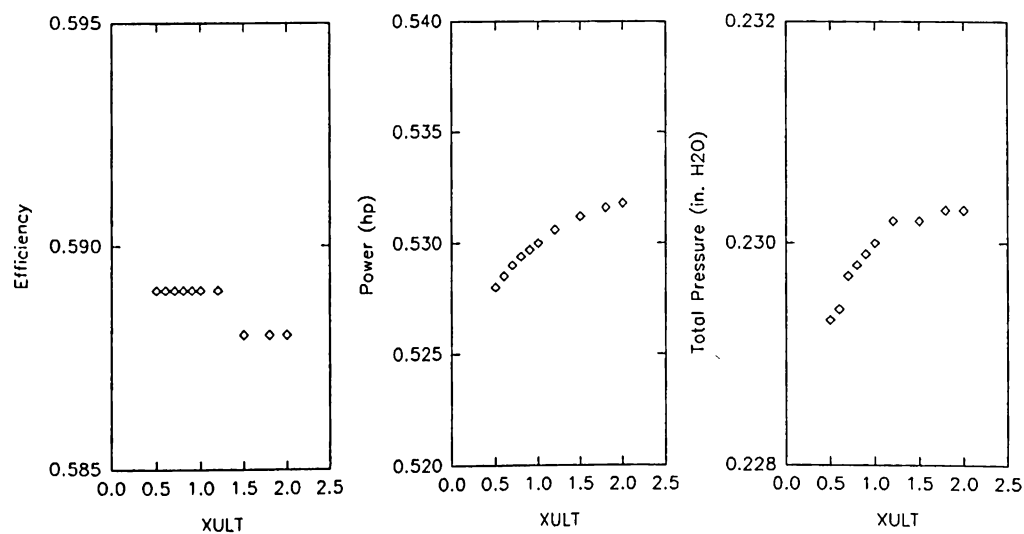


Figure 6.44 Plots of efficiency, power and P_{total} versus PSF-2 input variable XULT, distance downstream where wake pitch ceases to change

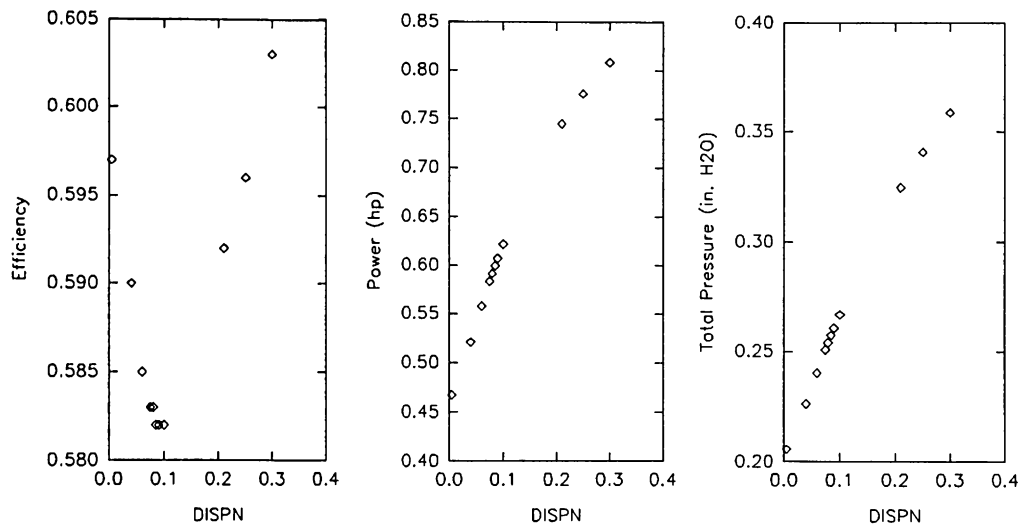


Figure 6.45 Plots of efficiency, power and P_{total} versus PSF-2 input variable DISPN, normal displacement of tip vortex collection point from trailing edge

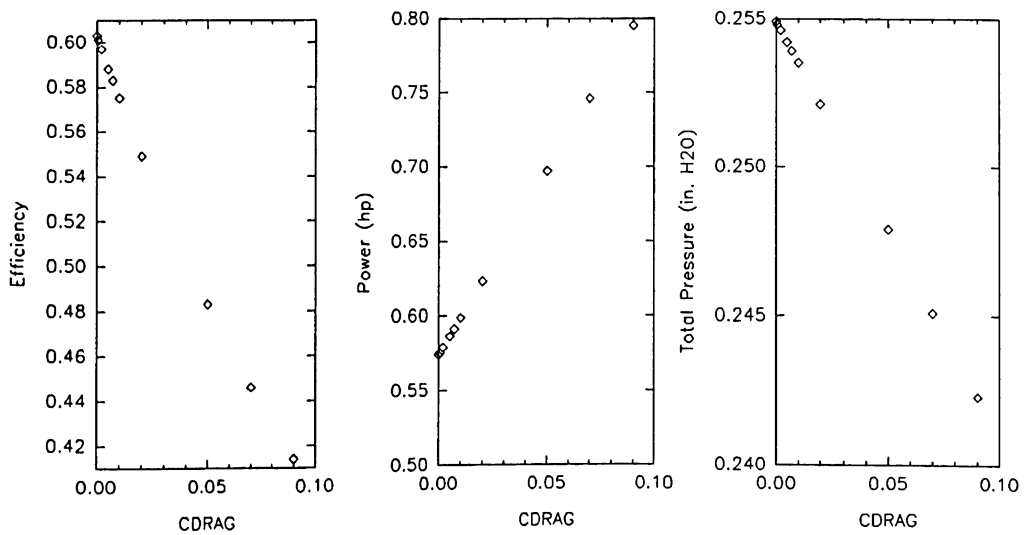


Figure 6.46 Plots of efficiency, power and P_{total} versus PSF-2 input variable CDRAG, section drag coefficient

Table 6.1 Percent change in PSF-2 output caused by changes of input variables shown in Figures 6.39-6.46

Variable name	Change in efficiency (%)	Change in power (%)	Change in P_{total} (%)
DCD	1.5	4.7	3.2
RULT	18.2	18.0	4.0
RHULT	0.2	0.2	0.4
SFC	1.4	1.2	0.1
XTW	3.4	4.5	6.9
XULT	0.2	0.7	0.4
DISPN	3.6	72.8	74.4
CDRAG	45.7	38.5	5.2

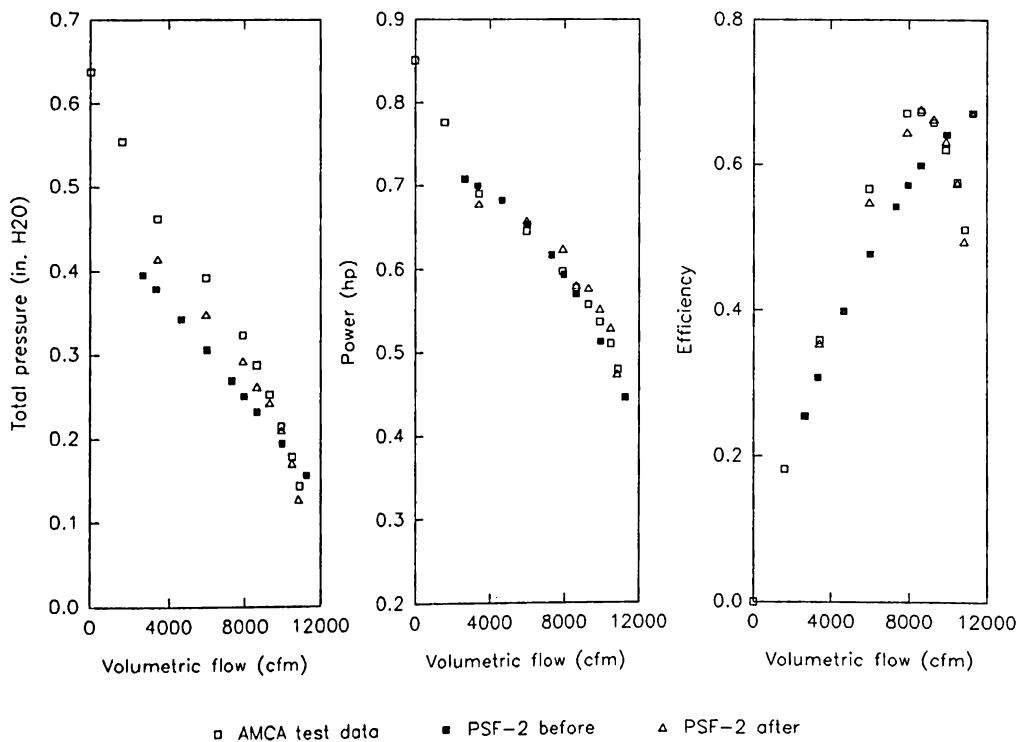


Figure 6.47 Measured and computed performance for the LP-36 fan at 850 rpm (computations before and after input variable "fitting" process)

6.4.2 PSF-2 Input Variable "Fitting" for the LP-36 Fan

The trend study results were used to guide an input variable "fitting" process which was used to select the best value of a given input variable at a given operating point based on comparison with measurement. The "fitting" process involved numerical experimentation at measured operating points to select the values of the input variables which minimized the error between the PSF-2 computation and prediction. The input variables XULT and RHULT were not "fitted" because of their minimal effect as determined by the trend study; constant values of $XULT = 1.5$ and $RHULT = 0.1$ were used. In Figure 6.47 the results of the performance tests and the PSF-2 computations before the "fitting" procedure are shown. These "PSF-2 before" results given in Figure 6.47 show good agreement in trend, considering they were run without knowledge of the best wake and blade section variables. Considering these variables, the lack of agreement in total pressure at low flow rates is probably caused by wake parameters and the under estimate in power (particularly at higher flow rates) is due to the absence of good drag estimation.

The input variables which best fit the performance measurements at flow rates ranging from 3406 to 10850 cfm are given in Figure 6.48. Some interesting trends appear for the variables CDRAG, DISPN, XTW, and RULT while the variables SFC and DCD appear to have no particular correlation to flow rate. These results are fascinating, considering that the variables were changed arbitrarily with no other purpose than to match measured performance. The values of DISPN and DCD ($DISPN = 0.08$ and $DCD = 7$ to 15 degrees) estimated from flow visualization at free-air (10,800 cfm) agree favorably with the results of the "fit" TESTING. Also, the "fitted" values of CDRAG are typical of those in the literature for thin cambered plates (Wallis, 1983 and Milgram, 1971). The best "fit" of XTW the transition wake length was found to be truncated at some operating points (at low flow rates). This behavior of XTW and an improved agreement with performance measurement is analogous to the work of Shi-cun (1990), who found that a prescribed decay in vortex element strength with down stream distance gave improved agreement for a helicopter rotor. A noticeable improvement in the predictive capability of the PSF-2 code with the "fitted" input variables can be seen in Figure 6.47 for the "PSF-2 after" performance data. The "after" data shows excellent agreement in efficiency and power prediction; total pressure, though improved, still shows increasing departure from measurement at low flow rates. The stalled flow (as visualized in Appendix F) at low flow rates would, however, be difficult for the VLM to predict due to the non-ideal flow phenomenon involved. In general, at low flow rates the PSF-2 wake calculations have trouble converging. Following the addition of graphical output of the wake model in the modified version of PSF-2, at low flow rates flow (visualized by the trailing vortex lines) is predicted to recirculate through the hub opening at low flow rates.

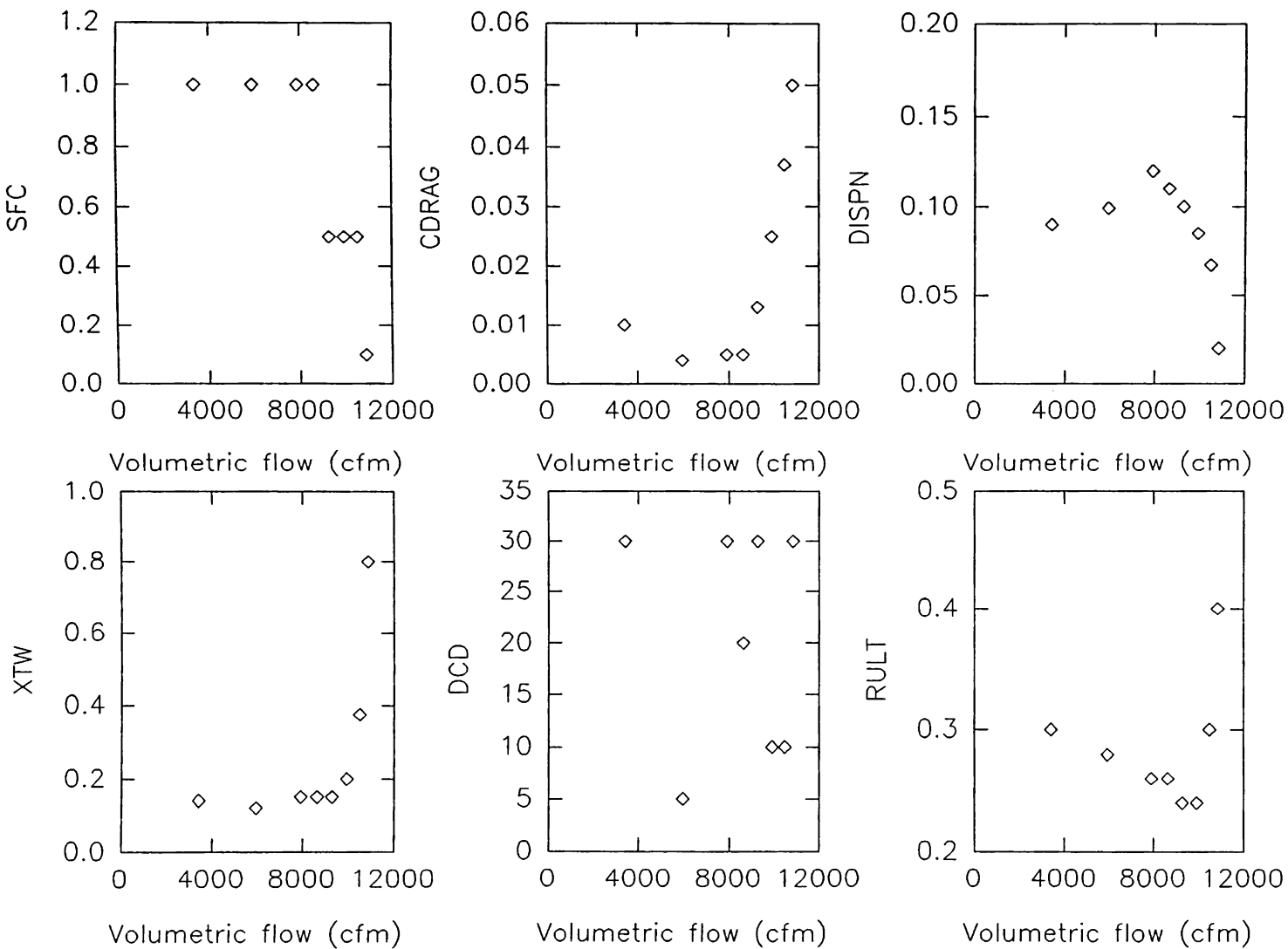


Figure 6.48 Input variable values which best match measured performance for the LP-36 fan at 850 rpm

Values for the input variables determined from the "fitting" process with the LP-36 rotor operating at 850 rpm were then used as input for computations for the rotor at 600 and 1100 rpm. Some of the input values found from the "fitting" process were such that wake convergence was difficult, and when they were used in the computations at 1100 rpm convergence was not possible. Of the five cases that did converge at 1100 rpm, there is some scatter to the results as shown in Figure 6.49 but results appeared good. At 600 rpm (also shown in Figure 6.49) the cases were not difficult to run and convergence was easily achieved. Both total pressure computations are low at 1100 and 600 rpm. However, the 10% shortfall at 600 rpm is the greater. The power calculation is low by even more, resulting in a peak efficiency that is much higher than the measurement for the 600 rpm case. Because the PSF-2 calculation of the volumetric flow does not account for flow in the motor/hub region, it is possible that the calculated flow rate should be higher which would shift the total pressure and power curves to the right, to improve the agreement. Even as it is, both the magnitude and the slopes of the computation and measurement data for pressure and power have good agreement.

From the flow visualization tests in Appendix F at 600 rpm it appeared that flow separation on the blade suction side occurred over a wider range of flow rates than at the higher rotational speeds (850 and 1100 rpm). Based on that evidence, the CDRAG is probably higher for the 600 rpm case and it would not be surprising that the wake input variables should also be different. When the "fitted" input variables were applied to a different fan, the six bladed ACME fan shown in Figure 5.2, there was again difficulty in achieving convergence in the wake alignment portion of the PSF-2 program. The ACME fan has a lower design rpm, 495, than the LP-36 fan but has similar performance. The power results of the PSF-2 computations for the ACME fan (shown in Figure 6.50) show considerable scatter and the efficiency plot indicates an efficiency peak at about the right flow rate but considerably lower than the measured value. The measured performance data (pressure and power) of the ACME fan has an interesting kink at around 7000 cfm which the PSF-2 computation does not capture. However, the computations agree fairly well, considering the input parameters were derived from a different fan operating at a different rotational speed.

Also shown in Figure 6.50, is a series of computations from the author's modified PSF-2 code, Fan Steady Flow (FSF), without the venturi panel option. In FSF an arbitrary CDRAG value can still be used but, also, wind tunnel test data of drag coefficient as a function of lift coefficient from several test curves in Wallis (1983) and Milgram (1971) can be interpolated using cubic-splines. The lift coefficient is estimated from the sum of the bound circulations over a given blade section. The results of FSF using this feature to estimate drag coefficient and "recommended" estimates for the other input variables ($DISPN = 0.08$, $XTW = 0.6$, $RULT = 0.4$ and $SFC = 0.33$) shows better agreement with the measurements than do the PSF-2 computations, although the efficiency is over estimated above about

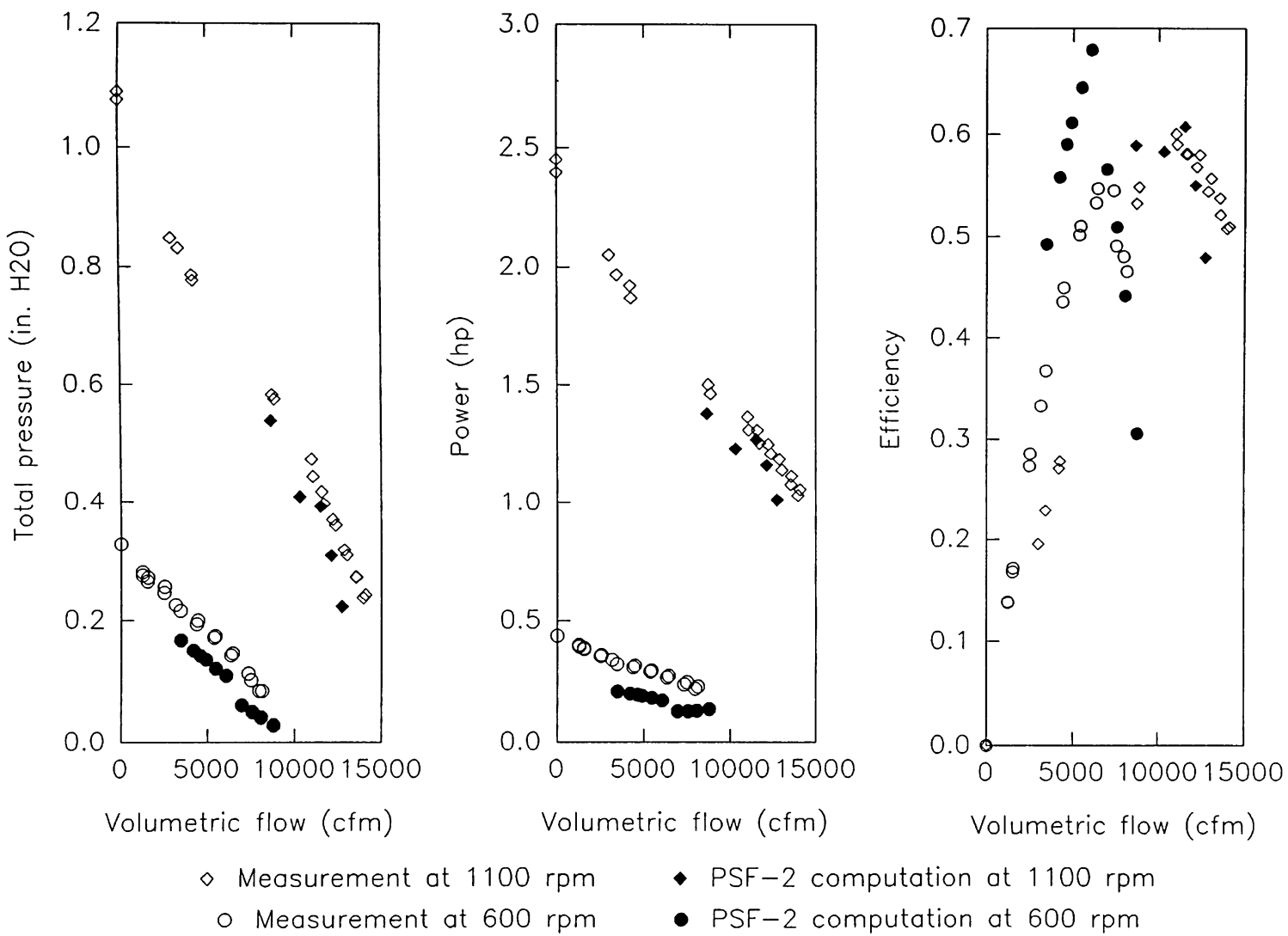


Figure 6.49 Measurements and PSF-2 computations of performance using "fitted" input variables at 600 and 1100 rpm

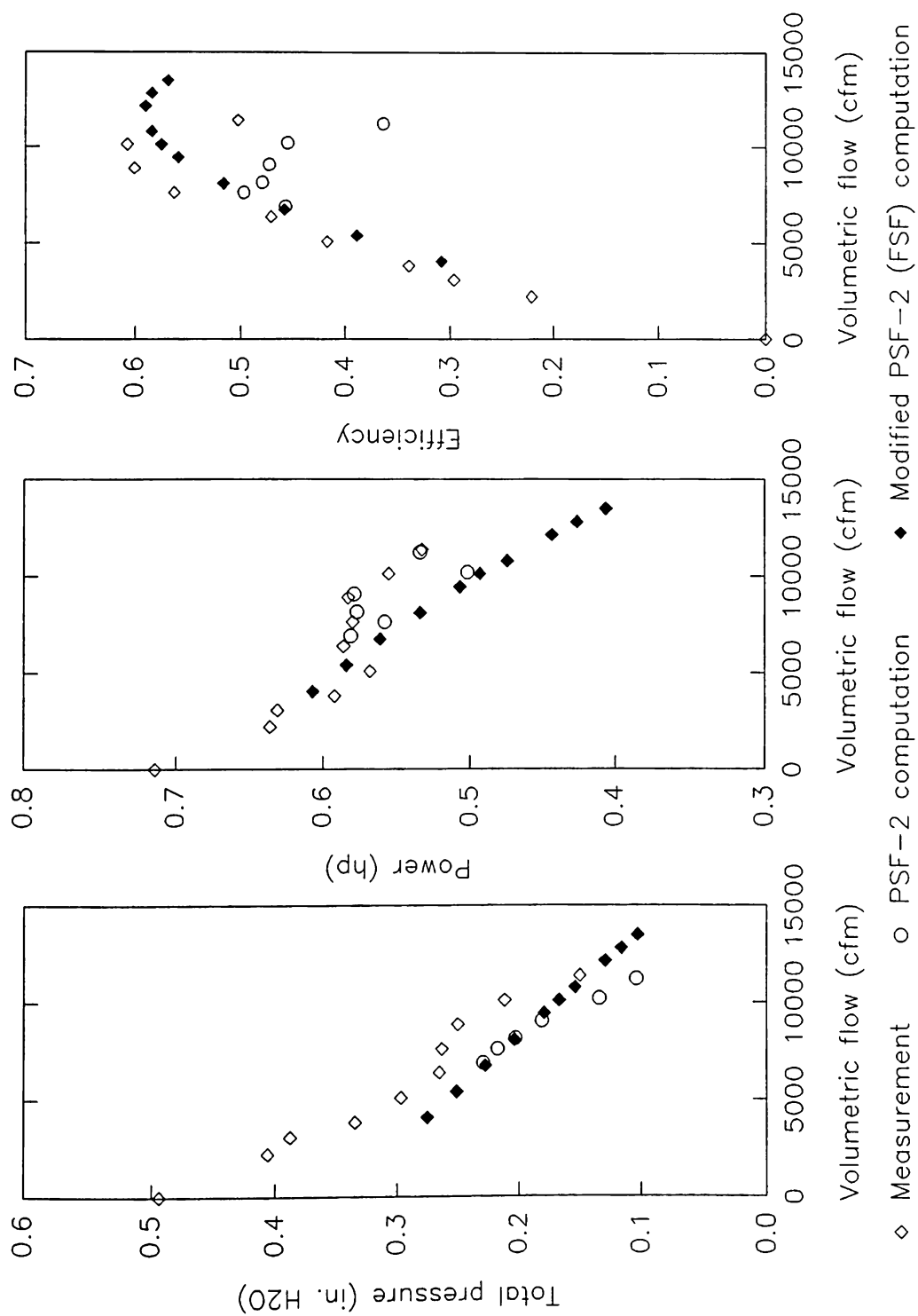


Figure 6.50 Measurements and PSF-2 computations of performance for the ACME fan using "fitted" input variables and the modified PSF-2 program

10000 cfm.

6.4.3 Computed Performance Using FSF

The PSF-2 code was modified as discussed in Chapter 4 in order to more thoroughly explore the lifting surface technique's ability to perform fan analysis. The modifications, briefly noted here, are:

- maximum number of panels on the key blade increased from 144 to 600
- like discretization performed on all blades and their trailing wakes (i.e. no longer is coarse spacing used on non-key blades, and tip vortex separation is now computed on all blades)
- tip vortex separation performed on all blades
- trailing wake alignment and interpolation indices may be selected by the user
- a venturi-panel duct model incorporated using vortex elements
- graphical postprocessing of the discretized blade, the trailing wake and the venturi duct added
- viscous drag estimated as a function of lift coefficient at a given spanwise section using wind-tunnel test data
- surface pressure estimations performed by using either element forces or by the Bernoulli equation to provide additional code verification output
- field point velocities can be estimated at points, surfaces offset from the blade or in prescribed axial planes
- the velocity field put into a form readily post-processed by PLOT3D
- the pressure difference field on the blade surface can also be put out in a form readily plotted using the contouring feature of the GNUPLOT program
- performance output using units commonly employed in ventilation fan testing or the dimensionless coefficients is possible

The modified PSF-2 code has been named **Fan Steady Flow (FSF)**.

Two sources of drag coefficient data (Wallis, 1983 and Milgram, 1971) were consulted to arrive at a basis upon which to estimate the spanwise section drag coefficient as a function of lift. There is some scatter in the data, and the author is unsure what is meant in Wallis (1983) by the term "Birnbaum" in describing the degree of camber of a given blade section. The drag data and the approximation currently used in the FSF program are given in Figure 6.51. The LP-36 blade has a largest camber of 8% near the root and a smallest value of 6% near the tip. Numerical experimentation has shown the computed "FSF approximation" results to agree best with the LP-36 measured performance with the "Milgram-12%" data consistently over predicting torque and the "Wallis-Birnbaum" data under predicting torque. Therefore the "FSF approximation" curve, which was

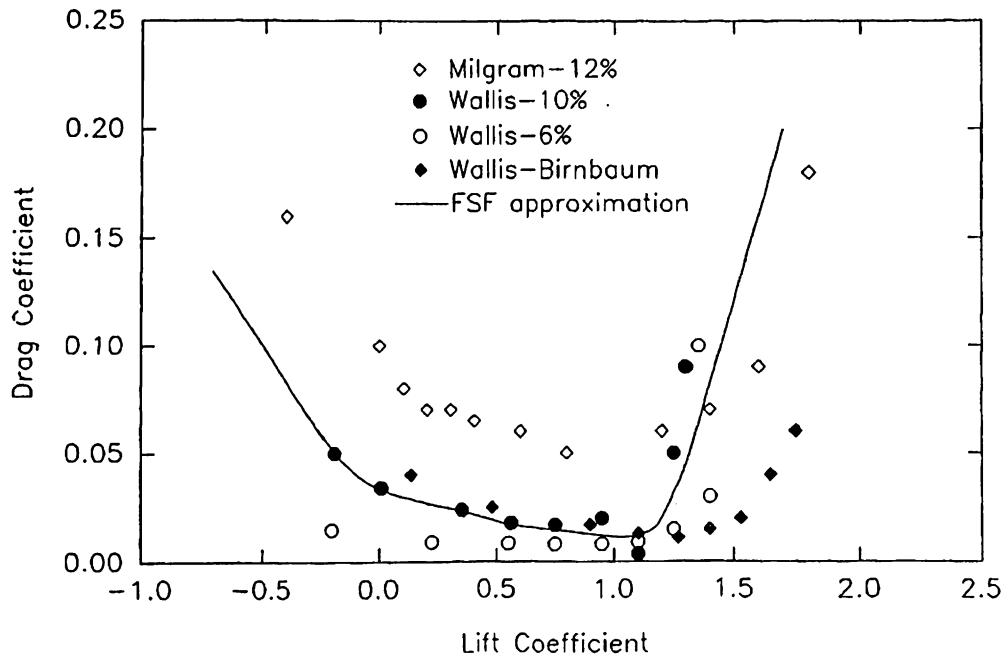


Figure 6.51 Drag data as a function of lift coefficients for thin plate blades of various amounts of camber (data from Wallis, 1983 and Milgram, 1971)

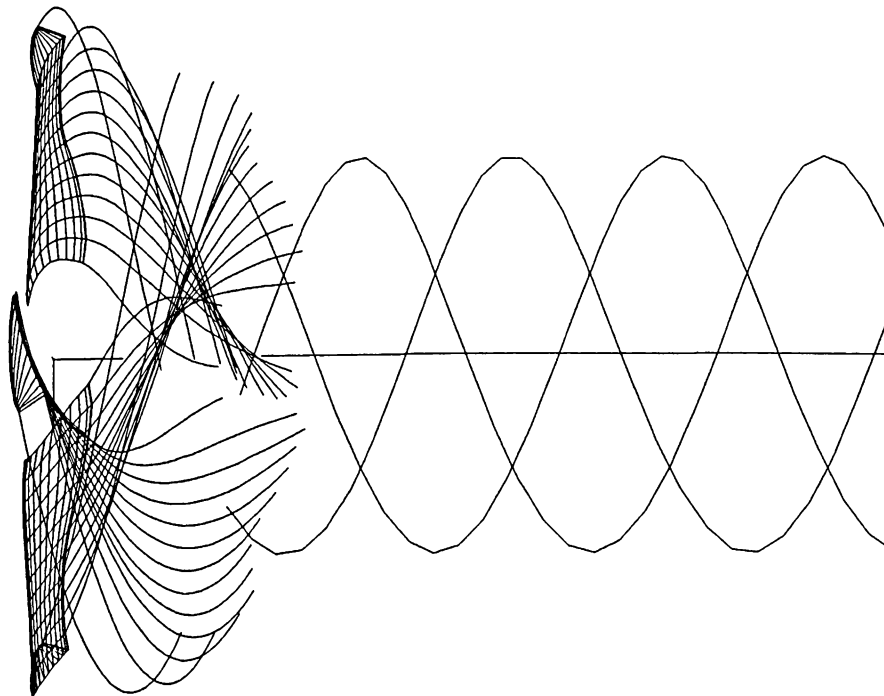


Figure 6.52 Computational lattice for LP-36 fan at 850 rpm and 10800 cfm (free-air) as modelled with FSF with a 12 x 12 blade grid

used in the results presented in this section, represents a reasonable determination of drag coefficient for the LP-36 blade. Although the viscous effects on drag have been empirically accounted for, other non-ideal flow phenomena occurring in the wake and at the blade tip were represented via the input parameters (DISPN, XTW and RULT).

The performance of the LP-36 fan was computed with the FSF program at 600, 850 and 1100 rpm with and without the venturi duct at various flow rates. Performance computations made with FSF were compared with the PSF-2 results with 144 panels (12 spanwise x 12 chordwise panels) using the "fitted input" variables (i.e. not using the drag estimation capability of FSF). Comparison of the PSF-2 performance with measurements using the fitted variable was shown in Figure 6.47. The FSF results with "fitted" parameters are very close as seen in Figure 6.53. The only difference appears to be slight increase in estimated power by FSF. Next, as seen in Figure 6.53, the same 12 x 12 lattice was computed using the drag coefficients computed as a function of the lift at a given spanwise station (as discussed with regard to Figure 6.51). The agreement between the two 12 x 12 grids in Figure 6.53 is remarkable considering that the "fitted" drag coefficients were constant over the entire blade span and determined solely on the basis of matching measured performance. With increasing panel number on the blade (see the 12 spanwise x 18 chordwise data in Figure 6.53), the results do not change much from the 12 x 12 grid. A small increase in both predicted power and pressure are observed for the 12 x 18 run.

The wake geometry at "free-air" (shown in Figure 6.52) was found to agree qualitatively with the wake observed using trailing edge streamers (Figures 6.33-35). Also, the best results were obtained using a transition wake of shorter length than typically used for propeller work. Perhaps this is another indication of the added importance of including a decay of trailing vortex element strengths in the fan wake.

Adding the venturi duct modelling capability of FSF to the calculations alters them. The panelling scheme used for the venturi duct calculations is shown in Figure 6.54 and consisted of 440 panels (40 in the circumferential direction and 11 in the axial direction). It is believed that duct panels in helical rather than cylindrical pattern will improve results (Kerwin et al., 1987), but this will be left to future studies. Also, the addition of panels extending further radially from the inlet (as seen in Figure 4.35), did not noticeably affect the "ducted" results. In Figure 6.55 a side view of the computed wake for the LP-36 fan at 850 rpm is given for a computation using the venturi duct (duct not shown in figure, however, so that the wake is easier to see). This computation was performed at the "free-air" state, and it is included for comparison with the flow visualization of Figures 6.33-35.

Computations using the duct modelling and a 12 x 12 blade panelling

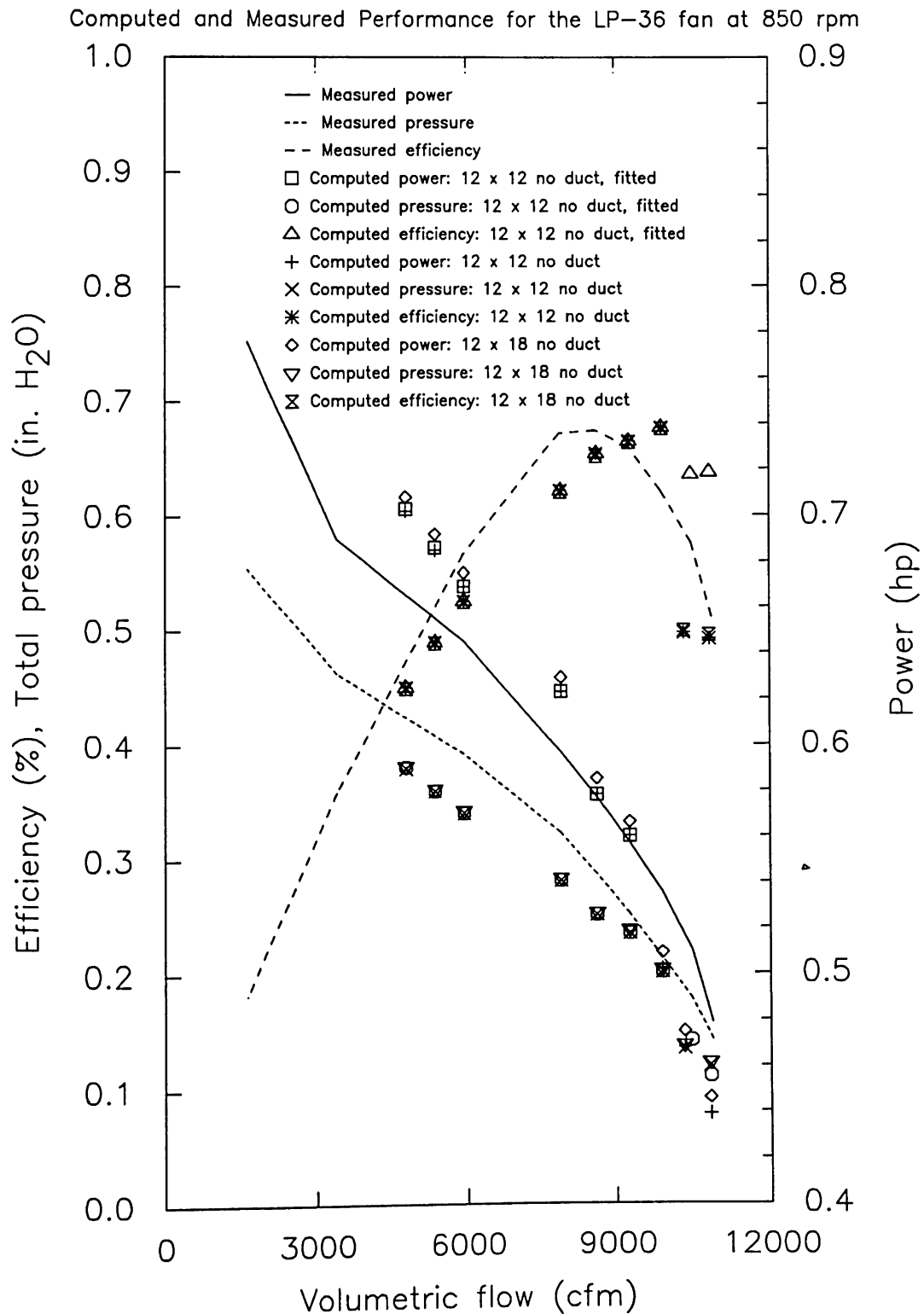


Figure 6.53 Computed and measured performance for the LP-36 at 850 rpm fan using FSF without the venturi duct capability

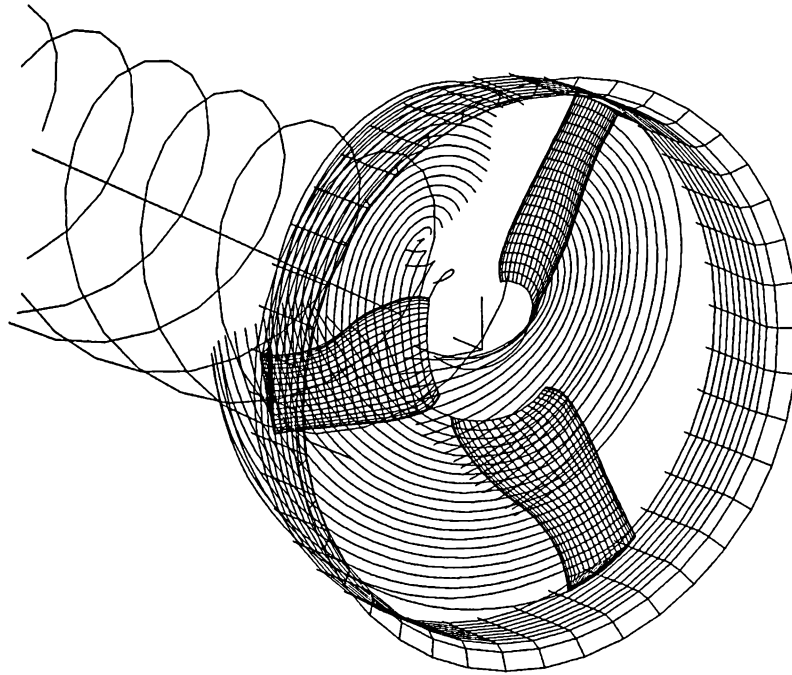


Figure 6.54 Duct panelling scheme used in FSF for all "duct" results presented in this section with 15 x 20 blade panels (computation at 850 rpm and "free-air")

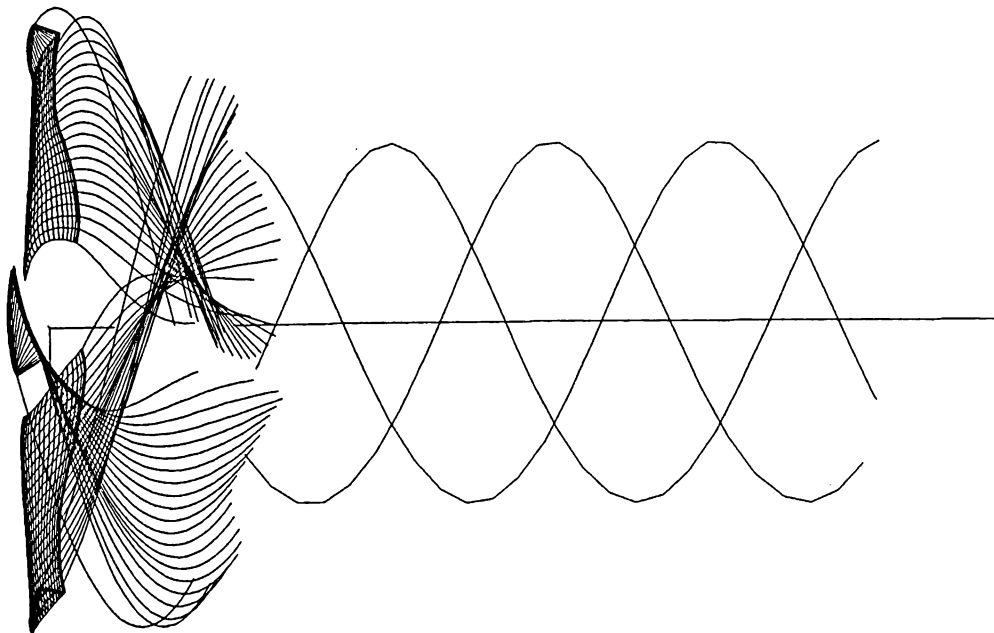


Figure 6.55 Side view of 15 x 20 panel blade lattice and trailing wake for the ducted LP-36 fan at 850 rpm and 10960 cfm (duct, used in calculation, not shown)

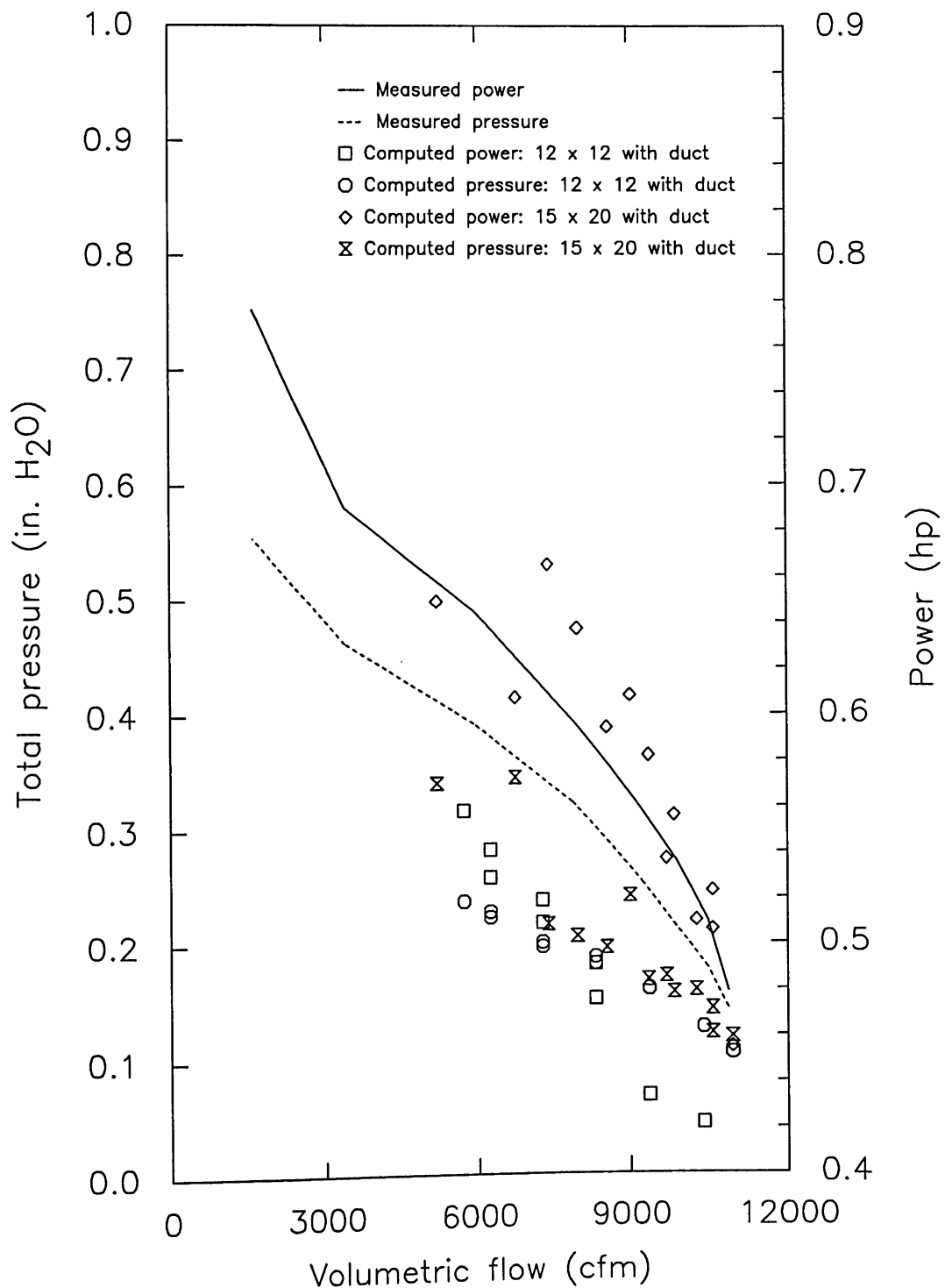


Figure 6.56 Computed and measured performance for the LP-36 at 850 rpm fan using FSF with the venturi duct capability (duct discretization shown in Figure 6.54)

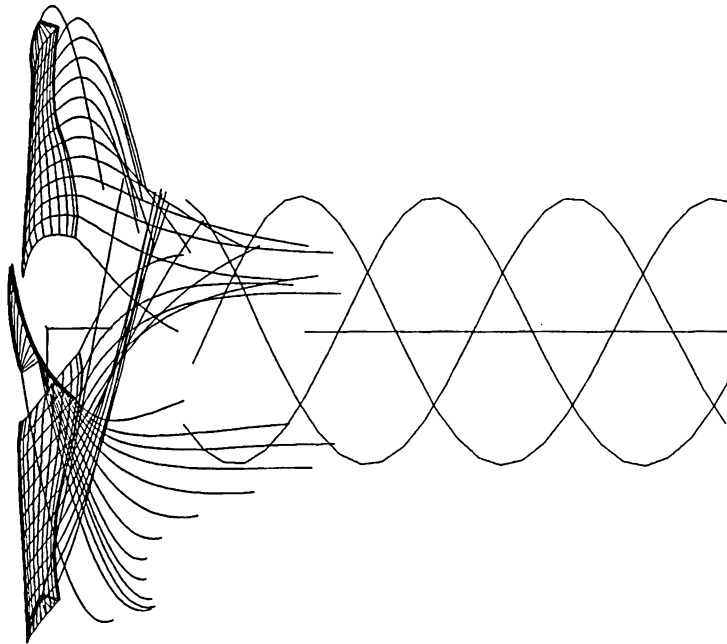


Figure 6.57 Side view of the blade lattice and wake elements for the 12 x 12 blade panels case at 850 rpm, 5730 cfm and with the venturi duct (duct, used in calculation, not shown)

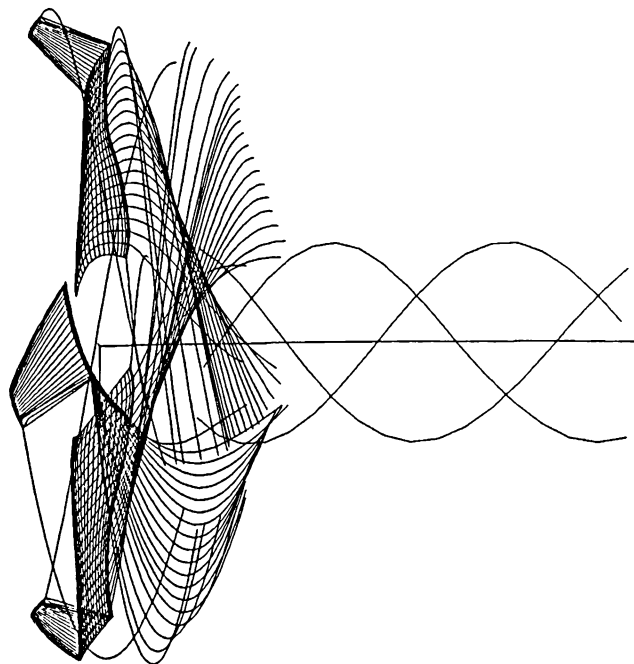


Figure 6.58 Side view of a 20 x 20 panel blade lattice and trailing wake for the ducted LP-36 fan at 850 rpm, 6760 cfm (duct, used in calculation, not shown)

scheme, underpredicted the power by a consistent value around 20%, as shown in Figure 6.56. Total pressure rise is also underpredicted, but agreement between the measured and predicted pressure rise improves as volumetric flow increases. As a result, the estimate of total pressure rise at "free-air" actually appears quite good. Following numerical experimentation with finer blade panel discretizations and various wake parameters, some results from these studies showed that by increasing the panels to 15 x 20 the short fall in predicted power was overcome. The pressure rise prediction for the "15 x 20" lattice "with duct" appears better than the more coarse lattice (as seen in Figure 6.56). Scatter in the predicted power and pressure for the 300 panel case is primarily due to wake parameter effects. For the fine discretization case, a firm handle on the best parameters and their functional dependence on flow rate was not studied. However, attempts to perform this at the lowest two volumetric flows for the 15 x 20 case indicated that it is possible to adjust the parameters to more closely match predicted power and pressure rise. The pressure is underestimated (again) for the 15 x 20 case, but parameter (XTW, RULT and DISPN) variation can be used to better match predicted and measured values of pressure as well.

Using the graphical post-processing capabilities of FSF, it is quite interesting to examine the variation of predicted wake geometry at the operating points studied. There are some interesting trends one sees in the wake geometries which best predict performance. Although an exhaustive study of this will not be presented here, the reader is alerted to some general trends in wake shapes. It was typically found (regardless of whether the duct model was used) that wakes which produced good agreement with measured performance at free-air conditions appeared as shown in Figure 6.55. As flow is decreased through the computational model, the iterative wake alignment procedure gives some interesting results. The wake produced for the 12 x 12 calculation with venturi duct (data in Figure 6.56) at 5730 cfm without "default" values of wake parameters (DISPN was computed, RULT = 0.5 and XTW = 1.0) underestimated both power and pressure, and produced the wake shown in Figure 5.57. This wake appears to be jet-like over the inner half of the blade span, and there is a definite transition to a helix of quite small pitch angle over the outer half of the blade span. Comparing the "default" parameter wake of Figure 6.57 with a 20 x 20 lattice at 6760 cfm (performance results virtually identical to that of the 15 x 20 run given in Figure 6.56 which agreed favorably with measured power and pressure) shown in Figure 6.58, a large prescribed value of DISPN (DISPN, tip vortex separation and collection point, = 0.26) was needed to achieve the agreement. This wake also possesses an ultimate wake of smaller diameter (RULT = 0.3). The innermost vortex filaments are seen to coil tightly with a noticeably smaller axial velocity component in the wake for Figure 6.58. A stalled flow pattern all along the leading edge of the blade was observe at this operating point (as documented in Appendix F) and by setting the value of DISPN to be large the complicated effects of this flow are modelled when using the venturi duct. However, when the venturi duct was not modelled,

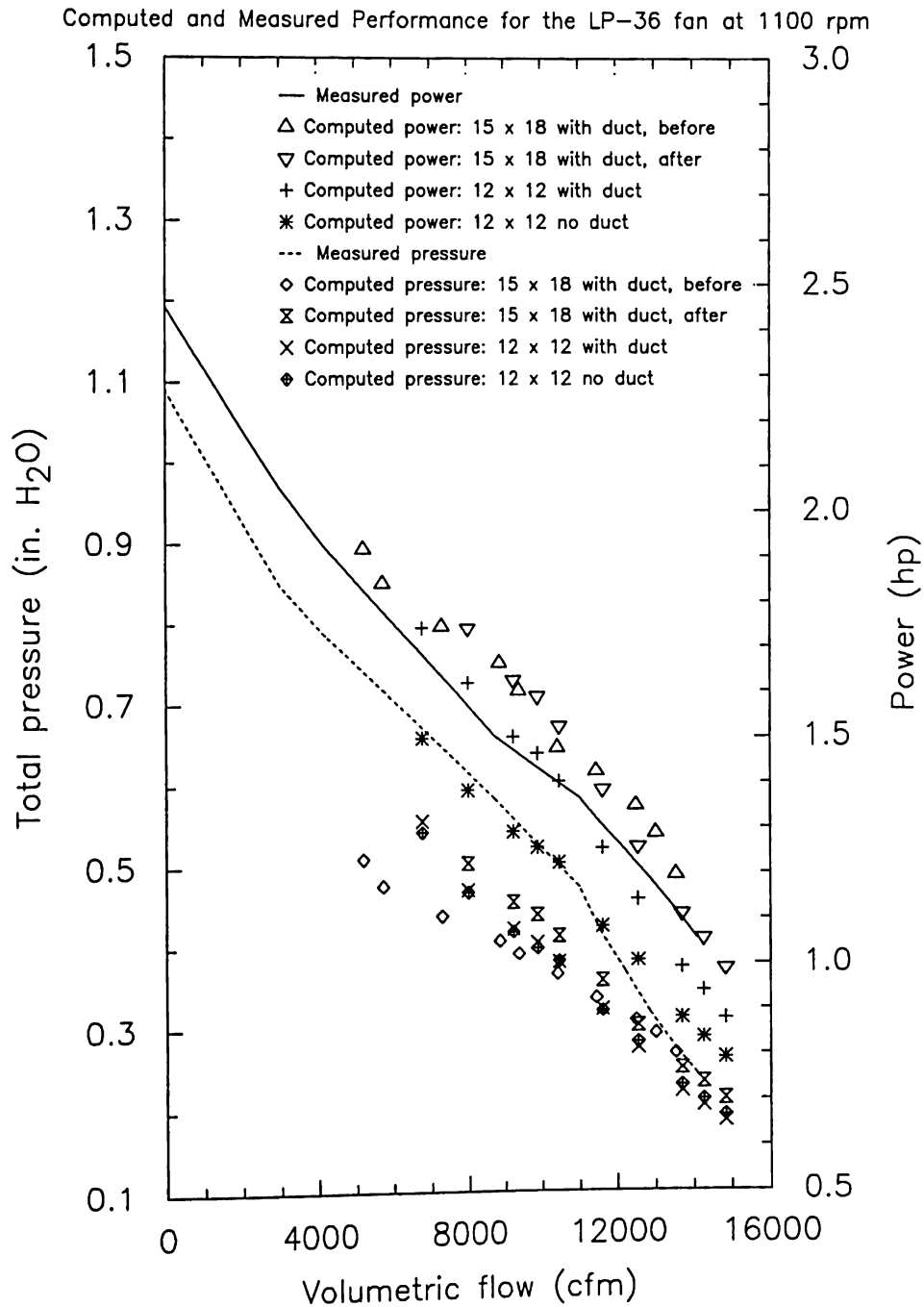


Figure 6.59 Computed and measured performance for the LP-36 at 1100 rpm fan using FSF without and with the venturi duct capability (duct discretization shown in Figure 6.54)

adequate performance predictions were achieved (i.e. see Figure 6.53) at this operating point with $DISPN = 0.1$.

At the 850 rpm speed, generally, the influence of the duct model does not appear favorable, but, perhaps, following a detailed input variable parameter study better agreement with measured performance at a wide range of operating points can be achieved. Still, the FSF program at the 850 rpm speed for the LP-36 fan does an adequate job of predicting performance in unstalled flow regimes. For instance, from experience using FSF, quite good agreement is achieved at "free-air" with and without the venturi duct for a wider variation of wake input parameters. Moreover, the parameter values determined from flow visualization at "free-air" conditions, $DCD = 13$ and $DISPN = 0.08$, with the other two important wake parameters set at $XTW = 0.8$ and $RULT = 0.4$, produced good performance agreement and a wake (see Figure 6.55) consistent with the trailing edge streamers photographs (Figures 6.33-35).

6.4.3.1 Computed Performance Using FSF at 600 and 1100 rpm

Unlike the results observed with using the duct modelling capability of FSF at 850 rpm, the addition of the duct model to performance prediction calculations at 600 and 1100 rpm noticeably improved the performance calculations. The improvement of the FSF predictions at 1100 rpm is quite apparent if one compares the 12 x 12 grid results without and, then, with the duct model as shown in Figure 6.59. Without incorporation of the venturi duct, the power for the 12 x 12 grid is underpredicted by 20 to 30% and addition of the duct with the same grid matched the measured power much better. No substantial difference in the predicted total pressure was observed with the addition of the duct for the 12 x 12 grid. Next, observe in Figure 6.59 the effect of increased panel number for the same wake input parameters as was used with the "12 x 12 with duct" case. This is the "15 x 18 with duct, before" case. Note that the effect of grid refinement from 144 to 290 panels improved the predictions of power and pressure close to the "free-air" state. However, at lower flow rates the predicted pressure is seen to depart from the measured values while power predictions remain good (even up to the lowest two flow rates in the plot). Following this case, observe the "15 x 18 with duct, after" case which incorporates the effect of slightly altering the input variables ($RULT$ and $DISPN$). The values of $RULT$ and $DISPN$ were constant at all operating points for the "before" case at 0.34 and 0.06 respectively, and were changed to a constant $DISPN = 0.09$ with $RULT$ varying between 0.55 and 0.34 for the "after" case. The "after" case produces excellent predictions from 12000 to 15000 cfm.

Figure 6.60 is included to show the difficulty in matching the measured efficiency data precisely. Also, this figure emphasizes that since predicted efficiency is (of course) derived from both predicted torque (power) and pressure

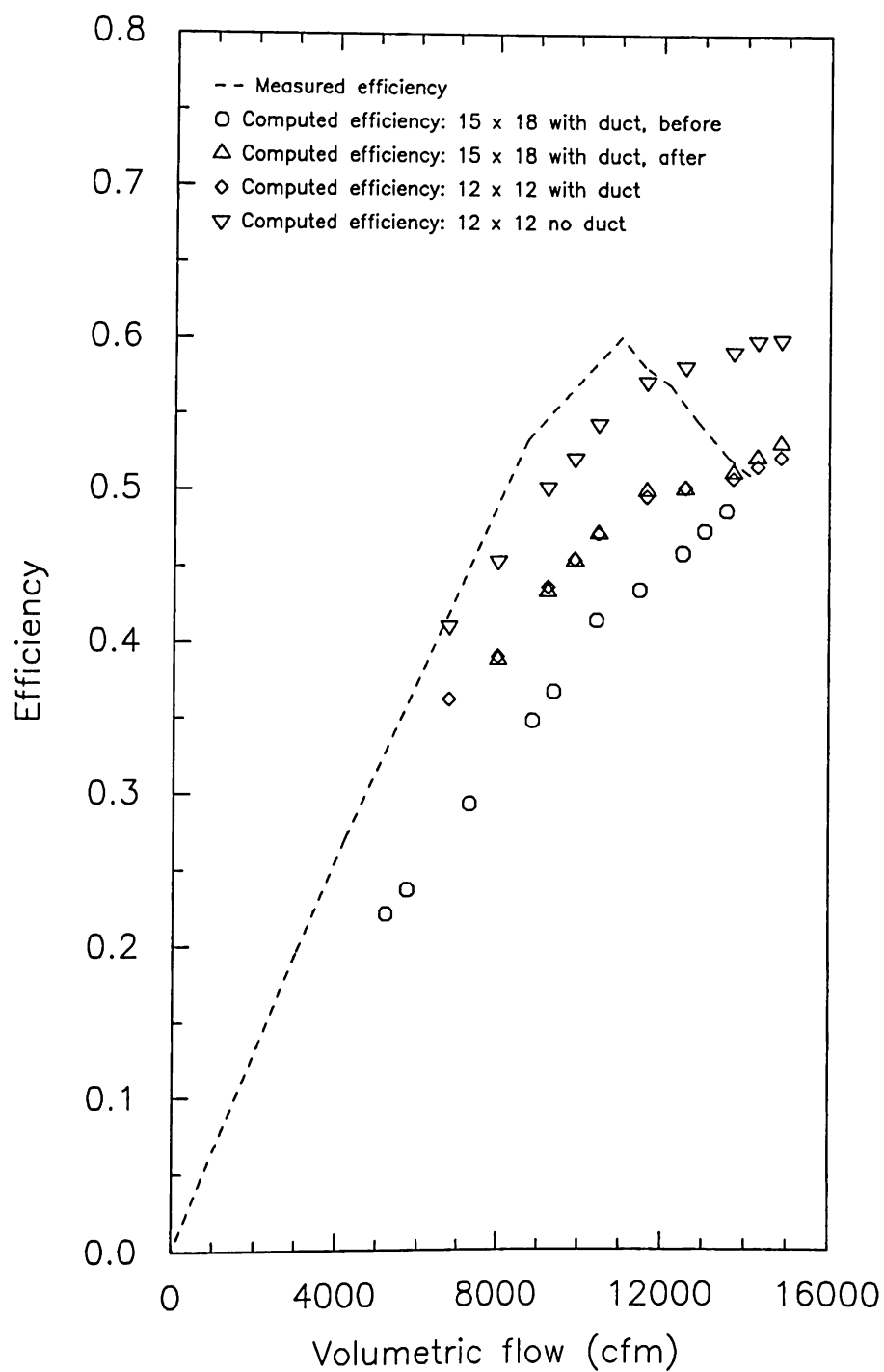


Figure 6.60 Computed and measured efficiency for the LP-36 at 1100 rpm fan using FSF without and with the venturi duct capability for cases shown in Figure 6.59

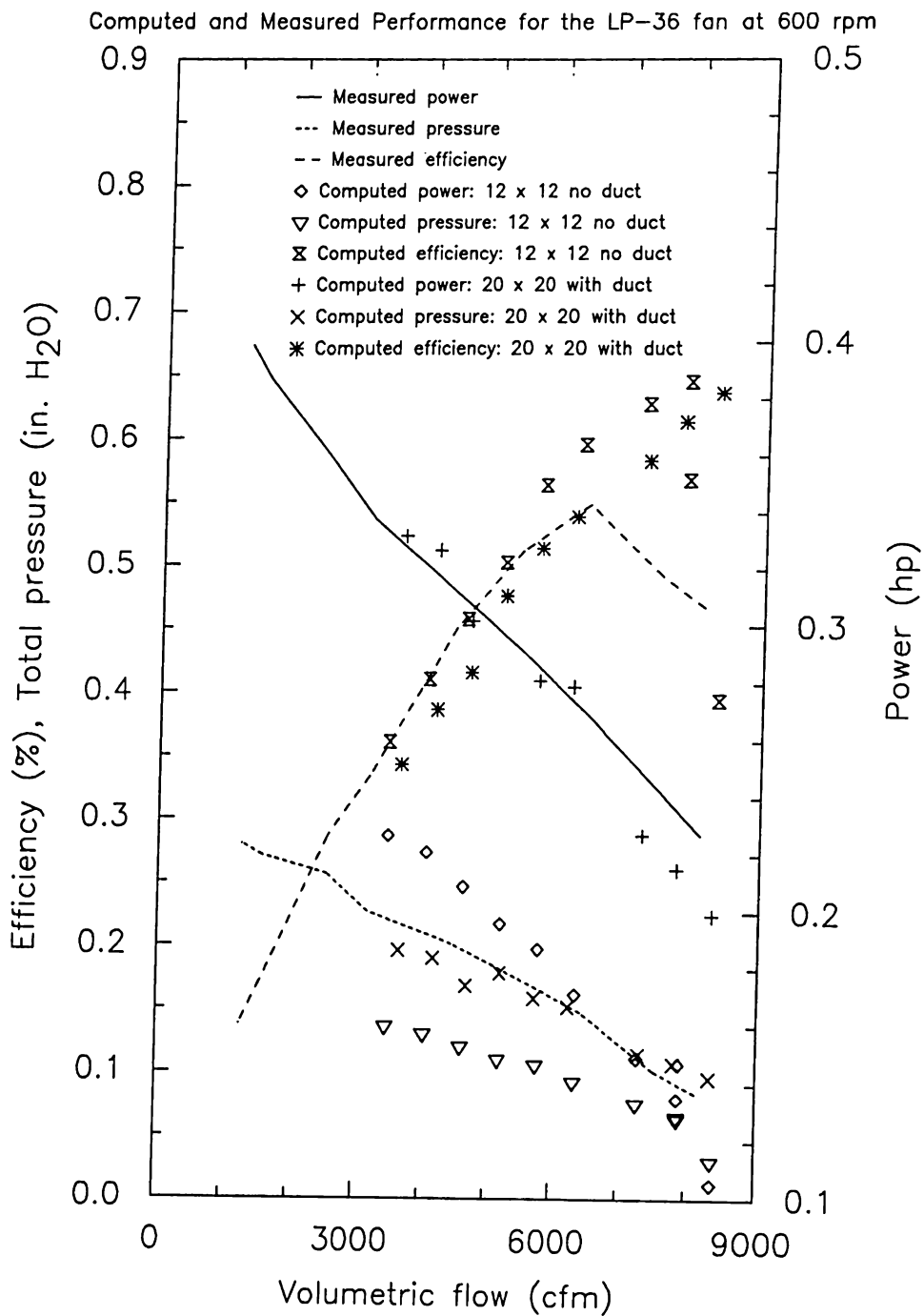


Figure 6.61 Computed and measured performance for the LP-36 at 600 rpm fan using FSF for a coarse lattice without and with a fine lattice and the venturi duct capability

rise, small discrepancies in their prediction can lead to larger errors in efficiency prediction. Also, it shows that poorer predicted power and pressure rise predictions can lead to a good efficiency prediction. This observation is meant as a caution to the user should the technique be used in some optimization procedure where predicted efficiency is an output variable being optimized. However, the trends in the prediction of the FSF program are consistent and, therefore, should assist one in attaining an "optimized" design with the understanding that the magnitudes of the actual power and pressure rise might depart from the VLM predictions.

Two extremes in the modelling capability of the FSF programs are demonstrated in Figure 6.61 for the LP-36 fan at 600 rpm. Earlier in Figure 6.49, the PSF-2 program was used to predicted performance for the LP-36 fan at 600 rpm with the result that power and pressure were underpredicted for a 12 x 12 lattice. Using the same blade discretization and the FSF program (the "12 x 12 no duct" data shown in Figure 6.61), similar power and pressure underprediction was observed. However, the drag calculation capability of FSF appears to better capture the efficiency curve than the PSF-2 results. Also, the FSF "12 x 12" calculation verifies again the agreement between PSF-2 and the FSF calculation for similar modelling cases. Then, presented in Figure 6.61, is the "extreme" case of computing the performance with FSF for a "20 x 20 with duct" model. The improvement in, especially, power and, also, pressure rise prediction is very good. It should be remarked that no wake parameter "fitting" was necessary to achieve these results, and some fine tuning of them between 7000 and 8500 cfm could match the measured results identically. The ducted capability and increased panel number possible with FSF can be used to produce excellent agreement between measured and predicted performance for this case.

6.5 Results of Unsteady Blade Aerodynamic Loading Measurements

A description of the method of measurement of the unsteady blade surface pressure differences (the aerodynamic loading) was previously discussed in Section 5.4. Here the results of those measurements, raw data and corrected data for the length of tubing are presented. Next, observations comparing the results of the unsteady pressure difference measurements and blade surface flow patterns will be made. Then comparisons will be made between the measured pressure differences and computed loadings from FSF. Unsteady pressure data were taken at three radial positions (position A at $R = 15.68$ in., position B at $R = 10.87$ in. and position C at $R = 7.67$ in.) with the chordwise position as a fraction of chord length of the blade at that radius indicated in Table 6.2. The data set at a given radius will be indicated using the position identification letters A, B or C.

The raw unsteady pressure difference measurements are presented as three dimensional contour plots in Figures 6.62-6.64. In these plots pressure on the top

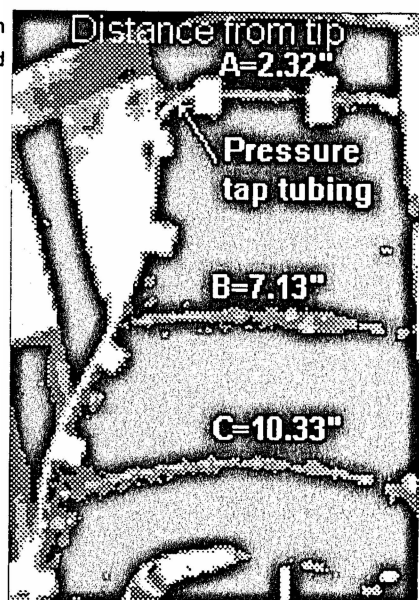
of one blade and the bottom of another blade were separately recorded at equal radial positions on the blades through one revolution (a period of 70.2 milliseconds). Lines were then drawn through every fourth data point, connecting adjacent tap position values at equal temporal positions. Finally, contours of constant pressure difference were interpolated from the data. In Appendix G the raw pressure differences are provided in a form more suited for determining the pressure difference values than for giving an overall impression of the unsteady measurements as seen in Figures 6.62-6.64. The corrected pressure differences are also presented in the form of contour plots in Figures 6.65-6.67, and given in an alternate form in Appendix G should more accurate numbers be needed. The method for correcting the unsteady pressure data was discussed in Section 5.4. Hereafter, for simplicity the pressure differences will be referred to as the data.

For the data at radius A, $R = 15.68$ in., the effects of the side walls and struts are noted in the corrected data at about 17, 30, 50 and 65 msec. These correspond with positions I, M, A to B, and E in Figure 5.4, respectively. Referring back to the surface flow visualization of Figures 6.22-6.24, it can be seen that the attached flow regions (i.e. F to G and B to C in Figure 5.4) correspond to the pressure measurements at 0 to 7 and 51 to 57 msec (for instance). That the regions of lowest blade loading occur at the diagonals of the inlet as measured is, therefore, substantiated by the surface flow visualization. Likewise, the regions of highest blade loading at the leading edge occur at the sidewalls and in the wakes of the motor support struts. The effect of the motor support struts is seen dramatically in Figure 6.62 at about 33 msec in the form of the double peak for the uncorrected data. The effect of the correction procedure appears to lessen the second peak by about 10% as seen by comparison of Figures 6.62 and 6.65. The surface flow visualization and the pressure measurements can be compared further by contrasting Figure 6.23 with Figures 6.62-6.67. At about 6 msec in Figure 6.23 a the flow appears to be nicely attached on the blade suction side. From about 7 to 13 msec in Figures 6.23 b, c and d the surface flow patterns go through increasingly stalled patterns and at position H the stalled flow is evident as also seen in Figure 6.24. The flow region corresponds to that in Figures 6.62-6.67 that peak at about 18 msec (between positions I and J in Figure 5.4) and later at about 52 msec (approximately position B in Figure 5.4).

Comparison of the unsteady pressure measurements at position B ($R = 10.87$ in. in Figures 6.63 and 6.66 for the raw and corrected data, respectively) reveals the disappearance of the effects of the walls at 7 and 52 msec. Again, this corresponds to positions H and A in Figure 5.4. This bears out the inlet and surface flow visualizations in Figures 6.13-6.24 which showed the effects at the side walls are weaker in the $R = 11$ in. region than they are at $R > 15$ in. Also, note that the effects of the struts are more equal for radial position B than they were for the position A case. This means that the laboratory table effect on the measurements taken behind the struts at 62 msec in Figures 6.63 and 6.66 also

Table 6.2 Pressure tap locations as a fraction of chord from blade leading edge on the LP-36 fan; position A at R = 15.68 in., position B at R = 10.87 in. and position C at R = 7.67 in.

Radius (in.)	Distance from leading edge (in.)	Chord length (in.)	Fraction of chord
15.68	0.84	13.11	0.06
15.68	2.15	13.11	0.16
15.68	3.34	13.11	0.25
15.68	4.59	13.11	0.35
15.68	5.86	13.11	0.45
15.68	7.16	13.11	0.55
15.68	8.45	13.11	0.64
15.68	9.77	13.11	0.75
15.68	11.10	13.11	0.85
15.68	12.49	13.11	0.95
10.87	1.04	15.60	0.07
10.87	2.46	15.60	0.16
10.87	3.73	15.60	0.24
10.87	5.11	15.60	0.33
10.87	6.50	15.60	0.42
10.87	7.88	15.60	0.51
10.87	9.22	15.60	0.59
10.87	10.68	15.60	0.69
10.87	12.07	15.60	0.77
10.87	13.45	15.60	0.86
10.87	14.81	15.60	0.95
7.67	0.92	20.37	0.05
7.67	2.26	20.37	0.11
7.67	3.59	20.37	0.18
7.67	4.93	20.37	0.24
7.67	6.29	20.37	0.31
7.67	7.65	20.37	0.38
7.67	9.02	20.37	0.44
7.67	10.38	20.37	0.51
7.67	11.74	20.37	0.58
7.67	13.10	20.37	0.64
7.67	14.46	20.37	0.71
7.67	15.87	20.37	0.78
7.67	17.20	20.37	0.84
7.67	18.57	20.37	0.91
7.67	19.87	20.37	0.98



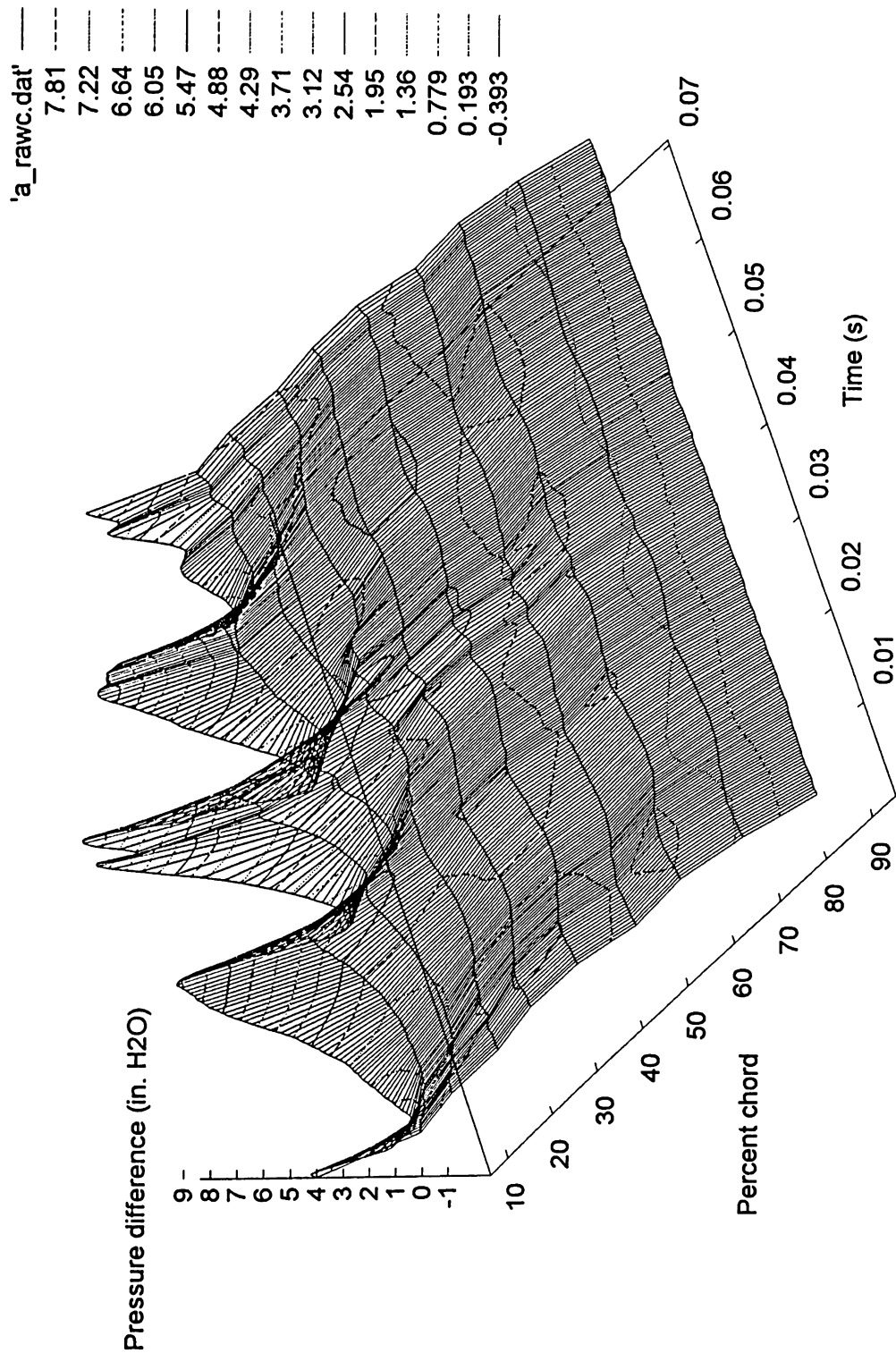


Figure 6.62 Uncorrected, "raw", unsteady pressure difference measurements at position A ($R = 15.68$ in.)

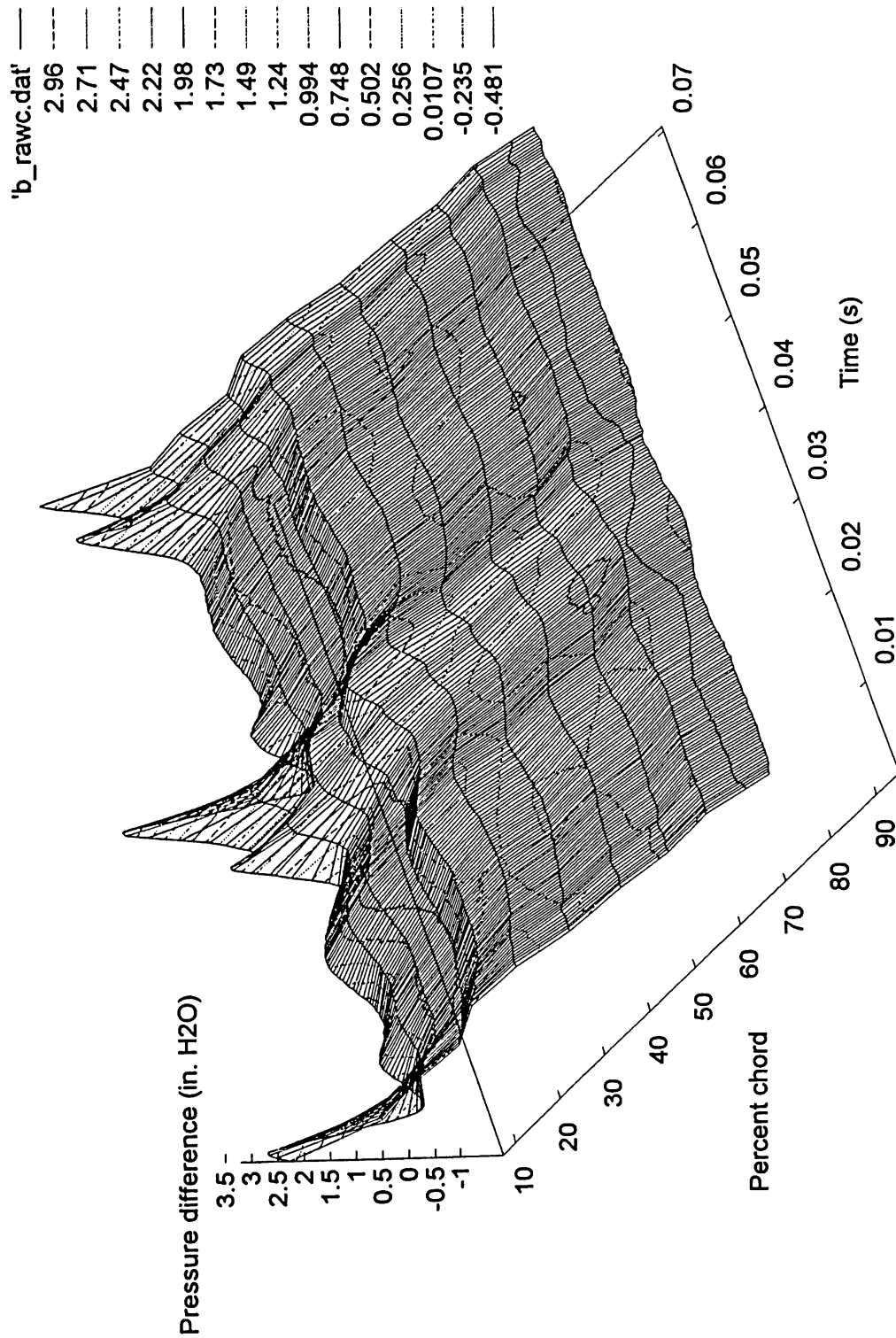


Figure 6.63 Uncorrected, "raw", unsteady pressure difference measurements at position B (R = 10.87 in.)

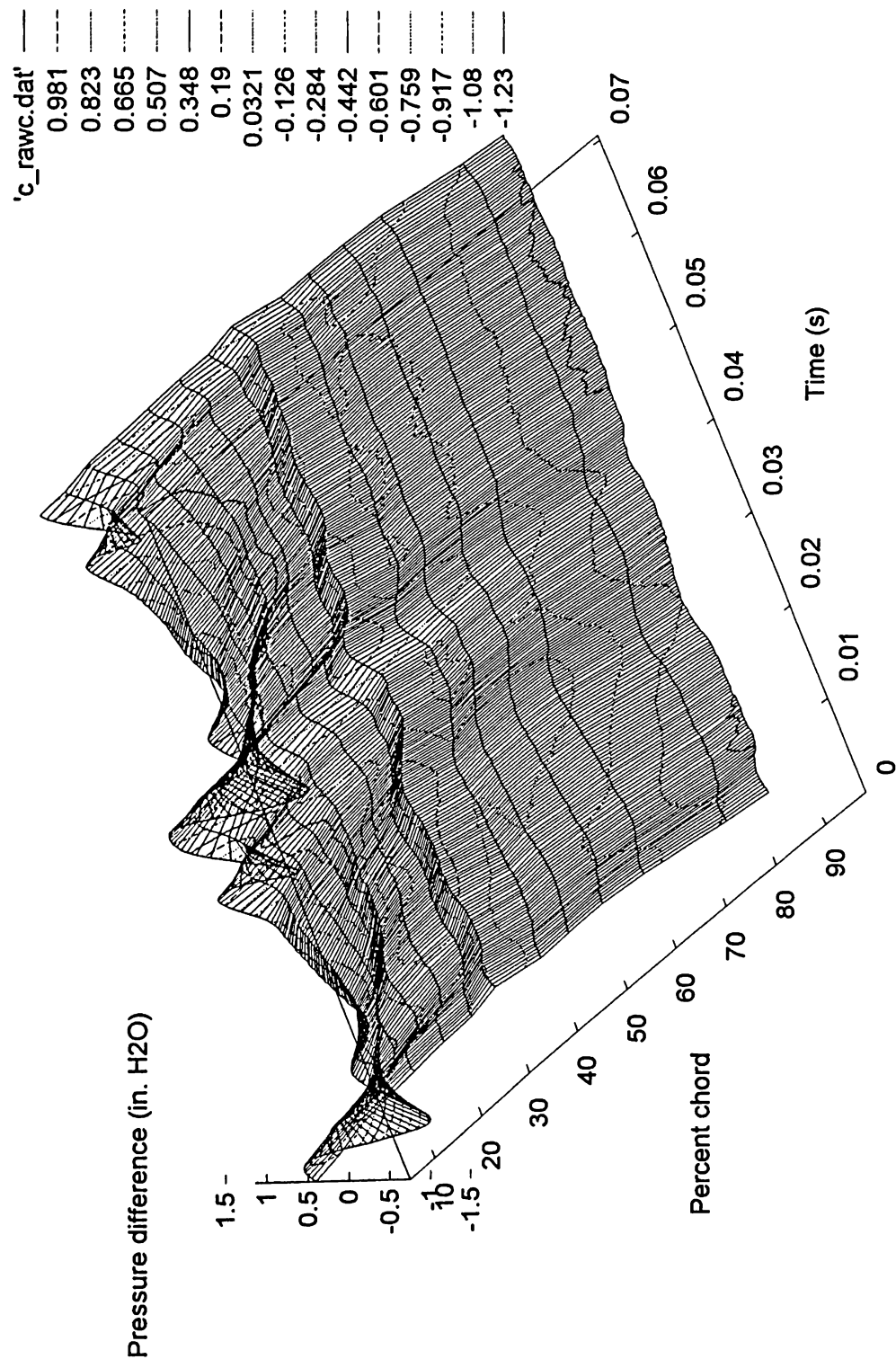


Figure 6.64 Uncorrected, "raw", unsteady pressure difference measurements at position C ($R = 7.67$ in.)

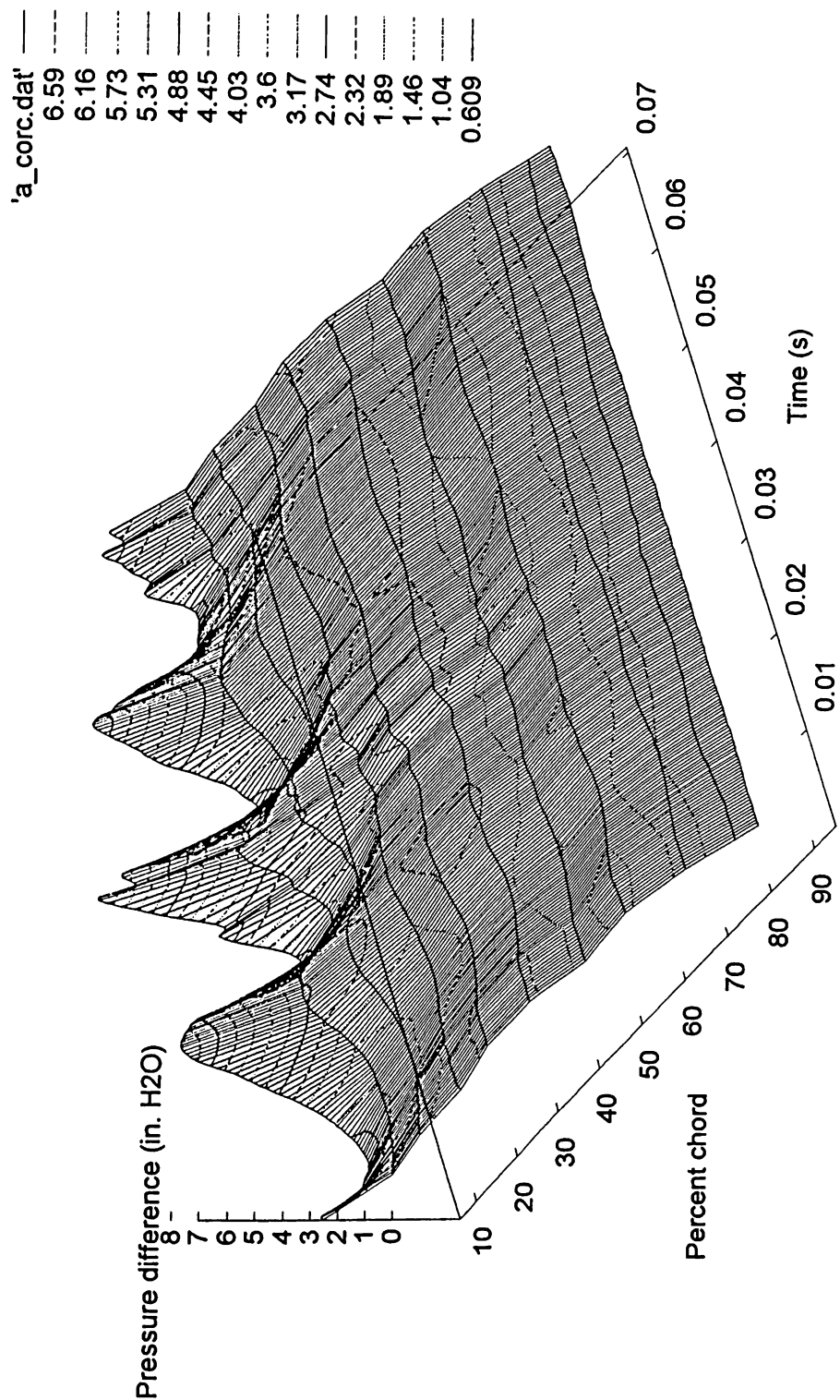


Figure 6.65 Unsteady pressure difference measurements at position A ($R = 15.68$ in.) corrected for tubing dynamic response

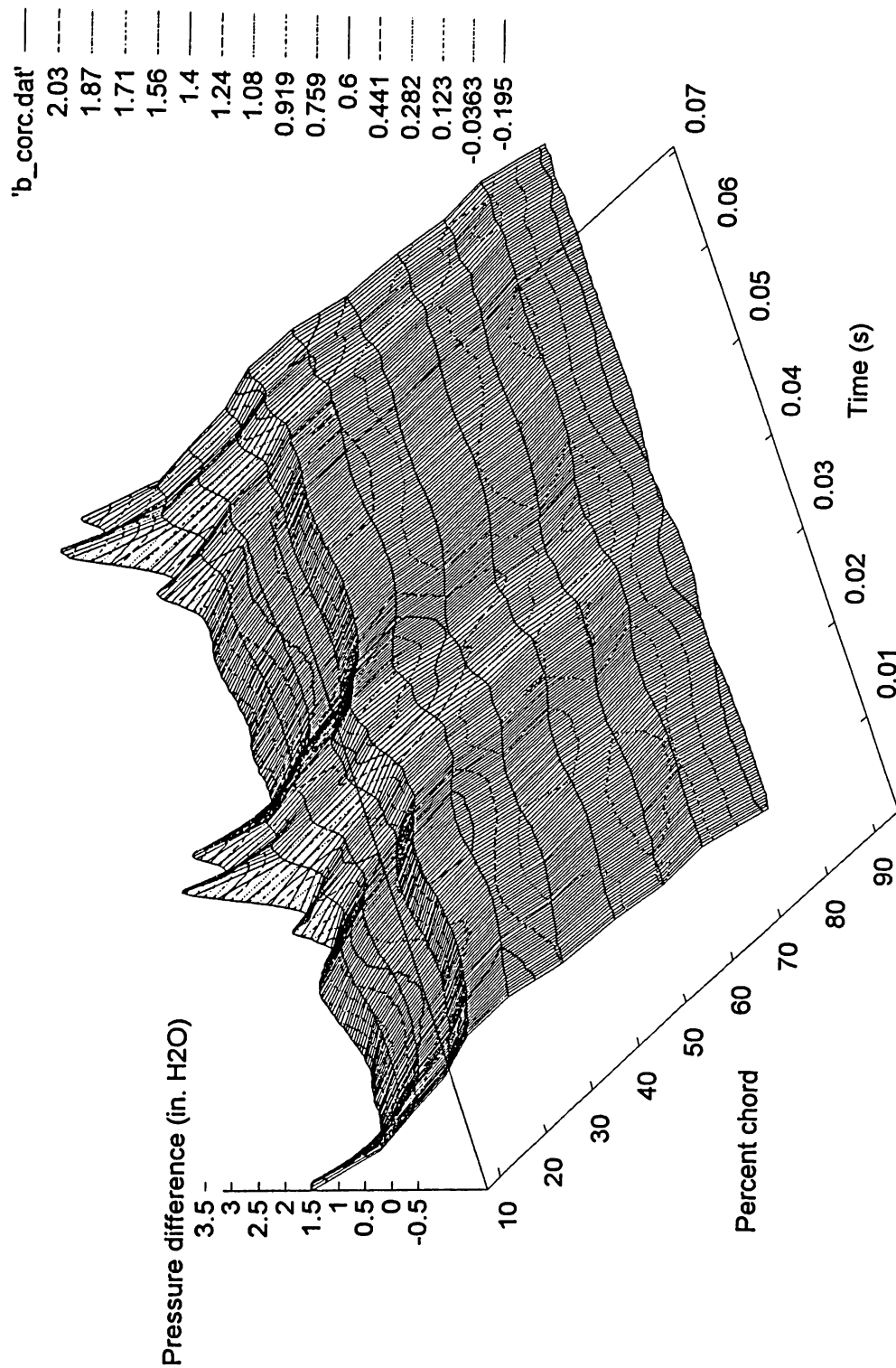


Figure 6.66 Unsteady pressure difference measurements at position B ($R = 10.87$ in.) corrected for tubing dynamic response

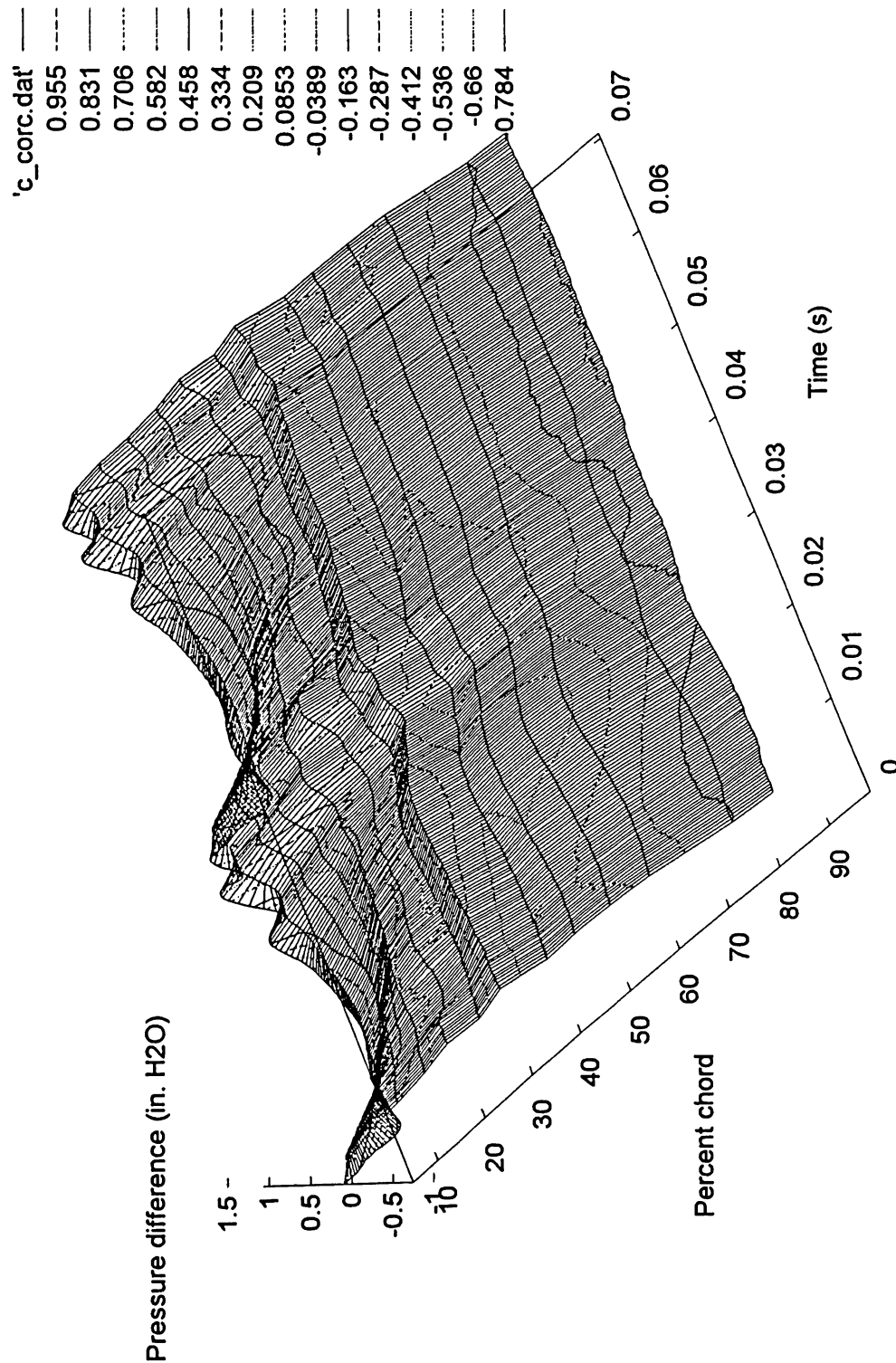


Figure 6.67 Unsteady pressure difference measurements at position C ($R = 7.67$ in.) corrected for tubing dynamic response

disappeared.

The surface tuft flow visualization in the region of radial position C ($R = 7.76$ in.) indicated from the separated flow pattern in Figures 6.27-6.29 that the blade section there experienced a negative angle of attack. This is borne out by the "raw" pressure difference data for this section shown in Figure 6.64 and also in Figure 6.67 for the corrected data. Again, no sidewall effect is seen in these figures. The motor support strut wakes are seen to lose their "sharp" effect and are seen approximately 4 msec earlier since that section of the blade "sees" the supports sooner than the blade tip.

There is, therefore, evidence from flow visualization of the LP-36 fan which supports the unsteady pressure measurements; The time at which a disturbance in the pressure occurs and the manner in which it occurs agree. The corrections to measured pressures are of small magnitude, account for the time lag in the system response caused by the tubing and improve the symmetry in the measurements. In short, outside of the correction for time lag, there is relatively little that the corrections change. The original data appears to be an adequate representation of the magnitudes of the unsteady blade loading.

6.5.1 Comparison of Measured and Computed Aerodynamic Loading

The major reason blade surface pressure measurements were made was to more thoroughly explore the application of the VLM to fan blades. However, as seen in the previous section, the measurements are in themselves interesting, and bring out understanding of the magnitude of the unsteady blade loading. It would be fortuitous should the steady flow modeled in FSF be in complete agreement with the real unsteady flow conditions. Therefore, the unsteady loading measurements and blade loading determined using the FSF program at the "free-air" condition will be compared in this section with this understanding.

The circumferentially averaged blade loadings (pressure differences) calculated from the unsteady measurements are presented in Figure 6.68. Circumferentially averaged values of loading for the "raw" data did not vary from the corrected data until the fifth significant figure, which is to be expected given the sinusoidal nature of the corrections. The overall loading increases from root to tip as expected. However, the averaged loading near the leading edge is higher for radial position B than A (surprising, considering the larger overall positive loadings experienced at position A). As can be seen in Figures 6.62-6.67, most of the unsteadiness in blade loading occurs over the leading 30% of the blade chord.

The post-processing of the VLM computations from FSF which are used to determine computed surface pressure differences were performed in two ways, via the Bernoulli equation from field point velocities and via the normal force on a

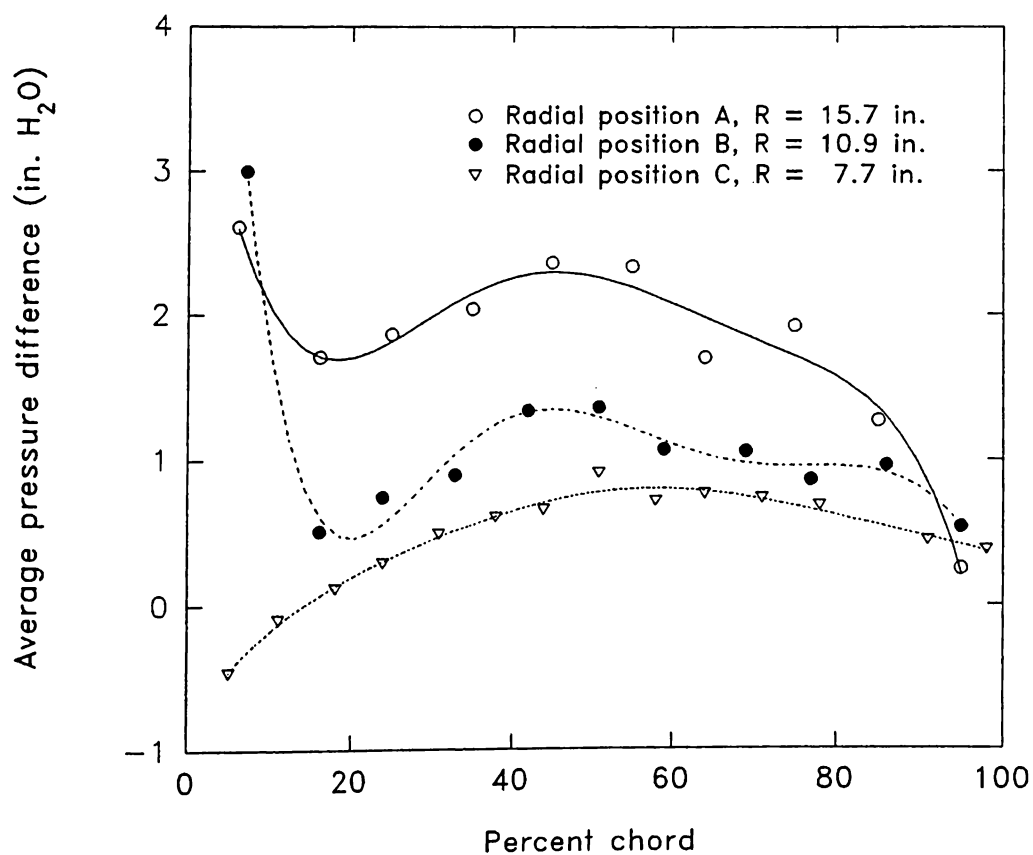


Figure 6.68 Circumferentially averaged blade pressure differences at the radial sections A, B and C at pressure tap chordwise locations

panel element divided by the panel area. Blade surface pressure differences at the three radial measurement locations were computed using the "Bernoulli" equation method and the "Element" method for 12 x 12 and 20 x 20 grids. These results are presented in Figures 6.69-6.71 for radial positions A, B and C, respectively. A single case of blade surface pressure difference using the "Element" method with the duct model and a 20 x 20 grid is also given in Figures 6.69-6.71 for each radial position and is identified in those figures as "Element with duct and 400 panels". There is a "hump" in the pressure difference data at 50% chord in the measures at each position; this "hump" diminishes at the smaller radii. No explanation for this hump has been devised.

The FSF pressure predictions for "Element with duct and 400 panels" appears to under predict the loading in all cases, agreeing with the observation that pressure rise is underpredicted for this case (see Figure 6.56). The disagreement is especially bad for the position A case as seen in Figure 6.69. Actually the influence of the duct model on the predicted pressure differences at positions B and C is small. For these reasons, the duct model results will not be examined further; the unducted results in Figures 6.69-6.71 are of greater interest.

Comparison of computed and measured pressure differences in Figure 6.69, reveals that the rise in the pressure difference as the leading edge is approached for the circumferentially averaged measurements is not predicted by any of the computed cases. This is due to the effects of the motor supports. Next, a circumferential position in the blade's rotation was sought where agreement between the FSF predictions and the measurements was good. This was found to be at approximately 10 msec as can be seen Figures 6.62-6.67, which correspond to the blade position between F and G (as seen in Figure 5.4) although similar measurement values are found at the three other symmetric, azimuthal positions. The agreement with the measured data from this azimuthal position (between F and G as seen in Figure 5.4) is in good agreement with predictions for the "144" and "400" panel cases with no duct regardless of the method of pressure difference calculations ("Bernoulli" or "Element").

At position B ($R = 10.87$ in.), computations made using the "Element" method for both the 144 and 400 panel discretizations under predict the loading by about 30% more than pressure difference computations made using the "Bernoulli" method. The computations of pressure difference made using the field point velocities and the "Bernoulli" method match the measurements within 0.2 in. H_2O (except at the "hump" discussed above) aft of the 0.3 chord fraction to the trailing edge. From the 0.3 chord fraction point to the leading edge, measurement and prediction using the "Bernoulli" method depart as seen in Figure 6.70. Also for this position, the 144 panel discretization appears to have reached a grid independent in as much as its prediction agrees with that of the 400 panel case.

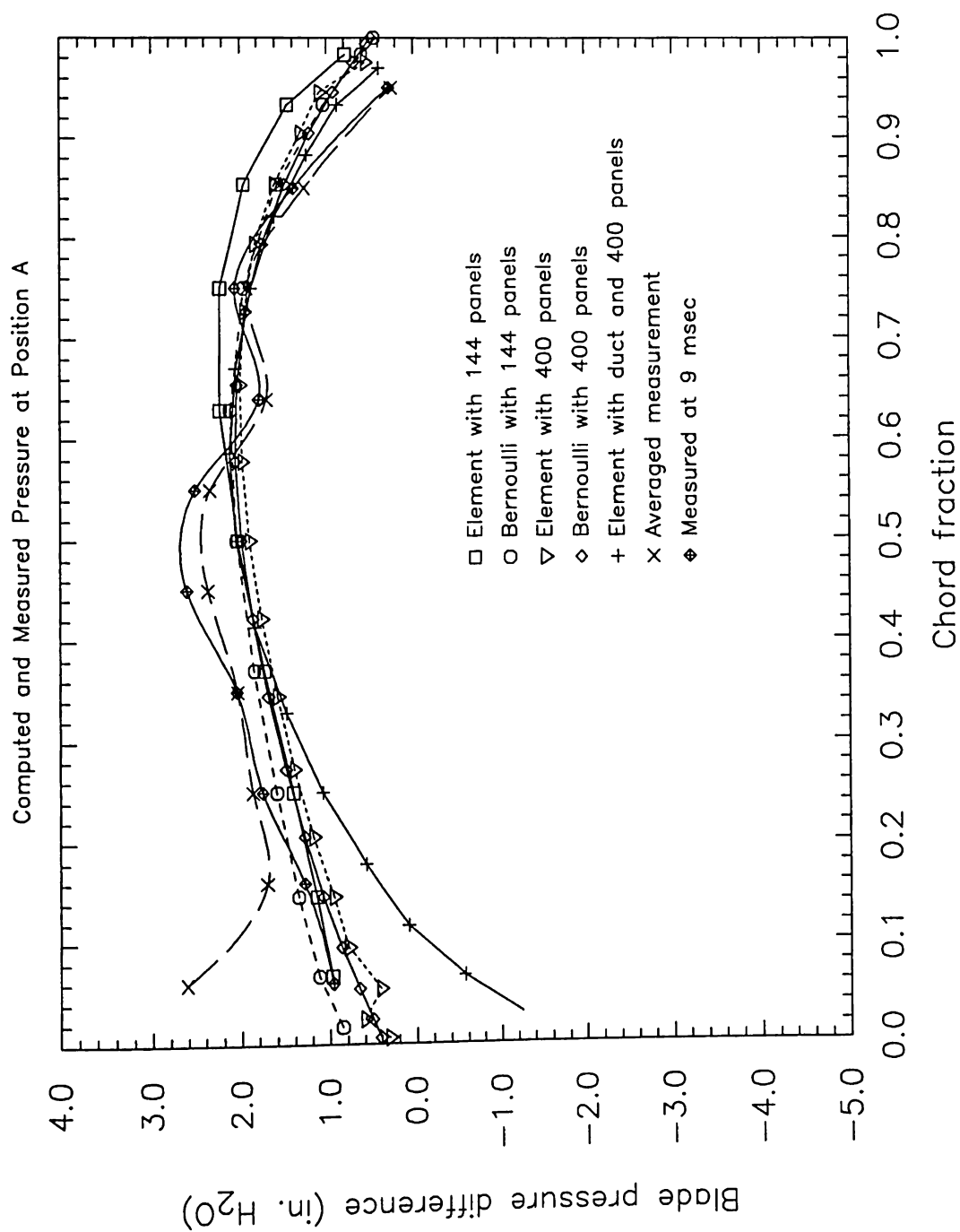


Figure 6.69 Comparison of measured computed pressure differences for the LP-36 fan at 850 rpm and "free-air" conditions at radial position A ($R = 15.68$ in.)

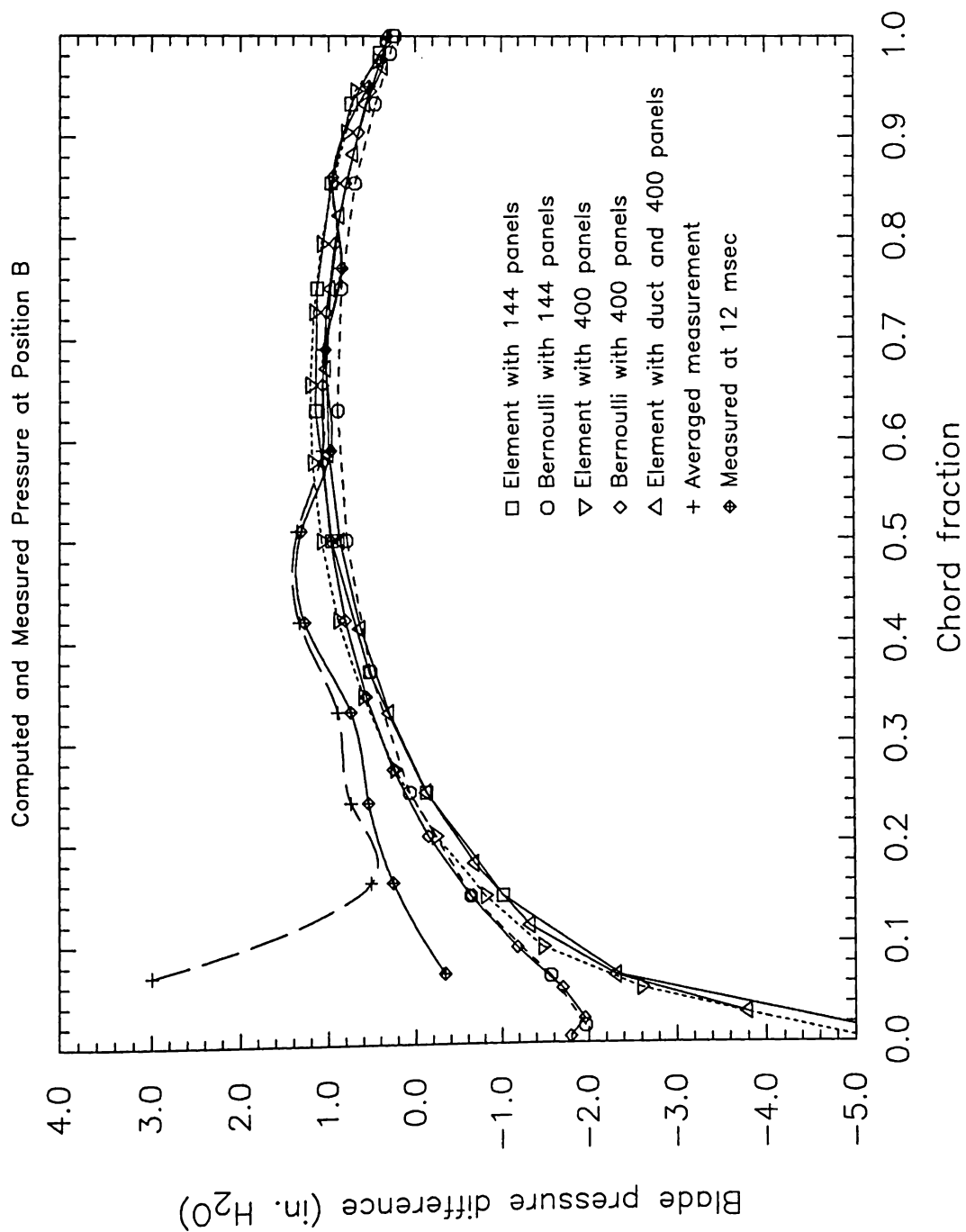


Figure 6.70 Comparison of measured computed pressure differences for the LP-36 fan at 850 rpm and "free-air" conditions at radial position B ($R = 10.87$ in.)

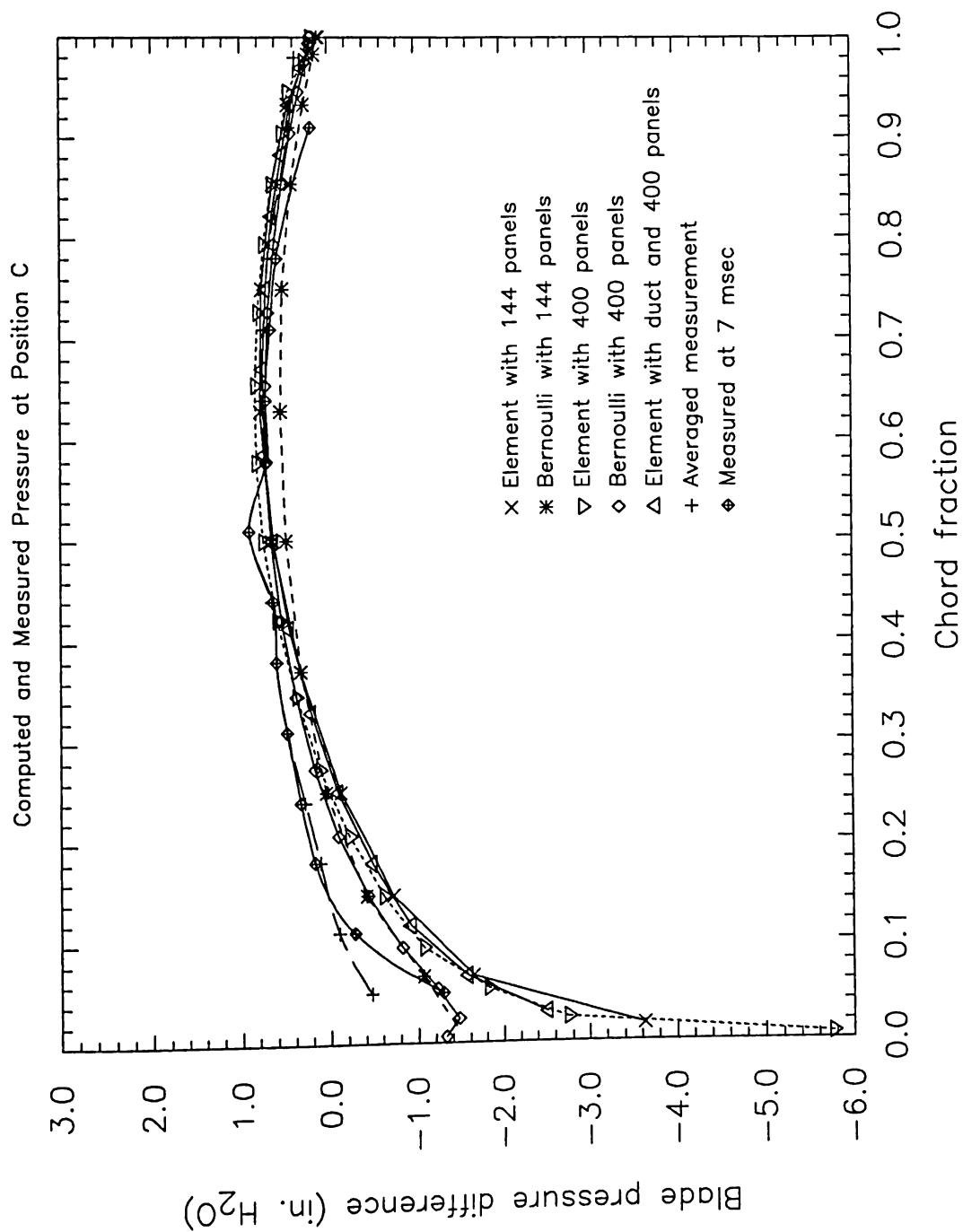


Figure 6.71 Comparison of measured computed pressure differences for the LP-36 fan at 850 rpm and "free-air" conditions at radial position C ($R = 7.67$ in.)

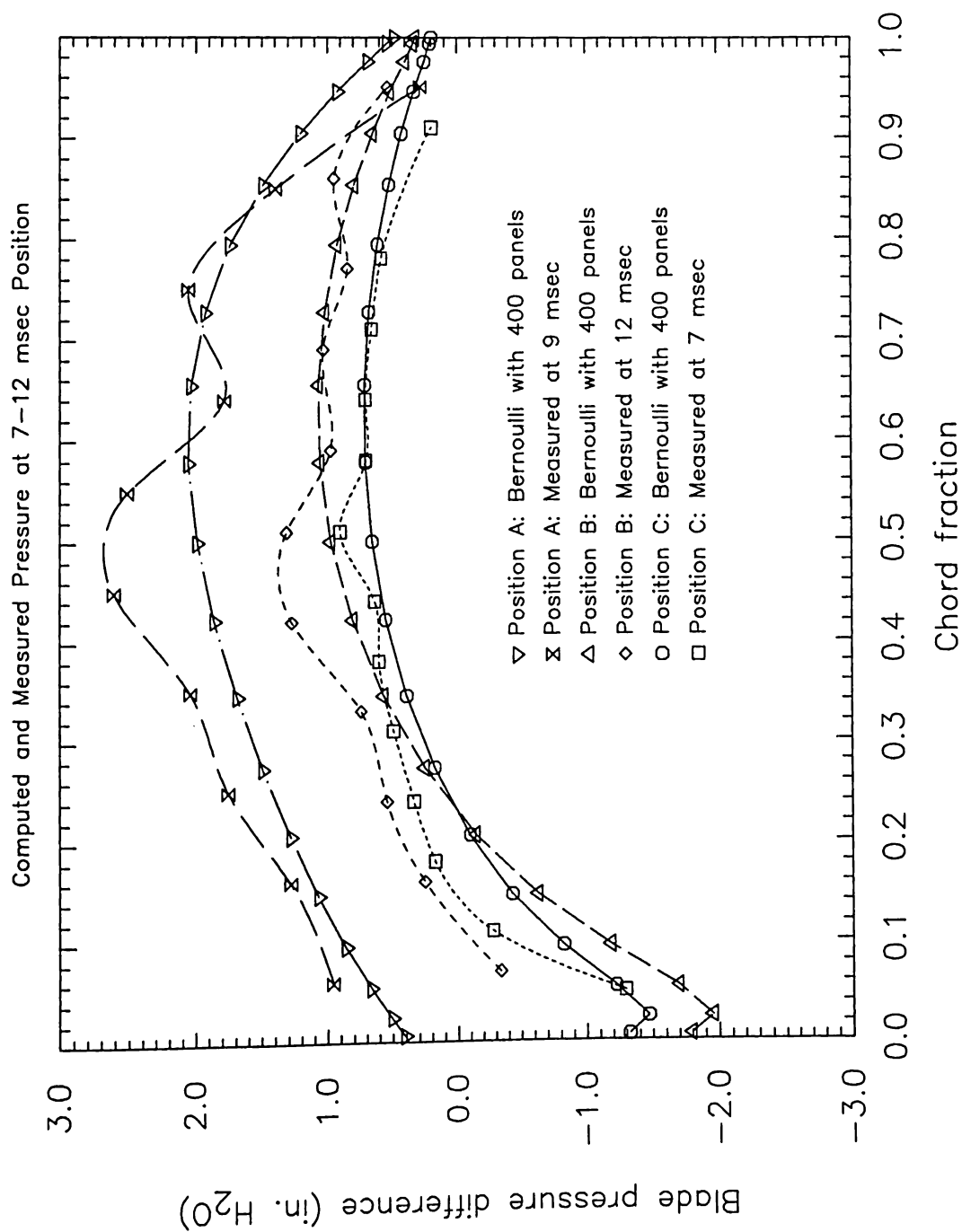


Figure 6.72 Measured pressure difference at azimuthal position (7-12 msec) compared with pressure predictions from FSF with a 400 panel (20 x 20) grid without duct at radial positions A, B and C

At radial position C ($R = 7.67$ in.), the comparison with the averaged measurement is, again, not as good as the measurement at the 7 msec point in the fan revolution period from just aft of 0.2 chord fraction to the leading edge. At the data point nearest the leading edge (0.03 chord fraction) the pressure data drops, agreeing with the predictions of the "Bernoulli" technique using both the 144 and the 400 panel grid. The predicted and measured drops at this point also agree in trend. Once again, the "Bernoulli" method does a slightly better job of predicting the pressure differences from the VLM than the "Element" method does.

Predicted versus measured blade pressure differences are in Figure 6.72 where measurements for the 7-12 msec azimuthal position is compared with predictions. The predicted "Bernoulli with 400 panels" data most consistently match the measurements. The remarkable agreement in predicting the trend in loading with radial position, especially over the back 50% of the blade chord is demonstrated. Considering the unsteadiness of the blade loading, the agreement is good. Also, the fact that prediction and measurement agree at the azimuthal position where the inlet flow is uniform suggests that the VLM accurately predicts blade loading for an axial-flow fan provided that the flow inlet conditions are uniform.

6.6 Conclusions and Recommendations

Flow visualization was used to visualize the flow pattern through an unducted LP-36 fan; a vortex ring was observed at the blade tip, covering the outer third of the blade span. Flow separation on the suction side of the blade was visualized by surface-tuft and surface oil flow techniques. The measured axial velocity profile in the inlet of the unducted fan slightly differed from that for the "typical" unducted fan profile discussed by Wallis (1983).

The inlet flow field was visualized at the "free-air" condition using vertical light sheets and helium bubble particles. Where the inlet flow was not disturbed by motor supports and wall/duct interactions, the velocity appeared to be mostly in the axial direction. Slight radial components were noticed for streaklines near the motor and tip. This guided the inlet profile hot-wire measurements made for the free-air condition. The measured inlet profile qualitatively agreed with the flow visualization and, when integrated, it agreed within 7% the volumetric flow determined from performance testing. Flow visualization on the ducted fan using surface tufts showed a variation in flow phenomena with azimuthal position. The surface tufts were used to estimate the tip vortex displacement (VLM code input parameter DISPN) from the trailing edge and helium bubble streaklines were used to determine the variation of wake contraction angle DCD with radius. Parameter studies using the VLM code at the "free-air" condition showed that values of DISPN and DCD which gave the best agreement between performance measurement and prediction were close to those estimated by flow visualization.

Considering that the fans studied operated in an unsteady condition due to inlet flow disturbances, the steady vortex-lattice method predicts magnitude and trends of performance variables surprisingly well. If one compares the predictive capability of PSF-2 as applied to ship propeller performance (in Figure 3.3) with the performance comparisons given in section 6.4, one sees comparable success in applying the VLM (PSF-2 and FSF) to axial-flow fans. The VLM should be considered as an analysis and design tool, since it has advantages over the blade element and cascade theory approaches. These advantages are that three-dimensional geometries incorporating twist, rake and sweep can be modelled. Such "exotic" blade geometries (recall Figure 3.2) have shown favorable performance and noise characteristics in ship and aircraft propeller work. The addition of a venturi duct model gave mixed results when comparing predicted and measured performance. This was, perhaps, due to the alignment of the duct trailing vortex elements with the axial direction, contrary to the helical geometry they actually follow as seen by flow visualization (see Figures 6.33-35).

The results of the pressure measurements, though at first sought for the purposes of code verification, are of interest in themselves. The measurement apparatus constructed and the technique used to extract the pressure difference across the blade is believed to be previously unreported as are resulting unsteady measurements that capture such effects as those of the motor support struts. There is, also, evidence from flow visualization of the flow through the fan which supports the unsteady pressure measurements; The time at which a disturbance in the pressure occurs and the manner in which it occurs agree. The results of the pressure measurement at an azimuthal position where the inlet is undisturbed agree in magnitude and trend with computations using the VLM. The major disagreement between the measured and predicted aerodynamic loading occurs near the leading edge. This type of disagreement is mentioned elsewhere in the literature as a drawback of the VLM (see discussion in Chapter 3 regarding comparison of Hess and Valarezo, 1985 and Kim and Kobayashi, 1984).

6.6.1 Recommendations for Future Work

It is recommended that a full-field solver be used to compute the flow through the LP-36 fan. Only after doing this can the advantages and trade-offs of the VLM and full-field solver be compared. An additional recommendation in this regard, is that the use of the VLM to provide an initial flow field to a full three-dimensional Navier-Stokes solver be explored with the goal of accelerating the full-field solver. In many finite volume CFD solvers, such as FLUENT, a rotating frame of reference problem often requires time consuming iterations. In the case of FLUENT, for instance, the developer's recommend first solving the problem without the rotating frame of reference followed by iterations where the rotational speed is gradually increased to the desired value. However, if one first solved the problem via a VLM computation and then computed the field point velocities for

the full field solver, the convergence of the full field solver might be accelerated. This process might even involve more levels of iteration between the VLM and the full-field solver where the full-field solver could feedback to the VLM the wake input parameters.

It is recommend that the computational ability of FSF be extend to fan installation problems where the interaction of the fan flow field within the context of a larger thermofluid system is important. For instance, the unsteady interaction of the motor support struts could be computed using an unsteady version of FSF. Unsteady VLM applications can be devised from steady computer codes for application in multistage and counter-rotating machines. The application of an unsteady VLM to the interaction of upstream disturbances is another advantage of continuing to pursue development of the VLM. It is recommended that the FSF program be used not only for analysis of design improvements but, also, used to provide a velocity flow fields for problems where the fan exhaust/wake may be of importance such as automobile engine and cooling fan wake interaction and fan/room ventilation flow fields.

There are a number of developments to the FSF program which might improve its agreement with measured performance data. It is recommended that an effort be made to develop a venturi duct model which uses either wake alignment or wake prescribed wake pitch rather than a "straight" axial-aligned trailing vortex elements. If possible, this improved duct model should also include modeling of the tip-gap effects, a topic of interest in its own right (Lakshminarayana, 1970). The importance of the wake input parameters has been established and discussed. Any future work on the treatment of the wake should be directed toward eliminating the need for these input parameters. A different wake alignment scheme employing "vortex chasing" needs to be explored. This method of alignment, though more computationally intensive, might eliminate the need for the wake parameters altogether. This effort might lead to a modified version of the Loukakis wake model currently used which would be more suitable for ventilation fans. Using FSF or some future modified version of FSF, it is recommended that post-processing with the PLOT-3D program be used to explore particle streakline and surface flow direction from the VLM output. These can compared with the flow visualization of the LP-36 fan surface flow as recorded in Appendix F.

One conclusion from this study has been the identification of large unsteady loading fluctuations on the fan blade caused by inlet disturbances. Certainly, better data for comparison with steady flow field solvers should be obtained by measurements of fan performance with motor mounting struts mounted downstream and a rounded box at the inlet to eliminate the side wall disturbances. Close attention to these effects may also improve the fan performance without even altering the blade geometry. It is recommended, therefore, that steady data be gathered for comparison.

If inlet flow disturbances are of importance, it is recommended that the unsteady blade pressure measurement system be used in real time to investigate the effects of motor mount configurations and inlet venturi shapes. Also, after construction of an accurate traversing mechanism, the pressure data acquisition system with strobe light can be used with the hot-wire anemometer to perform wake surveys. To provide more data for code verification, it is recommended that the unsteady pressure measurement system be altered to measure velocities (through the slip-rings) using a blade-mounted hot-wire anemometer (or with a laser-doppler anemometer) on the blades or in the inter-blade region while the fan is operating. Should more experimental data be required for comparison with results from full-field viscous flow solvers, it is advised that a pressure sensitive paint chemical be tested for applicability and a liquid crystal shear stress indicator ought to be used for flow visualization studies using the strobe light.

It is recommended that future performance, measurement and flow visualization testing be performed in the same facility to enable more consistent and more uniform results. It is recommended that the variation of inlet velocity profile with blade geometry characteristics (planform, tip shape, sweep, and rake) and operating point be acquired. Development of a "smart" blade with controllable flow control devices such as leading edge slots to control flow separation inherent in thin-plate blades should, also, be undertaken.

The final goal of most research and development projects is to produce some improved product. In this regard, a recommendation for future design advancements is the implementation of a design optimization code or an expert system with both an experimental and computational knowledge base. An attractive feature of the VLM is relatively fast run-time compared to full-field solvers. This makes the VLM ideal for design iterations and optimization. However, there are many complexities within the flow field not captured by the VLM and this should be accounted for by an experimental knowledge base in any advanced design system.

APPENDIX A

THIN-AIRFOIL THEORY

A brief discussion of thin-airfoil theory is given in this appendix. More detailed treatment of the thin-airfoil theory is found in Anderson (1984) and Lan (1988), but this discussion only overviews the salient points of the theory. Lan's development is used here.

Consider an airfoil of small thickness in relation to its length with a small camber. Define upper and lower surfaces of the airfoil (shown in Figure A.1) as

$$\begin{aligned} \text{upper surface, } z_u &= f_u(x) \\ \text{lower surface, } z_l &= f_l(x) \end{aligned} \quad (\text{A.1})$$

The x coordinate is the chord axis formed by the nose-to-tail line of the airfoil. The freestream velocity v_∞ can then be related to a velocity potential Φ_∞ as

$$\Phi_\infty = x v_\infty \cos(\alpha) + z v_\infty \sin(\alpha) \quad (\text{A.2})$$

where α is the angle of attack of the airfoil. Using potential theory, the overall velocity potential Φ of the flow in the presence of an airfoil can be written as the sum of the freestream potential Φ_∞ and a velocity potential ϕ due to small perturbation velocities caused by the presence of the airfoil as

$$\begin{aligned} \Phi &= \Phi_\infty + \phi(x, z) \\ \Phi &= x v_\infty \cos(\alpha) + z v_\infty \sin(\alpha) + \phi(x, z) \end{aligned} \quad (\text{A.3})$$

The derivatives of the total velocity potential will produce velocities as

$$\begin{aligned} v_x &= \frac{\partial \Phi}{\partial x} = v_\infty \cos(\alpha) + \frac{\partial \phi}{\partial x} \\ v_z &= \frac{\partial \Phi}{\partial z} = v_\infty \sin(\alpha) + \frac{\partial \phi}{\partial z} \end{aligned} \quad (\text{A.4})$$

Writing the perturbation velocities u and w in place of the derivatives of the perturbation potential with respect to x and z , respectively, and using the assumption of small angle of attack α from Equation (A.4), one has

$$\begin{aligned} v_x &\approx v_\infty + u \\ v_z &\approx v_\infty \alpha + w \end{aligned} \quad (\text{A.5})$$

where u and w are the components of the induced velocity, a perturbation in the flow caused by the airfoil. Blowing or suction at the surface will not be

considered, but could be added at the surface. Hence there is a flow tangency condition at the airfoil surface. For the upper surface this gives the expression

$$\frac{dz_u}{dx} = f'_u(x) = \left[\frac{v_z}{v_x} \right]_{\text{upper surface}} = \frac{v_\infty \alpha + w(x,z)}{v_\infty + u(x,z)} \quad (\text{A.6})$$

Using the assumptions of small perturbations in simplifying the binomial expansion of the final result in Equation (A.6), the flow tangency condition becomes

$$\frac{v_\infty \alpha + w(x,z)}{v_\infty + u(x,z)} = \left[\alpha + \frac{w(x,z)}{v_\infty} \right]_{\text{upper surface}} \quad (\text{A.7})$$

By using a Taylor series expansion, the second term on the right hand side of Equation (A.7) can be written in terms of the downwash about the chord line ($z=0$) as

$$\left[\alpha + \frac{w(x,z)}{v_\infty} \right]_{\text{upper surface}} = \alpha + \left[w(x,0) + \frac{\partial w(x,0)}{\partial z} z_u + \dots \right] \frac{1}{v_\infty} = \alpha + \frac{w(x,0)}{v_\infty} \quad (\text{A.8})$$

after omitting higher order terms. The resulting tangency condition using these simplifications can be constructed from Equations (A.5) and (A.7) as

$$f'_u(x) = \alpha + \frac{w(x,0)}{v_\infty} \quad (\text{A.9})$$

This boundary condition is called the mean surface approximation since it is not applied on the actual airfoil surface. It will work well for thin-plate fan blades, however. Hence, one method of developing the surface boundary condition for the **induced** velocities has been derived. It can be shown that Equation (A.9) holds for the lower surface as well. Far away from the surface under consideration, the induced velocities must vanish.

By arbitrarily splitting the induced velocity w into two components (w_1 and w_2) and adding and subtracting $\frac{1}{2}f'_l$, the tangency condition becomes

$$\alpha + \frac{w_1 + w_2}{v_\infty} = \frac{1}{2}[f'_u(x) + f'_l(x)] + \frac{1}{2}[f'_u(x) - f'_l(x)] \quad (\text{A.10})$$

The tangency condition Equation (A.10) can now be conveniently split into two

conditions, one of which is satisfied on the camber (mean camber line) slope as

$$\alpha + \frac{w_1}{V_\infty} = \frac{1}{2}[f_u'(x) + f_l'(x)] = \frac{dz_c}{dx} \quad (A.11)$$

where the mean camber is $z_c = \frac{1}{2}[f_u(x) + f_l(x)]$, and the other of which is satisfied by the thickness problem condition

$$\frac{w_2}{V_\infty} = \frac{1}{2}[f_u'(x) - f_l'(x)] = \frac{dz_t}{dx} \quad (A.12)$$

where the mean camber is $z_t = \frac{1}{2}[f_u(x) - f_l(x)]$. After looking in a similar manner at the lower surface, the problem of potential flow in the freestream can be divided into the solution for two velocity potentials. The total potential is then the superposition of the potential due to the thickness problem and the potential problem due to camber. The camber problem is the only solution that would be of interest in the study of plate bladed fans. The camber problem for potential flow about a thin airfoil is

equation for solution of perturbation velocity potential - $\nabla^2 \phi_{\text{camber}} = 0$

$$\text{upper surface boundary conditions} - \alpha + \frac{w_1}{V_\infty} \equiv \left[\frac{dz_c}{dx} \right]_{\text{upper surface}}$$

$$\text{lower surface boundary conditions} - \alpha + \frac{w_1}{V_\infty} \equiv \left[\frac{dz_c}{dx} \right]_{\text{lower surface}}$$

$$\text{far from the surface} - \frac{\partial \phi_c}{\partial x}, \frac{\partial \phi_c}{\partial z} \rightarrow 0 \quad (A.13)$$

The simplifications used and the linearization of the angle of attack ($\sin \alpha \approx \alpha$) leads to a formulation that does not predict pressures well at large angles of attack (i.e. greater than $\pm 8^\circ$ as seen in Anderson (1984, Figure 4.20, p.210). The sketch in Figure A.1 illustrates the concept of decomposing the potential flow problem into the camber and thickness problems.

From Equation (A.13) it is seen that the boundary condition on the lifting surface implies that the induced velocity w is continuous across the mean camber surface. Assuming incompressible flow, the Bernoulli equation for the flow about the mean camber surface can be written as

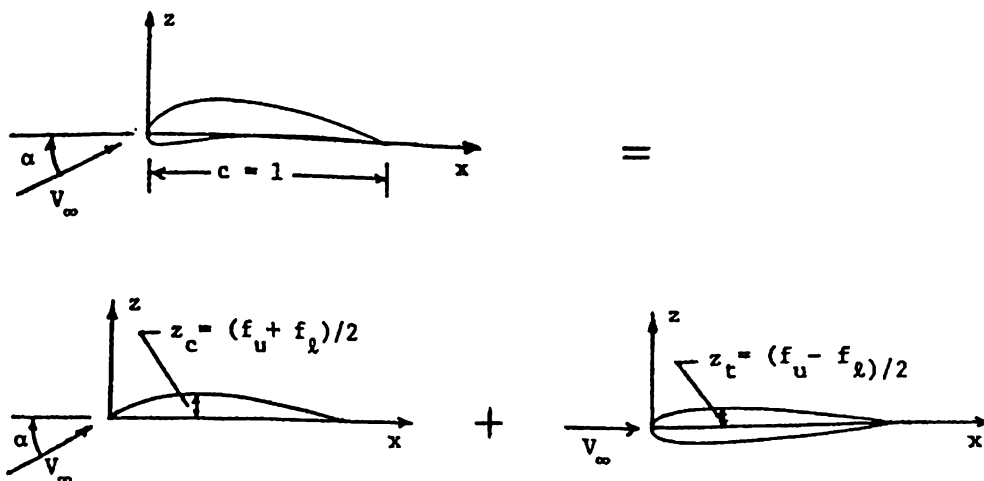


Figure A.1 Concept of decomposition of the potential flow problem into camber and thickness problems (Lan, 1988, p. 65)

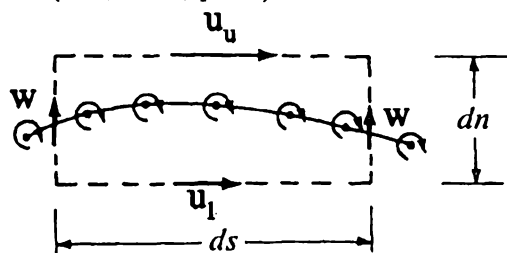


Figure A.2 The cambered surface with elemental vorticity γds (Anderson, 1984, p.196)

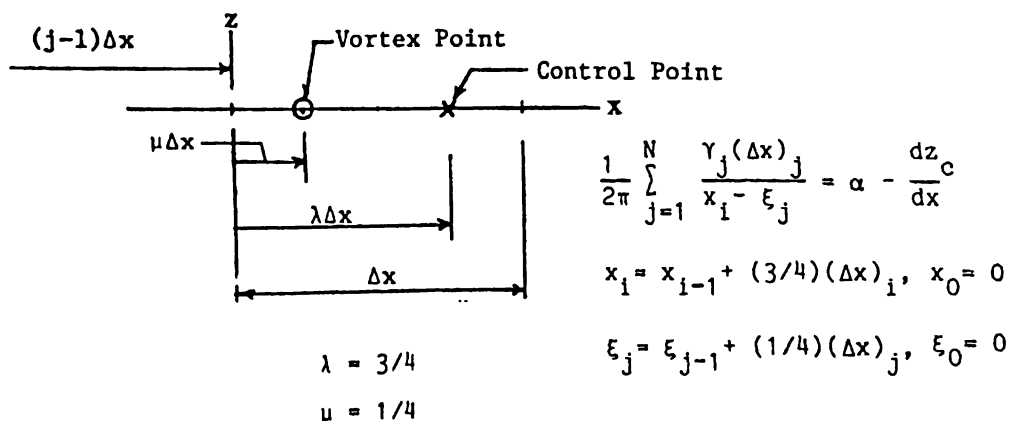


Figure A.3 Locations of vortex and control points in the VLM (Lan, 1988, p.73)

$$P_u + \frac{\rho}{2} [(v_\infty + u_u)^2 + (v_\infty \alpha + w_u)^2] = \quad (A.14)$$

$$P_l + \frac{\rho}{2} [(v_\infty + u_l)^2 + (v_\infty \alpha + w_l)^2]$$

where the assumption of small α has been used. Employing the fact that $w_u = w_l$, rewriting and expanding Equation (A.14) and neglecting products of induced velocities, the equation is linearized to

$$P_l - P_u = \frac{\rho}{2} [2v_\infty(u_u - u_l) + u_u^2 - u_l^2] \approx \rho v_\infty(u_u - u_l) \quad (A.15)$$

If the cambered surface, shown in Figure A.1, is generating lift, it can be considered to generate a circulation Γ defined as

$$\Gamma = \oint \vec{v} \cdot d\vec{s} \quad (A.16)$$

If the closed contour of integration is a rectangular box enclosing the airfoil of elemental vorticity $d\Gamma = \gamma ds$ (see Figure A.2), then

$$d\Gamma = \gamma ds = u_u ds - u_l ds \quad (A.17)$$

From Equations (A.15) and (A.17), it can be seen that a vorticity density γ can be used to represent velocity or pressure discontinuities at a surface by

$$\gamma = u_u - u_l = \frac{(\Delta P)}{\rho v_\infty} \quad (A.18)$$

where ΔP is the pressure difference between the upper and the lower surface. The pressure difference is responsible for generating lift on an airfoil, or generating pressure rise across and air flow through an axial flow fan.

Using the concept of a point vortex as developed in flow singularity theory, the stream function about such a singularity is

$$\psi = \frac{d\Gamma}{2\pi} \ln R \quad (A.19)$$

where $d\Gamma = \gamma ds$ is the strength of the point vortex, and R is the distance from the point vortex center. By the definition of the stream function, the differential velocity dw induced by such an elemental vortex is

$$dw = -\frac{\partial\psi}{\partial R} = -\frac{d\Gamma}{2\pi R} = -\frac{\gamma ds}{2\pi R} \quad (A.20)$$

The velocity $w(x, 0)$ induced by a vortex distribution on a straight line segment (as shown in Figure A.3) aligned on the x -axis, where $z = 0$, is found from Equation (A.20) to be

$$w(x,0) = -\frac{1}{2\pi} \int_0^1 \frac{\gamma(\xi)d\xi}{(x-\xi)} \quad (A.21)$$

where ξ is the location of the vortex of elemental strength γds , x is the point at which the induced velocity is evaluated, the chord length has been normalized to unity in the integration limits, and R is replaced by

$$R = \sqrt{(x-\xi)^2 + z^2} \quad (A.22)$$

Having developed an expression for the induced velocity at the mean camber line (of a straight line segment on the x -axis), the camber line boundary condition, that the flow is tangent to it (see Equation (A.13)), is written as

$$\alpha + \frac{w(x,0)}{v_\infty} = \alpha - \frac{1}{2\pi v_\infty} \int_0^1 \frac{\gamma(\xi) d\xi}{(x-\xi)} = \frac{dz_{\text{camber}}}{dx} \quad (A.23)$$

Equation (A.23) can then be cast in a form known as the fundamental equation of thin-airfoil theory, which is given by

$$\frac{1}{2\pi} \int_0^1 \frac{\gamma(\xi) d\xi}{(x-\xi)} = v_\infty \left[\alpha - \frac{dz_{\text{camber}}}{dx} \right] \quad (A.24)$$

The integral Equation (A.24) can be solved by applying a transformation (Anderson, 1984, p.212)

$$x = \frac{1}{2} (1 - \cos\theta) \quad \xi = \frac{1}{2} (1 - \cos\theta') \quad (A.25)$$

where the limits of integration are then from $\theta' = 0 \rightarrow \pi$. Then representing γ by a trigonometric series that satisfies the Kutta condition. The coefficients of the series are then determined in such a way that the camber line is a streamline of the flow, and are dependent on α and dz_c/dx . Making the transformation and using Equation (A.25) in Equation (A.24), it is found that

$$\frac{1}{2\pi} \int_0^\pi \frac{\gamma(\theta) \sin \theta}{\cos \theta - \cos \theta_0} d\theta = v_\infty \left[\alpha - \frac{dz_{\text{camber}}}{dx} \right] \quad (A.26)$$

Which leads to Anderson's solution in series form as given by

$$\gamma(\theta) = 2 v_{\infty} \left(A_0 \frac{1 + \cos \theta}{\sin \theta} + \sum_{n=1}^{\infty} A_n \sin (n \theta) \right) \quad (\text{A.27})$$

where the values of A_n for $n = 0, 1, 2, 3, \dots$ must be determined so that the camber line is a streamline to the flow. The results for the values of A_n are given by Anderson (1984), and only the general direction of the solution is given here. It is more interesting to examine Lan's presentation of the derivation.

Lan (1988) shows that the singular integral equation, Equation (A.26) can be exactly solved by isolating the unknown function $\gamma(\xi)$ by using Söhnngen's inversion formula¹. Then

$$\gamma(x) = -\frac{2 v_{\infty}}{\pi} \left[\frac{1-x}{x} \right]^{1/2} \int_0^1 \left[\alpha - \frac{dz_c}{dx} \right] \left[\frac{\xi}{1-\xi} \right]^{1/2} \frac{d\xi}{x-\xi} \quad (\text{A.28})$$

A classical solution for the γ distribution on a flat plate can be obtained by use of the transformations in Equation (A.25) with Equation (A.26) where there is no camber ($dz_c/dx = 0$). This solution is lengthy and involves the solution of the integral by Glauert's formula. The final result (Lan, 1988, p.67) is given by

$$\gamma(x) = 2v_{\infty} \alpha \left(\frac{1-x}{x} \right)^{1/2} \quad (\text{A.29})$$

Recall that this discussion was for small α with a normalized chord length. Without making those assumptions, Equation (A.29) would appear as

$$\gamma(x) = 2v_{\infty} \sin \alpha \left(\frac{c-x}{x} \right)^{1/2} \quad (\text{A.30})$$

¹ If $\gamma(x)$ is continuous on $0 < x < 1$, then the solution to

$$\frac{1}{2\pi} \int_0^1 \frac{\gamma(\xi) d\xi}{(x-\xi)} = h(x)$$

can be found from

$$\gamma(\xi) = -\frac{2}{\pi} \left[\frac{1-x}{x} \right]^{1/2} \left[\int_0^1 h(\xi) \left[\frac{\xi}{1-\xi} \right]^{1/2} \frac{d\xi}{x-\xi} \right] + \frac{C}{[x(1-x)]^{1/2}}$$

where C must be 0 at the trailing edge, as γ must be finite.

which is an analytic expression for the pressure loading of the plate in terms of γ .

The development thus far has been one of thin-wing theory, and has shown that the effects of blade loading (the problem of finding γ over an arbitrary mean camber line) and thickness can be treated separately. For the thin, flat plate blading of the fans studied, the solution of the loading in the manner described by placing a singularity distribution of γ on the mean camber line works well, except near the leading edge where a singularity occurs as $x \rightarrow 0$ in Equation (A.28).

Generally, Equations (A.24) and (A.26) cannot be analytically solved for an arbitrary camber shape; a numerical method must be used. A straight forward technique is the VLM method. In Figure A.3 is given a representation of a VLM element for two-dimensional flow briefly summarized as follows. The VLM method is based on the "three-quarter-chord theorem", placing a discrete vortex at the 1/4 chord point and placing a control point at the 3/4 chord point where the tangency condition of Equation (A.24) is applied, yields the exact circulation for a flat plate in parallel flow. Using x_i as control points, ξ_j as the locations of the discrete vortices and N as the total number of panels (sections containing the singularity and the control point), the formulation can be shown to be (Lan, 1988)

$$\frac{1}{2\pi} \sum_{j=1}^N \frac{\gamma_j(\Delta x)_j}{(x_i - \xi_j)} = v_\infty \left[\alpha - \frac{dz_{\text{camber}}}{dx} \right] \quad (\text{A.31})$$

where

$$\begin{aligned} x_i &= x_{i-1} + \frac{3}{4} (\Delta x)_i \quad \text{and} \quad x_0 = 0 \\ \xi_j &= \xi_{j-1} + \frac{1}{4} (\Delta x)_j \quad \text{and} \quad \xi_0 = 0 \end{aligned} \quad (\text{A.32})$$

which are illustrated in Figure A.3. This requires a solution of a system of linear algebraic equations for γ_j . Following the solution of the γ distribution, pressure coefficients and loadings can be computed using the Kutta-Joukowski law. The VLM does not give good results for pressure distributions near the leading and trailing edges due to the singularities at those positions not having been taken into account. These problems are reduced by using a cosine chordwise spacing arrangement which resolves the solution better at those points. Lan (1974) showed that by using a cosine spacing of discretization of Equation (A.24) (called the quasi-vortex-lattice method or QVLM) over the chord line, the leading edge suction force can be precisely computed.

APPENDIX B

PRESSURE DATA ACQUISITION PROGRAM

The data acquisition program for the pressure measurements made using the HP 54601A oscilloscope is given below in the Microsoft QuickBASIC language.

```

'
'      DATA ACQUISITION PROGRAM FOR FAN SURFACE PRESSURE DATA
'      LAST MODIFIED: by R Hardin 2/5/93
'
DECLARE SUB initialize ()
DECLARE SUB getit ()
DECLARE SUB saveit ()
DECLARE SUB retrieveit ()
DECLARE SUB graphit ()
DECLARE SUB outdat ()
DECLARE SUB enter (number!)
'
' Filename : fan_2.BAS
'
DIM SHARED preamble!(10)      'variable holding the preamble data
DIM SHARED waveform%(4000)    'variable holding the waveform data
DIM SHARED preamble2!(10)     'variable holding the preamble data
DIM SHARED waveform2%(4000)    'variable holding the waveform data
DIM SHARED V(4000)
DIM SHARED TIME(4000)
DIM SHARED Vtrig(4000)
DIM SHARED TIMEtrig(4000)

DIM SHARED lf$                'will be defined as LF char
'DEFINE VARIABLES
lf$ = CHR$(10)                ' define the LF char

wish$ = "?"

DO
PRINT "ENTER COMMAND ('?' FOR HELP, AND USE ONLY CAPITAL LETTERS)"
INPUT wish$

IF wish$ = "?" THEN
PRINT "LIST OF COMMANDS..."
PRINT "      INIT      - INITIALIZES COM PORT AND TRIGGER"
PRINT "      GET       - GET THE WAVE FORM, PICK CHANNEL"
PRINT "      SAVEBIN    - SAVE PREAMBLE AND WAVE FORM DATA TO A BINARY"
PRINT "      FILE"
PRINT "      RETRIEVE   - RETRIEVE THE DATA FROM A BINARY FILE"
PRINT "      GRAPH      - GRAPH THE RAW DATA CURRENTLY ACQUIRED"
PRINT "      SAVE       - SAVES THE VOLTAGE AND TIME DATA TO FILE IN"
PRINT "      ASCII"
PRINT "      ?         - DISPLAYS THIS SCREEN"
END IF

IF wish$ = "INIT" THEN CALL initialize      'initialize interface and scope
IF wish$ = "GET" THEN CALL getit           'get waveform from scope
IF wish$ = "SAVEBIN" THEN CALL saveit      'save waveform to a file
IF wish$ = "RETRIEVE" THEN CALL retrieveit 'retrieve waveform from file
IF wish$ = "GRAPH" THEN CALL graphit      'display the waveform data
IF wish$ = "SAVE" THEN CALL outdat        'save voltage and time data

LOOP UNTIL wish$ = "QUIT"

'PRINT "Press <enter> to quit...";
'LINE INPUT dummy$
END

```

```

SUB enter (number!)
*****
' This routine will read a real number from the RS-232 port defined as file
' #1. Either comma or LF will be treated as delimiter
*****
quit = 0
msg$ = ""
DO
    ' skip the leading LF and comma
    DO
        ch$ = INPUT$(1, #1)
        IF ch$ <> lf$ AND ch$ <> "," THEN
            ' get a byte from RS-232 port
            ' LF and comma are separators
            msg$ = msg$ + ch$
            ' append byte to string
        ELSE
            quit = 1
        END IF
    LOOP UNTIL quit = 1
LOOP UNTIL LEN(msg$) <> 0
number = VAL(msg$)
' until comma or LF is found
' until valid content is found
' convert the string into number
END SUB

SUB getit
PRINT "Waveform Data is being transferred to PC ..."
PRINT
PRINT
PRINT #1, ":waveform:points 1000"; lf$; 'get 1000 points from scope
PRINT #1, ":acquire:type AVERAGE"; lf$; 'set acquire to be normal
PRINT #1, ":ACQUIRE:COUNT 256"; lf$; 'take the average of 256 sweeps
PRINT #1, ":acquire:complete 100"; lf$; 'get data until 100% completion

PRINT "ENTER WHICH CHANNEL TO ACQUIRE FROM (1 OR 2)"
INPUT PORT
IF PORT = 1 THEN PRINT #1, ":waveform:source chan1"; lf$; 'get data from channel 1
IF PORT = 2 THEN PRINT #1, ":waveform:source chan2"; lf$; 'get data from channel 2

PRINT #1, ":waveform:format word"; lf$; 'get data in 16-bit word format
PRINT #1, ":waveform:byteorder msbf"; lf$; 'set lsb transferred first
IF PORT = 1 THEN PRINT #1, ":digitize channel1"; lf$; 'tell scope to gather data
IF PORT = 2 THEN PRINT #1, ":digitize channel2"; lf$; 'tell scope to gather data
'
' Get the preamble data for the waveform
' preamble(1)=format of waveform
' preamble(2)=type (ave,normal,peak detect)
' preamble(3)=points (number of data points)
' preamble(4)=count (always 1)
' preamble(5)=x increment
' preamble(6)=x origin
' preamble(7)=x reference
' preamble(8)=y increment
' preamble(9)=y origin
' preamble(10)=y reference
PRINT #1, ":waveform:preamble?"; lf$; 'ask for preamble informations
' IF PORT = 1 THEN 'get data from channel 1
' IF PORT = 2 THEN PRINT #1, ":waveform:source chan2"; lf$; 'get data from channel 2

IF PORT = 1 THEN
    FOR count% = 1 TO 10
        CALL enter(preamble!(count%))
    NEXT count%
END IF

IF PORT = 2 THEN
    FOR count% = 1 TO 10
        CALL enter(preamble2!(count%))
    NEXT count%
END IF

' Get the waveform from the scope in word format
' from port #1
'
IF PORT = 1 THEN
PRINT #1, ":waveform:data?"; lf$; 'ask for the waveform data
msg$ = INPUT$(10, #1) 'the arbitrary block header
length% = VAL(RIGHT$(msg$, 8)) / 2 'length is specified in last 8 bytes of
header 'length is measured in bytes

```



```

FOR count% = 1 TO length%           'get the waveform
    GET #1, , waveform%(count%)
NEXT count%
msg$ = INPUT$(1, #1)                 'get the last NL char.
END IF

' Get the waveform from the scope in word format
' from port 2

IF PORT = 2 THEN
PRINT #1, ":waveform:data?"; lf$;   'ask for the waveform data
msg$ = INPUT$(10, #1)               'the arbitrary block header
length% = VAL(RIGHT$(msg$, 8)) / 2  'length is specified in last 8 bytes of
header                               'length is measured in bytes

FOR count% = 1 TO length%           'get the waveform
    GET #1, , waveform2%(count%)
NEXT count%
msg$ = INPUT$(1, #1)                 'get the last NL char.
END IF

END SUB

SUB graphit

SCREEN 2                             'set screen mode to CGA
                                     '640 x 200 x 2
VIEW (1, 1)-(638, 128), , 15       'set viewport and draw the border
WINDOW (0, 0)-(10, 8)              'prepare to draw the grid
FOR i% = 1 TO 9                     'draw the grid
    LINE (i%, 0)-(i%, 8)
NEXT i%
FOR i% = 1 TO 7
    LINE (0, i%)-(10, i%)
NEXT i%

WINDOW (1, 0)-(preamble!(3), 255)  'use window to make the co-ordinates to be
                                     'device independent
FOR i% = 1 TO preamble!(3)
    PSET (i%, waveform%(i%))        'draw the pixels for channel 1
NEXT i%

FOR i% = 1 TO preamble2!(3)
    PSET (i%, waveform2%(i%))       'draw the pixels for channel 2
NEXT i%

'
' Use the preamble data to calculate the timebase and vertical settings
'
WIDTH 80, 25
VIEW PRINT 20 TO 24
LOCATE 20, 1
PRINT "V/Div = " + STR$(32 * preamble!(8)) + "V"
PRINT "Offset = " + STR$((128 - preamble!(10)) * preamble!(8) + preamble!(9)) +
    "V";

LOCATE 20, 41
PRINT "S/Div = " + STR$(preamble!(3) * preamble!(5) / 10) + "S"
LOCATE 21, 41
PRINT "Delay = " + STR$((preamble!(3) / 2 - preamble!(7)) * preamble!(5) +
preamble!(6)) + "S";
PRINT "Press <enter> to CONTINUE...";
LINE INPUT dummy$
SCREEN 0
CLS
END SUB

SUB initialize
' scope is connected to COM1 at 19200 baud rate
OPEN "COM1:19200,n,8,1,CD1000,CS1000,DS1000,rb4096" FOR RANDOM AS #1 LEN = 2
REM PRINT #1, "**RST"; lf$;          ' reset the scope
REM PRINT #1, ":autoscale"; lf$;    ' autoscale the input signal
PRINT #1, ":channel1:probe x1"; lf$; ' set probe factor to 1
PRINT #1, ":channel2:probe x1"; lf$; ' set probe factor to 1

PRINT #1, ":trigger:mode normal"; lf$; 'set trigger mode to normal

```

```

PRINT #1, ":trigger:source channel2"; lf$; 'set trigger source to channel 2
PRINT #1, ":trigger:level 3.25"; lf$; 'set trigger level
PRINT #1, ":timebase:range 0.1"; lf$; 'set time per div to 0.1/10 sec

CLS
END SUB

SUB outdat
PRINT "ENTER FILE NAME FOR OUTPUT DATA ----->";
LINE INPUT FILE$
SPACER$ = " "
OPEN FILE$ FOR OUTPUT AS #4
FOR count% = 1 TO 10
WRITE #4, preamble!(count%), preamble2!(count%)
NEXT count%

FOR count% = 1 TO preamble!(3)
V(count%) = ((waveform%(count%) - preamble!(10)) * preamble!(8)) + preamble!(9)
TIME(count%) = (count% - preamble!(7)) * preamble!(5) + preamble!(6)
Vtrig(count%) = ((waveform2%(count%) - preamble2!(10)) * preamble2!(8)) +
preamble2!(9)
TIMEtrig(count%) = (count% - preamble2!(7)) * preamble2!(5) + preamble2!(6)
NEXT count%

FOR count% = 1 TO preamble!(3)
PRINT #4, V(count%), SPACER$, TIME(count%), SPACER$, Vtrig(count%), SPACER$,
TIMEtrig(count%)
NEXT count%

CLOSE #4
END SUB

SUB retrieveit
PRINT "Waveform data has been saved to a file. The program will retrieve"
PRINT "the data from file 'wave.dat'. All subsequence operations"
PRINT "are based on the saved information. Press <enter> to continue."
LINE INPUT dummy$
CLS
OPEN "wave.dat" FOR BINARY AS #2
FOR count% = 1 TO 10
GET #2, , preamble!(count%)
NEXT count%
FOR count% = 1 TO preamble!(3)
GET #2, , waveform%(count%)
NEXT count%
CLOSE #2
END SUB

SUB saveit
PRINT "Waveform data is to be saved to a file. "
PRINT "The data will be saved to file 'wave.dat'. "
PRINT "Press <enter> to continue."
LINE INPUT dummy$
OPEN "wave.dat" FOR BINARY AS #2
FOR count% = 1 TO 10
PUT #2, , preamble!(count%)
NEXT count%
FOR count% = 1 TO preamble!(3)
PUT #2, , waveform%(count%)
NEXT count%
CLOSE #2
END SUB

```

APPENDIX C

PRESSURE MEASUREMENT SYSTEM CALCULATIONS AND DATA

The pressure measurement system calculations that follow were made with the aid of the Mathcad software package.

C1. Geometry data for the pressure tubing and the pressure transducer

length of the tubing $L_{\text{tube}} := 28 \text{ in}$

internal diameter of the tubing $Di_{\text{tube}} = 0.027 \text{ in}$

external diameter of the tubing $Do_{\text{tube}} := 0.092 \text{ in}$

modulus of elasticity of the tubing $E_{\text{tube}} := 2431 \frac{\text{lbf}}{\text{in}^2}$

volume of the reference pressure
port (P1) of the pressure transducer $V_{P1} := 0.06 \text{ cm}^3$

volume of the pressure
sensing port (P2) of the transducer $V_{P2} := 0.001 \text{ cm}^3$

Properties of air

air pressure $P_o := 1.013 \cdot 10^5 \frac{\text{N}}{\text{m}^2}$

specific heat ratio $\gamma := 1.402$

C.2 The transducer-to-tubing volume ratio computation

area of the tubing $A_{\text{tube}} := \pi \cdot \left(\frac{0.027}{2} \right)^2 \quad A_{\text{tube}} = 5.72555 \cdot 10^{-4} \text{ in}^2$

tubing volume is $V_{\text{tube}} := A_{\text{tube}} \cdot L_{\text{tube}} \quad V_{\text{tube}} = 0.01603 \text{ in}^3$

in SI units the tubing volume is $V_{\text{tube}} := V_{\text{tube}} \cdot 16.39 \frac{\text{cm}^3}{\text{in}^3}$

$$V_{\text{tube}} = 0.26276 \text{ cm}^3$$

The transducer to tubing volume ratio is $R := \frac{V_{P2}}{V_{tube}} \quad R = 0.00381$

The ratio indicates the transducer volume is only 0.4% of the pressure tap tubing volume.

C.3 The effect of tubing elasticity on speed of sound

In order to calculate the correction factor for the elasticity, the modulus of elasticity for the air and the thickness of the tube wall are computed.

The modulus of elasticity E_{air} of the air is $E_{air} := \gamma \cdot P_o$

or $E_{air} = 1.42023 \cdot 10^5 \frac{N}{m^2}$

Putting the tubing modulus of elasticity into SI units $E_{tube} := 16.7 \cdot 10^6 \frac{N}{m^2}$

The thickness t_{tube} of the tubing wall is $t_{tube} := \frac{D_{o\ tube} - D_{i\ tube}}{2}$

$t_{tube} = 0.0325 \text{ in}$

In SI units the tubing wall thickness is $t_{tube} := t_{tube} \cdot 2.54 \frac{cm}{in}$

$t_{tube} = 0.08255 \text{ cm}$

The correction factor F is then

$$F := \sqrt{\frac{1}{1 + \frac{D_{i\ tube} \cdot E_{air}}{t_{tube} \cdot E_{tube}}}} \quad F = 0.99861$$

The 0.14% correction is negligible, but will be applied to the measurement corrections.

APPENDIX D

FAST FOURIER TRANSFORM AND PRESSURE DATA CORRECTION PROGRAM

The program used to convert the pressure measurement data to a Fourier series and then correct each term in the series for attenuation and phase lag is given below.

```

PARAMETER (MCOEFF=707)
parameter(NDATA=1000)
C
COMMON SPEICH(50000)
REAL Xplot(1000),Yplot(1000),X2(1000),Y2(1000),FREQ(MCOEFF)
REAL A(MCOEFF/2),B(MCOEFF/2),R(MCOEFF),WSAVE(3*MCOEFF+15)
REAL DFTA(MCOEFF/2),DFTB(MCOEFF/2),C(MCOEFF/2),S(MCOEFF/2)
REAL XJ(MCOEFF),R2(MCOEFF),POWER(MCOEFF/2)
REAL XCORR(2000),YCORR(2000)
DIMENSION VP(NDATA),TIMEP(NDATA),RP(11),R2P(11)
$ .VtrigP(NDATA),TIMETrigP(NDATA), PRESSDATP(NDATA)
DIMENSION VS(NDATA),TIMES(NDATA),RS(11),R2S(11),DELTAP(NDATA)
$ .VtrigS(NDATA),TIMETrigS(NDATA), PRESSDATS(NDATA)
DIMENSION TIME(NDATA), DELTAP2(NDATA)
CHARACTER*28 FILEIN
character*13 fileinP, fileinS, fileout,fileZ
C
PI = ASIN(1.0)*2.0
C
C*****
C READ RAW VOLTAGE VS TIME DATA
C*****
C
C write(*,*)'enter pressure side file name to be read-->'
C READ(*, '(A)')fileinP
C
C write(*,*)'enter suction side file name to be read-->'
C READ(*, '(A)')fileinS
C
C write(*,*)'FILE NAME FOR RAW DELTA_P DATA-->'
C READ(*, '(A)')fileout
C
C write(*,*)'enter file name FOR Z VALUE RESULTS-->'
C READ(*, '(A)')fileZ
C
C OPEN(1,FILE=fileinP,STATUS='OLD')
C OPEN(11,FILE=fileinS,STATUS='OLD')
C OPEN(2,FILE=fileout,STATUS='NEW')
C OPEN(4,FILE=fileZ,STATUS='NEW')
C OPEN(13, FILE='PRESS.OUT', STATUS='OLD')
C
C READ(1,*)(RP(I),R2P(I),I=1,10)
C READ(1,*)(VP(I), TIMEP(I),VtrigP(I),TIMETrigP(I), I=1,NDATA)
C READ(11,*)(RS(I),R2S(I),I=1,10)
C READ(11,*)(VS(I), TIMES(I),VtrigS(I),TIMETrigS(I), I=1,NDATA)
C
C*****
C plotting DATA section
C*****
C write(*,*)' plot INPUT? 1 = yes, 0 = no'
C READ(*,*)iplot
C
C IF (iplot .eq. 1) THEN
C YMAX=-1000.0
C YMIN=1000.0
C DO 1 I=1,NDATA
C IF(VP(I) .GT. YMAX) YMAX=VP(I)

```

```

        IF(VS(I) .GT. YMAX) YMAX=VS(I)
        IF(VtrigS(I)/9.0-1.7 .GT. YMAX) YMAX=VtrigS(I)/9.0-1.7
        IF(VP(I) .LT. YMIN) YMIN=VP(I)
        IF(VS(I) .LT. YMIN) YMIN=VS(I)
        IF(VtrigS(I)/9.0-1.7 .LT. YMIN) YMIN=VtrigS(I)/9.0-1.7
        pressdats(I) = VtrigS(I)/9.0 - 1.7
        pressdatp(I) = VtrigP(I)/9.0 - 1.7
C
C 1 CONTINUE
C
        write(*,*)'Enter 1 for graphic, 0 for plot:'
        read(*,*)IOUT
        CALL EGATRM(15)
        IF (IOUT .EQ. 1)CALL EGATRM(15)
        IF (IOUT .EQ. 0) then
            CALL HPGL('PLOT1')
        END IF
        CALL NFRAME(210.,160.)
        CALL CORDEF(0,25000)
        CALL DEFPICT(180.,130.,20.,20.)
C WINDOW SETS THE AXIS
        CALL WINDOW(0.0,TIMEP(NDATA),YMIN,YMAX)
        CALL STFONT(0)
        CALL STVELO(4)
        CALL AXENR('GRID','TIME (MILLISECONDS)',19
        $ , 'VOLTAGE (V)',11)
        CALL POLYGO(TIMEP, VP, NDATA)
        CALL STTXTR(3)
        CALL STPEN(2)
        CALL POLYGO(TIMEP, VS, NDATA)
        CALL STTXTR(4)
        CALL POLYGO(timep,pressdatP, NDATA)
        CALL POLYGO(timep,pressdats, NDATA)
        CALL FINISH
C
        END IF
C
C CONVERT DATA TO A SINGLE 360 DEGREE SWEEP
C*****
C FIND A CYCLE OF DATA FOR THE PRESSURE SIDE OF BLADE
C*****
C FIND FIRST TRIGGER
C
        TRIGSTART=VtrigP(1)
        VMAX=-10000.0
        NUMTRIG=0
        I = 1
        DO 2 WHILE ( NUMTRIG .LT. 1 )
C FIND FIRST MAXIMUM VALUE AND STORE INDEX AND VALUE
C
        IF ( VtrigP(I) .GT. (TRIGSTART+ 0.1*(ABS(TRIGSTART))) ) THEN
            IF ( VtrigP(I) .GT. VMAX ) VMAX = VtrigP(I)
            IF ( VtrigP(I) .LT. (VMAX - 0.1*(ABS(VMAX))) ) THEN
                ISTART = I
                NUMTRIG = 1
            END IF
        END IF
        I = I + 1
2 CONTINUE
        write(*,*)'ISTART = >',ISTART
C
C SET IEND TO BE ISTART+707 WITH DATA POINTS EVERY
C 0.1 MSEC 706 DATA POINTS IN ONE CYCLES
C WORTH OF DATA AT 850 RPM
C
        IEND=ISTART+MCOEFF-1
        write(*,*)'IEND = >',IEND
        write(*,*)'THE NUMBER OF DATA POINTS ARE-->',IEND-ISTART+1
        NPDATA=IEND-ISTART+1
C*****
C CONVERT VOLTAGE TO A PRESSURE ADD CALIBRATION CURVE HERE
C*****
        DO 3 I=ISTART,IEND
            PRESSDATP(I-ISTART + 1) = 16.0977 + 9.21579 * VP(I)
            PRESSDATP(I-ISTART + 1) = 16.1729 + 9.2699 * VP(I)
            PRESSDATP(I-ISTART + 1) = 15.9592 + 9.7215 * VP(I)
3 CONTINUE

```

```

C*****
C FIND A CYCLE OF DATA FOR THE SUCTION SIDE OF BLADE
C*****
C FIND FIRST TRIGGER
C
    TRIGSTART=Vtrigs(1)
    VMAX=-10000.0
    NUMTRIG=0
    I = 1
    DO 4 WHILE ( NUMTRIG .LT. 1 )
C
C FIND FIRST MAXIMUM VALUE AND STORE INDEX AND VALUE
C
        IF ( Vtrigs(I) .GT.(TRIGSTART+ 0.1*(ABS(TRIGSTART))) ) THEN
            IF ( Vtrigs(I) .GT. VMAX ) VMAX = Vtrigs(I)
            IF ( Vtrigs(I) .LT. (VMAX - 0.1*(ABS(VMAX))) ) THEN
                ISTARTS = I
                NUMTRIG = 1
            END IF
        END IF
        I = I + 1
4    CONTINUE
    write(*,*)'ISTART = >',ISTARTS
C
C SET IEND TO BE ISTART+705 WITH DATA POINTS EVERY
C 0.1 MSEC 706 DATA POINTS IN ONE CYCLES
C WORTH OF DATA AT 850 RPM
C
    IENDS=ISTARTS+MCOEFF-1
C
    write(*,*)'IENDS = >',IENDS
    write(*,*)'THE NUMBER OF DATA POINTS ARE-->',IENDS-ISTARTS+1
    NSDATA=IENDS-ISTARTS+1
C
C*****
C CONVERT VOLTAGE TO A PRESSURE ADD CALIBRATION CURVE HERE
C*****
    DO 5 I=ISTARTS,IENDS
C*****
C -1.642 VOLTS ZERO CALIBRATION CURVE
C*****
        PRESSDATS(I-ISTARTS + 1) = 15.9592 + 9.7215 * VS(I)
C*****
C -1.741 VOLTS ZERO CALIBRATION CURVE
C*****
        PRESSDATS(I-ISTARTS + 1) = 16.1729 + 9.2699 * VS(I)
5    CONTINUE
        IF ( NPDATA .GT. NSDATA ) IEND = NSDATA
        IF ( NPDATA .LT. NSDATA ) IEND = NPDATA
        IF ( NPDATA .EQ. NSDATA ) IEND = NSDATA
        If ( IEND .GE. 702) IEND = 707
C
C
C
    DO 6 I = 1, IEND
        DELTAP(I)=PRESSDATS(I) - PRESSDATP(I)
        TIME(I)=TIMEP(I - 1 + ISTART) - TIMEP(ISTART)
6    CONTINUE
C*****
C plotting PRESSURE section
C*****
    write(*,*)'do you want to plot... 1 = yes, 0 = no'
    READ(*,*)iplot
    YMAX=-1000.0
    YMIN=1000.0
    DO 8 I=1,IEND
        IF(PRESSDATP(I) .GT. YMAX) YMAX=PRESSDATP(I)
        IF(PRESSDATS(I) .GT. YMAX) YMAX=PRESSDATS(I)
        IF(DELTAP(I) .GT. YMAX) YMAX=DELTAP(I)
        IF(PRESSDATP(I) .LT. YMIN) YMIN=PRESSDATP(I)
        IF(PRESSDATS(I) .LT. YMIN) YMIN=PRESSDATS(I)
        IF(DELTAP(I) .LT. YMIN) YMIN=DELTAP(I)
C
C 8 CONTINUE
C
    IF (IPL0T .EQ. 1) THEN
        write(*,*)'Enter 1 for graphic, 0 for plot:'
    
```

```

      read(*,*)IOUT
      CALL EGATRM(15)
      IF (IOUT .EQ. 1)CALL EGATRM(15)
      IF (IOUT .EQ. 0) THEN
C        CALL ZWFILE
          CALL HPGL('PLOT2')
        END IF
        CALL NFRAME(210.,160.)
        CALL CORDEF(0.25000)
        CALL DEFPIC(180.,130.,20.,20.)
C WINDOW SETS THE AXIS
        CALL WINDOW(0.0,TIME(IEND),YMIN,YMAX)
        CALL STFONT(1)
        CALL STVELO(4)
        CALL AXENR('NOGRID','TIME (SECONDS)',14
$ , 'PRESSURE (INCHES H2O)',21)
        CALL STTXTR(2)
        CALL POLYGO(TIME, PRESSDATP, IEND)
        CALL STTXTR(3)
        CALL STPEN(2)
        CALL POLYGO(TIME, PRESSDATS, IEND)
        CALL STTXTR(4)
        CALL POLYGO(TIME, DELTAP, IEND)
C*****DRAW LEGEND
        CALL STFONT(1)
        CALL STTXTR(2)
        CALL MOVETO(0.033,2.4)
        CALL MOVEON(0.04,2.4)
        CALL SWRITE('A: Air injected',
$ 2.4,0.0,0.042,2.4,15,'LM')
        CALL STTXTR(3)
        CALL MOVETO(0.033,2.2)
        CALL MOVEON(0.04,2.2)
        CALL SWRITE('B: Undisturbed',
$ 2.4,0.0,0.042,2.2,14,'LM')
        CALL STTXTR(4)
        CALL MOVETO(0.033,2.0)
        CALL MOVEON(0.04,2.0)
        CALL SWRITE('Difference between B and A',
$ 2.4,0.0,0.042,2.0,26,'LM')
C
      CALL FINISH
      END IF
C*****
C      WRITE RAW DELTA_P DATA TO FILE
C*****
      WRITE(*,*)'ENTER PERCENT CHORD FOR THIS TAP-> '
      READ(*,*)PERCHORD
      DO 9 I=1,IEND
        WRITE(2,*)PERCHORD, TIME(I), DELTAP(I)
      9 CONTINUE
C*****
C      DELTAP(1..IEND) IS NOW 1 CYLCE OF PRESSURE DIFFERENCE
C      AND TIME(1..IEND) ARE THE TIME VALUES IN SEC FOR
C      THE PRESSURE DATA
C*****
C*****
C      EZFFT FAST FOURIER TRANSFORM PART OF PROGRAM
C*****
      MCOEF = MCOEFF
      N = MCOEF
      PERIODL=70.6E-03
      DEL = 1.0E-4
      F = 1.0/PERIODL
      OMEGA = 2.0*PI*F
      WRITE(*,*)'NOW COMPUTING FFT...'
C
      DO 20 I=1,MCOEF
        XJ(I)=TIME(I)
        R(I)=DELTAP(I)
      20 CONTINUE
      XO=XJ(1)
      CALL EZFFT1 (N,WSAVE)
      DO 21 J = 1,N
C Compute sines and cosines to adjust output of EZFFT to give
C approximate Fourier coefficients.

```



```

                IF (J .LE. N/2) THEN
                    FREQ(J)=J*OMEGA
                    C(J) = COS(J*OMEGA*X0)
                    S(J) = SIN(J*OMEGA*X0)
                END IF
21    CONTINUE
        CALL EZFFT (N,R,AZERO,A,B,WSAVE)
C
C As a convenience this loop can go to N/2. If N is even last B is
C zero.
        DO 31 J = 1,N/2
            DFTA(J) = A(J)*C(J) - B(J)*S(J)
            DFTB(J) = A(J)*S(J) + B(J)*C(J)
31    CONTINUE
C*****
C      EVALUATE THE FFT OF THE DATA
C*****
        M = 706
        DEL2=DEL
        DO 40 K = 1,M
            X = TIME(K)
            TN = AZERO
            DO 41 J = 1,N/2
                TN = TN + DFTA(J)*COS(J*OMEGA*X) + DFTB(J)*SIN(J*OMEGA*X)
41    CONTINUE
            X2(K)=X
            Y2(K)=TN
            ER = TN - R(K)
            WRITE (4,*) X,TN,R(K),ER
40    CONTINUE
C
C      PERFORM LOOP TO COMPUTE THE POWER SPECTRUM
C
        PMAX=0.0
        DO 50 K=1,N/2
            POWER(K)=(DFTA(K)*DFTA(K)+DFTB(K)*DFTB(K))/2.0
            IF(POWER(K) .GT. PMAX) PMAX = POWER(K)
50    CONTINUE
C
C*****
C      DO YOU WANT TO PLOT THE DATA AND FFT?
C*****
        write(*,*)'do you want to plot data vs. fft'
        write(*,*)'1 = yes, 0 = no'
        READ(*,*)iplot
        IF (IPLOT .EQ. 1) THEN
C*****
            write(*,*)'Enter 1 for graphic, 0 for plot:'
            read(*,*)IOUT
            CALL EGATRM(15)
            IF (IOUT .EQ. 1)CALL EGATRM(15)
            IF (IOUT .EQ. 0) CALL ZWFILE
            CALL NFRAME(210.,160.)
            CALL CORDEF(0,25000)
            CALL DEFPIC(180.,130.,20.,20.)
C WINDOW SETS THE AXIS
            CALL WINDOW(0.0,TIME(IEND),YMIN,YMAX)
C            CALL WINDOW(0.0,PERIODL,0.0,20.0)
            CALL STFONT(0)
            CALL STVELO(4)
            CALL AXENR('GRID','TIME (SECONDS)',14
            $ , 'PRESSURE (INCHES H2O)',21)
C****PLOT DATA*****
            CALL STTXTR(1)
            CALL POLYGO(TIME, DELTAP, IEND)
C****PLOT FFT*****
            CALL STTXTR(2)
            CALL POLYGO(X2,Y2,M)
            CALL FINISH
            END IF
C*****
C      PLOT POWER SPECTRUM
C*****
        write(*,*)'do you want to plot POWER SPECTRUM'
        write(*,*)'1 = yes, 0 = no'
        READ(*,*)iplot
        IF (IPLOT .EQ. 1) THEN

```

```

      CALL NFRAME(210.,160.)
      CALL CORDEF(0,25000)
      CALL DEFPIC(180.,130.,20.,20.)
C WINDOW SETS THE AXIS
C      CALL WINDOW(0.0,(MCOEF/2)*OMEGA,0.0,PMAX)
      CALL WINDOW(0.0,4000.0,0.0,PMAX)
      CALL STFONT(0)
      CALL STNDIV(13,10)
      CALL AXENR('GRID','FREQ VALUE',10
$ , 'POWER VALUE',11)
      CALL POLYGO(FREQ,POWER,MCOEF/2)
      CALL FINISH
      END IF
C*****
C COMPUTE DYNAMIC CORRECTION
C*****
C TUBEL= TUBING LENGTH IN FT
C CSPEED= ACOUSTIC VELOCITY FT/SEC
      TUBEL=26.5/12.0
      CSPEED=1095.0
C***CORRECT SPEED OF PROPAGATION FOR TUBING*****
      CSPEED = 0.99861 * CSPEED
      PHICOR=(TUBEL/CSPEED)+0.1E-3
      write(*,*)'NOW CORRECTING FFT....'
C
      DO 200 K = 1,IEND
        TN = AZERO
        DO 201 J = 1,N/2
          CAOUT = DFTA(J)
          CBOUT = DFTB(J)
C
          CALL IBERALL(J*OMEGA,DELTA_0,PRATIO)
C
          TN1 = CAOUT*COS(J*OMEGA*TIME(K) + DELTA_0)
          TN2 = CBOUT*SIN(J*OMEGA*TIME(K) + DELTA_0)
          TN = TN + (TN1 + TN2)/PRATIO
C
201 CONTINUE
        XCORR(K)=TIME(K)
        YCORR(K)=TN
200 CONTINUE
C*****
C DO YOU WANT TO PLOT THE DATA AND CORRECTED FFT?
C*****
      write(*,*)'do you want to plot data vs. corrected'
      write(*,*)'fft 1 = yes, 0 = no'
      READ(*,*)iplot
      IF (IPLOT .EQ. 1) THEN
C*****
      write(*,*)'Enter 1 for graphic, 0 for plot:'
      read(*,*)IOUT
      CALL EGATRM(15)
      IF (IOUT .EQ. 1)CALL EGATRM(15)
      IF (IOUT .EQ. 0) CALL ZWFILE
      CALL NFRAME(210.,160.)
      CALL CORDEF(0,25000)
      CALL DEFPIC(180.,130.,20.,20.)
C WINDOW SETS THE AXIS
      CALL WINDOW(0.0,TIME(IEND),YMIN,YMAX)
      CALL STFONT(0)
      CALL STVELO(4)
      CALL AXENR('NOGRID','TIME (SECONDS)',14
$ , 'PRESSURE (INCHES H2O)',21)
C***PLOT DATA*****
      CALL STTXTR(1)
      CALL POLYGO(xcorr,ycorr, IEND)
C***PLOT FFT*****
      CALL STTXTR(2)
      CALL POLYGO(X2,Y2,M)
C***DRAW LEGEND
      CALL STFONT(1)
      CALL STTXTR(2)
      CALL MOVETO(0.033,5.9)
      CALL MOVEON(0.04,5.9)
      CALL SWRITE('Uncorrected FFT',
$ 2.4,0.0,0.042,5.9,15,'LM')
      CALL STTXTR(1)

```

```

      CALL MOVETO(0.033,5.3)
      CALL MOVEON(0.04,5.3)
      CALL SWRITE('Corrected FFT',
$ 2.4,0.0,0.042,5.3,13,'LM')
C
      CALL FINISH
      END IF
C*****
C      WRITE CORRECTED DELTA_P DATA TO FILE
C*****
      DO 300 I=1,IEND
      WRITE(13,*)PERCHORD, TIME(I), YCORR(I)
300   CONTINUE
      sum_raw = 0.0
      sum_cor = 0.0
      DO 400 I=1,IEND
      sum_raw = sum_raw + DELTAP(I)
      sum_cor = sum_cor + YCORR(I)
400   CONTINUE
      ave_raw = sum_raw/real(iend)
      ave_cor = sum_cor/real(iend)
      WRITE(*,*)'The average delta_p for raw data is ',
$ ave_raw, 'in. H2O'
      WRITE(*,*)'the average delta_p for corrected data is ',
$ ave_cor, 'in. H2O'
      STOP
      END
C*****
      SUBROUTINE IBERALL(OMEGIN,DELTA_O,PRATIO)
C*****
      REAL L,R,VTRANS,C,DYVISC,T,RHO,H,OMEGNAT,AIN,AOUT,
$          OMEGIN
C
C      CORRECTS DYNAMIC PRESSURE MEASUREMENTS USING EQUATIONS FROM IBERALL,
C      "ATTENUATION OF OSCILLATORY PRESSURES..."
C
C      VARIABLES:
C          R= RADIUS OF PRESSURE TRANSMITTING TUBE,FT
C          L= LENGTH OF PRESSURE TRANSMITTING TUBE, FT
C          C= SPEED OF SOUND IN MEDIUM,FT/SEC
C          DYVISC= DYNAMIC VISCOSITY OF MEDIUM,LBM/FT*SEC
C          T= TEMPERATURE OF MEDIUM IN KELVIN
C          RHO= DENSITY OF MEDIUM, KG/M^3
C          VISC_KIN = KINEMATIC VISCOSITY OF FLUID, FT^2/SEC
C          GAMMA = SPECIFIC HEAT RATIO
C
      VISC_KIN = 14.0E-6 * 3.875E+4/3600.0
      PI = ASIN(1.0)*2.0
      T=25.0+273.15
      R=0.027/(2.0*12.0)
      L=28.0/12.0
      C= 20.04*SQRT(T)*3.2808*0.9965
      DYVISC= 1.8462E-5*2419.1/3600.0
      GAMMA = 1.4
C
      COMPUTE Z FACTOR FOR THIS CASE
      Z= (2.0*R)**2 *OMEGIN/(4.0*VISC_KIN)
C
      COMPUTE THE DELAY TIME (SEC)
      D_OMEGA = OMEGIN*L/C
C
      COMPUTE THE PRESSURE AMPLITUDE RATIO
      PRATIO = SQRT( 2.0/(1.0 + COS(2.0*D_OMEGA)))
      PRATIO = ABS (1.0 / COS(D_OMEGA))
C      COMPUTE ATTENUATION FACTOR
      CHI_O = 32.0*DYVISC*OMEGIN* (L/(2.0*R))**2
C      COMPUTE TIME DELAY
      DELTA_O = ATAN(D_OMEGA * GAMMA *
$          SQRT(1.0/(Z*2.0))*TAN(D_OMEGA))
C
      DELTA_O = D_OMEGA
      RETURN
      END

```

APPENDIX E

INTEGRATION OF MEASURED INLET AXIAL VELOCITIES

The inlet velocity profile as a function of the radius R (ft) was fitted by the polynomial

$$V(R) := (2597.4 - 5537.3 \cdot R + 10548 \cdot R^2 - 6507.7 \cdot R^3 + 793.4 \cdot R^4) \frac{\text{ft}}{\text{min}}$$

Integrating the velocity profile over the inlet annulus area gives the volumetric flow rate as

$$\text{CFM} \equiv \left[\int_0^{2 \cdot \pi} \int_{\frac{3}{12}}^{\frac{18}{12}} (2597.4 - 5537.3 \cdot R + 10548 \cdot R^2 - 6507.7 \cdot R^3 + 793.4 \cdot R^4) \cdot R \, dR \, d\alpha \right] \frac{\text{ft}^3}{\text{min}}$$

where the limits of integration in the radial direction are from 3 to 18 in. The resulting volumetric flow from the integration of the axial velocity components is

$$\text{CFM} = 10076.252 \frac{\text{ft}^3}{\text{min}}$$

The difference between the volumetric flow rate estimated by integrating the velocity profile and that given on the manufacturer's data sheet (10910 cfm) differ by

$$\frac{\text{CFM} - 10910}{10910} \cdot 100 = -7.642\%$$

APPENDIX F

SURFACE FLOW VISUALIZATION OF THE LP-36 FAN AT ROTATIONAL SPEEDS OF 600, 850 AND 1100 RPM

Below are presented photographs of blade surface flow visualization photographs using marabou tufts on the LP-36 fan at 600, 1100 and 850 rpm made while obtaining the performance data presented in Figures 6.37 and 6.38. Before each set of photographs, the efficiency data is presented so that corresponding data point and photograph might be readily compared. The photographs of the suction side and pressure side are presented together at approximately the same points in the performance curves.

These photographs serve several purposes. They serve as a record of the flow patterns and can be compared with numerical computations of the surface velocities using either the author's field point velocity program or by some other numerical method in the future. Also, they document the success of the marabou tuft method on a rotating surface which the author has not yet seen in the literature. The flow behaviors on the blade surface at similar points in the three performance curves are similar.

Several details of the blade surface flow are of particular importance. At each maximum volumetric flow rate the free-air condition was reached, and at this point the flow is well behaved and attached all along the leading edge. As the flow rate was decreased in each case from the maximum the efficiency increases slightly but the leading edge flow on the suction side becomes less well behaved. Then, as the flow rate was decreased further, a stall pattern developed over the blade which, again, is similar in all three cases.

On the pressure side of the blade, radial flow toward the suction side through the tip gap is evident at all operating points. At maximum flow rate, the flow on the pressure side is well behaved except in the inner third of the blade span. There, a swirling and predominantly outward flow pattern is observed for each rotational speed. At lower and lower flow rates the blade sees an ever increasing positive angle of attack, and flow wraps around from the pressure to the suction side at the leading edge. This is further evidence of leading edge vortices playing a role in the flows associated with this type of fan.

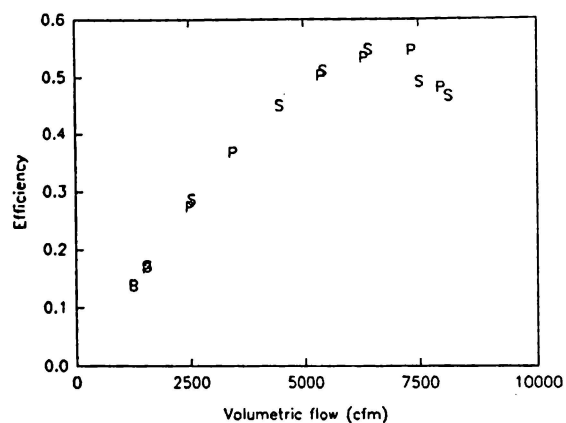


Figure F.1 Efficiency versus volumetric flow data for LP-36 fan at 600 rpm (S and P signify data for suction and pressure side photographs, respectively)

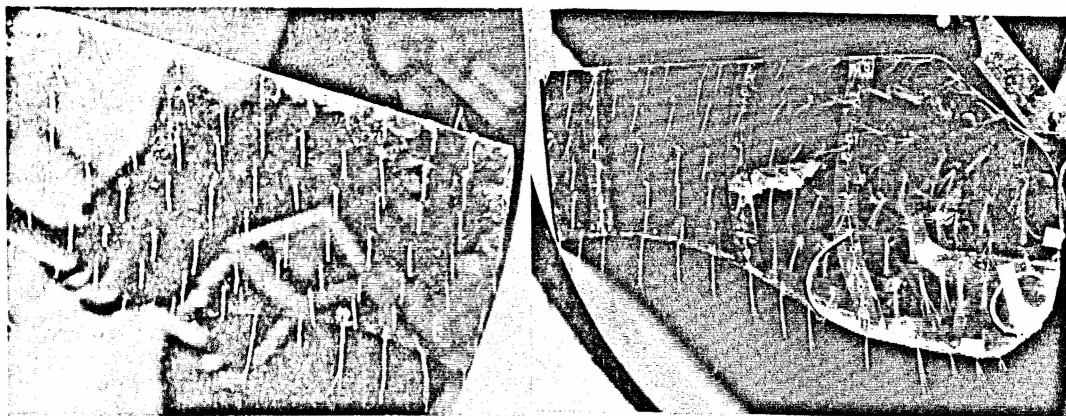


Figure F.2 Surface flow at 8141 cfm on suction side (left) and 7976 cfm on pressure side (right) for 600 rpm test data

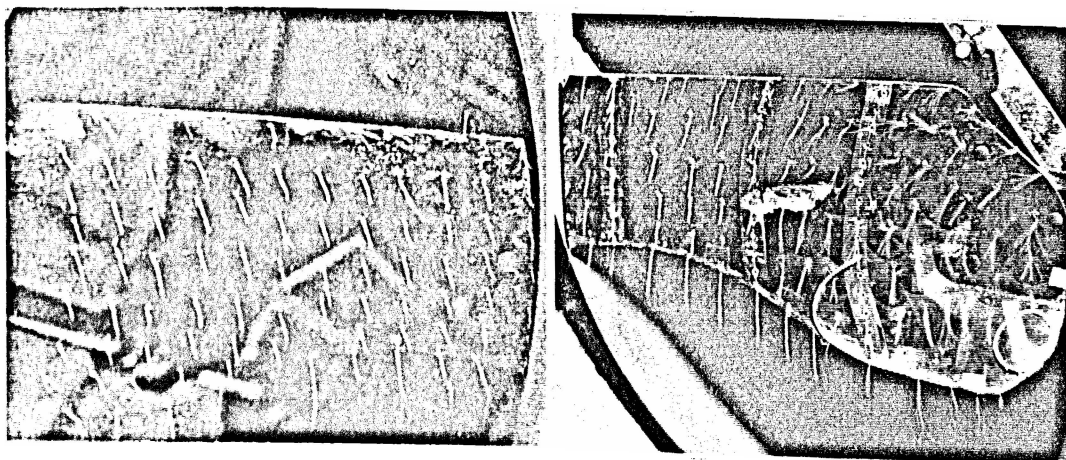


Figure F.3 Surface flow at 7516 cfm on suction side (left) and 7356 cfm on pressure side (right) for 600 rpm test data

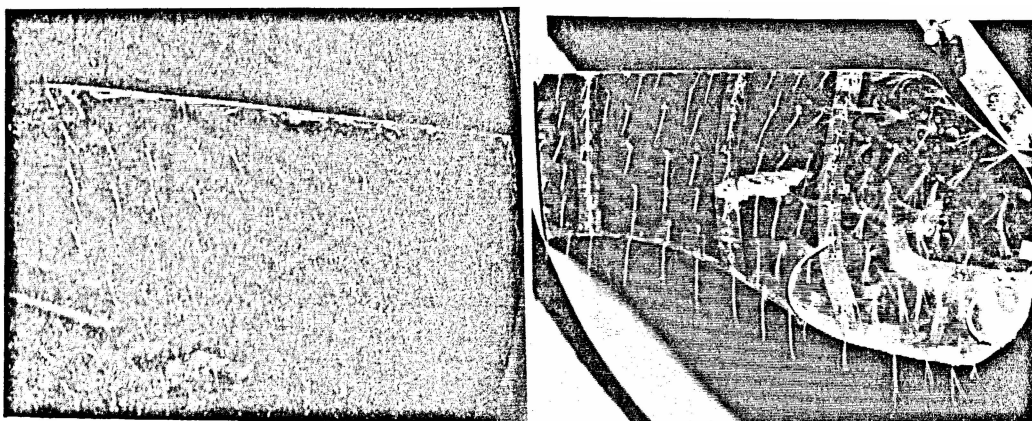


Figure F.4 Surface flow at 6432 cfm on suction side (left) and 6346 cfm on pressure side (right) for 600 rpm test data

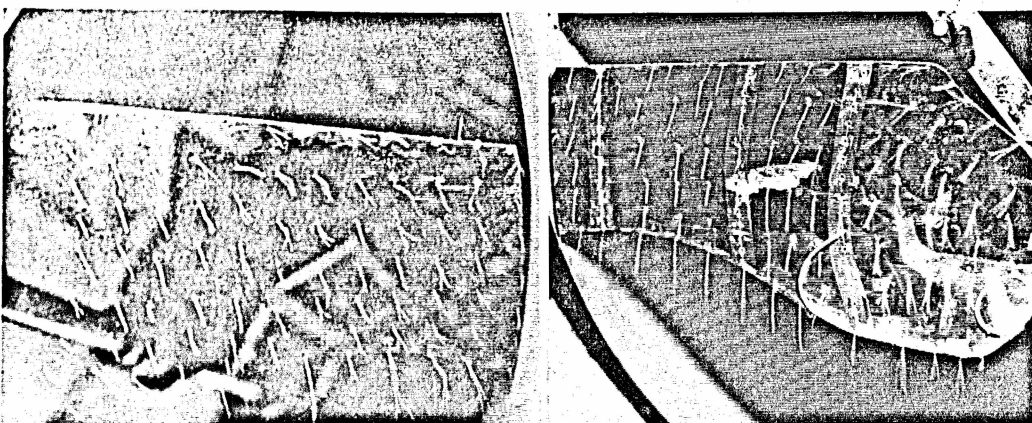


Figure F.5 Surface flow at 5442 cfm on suction side (left) and 5390 cfm on pressure side (right) for 600 rpm test data

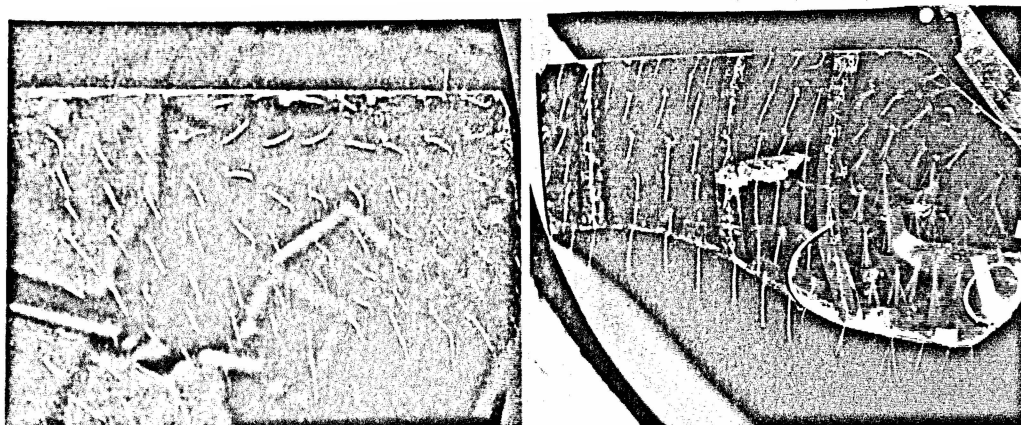


Figure F.6 Surface flow at 4456 cfm on suction side (left) and 3442 cfm on pressure side (right) for 600 rpm test data

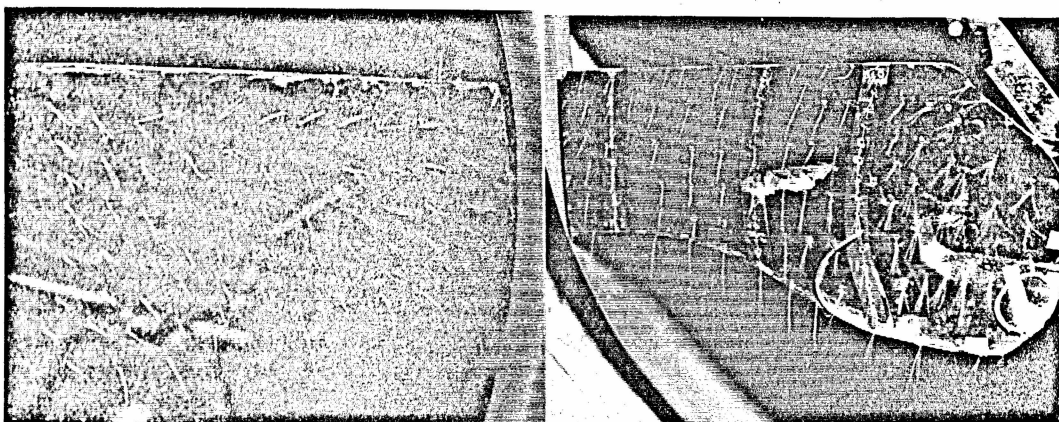


Figure F.7 Surface flow at 2537 cfm on suction side (left) and 2492 cfm on pressure side (right) for 600 rpm test data

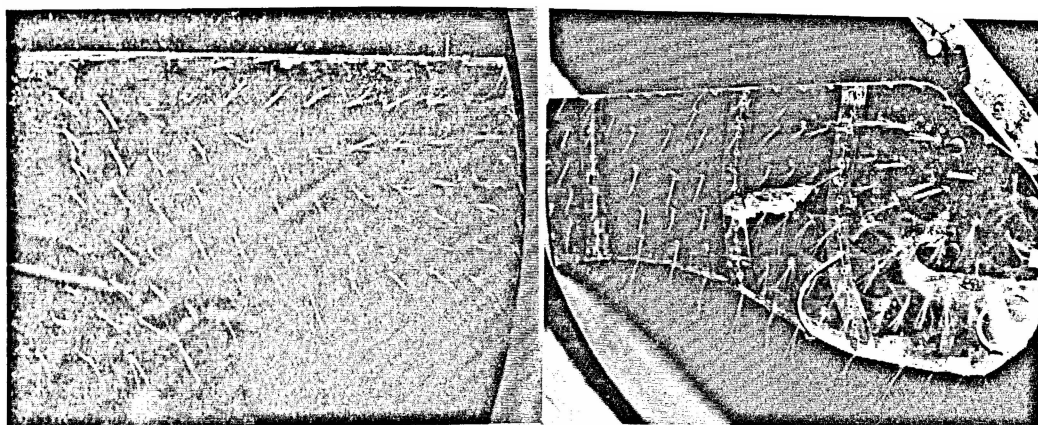


Figure F.8 Surface flow at 1554 cfm on suction side (left) and 1537 cfm on pressure side (right) for 600 rpm test data

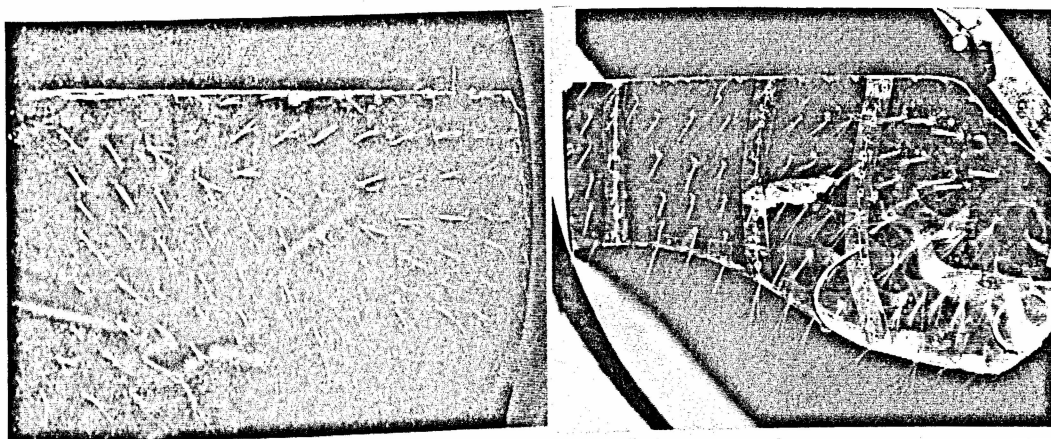


Figure F.9 Surface flow at 1247 cfm on suction side (left) and 1249 cfm on pressure side (right) for 600 rpm test data

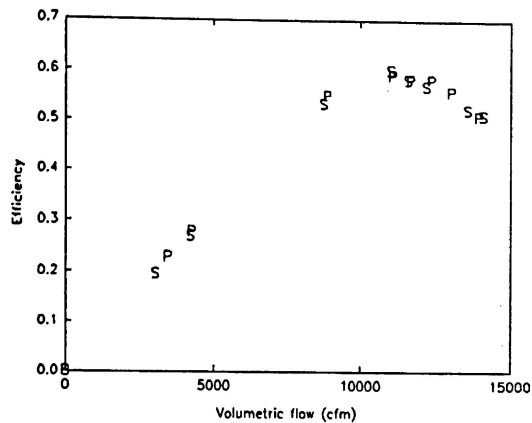


Figure F.10 Efficiency versus volumetric flow data for LP-36 fan at 1100 rpm (S and P signify data for suction and pressure side photographs, respectively)

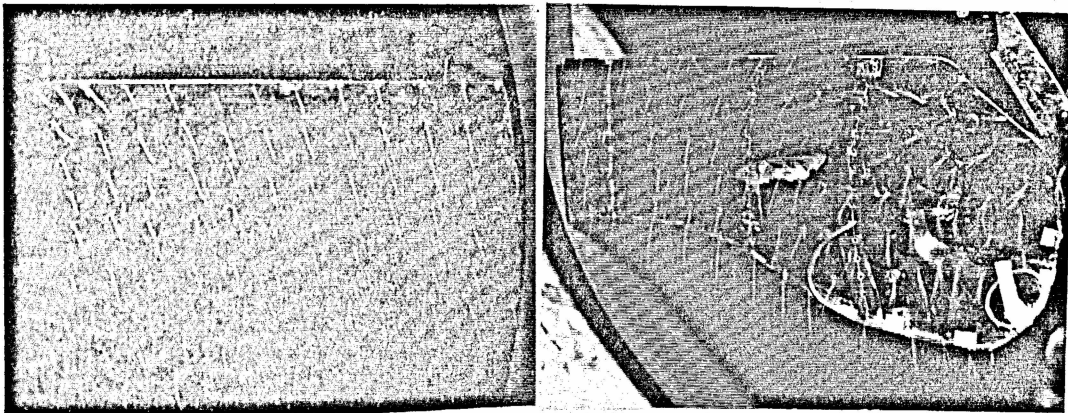


Figure F.11 Surface flow at 14096 cfm on suction side (left) and 13962 cfm on pressure side (right) for 1100 rpm test data

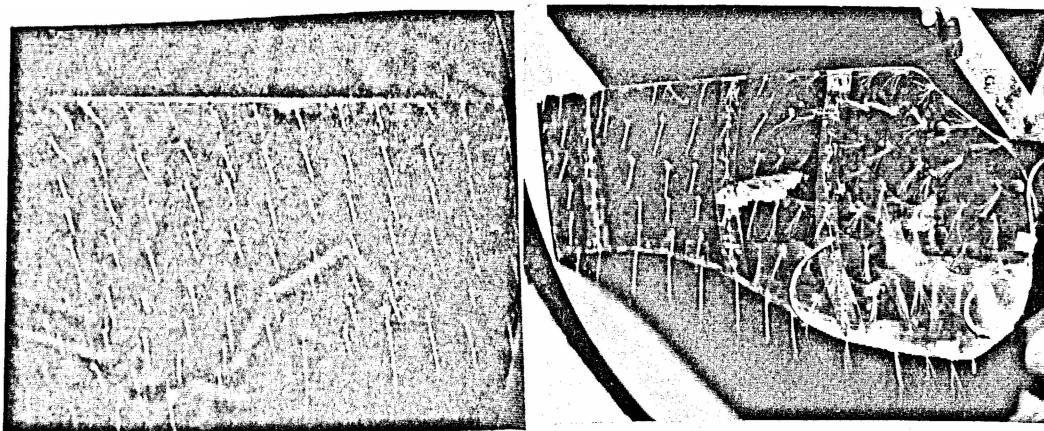


Figure F.12 Surface flow at 13578 cfm on suction side (left) and 13036 cfm on pressure side (right) for 1100 rpm test data

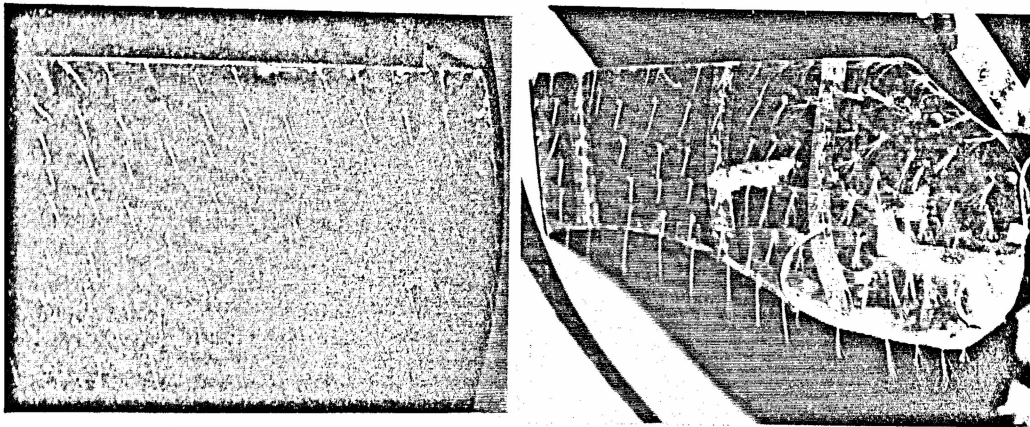


Figure F.13 Surface flow at 12208 cfm on suction side (left) and 12379 cfm on pressure side (right) for 1100 rpm test data

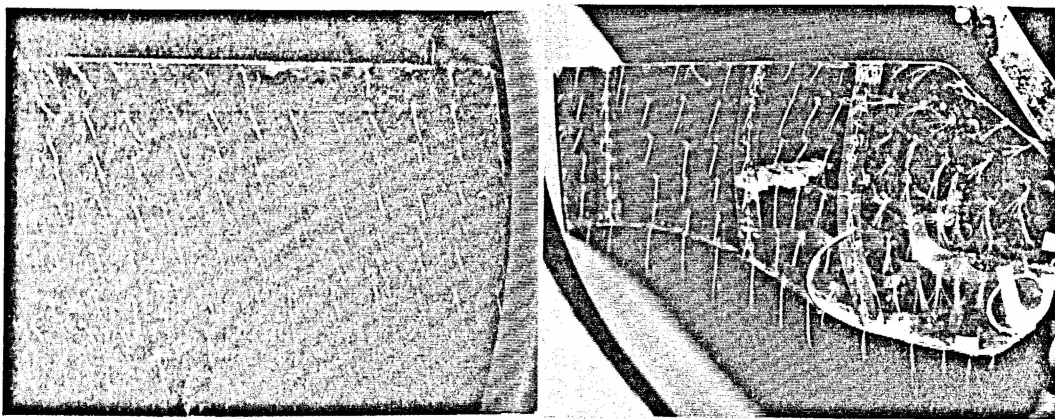


Figure F.14 Surface flow at 11578 cfm on suction side (left) and 11692 cfm on pressure side (right) for 1100 rpm test data

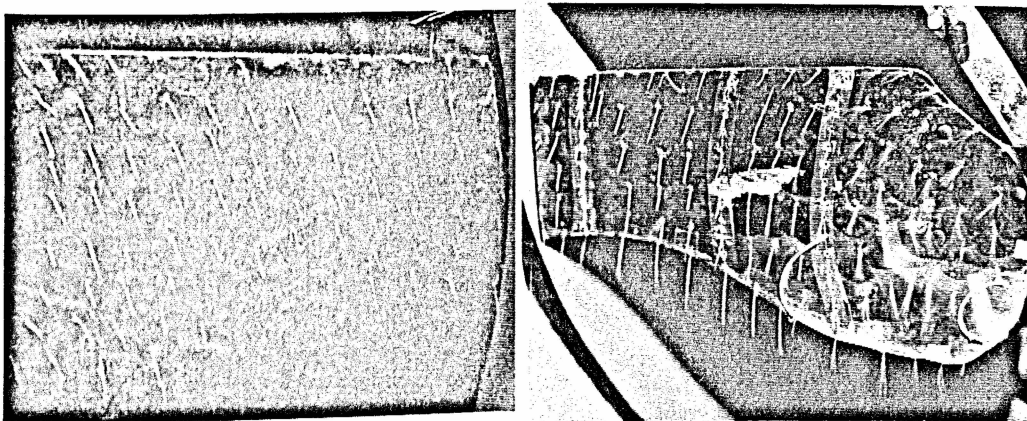


Figure F.15 Surface flow at 11002 cfm on suction side (left) and 11072 cfm on pressure side (right) for 1100 rpm test data

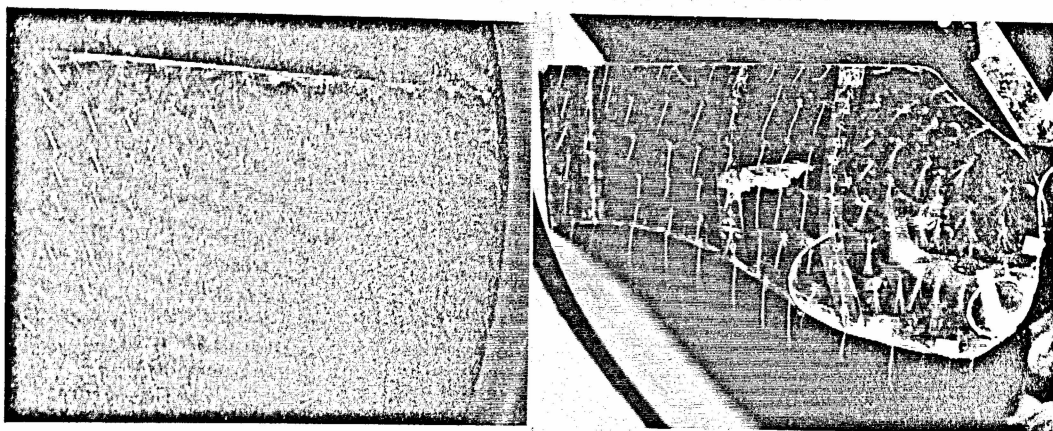


Figure F.16 Surface flow at 8729 cfm on suction side (left) and 8865 cfm on pressure side (right) for 1100 rpm test data

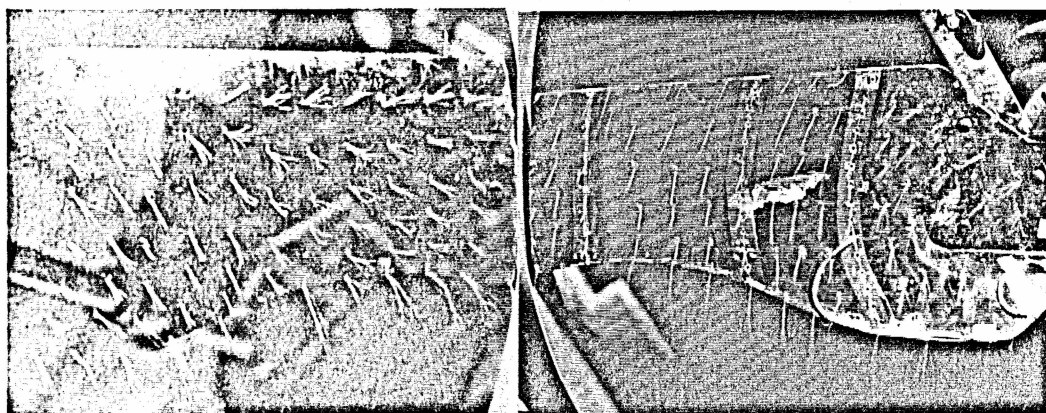


Figure F.17 Surface flow at 4200 cfm on suction side (left) and 4252 cfm on pressure side (right) for 1100 rpm test data

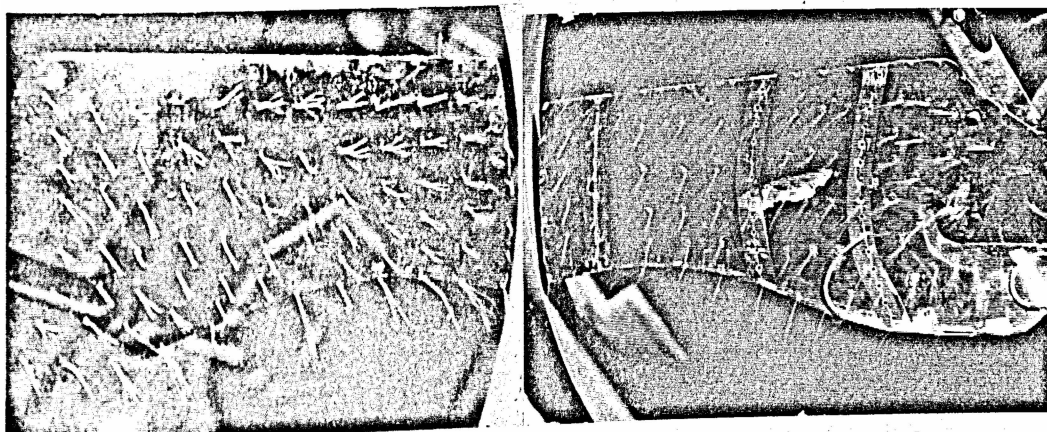


Figure F.18 Surface flow at 3002 cfm on suction side (left) and 3434 cfm on pressure side (right) for 1100 rpm test data

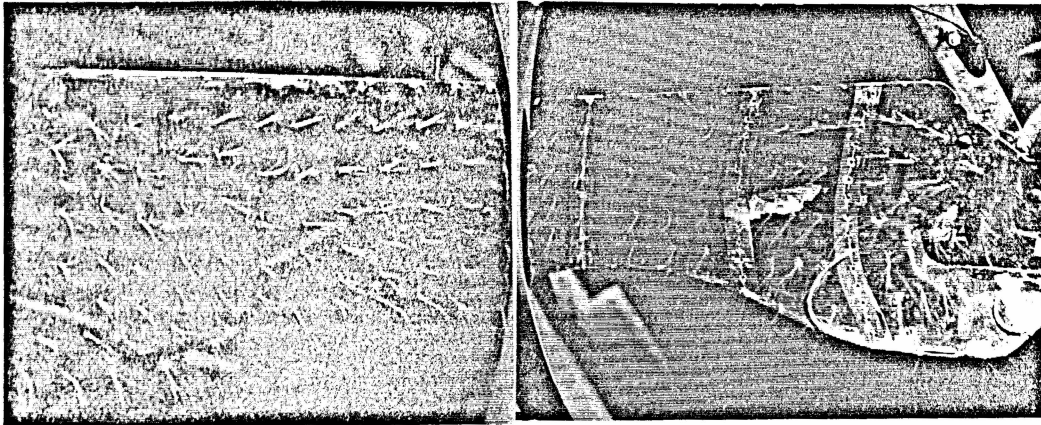


Figure F.19 Surface flow at 0 cfm on suction side (left) and 0 cfm on pressure side (right) for 1100 rpm test data

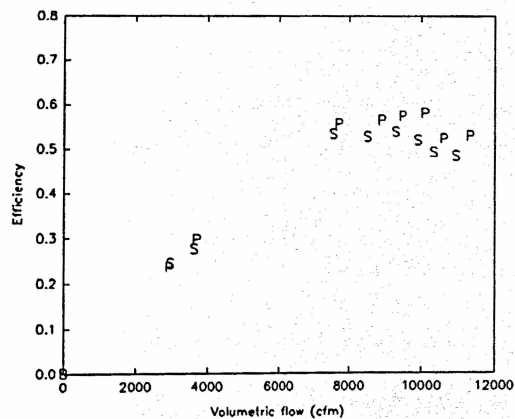


Figure F.20 Efficiency versus volumetric flow data for LP-36 fan at design speed of 850 rpm (S and P signify data for suction and pressure side photographs, respectively)

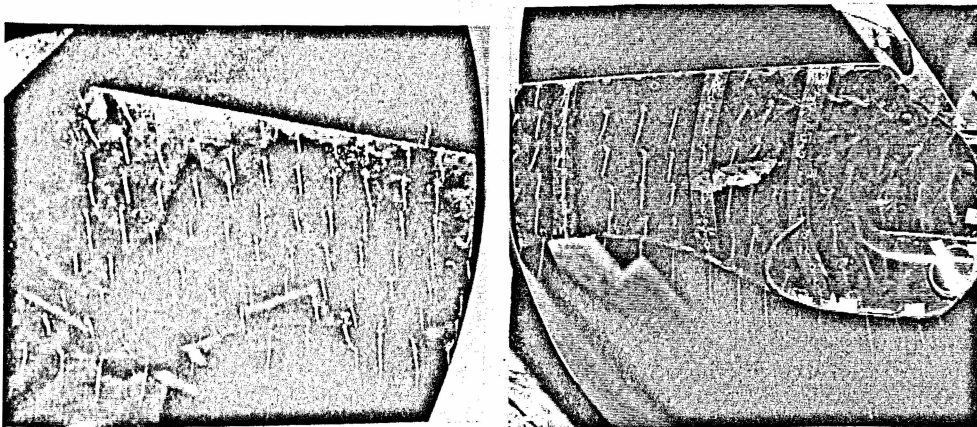


Figure F.21 Surface flow at 10947 cfm on suction side (left) and 11339 cfm on pressure side (right) for 850 rpm test data

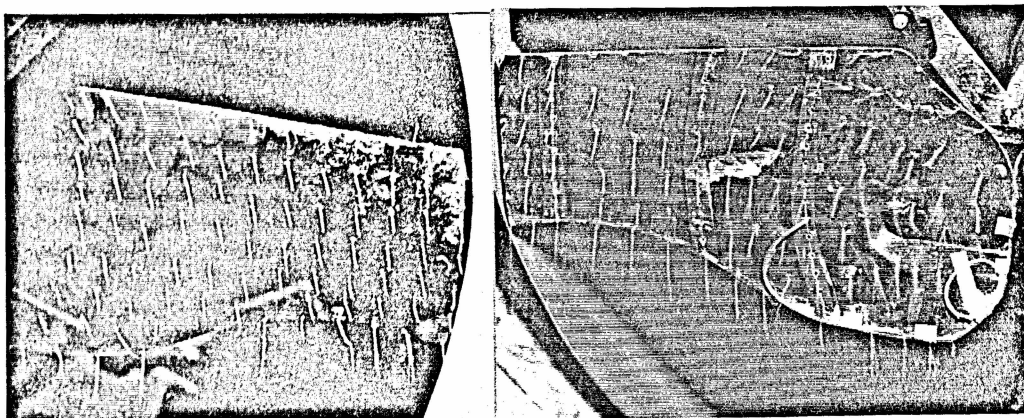


Figure F.22 Surface flow at 10327 cfm on suction side (left) and 10609 cfm on pressure side (right) for 850 rpm test data

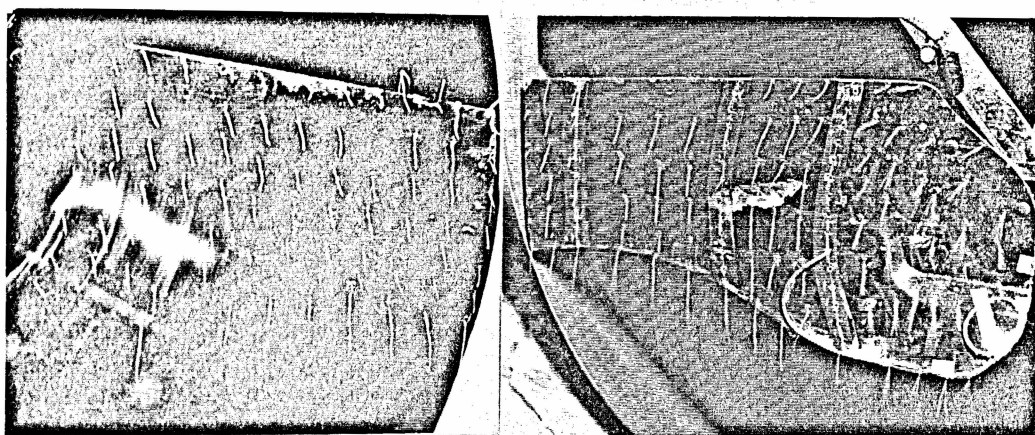


Figure F.23 Surface flow at 9903 cfm on suction side (left) and 10101 cfm on pressure side (right) for 850 rpm test data

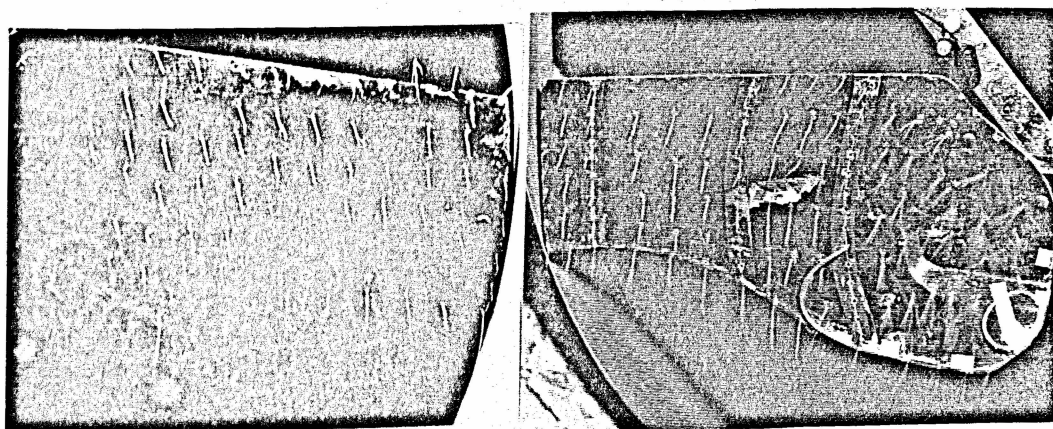


Figure F.24 Surface flow at 9270 cfm on suction side (left) and 9474 cfm on pressure side (right) for 850 rpm test data

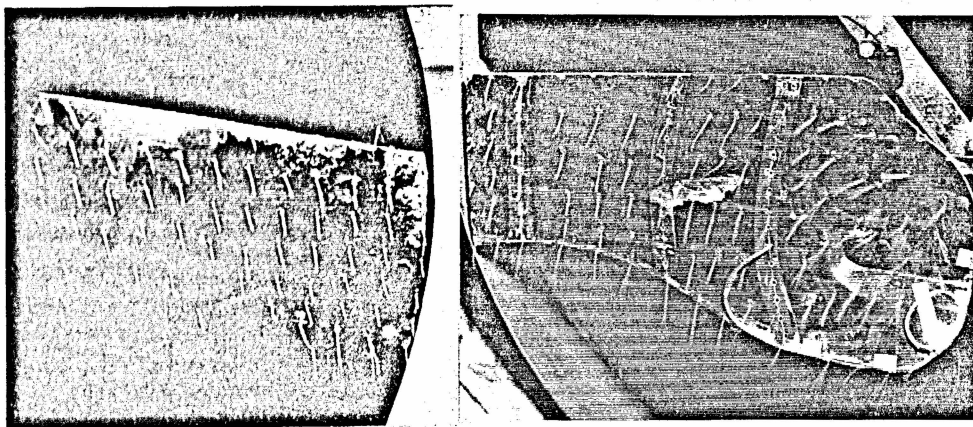


Figure F.25 Surface flow at 8497 cfm on suction side (left) and 8883 cfm on pressure side (right) for 850 rpm test data

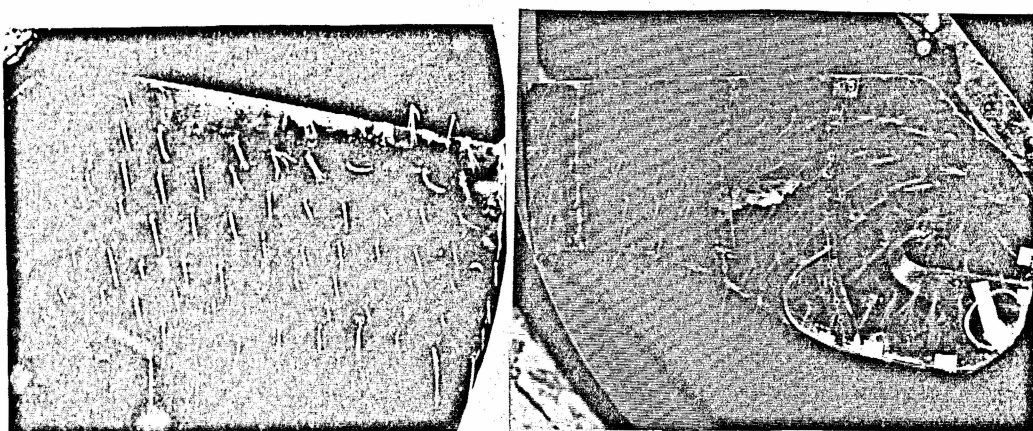


Figure F.26 Surface flow at 7548 cfm on suction side (left) and 7711 cfm on pressure side (right) for 850 rpm test data

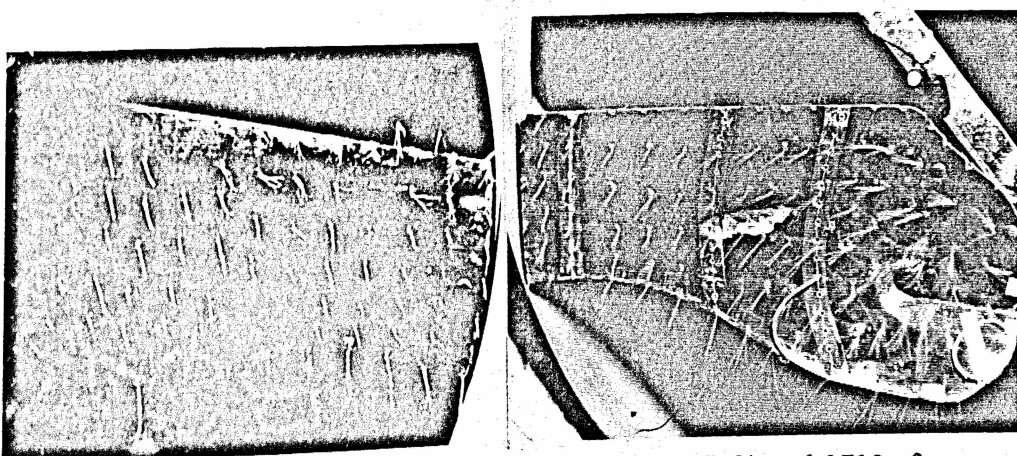


Figure F.27 Surface flow at 3640 cfm on suction side (left) and 3712 cfm on pressure side (right) for 850 rpm test data

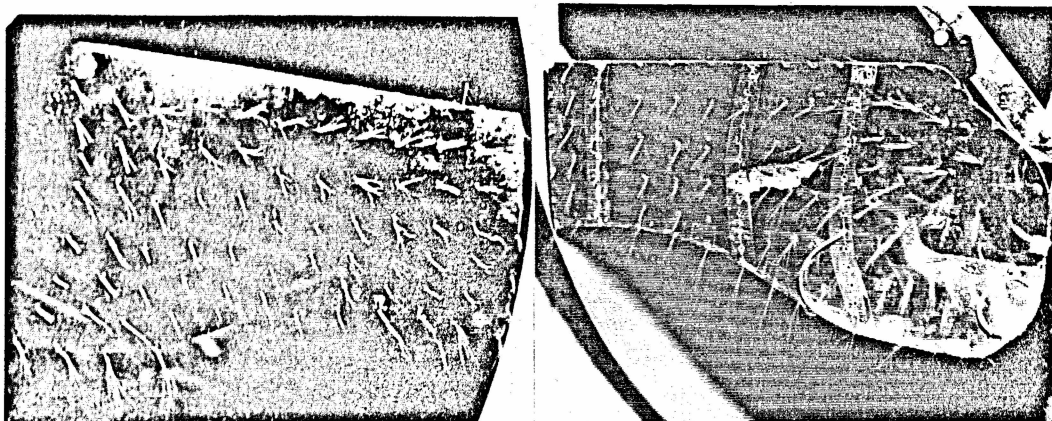


Figure F.28 Surface flow at 2972 cfm on suction side (left) and 2940 cfm on pressure side (right) for 850 rpm test data

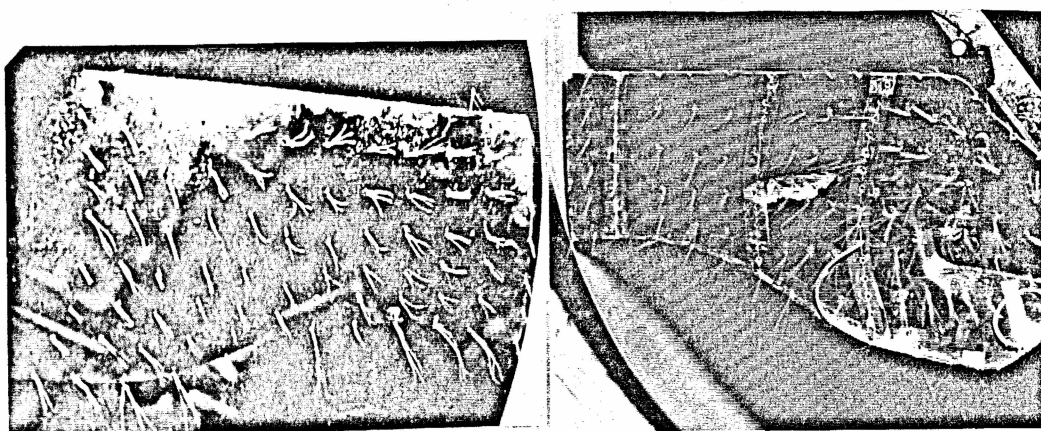


Figure F.29 Surface flow at 0 cfm on suction side (left) and 0 cfm on pressure side (right) for 850 rpm test data

APPENDIX G

UNSTEADY BLADE SURFACE PRESSURE DIFFERENCE MEASUREMENTS

The six figures included in this appendix provide a record of the raw pressure difference data and the corrected data for the three radial positions where pressure difference measurements were made (position A at $R = 15.68$ in., position B at $R = 10.87$ in. and position C at $R = 7.67$ in.).

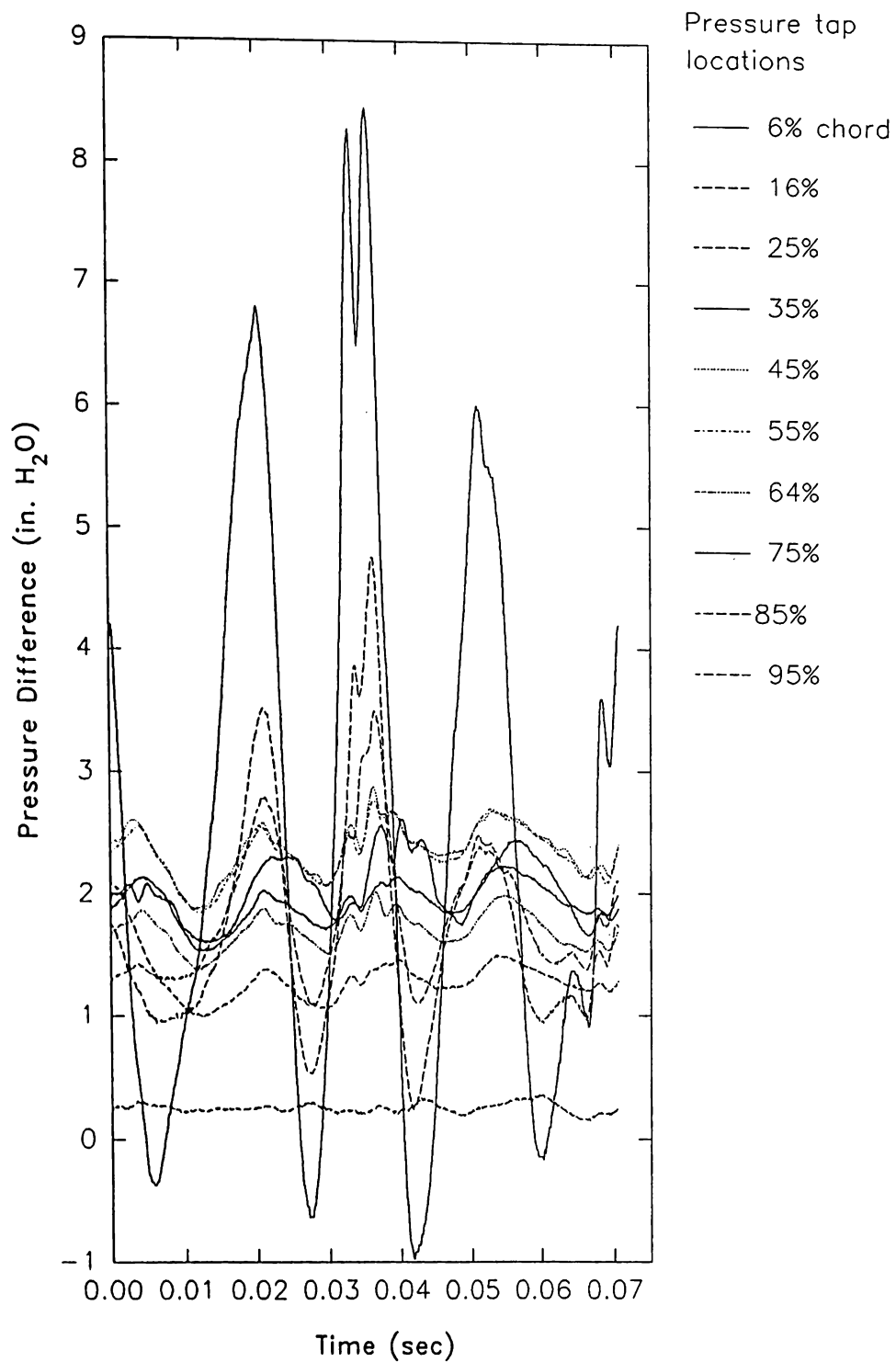


Figure G.1 Uncorrected, "raw", unsteady pressure difference measurements at position A ($R = 15.68$ in.)

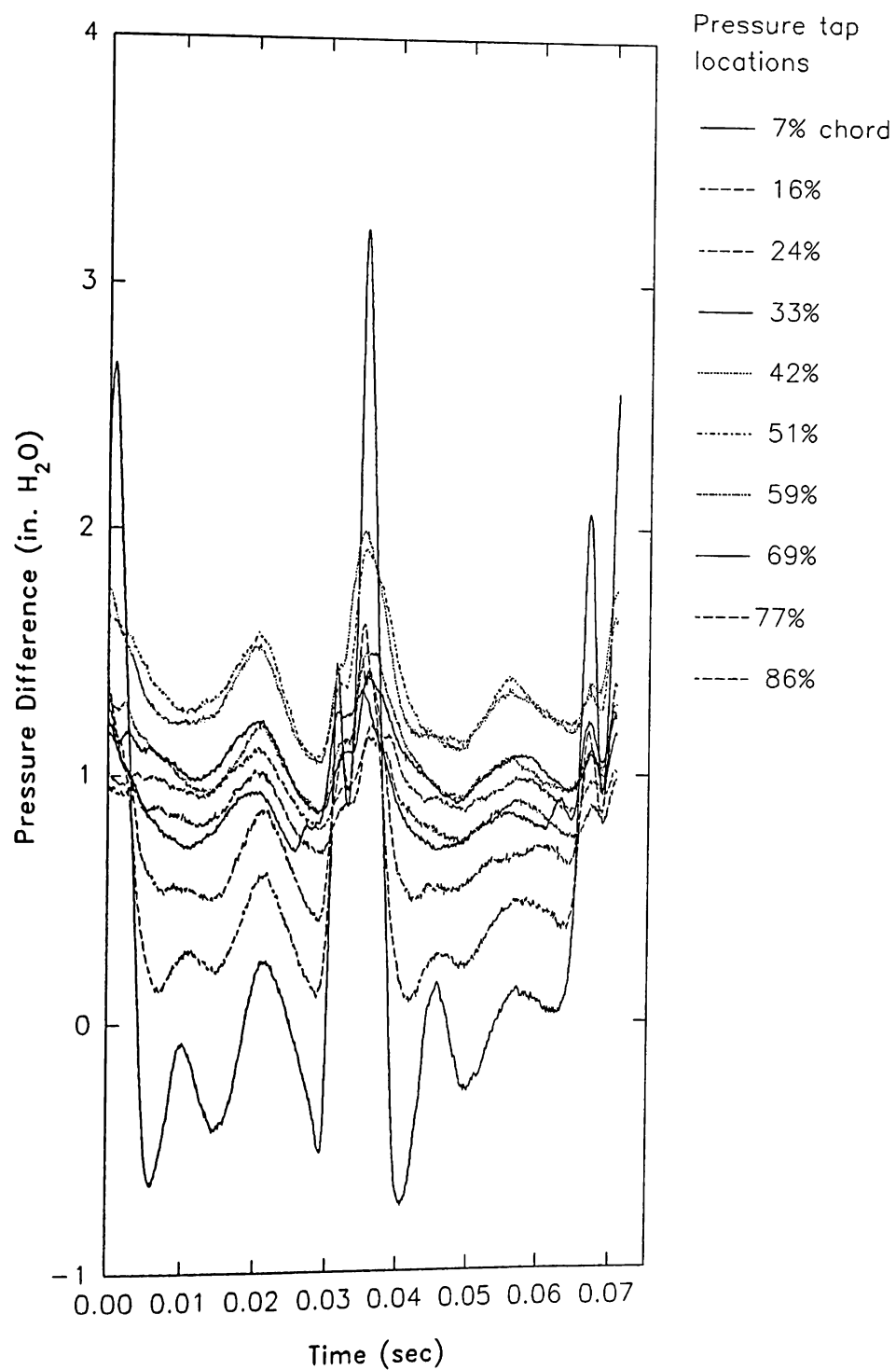


Figure G.2 Uncorrected, "raw", unsteady pressure difference measurements at position B ($R = 10.87$ in.)

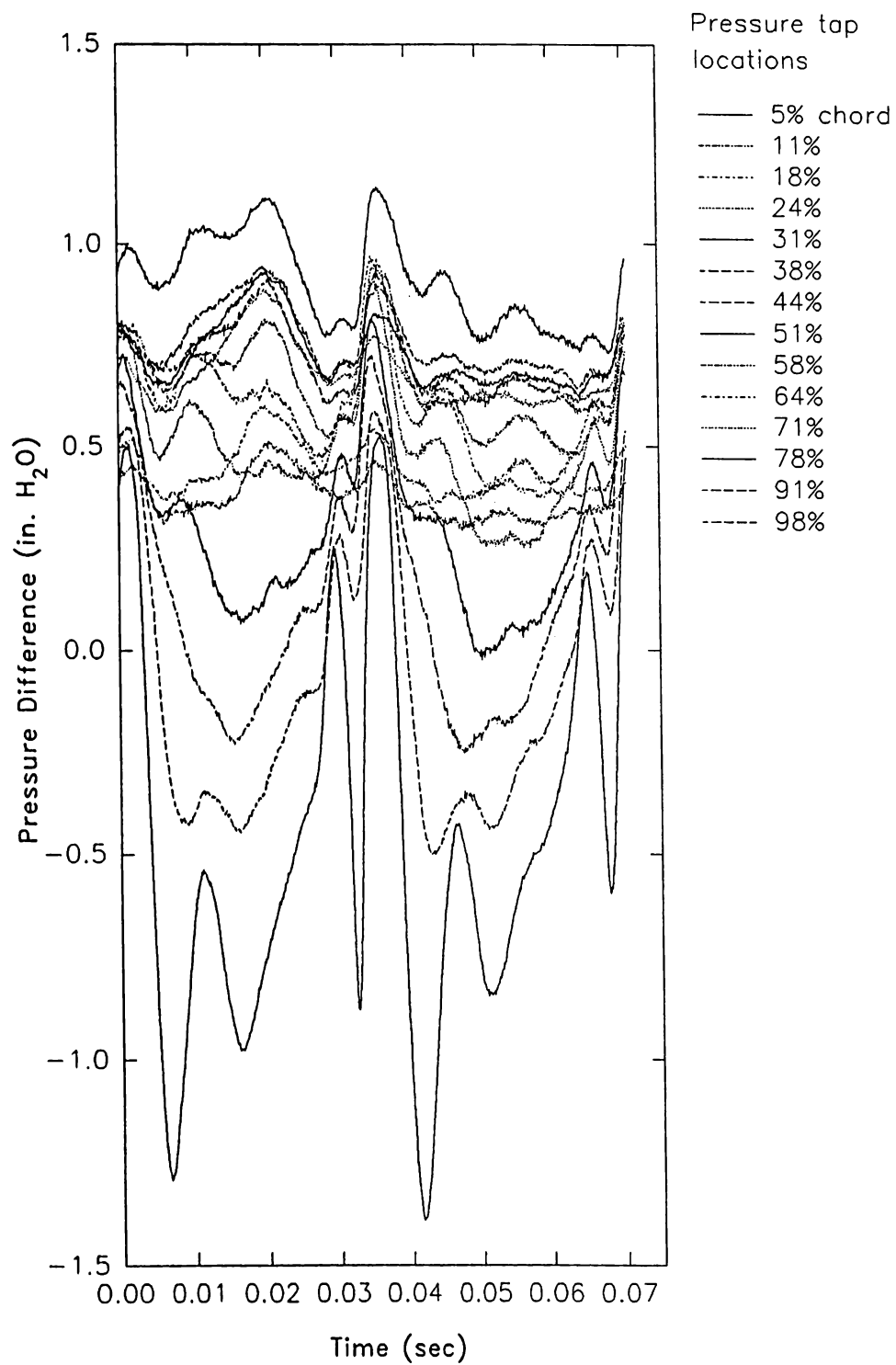


Figure G.3 Uncorrected, "raw", unsteady pressure difference measurements at position C ($R = 7.67$ in.)

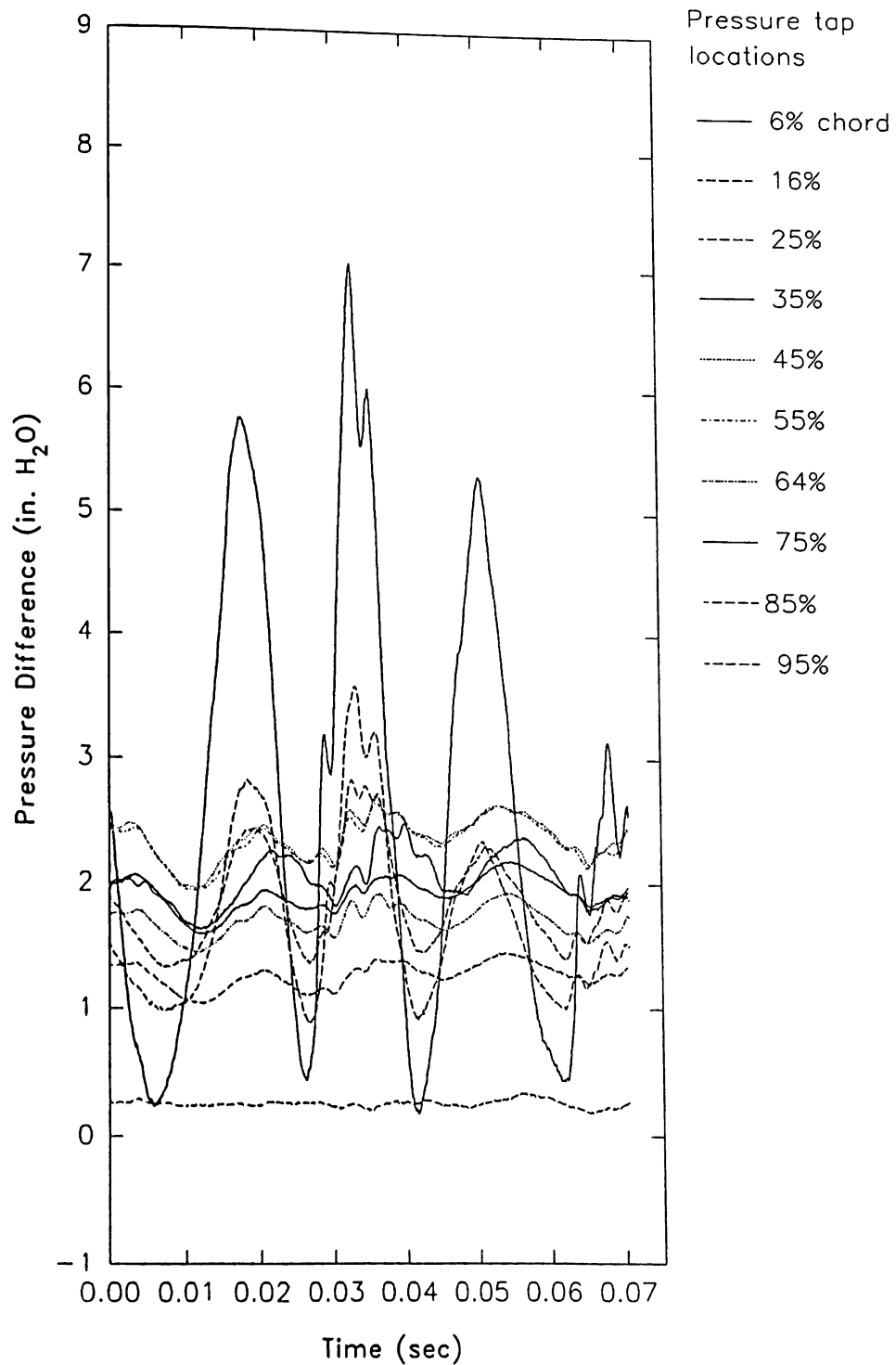


Figure G.4 Unsteady pressure difference measurements at position A ($R = 15.68$ in.) corrected for tubing dynamic response

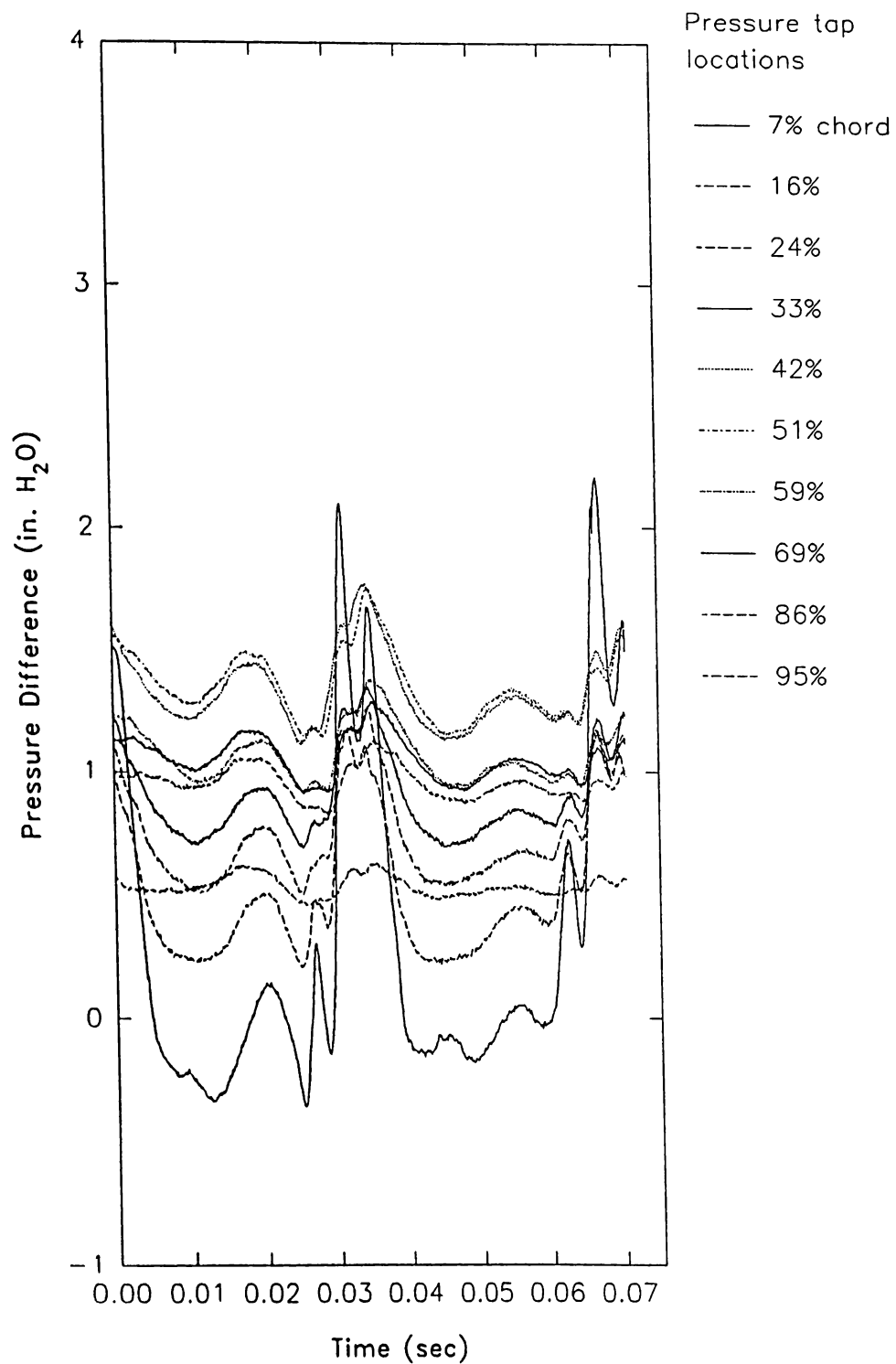


Figure G.5 Unsteady pressure difference measurements at position B ($R = 10.87$ in.) corrected for tubing dynamic response

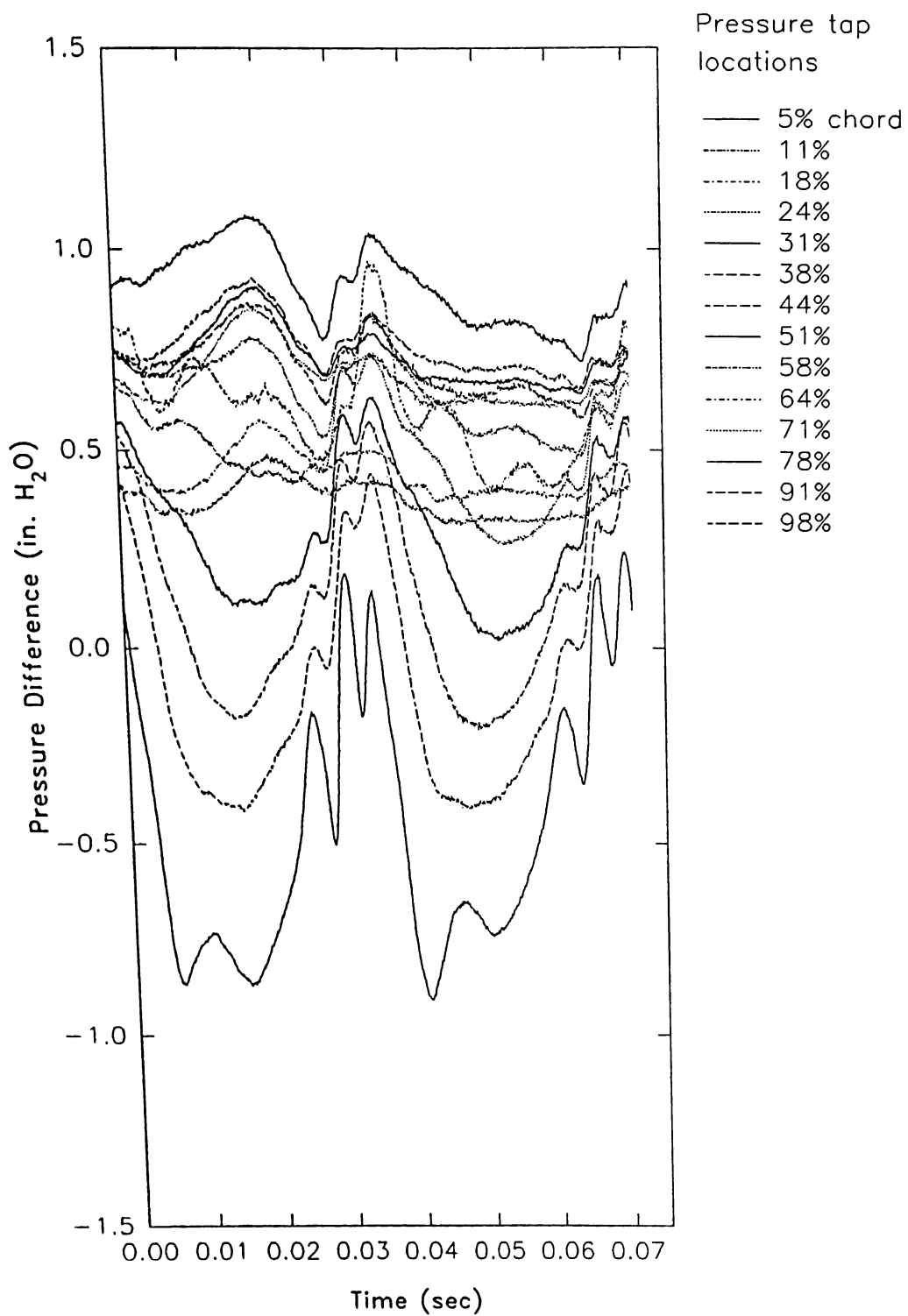


Figure G.6 Unsteady pressure difference measurements at position C ($R = 7.67$ in.) corrected for tubing dynamic response

REFERENCES

- Adrian, R. J., 1989, "Applications Particle Image Velocimetry," *Flow Visualization- 1989*, Winter Annual Meeting of the ASME, San Francisco, pp. 23-28.
- Ahmed, S. R., 1983, "Influence of Base Slant on the Wake Structure and Drag of Road Vehicles," *ASME Journal of Fluids Engineering*, Vol. 105, pp. 429-434.
- Akiyama, M., Suzuki, M., and Nishiwaki, I., 1979, " Transport Phenomena of Ventilating Flows in a Rectangular Room," *Flow Visualization*, Hemisphere, pp. 135-141.
- AMCA, 1985, *Laboratory Methods of Testing Fans for Rating*, ANSI/AMCA Standard 210-85, ANSI/ASHRAE Standard 51-1985, Air Movement and Control Association Inc. and the American Society of Heating, Refrigerating and Air-Conditioning Engineers.
- Anderson, J.D., 1984, *Fundamentals of Aerodynamics*, McGraw-Hill.
- Andrews, A.E., 1988, "Progress and Challenges in the Application of Artificial Intelligence to Computational Fluid Dynamics," *AIAA Journal*, Vol. 25, pp. 39-46.
- Arakawa, C., and Tagori, T., 1982, " Fundamental Experiments of Oil Films on a Rotating Disk," *Flow Visualization II*, Hemisphere,, pp. 127-131.
- Arieli, R., Tauber, M.E., Saunders, D.A., and Caughey, D.A., 1986, "Computation of Transonic Flow About Helicopter Rotor Blades," *AIAA Journal*, Vol.24, No.5, pp. 722-727.
- Atraghji, E., 1982, " More Than Meets the Eye: The Oil Dot Technique," *Flow Visualization II*, Hemisphere, Washington D. C., pp. 619-628.
- Baskin, V.E., Vil'dgrube. L.S., Vozhdayev, Y.S., and Maykapar, G.I., 1976, *Theory of the Lifting Airscrew*, NASA TT F-823.
- Bass, R.M., 1987, "Factors Influencing the Aerodynamic Design of Low Pressure Axial Fans," IMechE Seminar on *Industrial Fans- Aerodynamic Design*, pp. 1-6.
- Behr, R., and Wagner, S., 1988, "Ein Nichtlineares Wirbelgitterverfahren zur Berechnung von Interferenzeffekten zwischen Freien Wirbelschichten und Tragflächen," DGLR Fach Symposium-Strömungen mit Ablösung, Braunschweig, pp. 169-180.

- Betz, A., 1919, "Schraubenpropeller mit geringstem Energieverlust," *Nachrichten von der Königlichen Gesellschaft der Wissenschaften zu Göttingen, Math.-Phys. Klasse*, 2, p.193.
- Bell, J.H., and McLachlan, B.G, 1993, "Image Registration for Luminescent Paint Sensors," *AIAA Paper 93-0178*, 31st Aerospace Sciences Meeting, Reno, NV.
- Binder, R.C., 1958, *Advanced Fluid Mechanics*, Vol. 1, Prentice-Hall, p. 264.
- Blaho, M., 1975, "Optimum Design of Axial Flow Fans with Cambered Blades of Constant Thickness," *Period. Polytech. -Mech. Engng.*, Vol. 19, No. 2, pp. 79-89.
- Bradshaw, Peter, 1970, *Experimental Fluid Mechanics*, 2nd edition, Pergamon Press, pp. 144-179.
- Brand, A., Komerath, N., and McMahon, H., 1989, "Results from Laser Sheet Visualization of a Periodic Rotor Wake," *Journal of Aircraft*, Vol. 26, No. 5, pp. 438-443.
- Brockett, T., 1966, "Minimum Pressure Envelope for Modified NACA-66 Sections with NACA $a=0.8$ Camber and Buships Type I and Type II Sections," DTNSRDC Report.
- Brown, N.A., 1977, "The Use of Skewed Blades for Ship Propellers and Truck Fans," *Noise and Fluids Engineering*, R. Hickling, Ed., pp. 201-207.
- Brownell, R.B., Flack, R.D., Davis, M.C., and Rice J.G., 1987, "Flow Visualization in a Laboratory Vaned Diffuser," *International Journal of Heat and Fluid Flow*, Vol. 8, No. 1, pp. 37-43.
- Burmeister, L., and Amadian, M., 1988, *Preliminary Report to Lenexa Products*.
- Caglar, Saban, 1988, "Über die Auslegung von Axialventilatoren," *Strömungsmechanik und Strömungsmaschinen*, Vol. 39, pp. 7-12.
- Caradonna, F.X., 1990, "The Application of CFD to Rotary Wing Flow Problems," *AGARD Report No. 781 Aerodynamics of Rotorcraft*, pp. 5-1,5-38.
- Casale, G., Onorato, M., Quagliotti, F., and Savorelli, P., 1985, "Flow Visualization Methods for Vortical Flow Studies," *Flow Visualization III*, Hemisphere, pp. 397-401.
- Chen, C. J., and Emrich, R. J., 1963, "Investigation of the Shock Tube Boundary Layer by a Tracer Method", *The Physics of Fluids*, Vol. 6, No. 1, pp. 1-9.

Cheung, R.S.W., 1987, *Numerical Prediction of Propeller Performance by Vortex Lattice Method*, Ph. D. Thesis, Toronto University, UTIAS Technical Note No. 265.

Clark, D.H., and Leiper, A.C., 1970, "Free Wake Analysis A Method for the Prediction of Helicopter Rotor Hovering Performance," *Journal of the American Helicopter Society*, Vol. 15, No. 1, pp. 3-11.

Clark, R., 1985, "A New Iterative Matrix Solution Procedure for Three-Dimensional Panel Methods," *Proceedings of the 23rd Aerospace Sciences Meeting*, AIAA, Reno, Nevada.

Colladay, R.S., and Russell, R.M., 1976, "Streakline Flow Visualization of Discrete Hole Film Cooling for Gas Turbine Applications," *ASME Journal of Heat Transfer*, Vol. 98, pp. 245-250.

Crimi, P., 1965, *Theoretical Prediction of the Flow in the Wake of a Helicopter Rotor*, Cornell Aero. Lab. Report No. BB-1994-S-1, September.

Crowder, J.P., 1982a, "In-Flight Propeller Flow Visualization Using Fluorescent Minitufts," *Flow Visualization and Laser Velocimetry for Wind Tunnels*, NASA-CP-2243, pp. 91-95.

Crowder, J.P., 1982b, "Fluorescent Minitufts for Nonintrusive Surface Flow Visualization," *Flow Visualization II*, Hemisphere, pp. 663-667.

Crowder, J.P., 1985, "Fluorescent Minitufts for Flow Visualization on Rotating Surfaces," *Flow Visualization III*, Hemisphere, Washington D. C., pp. 55-59.

Daws, L.F., 1967, "Movement of Air Streams Indoors," *Building Research Station Research Paper 66*, Building Research Station, Garston, Watford, Hertsfordshire U.K.

Dhaubhadel, M.N., Akay, H.U., and Charles, H.N., 1988, "Three-Dimensional Finite Element Analysis for Aerodynamic Design of Fan Blades," *AIAA Paper 88-3641-CP*.

Douglas, J., and Gunn, J. E., 1964, "A General Formulation of Alternating Direction Methods- Part I. Parabolic and Hyperbolic Problems," *Numerische Mathematik*, Vol. 6, pp. 428-453.

Dragos, L., and Dinu, A., 1990, "Application of the Boundary Element Method to the Thin Airfoil Theory," *AIAA Journal*, Vol. 28, pp. 1822-1824.

Egolf, T.A., and Sparks, S.P., 1987, "A Full Potential Flow Analysis with Realistic Wake Influence for Helicopter Rotor Airload Prediction," NASA CR-4007.

Eichorn, R., 1959, *An Analytical Investigation of Combined Free and Forced Convection and a New Method to Measure Free Convection Velocity Profiles*, Ph.D. Thesis, University of Minnesota.

Emrich, R. J., 1983, "Flow Field Measurement by Tracer Photography," *Experiments in Fluids*, Vol. 1, pp. 179-184.

Fingerson, L.M., and Freymuth, P., 1983, "Thermal Anemometers," *Fluid Mechanics Measurements*, R. J. Goldstein editor, Hemisphere, p. 118.

Forman, G.W., and Kelly N.W., 1961, "Cooling Tower Fans Performance," *Transactions of the ASME, Journal of Engineering for Power*, April, pp. 155-160.

Franke, G., 1978, *Investigation of the Unsteady Pressure Distribution on the Blades of an Axial Flow Fan*, M.S. Thesis, Pennsylvania State University, Applied Research Lab Report No. ARL/PSU/TM-78-300.

Fratello, G.F., Favier, D.F., and Maresca, C.M., 1991, "Experimental and Numerical Study of the Propeller/Fixed Wing Interaction," *Journal of Aircraft*, Vol. 28, No. 6, pp. 365-373.

Freymuth, P., Bank, W. and Palmer, M., 1985, "Use of Titanium Tetrachloride for Visualization of Accelerating Flow Around Airfoils," *Flow Visualization III*, Hemisphere, pp. 99-105.

Gilmore, D.C., and Gartshore, I.S., 1972, "The Development of an Efficient Hovering Propeller/Rotor Performance Prediction Method," *AGARD-CP-111 Aerodynamics for Rotary Wings*, Fluid Dynamics Panel Specialists Meeting, Marseilles, France.

Glauert, H., 1926, *The Elements of Aerofoil and Airscrew Theory*, Cambridge University Press, London, p. 208.

Glauert, H., 1959, *The Elements of Aerofoil and Airscrew Theory*, Cambridge.

Goldstein, S., 1929, "On the Vortex Theory of Screw Propellers," *Proceedings of the Royal Society of London, Series A*, Vol. 123.

Graber, A., and Rosen, A., 1987, "Velocities Induced by Semi-Infinite Helical Vortex Filaments," *Journal of Aircraft*, Vol. 24, No. 5, pp. 289-290.

Gray, R.B., 1992, "Vortex Modeling for Rotor Aerodynamics- The 1991 Alexander A. Nikolsky Lecture," *Journal of the American Helicopter Society*, Vol. 37, No. 1, pp. 3-14.

Gray, R.B., and Brown, G.W., 1972, "A Vortex Wake Analysis of a Single Bladed Hovering Rotor and a Comparison with Experimental Data," *AGARD-CP-111 Aerodynamics for Rotary Wings*, Fluid Dynamics Panel Specialists Meeting, Marseilles, France.

Greeley, D.S., 1982, *Marine Propeller Blade Tip Flows*, M.I.T. Department of Ocean Engineering Report 82-3, Cambridge, MA.

Greeley, D.S., and Kerwin, J.E., 1982, "Numerical Methods for Propeller Design and Analysis in Steady Flow," *Transactions of the SNAME*, Vol. 90.

Hanson, D. B., 1982, "Compressible Lifting Surface Theory for Propeller Performance Calculation," *AIAA Paper No. 82-0020*.

Hanson, D.B., 1983, "Compressible Helicoidal Surface Theory for Propeller Noise and Aerodynamics," *AIAA Journal*, Vol. 21, No. 6, pp. 881-889.

Hardin, R.A., 1988, *Flow Visualization Techniques for a Convection Oven*, M.S. Thesis, University of Kansas.

Hawthorne, W.R., and Horlock, J.H., 1962, "Actuator Disc Theory of the Incompressible Flow in Axial Compressors," *Proceedings of the Institution of Mechanical Engineers*, IMechE, Vol. 176, No. 30, pp. 789-814.

Hay, N., Mather, J., and Metcalfe, S., 1987, "Fan Blade Selection for Low Noise," IMechE Seminar on *Industrial Fans- Aerodynamic Design*, pp. 51-57.

Harvald, S.A., 1983, *Resistance and Propulsion of Ships*, John-Wiley & Sons.

Hay, N., Metcalf, R., 1978, "A Simple Method for the Selection of Axial Fan Blade Profiles," *Proceedings of the Institution of Mechanical Engineers*, IMechE, Vol. 192, pp. 269-275.

Heidelberg, L., 1992, Private Communication, NASA-Lewis, (216) 433-3859.

Hess, J.L., 1974, "The Problem of Three-Dimensional Lifting Potential Flow and Its Solution by Means of Surface Singularity Distribution," *Computer Methods in Applied Mechanics and Engineering*, Vol. 4, pp. 283-319.

Hess, J.L., 1975, "The Use of Higher-Order Surface Singularity Distributions to

Obtain Improved Potential Flow Solutions for Two-Dimensional Lifting Airfoils ,"
Computer Methods in Applied Mechanics and Engineering, Vol. 5, Jan., pp. 11-33.

Hess, J.L., and Valarezo, W.O., 1985, "Calculation of Steady Flow About Propellers using a Surface Panel Method," *AIAA Journal of Propulsion*, Vol. 1, pp. 470-476.

Hewlett-Packard, 1991, *Programmer's Guide-HP 54600A-54601A Oscilloscopes*, Publication 54600-90909, Hewlett-Packard Company.

Hinze, J.O., 1975, Turbulence, 2nd edition, McGraw-Hill.

Hoerner, S.F., 1965, *Fluid Dynamic Drag*, published by author.

Homicz, G.F., Lordi, J.A., Ludwig, G.R., 1979, *Aerodynamic and Acoustic Investigations of Axial Flow Fan and Compressor Blade Rows, Including Three-Dimensional Effects*, Final report Air Force Aero Propulsion Lab., AFAPL-TR-79-2061, Calspan Advanced Technology Center, Buffalo, NY.

Hough, G.R., 1973, "Remarks on Vortex-Lattice Methods," *Journal of Aircraft*, Vol. 10, No. 5.

Howarth, A.T., Morton, A.S., and Sherratt, A.F.C., 1972, "A New Method of Comfort Heating with Warm Air," *Heat and Mass Transfer by Combined Forced and Natural Convection: A Symposium Arranged by the Thermodynamics and Fluid Mechanics Group of the Institution of Mechanical Engineers*, The Institution of Mechanical Engineers, London, pp. 54-62.

Hsieh, C.K., 1977, "The Natural Convection of Air Over a Heated Plate with Forward Facing Step," *ASME Journal of Heat Transfer*, Vol. 99, pp. 439-442.

Hughes, M.J., Kinnas, S.A., and Kerwin, J.E., 1992, "Experimental Validation of a Ducted Propeller Analysis Method," *Journal of Fluids Engineering*, Vol. 114, June, pp. 214-219.

Iberall, A.S., 1950, "Attenuation of Oscillatory Pressures in Instrument Lines," *Journal of Research*, National Bureau of Standards, Vol. 45, July, Research Paper 2115.

Jackson, T.W., and Lilley, D.G., 1986, "Accuracy and Directional Sensitivity of the Single-Wire Technique," *AIAA Journal*, , Vol. 24, No. 3, pp. 451-458.

James, R.M., 1972, "On the Remarkable Accuracy of the Vortex Lattice Method,"

Computer Methods in Applied Mechanics and Engineering, Vol. 1.

Jameson, A. and Caughey, D.A., 1977, "Numerical Calculation of Transonic Flow Past a Swept Wing," Courant Institute of Mathematical Sciences, New York University, New York, C00-7077-140, June 1977.

Javur, M.M., Murthy, K.S., and Kar, S., 1982, "The Introduction of Leading Edge Slats to Improve the Off-Design Performance of Axial Flow Fans," *Papers presented at the International Conference on Fan Design and Applications*, BHRA Fluid Engineering, Guilford, England, pp.281-294.

Johnsen, I.A., and Bullock, R.O.(Eds.), 1965, *Aerodynamic Design of Axial Flow Compressors*, NASA SP-36, National Aeronautics and Space Administration.

Johnson, W., 1986, "Recent Developments in Rotary-Wing Aerodynamic Theory," *AIAA Journal*, Vol. 24, No. 8, pp. 1219-1244.

Jun, Wei, and Fangyuan, Zhong, 1988, "The Effect of Forward Skewed Rotor Blades on the Aerodynamic and Aeroacoustic Performance of Axial-Flow Fans," *AIAA Paper 88-3783-CP*.

Kahaner, D., Moler, C., and Nash, S., 1989, *Numerical Methods and Software*, Prentice Hall.

Kent, J.C., and Eaton, A.R., 1982, "Stereo Photography of Neutrally Density He-Filled Bubbles for 3-D Fluid Motion Studies in an Engine Cylinder," *Applied Optics*, Vol. 21, No. 5, pp. 904-912.

Kerwin, J.E., and Lee, C.S., 1978, "Prediction of Steady and Unsteady Marine Propeller Performance by a Numerical Lifting-Surface Theory," *SNAME Transactions*, Vol. 86, pp. 218-253.

Kerwin, J.E, Kinnas, S.A., Lee, J.T., and Shih, W.Z., 1987, "A Surface Panel Method for the Hydrodynamic Analysis of Ducted Propellers," *Transactions of the SNAME*, Vol. 95.

Kerwin, J.E., 1986, *13.04 Lecture Notes- Hydrofoils and Propellers*.

Kerwin, J.E, 1988, Private Communication, Department of Ocean Engineering, Massachusetts Institute of Technology, 77 Massachusetts Ave., Cambridge, Massachusetts 72139, (617) 253-5139.

Kerwin, J.E., 1989, "Marine Propellers," *Annual Review of Fluid Mechanics*, Vol. 18, pp. 367-403.

- Khalighi, B., 1989, "Study of the Intake Swirl Process in an Engine Using Flow Visualization and Particle Tracking Velocimetry," *Flow Visualization- 1989*, Winter Annual Meeting of the ASME, San Francisco, pp. 37-47.
- Khalighi, B., Braun, M. J., and Freitas, C. J., 1991, *Experimental and Numerical Flow Visualization FED-Vol. 128*, Winter Annual Meeting of the ASME, Atlanta, Georgia.
- Kim, K., and Kobayashi, S., 1984, "Pressure Distribution on Propeller Blade Surface Using Numerical Lifting -Surface Theory," *Proceeding of the SNAME Symposium- Propellers 84*, Virginia Beach, Virginia.
- Kimura, T., and Nishio, N., 1989, "New Method for Measurement of Surface Pressure Using Magnetic Tape," *AIAA Journal*, Vol.27, No.11, pp. 1579-1583.
- Kinnas, S.A., and Coney, W.B., 1988, " On the Optimum Ducted Propeller Loading," *SNAME Symposium- Propellers 88*.
- Kinnas, S.A., 1991, Private Communication, Department of Ocean Engineering, Massachusetts Institute of Technology, Room 5-221, 77 Massachusetts Ave., Cambridge, Massachusetts 72139, -
(617) 253-5990.
- Kinnas, S.A., and Hsin, C., 1992, "Boundary Element Method for the Analysis of the Unsteady Flow Around Extreme Propeller Geometries," *AIAA Journal*, Vol.30, No.3, pp. 688-696.
- Kobayakawa, M., and Onuma, H., 1985, "Propeller Aerodynamic Performance by Vortex-Lattice Method," *Journal of Aircraft*, Vol. 22, No. 8, pp. 649-654.
- Kocurek, J.D., and Tangler, J.L., 1977, "A Prescribed Wake Lifting Surface Hover Performance Analysis," *Journal of the American Helicopter Society*, Vol. 22, No., 1, January, p. 24-35.
- Kodak, 1989, *KODAK T-MAX Professional Films*, KODAK Publication No. F-32.
- Kumar, R., Conover, T., and Pan, Y., 1993, "Three-Dimensional Turbulent Swirling Flow in a Cylinder: PTV Experiments and Computations," *FED-Vol. 161, Fluid Measurement and Instrumentation Forum*, Gore, Morrow, and Jones eds., pp. 107-112.
- Küssner, H.G., 1940, "General Lifting Surface Theory", *Luftfahrtforschung*, Vol. 11, No. 11/12.

Lakshminarayana, B., 1970, "Method of Predicting the Tip Clearance Effects in Axial Flow Turbomachinery," *Trans. ASME*, Sept., pp. 476-482.

Lamb, H., 1945, *Hydrodynamics*, Dover.

Landgrebe, A.J., 1969, "An Analytical Method for Predicting Rotor Wake Geometry," *Journal of the American Helicopter Society*, October, pp.20-32.

Landgrebe, A.J., 1972, "The Wake Geometry of a Hovering Helicopter Rotor and Its Influence on Rotor Performance," *Journal of the American Helicopter Society*, October, pp.3-15.

Langrebe, A.J., and Cheney, M.C., 1972, "Rotor Wakes- Key to Performance Prediction," *AGARD-CP-111 Aerodynamics for Rotary Wings*, Fluid Dynamics Panel Specialists Meeting, Marseilles, France.

Lan, C.E., 1974, "A Quasi-Vortex Lattice Method in Thin Wing Theory," *Journal of Aircraft*, Vol. 11, pp.518-527.

Lan, C.E., 1988, *Applied Wing and Airfoil Theory*, Cheng Chung Book Company, Taipei.

Lee, C.S., 1979, *Prediction of Steady and Unsteady Performance of Marine Propellers with or without Cavitation by Numerical Lifting-Surface Theory*, PhD. thesis, Massachusetts Institute of Technology.

Leinbach, H., and Schmid, H., 1988, *Einführung in das Grafikpaket PICASSO*, RUS-Regionales Rechenzentrum der Universität Stuttgart.

Lewis, R.I., 1991, *Vortex Element Methods for Fluid Dynamic Analysis of Engineering Systems*, Cambridge University Press, Cambridge.

Loukakis, T.A., 1971, *A New Theory for the Wake of Marine Propellers*, MIT Department of Ocean Engineering Report 71-1, Cambridge, Mass., May.

Magness, C., Utsch, T., and Rockwell, D., 1990, "Flow Visualization via Laser-Induced Reflection from Bubble Sheets," *AIAA Journal*, Vol. 28, No. 7, pp. 1199-1200.

Maltby, R. L., Keating, R. F. A., 1962, "Smoke Techniques for Use in Low Speed Wind Tunnels," *Flow Visualization in Wind Tunnels Using Indicators* (compiled by R. L. Maltby), AGARDograph No. 70, pp. 87-109.

Maltby, R. L., and Keating, R.F.A., 1962, "The Surface Oil Flow Technique for

- use in Low Speed Wind Tunnel Tests, " *Flow Visualization in Wind Tunnels Using Indicators* (compiled by R. L. Maltby), AGARDograph No. 70, pp. 29-38.
- Maser, J.G., Fertis, D.G., Aiello, R.A., and Chamis, C.C., 1990, "Parametric Studies of Advanced Turboprops," *Journal of Propulsion*, Vol. 6, No. 1, pp.58-62.
- Masquelier, M.L., 1982, *Application of the Vortex-Lattice Method to Propeller Performance Analysis*, M.S. Thesis, Air Force Institute of Technology.
- Maskew, B., 1982, "Prediction of Subsonic Aerodynamic Characteristics: A Case for Low-Order Panel Methods," *Journal of Aircraft*, Vol. 19, February, pp. 157-163.
- Matisse, P., and Gorman, M., 1984, "Neutrally Buoyant Anisotropic Particles for Flow Visualization," *Physics of Fluids*, Vol. 27, No. 4., pp. 759-760.
- McKenzie, A.B., 1987, "The Selection of Fan Blade Geometry for Optimum Efficiency," IMechE Seminar on *Industrial Fans- Aerodynamic Design*, pp. 45-50.
- McEwen, D., Wilson, G., and Neal, A.N., 1987, "The Design of a Mixed Flow Fan of Simple Blade Geometry ," IMechE Seminar on *Industrial Fans- Aerodynamic Design*, pp. 27-34.
- Mello, O.A.F., and Rand, O., 1991, "Unsteady, Frequency-Domain Analysis of Helicopter Non-Rotating Lifting Surfaces," *Journal of the American Helicopter Society*, April, pp. 70-81.
- Merzkirch, Wolfgang, 1987, *Flow Visualization*, 2nd edition, Academic Press, Orlando, Florida.
- Milgram, J. H., 1971, *Section Data for Thin Highly Cambered Airfoils in Incompressible Flow*, NASA CR-1767.
- Min, K.S., 1978, *Numerical and Experimental Methods for the Prediction of Field Point Velocities Around Propeller Blades*, MIT Department of Ocean Engineering Report 78-12, Cambridge, MA.
- Morino, L., and Kuo, C.C., 1974, "Subsonic Potential Aerodynamics for Complex Configurations: A General Theory," *AIAA Journal*, Vol. 12, No. 2, pp. 191-197.
- Morris, M.J., Dononvan, J.F., Kegelmann, J.T., Schwab, S.D., Levy, R.L., and Crites, R.C., 1993, "Aerodynamic Applications of Pressure Sensitive Paint," *AIAA Journal*, Vol. 31, No. 3, pp. 419-425.

- Mueller, T. J., 1985, "Recent Developments in Smoke Flow Visualization," *Flow Visualization III*, Hemisphere, pp. 30-40.
- Mueller, T. J., 1983, "Flow Visualization by Direct Injection," *Fluid Mechanics Measurements*, R. J. Goldstein editor, Hemisphere, pp. 307-375.
- Müller, R.H.G., 1990, "Special Vortices at a Helicopter Rotor Blade," *Journal of the American Helicopter Society*, October, pp. 16-22.
- Murai, H., Ihara, A., and Narasaka T., 1982, " Visual Investigation of Formation Process of Oil-Flow Pattern," *Flow Visualization II*, Hemisphere, pp. 629-633.
- Nagib, H. M., 1979, "Visualization of Turbulent and Complex Flows Using Controlled Sheets of Smoke Streaklines," *Flow Visualization*, Hemisphere, Washington D. C., pp.257-263.
- NASA SP-405, 1976, *Vortex Lattice Utilization*.
- van Niekerk, B., 1986, "Lifting Surface Theory for the Rest of Us," *AIAA/ASME/ASCE/AHS 27th Structures, Structural Dynamics, and Materials Conference*, Part 1, pp. 739-745.
- Obata, M., Miyao, S., Kurata, K., and Kusakari, K., 1979, " Visualization of Gas Flows in Natural Circulation Boilers," *Flow Visualization*, Hemisphere, pp. 189-194.
- Panton, R., 1984, *Incompressible Flow*, John Wiley and Sons.
- Payne, F. M., 1987, *The Structure of Leading Edge Vortex Flow Including Vortex Breakdown*, Ph.D. thesis, University of Notre Dame.
- Pelletier, D.H., and Schetz, J.A., 1985, "A Turbulence Model for Finite Element Simulation of 3-D Turbulent Flows Near Propellers and Windmills," *Numerical Methods in Laminar and Turbulent Flow, Part 2, Proceedings of the Fourth International Conference held at Swansea*, C. Taylor et al., Eds., pp. 1586-1598.
- Philbert, M., Beaupoil, R., Faléni, J.P., 1979, "Application d'un dispositif d'éclairage laminaire à la visualisation des écoulements aérodynamiques en soufflerie par émission de fumée," *La Recherche Aéronautique*, No. 1979-3, Mai-Juin.
- Pierzga, M. J., 1980, *Experimental Verification of the Streamline Curvature Numerical Analysis*, M.S. Thesis Pennsylvania State University.

- Polhamus, E. C., 1966, "A Concept of the Vortex Lift of Sharp-Edged Delta Wings Based on a Leading-Edge-Suction Analogy, " NASA TN D-3767.
- Polhamus, E. C., 1968, "Application of Leading-Edge-Suction Analogy of Vortex Lift to the Drag Due to Lift of Sharp-Edge Delta Wings," NASA TN D-4739.
- Pope, A., 1984, *Low-speed wind tunnel testing*, 2nd edition, Wiley.
- Portiero, J.L.F., Norton, D.J., and Pollock, T.C., 1985, " Space Shuttle Ice Prevention Studies," *Flow Visualization III*, Hemisphere, pp. 772-776.
- Rangwalla, A.A., and Wilson, L.N., 1987, "Application of a Panel Code to Unsteady Wing-Propeller Interference," *Journal of Aircraft*, Vol. 24, No. 8, pp. 568-571.
- Rom, J., Almosnino, D., and Gordon, R., 1987, "High Angle of Attack Subsonic Non-linear Vortex Flow Calculations," *AIAA Paper 87-2275*.
- Rosen, A., and Graber, A., 1988, "Free Wake Model of Hovering Rotors Having Straight or Curved Blades," *Journal of the American Helicopter Society*, July, pp. 11-19.
- Sadler, G.S., 1971, " Development and Application of a Method for Predicting Rotor Free Wake Positions and resulting Rotor Blade Air Loads," NASA CR-1911.
- Sage Action Incorporated, 1973, *Operating Instructions for Helium Bubble Generator, Model 3*.
- SAI (Sage Action Incorporated), 1990, private communication with company representative Brad Ordway, phone (607) 844-8448.
- Sallam, T.M., Kaji, M., Nakanishi, S., and Ishigai, S., 1982, " Visualization of Recirculating Flows in Reversed-Flow Furnace Models," *Flow Visualization II*, Hemisphere, pp. 57-62.
- Sandborn, V.A., 1972, *Resistance Temperature Transducers*, Metrology Press, p. 189.
- Santanam, Chandran B., Tietbohl, Gregory L., 1985, "Complex Flow Visualization by a Unique Method," *Flow Visualization III*, Hemisphere, pp. 1-6.
- Schuder, C.B., and Binder, R.C., 1959, "The Response of Pneumatic Transmission Lines to Step Inputs," *Transactions of the ASME Journal of Basic Engineering*, December, pp. 578-584.

Scoles, J., and Ollerhead, J. B., 1981, *Experimental Study of the Effects of an Inlet Flow Conditioner on the Noise of an Axial Flow Fan*, Department of Transport Technology(UK), TT (Report) n. 8101.

Seddon, J., 1990, *Basic Helicopter Aerodynamics*, AIAA Inc.

Settles, G. S., and Teng, H.Y., 1983, " Flow Visualization Methods for Separated Three-Dimensional Shock Wave/Turbulent Boundary-Layer Interactions," *AIAA Journal*, Vol. 21, No. 3, pp. 390-397.

Settles, G.S., 1986, " Modern Developments in Flow Visualization," *AIAA Journal*, Vol. 24, No. 8, pp. 1313-1323.

Shi-cun, W., 1990, "Analytical Approach to the Induced Flow of a Helicopter Rotor in Vertical Descent," *Journal of the American Helicopter Society*, January, pp. 92-98.

Singleton, R.E., 1992, "CFD Joins the Army," *Aerospace America*, Vol. 30, No.2, pp. 22-26.

Smith, T.W., 1987, "A Practical Approach to the Design of Axial and Mixed Flow Fans," IMechE Seminar on *Industrial Fans- Aerodynamic Design*, pp. 7-12.

Snyder, A., 1987, "Numerical Simulation of Transonic Propeller Flow Using a Three-Dimensional Small Disturbance Code Employing Novel Helical Coordinates," *AIAA 87 -1162, AIAA 8th Computational Fluid Dynamics Conference*, pp.647-666.

Somerscales, E.F.C., 1981, "Tracer Methods," *Methods of Experimental Physics: Fluid Dynamics Part A*, R.J. Emrich editor, Academic Press, pp. 6-64.

Sonntag, R.E., and Van Wylen, G.J., 1985, *Fundamentals of Classical Thermodynamics*, 3rd ed., John Wiley and Sons, pp. 224-227.

Sparks, George W. and Ezekiel, Shaoul, 1977, "Laser Streak Velocimetry for Two-Dimensional Flows in Gases," *AIAA Journal*, Vol. 15, No. 1, pp. 110-113.

Squire, L.C., Maltby, R. L., Keating, R.F.A., and Stanbrook, A., 1962, " The Surface Oil Flow Technique, " *Flow Visualization in Wind Tunnels Using Indicators* (compiled by R. L. Maltby), AGARDograph No. 70, pp. 1-74.

Srinivasan, G.R., and McCroskey, W.J., 1988, "Navier-Stokes Simulations of Tip Vortices for Fixed and Rotating Helicopter Blades," *Computational Fluid Dynamics*, pp. 651-662.

Stanbrook, A., 1962, " The Surface Oil Flow Technique for use in High Speed Wind Tunnel Tests, " *Flow Visualization in Wind Tunnels Using Indicators* (compiled by R. L. Maltby), AGARDograph No. 70, pp. 39-74.

Stanislas, M., 1985, "Ultra High Speed Visualization of Unsteady Flows Using a Pulsed Ruby Laser," *Flow Visualization III*, Hemisphere, pp. 41-44.

Stastny, M., 1982, " Visualization of Some Phenomena Connected with Non-Potentiality of the Flow in Steam Turbines," *Flow Visualization II*, Hemisphere, pp. 147-152.

Stefko, G.L., Paulovich, F.J., Greissing, J.P., and Walker, E.D., 1982, "Propeller Flow Visualization Techniques," *Flow Visualization and Laser Velocimetry for Wind Tunnels*, NASA-CP-2243, pp.75-89.

Steinhoff, J. and Ramachandran, K., 1989, "A Vortex Embedding Method for Free Wake Analysis of Helicopter Rotor Blades in Hover," *Vertica*, Vol. 13, No. 2, pp. 133-141.

Steinhoff, J. and Ramachandran, K., 1990, "Free-Wake Analysis of Compressible Rotor Flows," *AIAA Journal*, Vol. 28, No. 3, pp. 426-431.

Stedman, D. H., Carignan, G. R., 1985, "Flow Visualization Using Ozone," *Flow Visualization III*, Hemisphere, pp. 87-92.

Stepniewski, W.Z., 1979, *Rotary Wing Aerodynamics*, NASA CR-3082.

Stinebring, D.R., and Treaster, A.L., 1985, " Water Tunnel Flow Visualization by the Use of Fluorescent Minitufts," *Flow Visualization III*, Hemisphere, pp. 65-70.

Strawn, R.C., and Caradonna, F.X., 1986, "Numerical Modeling of Rotor Flows with a Conservative Form of the Full-Potential Equation," *AIAA 24th Aerospace Sciences Meeting*, Reno, Nevada, January 6-9.

Sucker, D., Boenecke, H., 1982, "Practical Application of Fluid-Dynamic Models on Power and Process Engineering in the Iron and Steel Industry," *Flow Visualization II*, Hemisphere, pp. 185-192.

Sullivan, J.P., 1977, "The Effect of Blade Sweep on Propeller Performance," *AIAA Paper 77-716*.

Swarztrauber, P., 1975, *Efficient Subprograms for the Solution of Elliptic Partial Differential Equations*, Report TN/LA-109, National Center for Atmospheric Research, Boulder, Colorado.

- Tanner, L.H., 1982, " Surface Flow Visualization and Measurement by Oil Film Interferometry," *Flow Visualization II*, Hemisphere, pp. 613-617.
- Theodorsen, T., 1948, *Theory of Propellers*, McGraw-Hill.
- Tong, S. S., 1985, "Design of Aerodynamic Bodies Using Artificial Intelligence/Expert System Technique," *AIAA-85-0112*.
- Tsao, S.K., 1975, *Documentation of Programs for the Analysis of Performance and Spindle Torque of Controllable Pitch Propellers*, MIT, Department of Ocean Engineering Report 75-8, May.
- Vaczy, C.M., and McCormick, D.C., 1987, "A Study of the Leading Edge Vortex and Tip Vortex on Prop-Fan Blades," *ASME Journal of Turbomachinery*, Vol. 109, pp. 325-331.
- Valarezo, W., and Liebeck, R., 1988, "Three-Dimensional Calculation of Windmill Surface Pressures," *AIAA Paper No. 88-2533*.
- Valarezo, W., 1989, "On the Use of Proplets as a Means of Reducing Blade Compressibility Losses," *AIAA Paper No. 89-2213*.
- Valarezo, W., 1991, "Surface Panel Method for Installed Multiple Rotor Flows," *Journal of Aircraft*, Vol. 28, No. 8, pp. 496-501.
- Van Houten, R., 1986, *Analysis of Ducted Propeller in Steady Flow, Technical Report 4.76-1*, Airflow Research and Manufacturing Corp., Watertown, MA.
- Van Meel, D.A., and Vermij, H., 1961, "A Method for Flow Visualization and Measurement of Velocity Vectors in Three-Dimensional Flow Patterns in Water Models by Using Color Photography," *Applied Scientific Research*, Section A, No. 10, pp. 109-117.
- Vavra, M.H., 1974, *Aero-thermodynamics and Flow in Turbomachines*, R. E. Krieger Publishing Co.
- Wada, K., and Hayafuji, H., 1985, "Quantification of Downwash and Ground Vortex of a Lifting Rotor Model by Flow Visualization Technique," *Flow Visualization III*, Hemisphere, pp. 428-433.
- Walatka, P. P., and Buning, P. G., 1989, *PLOT3D User's Manual*, NASA TM-101067.
- Wallis, R.A., 1968a, "A Rationalised Approach to Blade Element Design, Axial

Flow Fans," Paper No. 2599, The Institution of Engineers, Australia, *Third Australian Conference on Hydraulics and Fluid Mechanics*.

Wallis, R.A., 1968b, "Optimisation of Axial Flow Fans Design," The Institution of Engineers, Australia, *Mechanical and Chemical Engineering Transactions*, May, pp. 31-36.

Wallis, R.A., 1972, "The Development of Blade Sections for Axial Flow Fans," The Institution of Engineers, Australia, *Mechanical and Chemical Engineering Transactions*, November, pp. 111-116.

Wallis, R.A., 1983, *Axial Flow Fans and Ducts*, John Wiley and Sons, New York.

Wang, Mo-Hwa, 1985, "Hub Effects in Propeller Design and Analysis," Technical Report No. 85-12, Department of Ocean Engineering, MIT.

Wei, J., and Zhong, F., 1988, "The Effect of Forward Skewed Rotor Blades on Aerodynamic and Aeroacoustic Performance of Axial-Flow Fans," *AIAA Paper 88-3783-CP, AIAA/ASME/SIAM/APS 1st National Fluid Dynamics Conference*, pp. 1983-1990.

White, F.M., 1974, *Viscous Fluid Flow*, McGraw Hill.

Whitfield, D.L., Swafford, T.W., Janus, J.M., Mulac, R.A., and Belk, D.M., 1987, "Three-Dimensional Unsteady Euler Solutions for Propfans and Counter-Rotating Propfans in Transonic Flow," *AIAA Paper 87-1197*.

Williams, M.H., and Hwang, C., 1986, "Three Dimensional Unsteady Aerodynamics and Aeroelastic Response of Advance Turboprops," *AIAA/ASME/ASCE/AHS 27th Structures, Structural Dynamics and Materials Conference*, San Antonio, Texas, pp. 116-124.

Wilson, J.C., 1987, "Accomplishments at NASA Langley Research Center in Rotorcraft Aerodynamics Technology", NASA CP-2495, pp. 7-33.

Wright, T., and Simmons, W.E., 1990, "Blade Sweep for Axial Flow Fans," *ASME Journal of Turbomachinery*, Vol. 112, pp. 151-158.

Wright, T., and Ralston, S., 1987, "Computer-Aided Design of Axial Flow Fans Using Small Computers," *ASHRAE Transactions*, Vol. 93, Part 2, pp. 282-294.

Yadav, R., and Singh, R.K., 1987, "Prediction of Flow Field in Impellers of Centrifugal Pumps," *Numerical Methods in Laminar and Turbulent Flow*, Vol. 5, Part 2, pp. 1977-1988.

Yamamoto, O., Barton, J.M., and Bober, L.J., 1986, "Improved Euler Analysis of Advanced Turboprop Propeller Flows," *AIAA Paper 86-1521*.

Yausa, H., and Ishii, N., 1982, "Leading-Edge Separating Vortex and Pressure Distributions on Propeller Blades," *Proceeding of the Second International Symposium on Flow Visualization*, Bochum, Germany, Sept. 1980, Hemisphere Publishing Corp., New York, pp. 256-260.

Yon, S., Katz, J., and Ashby, D.L., 1991, "Unsteady Fluid Dynamic Model for Propeller Induced Flow Fields," *AIAA Paper 91-1664, AIAA 22nd Fluid Dynamics, Plasma Dynamics, and Lasers Conference*.

Zimmer, H., 1972, "The Rotor in Axial Flow," *AGARD-CP-111 Aerodynamics for Rotary Wings*, Fluid Dynamics Panel Specialists Meeting, Marseilles, France.